

# **BULGARIAN CHEMICAL COMMUNICATIONS**

**2016** Volume 48 / Number 3

*Journal of the Chemical Institutes  
of the Bulgarian Academy of Sciences  
and of the Union of Chemists in Bulgaria*



## Mechanism of hydrogen transfer from 1-methylbutyl peroxide to hydroxyl radical

S. Q. Zhou\*, H. W. Kuai, Y. X. Gu, W. Zhou, A. P. Li

Faculty of Chemical Engineering, Huaiyin Institute of Technology, Huai'an, 223003, P. R. China

Received November 4, 2014, Accepted December 28, 2015

The density functional theory method was used to study the mechanism for the hydrogen transfer from 1-methylbutyl peroxide [ $n\text{-C}_3\text{H}_7\text{CH}(\text{CH}_3)\text{OOH}$ ] to hydroxyl radical. The B3LYP method was used in conjunction with the 6-311++G\*\* basis set. The geometrical configurations of reactants, products and transition states were fully optimized on the potential energy surfaces. The activation energies for the hydrogen transfer are in the range from 0.37 to 7.9 kJ/mol. The results suggest that the alkyl  $\beta\text{-H}$  is the easiest to transfer in view of both thermodynamics and kinetics. On the contrary, the  $\gamma\text{-H}$  transfer requires larger activation energy compared to  $\alpha\text{-}$  and  $\beta\text{-H}$ . All three types of hydrogen transfers become much easier in the presence of hydroxyl radical compared to the intramolecular hydrogen transfer, which is in good agreement with the experimental fact that the emulsification of diesel oil and water results in improved combustion properties.

**Keywords:** 1-Methylbutyl peroxide, Hydroxyl radical, Intermolecular hydrogen-atom transfer, Density functional theory.

### INTRODUCTION

The diesel engine is still one of the most fuel-efficient combustion engines at present [1-4]. Diesel emulsion is considered one of the possible alternative fuels for curtailing the emission pollution of combustion equipment such as diesel engines and large power boilers [5-8]. Emulsion fuels are defined as emulsions of water in fuel with the typical composition of 5–20% of water, surfactant and based fuel such as kerosene or diesel. It is consistently proven that emulsion fuels significantly lower emissions of hydrocarbons, carbon monoxide/dioxide and especially hazardous nitrous oxides and particulate matters [9-12].

Diesel oil primarily consists of hydrocarbons with  $n\text{-alkanes}$  being the dominant components. It converts to self-ignited peroxides of hydrocarbons prior to complete combustion. The easiness of formation of hydrocarbon peroxides determines whether or not the engine is knocking. Of all types of peroxides, the di-peroxyl hydrocarbons have been believed to be the precursors of the final products carbon oxide and water. These di-peroxyl hydrocarbons are expected to play an important role in eliminating the diesel engine knocking. The key steps to produce di-peroxyl hydrocarbons are the intramolecular hydrogen-atom transfer reactions [13-16]. However, on the condition of water existing, the hydroxyl radical that is produced from water takes part in the process of the formation of di-peroxyl hydrocarbons (Fig. 1). Hydroxyl radical

assimilates a hydrogen atom from the mono-peroxyl hydrocarbon. The process yields the formation of a carbon radical. Once the products of alkyl radicals come into being, they are easy to further react with oxygen to produce di-peroxyl hydrocarbons. Here, 1-methylbutyl peroxide was used as the computational model of hydrocarbon peroxide.

The main objective of this work is to explore energies and mechanisms for the hydroxyl assimilating a hydrogen from 1-methylbutyl peroxide [synonym, 2-pentyl peroxide, chemical formula  $n\text{-C}_3\text{H}_7\text{CH}(\text{CH}_3)\text{OOH}$ ] as a computational model.

### COMPUTATIONAL METHODS

The molecular structures and energies of the reaction stationary points were calculated with the density functional theory (DFT) B3LYP technique [17-19]. Unrestricted wave function was employed for the open-shell systems. The geometries of all species (reactants, transition states and products) were optimized at the B3LYP/6-311++G\*\* level. The corresponding vibration frequencies were calculated at the same level. All located transition states exhibited one normal imaginary frequency with a transition vector corresponding to the motion of a H-atom during the intermolecular H-atom-transfer process. All calculations were performed with Gaussian 03 package of programs [20].

\* To whom all correspondence should be sent:  
E-mail: zhousuqin7803@sina.com

## RESULTS AND DISCUSSION

*Structures and geometries*

Fig. 2 shows the optimized geometries of the transition states. The imaginary frequencies of TS1, TS2, TS3 and TS4 are  $-446.16$ ,  $-257.60$ ,  $-823.85$  and  $-240.27$   $\text{cm}^{-1}$ , respectively. The vibrational normal modes of the four transition states correspond to the wagging of a hydrogen atom towards the hydroxyl radical. On going from the reactant to TS, one of the C–H bonds elongates toward the hydroxyl radical. The O $\cdots$ H lengths of partially formed water moiety in TS1, TS2, TS3 and TS4 are 1.412 Å, 1.460 Å, 1.333 Å and 1.444 Å, respectively. The lengths of the C–H bonds associated with the transfer of a H atom are 1.188 Å, 1.167 Å, 1.211 Å and 1.172 Å, for TS1, TS2, TS3 and TS4, respectively. The lengths of these C–H bonds are increased by about 10% compared to their corresponding C–H bond lengths in the reactants. The structure of TS2 differs more from that of its product than that of the other three TS. However, there is a six-membered ring with an intramolecular hydrogen bond in TS2, which attributes it with lower activation energy as discussed below.

*Change of energy*

The hydroxyl radical approaches the alkyl hydrogen atoms, resulting in the formation of TS1-TS4. Table 1 collects the total energies, zero point vibrational energies and relative energies at the B3LYP/6-311++G\*\* level. The relative energy, after being corrected for the zero point vibrational energy, refers to the corresponding reactant, i.e., the complex of 1-methylbutyl peroxide and hydroxyl radical. The relative energy is the energy barrier needed to be overcome during the intermolecular hydrogen transfer reaction. As can be seen from Table 1 and Fig. 3, for  $\alpha$ -H, the methylene hydrogen is energetically favorable to be transferred in comparison with methyl hydrogen. In other words, the  $\alpha$ -H transfer from methylene to hydroxyl results in the largest energy release. All four reactions are firstly endothermic to overcome the energy barrier from the reactants to the transition states. But these reactions are exothermic from the reactants to the products. The activation energy of 0.37 kJ/mol for reaction (2) is the lowest one, that is, the alkyl  $\beta$ -H is the easiest to transfer. The  $\beta$ -H transfer is a favorable process in view of both thermodynamics and kinetics. On the contrary, the reaction (4) of alkyl  $\gamma$ -H transfer requires the largest activation energy. Table 1 also lists the relative energies of the transition states for the

corresponding intrahydrogen transfers.  $\beta$ -H is the easiest to transfer in the process of intramolecular hydrogen transfer in comparison with  $\alpha$ -H and  $\gamma$ -H. Notably,  $\beta$ -H is also the easiest to transfer assisted by hydroxyl in comparison of  $\alpha$ -H and  $\gamma$ -H. However, all types of H transfer become much easier in the presence of hydroxyl radical. This finding can explain the fact that the combustion of diesel oil is accelerated by the addition of small amounts of water.

*Atomic Mulliken charge and spin density*

As can be seen from Table 2, the Mulliken charges on C<sub>3</sub>, C<sub>2</sub>, C<sub>5</sub> and C<sub>1</sub> atoms for TS1, TS2, TS3 and TS4, respectively, decrease (more negatively charged) in comparison with those of the reactant. However, their corresponding charges on C<sub>3</sub>, C<sub>2</sub>, C<sub>5</sub> and C<sub>1</sub> atoms increase on going from reactant to products. It is interesting to note that the C<sub>3</sub> and C<sub>2</sub> atoms, for P1 and P2, respectively, are positively charged with 0.3 a.u.; on the contrary, the C<sub>5</sub> and C<sub>1</sub> atoms, for P3 and P4, respectively, are negatively charged with  $-0.4$  a.u. This large difference of charges is due to the C<sub>5</sub> and C<sub>1</sub> atoms being at the end of the carbon chain. There are less hyper-conjugation effects between the single electron on the end carbon and its neighbor C-H bond. More electron charges (negative charges) are built up on O<sub>7</sub> on going from reactants to products. And much more electron charges (negative charges) are built up on O<sub>8</sub> on going from reactants to products.

The electrons on the transferred hydrogen atoms are attracted by the hydroxyl oxygen atom in the reaction process. On going from the reactants to their corresponding TS1-TS4, the Mulliken charges on the transferred H<sub>11</sub> atom increase dramatically, since its electrons are shared by both neighbor carbon and oxygen atoms. On going from the TS1-TS3 to their corresponding products P1-P3, the Mulliken charges on the transferred H<sub>11</sub> atom decrease just slightly. Although the electronegativity of oxygen is larger than that of carbon, the transferred H<sub>11</sub> atom is closer to carbon than to oxygen.

Table 3 lists the spin densities of hydroxyl atoms, transferred hydrogen atom and its neighbor carbon. The total spin density of hydroxyl for the reactant is 1.0 a.u. However, on going from reactant to TS1-TS4, the spin densities of hydroxyl oxygen atoms decrease by about 0.3 a.u., but those of the carbon atoms increase from near zero to 0.3-0.4 a.u. This indicates that a hydrogen atom is partially transferred from carbon to hydroxyl oxygen.

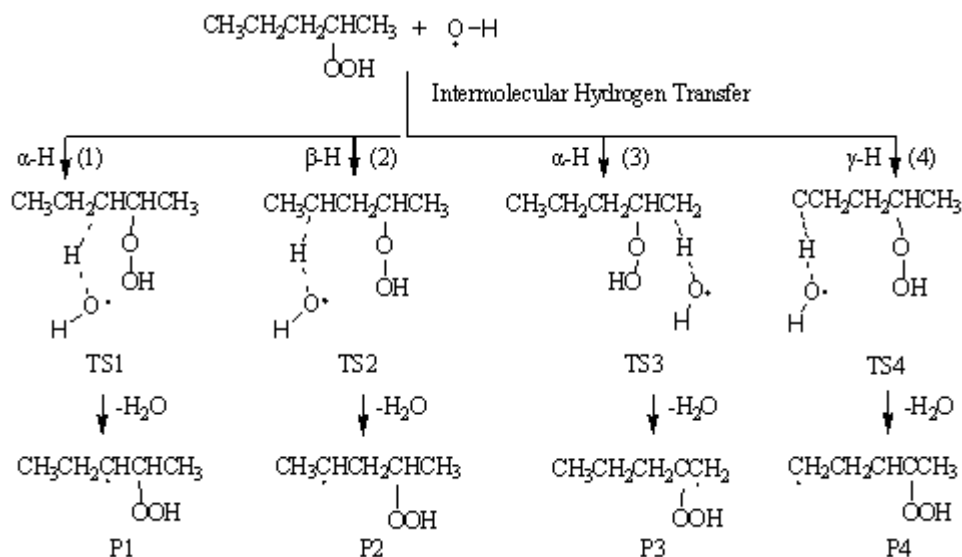


**Fig. 1.** Intermolecular hydrogen-atom transfer from 1-methylbutyl peroxide to hydroxyl radical for hydrogen at different positions.

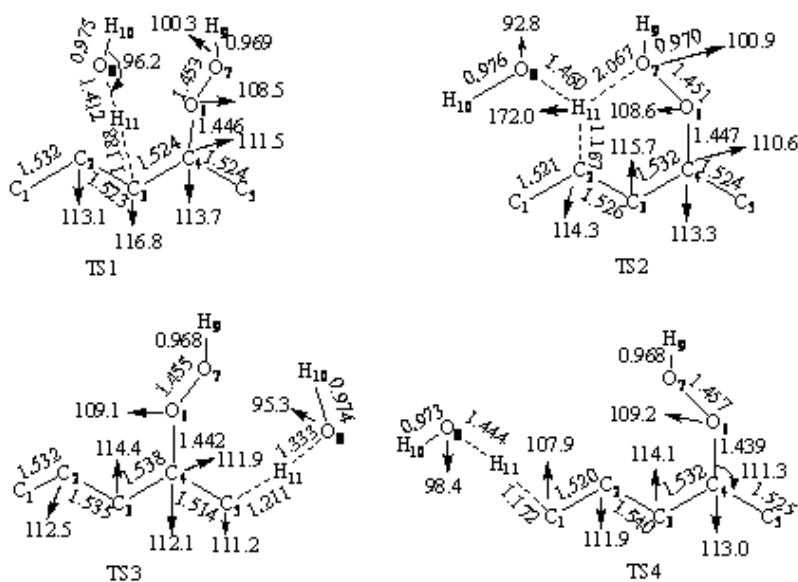


**Fig. 2.** Optimized structures of transition states (bond length in Angström, bond angle in degree).

**Table 1.** Total energies ( $E$ , in Hartree), zero point vibrational energies ( $E_{\text{vib}}$ , in kJ/mol) and relative energies ( $\Delta E$ , in kJ/mol) at the B3LYP level <sup>a</sup>

Species	$E$	$E_{\text{vib}}$	$\Delta E$	$\Delta E^c$	Species	$E$	$E_{\text{vib}}$	$\Delta E^d$
Reactant <sup>b</sup>	-423.997945	468.80	0.00	—	P1	-347.557871	400.87	-60.52
TS1	-423.993055	458.61	2.65	140.41	P2	-347.559594	399.39	-66.52
TS2	-423.994906	461.19	0.37	90.02	P3	-347.551672	399.32	-45.79
TS3	-423.990191	456.34	7.90	152.10	P4	-347.554205	399.76	-52.00
TS4	-423.989281	458.27	12.22	100.76	H <sub>2</sub> O	-76.458531	55.87	—

<sup>a</sup>  $\Delta E$  were corrected with zero-point vibrational energy. Relative energy refers to the corresponding reactant, i.e., the complex of 1-methylbutyl peroxide and hydroxyl radical. <sup>b</sup> Complex of 2-pentyl peroxide and hydroxyl radical. <sup>c</sup> Relative energies of transition states for the corresponding intrahydrogen transfers from Ref. [4]. <sup>d</sup> Energy of water is included.

**Table 2.** Atomic Mulliken charges along the reaction pathways at the B3LYP/6-311++G\*\* level.

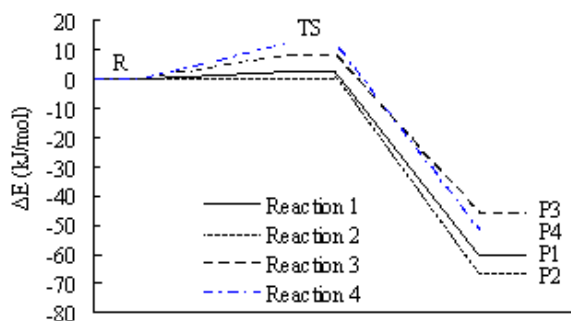
Atom	Reactant	TS1	TS2	TS3	TS4	P1	P2	P3	P4
C <sub>1</sub>	-0.625	-0.604	-0.644	-0.635	-0.644	-0.453	-0.755	-0.620	-0.386
C <sub>2</sub>	0.054	-0.100	-0.100	-0.040	-0.100	-0.442	0.318	-0.046	-0.136
C <sub>3</sub>	-0.336	-0.397	-0.451	-0.297	-0.451	0.331	-0.424	-0.490	-0.313
C <sub>4</sub>	-0.130	-0.183	0.029	-0.114	0.029	-0.326	-0.122	0.152	-0.023
C <sub>5</sub>	-0.585	-0.576	-0.615	-0.634	-0.615	-0.652	-0.592	-0.473	-0.607
O <sub>6</sub>	-0.088	-0.067	-0.090	-0.009	-0.090	-0.044	-0.056	-0.066	-0.059
O <sub>7</sub>	-0.188	-0.192	-0.197	-0.258	-0.197	-0.214	-0.207	-0.198	-0.198
O <sub>8</sub>	-0.248	-0.318	-0.358	-0.367	-0.358	-0.502	-0.502	-0.502	-0.502
H <sub>11</sub> <sup>a</sup>	0.097–0.189	0.361	0.333	0.301	0.239	0.251	0.251	0.251	0.251

<sup>a</sup> Refers to the transferred hydrogen atom.

**Table 3.** Atomic spin densities for the transferred hydrogen atom and its neighbor atoms along the reaction pathways at the B3LYP/6-311++G\*\* level.

Atom <sup>a</sup>	Reactant	TS1	TS2	TS3	TS4	P1	P2	P3	P4
O <sub>8</sub>	1.021	0.685	0.721	0.629	0.712	0.000	0.000	0.000	0.000
H <sub>10</sub>	-0.021	-0.003	0.001	0.002	-0.011	0.000	0.000	0.000	0.000
C	-0.005–0.002	0.344	0.293	0.410	0.300	1.018	1.095	1.117	1.156
H	0.00	-0.020	-0.023	-0.028	-0.016	0.000	0.000	0.000	0.000

<sup>a</sup> H and C atoms refer to the transferred hydrogen atom and its neighbor carbon, respectively.

**Fig. 3.** Energy changes along the reaction pathway at B3LYP/6-311++G\*\* level.

All the spin density primarily locates on the carbon atom in the products. This clearly indicates that it is the hydrogen radical that transfers from the carbon atom to the hydroxyl oxygen atoms with water as a leaving moiety.

## CONCLUSIONS

The reactions of hydrogen atom migration from one of the C–H of 1-methylbutyl peroxide to hydroxyl radical were investigated by the DFT-B3LYP method. Transition states with six-membered rings were formed in the process of  $\beta$ -H transfer when the hydrogen atom migrates from the

methylene group to hydroxyl radical. The six-membered ring facilitates the formation of transition state. The atomic charges and spin distribution on the radical seem to be adequate in helping to understand the trends of the intermolecular hydrogen transfer. The  $\beta$ -H is easier to transfer than the  $\alpha$ - and  $\gamma$ -H. The hydroxyl radical greatly facilitates all three types of hydrogen transfer. This presents a rational explanation of the fact that the combustion of diesel oil is accelerated by the addition of small amounts of water.

**Acknowledgements:** We gratefully thank for the support by the Nature Science Foundation of Jiangsu Higher Education Institutions of China (Grant No. 13KJB530002) and the National Natural Science Foundation of China (Grant No. 11404127). S.-Q. Zhou thanks the Research Support of Huaiyin Institute of Technology (Grant No. HGA1008).

## REFERENCES

1. F. -F. Pischinger, in: E. Sher (ed.). Handbook of Air Pollution from Internal Combustion Engines. London: Academic Press, 1998, p. 261.
2. M. Lapuerta, R. García-Contreras, J. Campos-Fernández, *Energ. Fuel*, **24**, 4497 (2010).

3. Y.-C. Lin, W.-J. Lee, H.-R. Chao, *Environ. Sci. Technol.*, **42**, 3849 (2008).
4. J.-B. Huang, D. Wu, H. Tong, W.-M. Li, *J. Energy Inst.*, **86**, 189 (2013).
5. G. Chen, D. Tao, *Fuel Process. Technol.*, **86**, 499 (2005).
6. Y. Liu, G.-H. Huang, Y.-P. Cai, C. Dong, *Int. J. Green Energy*, **11**, 1013 (2014).
7. P. Manivasagan, P. Sivasankar, J. Venkatesan, K. Sivakumar, S.-K. Kim, *Bioprocess Biosyst. Eng.*, **37**, 783 (2014).
8. Y.-P. Li, T.-J. Wang, W. Liang, C.-Z. Wu, *Energ. Fuel*, **24**, 1987 (2010).
9. A. -M. Al-Sabagh, M. -E. Mostafa, E. -M. -R. Noor, W. -R. Aly, *Egypt. J. Petrol.*, **20**, 17 (2011).
10. G. -R. Yu, J. -J. Zhao, D. -D. Song, *Ind. Eng. Chem. Res.*, **50**, 11690 (2011).
11. M. Lapuerta, O. Armas, R. García-Contreras, *Energ. Fuel*, **23**, 4343 (2009).
12. M.-V.-E. Santana, Q. Zhang, J.-R. Mihelcic, *Environ. Sci. Technol.*, **48**, 3084 (2014).
13. E.-B. Webb, C.-A. Koh, M.-W. Liberatore, *Ind. Eng. Chem. Res.*, DOI: 10.1021/ie5008954.
14. P.-B.-L. Fregolente, L.-V. Fregolente, M.-R.-W. Maciel, *J. Chem. Eng. Data*, **57**, 1817 (2012).
15. K.-Y. Lee, J.-J. Blaker, R. Murakami, J.-Y.-Y. Heng, A. Bismarck, *Langmuir*, **30**, 452 (2014).
16. M. Li, L. -F.Xie, X. -H. Ju, F. -Q. Zhao, *Petrol. Chem.*, **53**, 431 (2013).
17. J.-M. Seminario, P. Politzer, *Modern Density Functional Theory: A Tool for Chemistry*, Elsevier: Amsterdam, 1995.
18. L.-F. Xie, C.-C. Ye, X.-H. Ju, F.-Q. Zhao, *J. Struct. Chem.*, **53**, 659 (2012).
19. M. Wang, J.-J. Geng, Z.-B. Wei, Z.-Y. Wang, *Chinese J. Struct. Chem.*, **32**, 890 (2013).
20. M.-J. Frisch, G.-W. Trucks, H. -B. Schlegel, Gaussian, Inc. Pittsburgh PA, 2003.

## МЕХАНИЗЪМ НА ПРЕНОСА НА ВОДОРОД ОТ 1-МЕТИЛ-БУТИЛОВ ПЕРОКСИД КЪМ ХИДРОКСИЛЕН РАДИКАЛ

С. К. Жоу, Х. В. Куай, И. Х. Гу, В. Зоу, А. Р. Ли

Факултет по инженерна химия, Технологичен институт Хуайин, Хуаян, 223003, КНР

Постъпила на 4 ноември, 2014 г.; приета на 28 декември, 2015 г.

(Резюме)

Използван е DFT-методът за да се изследва механизма на преноса на водород от 1-метил-бутилов пероксид [ $n\text{-C}_3\text{H}_7\text{CH}(\text{CH}_3)\text{OOH}$ ] към хидроксилен радикал. Използван е B3LYP-методът заедно с базисна мрежа 6-311++G\*\*. Геометричната конфигурация на реагентите, продуктите и преходните състояния са оптимизирани на повърхностите на потенциалната енергия. Активиращите енергии на пренос на водорода са в интервала от 0.37 до 7.9 kJ/mol. Резултатите показват, че  $\beta\text{-H}$  е най-лесен за пренос от термодинамична и кинетична гледна точка. Обратно, преносът  $\gamma\text{-H}$  изисква по-големи активиращи енергии спрямо  $\alpha\text{-}$  and  $\beta\text{-H}$ . Тези три типа пренос на водород се извършват по-лесно в присъствие на хидроксилни радикали, отколкото вътрешно-молекулния пренос, което е в добро съгласие с експерименталния факт, че емулсификацията на дизелово гориво във вода води до по-добри горивни качества.

## Two ammonium ionic liquids as efficient catalysts for the one-pot green synthesis of 3,4,5-substituted furan-2(5H)-ones

S. Salahi<sup>1</sup>, M. T. Maghsoodlou<sup>1\*</sup>, N. Hazeri<sup>1</sup>, M. Lashkari<sup>2</sup>, R. Doostmohammadi<sup>1</sup>, A. Kanipour<sup>1</sup>, F. Farhadpour<sup>1</sup>, A. Shojaei<sup>1</sup>

<sup>1</sup>Department of Chemistry, Faculty of Science, University of Sistan & Baluchestan, P. O. Box 98135-674 Zahedan, Iran

<sup>2</sup>Faculty of Science, Velayat University, Iranshahr, Iran

Received September 9, 2014; Accepted September 16, 2015

An efficient and environmentally friendly method for one-pot preparation of 3,4,5-substituted furan-2(5H)-ones is described by condensation of aromatic aldehydes, aromatic amines and dialkyl acetylenedicarboxylates under solvent-free conditions using ammonium ionic liquids as catalysts. This synthetic approach benefits from cleaner reaction profiles, use of easily available, inexpensive, recyclable and environmentally benign catalyst, high yields, and simple experimental and work-up procedures.

**Keywords:** Ammonium ionic liquids ([Et<sub>2</sub>NH<sub>2</sub>][HSO<sub>4</sub>], [Et<sub>3</sub>NH][HSO<sub>4</sub>]), Multi-component reaction, Green chemistry, Furan-2(5H)-ones.

### INTRODUCTION

2(5H)-Furanones are attractive for organic chemists since they are key structural elements in many biologically active natural products [1]. They are abundant in nature and recently have been widely used as plant-growth regulators, antiulcer agents, and fish-growth promoters [2]. Attempts are ongoing to develop new synthetic approaches for the efficient preparation of natural products containing furanone ring units (Figure 1: freelingyne 1, tetrenoline 2, and sarcophine 3) because of their importance in biological activities such as antibacterial, antifungal, antimicrobial, antiviral, anticancer, anti-inflammatory, antipsoriasis, and anti-phospholipase A2 activities [3]. The wide range of application of compounds containing the butenolide ring results in considerable attention toward the synthesis of these compounds.

Recently, a multi-component reaction (MCR) of aromatic amines, aldehydes and dialkyl acetylenedicarboxylate has been used for the synthesis of furan-2(5H)-ones. Multi-component reactions offer an efficient and powerful mode of synthesis of complex structures, which is a convenient route for the synthesis of new drugs and chemical compounds by the combination of various starting materials [4].

Narayana *et al.* applied  $\beta$ -cyclodextrin for the synthesis of 2(5H)-furanone by condensation of anilines, aldehydes and diethyl acetylenedicarboxylate in a one pot three-

component reaction [5]. Other synthetic methods have also been developed by employing nano-ZnO [6], Al(HSO<sub>4</sub>)<sub>3</sub> [7], KOH [8] and SnCl<sub>2</sub>·2H<sub>2</sub>O [9].

Ionic liquids (ILs) are considerably popular among chemists since they have some specific characteristics such as very low vapor pressure, non-explosiveness, thermal stability in a wide temperature range and environmental safety, which make them a green alternative to conventional organic solvents [10-13].

ILs are categorized in a wide range such as acidic ILs, basic ILs, metal-containing ILs, guanidinium ILs, chiral ILs, and ILs containing OH groups [14]. Because of their usefulness, preparation and application of various kinds of ionic liquids in chemical processes have been quickly developed. Of the many different kinds of ILs available, the Brønsted acidic ILs offer the greatest potential for the development of environmentally friendly acid catalysts for organic synthesis [15,16]. Combination of a Brønsted acid and a Brønsted base produces protic ionic liquids [17]. Protic ionic liquid such as [Et<sub>3</sub>NH][HSO<sub>4</sub>] has been used by Li as a catalyst and green solvent for the cracking reactions of dialkoxypropanes [18].

In continuation of our research [19-22], herein we present the ionic liquids ([Et<sub>2</sub>NH<sub>2</sub>][HSO<sub>4</sub>] and [Et<sub>3</sub>NH][HSO<sub>4</sub>]) as catalysts in a simple and efficient method for the synthesis of 4,5-substituted furan-2(5H)-ones by one-pot condensation of aromatic aldehydes, aromatic amines and dialkyl acetylenedicarboxylates under solvent-free conditions.

\* To whom all correspondence should be sent:

E-mail: mt\_maghsoodlou@chem.usb.ac.ir ,  
mt\_maghsoodlou@yahoo.com

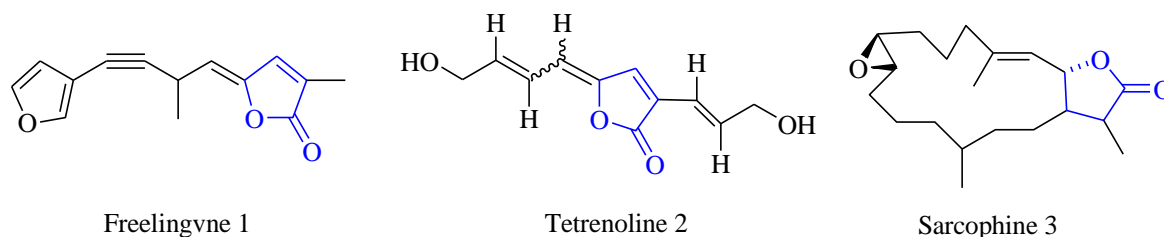


**Fig. 1.** Natural products containing a furanone ring fragment.

## EXPERIMENTAL

### General

Melting points and IR spectra of all compounds were measured on an Electrothermal 9100 apparatus and a JASCO FTIR 460 Plus spectrometer, respectively. The  $^1\text{H}$  and  $^{13}\text{C}$  NMR spectra were obtained on a Bruker DRX-400 Avance instrument with  $\text{CDCl}_3$  as a solvent. All reagents and solvents were purchased from Fluka and Merck and were used without further purification.

#### Preparation of diethylamine hydrogen sulfate [Et<sub>2</sub>NH<sub>2</sub>][HSO<sub>4</sub>]

In an ice bath, 0.5 mol sulfuric acid was added dropwise to the solution of diethylamine (0.5 mol diethylamine in 150 mL chloroform) under vigorous stirring. After completion of the reaction, the chloroform was removed on a rotary evaporator. Finally, after cooling the ionic liquid a white solid was obtained. This white crystalline powder was dried in high vacuum at 50°C overnight (>99% yield) [23].

#### Preparation of triethylamine hydrogen sulfate [Et<sub>3</sub>NH][HSO<sub>4</sub>]

Solution of sulfuric acid 98% (19.6 g, 0.2 mol) in water was dropped into triethylamine (20.2 g, 0.2 mol) under stirring at 60 °C for 1 h. Afterwards, the reaction mixture was stirred for another 1 h at 70 °C to ensure completion of the reaction. Finally, in order to remove the traces of water, the residue was heated at 80°C in high vacuum until the weight of the residue remained constant [24].

#### General procedure for the synthesis of 3,4,5-substituted furan-2(5H)-one derivatives

The mixture of aldehyde (1.0 mmol), amine (1.0 mmol), dialkylacetylenedicarboxylate (1.0 mmol) and 40 mol % of the ionic liquids [Et<sub>2</sub>NH<sub>2</sub>][HSO<sub>4</sub>] and [Et<sub>3</sub>NH][HSO<sub>4</sub>] was stirred for 10-15 minutes at 70-80°C. After completion of the reaction monitored by thin-layer chromatography (TLC), the reaction mixture was filtrated and washed with water/ethanol (3×3 mL) to purify the product and

separate the catalyst. The analytical and spectral data for the unknown products (**4p** and **4q**) are represented below:

#### *t*-Butyl-2,5-dihydro-5-oxo-2-(4-bromophenyl)-4-(phenylamino)furan-3-carboxylate (**4p**)

White powder; m.p. 169-172 °C; IR (KBr):  $\nu$  3208, 1716, 1677, 1596, 1499  $\text{cm}^{-1}$ ;  $^1\text{H}$  NMR ( $\text{CDCl}_3$ , 400 MHz):  $\delta$ = 1.39 (s, 9H, 3×Me), 5.65 (s, 1H, H<sub>benzylic</sub>), 7.09-7.14 (m, 3H, H<sub>Ar</sub>), 7.27-7.31 (m, 2H, H<sub>Ar</sub>), 7.38-7.41 (m, 2H, H<sub>Ar</sub>), 7.34-7.45 (m, 2H, H<sub>Ar</sub>), 9.32 (brs, 1H, NH);  $^{13}\text{C}$  NMR ( $\text{CDCl}_3$ , 100 MHz):  $\delta$ =28.0 (3×Me), 61.0 (C<sub>benzylic</sub>), 83.5 (OCMe<sub>3</sub>), 114.0, 122.3, 122.4, 125.9, 129.0, 129.3, 131.6, 134.5, 136.0 and 156.9 (C<sub>Ar</sub> and C=C), 162.7 and 164.8 (C=O).

#### *t*-Butyl-2,5-dihydro-5-oxo-2-phenyl-4-(3-nitrophenylamino)furan-3-carboxylate (**4q**)

White powder; m.p. 165-168 °C; IR (KBr):  $\nu$  3142, 1715, 1681, 1531, 1456  $\text{cm}^{-1}$ ;  $^1\text{H}$  NMR ( $\text{CDCl}_3$ , 400 MHz):  $\delta$ = 1.37 (s, 9H, 3×Me), 5.76 (s, 1H, H<sub>benzylic</sub>), 7.24-7.32 (m, 5H, H<sub>Ar</sub>), 7.64 (t, 1H,  $J$ =8.0 Hz, H<sub>Ar</sub>), 7.93 (ddd,  $J$ =8.0, 2.0, 0.8 Hz, 1H, H<sub>Ar</sub>), 8.09 (ddd,  $J$ =8.4, 2.4, 0.8 Hz, 1H, H<sub>Ar</sub>), 8.32 (t, 1H,  $J$ =2.4 Hz, H<sub>Ar</sub>), 9.40 (brs, 1H, NH);  $^{13}\text{C}$  NMR ( $\text{CDCl}_3$ , 100 MHz):  $\delta$ =  $^{13}\text{C}$  NMR ( $\text{CDCl}_3$ , 100 MHz):  $\delta$ =27.9 (3×Me), 61.3 (C<sub>benzylic</sub>), 83.8 (OCMe<sub>3</sub>), 115.1, 115.9, 119.9, 127.3, 127.5, 128.8, 128.9, 129.8, 134.4, 137.6, 148.3 and 156.9 (C<sub>Ar</sub> and C=C), 163.1 and 164.9 (C=O).

## RESULTS AND DISCUSSION

To examine the effect of catalyst loading and temperature on the three-component condensation reaction of 4,5-substituted furan-2(5H)-ones, the reaction of aromatic aldehydes, aromatic amines and dialkyl acetylenedicarboxylates was selected as a model in the presence of the ionic liquids, diethylamine hydrogen sulfate [Et<sub>2</sub>NH<sub>2</sub>][HSO<sub>4</sub>] and triethylammonium hydrogensulfate ([Et<sub>3</sub>NH][HSO<sub>4</sub>]) as catalysts (Table 1). Different amounts of diethylamine hydrogensulfate and triethylammonium hydrogensulfate were applied as catalysts (15, 20, 30, 40, 50 and 55 mol %) at various temperatures (45, 50, 60, 70, 80, 90 and 100

°C) (Table 1). As the Table shows, the addition of 40 mol % of acidic ionic liquid catalyst at 80 and 70 °C results in a corresponding product within 15 min with 85 % yield. Afterwards, the three-component condensation reaction of aromatic aldehydes, aromatic amines and dialkyl acetylenedicarboxylates was investigated under optimized conditions for preparation of 4,5-substituted furan-2(5*H*)-one derivatives (Table 2).

To better understanding the effect of the substituent, diverse substituted aldehydes were used

to synthesize the desired products in high to excellent yields using the ammonium ionic liquids ([Et<sub>2</sub>NH<sub>2</sub>][HSO<sub>4</sub>], [Et<sub>3</sub>NH][HSO<sub>4</sub>]) as catalysts (Table 2).

The proposed speculative mechanism for the formation **4** is shown in Scheme 2. The mechanism can proceed through Michael addition, iminium-enamine tautomerization and  $\gamma$ -lactonization [25,26].

**Table 1.** Optimization of reaction conditions in the presence of different amounts of ionic liquids, A: diethylamine sulfate [Et<sub>2</sub>NH<sub>2</sub>][HSO<sub>4</sub>] B: triethylamine sulfate [Et<sub>3</sub>NH][HSO<sub>4</sub>] as catalysts at different temperatures <sup>a</sup>

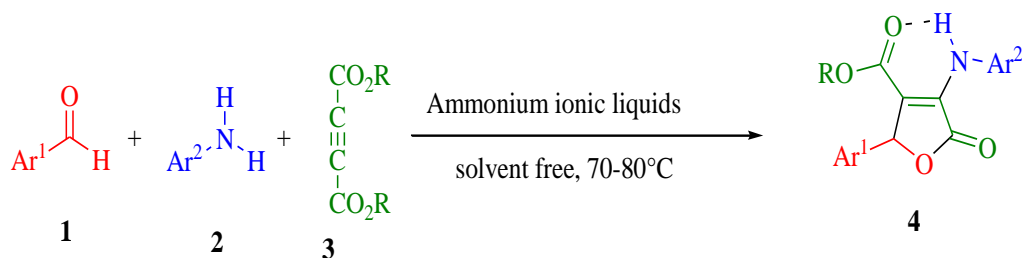
Entry	Catalyst/mol %		Temperature/ °C		Time/min		Isolated Yield/ %	
	A	B	A	B	A	B	A	B
1	15	15	80	70	15	15	36	49
2	15	15	80	70	20	20	57	55
3	20	20	80	70	15	15	65	67
4	30	30	80	70	15	15	83	81
<b>5</b>	<b>40</b>	<b>40</b>	<b>80</b>	<b>70</b>	<b>15</b>	<b>15</b>	<b>85</b>	<b>85</b>
6	50	50	80	70	15	15	87	83
7	55	55	80	70	15	15	88	83
8	30	40	45	45	20	20	56	46
9	30	40	50	50	20	20	57	50
10	30	40	60	60	15	15	61	73
11	30	40	70	70	15	15	74	81
12	30	40	80	80	15	15	83	77
13	30	40	90	90	15	15	66	72
14	30	40	100	100	15	15	70	70
15	30	40	80	70	5	5	66	61
16	30	40	80	70	10	10	78	79
17	30	40	80	70	15	15	83	81
18	30	40	80	70	20	20	80	77

<sup>a</sup> Reaction conditions: benzaldehyde (1.0 mmol), aniline (1.0 mmol), diethyl acetylenedicarboxylate (1.0 mmol)

**Table 2.** Synthesis of furan-2(5*H*)-one derivatives in the presence of ammonium ionic liquids, A: diethylammonium hydrogensulfate [Et<sub>2</sub>NH<sub>2</sub>][HSO<sub>4</sub>] B: triethylammonium hydrogensulfate [Et<sub>3</sub>NH][HSO<sub>4</sub>] as catalysts.

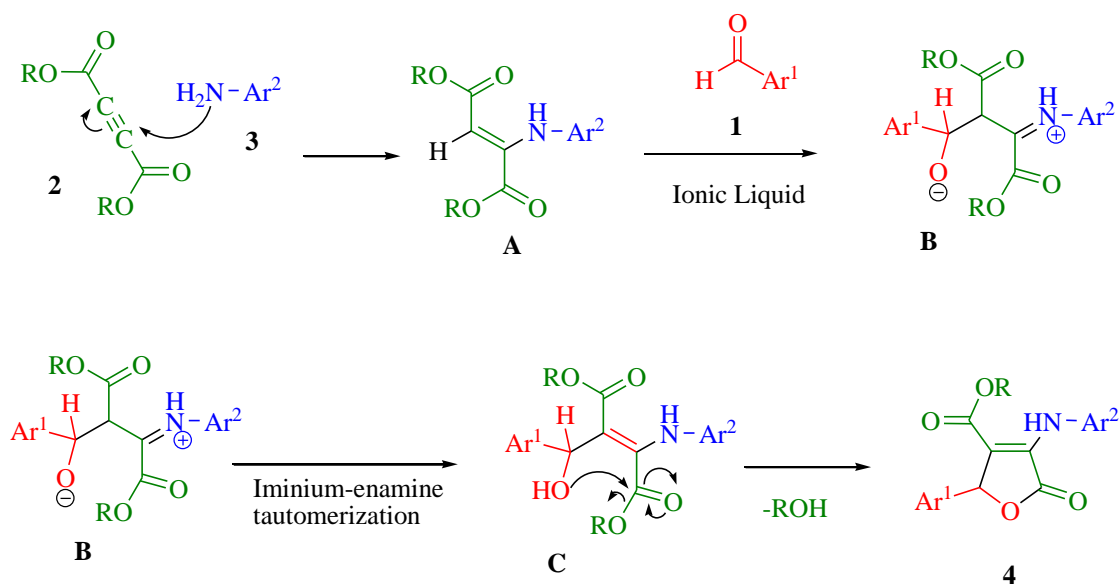
Entry	Ar <sup>1</sup>	Ar <sup>2</sup>	R	Products	Isolated Yield/ %		Ref.
					A	B	
1	Ph	Ph	CH <sub>3</sub>	<b>4a</b>	88	85	7
2	4-Me- C <sub>6</sub> H <sub>4</sub>	Ph	CH <sub>3</sub>	<b>4b</b>	80	76	7
3	3-NO <sub>2</sub> - C <sub>6</sub> H <sub>4</sub>	Ph	CH <sub>3</sub>	<b>4c</b>	81	78	7
4	4-NO <sub>2</sub> -C <sub>6</sub> H <sub>4</sub>	Ph	CH <sub>3</sub>	<b>4d</b>	89	85	19
5	4-OMe- C <sub>6</sub> H <sub>4</sub>	Ph	CH <sub>3</sub>	<b>4e</b>	88	87	19
6	Ph	4-F-C <sub>6</sub> H <sub>4</sub>	CH <sub>3</sub>	<b>4f</b>	71	67	19
7	Ph	4-Cl-C <sub>6</sub> H <sub>4</sub>	CH <sub>3</sub>	<b>4g</b>	72	69	19
8	Ph	3-NO <sub>2</sub> -C <sub>6</sub> H <sub>4</sub>	CH <sub>3</sub>	<b>4h</b>	79	78	19
9	Ph	Ph	CH <sub>3</sub> CH <sub>2</sub>	<b>4i</b>	89	85	5
10	Ph	4-Me-C <sub>6</sub> H <sub>4</sub>	CH <sub>3</sub> CH <sub>2</sub>	<b>4j</b>	90	87	5
11	4-Me-C <sub>6</sub> H <sub>4</sub>	Ph	CH <sub>3</sub> CH <sub>2</sub>	<b>4k</b>	85	82	5
12	4-Cl-C <sub>6</sub> H <sub>4</sub>	Ph	CH <sub>3</sub> CH <sub>2</sub>	<b>4m</b>	91	89	5
13	4-OMe-C <sub>6</sub> H <sub>4</sub>	Ph	CH <sub>3</sub> CH <sub>2</sub>	<b>4n</b>	90	85	5
14	1- naphthyl	Ph	CH <sub>3</sub> CH <sub>2</sub>	<b>4o</b>	64	63	5
15	4-Br-C <sub>6</sub> H <sub>4</sub>	Ph	<i>t</i> -Bu	<b>4p</b>	86	81	<i>a</i>
	Ph-C <sub>6</sub> H <sub>4</sub>	3-NO <sub>2</sub> -C <sub>6</sub> H <sub>4</sub>	<i>t</i> -Bu	<b>4q</b>	80	76	<i>a</i>

<sup>a</sup> New compounds synthesized in this work.



Ammonium ionic liquids: [Et<sub>2</sub>NH<sub>2</sub>][HSO<sub>4</sub>], [Et<sub>3</sub>NH][HSO<sub>4</sub>]

**Scheme 1.** Synthesis of 3,4,5-substituted furan-2(5*H*)-one derivative.



**Scheme 2.** Proposed mechanism for the formation of furan-2(5*H*)-one derivatives.

## CONCLUSION

In summary, a simple method for the preparation of furan-2(5*H*)-one derivatives in solvent-free conditions *via* one-pot three-component reaction from commonly available starting materials was developed. The products can be easily collected by filtration.

**Acknowledgements:** We gratefully acknowledge financial support from the Research Council of the University of Sistan and Baluchestan.

## REFERENCES

1. Y. S. Rao, *Chem. Rev.*, **76**, 625 (1976).
2. (a) V. V. Nemchenko, N. P. Ivanova, *Khim. Sel'sk. Khoz.*, **1**, 91 (1991); (b) H. Aihara, M. Muramatsu, I. Arai, *Jpn Kokai Tokyo Koho*, 225315 (1988); (c) L. N. Tsen, V. S. Suleimanyan, *Rybn. Khoz.*, **5**, 37 (1982).
3. (a) R. A. Massy-Westropp, G. D. Reynolds, T. M. Spotswood, *Tetrahedron Lett.*, **7**, 1939 (1966); (b) A. Khalid, E. Sayed, Y. Khaled, D. Orabi, C. Dunbar, M. T. Hamann, A. A. Mitchell, A. S. Yogesh, S. M. Jaber, El-Feraly, S. Farouk *Tetrahedron*, **58**, 3699 (2002); (c) S. Ma, Z. Shi, *J. Org. Chem.*, **63**, 6387 (1998); (d) A. Alaa, Y. El-Tombary, A. S. F. B. Abdel-Ghany, A. Shams, S. El-Dine, S. G. S. Farid, *Med. Chem. Res.*, **20**, 865 (2011).
4. (a) J. Zhu, H. Bienaymé, *Multicomponent Reactions*, Wiley-VCH, Weinheim, 2005; (b) A. Aminkhani, G. Marandi, *Lett. Org. Chem.*, **9**, 7 (2012); (c) J.-N. Sangshetti, N.-D. Kokare, D.-B. Shinde, *Chin. J. Chem.*, **26**, 1506 (2008); (d) S. Song, Z. Shan, Y. A. Jin, *Lett. Org., Chem.*, **7**, 64 (2010).
5. S. N. Murthy, B. Madhav, A. V. Kumar, K. R. Rao, Y. V. D. Nageswar, *Tetrahedron*, **65**, (2009).
6. S. U. Tekale, S. S. Kauthale, V. P. Pagore, V. B. Jadhav, R. P. Pawar, *J. Iran Chem. Soc.*, **10**, 1271 (2013).
7. M. R. Mohammad Shafiee, S. S. Mansoor, M. Ghashang, A. Fazlinia, *C. R. Chimie*, **17**, 131 (2014).
8. S. Ramesh, R. Nagarajan, *Synthesis*, **20**, 3307 (2011).
9. L. Nagarapu, U. N. Kumar, P. Upendra, R. Bantu, *Synth. Commun.*, **42**, 2139 (2012).
10. (a) R. D. Rogers, K. R. Seddon, *Science*, **302**, 792 (2003); (b) R. Sheldon, *Green Chem.*, **7**, 267 (2005); (c) P. Wasserscheid, W. Keim, *Angew. Chem. Int. Ed.*, **39**, 3773 (2000).
11. (a) J. S. Wilkes, J. A. Levisky, R. A. Wilson, C. L. Hussey, *Inorg. Chem.*, **21**, 1263 (1982); (b) J. S. Wilkes, M. J. Zaworotko, *J. Chem. Soc., Chem. Commun.*, 965 (1992).
12. M. A. Zolfigol, A. Khazaei, A. R. Moosavi-Zare, A. Zare, V. Khakyzadeh, *Appl. Catal. A: General*, **400**, 70 (2011).
13. A. R. Moosavi-Zare, M. A. Zolfigol, V. Khakyzadeh, C. Böttcher, M. H. Beyzavi, A. Zare, A. Hasaninejad, R. Luque, *J. Mater. Chem. A*, **2**, 770 (2014).
14. C.B. Yue, D. Fang, L. Liu, T.F. Yi, *J. Mol. Liq.*, **163**, 99 (2011).
15. A. Zare, A. R. Moosavi-Zare, M. Merajoddin, M. A. Zolfigol, T. Hekmat-Zadeh, A. Hasaninejad, A. Khazaei, M. Mokhlesi, V. Khakyzadeh, F. Derakhshan-Panah, M. H. Beyzavi, E. Rostami, A. Arghoon, R. Roohandeh, *J. Mol. Liq.*, **167**, 69 (2012).
16. A. Zare, F. Abi, A. R. Moosavi-Zare, M. H. Beyzavi, M. A. Zolfigol, *J. Mol. Liq.*, **178**, 113 (2013).
17. T. L. Greaves, C. J. Drummond, *Chem. Rev.*, **108**, 206 (2008).
18. C. Wang, L. Guo, H. Li, Y. Wang, J. Weng, L. Wu, *Green Chem.*, **8**, 603 (2006).
19. R. Doostmohammadi, M. T. Maghsoodlou, N. Hazeri, S. M. Habibi-Khorassani, *Res. Chem. Intermed.*, **39**, 4061 (2013).
20. R. Doostmohammadi, M.T. Maghsoodlou, N. Hazeri, S.M. Habibi-Khorassani, *Chin. Chem. Lett.*, **24**, 901 (2013).
21. N. Hazeri, M. T. Maghsoodlou, N. Mahmoudabadi, R. Doostmohammadi, S. Salahi, *Current Organocatal.*, **1**, 45 (2014).
22. R. Doostmohammadi, N. Hazeri, *Lett. Org. Chem.*, **10**, 199 (2013).
23. J. Weng, C. Wang, H. Li, Y. Wang, *Green Chem.*, **8**, 96 (2006).
24. Z. Zhou, X. Deng, *J. Mol. Catal. A: Chem.*, **367**, 99 (2013).
25. J. Safaei-Ghomi, F. Salimi, A. Ramazani, F. Zeinali Nasrabadi, Y. Ahmadi, *Turk. J. Chem.*, **36**, 485 (2012).
26. M. B. Teimouri, T. Abbasi, *Tetrahedron*, **66**, 3795 (2010).

## ДВЕ АМОНИЕВИ ЙОННИ ТЕЧНОСТИ КАТО ЕФЕКТИВНИ КАТАЛИЗАТОРИ ЗА ЕДНОСТАДИЙНА ЗЕЛЕНА СИНТЕЗА НА 3,4,5-ЗАМЕСТЕНИ ФУРАН-2(5*H*)-ОНИ

С. Салахи<sup>1</sup>, М.Т. Максудлу<sup>1</sup>, Н. Хазери<sup>1</sup>, М. Лашкари<sup>2</sup>, Р. Дустмохамади<sup>1</sup>, А. Канипур<sup>1</sup>, Ф. Фархадпур<sup>1</sup>, А. Шоджаеи<sup>1</sup>

<sup>1</sup>Департамент по химия, Научен факултет, Университет в Систан и Балучестан, Захедан, Иран

<sup>2</sup>Научен факултет, Велаят, Иранишахр, Иран

Постъпила на 9 септември, 2014 г.; приета на 16 септември, 2015 г.

(Резюме)

Описана е едностадийна и екологично съвместима кондензация на ароматни алдехиди, ароматни амини и диалкил-ацетилен-дикарбоксилати за синтезата на 3,4,5-заместени фуран-2(5*H*)-они без разтворител с амониеви йонни течности като катализатори. Този подход има предимствата на чисти реакционни профили, използването на лесно достъпни, евтини, рециклируеми и екологично съвместими катализатори и проста процедура.

## Convenient approach for the one-pot, three-component synthesis of 1-(benzothiazolylamino)methyl-2-naphthol using fumaric acid as a green catalyst

M. T. Maghsoodlou<sup>1\*</sup>, M. Karima<sup>1</sup>, M. Lashkari<sup>2</sup>, B. Adrom<sup>1</sup>, N. Hazeri<sup>1</sup>

<sup>1</sup>Department of Chemistry, Faculty of Science, University of Sistan and Baluchestan, P. O. Box 98135-674 Zahedan, Iran

<sup>2</sup>Faculty of Science, Velayat University, Iranshahr, Iran

Received August 24, 2014; Accepted September 15, 2015

One-pot, efficient three-component condensation of aldehydes, 2-naphthol, and 2-aminobenzothiazole in the presence of fumaric acid as an effective catalyst for the synthesis of 1-(benzothiazolylamino)methyl-2-naphthol derivatives under thermal and solvent-free conditions is described. The present approach of this methodology offers several advantages such as mild conditions, high yields, clean reaction profiles, operational simplicity, and environmentally benign and simple work-up procedures.

**Keywords:** Green protocol, 1-(Benzothiazolylamino)methyl-2-naphthol, Multi-component reaction, Fumaric acid, Solvent-free conditions.

### INTRODUCTION

Multicomponent condensation reactions have a wide range of applicability in the field of synthetic organic chemistry. They constitute an especially attractive synthetic strategy because they provide easy and rapid access to large libraries of organic compounds with diverse substitution patterns. Being one-pot reactions, they are easier to carry out than multistep syntheses, and the products are formed in a single step. Diversity can be achieved simply by varying the components [1]. In the past few years, combinatorial methods using multicomponent reactions have been closely examined as fast and convenient solutions for the synthesis of diverse classes of compounds [2]. Recently, this strategy became important in drug discovery in the context of synthesis of biologically active compounds. This method increases the efficiency of the reactions and decreases the number of laboratory operations along with solvents and chemicals used. It also reduces reaction time and increases the yield of products in comparison with normal multistep methods [3].

2-Aminobenzothiazoles are unique scaffolds that are widely used in medicinal and biological chemistry [4]. Their diverse functions range from electron transfer facilitation in the firefly luciferin cycle [5], through antitumor [6], and antidiabetic activity [7] to Alzheimer's disease tracer (8) and anticancer agent in pharmaceutical chemistry [9].

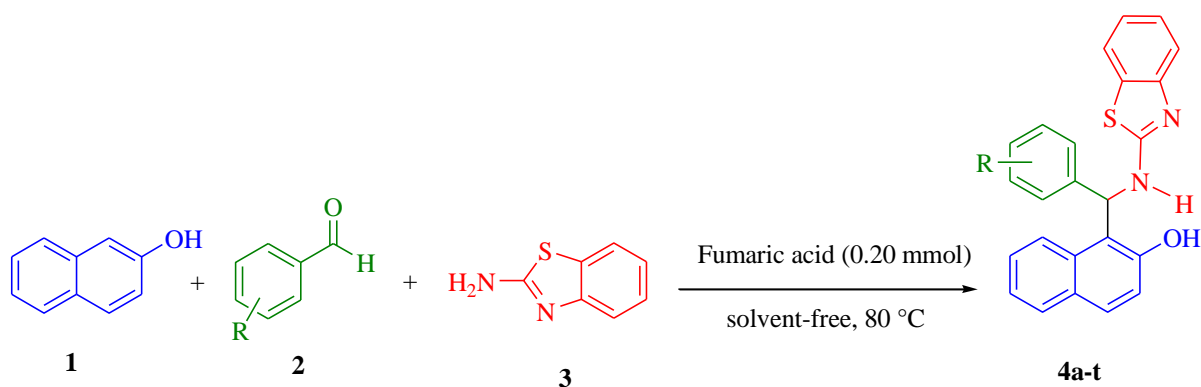
Also, benzothiazoles are commercially important as reactive dyes [10], hair dyes [11], agrochemical fungicides, insecticides, acaricides, herbicides, plant desiccants and defoliants [12].

Fumaric acid (C<sub>4</sub>H<sub>4</sub>O<sub>4</sub>) is an organic acid widely found in nature, and is a component of organic biosynthesis in humans. Chemically, it is an unsaturated dicarboxylic acid. It exists as white or nearly white crystals, odorless, with a very tart taste. Fumaric acid is generally nontoxic and nonirritant. Fumaric acid has been used in food and beverage products since the 1940s. Food research shows that fumaric acid can improve quality and reduce the costs of many food and beverage products. It is non-hygroscopic (absorbs no moisture). In the cosmetic industry, it is used as a bath salt cleaning agent for dentures. It is also used in animal feeds. Fumaric acid is used in oral pharmaceutical formulations and clinically in the treatment of psoriasis.

Because of the above-mentioned properties of 2-aminobenzothiazole and fumaric acid and as a part of our ongoing program on multi-component reactions [13,14], herein we present an eco-friendly, simple and efficient method for the synthesis of 1-(benzothiazolylamino)methyl-2-naphthol compounds *via* a one-pot three-component reaction using 2-naphthol, 2-aminobenzothiazole and aromatic aldehydes in the presence of fumaric acid under solvent-free conditions (Scheme 1).

\* To whom all correspondence should be sent:

E-mail: mt\_maghsoodlou@chem.usb.ac.ir ,  
mt\_maghsoodlou@yahoo.com



**Scheme 1.** Fumaric acid catalyzed synthesis of 1-(benzothiazolylamino)methyl-2-naphthols **4a-t**.

## EXPERIMENTAL

### General

Melting points and IR spectra were measured on an Electrothermal 9100 apparatus and a JASCO FT/IR- 460 plus spectrometer, respectively. The  $^1\text{H}$  and  $^{13}\text{C}$  NMR spectra were obtained on a Bruker DRX-400 Avance instrument with DMSO as a solvent. All reagents and solvents were purchased from Fluka and Merck and were used without further purification.

### Typical procedure for the synthesis of 1-amidoalkyl-2-naphthols (**4a-t**)

Fumaric acid (0.20 mmol, 0.023 g) was added into a mixture of benzaldehyde (1.0 mmol), 2-naphthol (1.0 mmol) and 2-aminobenzothiazole (1.0 mmol), then the reaction mixture was stirred at 80 °C for the appropriate time (Table 1). After completion of the reaction (monitored by TLC), the reaction mixture was washed with  $\text{H}_2\text{O}$  ( $3 \times 10$  mL). As the catalyst is soluble in water, it was removed from the reaction mixture. Then, the residue was recrystallized from EtOH.

### 1-((Benzo[d]thiazol-2-ylamino)(2,5-dimethoxyphenyl)methyl)naphthalen-2-ol (**4s**)

Yield: 90 %; m.p. 209-211 °C; IR (KBr,  $\text{cm}^{-1}$ ): 3368 (N-H), 3060 (O-H), 1628 (C=N),  $^1\text{H}$  NMR (400 MHz, DMSO- $d_6$ ):  $\delta$  = 3.50 and 3.64 (2s, 6H, 2OCH<sub>3</sub>), 6.76 (d, 1H,  $J=8.4$  Hz,  $\text{H}_{\text{Ar}}$ ), 6.84 (d, 1H,  $J=8.8$  Hz,  $\text{H}_{\text{Ar}}$ ), 6.98 (d, 1H,  $J=7.2$  Hz,  $\text{H}_{\text{Ar}}$ ), 7.15-7.45(m, 7H,  $\text{H}_{\text{Ar}}$ , 1 $\text{H}_{\text{benzylic}}$ ), 7.63 (d, 1H,  $J=7.6$  Hz,  $\text{H}_{\text{Ar}}$ ), 7.71 (d, 1H,  $J=8.8$  Hz,  $\text{H}_{\text{Ar}}$ ), 7.77 (d, 1H,  $J=8\text{Hz}$ ,  $\text{H}_{\text{Ar}}$ ), 8.26 (d, 1H,  $J=8.4$  Hz,  $\text{H}_{\text{Ar}}$ ), 8.61 (brs, 1H, NH), 9.92 (s, 1H, OH).  $^{13}\text{C}$  NMR (100 MHz, DMSO- $d_6$ ):  $\delta$  = 50.56, 55.69, 56.44, 111.64, 112.41, 116.22, 118.46, 118.72, 119.06, 121.22, 121.26, 122.66, 123.89, 125.82, 126.39, 128.70, 128.80, 129.51, 131.07, 131.70, 133.06, 151.37, 152.74, 153.24, 153.81, 166.14.

### 1-((Benzo[d]thiazol-2-ylamino)(2-hydroxy-3-methoxyphenyl)methyl)naphthalen-2-ol (**4t**)

Yield: (92%); m.p. 200-202 °C ; IR (KBr,  $\text{cm}^{-1}$ ): 3366 (N-H), 3141 (O-H), 1632 (C=N);  $^1\text{H}$  NMR (400 MHz, DMSO- $d_6$ ):  $\delta$  = 3.74 (s, 3H, OCH<sub>3</sub>), 6.67 (t, 1H,  $J=7.6$  Hz,  $\text{H}_{\text{Ar}}$ ), 6.82 (d, 1H,  $J=7.6$  Hz,  $\text{H}_{\text{Ar}}$ ), 6.96 (t, 1H,  $J=7.6$  Hz,  $\text{H}_{\text{Ar}}$ ), 7.01 (d, 1H,  $J=7.2$  Hz,  $\text{H}_{\text{Ar}}$ ), 7.14-7.40 (m, 6H,  $\text{H}_{\text{Ar}}$ , 1 $\text{H}_{\text{benzylic}}$ ), 7.61 (d, 1H,  $J=7.2$  Hz,  $\text{H}_{\text{Ar}}$ ), 7.71 (d, 1H,  $J=8$  Hz,  $\text{H}_{\text{Ar}}$ ), 7.76 (d, 1H,  $J=8$  Hz,  $\text{H}_{\text{Ar}}$ ), 8.18 (d, 1H,  $J=8.4$  Hz,  $\text{H}_{\text{Ar}}$ ), 8.64 and 8.79 (brs, 2H, NH and OH), 9.95 (brs, 1H, OH).  $^{13}\text{C}$  NMR (100 MHz, DMSO- $d_6$ ):  $\delta$  = 50.90, 56.12, 56.27, 110.81, 118.29, 118.53, 118.86, 119.16, 121.13, 121.24, 122.66, 123.43, 125.81, 126.42, 128.82, 129.30, 130.96, 132.17, 133.22, 144.29, 147.79, 151.68, 152.69, 153.66, 166.27.

## RESULTS AND DISCUSSION

Our initial aim was to develop an efficient one-pot procedure for the synthesis of 1-(benzothiazolylamino)methyl-2-naphthol derivatives through the reaction of 2-naphthol, 2-aminobenzothiazole and aldehydes in the presence of fumaric acid. To find out the optimum amount of fumaric acid, the reaction was carried out by varying the quantity of catalyst. The maximum yield was obtained when 0.20 mmol of catalyst was used (Table 1). Further increase in the amount of fumaric acid did not have any significant effect on the product yield. The results are summarized in Table 1. As shown in Table 1, the shortest time and best yield were achieved at 80 °C.

In order to evaluate the generality of the process, several examples illustrating the present method for the synthesis of 1-(benzothiazolylamino)methyl-2-naphthols (**4**) were studied (Table 2). The reactions of 2-naphthol with various aromatic aldehydes and 2-aminobenzothiazole were carried out in the presence of 0.20 mmol fumaric acid at 80°C. In all reactions, good to excellent yields were obtained at

short reaction times (4–15 min). Using these optimized reaction conditions, the generality of the reaction was examined using several types of aldehydes. As shown in Table 2, the direct three-component reaction worked well with a variety of aryl aldehydes including those bearing electron-withdrawing and electron-donating groups, and the desired compounds were obtained in good yields. However, the yield of product was lower in

comparison with aryl aldehydes containing electron-withdrawing substituents (Table 2).

The products were identified by IR, <sup>1</sup>H NMR and <sup>13</sup>C NMR spectroscopy. The <sup>1</sup>H NMR spectrum of **4s** exhibited a multiplet at  $\delta = 7.15$ – $7.45$  for the 7 aromatic hydrogens and benzylic hydrogen and two singlets at  $\delta = 8.61$  and  $\delta = 9.92$  for the NH and OH groups, respectively.

**Table 1.** Optimization of catalyst for the synthesis of 1-(benzothiazolylamino)methyl-2-naphthols.<sup>a</sup>

Entry	Catalyst (mmol)	Temperature (°C)	Time (min)	Isolated Yield (%)
1	Fumaric acid (0.10)	80	15	78
2	Fumaric acid (0.15)	80	14	84
<b>3</b>	<b>Fumaric acid (0.20)</b>	<b>80</b>	<b>12</b>	<b>93</b>
4	Fumaric acid (0.30)	80	9	87
5	Fumaric acid (0.20)	50	60	10
6	Fumaric acid (0.20)	60	20	35
7	Fumaric acid (0.20)	100	10	52

<sup>a</sup> Reaction conditions: 2-naphthol (1.0 mmol), 2-aminobenzothiazole (1.0 mmol) and benzaldehyde (1.0 mmol) in the presence of catalyst at different temperatures.

**Table 2.** Synthesis of 1-(benzothiazolylamino)methyl-2-naphthol derivatives

Entry	R	Time (min)	Yield (%) <sup>a</sup>	Product	M.p. (lit. m.p.) (°C)[Ref.]
1	4-NO <sub>2</sub>	15	52	<b>4a</b>	188–190 (189–191)[15]
2	4-Cl	4	89	<b>4b</b>	208–210(209–210)[16]
3	3-NO <sub>2</sub>	5	50	<b>4c</b>	190–192( 191-194)[17]
4	2,4-Cl <sub>2</sub>	5	82	<b>4d</b>	204–206(206–207)[15]
5	3-MeO	5	89	<b>4e</b>	185–187(184–186)[17]
6	4-Me	10	92	<b>4f</b>	183–185(182–183)[16]
7	2-Cl	4	88	<b>4g</b>	187–189(189–190)[15]
8	2,4-(MeO) <sub>2</sub>	9	89	<b>4h</b>	162-164(161-163)[17]
9	4-OMe	7	92	<b>4i</b>	173-175(175-176)[16]
10	2-NO <sub>2</sub>	15	58	<b>4j</b>	212–214(215–216)[15]
11	2,6-Cl <sub>2</sub>	7	86	<b>4k</b>	194–196(193–195)[20]
12	3-Br	4	90	<b>4l</b>	200–202(202–204)[17]
13	4- Br	4	90	<b>4m</b>	200–202(200–202)[20]
14	4-F	11	82	<b>4n</b>	175–177(176–178)[17]
15	5-Br,2-HO	7	90	<b>4o</b>	181-183(183–185)[20]
16	Thienyl	8	90	<b>4p</b>	190–192(191–193)[20]
17	2,3-(MeO) <sub>2</sub>	10	93	<b>4q</b>	200–202(201–203)[20]
18	H	8	89	<b>4r</b>	202-204(202–203)[15]
19	2,5-(MeO) <sub>2</sub>	10	90	<b>4s</b>	209-211 <sup>b</sup>
20	5- MeO,2-HO	6	92	<b>4t</b>	200-202 <sup>b</sup>

<sup>b</sup> New compounds synthesized in this work. All known products reported previously in the literature were characterized by comparison of m.p., IR and NMR spectra with those of authentic samples.

## CONCLUSION

In summary, an efficient method for the synthesis of 1-(benzothiazolylamino)methyl-2-naphthol derivatives is described. The reactions were carried out under solvent-free conditions with short reaction times and gave the corresponding products in good yields. The present methodology offers several advantages such as good yields, simple procedure, shorter reaction times, clean reaction conditions. Moreover, the products were purified without chromatography.

**Acknowledgements:** We gratefully acknowledge financial support from the Research Council of the University of Sistan and Baluchestan.

## REFERENCES

1. (a) J. Zhu, H. Bienayme, (eds.) Multicomponent Reactions; Wiley-VCH: Weinheim, 2005, p. 1; (b) C. O. Kappe, *Curr. Opin. Chem. Biol.*, **6**, 314 (2002); (c) A. Dömling, I. Ugi, *Angew. Chem., Int. Ed.*, **39**, 3168 (2000); (d) K. Kumaravel, G. Vasuki, *Curr. Org. Chem.*, **13**, 1820 (2009); (e) I. Ugi, A. Dömling, W. Hörl, *Endeavour*, **18**, 115 (1994); (f) B. Ganem, *Acc. Chem. Res.*, **42**, 463 (2009); (g) I. Ugi, *Pure Appl. Chem.*, **73**, 187 (2001); (h) J. Zhu, H. Bienayme, (eds.) Multicomponent Reactions, Wiley-VCH: Weinheim, 2005.
2. (a) L. F. Tietze, *Chem. Rev.*, **96**, 115 (1996); (b) Dömling, A. *Chem. Rev.*, **106**, 17 (2006); (c) D. J. Ramon, M. Yus, *Angew. Chem., Int. Ed.*, **44**, 1602 (2005).
3. (a) M. Zhang, H.-F. Jiang, H.-L. Liu, Q.-H. Zhu, *Org. Lett.*, **9**, 4111 (2007); (b) J.-P. Zhu, H. Bienayme, (eds.) Multicomponent Reactions, Wiley-VCH: Weinheim, 2005, p. 1499; (c) R. M. Armstrong, A. P. Combs, P. A. Tempest, S. D. Brown, T. A. Keating, *Acc. Chem. Res.*, **29**, 123 (1996).
4. A.R. Katritzky, D.O. Tymoshenko, D. Monteux, V. Vvedensky, G. Nikonov, C.B. Cooper, M. Deshpande, *J. Org. Chem.*, **65**, 8059 (2000).
5. E. H. White, F. McCapra, G.F. Field, *J. Am. Chem. Soc.*, **85**, 337 (1963).
6. C. G. Mortimer, G. Wells, J. P. Crochard, E. L. Stone, T. D. Bradshaw, M. F. G. Stevens, A.D. Westwell, *J. Med. Chem.*, **49**, 179 (2006).
7. M. C. V. Zandt, M. L. Jones, D. E. Gunn, L. S. Geraci, J. H. Jones, D. R. Sawicki, J. Sredy, J. L. Jacot, A. T. DiCioccio, T. Petrova, A. Mitschler, A. D. Podjarny, *J. Med. Chem.*, **48**, 3141 (2005).
8. C. Rodrigues-Rodrigues, N. S. Groot, A. Rimola, A. Alvarez-Larena, V. Lloveras, J. Vidal-Gancedo, S. Ventura, J. Vendrell, M. Sodupe, P. Gonzalez-Duarte, *J. Am. Chem. Soc.*, **131**, 1436 (2009).
9. S.T. Huang, I.J. Hsei, C. Chen, *Bioorg. Med. Chem.*, **14**, 6106 (2006).
10. C.K. Desai, K.R. Desai, *Orient. J. Chem.*, **16**, 311 (2000).
11. H. Moller, D. Oberkobusch, H. Hoeffkes, *Chem. Abstr.*, **134**(12), 168045c (2001).
12. U. Heinemann, H. Gayer, P. Gerdes, B. Krueger, F. Maurer, M. Vaupel, A. Mauler-Machnik, U. Wachendorff-Neumann, G. Haenssler, K. Kuck, C. Erdelen, P. Loesel, *Chem. Abstr.*, **135**(4), 46178y (2001).
13. A. Aminkhani, R. Kabiri, S. M. Habibi-Khorassani, R. Heydari, M. T. Maghsoodlou, G. Marandi, M. Lashkari, M. Rostamizadeh, *J. Sulfur Chem.*, **30**, 500 (2009).
14. M. T. Maghsoodlou, R. Heydari, S. M. Habibi Khorassani, M. K. Rofouei, M. Nassiri, E. Mosaddegh, A. Hassankhani, *J. Sulfur Chem.*, **27**, 341 (2006).
15. Y. Yi, G. Hongyunv, *Chin. J. Org. Chem.*, **31**, 96 (2011).
16. A. Shaabani, A. Rahmati, E. Farhangi, *Tetrahedron Lett.*, **48**, 7291 (2007).
17. A. Kumar, M.-S. Rao, V.-K. Rao, *Aust. J. Chem.*, **63**, 1538 (2010).
18. B. Adrom, N. Hazeri, M. T. Maghsoodlou, M. Mollamohammadi, *Res. Chem. Intermed.*, in press DOI 10.1007/s11164-014-1564-2.
19. S. Javanshir, A. Ohanian, M.M. Heravi, M.R. Naimi-Jamal, F. F. Bamoharram, *J. Saudi Chem. Soc.*, **18**, 502 (2014).
20. A. Hosseinian, H. R. Shaterian, *Phosphorus, Sulfur, and Silicon*, **187**, 1056 (2012).

## УДОБЕН ПОДХОД ЗА ЕДНОСТАДИЙНА ТРИ-КОМПОНЕНТНА СИНТЕЗА НА 1-(БЕНЗОТИАЗОЛАМИНО) МЕТИЛ-2-НАФТОЛ С ФУМАРОВА КИСЕЛИНА КАТО ЗЕЛЕН КАТАЛИЗАТОР

М.Т. Максудлу<sup>1</sup>, М. Карима<sup>1</sup>, М. Лашкари<sup>2</sup>, Б. Адром<sup>1</sup>, Н. Хазери<sup>1</sup>

<sup>1</sup> Департамент по химия, Научен факултет, Университет в Систан и Балучестан, Захедан, Иран

<sup>2</sup> Научен факултет, Велаят, Иранияхр, Иран

Постъпила на 24 август, 2014 г.; приета на 16 септември, 2015 г.

(Резюме)

Описана е едностадийна три-компонентна кондензация на алдехиди, 2-нафтол и 2-аминобензотиазол за синтезата на 1-(бензотиазоламино) метил-2-нафтолови производни с фумарова киселина като ефективен катализатор при висока температура и в отсъствието на разтворител. Този подход предлага няколко предимства: меки условия, високи добиви, чист реакционен профил, оперативна простота, екологично съвместима и проста процедура.

## BTTPC-catalyzed one-pot synthesis of 1,4-dihydropyridine derivatives *via* Hantzsch condensation under solvent-free conditions

M. Alikarami<sup>1\*</sup>, M. Ghasemian<sup>2</sup>

<sup>1</sup>Department of Chemistry, Ilam Branch, Islamic Azad University, Ilam, Iran.

<sup>2</sup>Department of Chemistry, Borujerd Branch, Islamic Azad University, Borujerd, Iran.

Received September 17, 2014, Accepted November 16, 2015

Benzyltriphenylphosphonium chloride (BTTPC) catalyzed efficient Hantzsch reaction *via* three-component coupling reactions of aldehydes, ethyl acetoacetate and ammonium acetate under solvent-free conditions is described for the preparation of 1,4-dihydropyridine derivatives. The process presented here is operationally simple, environmentally benign, inexpensive and gives good to excellent yields.

**Keywords:** Hantzsch reaction, BTTPC, Solvent free, Three-component coupling.

### INTRODUCTION

Five- and six-member heterocyclic compounds are important constituents that often exist in biologically active natural products and synthetic compounds of medicinal interest [1-4]. Among these compounds, 1,4-dihydropyridine (1,4-DHP) heterocyclic rings are a common feature of various bioactive compounds such as vasodilator, bronchodilator, anti-atherosclerotic, anti-cancer and anti-diabetic agents [5–8]. Furthermore, 1,4-DHPs have several other medicinal applications which include neuroprotecting [9] and cerebral anti-ischemic properties for the treatment of Alzheimer's disease [10,11]. Classical method used for the synthesis of these compounds is one-pot condensation of aldehyde with ethyl acetoacetate and ammonia in acetic acid or in refluxing alcohol [12]. This method suffers from several disadvantages such as long reaction time, harsh refluxing conditions, excessive use of volatile organic solvents and low yields. In recent years, due to the importance of 1,4-DHPs, the attention to the synthesis of 1,4-DHPs increased. Different approaches for the synthesis of 1,4-dihydropyridine derivatives using various catalysts, such as cellulose-sulfuric acid [13] triphenylphosphine [14] iron (III) trifluoroacetate [15], ionic liquid [tbmim]Cl<sub>2</sub>/AlCl<sub>3</sub> [16], nickel nanoparticles [17], aluminium phosphate [18], titanium dioxide nanoparticles [19], diphenylammonium triflate [20], visible light [21], melamine trisulfonic acid [22], Cu(OTf)<sub>2</sub> [23], Fe<sub>2</sub>(SO<sub>4</sub>)<sub>3</sub>.xH<sub>2</sub>O [24], Fe<sub>3</sub>O<sub>4</sub>@SiO<sub>2</sub> nanoparticles [25], *p*-TSA [26] and hydrotalcites or hydrotalcite-like materials [27]

have been reported.

Unfortunately, many of these reported methods suffer from major or minor limitations such as the use of expensive reagents, low yields, long reaction times, tedious work-up procedures or the use of hazardous and volatile organic solvents. Thus, the search for new reagents and methods is still of growing importance.

Herein, we report a simple, efficient and cost-effective one-pot method for the synthesis of DHPs from ethyl acetoacetate, ammonium acetate and an aldehyde, using the BTTPC catalyst (Scheme 1).

### RESULTS AND DISCUSSION

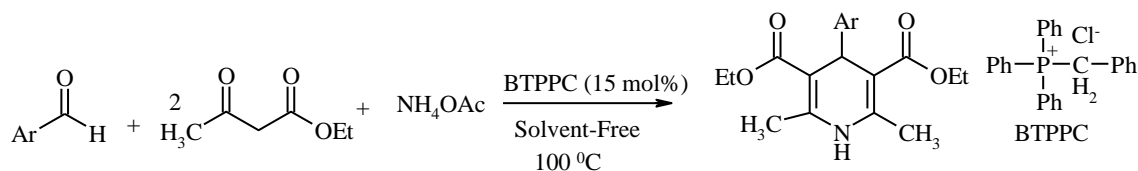
Initially, benzaldehyde was used to react with ethyl acetoacetate and ammonium acetate in the presence of 15 mol% BTTPC in various solvents like EtOH, THF, CHCl<sub>3</sub>, CH<sub>3</sub>CN and DMF at reflux temperature in order to optimize the reaction conditions (Table 1, entries 1–5). The reaction was studied under solvent-free conditions too.

It was found that the best results were obtained with 15 mol% BTTPC under solvent-free conditions (Table 1, entry 6). The reaction was completed within 30 min and the expected product was obtained in a 90% yield.

Next, we studied the effect of temperature on the model reaction. The reaction was studied at various temperatures like room temperature, 60, 100 and 130 °C. The yield of the product increased up to 100°C. After 100°C, the increase in the temperature did not lead to an increase in the yield.

Therefore, our optimized conditions were: 15 mol% of BTTPC, solvent-free at 100 °C, Table 2.

\* To whom all correspondence should be sent:  
E-mail: alikarami58@yahoo.com



**Scheme 1.** Synthesis of 1,4-dihydropyridine derivatives using BTPPC under solvent-free conditions.

**Table 1.** Synthesis of 2,6-dimethyl-4-(phenyl)-1,4-dihydropyridine-3,5-diethylcarboxylate from benzaldehyde, ethyl acetoacetate and ammonium acetate catalyzed by BTPPC under various conditions <sup>a</sup>.

Entry	Solvent	Amount of Catalyst (mol %)	Time (h)	Yield (%) <sup>b</sup>
1	EtOH	15	5	48
2	THF	15	5	43
3	CHCl <sub>3</sub>	15	5	45
4	CH <sub>3</sub> CN	15	5	55
5	DMF	15	5	38
6	None	15	0.5	90

<sup>a</sup> Reaction conditions: benzaldehyde (1 mmol), ethyl acetoacetate (2 mmol) and ammonium acetate (1.5 mmol), the amount of solvent used for entries 1–5 was 5 mL.

<sup>b</sup> Isolated yields.

**Table 2.** Optimisation of temperature using BTPPC (15 mol%) as catalyst <sup>a</sup>.

Entry	Temperature (°C)	Time (h)	Yield (%) <sup>b</sup>
1	r.t	5	-
2	60	1	78
3	100	0.5	90
4	130	0.5	90

<sup>a</sup> Reaction conditions: benzaldehyde (1 mmol), ethyl acetoacetate (2 mmol) and ammonium acetate (1.5 mmol), under solvent-free conditions.

<sup>b</sup> Isolated yields.

**Table 3.** Synthesis of 1,4-dihydropyridine derivatives using aldehyde, ethyl acetoacetate and ammonium acetate in the presence of BTPPC (15 mol%) under solvent-free conditions <sup>a</sup>.

Entry	Ar-H	Product	Yield (%)	Time (min)	M.p. [Lit. m.p. °C]
1			90	30	158 [158-160] <sup>28</sup>
2			75	40	138-140 [140-142] <sup>29</sup>

Table 3 continues on the next page

Table 3 – continuation

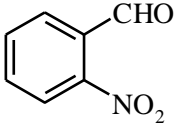
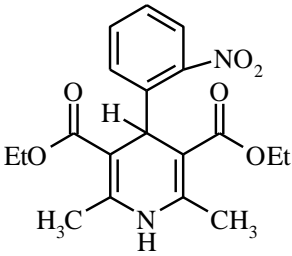
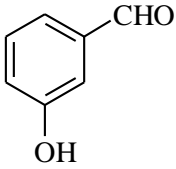
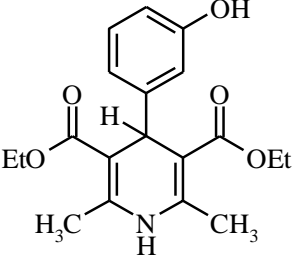
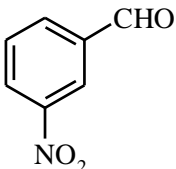
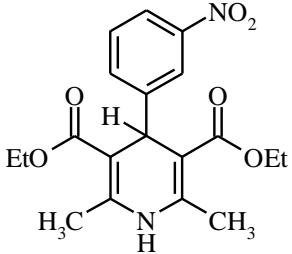
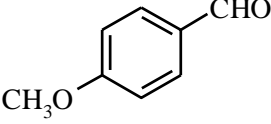
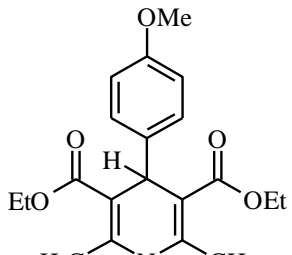
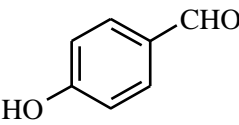
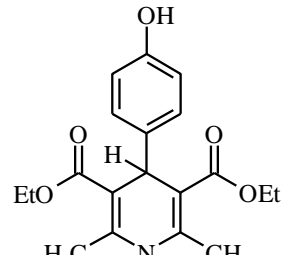
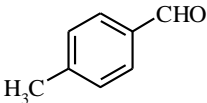
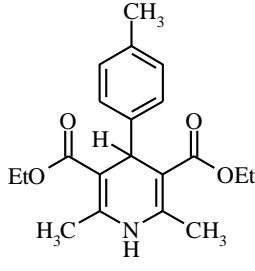
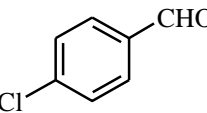
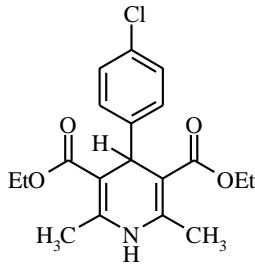
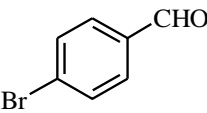
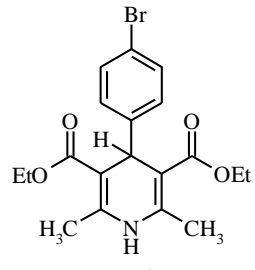
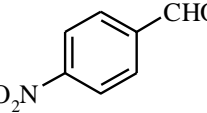
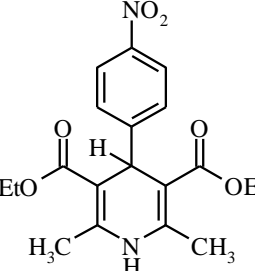
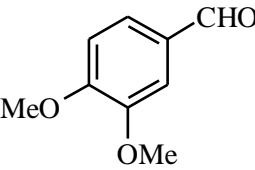
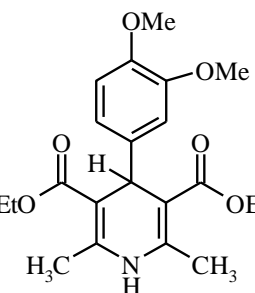
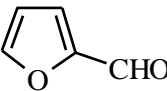
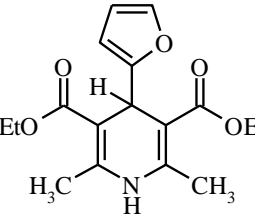
3			75	45	117-119 [118] <sup>21</sup>
4			79	35	179-181 [180-182] <sup>30</sup>
5			80	40	159-161 [161-163] <sup>31</sup>
6			87	30	160-162 [158-160] <sup>30</sup>
7			80	38	230-232 [229-232] <sup>29</sup>

Table 3 continues on the next page

Table 3 – continuation

8			84	35	139-140 [137-139] <sup>32</sup>
9			84	35	143-145 [144-145] <sup>23</sup>
10			82	35	164-166 [160-162] <sup>30</sup>
11			82	35	130-132 [130-131] <sup>31</sup>
12			85	35	160-162 [156-158] <sup>33</sup>
13			87	30	161-163(160-162) <sup>29</sup>

<sup>a</sup> Reaction conditions: aldehyde (1 mmol), ethyl acetoacetate (2 mmol) and ammonium acetate (1.5 mmol), under solvent-free conditions at 100 °C.

<sup>b</sup> Isolated yields.

A series of 1,4-dihydropyridines were synthesized by using diverse aldehydes, ethyl acetoacetate and ammonium acetate in the presence of BTPPC (15 mol%) as a catalyst under solvent-free conditions (Table 3).

As shown in Table 3, the reaction proceeds equally well irrespective of the nature of the carbonyl compounds (aromatic, heteroaromatic) to afford the corresponding products in excellent yields (75–90%). The catalytic system works well. It is noteworthy to mention that the effect of the nature of the substituents on the aromatic ring showed no obvious effect on the conversion, because they were obtained in high yields in relatively short reaction times.

The mechanism of this reaction in the presence of BTPPC is similar to that of Hantzsch reaction mechanism. BTPPC may increase the electrophilic character of the carbonyl carbon of the aldehydes by forming intermolecular bonds between the phosphonium cations and the carbonyl oxygen of the aldehydes.

## CONCLUSIONS

In conclusion, BTPPC was found to be an efficient catalyst in the one-pot reaction of aldehydes, ethyl acetoacetate and ammonium acetate to afford 1,4-dihydropyridines.

The low cost, availability, low toxicity and stability of the catalyst under normal temperatures and pressures, good to excellent yields of products and short reaction times make this methodology a valid contribution to the existing processes in the field of 4-substituted-1,4-dihydropyridines derivatives synthesis.

## EXPERIMENTAL

### Chemicals and Apparatus

All chemicals were obtained from Merck and Fluka Companies. The melting points were measured using an Electrothermal IA 9100 digital melting point apparatus. The IR spectra were recorded on a Bruker (4000–400  $\text{cm}^{-1}$ ) spectrometer.  $^1\text{H}$  NMR spectra were recorded on a 400 MHz spectrometer using TMS as internal standard.

### General Procedure

A mixture of aldehyde (1 mmol), ethyl acetoacetate (2 mmol), and ammonium acetate (1.5 mmol) was stirred at 100 °C in the presence of BTPPC (15 mol%) for the appropriate time. After completing the reaction, as indicated by TLC, the reaction mixture was dissolved in ethanol and

poured into water. The resulting precipitate was filtered and purified by recrystallization from ethanol to afford the desired compound in pure form. All products were identified by comparison of their physical and spectroscopic data with those reported for authentic samples.

Diethyl 1,4-dihydro-2,6-dimethyl-4-phenylpyridine-3,5-dicarboxylate (**Entry 1, Table 3**): IR (KBr):  $\gamma_{\text{max}}$  3342, 1689, 1651, 1491, 1218, 1127, 704 $\text{cm}^{-1}$ .  $^1\text{H}$ NMR (400 MHz, DMSO- $d_6$ ,  $\delta/\text{ppm}$ ): 1.12 (t,  $J= 7.2$  Hz, 6H), 2.25 (s, 6H), 3.98 (m, 4H), 4.85 (s, 1H), 7.21-7.07 (m, 5H), 8.80 (s, 1H).  $^{13}\text{C}$ NMR (100 MHz, DMSO- $d_6$ ,  $\delta/\text{ppm}$ ): 14.2, 19.5, 39.6, 59.7, 104.1, 126.1, 127.8, 128.0, 143.9, 143.7, 167.6.

1,4-Dihydro-2,6-dimethyl-4-(4-methoxyphenyl)pyridine-3,5-dicarboxylate (**Entry 6, Table 3**): IR (KBr):  $\gamma_{\text{max}}$  3342, 2983, 1694, 1491 $\text{cm}^{-1}$ .  $^1\text{H}$ NMR (400 MHz,  $\text{CDCl}_3$ ,  $\delta/\text{ppm}$ ): 1.24 (t,  $J= 7.2$  Hz, 6H), 2.33 (s, 6H), 3.76 (s, 3H), 4.01 (m, 4H), 4.94 (s, 1H), 5.70 (s, 1H), 6.76 (d,  $J= 8.8$  Hz, 2H), 7.21 (d,  $J= 8.8$  Hz, 2H).  $^{13}\text{C}$ NMR (100 MHz,  $\text{CDCl}_3$ ,  $\delta/\text{ppm}$ ): 14.2, 19.5, 38.7, 55.1, 59.7, 104.3, 113.1, 128.9, 140.3, 143.5, 157.8, 167.7.

Diethyl 1,4-dihydro-2,6-dimethyl-4-(4-nitrophenyl)pyridine-3,5-dicarboxylate (**Entry 11, Table 3**): IR (KBr):  $\gamma_{\text{max}}$  3326, 1694, 1646, 1523, 1346, 1218, 1116, 704 $\text{cm}^{-1}$ .  $^1\text{H}$ NMR (400 MHz,  $\text{CDCl}_3$ ,  $\delta/\text{ppm}$ ): 1.23 (t,  $J= 7.2$  Hz, 6H), 2.37 (s, 6H), 4.11 (m, 4H), 5.10 (s, 1H), 5.79 (s, 1H), 7.46 (d,  $J= 8.4$  Hz, 2H), 8.10 (d,  $J= 8.4$  Hz, 2H).  $^{13}\text{C}$ NMR (100 MHz,  $\text{CDCl}_3$ ,  $\delta/\text{ppm}$ ): 14.2, 19.6, 40.1, 60.0, 103.2, 123.3, 128.9, 144.6, 146.3, 155.1, 167.0.

Diethyl 1,4-dihydro-2,6-dimethyl-4-(3,4-dimethoxyphenyl)pyridine-3,5-dicarboxylate (**Entry 12, Table 3**):  $^1\text{H}$ NMR (400 MHz, DMSO- $d_6$ ,  $\delta/\text{ppm}$ ): 1.15 (t,  $J= 7.2$  Hz, 6H), 2.25 (s, 6H), 3.67 (s, 6H), 4.10-3.90 (m, 4H), 4.79 (s, 1H), 6.63 (dd,  $J= 8.4$  Hz, 2.0 Hz, 1H), 6.73 (d,  $J= 2$  Hz, 1H), 6.79 (d,  $J= 8.4$  Hz, 1H), 8.77 (s, 1H).  $^{13}\text{C}$ NMR (100 MHz, DMSO- $d_6$ ,  $\delta/\text{ppm}$ ): 14.7, 18.6, 38.7, 55.7, 55.8, 59.4, 102.4, 111.9, 112.1, 119.6, 141.4, 145.5, 147.5, 148.3, 167.5.

**Acknowledgement:** Financial support of this work from the Research Council of Islamic Azad University of Ilam is gratefully acknowledged.

## REFERENCES

1. A. Mobinikhaledi, N. Foroughifar, S. M. Shariatzade, M. Fallah, *Heterocycl. Commun*, **12**, 427 (2006).
2. G. D. Henry, *Tetrahedron*, **60**, 6043 (2004).
3. J. P. Michael, *Nat. Prod. Rep.*, **22**, 627 (2005).
4. N. I. Abdel-sayed, *Bulg. Chem. Commun.* **42**, 20 (2010).

5. A. Sausins, G. Duburs, *Heterocycles*, **27**, 269 (1988).
6. M. F. Gordeev, D.V. Patel, E. M. Gordon, *J. Org. Chem.*, **61**, 924 (1996).
7. R. A. Coburn, M. Wierzba, M. J. Suto, A. J. Solo, A. M. Triggler, D. J. Triggler, *J. Med. Chem.*, **31**, 2103 (1988).
8. T. Godfraind, R. Miller, M. Wibo, *Pharmacol. Rev.*, **38**, 321 (1986).
9. V. Klusa, *Drugs Fut.*, **20**, 135 (1995).
10. R. G. Bretzel, C. C. Bollen, E. Maeser, K. F. Federlin, *Drugs Fut.*, **17**, 465 (1992).
11. G. Tenti, E. Parada, R. León, J. Egea, S. Martínez-Revelles, A. M. Briones, V. Sridharan, M. G. López, M. T. Ramos, J. C. Menéndez, *J. Med. Chem.*, **57**, 4313 (2014).
12. A. Hantzsch, *Ber. Dtsch. Chem. Ges.*, **21**, 942 (1888).
13. J. Safari, S. H. Banitaba, S. D. Khalili, *J. Mol. Catal. A: Chem.*, **335**, 46 (2011).
14. A. Debache, W. Ghalem, R. Boulcina, A. Belfaitah, S. Rhouati, B. Carboni, *Tetrahedron Lett.*, **50**, 5248 (2009).
15. H. Adibi, H.A. Samimi, M. Beygzadeh, *Catal. Commun.*, **8**, 2119 (2007).
16. B.P. Reddy, K. Rajesh, V. Vijayakumar, *Arab. J. Chem.*, **8**, 138 (2015).
17. L. Saikia, D. Dutta, D. K. Dutta, *Catal. Commun.*, **19**, 1 (2012).
18. K. Purandhar, V. Jyothi, P.P. Reddy, M. A. Chari, K. Muktantid., *J. Heterocycl. Chem.*, **49**, 232 (2012).
19. M. Tajbakhsh, E. Alaee, H. Alinezhad, M. Khanian, F. Jahani, S. Khaksar, P. Rezaee, *Chin. J. Catal.*, **33**, 1517 (2012).
20. J. Li, P. He, Ch. Yu, *Tetrahedron*, **68**, 4138 (2012).
21. S. Ghosh, F. Saikh, J. Das, A. K. Pramanik, *Tetrahedron Lett.*, **54**, 58 (2013).
22. S. Sheik Mansoor, K. Aswin, K. Logaiya, S.P.N. Sudhan, *Journal of King Saud University – Science*, **25**, 191 (2013).
23. A. S. Paraskar, A. Sudalai, *Indian J. Chem.*, **46B**, 331 (2007).
24. K. Islama, D. K. Dasa, A. T. Khana, *Tetrahedron Lett.*, **55**, 5613-5617, (2014).
25. B. Dam, S. Nandi, A. K. Pal, *Tetrahedron Lett.*, **55**, 5236 (2014).
26. M. Nasr-Esfahani, M. Montazerzohori, R. Raeatikia, *Maejo Int. J. Sci. Technol.*, **8**, 32-40 (2014).
27. Ch. A. Antonyraj, S. Kannan, *Applied Catalysis A: General*, **338**, 121 (2008).
28. A. Debache, L. Chouguiat, R. Boulcina, B. Carboni, *The Open Organic Chemistry Journal*, **6**, 12 (2012).
29. L. Ming, G. Wei-Si, W. Li-Rong, L. Ya-Feng, Y. Hua-Zheng, *J. Mol. Catal. A: Chem.*, **258**, 133 (2006).
30. Y. L. N. Murthy, A. Rajack, M. T. Ramji, J. J. Babu, Ch. Praveen, K. A. Praveen, *Bioorg. Med. Chem. Lett.*, **22**, 6016 (2012).
31. S. Sajjadifar, H. Saeidian, S. Zare, H. Veisi, S. Rezaeyati, *Iranian Chem. Commun.*, **1**, 7 (2013).
32. S. M. Vahdat, F. Chekin, M. Hatami, M. Khavarpour, S. Bagheri, Z. Roshan-Kouhi, *Chinese Journal of Catalysis*, **34**, 758 (2013).
33. T. Shahani, H. K. Fun, B. P. Reddy, V. Vijayakumar, S. Sarveswari, *Acta Crystallographica Section E: Struct. Rep. Online*, **66**, 1355 (2010).

## ВТРРС-КАТАЛИЗИРАНА ЕДНОСТАДИЙНА СИНТЕЗА НА 1,4-ДИХИДРОПИРИДИНОВИ ПРОИЗВОДНИ ЧРЕЗ КОНДЕНЗАЦИЯ НА HANTZSCH БЕЗ РАЗТВОРИТЕЛ

М. Аликарами<sup>1</sup>, М. Гасемян<sup>2</sup>

<sup>1</sup> Департамент по химия, Клон Илам, Ислямски университет „Азад“, Илам, Иран

<sup>2</sup> Департамент по химия, Клон Боруджерд, Ислямски университет „Азад“, Боруджерд, Иран

Постъпила на 17 септември, 2014 г.; приета на 16 ноември, 2015 г.

(Резюме)

Бензил-трифенил-фосфониев хлорид (ВТРРС) катализира ефективна реакция на Hantzsch чрез три-компонентна синтеза на 1,4-дихлоропиридинови производни от алдехиди, етилацетат и амониев ацетат в условия без разтворител. Процесът е прост за изпълнение, екологично съвместим, евтин и с добри до отлични добиви.

## Chromium(VI) removal from water by using polyaniline biocomposites with *Madhuca longifolia* and *Szygium cumini* leaves

F. Kanwal, R. Rehman\*, S. Rasul, K. Liaqat

*Institute of Chemistry, University of the Punjab, Lahore-54590, Pakistan*

Received December 12, 2014; Revised February 26, 2016

Biocomposites of polyaniline with *Madhuca longifolia* (PANI/ML) and *Szygium cumini* (PANI/SC) were synthesized, characterized and used for batch-wise adsorption of Cr(VI) from water. Optimum conditions for PANI/ML: 20 min contact time, adsorbent dose 0.3 g in 50 mL solution of Cr(VI), 50° C temperature and pH 2; and for PANI/SC: 80 min contact time, adsorbent dose 0.1 g in 50 mL solution of Cr(VI), 10° C temperature and pH 5. Langmuir isotherm shows that chemisorptive monolayer removal of Cr(VI) has occurred on the composite binding sites. 13.334 mg/g is the maximum adsorption capacity of PANI/ML, in case of PANI/SC it is 4 mg/g.  $\Delta G^\circ$  negative value confirms the feasibility and spontaneity of the adsorption process. Freundlich isotherm tells about heterogeneously distributed sites and physio-sorptive metal ion removal. For PANI/ML and PANI/SC the constant  $K_F$  values are 0.019 and 0.005, respectively. Results revealed that PANI/ML is a better ecofriendly biocomposite for Cr(VI) removal from water as compared to PANI/SC.

**Keyword:** Cr(VI), Polyaniline composites, ecofriendly, leaves, water.

### INTRODUCTION

In Pakistan uncontrolled industrialization has become the main cause of environmental degradation. Industrial effluents which contain hazardous substances and heavy metals are disposed either into water bodies or onto open land directly or indirectly. Through different routes these hazardous substances enter and disturb the lifecycle and also cause diseases, e.g, cancer [1]. One of these toxic substances is chromium which is present in aqueous systems in trivalent and hexavalent form. Different industries, for example metal finishing, pigments, glass, inks, dyes, certain glues and ceramics use chromium [2]. Heavy metals are not biodegradable and bring high level toxicity to the environment [3].

The French chemist Vauquelin discovered chromium in 1798 [4]. Cr(VI) is more poisonous than Cr(III) [5]. Cr (VI) compounds are responsible for many clinical problems. Its retention and inhalation can cause asthma, nasal septum perforation, pneumonitis, bronchitis, liver and larynx inflammation, and bronchogenic carcinoma [6-8]. For Cr(VI) removal, adsorption on activated carbon is a very efficient process but it is very expensive [9]. In the last decades, metal ion adsorption by conducting polymers as PANI and polythiophene has been reported [10]. Among conducting polymers polyaniline (PANI) is very efficient. Abundant amine and imine groups in it

can chelate metal ions [8]. In this research work, polyaniline composites with plant leaves of *Szygium cumini* (Jamun) PANI/SC, and *Madhuca longifolia* (Mahva) PANI/ML were prepared and used for Cr(VI) adsorption in batch mode.

### EXPERIMENTAL WORK

Instruments used were: Digital balance, Chiller apparatus Caoran CAN-7000-B, FT-IR spectrophotometer, atomic absorption spectrophotometer (Perkin Elmer Analyst 100). Chemicals used were: aniline monomer, anhydrous ferric chloride, HCl (AnalaR), DMF (PRS Panreac), acetone (BDH). Aniline was purified by distillation before use. The middle fraction of the distillate was collected, kept under nitrogen atmosphere and stored in a refrigerator. Aniline polymerization was carried out as already reported [7].

#### *Synthesis of PANI composites with Szygium cumini, Madhuca longifolia leaves*

The composites were prepared in a similar way as already reported [11] and characterized by UV/Visible spectroscopy and FT-IR.

#### *Preparation of stock solution and standards for adsorption studies of Cr (VI):*

For a stock solution of 1000 ppm, 2.82 g of potassium dichromate was dissolved in 1000 ml of water and further standards were prepared by dilution.

\* To whom all correspondence should be sent:  
E-mail: grinorganic@yahoo.com

### ADSORPTION STUDIES

The adsorption studies of Cr(VI) were carried out in batch mode separately for both composites as described earlier [7]. The percent removal of Cr(VI) ions was calculated by:

$$\text{Adsorption \% age} = [(C_{in} - C_{fin}) / C_{in}] \times 100$$

where  $C_{in}$  is the initial concentration of Cr(VI),  $C_{fin}$  is Cr(VI) concentration after adsorption.

### RESULTS AND DISCUSSION

#### UV/VISIBLE spectroscopic analysis

PANI and its composites were analyzed after dissolution in dimethyl formamide and their spectra were taken. The  $\lambda_{max}$  of PANI and its composites are given in Table 1. Absorption at  $\lambda_{max1}$  330 nm is due to a  $\pi - \pi^*$  transition of aniline in the benzenoid ring [11]. Absorption at 645 nm is due to an excitonic transition of benzenoid to quinonoid ring. Presence of two peaks in the UV/Vis spectra shows that two non equivalent rings, benzenoid and quinonoid, are present in the polymer chain.

#### FT-IR Characterization

FT-IR was used to characterize PANI and its composites (PANI/ML, PANI/SC) and relevant peaks are given in Table 2 [12]. By comparing the FT-IR spectra of PANI and its composites (PANI/ML, PANI/SC) it was observed that the

band (due to amino group (N-H) [13] stretching frequency) for PANI at  $3431 \text{ cm}^{-1}$  is shifted to  $3425 \text{ cm}^{-1}$  in case of PANI/ML and PANI/SC. The absorption band at  $1571 \text{ cm}^{-1}$  is due to benzenoid to quinonoid rings nitrogen bond, because of benzenoid to quinonoid transition. In case of PANI/ML it is shifted to  $1584 \text{ cm}^{-1}$  and in case of PANI/SC - to  $1575 \text{ cm}^{-1}$ . Peaks due to secondary amine stretching [14] are shifted from  $1293 \text{ cm}^{-1}$  (PANI) to  $1288 \text{ cm}^{-1}$  (PANI/ML) and  $1266 \text{ cm}^{-1}$  (PANI/SC). Bands in the range of  $1571\text{-}1116 \text{ cm}^{-1}$  are due to the conductive nature of PANI.

#### CONDUCTIVITY MEASUREMENTS

The conductivity of PANI and its composites was measured by the Four Probe Method using Keithley 4200-SCS. The conductivity of polymers depends upon their size, type of monomer, doping level, shape, and interaction between filler molecules. Temperature dependent conductivity measurements were carried out with the samples at room temperature. Results in Table 3 show that PANI/ML is less conductive than PANI/SC. Its lower conductivity is due to the poorer connectivity between grinded leaves and polymer due to which its compactness and packing density decrease, because of the presence of chains of polymer not supported by leave particles, so conductivity also decreases [11].

**Table 1.**  $\lambda_{max}$  of PANI and its composites

Sample	$\lambda_{max1}$ (nm)	Absorbance	$\lambda_{max2}$ (nm)	Absorbance
PANI	330	0.376	645	.285
PANI/SC	330	0.373	635	.227
PANI/ML	325	0.327	645	.169

**Table 2.** FT-IR analysis of PANI and its composites

Vibrational Assignment	Reference absorption band ( $\text{cm}^{-1}$ )	PANI ( $\text{cm}^{-1}$ )	PANI/ML ( $\text{cm}^{-1}$ )	PANI/SC ( $\text{cm}^{-1}$ )
N-H Stretching	3426	3431	3425	3425
N=Q=N	1577	1571	1583	1575
N=B=N	1489	1493	1499	1499
-C=N Stretching	1295	1293	1288	1266
Aromatic C-N-C	1121	1116	1132	1132

**Table 3.** Conductivity, resistivity and thickness of PANI and its composites.

Sr. No.	Samples	Thickness (cm)	Resistivity ( $\Omega$ )	Conductivity (S/cm)
1.	PANI	0.014	60.3613	$16.5669 \times 10^{-3}$
2.	PANI/ML	0.0172	$1.6495 \times 10^3$	$606.2393 \times 10^{-6}$
3.	PANI/SC	0.0188	76.42753	$1.3084 \times 10^{-2}$

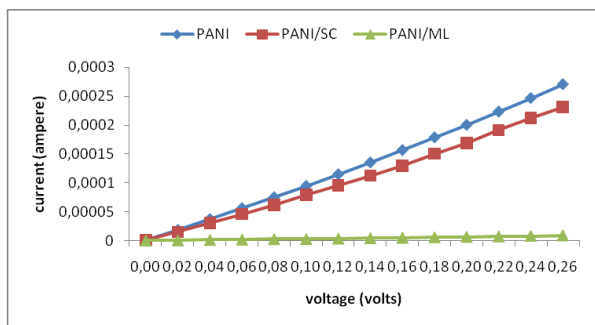


Fig.1. I-V Plots by PANI and its composites.

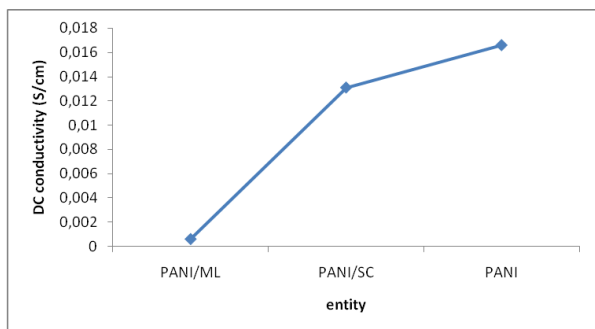


Fig.2. Comparison of conductivity of PANI and its composites.

## BATCH ADSORPTION EXPERIMENTS

### ADSORBENT DOSE

The effect of various adsorbent doses was studied for the percent removal of Cr(VI) metal. The results are given in Fig.3. The maximum percent removal of Cr (VI) was observed with 0.1 g of PANI/SC (89.52% removal) and 0.3 g of PANI/ML (91.03% removal). The results revealed that preventing the PANI/ML particles from aggregation and exposing Cr(VI) towards available active sites for adsorption showed greater efficiency in its removal. In case of PANI/ML adsorption firstly increases and then decreases because of adsorbent particles coagulation, due to which the number of sites available for adsorption decreases [12].

### CONTACT TIME

Adsorption phenomenon is time dependent. The effect of different time intervals on the percent removal of Cr (VI) by PANI/ML and PANI/SC was observed. Results are shown in Fig.4. The maximum percent removal value was 82 % for PANI/SC composite for 80 min, and 88.236 % for PANI/ML composite for 20 min. The reduced time interval for maximum removal of Cr(VI) using PANI/ML composite showed that it has more adsorption sites which are available for adsorption of metal ions. After the maximum removal of Cr (VI), the adsorption decreased with increase in

contact time because all available sites were occupied [13]. PANI/ML was more appropriate for removal of Cr (VI) than PANI/SC.

### METAL SOLUTION pH

The results of the pH study are shown in Fig.5. Solution pH is responsible for the type and ionic state of functional groups present on the sorbing material and the ionic state of chromium. Cr(VI) is converted to Cr(III) in acidic medium, which is further converted to  $\text{Cr(OH)}_2^{2+}$  and  $\text{Cr(OH)}_2^+$ , that can interact with  $-\text{NH}$ ,  $\text{N}=\text{Q}=\text{N}$  and  $\text{N}=\text{B}=\text{N}$  functional groups of PANI composites [14-18]. The Cr(VI) adsorption mechanism on the composites may be an exchange between the  $\text{Cl}^-$  and  $\text{Cr}_2\text{O}_7^-$  anions [19,21]. The maximum percent removal value was 88.666 % for PANI/SC composite at pH 5 and 91.03 % for PANI/ML composite at pH 2. PANI/ML was more appropriate for removal of Cr(VI) than PANI/SC.

### TEMPERATURE

The adsorption of Cr (VI) was studied at various temperatures ranging from 10 to 100° C on PANI/ML and PANI/SC (Fig.6). The maximum percent removal of Cr(VI) was observed at 10 °C using PANI/SC and at 50 °C using PANI/ML composite. The percent removal values were 85.655 and 87.161% for PANI/SC and PANI/ML composites, respectively. The results showed that PANI/ML was more appropriate for removal of Cr(VI) than PANI/SC.

### ADSORPTION ISOTHERMS

The Langmuir and Freundlich isotherms for PANI/ML and PANI/SC are shown in Tables 4 and 5, respectively.

Table 4. Langmuir isothermal parameters

Adsorbent	Slope	Intercept	R <sup>2</sup>	q <sub>m</sub> (mg/g)	b (L/mg)	ΔG° (KJ/mol)	R <sub>L</sub>
PANI/ML	13.27	0.075	0.912	13.334	0.005	-13.129	0.7
PANI/SC	13.99	0.250	0.979	4.0	0.017	-10.096	0.5

Table 5. Freundlich isothermal parameters

Adsorbent	Slope	Intercept	R <sup>2</sup>	K <sub>F</sub>	n
PANI/ML	1.730	1.710	0.853	0.019	0.578
PANI/SC	1.749	2.272	0.862	0.005	0.571

Langmuir isotherm indicated that monolayer chemisorptive removal of Cr(VI) ions has occurred on the homogeneously distributed composites' binding sites [22-24]. It is predominant over the Freundlich model. This means that chemisorption is predominant over physisorption, as indicated by the greater R<sup>2</sup> value of Langmuir than Freundlich. Maximum adsorption capacity (q<sub>m</sub>) values for

PANI/ML and PANI/SC are 13.34 and 4 mg/g, respectively.

The negative sign of  $\Delta G^\circ$  showed that the adsorption process is feasible and spontaneous. Results revealed that PANI/ML shows better adsorption than PANI/SC, where 'n' and 'K<sub>F</sub>' are Freundlich isotherm constants. 'K<sub>F</sub>' value was 0.019 and 0.005 for PANI/ML and PANI/SC, respectively. For Cr(VI) ions the value of 'n' was 0.578 for PANI/SC and 0.571 for PANI/JL. Separation factor R<sub>L</sub> value is between 0 and 1, indicating the favorability of this process [23]. At higher values of 'n' the affinity and heterogeneity of adsorbent sites will be greater.

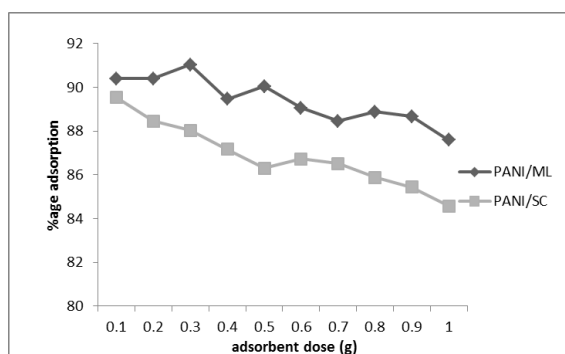


**Fig. 3.** Comparative graph of PANI/ML and PANI/SC showing the effect of adsorbent dose on the % adsorption of Cr(VI).

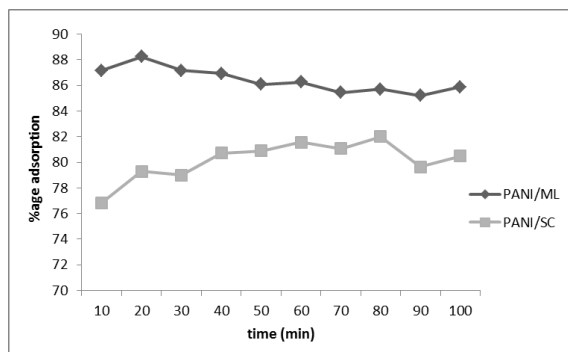


**Fig. 4.** Comparative graph of PANI/ML and PANI/SC showing the effect of contact time on the % adsorption of Cr(VI).

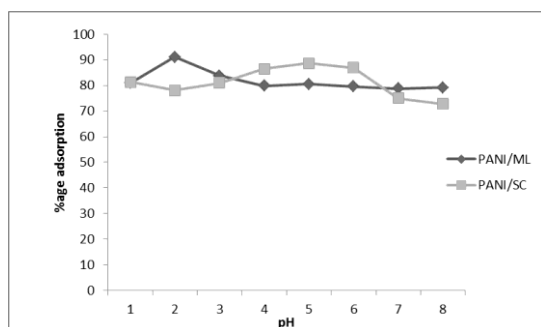


**Fig. 5.** Comparative graph of PANI/ML and PANI/SC showing effect of pH on the % adsorption of Cr(VI).

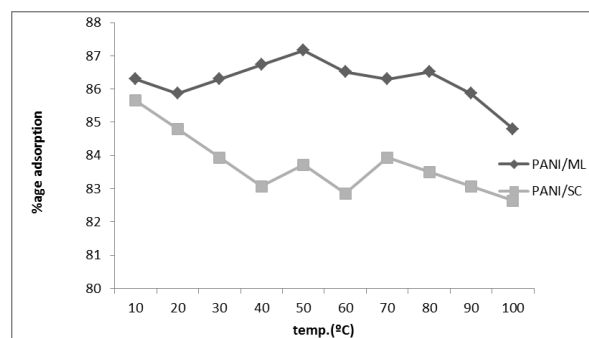


**Fig. 6.** Comparative graph of PANI/ML and PANI/SC showing the effect of temperature on the % adsorption of Cr(VI).

## CONCLUSIONS

Polyaniline composites PANI/ML and PANI/SC were synthesized, characterized and used as adsorbents for Cr(VI) removal from water. It was observed that PANI composite formation enhanced the adsorption capacity due to morphology modification and prevention of polyaniline particles aggregation. The batch experiments showed that Langmuir adsorption isothermal model is better fitted during adsorption of Cr(VI), which suggested that chemisorption occurred during removal of Cr(VI). The negative value of  $\Delta G^\circ$  confirmed the spontaneity and feasibility of the adsorption process. The observed trend of adsorption is

$$\text{PANI/ML} > \text{PANI/SC}.$$

Results revealed that polyaniline composites with *Syzygium cumini* (PANI/SC), and *Madhuca longifolia* (PANI/ML) are good adsorbents for removal of Cr(VI).

## REFERENCES

1. S.A. Khan, Riaz-ur-Rehman, M. Ali Khan, *Waste Manag.*, **15**, 271 (1995).
2. C. Namasivayam, R.T. Yamuna, *Chemosphere*, **30**, 561 (1995).
3. R.K. Gupta, R.A. Singh, S.S. Dubey, *Sep. Purif. Tech.*, **38**, 225 (2004)
4. A.K. Shanker, C.Cervantes, H. Loza-Tavera, S. Avudainayagam, *Env. Int.*, **31**, 739 (2005).
5. M.R. Samani, S.M. Borghei, A.Olad, M.J. Chaichi, *J. Hazard. Mat.*, **184**, 248 (2010).
6. J. Kotas, Z. Stasicka, *Env. Poll.*, **107**, 263 (2000).
7. F.Kanwal, R.Rehman, J. Anwar , M. Saeed, *J. Chem. Soc. Pak.*, **34**,1134 (2012).
8. Q. Li, L. Sun, Y. Zhang, Y. Qian, J. Zhai, *Desalination*, **266**, 188 (2011).
9. E. Malkoc, Y. Nuhoglu, M. Dundar, *J. Hazard. Mat.,B*, **138**, 142 (2006).
10. A.G Yavuz, E. Dincturk-Atalay, A.Uygun, F. Gode, E. Aslan, *Desalination*, **279**, 325, (2011).

11. F.Kanwal, A. Batool, S. Rasool, S. Naseem, R. Rehman, *Asian J. Chem.*, **26**, 7519 (2014).
12. K.Y. Xu, X. Zheng, C.L. Li and W.L. She, *Phys. Rev.*, **71**, 066604 (2005).
13. J.B. Pendry, A.J. Holden, W.J. Stewart, I. Youngs, *Phys. Rev. Lett.*, **76**, 4773 (1996).
14. L. Ai, J. Jiang, R. Zhang, *Syn Mat*, **160**, 762 (2010).
15. A.Olad, A. Rashidzadeh, *Iranian J. Chem. Eng.*, **5**, 45 (2008).
16. O.V.Dalgov, D.A.Kirzh, E.G.Maksimov, *Rev. Mod. Phys.*, **53**, 81, (1981).
17. P.A.Kumar, S.Chakraborty, M.Ray, *J. Chem. Eng.*, **141**, 130 (2008).
18. J.Anwar, U.Shafique, W.Zaman, M.Salman, Z.Hussain, M.Saleem, N.Shahid, S.Mahboob, S.Ghafoor, M.Akram, R.Rehman, N. Jamil, *Green Chem. Lett. Revs.*, **3**, 239 (2010).
19. Y.Zhang, Q.Li, L.Sun, R.Tang, J.Zhai, *J. Hazard. Mat.*, **175**, 404 (2010).
20. F.Kanwal, R. Rehman, J. Anwar, T. Mahmud, *EJEAFChe*, **10**, 2972, (2011).
21. R.Rehman, J. Anwar, T. Mahmud, *J. Chem. Soc. Pak.*, **34**, 460 (2012).
22. Li. X, M. Zhong, *J. Sep. Sci.*, **31**, 2839, (2008).
23. F. Kanwal, R.Rehman, J. Anwar and T. Mahmud, *J. Chil. Chem. Soc.*, **57**, 1058 (2012).
24. J. Anwar, U. Shafique, M. Salman, W. Zaman, S. Anwar, *J. Hazard. Mat.*, **171**, 797 (2009).

## ОТСТРАНЯВАНЕ НА ХРОМ (VI) ОТ ВОДИ С ИЗПОЛЗВАНЕТО НА ПОЛИАНИЛИНОВИ БИОКОМПОЗИТИ С ЛИСТА ОТ *Madhuca longifolia* И *Szygium cumini*

Ф. Канвал, Р. Рехман\*, С. Расул, К. Лиакат

*Институт по химия, Университет на Пунджаб, Лахор-54590, Пакистан*

Постъпила на 12 декември, 2014 г.; коригирана на 26 февруари, 2016 г.

(Резюме)

Синтезирани са биоконпозити от полианилин с листа от *Madhuca longifolia* (PANI/ML) и *Szygium cumini* (PANI/SC). Те са охарактеризирани и използвани за периодична адсорбция на Cr(VI) от вода. Оптималните условия за PANI/ML са: контактно време 20 мин., доза адсорбент 0.3 г в 50 mL разтвор на Cr(VI), 50° C и pH 2. За PANI/SC: контактно време 80 мин., доза адсорбент 0.1 г в 50 mL разтвор на Cr(VI), 10° C и pH 5. С помощта на изотермата на Лангмюир е показано, че отстраняването на хрома става чрез мономолекулярна хемисорбция върху активните центрове на адсорбента. Максималният адсорбционен капацитет на PANI/ML е 13.334 mg/g, докато за PANI/SC той е 4 mg/g. Отрицателната стойност на  $\Delta G^\circ$  потвърждава надеждността и спонтанността на адсорбционния процес. Изотермата на Freundlich свидетелства за хетерогенно разположени активни центрове и физичното отстраняване на металните йони. Стойностите на  $K_F$  за PANI/ML и PANI/SC са съответно 0.019 и 0.005. Резултатите показват, че PANI/ML е екологично по-добър биоконпозит за отстраняването на Cr(VI) от води спрямо биоконпозита PANI/SC.

## Effect of ultraviolet radiation on the free radicals formation in hypothyroid rat's liver

M. L. Valcheva-Traykova<sup>1\*</sup>, G. S. Bocheva<sup>2</sup>

<sup>1</sup>Department of Medical Physics and Biophysics, Faculty of Medicine, Sofia Medical University, 2 Zdrave Street, 1431 Sofia, Bulgaria

<sup>2</sup>Department of Pharmacology and Toxicology, Faculty of Medicine, Sofia Medical University, 2 Zdrave Street, 1431 Sofia, Bulgaria

Submitted February 27, 2015; Accepted September 3, 2015

Prolonged exposure to sunlight or solar simulated UV irradiation (SSUV) leads to oxidative stress in tissues. The literature data concerning the effect of this factor on hypothyroidism are controversial. The aim of this study was to investigate the influence of hypothyroidism and UV radiation on free radicals formation in rat's liver. After one week of adaptation, hypothyroid model was developed in 4 weeks, by continuous administration of 0.01% 6-n-propyl-2-thiouracil in the drinking water of male Wistar-Albino rats. Hypothyroidism was confirmed by the significant reduction of blood free thyroxin (approximately 0.44 ng/l, while 18 ng/l in the controls). The model was also proved by the loss of both appetite and body weight gain of the hypothyroid rats. During the 6-th week of the experiment, half of the PTU treated rats were irradiated with SSUV lamp for 60 min, divided into 4 portions with respective 15 min breaks. After decapitation, the accumulation of free radicals in rats' livers was measured spectrophotometrically using MTT-assay. Data were presented as percentage of the corresponding data for controls.

Alone, SSUV irradiation increased, while hypothyroidism decreased the free radicals accumulation in the rat liver. This was in agreement with the literature data about the individual effects of these factors on the oxidative stress. When the SSUV irradiation was applied on the hypothyroid rats, the relative increase of the free radicals in the liver was much higher than that in the livers of SSUV irradiated normothyroid animals.

**Key words:** hypothyroidism, UV radiation, free radicals, liver

### INTRODUCTION

Prolonged exposure to sun or solar simulated UV (SSUV) irradiation leads to accumulation of free radicals in the skin [1], immune suppression and synthesis of excessive proinflammatory cytokines, all resulting in oxidative stress in different tissues [2,3]. The sunburn and UV-radiation are major factors for set-up and development of UV-initiated diseases [4-7]. Clinical, biochemical and histological observations showed that both humans and animals develop hypothyroidism during long lasting spaceflight [8]. This has been associated with effects of sub-apoptotic doses of UVC [9], which compromised thyrocytes proliferation and the expression of genes involved in thyroid hormones production.

Thyroid hormones are involved in setting of the basal metabolic rates in the liver [10] and in decreasing of the oxidative stress-induced toxicity both in animals and humans [11,12]. But literature data about oxidative stress levels in hypothyroidism are controversial. Thyroid dysfunction was associated with enhanced oxidative stress [13] due to reduced antioxidant defense [14,15] and

increased free radicals production [16,17], although the interrelation is complicated. The oxidative stress in subclinical hypothyroidism has been associated with secondary hypercholesterolemia to thyroid dysfunction, but not to the hypothyroidism *per se* [18]. Other experimental data proved that the decreased metabolic rates due to hypothyroidism can diminish the tissue damages, opposing the deleterious effects of both increased free radicals and incapacitated antioxidant defense [19-21].

As thyroid hormones are involved in the control over the oxidative stress in a very complex manner, and the pre-exposition to solar (or solar simulated) UV radiation tends to initiate oxidative stress in tissues, the question arises about the effect of the prolonged exposition to sun or SSUV radiation on individuals with hypothyroidism.

In the present work, the effect of systemic pre-exposition to SSUV radiation on the free radicals production in the liver of hypothyroid rat model was estimated. The aim of the study was to monitor the individual and mutual effects of SSUV and hypothyroidism on the free radicals accumulation in the liver, and to compare this parameter with the corresponding level for the control animals. The accumulation of free radicals in a tissue is among the major factors for developing of the oxidative stress, later resulting in tissue damage. The free radicals accumulation was monitored by using

\* To whom all correspondence should be sent:  
E-mail: m\_traykova@mail.bg

spectrophotometric method, with MTT as a marker molecule. The activity of xanthine oxidase was estimated using uric acid as a marker.

## MATERIALS AND METHODS

*Animal model:* 30 male Wistar albino rats of body weight  $135 \pm 5$  g were separated in 4 groups named C (control), UV (normothyroid rats exposed to SSUV), PTU (hypothyroid rats) and PTU+UV (hypothyroid rats exposed to SSUV), housed in transparent standard containers. All animals were treated in agreement with the General regulations for treatment of experimental animals, established by the Ethic Committee at the Medical University of Sofia, in agreement with the "Guide to the care and use of Experimental Animal Care" (Canadian Council on Animal Care Guidelines, 1984).

After one week of adaptation, the groups PTU and PTU+UV were provided with 0.01% (w/w) aqueous solution of 6-n-propyl-2-thiouracil (Sigma-Aldrich), *ad libitum* for 5 weeks. The water and food consumptions were measured everyday, at the same hour, and data were used to calculate the average daily food and water consumption of one animal of a group. The body weight of the rats was measured two times per week, and the weekly body weight gain of an animal in a group was estimated. The average daily dose of 6-n-propyl-2-thiouracil consumed by the model animals was  $16 \pm 3$  mg/kg<sub>BW</sub>. At the end of the fourth week of the experiment, FT<sub>4</sub> was measured for each group. During the 5-th week, the normothyroid UV group and the hypothyroid PTU+UV group were exposed to ultraviolet radiation, by using UV lamp (type "Helios" 125W, IBORA, Bulgaria). The lamp combined UV (180 – 400 nm) and IR sources adjusted to mimic sunlight. The SSUV source was positioned at a distance of one meter from the animals' cage. The two groups were irradiated for 15 min four times per day, with periods of 15 min pause between sessions.

*Preparation of the supernatanta:* After the 7-th day of SSUV-exposure all animals were decapitated under anesthesia (Urethane, 2 mg/100 g BW). Livers were extracted and homogenized in sonified ice-cold PBS (50 mM, pH 7.45) solution of 0.04% BHT (for preventing the autooxidation with oxygen in the air). The homogenates were prepared using "Mechanik Prezsizna" type 302 homogenizer, at a speed of 2500 rpm and 20 vertical movements of the vessel. After centrifugation at 4°C and 2500 rpm for 10 min in a centrifuge (JERNETZKI K24), the supernatanta was collected and stored in ice-cold bath.

The amount of proteins in the supernatanta was determined as described by Stoscheck [22].

*Xanthine oxidase activity assessment:* The activity of xanthine oxidase was determined by measuring the relative change of the absorbance at 293 nm due to transformation of xanthine to uric acid, in a quartz cuvette, as previously described [23]. Briefly, one milliliter of the cuvette contained 0.02 ml xanthine solution, 0.02 ml supernatanta, and 0.96 ml PBS, against reference cuvette containing PBS. The blank measurement was performed by estimation of the relative change of the absorbance at 293 nm in a sample in PBS alone, with reference cuvette containing PBS. The amount of uric acid formed in the cuvette for one minute was calculated after subtracting the relative change of the absorbance at 293 nm measured in the blank sample. The activity of xanthine oxidase was calculated in mU/mg proteins, one unit of the enzyme being the amount needed to convert 1  $\mu$ mole of xanthine to uric acid for one minute at 25°C. To assess the effect of the treatment on the xanthine oxidase activity, the latter was presented as a percentage of this for the control group.

*Measurement of the free radicals accumulation:* The accumulation of free radicals in the liver supernatanta was evaluated using a marker molecule named MTT (Nitroblue tetrazolium bromide; Sigma-Aldrich) [23,24]. In presence of free radicals MTT transforms to formazan [25], with characteristic absorbance at 578 nm [25,26]. Recently, MTT has been successfully used in evaluations of free radicals accumulation in presence of pharmaceuticals [24,27], plant extracts [28,29] and animal tissues [30], proving to be very efficient and cheap. One ml of the cuvette contained 0.02 ml liver supernatanta, 0.02 ml xanthine, 0.1 ml MTT and PBS. The relative change of the absorbance at 576 nm was monitored for 5 min. The amount of MTT formazan formed for one minute in the presence of supernatanta, containing 1 mg proteins was calculated, and then data were presented as percentage of these for the control animals.

*Statistical analysis.* All parameters were presented as percentages of the corresponding parameter for the control animals. The activity of the xanthine oxidase and the formation of MTT-formazan were treated as two factors, each of them having four levels ("control", "hypothyroid", "SSUV- irradiated", and "hypothyroid and SSUV- irradiated").

The statistical significance of the mean values and standard deviations for each factor were

analyzed using Bartlett test, followed by ANOVA and Bonferoni post-test.

## RESULTS

The hypothyroidism was achieved at the end of the 4-th week, as proved by both low free thyroxin ( $0.44 \pm 0.31$  ng/l compared with  $18.41 \pm 0.28$  ng/l for the controls), loss of appetite, as well as by the loss of weight gain ( $p < 0.01$ , Figure 1).

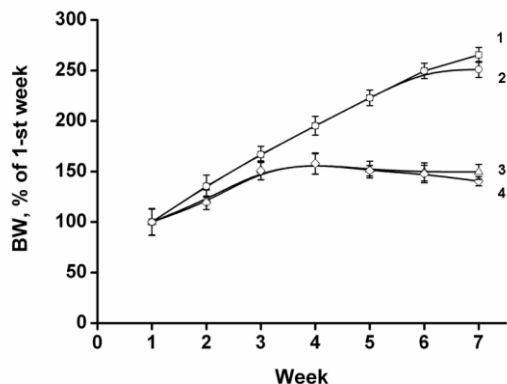


**Fig. 1.** Effect of 6-n-propyl-2-thiouracil on the body weight gain (BW, % of the 1-st week) of the experimental animals: 1 (□)- body weight of the control norm thyroid animals (group C); 2 (○)- body weight of the normothyroid rats exposed to SSUV-radiation (group UV); 3 (Δ)- body weight of the hypothyroid animals (group PTU); 4 (◇)- body weight of the hypothyroid animals exposed to SSUV-radiation for one week (group PTU+UV).

In agreement with literature [31-33], the loss of the body weight gain was associated with the decreased appetite of the animals, due to drastically decreased thyroid hormones levels.

Our data, presented in Figure 1, suggested that the hypothyroidism was the main factor for the loss of body weight gain ( $p < 0.001$ ). The SSUV exposure resulted in a slight but statistically significant ( $p < 0.05$ ) additional body weight loss for the normothyroid group.

When applied alone, SSUV treatment increased, while 6-n-propyl-2-thiouracil decreased the activity of xanthine oxidase, compared with the control group (Figure 2).

The activity of xanthine oxidase in the livers of the hypothyroid rats (group PTU) was ( $47 \pm 4$ )% of this in the livers of the control animals. This decrease could be related with the decreased overall metabolic rates of the animals due to 6-n-propyl-2-thiouracil-induced hypothyroidism [18, 20,21].

After one week of SSUV irradiation, the xanthine oxidase activity in the liver relatively increased to ( $115 \pm 1$ )% and ( $170 \pm 2$ )% for normothyroid and hypothyroid rats, respectively, compared to this in the livers of the corresponding

untreated groups. In accordance with previously published data, this increased activity can be explained with adaptation-related oxidative stress [2,3].

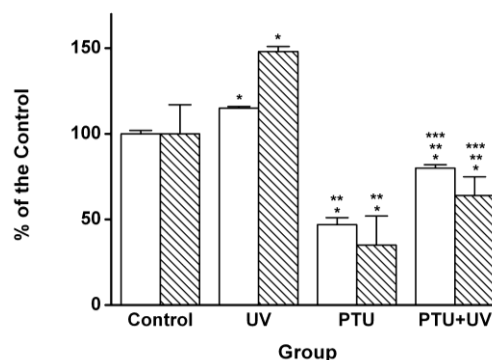


**Fig. 2.** Effects of SSUV-radiation and hypothyroidism alone and in combination on the activity of xanthine oxidase (□) and on the production of MTT- formazan (▨) in the liver homogenate of the model animals: Control – control group, PTU- hypothyroid rats, UV- normothyroid rats exposed to SSUV-radiation for 1 week, PTU+UV- hypothyroid rats irradiated for 1 week with SSUV. Data are presented as percentages of the corresponding parameters for the control group (\* -  $p < 0.05$ , \*\* -  $p < 0.01$ , \*\*\* -  $p < 0.001$ ).

However, we found, that even after SSUV exposure, the activity of xanthine oxidase in the livers of the group PTU+UV was still significantly lower than this of the control group. Statistical analysis suggested that in the hypothyroid-induced suppressed metabolism, the effect of the SSUV induced adaptive oxidative stress ( $p < 0.001$ ) due to the domination of xanthine oxidase activity in the rat liver.

The formation of MTT-formazan in the liver was enhanced due to SSUV irradiation to ( $148 \pm 3$ )%. In the hypothyroid state, the MTT-formazan decreased to ( $35 \pm 17$ )% in comparison with control animals. The SSUV exposure resulted in relatively more MTT-formazan in livers of normothyroid ( $148 \pm 3$ )% and hypothyroid ( $182 \pm 11$ )% rats, compared with the corresponding SSUV- untreated groups. The statistically significant ( $p < 0.001$ ) collective effect of SSUV and hypothyroidism on the MTT-formazan in the rat livers ( $64 \pm 11$ )%, compared to this of the control group ( $100 \pm 17$ )% indicated the prevailing impact of the SSUV.

## DISCUSSION

As the MTT-formazan was formed by interaction of MTT with free radicals [23-30], its appearance in presence of our model systems indicated free radicals formation. In our investigation, the formation of free radicals in the

liver supernatanta was prompted by addition of xanthine to the system. The increased content of xanthine provided enough substrate for xanthine oxidase to produce uric acid and reactive oxygen species [34,35].

Our study proved that, if applied alone, the 6-n-propyl-2-thiouracil-induced hypothyroidism decreased, while the SSUV-radiation increased the xanthine oxidase activity and free radicals liver accumulation. The former effect was associated with the decreased metabolic rates in the hypothyroid rats, while the latter was associated with adaptive UV-radiation induced oxidative stress.

The effects of the SSUV radiation on both xanthine oxidase activity and free radicals accumulation were stronger within the hypothyroid than within the normothyroid rats.

### CONCLUSIONS

1. SSUV irradiation and hypothyroidism alone result in opposite effects on the oxidative stress in rat's liver: the former increases, while the latter decreases the free radicals accumulation in the liver tissue.
2. The SSUV treatment of hypothyroid rats resulted in less free radicals in their livers than these accumulated in the livers of normothyroid animals.
3. The relative increase of the oxidative stress in the hypothyroid rat's liver is higher than this in the normothyroid animal.

**Acknowledgement:** This work is financially supported by Grant № 73/2013 of the Scientific Board at the Medical University of Sofia, Bulgaria

### REFERENCES:

1. F. A. Wagener, C. E. Carels, D. M. Lundvig, *Int. J. Mol. Sci.*, **14**, 9126 (2013).
2. H. Wei, X. Zhang, Y. Wang, M. *Cancer Lett.*, **185**, 21 (2002).
3. G. M. Halliday, D. L. Damian, S. Rana, S. N. Byrne, *J. Dermatol. Sci.*, **66**, 176 (2012).
4. R. K. Singh, M., Gutman, R. Reich, M., *Cancer Res.*, **55**, 3669 (1995).
5. A. Monnereau, S. L. Glaser, C. W. Schupp, K. Ekström Smedby, S. de Sanjosé, E. Kane, M. Melbye, L. Forétova, M. Maynadié, A. Staines, N. Becker, A. Nieters, P. Brennan, P. Boffetta, P. Cocco, I. Glimelius, J. Clavel, H. Hjalgrim, E. T. Chang, *Blood*, **122**, 3492 (2013).
6. P. Boffetta, O. van der Hel, A. Krickler, A. Nieters, S. de Sanjosé, M. Maynadié, P. L. Cocco, A. Staines, N. Becker, R. Font, A' Mannetje, C. Goumas, P. Brennan, *Int. J. Epidemiol.*, **37**, 1080 (2008).

7. T. Bald, T. Quast, J. Landsberg, M. Rogava, N. Glodde, D. Lopez-Ramos, J. Kohlmeyer, S. Riesenberger, D.-van den Boorn-Konijnenberg, C. Hömig-Hölzel, R. Reuten, B. Schadow, H. Weighardt, D. Wenzel, I. Helfrich, D. Schadendorf, W. Bloch, M. E. Bianchi, C. Lugassy, R. L. Barnhill, M. Koch, B. K. Fleischmann, I. Förster, W. Kastenmüller, W. Kolanus, M. Hölzel, E. Gaffal, T. Tüting, *Nature*, **507**, 109 (2014).
8. P. Dayanandan, *J. Biosci.*, **36**, 911 (2011).
9. E. Baldini, M. D'Armiento, S. Sorrenti, M. Del Sordo, R. Mocini, S. Morrone, L. Gnessi, F. Curcio, S. Ulisse, *Astrobiology*, **13**, 536 (2013).
10. A. Guerro, R. Pamplona, M. Postero-Olin, J. Barja, M. Lopez-Torrez, *Free Rad. Biol. Med.*, **26**, 73 (1999).
11. R. Gredilla, G. Barja, M. López-Torres, *Free Rad. Res.*, **35**, 417 (2001).
12. N. Petrovic, G. Cvijic, J. Djordjevic, V. Davidovic, *Ann. N.-Y. Acad. Sci.*, **1040**, 431 (2005).
13. U. Resch, G. Hersel, F. Tatzber, H. Sinzinger, *Clin. Chem. Lab. Med.*, **40**, 1132 (2002).
14. A. N. Torun, S. Kulaksizoglu, M. Kulaksizoglu, B. Q. Pamuk, E. Isbilen, N. B. Tutunku, *Clin. Endocrinol. (Oxf)*, **70**, 469 (2009).
15. P. Pasupathi, R. Latha *Thyroid Sci.*, **3**, CLS1-6 (2008).
16. S. Mukherjee, L. Samanta, A. Roy, S. Bhanja, G. B. Chainy, *Biomed Res. Int.*, Article ID 590897 (2014).
17. S. Yilmaz, S. Ozan S, F. Benzer, H. Canatan, *Cell Biochem. Funct.*, **21**, 325 (2003).
18. A. Santi, M. M. Duarte, C. C. Menezes, V. L. Loro, *Int. J. Endocrinol.*, Article ID 856359 (2012).
19. P. Venditti, M. Balestrieri, S. Di Meo, T. De Leo, *J. Endocrinol.*, **155**, 151 (1997).
20. M. J. Coria, A. I. Pastrán, M. S. Gimenez, *Acta Biomed.*, **80**, 135 (2009).
21. M. Messarah, A. Boumendjel, A. Chouabia, F. Klilet, C. Abdenour, M. S. Boulakoud, A. E. Feki, *Exp. Toxicol. Pathol.*, **62**, 301 (2010).
22. C. M. Stoscheck, *Methods Enzymol.*, **182**, 50 (1990).
23. B. Memedi, M. Traykova, N. Boyadjieva, *Trakia J. Sci.*, **10**, 321 (2012).
24. I. Kostova, M. Traykova, V. K. Rastogi, *Med. Chem.*, **4**, 371 (2008).
25. M. V. Berridge, P. M. Herst, A. S. Tan, *Biotechnol. Annu. Rev.*, **11**, 127 (2005).
26. R. H. Burdon, V. Gill, C. Rice-Evans, *Free Radic. Res. Commun.*, **18**, 369 (1993).
27. I. Kostova, M. Traykova, *Med. Chem.*, **2**, 463 (2006).
28. I. A. Muraina, M. M. Suleiman, J. N. Eloff, *Phytomedicine*, **16**, 665 (2009).
29. Y. Liu, M. G. Nair, *J. Nat. Prod.*, **73**, 1193 (2010).
30. M. Traykova, L. Astasidi, T. Traykov, N. Boyadjieva, *Trakia J. Sci.*, **10**, 336 (2012).
31. V. Welch-White, N. Dawkins, T. Graham, R. Pace, *Lipids Health Dis.*, **12**, 100 (2013).
32. S. Walrand, K. R. Short, L. A. Heemstra, C. M. Novak, J. A. Levine, J. M. Coenen-Schimke, K. S. Nair, *FASEB J.*, **28**, 1499 (2014).
33. R. Mullur, Y. Y. Liu, G. A. Brent, *Physiol. Rev.*, **94**, 355 (2014).

34. Y. Y. Sautin, R. J. Johnson, *Nucleosides Nucleotides Nucleic Acid*, **27**, 608 (2008).

35. G. Deliconstantinos, V. Villiotou, J. C. Stavrides, *Biochem. Pharmacol.*, **51**, 1727 (1996).

## ЕФЕКТ НА УЛТРАВИОЛЕТОВОТО ОБЛЮЧВАНЕ ВЪРХУ ОБРАЗУВАНЕТО НА СВОБОДНИ РАДИКАЛИ В ЧЕРЕН ДРОБ НА ПЛЪХОВЕ С ХИПОТИРЕОИДИЗЪМ

М. Л. Вълчева-Трайкова<sup>1</sup>, Г. С. Бочева<sup>2</sup>

<sup>1</sup>*Катедра по медицинска физика и биофизика, Медицински факултет, Медицински Университет – София, ул. Здраве 2, 1431 София, България*

<sup>2</sup>*Катедра по фармакология и токсикология, Медицински факултет, Медицински Университет – София, ул. Здраве 2, 1431 София, България*

Получена на 27 февруари 2015 г., приета на 3 септември 2015 г.

(Резюме)

Продължителното облъчване на здрави тъкани със симулирана слънчева ултравиолетова радиация (ССУВР) води до окислителен стрес в тях. Литературните данни за ефекта на този фактор при хипотиреоидизъм са противоречиви. Цел на това изследване бе да се проучи влиянието на хипотиреоидизма и УВ радиацията върху образуването на свободни радикали в черен дроб на плъх. След едноседмична адаптация на мъжки бели плъхове от линията Вистар, хипотиреоидизмът у тях беше постигнат чрез хронично администриране на 0.01% б-п-пропил-2-тиоурацил (пропицил) в питейната им вода за 4 седмици. Хипотиреоидизмът бе потвърден от значителното намаление на тироксина в кръвта на моделните животни (около 0.44 нг/л, при 18 нг/л за нормотиреоидните плъхове). Хипотиреоидизмът бе потвърден и от загубата на апетит, и от забавеното относително нарастване на телесното тегло на моделните животни.

През шестата седмица на опита, половината от третираните с пропицил плъхове бяха облъчвани с лампа, симулираща слънчева УВ радиация в продължение на 60 минути, групирани в 4 равни интервала, с междинни прекъсвания от по 15 минути.

След декапитиране на опитните животни, натрупването на свободни радикали в черния дроб бе изследвано спектрофотометрично, с прилагането на МТТ-методика. Резултатите за моделната група бяха представени като процент от съответните данни за контролната група.

Приложени поотделно, ССУВР увеличаваше, докато хипотиреоидизмът намаляваше натрупването на свободни радикали в черен дроб на плъх. Този резултат бе в съгласие с литературните данни за индивидуалните ефекти на тези фактори върху окислителния стрес. След прилагане на ССУВР върху хипотиреоидни плъхове, натрупването на свободни радикали в черния им дроб беше много по-голямо от това в черния дроб на третирани по същия начин нормотиреоидни животни.

## H<sub>3</sub>PW<sub>12</sub>O<sub>40</sub> (PW<sub>12</sub>) encapsulated on cotton-like mesoporous (CLM) silica as an efficient, reusable nano photocatalyst for the decolorization of Rhodamine B

R. Fazaeli\*

Department of Chemistry, Shahreza Branch, Islamic Azad University, 86145-311, Iran.

Received January 26, 2015; Revised February 3, 2016

Cotton-like mesoporous silica (CLM) was prepared by sol-gel technology. PW<sub>12</sub>-containing cotton-like mesoporous silica system (PW<sub>12</sub>@CLM) was studied with regard to its performance towards photodecolorization of Rhodamine B (RhB) dye solutions. The surface properties of the functionalized catalyst were analyzed by a series of characterization techniques like FTIR, XRD, N<sub>2</sub> adsorption–desorption, UV-vis and TEM. The photoefficiency of PW<sub>12</sub>@CLM towards photodecolorization of RhB was investigated in a photocatalytic reactor using UV lamp as a light source.

**Keywords:** Supported photocatalyst; Encapsulation method; cotton-like mesoporous (CLM) silica; Rhodamine B.

### INTRODUCTION

Azo dye containing waste water released into water bodies without decolorization is toxic to the ecosystem and also has significant influence on human health. Therefore, such pollutants have to be treated prior to discharging into the environment. They can be efficiently eliminated by photocatalytic decolorization, as an advanced oxidation process [1,2]. Rhodamine B (RhB) is a highly water soluble, basic red dye of the xanthenes class. It is widely used as a colorant in textiles and food stuffs, and is also a well-known fluorescent water tracer. RhB is highly soluble in water and organic solvents, and its color is fluorescent bluish-red. This compound is now banned from use in foods and cosmetics because it has been found to be potentially toxic and carcinogenic. So the photodecolorization of RhB is important with regard to the purification of dye effluents [3,4]. Many catalysts such as PbMoO<sub>4</sub> [5], MgFe<sub>2</sub>O<sub>4</sub>/TiO<sub>2</sub> [6], TiO<sub>2</sub> bilayer films [7], TiO<sub>2</sub>/AC [8] and GdVO<sub>4</sub>/g-C<sub>3</sub>N<sub>4</sub> [9] have been developed for degradation of RhB.

The photo-oxidation efficiency of POMs is comparable to that of the semiconductor TiO<sub>2</sub> [10-12]. Incorporation of H<sub>3</sub>PW<sub>12</sub>O<sub>40</sub> (PW<sub>12</sub>) into a silica matrix to prepare insoluble POMs with mesoporous structure has been used in photocatalytic reactions [13-15].

It is well known that the size, morphology, and structure of mesoporous materials significantly influence their physical and chemical properties and, therefore, their applications [16]. Recently,

much effort has been devoted to developing novel approaches for tailoring the structure of mesoporous materials to have specific morphologies, which is an important goal of material scientists. Studies have shown that combinations of various micelle interactions have led to the development of helical rods [17], helical fibers [18], shells [19], hollow or solid spheres [20,21], and faceted rhombododecahedra [22]. Based on this idea, a series of mesoporous materials with special morphologies, including solid spheres, hollow spheres and leaf shapes have been synthesized using different dual-template combinations [23-26].

The focus of the present work is to synthesize PW<sub>12</sub>@CLM and apply it in the photodecolorization of RhB (C.I.No: 45170, formula weight=479.02, structure shown in Fig. 1), using UV irradiation. The effect of different parameters like initial dye concentration, catalyst loading, pH of the medium, temperature of the dye solution on the photodecolorization of RhB were studied in detail.

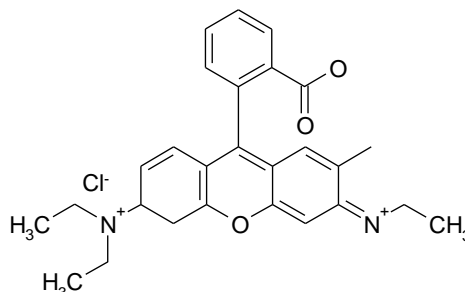


Fig. 1. Structure of Rhodamine B (RhB).

\* To whom all correspondence should be sent:  
E-mail: fazaeli@iaush.ac.ir

### Preparation of CLM

LSM was synthesized using dodecylamine (DDA, 1.17 g) and F127 (0.5 g) as templates. The templates were dissolved in a mixture of ethanol (12 mL) and water (23 mL) under stirring for 30 min. TEOS (5 mL) was then added and the mixture was stirred for 24 h at ambient temperature. The solid product was recovered by filtration, then dried for 4 h at 110 °C and calcined for 4 h at 350 °C [27].

### Preparation of $PW_{12}$ @CLM

The supported  $PW_{12}$  catalyst was prepared under hydrothermal conditions. In a typical process, a 50 mg portion of  $PW_{12}$  was dissolved in deionized water and impregnated dropwise into 100 mg support (CLM) in 25 ml distilled water. The mixture was added to a Teflon container and kept under static conditions at 493 K for 8 h. The resulting solid was dried at 110 °C for 4 h and calcined at 350 °C for 4 h. According to elemental analysis, the loading was 27 wt% (Fig.2).

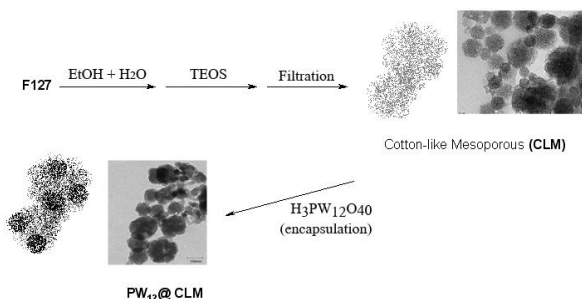


Fig. 2. Preparation of CLM and  $PW_{12}$ @CLM

## RESULTS AND DISCUSSION

### Physico-chemical characterization

The surface properties of  $PW_{12}$ @CLM were analyzed by a series of characterization techniques like FTIR, XRD,  $N_2$  adsorption–desorption, UV-vis and TEM.

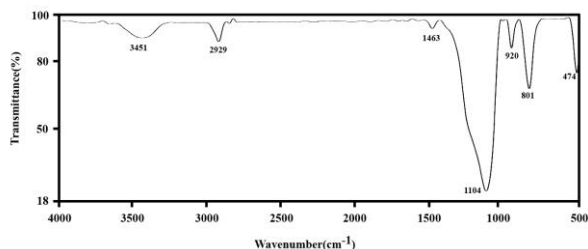


Fig. 3. FT-IR spectrum of  $PW_{12}$ @CLM.

FT-IR spectroscopy proved to be a powerful technique for studying the surface interaction between HPA and organic and inorganic supports.

Fig. 3 presents the FT-IR spectrum in the skeletal region of 4000–400  $cm^{-1}$  for the  $PW_{12}$ @CLM materials. In the spectrum of the parent CLM silica, a main band at 1090  $cm^{-1}$  with a shoulder at 1201  $cm^{-1}$  is observed that is due to asymmetric Si–O–Si stretching modes. Also, the corresponding symmetric stretching bands are observed at 812 and 961  $cm^{-1}$  [21]. The FT-IR spectrum of  $PW_{12}$ @CLM indicates that most of the characteristic bands of the parent Keggin structure, which could be found in the  $PW_{12}$  fingerprint region (1250–500  $cm^{-1}$ ), are not shown or appeared in the same assignable position of the bands corresponding to the ordered mesoporous silica host materials [28].

Fig.4 shows the XRD patterns of the parent CLM and  $PW_{12}$ @CLM in the low angle region ( $2\theta = 0.6-8^\circ$ ). The main diffraction peak for CLM and  $PW_{12}$ @CLM is observed at  $2\theta=3.93$  and  $2\theta=4.02$ , respectively. For  $PW_{12}$ @CLM systems, on low-angle X-ray diffraction, a slight shift of the primary peak to higher  $2\theta$  values, with a corresponding decrease in the peak intensity was also noted. The shift of the primary peak to higher scattering angles can be taken as an indication of a slight decrease in the sphere diameters, possibly due to a contraction of their frameworks with increasing  $PW_{12}$  loading during the calcination procedure. For  $PW_{12}$ @CLM, the intensities of the reflections decrease, indicating that the adopted synthesis procedure leads to less ordered materials than traditional CLM [29]. However, the arrangement of the CLM framework was still well retained after incorporation of  $PW_{12}$ , as can be seen from the TEM and  $N_2$  adsorption data.

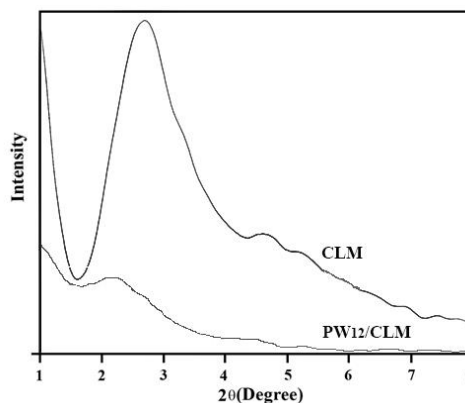


Fig.4. XRD patterns of CLM and  $PW_{12}$ @CLM.

The TEM image of the  $PW_{12}$ @CLM sample is shown in Fig. 5. The synthesized cotton-like mesoporous material clearly displayed a cotton shape and worm-like porous structure [27]. The same morphology was obtained for  $PW_{12}$ @CLM. TEM analyses indicate that the wrinkled porous structure of the CLM is robust enough to survive

the  $PW_{12}$  incorporation process and so offers an excellent matrix to support highly dispersed  $PW_{12}$  species. The places with darker contrast could be assigned to the presence of  $PW_{12}$  particles with different dispersion. The small dark spots in the image could be ascribed to  $PW_{12}$  particles, probably located in the  $PW_{12}@CLM$  cavities. The larger dark areas over the cavities most likely correspond to  $PW_{12}$  agglomerates on the external surface.

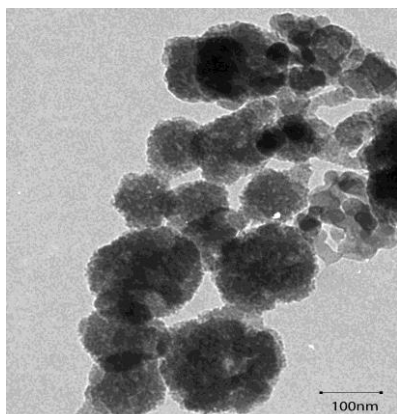


Fig. 5. TEM image of  $PW_{12}@CLM$ .

Structural properties of CLM and  $PW_{12}@CLM$  are listed in Table 1. CLM showed BET surface area of  $1255 \text{ m}^2/\text{g}$  and pore volume of  $1.21 \text{ cm}^3/\text{g}$ . After  $PW_{12}$  modification, the nitrogen adsorption isotherm (Fig. 6) became an even line and the adsorbed volume decreased distinctly, suggesting the occupation of the pore by  $PW_{12}$ . BET surface area and pore volume of  $PW_{12}@CLM$  samples decreased which confirms that  $PW_{12}$  has occupied the channels in CLM.

Two main absorptions are present in the DRUV-vis spectrum of pure  $PW_{12}$ : the first one is centered at 255 nm, and is attributed to the oxygen-tungsten charge-transfer absorption band for Keggin anions [30]. The second broad absorption in the  $PW_{12}$  is centered at 360 nm with a shoulder at 345 nm. For  $PW_{12}@CLM$  (Fig. 7), these bands are clearly observed, and since pure nano- $\text{SiO}_2$  shows no UV absorption peak, therefore, these results indicated that a primary Keggin structure has been introduced into the nanostructure framework.

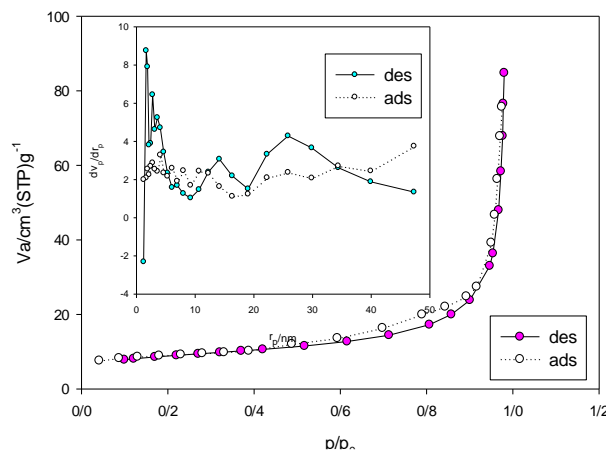


Fig. 6.  $\text{N}_2$ -adsorption-desorption isotherms of  $PW_{12}@CLM$ .

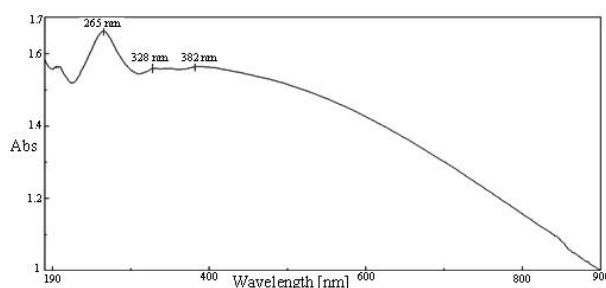


Fig. 7. DRUV-vis spectrum of  $PW_{12}@CLM$ .

#### Photocatalytic activity

After characterizing  $PW_{12}@CLM$ , the obtained material was used for the photocatalytic decolorization of a 40 ppm RhB dye solution containing  $1 \text{ g L}^{-1}$  photocatalyst under UV irradiation at varied conditions. A negligible decrease in the concentration of dye was observed under irradiation in the absence of photocatalyst or in the presence of photocatalyst without a light source. It is evident from the following results that the photolysis of the RhB solution in the presence of photocatalyst leads to the disappearance of the compound. In the absence of catalyst, direct photolysis of RhB was very slow and no appreciable photodecolorization, about 7 %, was observed during 60 min of UV irradiation, while in the presence of catalyst, the percentage of dye degraded after 60 min ranged from 7% to 92%.

Table 1. Texture parameters of CLM and  $PW_{12}@CLM$  samples.

Material	Surface area ( $\text{m}^2/\text{g}$ )	Texture parameters ( $\text{N}_2$ adsorption)	
		Pore volume ( $\text{cm}^3/\text{g}$ ) <sup>a,b</sup>	Pore diameter (nm)
CLM	1255	1.21	3.3
$PW_{12}@CLM$	380	0.96	1.8

<sup>a</sup>Total pore volume measured at  $p/p_0 = 0.99$ .

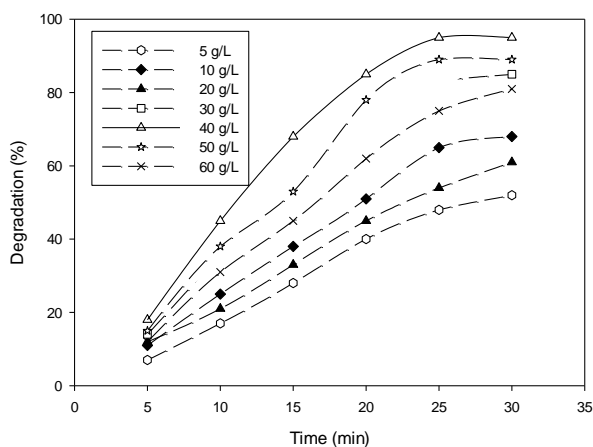
<sup>b</sup>Pore volume and pore size (by BJH method) determined from  $\text{N}_2$  adsorption at 77K.

### Effect of photocatalyst dosage

The effect of the amount of  $PW_{12}@CLM$  on the photodecolorization of RhB *versus* time is shown in Fig. 8a. It was observed that the decolorization percentage increased with increasing the amount of photocatalyst, reached the highest value ( $0.40 \text{ g L}^{-1}$  of the photocatalyst) and then decreased. The reason for this decrease is thought to be the fact that when the concentration of the catalyst rises, the solid particles increasingly block the penetration of the photons.

So, the overall number of photons that can reach the catalyst particles and the production of OH radicals decrease with the loading of the catalyst. Another reason may be the decolorization of solid particles while using large amounts of catalyst [31].

a)



b)

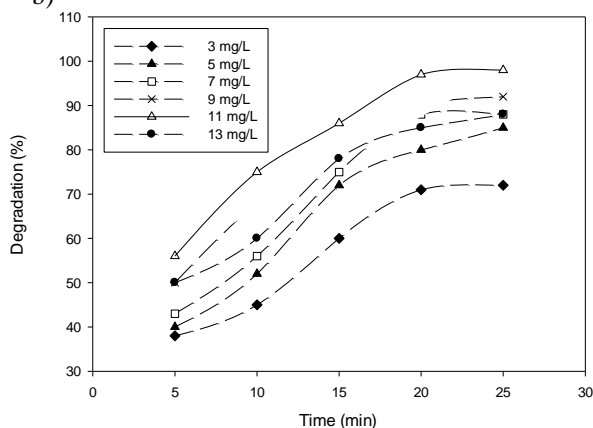


**Fig. 8.** (a) Effect of  $PW_{12}@CLM$  dosage on decolorization efficiency; initial RhB concentration,  $11 \text{ mg L}^{-1}$ ; initial pH, 9; (b) Effect of initial dye concentration on RhB decolorization efficiency;  $0.40 \text{ g L}^{-1}$  of the catalyst; initial solution pH= 9.

### Effect of the initial dye concentration

After optimizing the photocatalyst dosage, the effect of initial dye concentration ranging from 3 to  $13 \text{ mg L}^{-1}$  on the photodecolorization of RhB was investigated. The obtained results are shown in Fig.

8b. It can be seen that the rate of photodecolorization increases with increasing dye concentration up to  $11 \text{ mg L}^{-1}$ . This may be due to the fact that as the dye concentration was increased, more dye molecules were available for consecutive decolorization. The rate of photodecolorization was found to decrease with further increase in dye concentration, i.e., above  $11 \text{ mg L}^{-1}$ . The reason for this decrease is attributed to the shielding effect of the dye at high concentration that retards the penetration of light to the dye molecules deposited over the catalyst surface.

### Influence of pH

The effect of pH in the range of 1-11 on RhB dye decolorization efficiency *versus* time is presented in Fig. 9. The pH value of the original solution of RhB is 9. Dilute hydrochloric acid solution or potassium hydroxide solution was used to tune the pH value when necessary. The initial concentration of RhB solution and dosage of the photocatalyst were kept at  $11 \text{ mg L}^{-1}$  and  $0.40 \text{ g L}^{-1}$ , respectively. Cationic dyes, such as RhB, undergo efficient degradation in the presence of  $PW_{12}@CLM$  under UV-Vis irradiation in alkaline media. These observations suggest that the charge characteristics of the dye substrates greatly influence their degradation. The effect of pH on the degradation of dyes in the presence of  $\text{SiO}_2$  has been explained on the basis of point of zero charge ( $\text{pH}_{\text{pzc}}$ ) of  $\text{SiO}_2$  particles. The  $\text{pH}_{\text{pzc}}$  of  $\text{SiO}_2$  particles is 5.5 [32]. Thus,  $\text{SiO}_2$  is positively charged in acidic solution ( $\text{pH} < 5.5$ ) and negatively charged in alkaline solution. According to this explanation and because of electrostatic interactions, cationic dyes (Rh.B) should be degraded at alkaline solution (Fig. 9). In alkaline solutions, the interaction between catalyst surface ( $\text{Si-O}^-$ ) and dye [specifically the nitrogen group, such as RhB, (Fig. 1)] favors the adsorption of the dye on the surface and accordingly, the photocatalytic activity increases [33].

### Reusability of the catalyst

In our experiments, the stability and reusability of the photocatalyst were examined by repetitive use of the catalyst. After the dye was degraded in the first cycle, the photocatalyst was removed by filtration, washed several times with deionized water and dried at 90 and  $350 \text{ }^\circ\text{C}$  for 2 h. This recovered catalyst was used again with the same concentration of RhB solution. The decomposition of RhB in the second cycle was almost as fast as in the first run. The fourth run of the decolorization of RhB showed no significant loss of photoactivity of

the catalyst, which indicated the considerable stability of the photocatalyst under the present conditions.

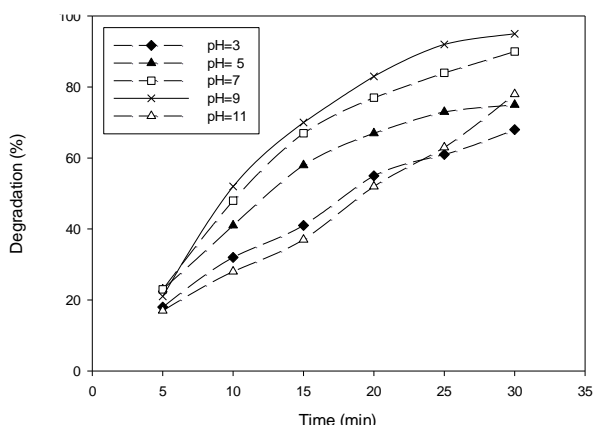


**Fig. 9.** Influence of solution pH on the RhB dye decolorization;  $0.40 \text{ g L}^{-1}$  of the catalyst; initial RhB concentration,  $11 \text{ mgL}^{-1}$ .

Comparison of  $PW_{12}@CLM$  with recently reported catalysts [5-9] for degradation of RhB shows that the photocatalytic activity of  $PW_{12}@CLM$  seems to be comparable with that of other known catalysts.

## CONCLUSIONS

The results of this research demonstrated that  $PW_{12}@CLM$  is an efficient catalyst for the photodegradation of RhB. The results of the UV-Vis spectral changes indicate that the photocatalytic process can be used for complete decolorization and mineralization of RhB in the presence of  $PW_{12}@CLM$  in a photochemical reactor.

**Acknowledgements:** We gratefully thank Shahreza Branch, Islamic Azad University, for financial support.

## REFERENCES

- C.G. Feng, X.X. Zhuo, X. Liu, *J. Rare Earths*, **25**, 717 (2009).
- K. Bubacz, J. Choina, D. Dolat, A.W. Morawski, *Polish. J. Env. Stud.*, **19**, 685 (2010).
- N. Barka, S. Qourzal, A. Assabbane, A. Nounah, Y. Ait-ichou, *J. Photochem. Photobiol. A.*, **195**, 346 (2008).
- L. You-ji, C. Wei, *Catal. Sci. Technol.*, **1**, 802 (2011).
- D.B. Hernández-Uresti, J.A. Aguilar-Garib, A.M. la Cruz, *J. Microwave Power EE*, **46** (3), 163 (2012).
- L. Zhang, Y. He, Y. Wu, T. Wu, *Mater. Sci. Eng. B.*, **176**, 1497 (2011).
- J. Zhuang, W. Dai, Q. Tian, Z. Li, L. Xie, J. Wang, P. Liu, *Langmuir*, **26**(12), 9686 (2010).
- Y. Li, S. Sun, M. Ma, Y. Ouyang, W. Yan, *Chem. Eng. J.*, **142**, 147 (2008).
- Y. He, J. Cai, T. Li, Y. Wu, H. Lin, L. Zhao, M. Luo, *Chem. Eng. J.*, **215-216**, 721 (2013).
- A. Pearson, S. K. Bhargava, V. Bansal, *Langmuir*, **27**, 9245 (2011).
- C. Yang, L. Tian, L. Ye, T. Peng, K. Deng, L. Zan, *J. Appl. Polymer Sci.*, **120**, 2048 (2011).
- Z. Jiang, J. Han, X. Liu, *Adv. Mater. Res.*, **152-153**, 202 (2011).
- Y.H. Guo, C.W. Hu, X.L. Wang, Y.L. Wang, E.B. Wang, Y.C. Zou, H. Ding, S.H. Feng, *Chem. Mater.*, **13**, 4058 (2001).
- Y. Guo, Y. Wang, C. Hu, Y. Wang, E. Wang, Y. Zhou, S. Feng, *Chem. Mater.* **12**, 3501 (2000).
- G. Marci, E. García-López, M. Bellardita, F. Parisi, C. Colbeau-Justin, S. Sorgues, L. F. Liotta, L. Palmisano, *Phys. Chem. Chem. Phys.*, **15**, 13329 (2013).
- H.L. Xu, W.Z. Wang, *Angew. Chem. Int. Ed.* **46**, 1489 (2007).
- S. Yang, L.Z. Zhao, C.Z. Yu, X.F. Zhou, J.W. Tang, P. Yuan, D.Y. Chen, D.Y. Zhao, *J. Am. Chem. Soc.* **128**, 10460 (2006).
- G.L. Lin, Y.H. Tasi, H.P. Lin, C.Y. Tang, C.Y. Lin, *Langmuir*, **23**, 4115 (2007).
- Y.Q. Yeh, B.C. Chen, H.P. Lin, C.Y. Tang, *Langmuir*, **22**, 6 (2006).
- Y.F. Zhu, J.L. Shi, H.R. Chen, W.H. Shen, X.P. Dong, *Micropor. Mesopor. Mat.*, **85**, 75 (2005).
- W.Q. Wang, J.G. Wang, P.C. Sun, D.T. Ding, T.H. Chen, *J. Colloid Interf. Sci.* **331**, 156 (2009).
- B.C. Chen, M.C. Chao, H.P. Lin, C.Y. Mou, *Micropor Mesopor Mat.*, **81**, 241 (2005).
- J.G. Wang, F. Li, H.J. Zhou, P.C. Sun, D.T. Ding, T.H. Chen, *Chem. Mater.*, **21**, 612 (2009).
- H. Blas, M. Save, P. Pasetto, C. Boissiere, C. Sanchez, B. Charleux, *Langmuir*, **24**, 13132 (2008).
- Z. Feng, Y.S. Li, D.C. Niu, L. Li, W.R. Zhao, H.R. Chen, L. Lei, J.H. Gao, M.L. Ruan, J.L. Shi, *Chem. Commun.*, 2629 (2008).
- F. Cavani, N. Ballarini, A. Cericola, *Catal. Today*, **127**, 113 (2007).
- L. Du, H. Song, S. Liao, *Appl. Sur. Sci.* **255**, 936 (2009).
- R. Fazaeli, H. Aliyan, S. Parishani Froushani, Z. Mohagheghian, *Turk. J. Chem.*, **38**, 372 (2014).
- R. Fazaeli, H. Aliyan, E. Naderi, *Phosphorus, Sulfur*, **188**, 745 (2013).
- J. Juan-Alcaniz, E. V. Ramos-Fernandez, U. Lafont, J. Gascon, F. Kapteijn, *J. Catal.*, **269** 229 (2010).
- H. Aliyan, R. Fazaeli, R. Jalilian, *Appl. Sur. Sci.*, **276**, 147 (2013).
- M. Guedes, J.A.F. Ferreira, A.C. Ferro, *J. Colloid Inter. Sci.* **337**, 439 (2009).
- H. Aliyan, R. Fazaeli, R. Jalilian, *Appl. Sur. Sci.*, **276**, 147 (2013).

**H<sub>3</sub>PW<sub>12</sub>O<sub>40</sub> (PW<sub>12</sub>) КАПСУЛИРАН В ПАМУКО-ПОДОБЕН МЕЗОПОРЪОЗЕН СИЛИЦИЕВ ДИОКСИД (CLM) КАТО ЕФЕКТИВЕН И МНОГОКРАТНО УПОТРЕБЯВАН НАНО-ФОТОКАТАЛИЗАТОР ЗА ОБЕЗЦВЕТЯВАНЕТО НА RHODAMINE B**

**Р. Фазаели**

*Департамент по химия, Клон Шахреза, Ислямски университет „Азад“, 86145-311, Иран*

Постъпила на 26 януари, 2015 г.; коригирана на 3 февруари, 2016 г.

(Резюме)

Приготвен е памуко-подобен мезопоръозен силииев диоксид (CLM) по зол-гел технология. Изследвана е PW<sub>12</sub>-съдържаща система с памуко-подобен мезопоръозен силииев диоксид (PW<sub>12</sub>@CLM) по отношение на фото-химичното обезцветяване на Rhodamine B (RhB) в багрилни разтвори. Повърхностните свойства на този катализатор са анализирани с различни техники, като FTIR, XRD, N<sub>2</sub> адсорбция/десорбция, UV-Vis и TEM. Ефективността спрямо PW<sub>12</sub>@CLM фото-обезцветяването на RhB е изследвана във фото-каталитичен реактор с UV-лампа като светлинен източник.

## A novel eco-friendly method for the synthesis of 2,3-dihydroquinazolin-4(1H)-ones in aqueous media under ultrasonication using ZrOCl<sub>2</sub>-MCM-41 as a highly efficient nanocatalyst/nanoreactor

Ali Mohammad Amani<sup>\*1,2,3</sup>, Younes Ghasemi<sup>1,2</sup>, Amir Savardashtaki<sup>4</sup>, Kamiar Zomorodian<sup>5</sup>, Esmaeil Mirzaei<sup>1</sup>, Bijan Zare<sup>4</sup>, Hamid Sepehrian<sup>6</sup>

<sup>1</sup>Department of Medical Nanotechnology, School of Advanced Medical Sciences and Technologies, Shiraz University of Medical Sciences, Shiraz, Iran

<sup>2</sup>Pharmaceutical Sciences Research Center, Shiraz University of Medical Sciences, Shiraz, Iran

<sup>3</sup>Department of Chemistry Shiraz University of Technology Shiraz, Iran

<sup>4</sup>Department of Medical Biotechnology, School of Advanced Medical Sciences and Technologies, Shiraz University of Medical Sciences, Shiraz, Iran

<sup>5</sup>Basic Sciences in Infectious Diseases Research Center, Shiraz University of Medical Sciences. Postal code 71348-45794, Shiraz, Iran.

<sup>6</sup>Nuclear Science and Technology Research Institute, Tehran, Iran

Received August 26, 2015, Revised September 25, 2015

Simple, convenient, and green synthetic protocols are developed for the one-pot synthesis of 2,3-disubstituted quinazolin-4(1H)-ones through one-pot condensation of arylaldehydes, isatoic anhydride and ammonium acetate in the presence of ZrOCl<sub>2</sub>-MCM-41 as a highly efficient novel nanocatalyst/nanoreactor under sonication. The main advantages of this protocol include short reaction times, practical simplicity, high yields, recyclable catalysts, safety, and cheapness of benign solvents.

**Keywords:** ZrOCl<sub>2</sub>-MCM-41, Nanocatalyst, Ultrasound irradiation, 2,3-Dihydroquinazolinone, Heterocycles, Multicomponent reactions, Solvent-free conditions

### INTRODUCTION

Quinazolin-4-ones are pharmacologically the most important classes of heterocyclic compounds and occur widely in natural products such as rutaecarpine (Figure 1) [1]. These compounds possess versatile types of biological activities; some of these are well known for their anticancer [2,3], antitubercular [4], antibacterial [5], antifungal [6], anti-HIV [7], antihelminthic [8], anti-inflammatory [9] and antihypertensive activities [10].

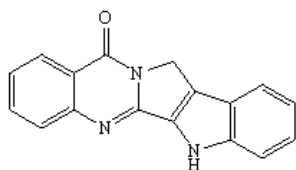


**Fig. 1.** Structure of rutaecarpine

Multicomponent reactions (MCRs) leading to interesting heterocyclic scaffolds are particularly useful for the creation of diverse chemical libraries of drug-like molecules for biological screening [11]. Some reported synthetic routes include the

reaction of isatoic anhydride and aldehydes with ammonium acetate or primary amine in the presence of various reagents or catalysts [12-28].

Recently, we have reported the preparation of 2,3-disubstituted quinazolin-4(3H)-ones via multicomponent reactions [29]. Now, a three-component one-step synthesis of 2,3-dihydroquinazolin-4(1H)-ones has been designed. For this, the use of ZrOCl<sub>2</sub> incorporated in MCM-41, which is relatively non-toxic and inexpensive, was at the centre of our study. In the course of our work on the application of zirconium containing MCM-41 in different organic reactions, we have found it as an effective promoter for the preparation of 2,3-dihydroquinazolin-4(1H)-ones.

Zirconia is a special transition metal oxide that is widely used in catalytic processes as a catalyst, a support, and a promoter [30]. However, its relatively low surface area (usually below 50 m<sup>2</sup> g<sup>-1</sup>) limits the number of active sites [31]. Ordered mesoporous silicas with a tunable pore structure and tailored composition have received considerable interest with broad application ranging from adsorption [32], gas separation [33], and catalysis [34] to biological uses [35]. Some properties of these materials are: mechanically stable structure, high surface area, and large, ordered pores with narrow size distribution of an

\* To whom all correspondence should be sent:  
E-mail: amani\_a@sums.ac.ir, amani@sutech.ac.ir;  
amani@chemist.com

inorganic backbone. Therefore, it would be reasonable to consider these materials as numerous combined nanosized vessels of the same properties. One of the best-known nanosized inorganic backbones is MCM-41, which is a structurally well ordered mesoporous material with a narrow pore size distribution between 1.5 and 10 nm, depending on the surfactant cation and a very high surface area of up to 1500 m<sup>2</sup> g<sup>-1</sup> [36]. While several types of solid sulfonic acids, based on ordered mesoporous silicas, have been created in recent years [34], there have been only a few reports of their applications as catalysts in chemical transformations. Herein, we report the preparation of ZrOCl<sub>2</sub>-MCM-41 as a new modified Lewis acid.

The application of ultrasonic irradiation in reactions using heterogeneous catalysts is a promising technique. Compared with traditional methods, the procedure is more convenient and can be carried out in a shorter reaction time and milder conditions under ultrasound irradiation to give a higher yield of products. Sonication accelerates the reaction by providing driving energy by cavitation and formation and collapse of bubbles (production of high pressure and high temperature) and ensures a better contact, increasing the reaction rate and selectivity [37]. Our efforts for development of new green synthetic methods for various heterocyclic compounds prompted us to investigate the utility of ZrOCl<sub>2</sub>-MCM-41 as a heterogeneous nanocatalyst under sonication to afford substituted quinazolinones.

Therefore, we present a versatile procedure for the selective production of mono and di-substituted 2,3-dihydroquinazolin-4(1H)-ones in the presence of ZrOCl<sub>2</sub>-MCM-41 employing three-component reactions of isatoic anhydride with aldehydes and primary amines (or ammonium salts) (Scheme 1).

## EXPERIMENTAL

### Reagents

All the chemicals used were of analytical grade (E. Merck or Fluka).

### Apparatus

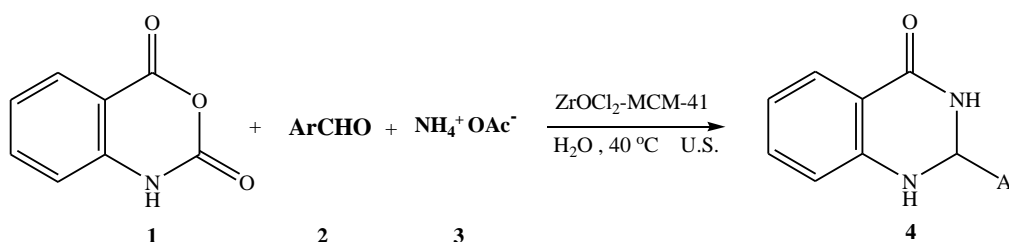
**Nanocatalyst:** A Philips X'pert powder diffractometer system with Cu-K $\alpha$  ( $\lambda=1.541\text{\AA}$ )

radiation was used for the X-ray studies. Nitrogen sorption studies were made with a Quantachrome NOVA instrument and scanning electron micrographs were recorded using a Philips microscope XL30. FT-IR spectra were obtained using a Bruker FT-IR spectrophotometer model Vector-22. Thermogravimetric analysis was performed on a Rheometric Scientific model STA-1500.

**Products:** Melting points were measured on a Buchi B-540 apparatus. IR spectra were obtained on an ABB Bomem Model FTLA200-100 spectrophotometer. <sup>1</sup>H and <sup>13</sup>C NMR spectra were recorded on a Bruker Avance DRX-300 spectrometer at 300 and 75 MHz, using TMS as an internal standard. Mass spectra were obtained on a Shimadzu QP 1100 EX with an ionization potential of 70 eV.

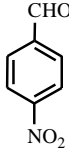
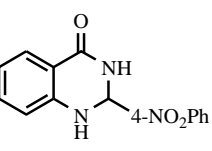
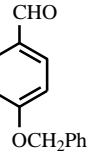
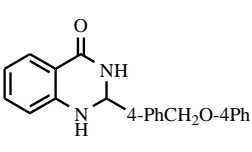
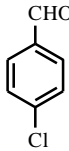
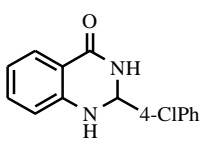
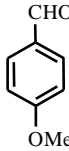
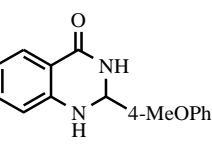
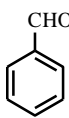
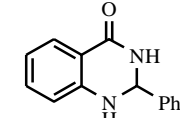
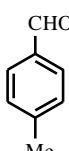
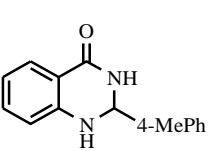
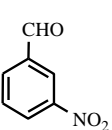
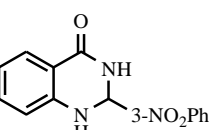
### Preparation of Mesoporous Zirconium Silicate

Five different samples of mesoporous zirconium silicate were prepared by mixing sodium silicate as a silicon source, zirconium oxychloride as a zirconium source, and cetyltrimethylammonium bromide (CTMABr) as a surfactant under non-thermal conditions. In a typical procedure, 0.6 g of CTMABr was added in 23 g of demineralized water, the mixture was stirred at 3270 H for 15 min (140 rpm), after that 3 g of sodium silicate was added to the mixture and it was further stirred for 30 min. The pH value was adjusted at 9 by adding sulfuric acid (2M). Then a solution of ZrOCl<sub>2</sub>.8H<sub>2</sub>O (0.45 g in 50 mL demineralized water) was dropwise added. The stirring was continued for 4 h. A bulky white precipitate was formed. It was filtered, washed five times with demineralized water, and dried in an air oven at 50°C for 48 h. A small portion of this material was calcined at 600 °C for 6 h. The material was digested in 0.1M HNO<sub>3</sub> for 24 h and then washed with demineralized water. The samples prepared had Si/Zr molar ratios: 10; 20; 40; and 80. They were marked as: Zr<sub>x</sub>MCM-41 where x indicated the Si/Zr molar ratio and MCM-41 indicated a hexagonal ordered mesoporous silicate.



**Scheme 1.** Synthesis of new substituted 2,3-dihydroquinazolinones.

**Table 1.** Synthesis of 2-aryl substituted 2,3-dihydroquinazolin-4(1H)-ones in the presence of ZrOCl<sub>2</sub>-MCM-41.

Entry	Ar	Product	Time (min)	Yield (%) <sup>a</sup>	M.P. (°C)	
					Found	Reported [Ref]
1		 <b>(4a)</b>	8	87	300-302	310-312[29]
2		 <b>(4b)</b>	5	79	238-240	238-240[29]
3		 <b>(4c)</b>	10	75	207-208	207-208[29]
4		 <b>(4d)</b>	15	75	183-184	183-184[29]
5		 <b>(4e)</b>	20	86	225-226	225-226[29]
6		 <b>(4f)</b>	25	70	228-230	229-231[29]
7		 <b>(4g)</b>	8	87	180-182	180-182[29]

<sup>a</sup>Isolated yields

#### General Procedure for the Synthesis of 2, 3-Dihydroquinazolin-4(1H)-ones

A mixture of 0.163 g isatoic anhydride (1 mmol), aromatic aldehyde (1 mmol), and ammonium acetate (1.2 mmol) was added to 5 mg of ZrOCl<sub>2</sub>-MCM-41 (Zr/Si molar ratio 0.27) and water (5 mL) and the temperature was then raised to 40 °C and maintained under ultrasonic irradiation (25 kHz) for the appropriate time (Table 1). When the reaction was complete (TLC; n-hexane-EtOAc, 2:1) the water was evaporated, CHCl<sub>3</sub>:methanol (10 mL, 3:1) was added. The mixture was stirred for at least 10 min and the solid catalyst was separated by

filtration. The mixture was evaporated in vacuum; the residues were purified by recrystallization from EtOH.

#### General Procedure for the Synthesis of 2, 3-Dihydroquinazolin-4(1H)-ones

A mixture of 0.163 g isatoic anhydride (1 mmol), aromatic aldehyde (1 mmol), and ammonium acetate (1.2 mmol) was added to 5 mg of ZrOCl<sub>2</sub>-MCM-41 (Zr/Si molar ratio 0.27) and water (5 mL) and the temperature was then raised to 40 °C and maintained under ultrasonic irradiation (25 kHz) for the appropriate time (Table 1). When

the reaction was complete (TLC; n-hexane–EtOAc, 2:1) the water was evaporated and CHCl<sub>3</sub>:methanol (10 mL, 3:1) was added. The mixture was stirred for at least 10 min and the solid catalyst was separated by filtration. The mixture was evaporated in vacuum; the residues were purified by recrystallization from EtOH.

#### Compound 4a

IR (KBr):  $\bar{\nu}$  = 3360, 3345, 3065, 1679, 1608 cm<sup>-1</sup>; <sup>1</sup>H-NMR (300 MHz, DMSO-d<sub>6</sub>),  $\delta$ : 7.56(t, *J*=6/0 Hz, 1H, 1CH), 7.86(m, 3H, 2CH, 1NH), 8.16(d, *J*=6/0 Hz, 1H, CH), 8.39(m, 5H, CH), 12.8(s, 1H, NH) ppm; <sup>13</sup>C-NMR (75 MHz, DMSO-d<sub>6</sub>),  $\delta$ : 65.5, 121.2, 123.6, 125.9, 127.7, 129.3, 134.8, 138.6, 148.3, 149.0, 150.8, 162.1 ppm; MS, *m/z* (regulatory intensity): 50(45), 76(50), 92(29), 119(97.5), 192(24), 221(43), 267(100), 269(2.5)[M<sup>+</sup>].

#### Compound 4d

IR (KBr):  $\bar{\nu}$  = 3291, 3178, 3060, 2931, 2829, 1663 cm<sup>-1</sup>; <sup>1</sup>H-NMR (300 MHz, DMSO-d<sub>6</sub>),  $\delta$ : 3.84-3.9(s, 3H, CH<sub>3</sub>), 4.34(s, 1H, NH), 5.72(s, 1H, NH), 5.86(s, 1H, CH), 6.65-6.8(d, *J*=8.0 Hz, 1H, CH, Ph), 6.88-7.00(m, 3H, CH, Ph), 7.31-7.36(d, *J*=7.8Hz, 1H, CH, Ph), 7.51-7.53(d, *J*= 8.6 Hz, 2H, CH, Ph), 7.93-7.96(d, *J*=7.7Hz, 1H, CH, Ph) ppm.

#### Compound 4g

IR (KBr):  $\bar{\nu}$  = 3350, 3245, 3050, 2910, 1608 cm<sup>-1</sup>; <sup>1</sup>H-NMR (300 MHz, DMSO-d<sub>6</sub>),  $\delta$ : 5.93(s, 1H, CH), 6.66(t, *J*= 6.0Hz, 1H, CH), 6.77(d, *J*=6.0Hz, 1H, CH), 7.26(d, t, *J*<sub>1</sub>=1.2Hz, *J*<sub>2</sub>=9.0Hz, 1H, CH), 7.33(s, 1H, NH), 7.59(d, *J*=9.0Hz, CH), 7.83(m, 1H, CH), 7.92(d, 1H, *J*=9.0Hz, CH), 8.19(d, *J*=6.0Hz, 1H), 8.34(s, 1H, CH), 8.54(s, 1H, NH) ppm; <sup>13</sup>C-NMR (75 MHz, DMSO-d<sub>6</sub>),  $\delta$ : 65.1, 114.6, 114.9, 117.5, 121.6, 122.7, 123.3, 125.9, 127.4, 131.3, 133.4, 133.6, 134.7, 144.3, 147.3, 147.7, 163.3 ppm; MS, *m/z* (regulatory intensity): 50(15), 92(35), 119(29), 120(40), 147(100), 221(15), 269(6.7) [M<sup>+</sup>].

## RESULTS AND DISCUSSION

In continuation of our search for application of functionalized ordered mesoporous silicas [38], our attempt was focused on the application of novel nanoreactors for ultrasound assisted synthesis of substituted quinazolinones. These Lewis acidic nanoporous zirconium silicates were prepared with various mole ratios of Si/Zr. Infrared spectra of these nanocatalysts were measured by a standard KBr disc technique. The FT-IR spectrum of the Zr10MCM-41 nanocatalyst shown in Fig. 2 is closely similar to that of mesoporous molecular

sieves which also show a series of bands that are characteristic of the SiO<sub>4</sub> tetrahedron and its modification by introduction of metal ions [39]. The spectrum shows five main absorption bands in the regions 3000–3700, 1055–1090, 960–970, 790–850, 440–465 cm<sup>-1</sup>. The band in the region 1055–1090 cm<sup>-1</sup> is due to the internal asymmetric stretching mode of SiO<sub>4</sub> (TO<sub>4</sub>) skeleton, the strongest band in the spectra of silicates [40]. The peak in the region 960–970 cm<sup>-1</sup> is generally considered as a proof for the incorporation of a heteroatom into the framework [41]. Camblor *et al.* have proposed that the band at 960 cm<sup>-1</sup> is due to the Si-O stretching vibrations of the Si-OH groups present.

The SEM image of the mesoporous Zr10MCM-41 was taken using gold coating during 2 minutes for high magnification and is shown in Fig. 3. The SEM image of the mesoporous Zr10MCM-41 exhibits uniform spherical crystallites ~0.4–0.8 mm in size.

XRD analysis was performed from 1.5° (2 $\theta$ ) to 10.0° (2 $\theta$ ) at a scan rate of 0.02° (2 $\theta$ )/sec. The XRD patterns after calcination of the synthesized zirconium silicate samples are presented in Fig. 4. There is a strong diffraction at 2 $\theta$  smaller than 3° along with the presence of small peaks, which confirms the formation of mesoporous materials [42].

The thermogravimetric analysis of these nanocatalysts was performed from ambient temperature to 900°C at a heating rate of 10°C/min. The thermograms of the nanocatalysts are presented in Fig. 5. The thermograms of the uncalcined samples show a gradual weight loss up to 900°C. The TGA curve of the samples shows five steps of weight loss (35-130, 130-300, 300-380, 380-480, and 480-600 °C). The weight loss is ~4.0% in the first step and is due to desorption of the physisorbed water in the pores of the uncalcined samples. The weight losses in the second (~20.0%) and third (~7.0%) steps are mainly associated with oxidative decomposition of templates; in the fourth step, the weight loss (~7.0%) is due to removal of coke formed in the previous steps by the decomposition of templates. In the final step, the weight loss (~2.0%) is mainly due to the loss of water formed by condensation of the silanol groups.

In the present communication, we report a simple and ecofriendly synthesis of 2-aryl substituted 2,3-dihydroquinazolin-4(1H)-ones by treatment of isatoic anhydride, aromatic aldehyde, and ammonium acetate in the presence of ZrOCl<sub>2</sub>-MCM-41 as catalyst under ultrasound irradiation (Scheme 1).

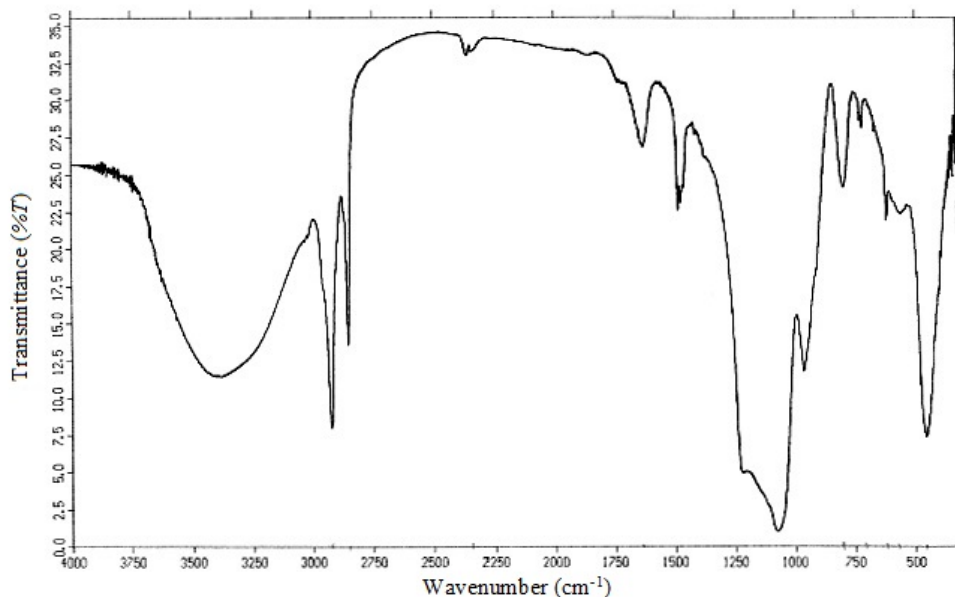


Fig. 2. FT-IR spectrum of the synthesized  $ZrOCl_2$ -MCM-41.

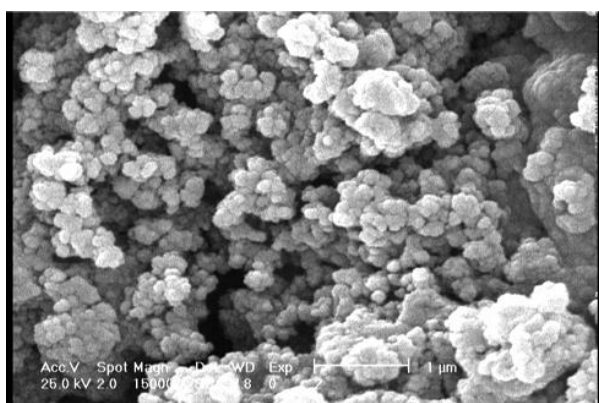


Fig. 3. SEM image of  $ZrOCl_2$ -MCM-41.

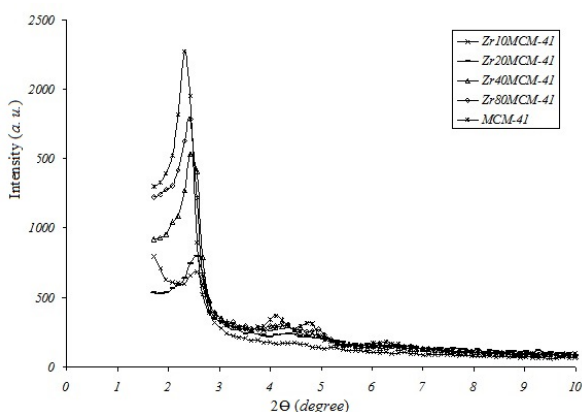


Fig. 4. XRD patterns of the synthesized  $ZrOCl_2$ -MCM-41 and MCM-41

The results showed that the reaction without ultrasound irradiation needs very long time and gives relatively low yields. Thus, it seemed that ultrasound irradiation played the main role in

enhancement of the reaction rate and the combination of ultrasound and  $ZrOCl_2$ -MCM-41 was found to be ideal for the faster synthesis in high yield.

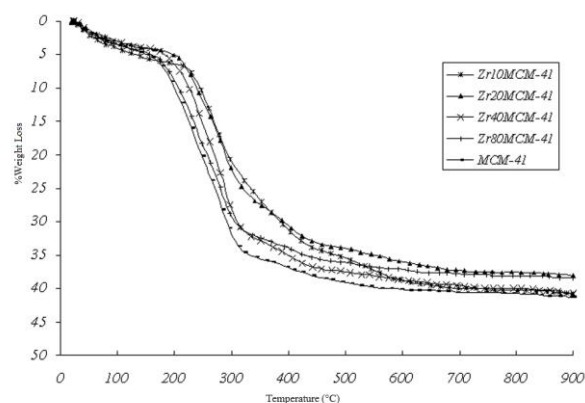


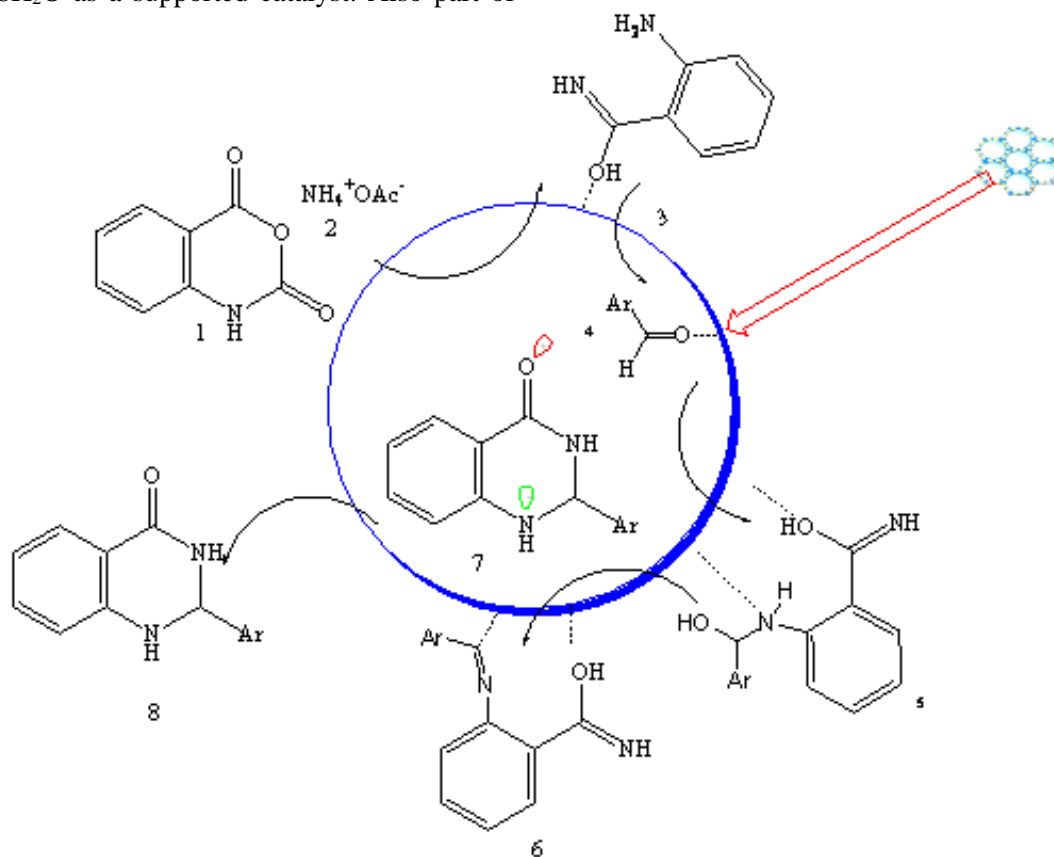
Fig. 5. TGA curve of the synthesized  $ZrOCl_2$ -MCM-41 and MCM-41.

A variety of aldehydes including heterocyclic and aromatic aldehydes, possessing both electron-donating and electron-withdrawing groups, were employed for the formation of 2,3-dihydroquinazolin-4(1H)-ones. In all cases, the yields were excellent (Scheme 1, Table 1). Among the various benzaldehydes tested, the reaction worked well with electron-donating groups (Me, MeO) (entries 6 and 4, Table 1), as well as electron-withdrawing groups ( $NO_2$ , Cl) (entries 1 and 3, Table 1) giving various 2,3-dihydroquinazolin-4(1H)-ones in 75–87% yields.

We have found that  $ZrOCl_2$ -MCM-41 is an effective eco-friendly and efficient promoter for the synthesis of 2,3-dihydroquinazolin-4(1H)-ones. A plausible mechanistic pathway to 2-aryl-substituted

2,3-dihydroquinazolin-4(1H)-ones is illustrated in Scheme 2. In the initial step, the reaction of isatoic anhydride (1), and ammonium acetate (2) within the  $ZrOCl_2$ -MCM-41 tunnels, together with decarboxylation, gives 2-aminobenzamide (5). The intermediate (3) is formed through nucleophilic attack of the amino group in 2-aminobenzamide at the activated carbonyl group in the aldehyde by  $ZrOCl_2 \cdot 8H_2O$  as a supported catalyst. Also part of

the amide in the imine intermediate (5) is converted into its tautomer in the presence of the catalyst. Then the Schiff base intermediate (6) is produced by intermediate (5) dehydration. The intramolecular nucleophilic addition reaction between the amide group nitrogen and the activated Schiff base carbon gives intermediate (7), which is followed by a 1,5-proton transfer giving the products.



**Scheme 2.** Proposed reaction mechanism

## CONCLUSION

In conclusion, a simple green method for the synthesis of a novel class of the quinazolinone family is developed.  $ZrOCl_2$ -MCM-41 is an efficient nanoreactor for the synthesis of 2,3-dihydroquinazolinones. The method offers several advantages, such as avoiding toxic solvents or catalysts, simple work-up procedure without using any chromatographic method, and improved yields. Starting materials are inexpensive and commercially available. We believe that many biologically active derivatives could be synthesized by this multi-component reaction with high atomic economy.

## REFERENCES

1. a) Z.Z. Ma, Y. Hano, T. Nomura, Y. J. Chen, *Heterocycles.*, **46**, 541(1997); (b) A.L. Chen, K.K. Chen, *J. Am. Pharm. Assoc.*, **22**, 716 (1933).
2. J.B. Jiang, D.P. Hesson, B.A. Dusak, D.L. Dexter, G.J. Kang, E. Hamel, *J. Med. Chem.*, **33**, 1721(1990).
3. Y. Xia, Z.N. Yang, M.J. Hour, S.C. Kuo, P. Xia, K.F. Bastow, Y. Nakanishi, P. Nampoothiri, T. Hackl, E. Hamel, K.H. Lee, *Bioorg. Med. Chem. Lett.*, **11**, 1193 (2001).
4. P.B. Trivedi, N.K. Undavia, A.M. Dave, K.N. Bhatt, N.C. Desai, *Indian J. Chem.*, **32B**, 497 (1993).
5. N.A. Gangwal, U.R. Kothawade, A.D. Galande, D.S. Pharande, A.S. Dhake, *Indian J. Het. Chem.*, **10**, 291 (2001).
6. J. Bartroli, E. Turmo, M. Alguero, E. Boncompte, M.L. Vericat, L. Conte, J. Ramis, M. Merlos, J.G. Rafanell, J. Forn, *J. Med. Chem.*, **41**, 1869 (1998).
7. V. Alagarsamy, R. Revathi, S. Meena, K.V. Ramaseshu, S. Rajasekaran, E. De-Clerco, *Indian J. Pharm. Science.*, **4**, 459 (2004).

8. D. P. Gupta, S. Ahmad, K. Ashok, K. Shanker, *Indian J. Chem.*, **27B**, 1060 (1988).
9. Q. Chao, L. Deng, H. Shih, L.M. Leoni, D. Genini, D.A. Carson, H. B. Cottam., *J. Med. Chem.*, **42**, 3860 (1999).
10. W.B. Wright, A.S. Tomcufcik, P.S. Chan, J.W. Marsico, J.B. Press, *J. Med. Chem.*, **30**, 2277 (1987).
11. (a) A. Domling, *Curr. Opin. Chem. Biol.*, **6**, 306 (2002) (b) L. Weber, *Drug Discovery Today*, **7**, 143 (2002).
12. (a) P. Salehi, M. Dabiri, M.A. Zolfigol, M. Baghbanzadeh, *Synlett.*, **1155**(2005); (b) M. Dabiri, P. Salehi, S. Otokesh, M. Baghbanzadeh, G. Kozehgary, A.A. Mohammadi, *Tetrahedron Lett.*, **46**, 6123 (2005).
13. M. Narasimhulu, Y.R. Lee, *Tetrahedron*, **67**, 9627 (2011).
14. J.X. Chen, D.Z. Wu, F. He, M.C. Liu, H.Y. Wu, J.C. Ding, W.K. Su, *Tetrahedron Lett.*, **49**, 3814 (2008).
15. A. Ghorbani-Choghamarani, T. Taghipour, *Lett. Org. Chem.*, **8**,470 (2011).
16. K. Niknam, N. Jafarpour, E. Niknam, *Chin. Chem. Lett.*, **22**, 69 (2011).
17. K. Niknam, M.R. Mohammadizadeh, S. Mirzaee, *Chin. J. Chem.*, **29**, 1417 (2011).
18. M. Dabiri, P. Salehi, M. Baghbanzadeh, M.A. Zolfigol, M. Agheb, S. Heydari, *Catal. Commun.*, **9**, 785 (2008).
19. M. Wang, T.T. Zhang, Y. Liang, J.J. Gao, *Chin. Chem. Lett.*, **22**, 1423 (2011).
20. Z.H. Zhang, H.Y. Lü, S.H. Yang, J.W. Gao, *J. Comb. Chem.* **12**, 643(2010).
21. H.R. Shaterian, A.R. Oveisi, M. Honarmand, *Synth. Commun.*, **40**, 1231 (2010).
22. P. Salehi, M. Dabiri, M. Baghbanzadeh, M. Bahramnejad, *Synth. Commun.*, **36**, 2287 (2006).
23. M.Z. Kassae, S. Rostamizadeh, N. Shadjou, E. Motamedi, M. Esmaelzadeh, *J Heterocyclic Chem.*, **47**, 1421 (2010).
24. M. Baghbanzadeh, P. Salehi, M. Dabiri, G. Kozehgary, *Synthesis*, **344** (2006).
25. (a) J. Chen, W. Su, H. Wu, M. Liu, C. Jin, *Green Chem.*, **9**, 972 (2007); (b) N.B. Darvatkar, S.V. Bhilare, A.R. Deorukhkar, D.G. Raut, M.M. Salunkhe, *Green Chem. Lett. Rev.*, **3**, 301 (2010).
26. M.P. Surpur, P.R. Singh, S.B. Patil, S.D. Samant, *Synth. Commun.*, **37**, 1965 (2007)..
27. J. Safari, S. Gandomi-Ravandi, *J. Mol. Catal A: Chem.*, **371**, 135 (2013).
28. B.H. Chen, J.T. Li, G.F. Chen, *Ultrasonics Sonochem.*, **23**, 59 (2015).
29. a) S. Rostamizadeh, A. M. Amani, R. Aryan, H. R. Ghaieni, N. Shadjou, *Synth. Commun.*, **38**, 3567 (2008) b) S. Rostamizadeh, A.M. Amani, G.H. Mahdavinia, H. Sepehrian, S. Ebrahimi, *Synthesis*, **8**, 1356 (2010).
30. H. Teterycz, R. Klimkiewicz, M. Laniecki, *Appl. Catal. A.*, **249**, 313(2003).
31. T. Yamaguchi, *Catal. Today*, **20**,199 (1994).
32. H. Yoshitake, *New J. Chem.*, **29**, 1107 (2005).
33. P.J.E. Harlick, A. Sayari, *Ind. Eng. Chem. Res.*, **46**, 446 (2007).
34. B. Karimi, D. Zareyee, *Org. Lett.*, **10**, 3989 (2008).
35. M. Hartmann, *Chem. Mater.*, **17**, 4577 (2005).
36. W. Zhang, T.R. Pauly, T. Pinnavaia, *J. Chem. Mater.*, **9**, 2491 (1997).
37. a)R. Cella, H.A. Stefani, *Tetrahedron*, **65**, 2619 (2009); b)T.J. Mason. Practical Sonochemistry, A user's guide to applications in chemistry and chemical engineering, Ellis Horwood Limited, New York; 1991: c) M. Mečiarová, Š. Toma, P. Babiak, *Chem. Pap.*, **55**, 302 (2001).
38. a) S. Rostamizadeh, A.M. Amani, G.H. Mahdavinia, G. Amiri, H. Sepehrian *Ultrasonics Sonochem.*, **17**, 306 (2010) b) H. Sepehrian, R. Yavari, S. Waqif-Husain, M. Ghannadi-Maragheh, *Sep. Sci. Tech.*, **43**, 3269 (2008).
39. X. Chen, L. Huan, , G. Ding, Q. Li, *Catal. Lett.*, **44**, 123 (1997).
40. C.Y. Chen, S.L. Burkett, H.X. Lin, M.E. Davis, *Microporous Mater.*, **2**, 27 (1993).
41. M.A. Camblor, A. Corma, J. Perez-Pariente, *J. Chem. Soc. Chem. Commun.* **13**, 557 (1993).
42. C.T. Kresge, M.E. Leonowics, W.J. Roth, J.C. Vartuli, J.S. Beck, *Nature*, **359**, 710 (1992).

НОВ ЕКОЛОГИЧНО СЪВМЕСТИМ МЕТОД ЗА СИНТЕЗА НА 2,3-ДИГИДРОХИНАЗОЛИН-4(1H)-ОНИ ВЪВ ВОДНА СРЕДА ПРИ УЛТРАЗВУКОВО ВЪЗДЕЙСТВИЕ, ИЗПОЛЗВАЙКИ  $ZrOCl_2$ -МСМ-41 КАТО ВИСОКОЕФЕКТИВЕН НАНОКАТАЛИЗАТОР/НАНОРЕАКТОР

А.М. Амани<sup>1,2,3\*</sup>, Ю. Гасеми<sup>1,2</sup>, А. Савардацаки<sup>4</sup>, К. Зомородиан<sup>5</sup>, Е. Мирзаеи<sup>1</sup>, Б. Заре<sup>4</sup>, Х. Сефериан<sup>6</sup>

<sup>1</sup>Департамент по медицински нанотехнологии, Училище за нови медицински науки и технологии, Университет за медицински науки в Шираз, Иран

<sup>2</sup>Изследователски фармацевтичен център, Университет за медицински науки в Шираз, Иран

<sup>3</sup>Департамент по химия, Технологичен университет, Шираз, Иран

<sup>4</sup>Департамент по медицинска биотехнология, Училище по модерна медицина и технология, Университет за медицински науки в Шираз, Иран

<sup>5</sup>Изследователски център по инфекциозни болести, Университет за медицински науки в Шираз, Иран

<sup>6</sup>Изследователски институт по ядрени науки и технологии, Техеран, Иран

Постъпила на 26 август, 2015 г.; коригирана на 25 септември, 2015 г.

(Резюме)

Прости, удобни и „зелени“ рецептури са разработени за едностадийната синтеза на 2,3-дихидрохиназолин-4(1H)-они чрез кондензация на арилалдехиди, изатинов анхидрид и амониев ацетат в присъствие на  $ZrOCl_2$ -МСМ-41 като високоефективен нанокатализатор/нанореактор при ултразвуково действие. Главните предимства на метода са кратките времена, високите добиви, рециклирания катализатор, безопасността и ниската цена на разтворителя.

## Spectroscopic studies of charge-transfer complexes of 2,3-dichloro-5,6-dicyano-p-benzo-quinone with p-nitroaniline

N. Singh, A. Ahmad\*

*Department of Chemistry, Faculty of Science, Aligarh Muslim University, Aligarh -202002, India*

Received August 2, 2015, Accepted October 5, 2015

The charge-transfer complexes of the donor p-nitroaniline (PNA) with the acceptor 2, 3-dichloro-5,6-dicyano-p-benzoquinone (DDQ) were studied spectrophotometrically in various solvents such as CH<sub>2</sub>Cl<sub>2</sub>, CHCl<sub>3</sub>, and CCl<sub>4</sub> at different temperatures. Two charge-transfer bands were observed in each case. The results indicate that the formation of the CT-complex in a less polar solvent is comparatively high. The stoichiometry of the CT-complex was found to be 1:1. The physical parameters of the CT-complex were evaluated by the Benesi–Hildebrand equation. The data are discussed in terms of the formation constant ( $K_{CT}$ ), molar extinction coefficient ( $\epsilon_{CT}$ ), standard free energy ( $\Delta G^\circ$ ), oscillator strength ( $f$ ), transition dipole moment ( $\mu_{EN}$ ), resonance energy ( $R_N$ ) and ionization potential ( $I_D$ ). The results indicate that the formation constant ( $K_{CT}$ ) for the complex is dependent upon the nature of electron acceptor, donor and polarity of solvents used. The formation of the complex was confirmed by UV-visible, FT-IR, and <sup>1</sup>H-NMR techniques. The possible structure of the CT-complex between DDQ and PNA was proposed.

**Keywords:** Charge-transfer complex; 2, 3-dichloro-5, 6-dicyano-p-benzo-quinone (DDQ); p-nitro aniline (PNA); UV-Visible, FT-IR, <sup>1</sup>H-NMR.

### INTRODUCTION

Various aromatic molecules can behave as electron donors and form molecular complexes with electron acceptor molecules such as halogens, nitro compounds and quinines [1-2]. Extensive works have been carried out to elucidate the nature of intermolecular interactions in these molecular complexes. Mulliken has developed the theory of the intermolecular CT interactions, which has been successfully applied to the interpretation of the absorption bands characteristic of molecular complexes in various systems [3]. DDQ is a strong electron acceptor having electron affinity of 1.9 e.v. [4].

In the present paper, spectrophotometric studies were carried out for CT complexes of DDQ with p-nitroaniline, special attention being paid to the appearance of two CT bands. Orgel first reported two bands in the case of methylbenzene complexes of chloranil and 1, 2, 5-trinitrobenzene [5]. Orgel related the two ionization potentials of the donor molecules to the frequencies of the CT bands.

This paper presents studies of the charge-transfer interaction between DDQ and p-nitroaniline in both liquid and solid states. The aim of the work is to determine the reaction stoichiometry, the nature of bonding between DDQ and PNA, and also some physical parameters. In

addition, the nature and structure of the reaction product (CT-complex) in both solution and solid states can be estimated using spectroscopic techniques like FT-IR, <sup>1</sup>H NMR and UV-Vis electronic absorption to obtain the stoichiometry, molecular structure and nature of interaction for the CT-complexes [6-9].

### EXPERIMENTAL

#### *Materials*

Analytical grade (AR) chemicals were used throughout. 2,3-Dichloro-5,6-dicyano-p-benzoquinone (DDQ) and p-nitro aniline (PNA) were obtained from Sigma Aldrich, (CDH). Dichloromethane (Merck), chloroform (Merck) and carbon tetrachloride (Merck) were used without further purification.

#### *Preparation of standard solutions*

Solutions of the donor of different concentrations, 0.01M, 0.02M, 0.03M, 0.04M, and 0.05M, were prepared in different volumetric flasks by dissolving accurately weighed amounts of p-nitro aniline in different solvents such as carbon tetrachloride, chloroform and dichloromethane.

A standard solution of the acceptor, DDQ (0.01M) was prepared by dissolving accurately weighed amounts of the acceptor in the above solvents in different volumetric flasks.

\* To whom all correspondence should be sent:

E-mail: afaqahmad212@gmail.com;  
neetisingh72@gmail.com

### Synthesis of solid CT- complex

Analar R grade samples of DDQ and p-nitroaniline were employed for the synthesis of the title compound. Equimolar solutions of the two reactants were separately prepared in methanol and mixed together. The resulting solution was stirred well for about thirty min.

The precipitated adduct was filtered off at the pump and repeatedly recrystallised from methanol to enhance the degree of purity of the synthesized compound.

### Analyses

The electronic absorption spectra of the donor P-nitroaniline, acceptor DDQ and the resulting complex in dichloromethane, chloroform and carbon tetrachloride were recorded at different temperatures, i.e. 20°C, 25°C and 30°C in the visible range 200 nm–600 nm using a UV- visible spectrophotometer Perkin-Elmer-  $\lambda$ -850 with a 1 cm quartz cell path length. The FT-IR spectra of the reactants and the resulting CT-complex were recorded with the help of the FT-IR spectrometer INTERSPEC– 2020 (spectra lab U.K.) in KBr pellets. The <sup>1</sup>H NMR spectrum of the CT-complex was measured in acetone using Bruker Advance II 400 NMR spectrometer.

## RESULTS AND DISCUSSION

### Observation of CT- bands

3-ml volumes of the donor and the acceptor were scanned separately by spectrophotometric titration [10] at their wavelengths of maximum absorption: 280 nm for DDQ, 400 nm for PNA, 320 nm for the blank solvent (dichloromethane) and 440 nm and 560 nm for the CT-complex of 0.01M PNA and 0.01M DDQ in dichloromethane, as shown in Fig 1. The reaction mixture of the donor (10 ml) and the acceptor (10 ml) in the different solvents, viz., carbon tetrachloride, chloroform and dichloromethane, formed a yellow colored charge transfer complex. The complex for each of the reaction mixtures was let to standing overnight at different temperatures i.e. 20°C, 25°C and 30°C to form a stable complex before analysis at the maximum absorbance 440 nm and 560 nm for dichloromethane, 430 nm and 550 nm for chloroform and 420 nm and 540 nm for carbon tetrachloride.

The concentration of the donor in the reaction mixture was kept higher than that of the acceptor,  $[D_0] \gg [A_0]$  [11, 12] and changed over a wide range of concentrations from 0.01M to 0.5M while the concentration of the  $\pi$ -acceptor (DDQ) was kept

fixed [11] at 0.01M in each solvent; these produced solutions with donor: acceptor molar ratios varying from 1:1 to 50:1, these concentration ratios were used to obtain a straight line diagram for determination of the formation constants of the CT-complex.

The spectra of the solutions of 0.01M PNA, and 0.01M DDQ in different solvents were recorded with solvents used as a reference, the longest wavelength peak was considered as the CT-peak [13]. The changes of the absorption intensity to higher values for all complexes in this study when adding the donor were detected and investigated, as shown in Table 5. These measurements were based on the CT-absorption bands exhibited in the spectra of the above mentioned systems given in Figs. 2- 4. In all systems studied the absorption spectra are of similar nature except for the position of the absorption maxima ( $\lambda_{CT}$ ) of the complexes. The CT-complex absorption spectra were analyzed by fitting to the Gaussian function

$$y = y_0 + [A/ w\sqrt{(\pi/2)}] \exp [-^2 (x - x_c)^2/w^2]$$

where  $x$  and  $y$  denote wavelength and absorbance, respectively. The results of the Gaussian analysis for all systems under study are shown in Table 1. The wavelengths of these new absorption maxima ( $\lambda_{CT} = x_c$ ) and the corresponding transition energies ( $h\nu$ ) are summarized in Tables 2-4.

### Determination of the ionization potentials of the donor

The ionization potentials of the donor ( $I_D$ ) in the charge transfer complexes were calculated using the empirical equation derived by Aloisi and Piganatro [14]

$$I_D \text{ (eV)} = 5.76 + 1.53 \times 10^{-4} \nu_{CT} \quad (1)$$

where  $\nu_{CT}$  is the wave number in  $\text{cm}^{-1}$  of the complex determined in different solvents, viz., carbon tetrachloride, chloroform and dichloromethane. The data are summarized in Tables 2-4.

### Determination of oscillator strength, ( $f$ ), and transition dipole moment, ( $\mu EN$ )

From the CT-absorption spectra, one can determine the oscillator strength. The oscillator strength  $f$  is estimated using the formula

$$f = 4.32 \times 10^{-9} \int \epsilon_{CT} dv \quad (2)$$

where  $\int \epsilon_{CT} dv$  is the area under the curve of the extinction coefficient of the absorption band in question vs. frequency. To a first approximation

$$f = 4.32 \times 10^{-9} \epsilon_{CT} \Delta\nu_{1/2} \quad (3)$$

where  $\epsilon_{CT}$  is the maximum extinction coefficient of

the band and  $\Delta v_{1/2}$  is the half-width, i.e., the width of the band at half the maximum extinction. The observed oscillator strengths of the CT-bands are summarized in Tables 2-4.

The extinction coefficient is related to the transition dipole by

$$\mu_{EN} = 0.0952 [\epsilon_{CT} \Delta v_{1/2} / \Delta v]^{1/2} \quad (4)$$

where  $\Delta v \approx v$  at  $\epsilon_{CT}$  and  $\mu_{EN}$  is defined as  $-e \int \psi_{ex} \sum_i r_i \psi_{yg} dt$ .  $\mu_{EN}$  for the complexes of PNA with DDQ is given in Tables 2-4.

#### Determination of resonance energy ( $R_N$ )

Briegleb and Czekalla [15] theoretically derived the relation

$$\epsilon_{CT} = 7.7 \times 10^{-4} / [h\nu_{CT} / [R_N] - 3.5], \quad (5)$$

where  $\epsilon_{CT}$  is the molar extinction coefficient of the complex at the maximum of the CT absorption,  $\nu_{CT}$  is the frequency of the CT-peak and  $R_N$  is the resonance energy of the complex in the ground state, which is obviously a contributing factor to the stability constant of the complex (a ground state property). The values of  $R_N$  for the complexes under study are given in Tables 2-4.

**Table 1.** Gaussian curve analysis for the CTC in the spectra of DDQ with PNA in different polar solvents.

Complex	Solvent	Temperature	A	W	Xc	Y <sub>0</sub>
DDQ + PNA	CH <sub>2</sub> Cl <sub>2</sub>	20°C	34.75 ± 6.66	95.74±15.05	419.37	0.8232±0.0235
DDQ + PNA	CHCl <sub>3</sub>	20°C	28.28 ± 4.52	67.84±9.66	421.56	0.9350±0.0197
DDQ + PNA	CCl <sub>4</sub>	20°C	32.42 ± 4.69	49.17±6.18	423.69	1.042±0.0290

**Table 2.** CT-complex absorption maxima ( $\lambda_{CT}$ ), transition energies ( $h\nu_{CT}$ ), of the DDQ+PNA complexes, experimentally determined values of ionization potentials ( $I_D$ ), oscillator strength ( $f$ ), dipole moments ( $\mu_{EN}$ ), and resonance energies ( $R_N$ ) of the complexes in dichloromethane.

Complex	Solvent	Temp.	$\lambda_{CT}$ (nm)	$f \times 10^{-5}$	$\mu_{EN}$ (Debye)	$R_N$ (ev)	$h\nu_{CT}$ (ev)	$I_D$ (ev)	$\Delta G$
DDQ + PNA	CH <sub>2</sub> Cl <sub>2</sub>	20°C	419.37nm	3.63×10 <sup>-5</sup>	0.892	0.00671	2.96	9.40	13.408
DDQ + PNA	CH <sub>2</sub> Cl <sub>2</sub>	20°C	549.17nm	3.48×10 <sup>-5</sup>	0.757	0.00370	2.26	8.54	14.721
DDQ + PNA	CH <sub>2</sub> Cl <sub>2</sub>	25°C	423.39nm	2.36×10 <sup>-5</sup>	0.912	0.00694	2.93	9.37	13.465
DDQ + PNA	CH <sub>2</sub> Cl <sub>2</sub>	25°C	558.46nm	1.73×10 <sup>-5</sup>	0.775	0.00381	2.22	8.49	14.778
DDQ + PNA	CH <sub>2</sub> Cl <sub>2</sub>	30°C	428.15nm	2.64×10 <sup>-5</sup>	0.934	0.00720	2.90	9.32	13.636
DDQ + PNA	CH <sub>2</sub> Cl <sub>2</sub>	30°C	530.30nm	6.58×10 <sup>-5</sup>	0.798	0.00425	2.34	8.63	14.492

**Table 3.** CT-complex absorption maxima ( $\lambda_{CT}$ ), transition energies ( $h\nu_{CT}$ ), of the DDQ+PNA complexes, experimentally determined values of ionization potentials ( $I_D$ ), oscillator strength ( $f$ ), dipole moments ( $\mu_{EN}$ ), and resonance energies ( $R_N$ ) of the complexes in chloroform.

Complex	Solvent	Temp.	$\lambda_{CT}$ (nm)	$f \times 10^{-5}$	$\mu_{EN}$ (Debye)	$R_N$ (ev)	$h\nu_{CT}$ (ev)	$I_D$ (ev)	$\Delta G$
DDQ + PNA	CHCl <sub>3</sub>	20°C	421.56nm	$2.65 \times 10^{-5}$	0.905	0.00690	2.95	9.38	13.808
DDQ + PNA	CHCl <sub>3</sub>	20°C	563.95nm	$2.42 \times 10^{-5}$	0.801	0.00403	2.20	8.47	14.549
DDQ + PNA	CHCl <sub>3</sub>	25°C	425.36nm	$1.93 \times 10^{-5}$	0.914	0.00695	2.92	9.35	14.549
DDQ + PNA	CHCl <sub>3</sub>	25°C	575.23nm	$6.75 \times 10^{-5}$	0.736	0.00334	2.16	8.40	15.120
DDQ + PNA	CHCl <sub>3</sub>	30°C	425.23nm	$2.13 \times 10^{-5}$	0.930	0.00718	2.92	9.35	14.778
DDQ + PNA	CHCl <sub>3</sub>	30°C	579.73nm	$7.57 \times 10^{-5}$	0.752	0.00345	2.14	8.39	15.006

**Table 4.** CT-complex absorption maxima ( $\lambda_{CT}$ ), transition energies ( $h\nu_{CT}$ ), of the DDQ+PNA complexes, experimentally determined values of ionization potentials ( $I_D$ ), oscillator strength ( $f$ ), dipole moments ( $\mu_{EN}$ ), and resonance energies ( $R_N$ ) of the complexes in carbon tetrachloride

Complex	Solvent	Temp.	$\lambda_{CT}$ (nm)	$f \times 10^{-5}$	$\mu_{EN}$ (Debye)	$R_N$ (ev)	$h\nu_{CT}$ (ev)	$I_D$ (ev)	$\Delta G$
DDQ + PNA	CCl <sub>4</sub>	20°C	423.69nm	$2.07 \times 10^{-5}$	0.939	0.00735	2.93	9.37	15.120
DDQ + PNA	CCl <sub>4</sub>	20°C	572.066nm	$6.26 \times 10^{-5}$	0.775	0.00372	2.17	8.43	14.835
DDQ + PNA	CCl <sub>4</sub>	25°C	421.65nm	$1.87 \times 10^{-5}$	0.949	0.00753	2.94	9.38	15.291
DDQ + PNA	CCl <sub>4</sub>	25°C	512.78nm	$1.54 \times 10^{-5}$	0.798	0.00440	2.42	8.74	14.435
DDQ + PNA	CCl <sub>4</sub>	30°C	418.89nm	$2.27 \times 10^{-5}$	0.972	0.00795	2.96	9.40	15.291
DDQ + PNA	CCl <sub>4</sub>	30°C	513.89nm	$1.22 \times 10^{-5}$	0.829	0.00474	2.42	8.72	14.093

**Table 5.** Absorption maxima  $\lambda_{CT}$ , association constants (K), molar absorptivities ( $\epsilon$ ), of the CT-complex of DDQ and PNA in dichloromethane, chloroform and carbon tetrachloride at 20°C, 25°C and 30°C.

Systems	Solvent	$\lambda_{CT}$ (nm)		$K_{20}$ (l mol <sup>-1</sup> )		$K_{25}$ (l mol <sup>-1</sup> )		$K_{30}$ (l mol <sup>-1</sup> )		$\epsilon_{20}$ (l mol <sup>-1</sup> cm <sup>-1</sup> )		$\epsilon_{25}$ (l mol <sup>-1</sup> cm <sup>-1</sup> )		$\epsilon_{30}$ (l mol <sup>-1</sup> cm <sup>-1</sup> )	
DDQ + PNA	CH <sub>2</sub> Cl <sub>2</sub>	44 0	56 0	22 8	383	234	39 3	24 7	35 1	176	127	184	133	193	141
DDQ + PNA	CHCl <sub>3</sub>	43 0	55 0	26 9	362	356	455	39 3	43 4	181	142	185	120	191	125
DDQ + PNA	CCl <sub>4</sub>	42 0	54 0	45 3	399	482	340	48 8	30 1	195	133	199	141	209	152

**Table 6.** Characteristic infrared frequencies\*(cm<sup>-1</sup>) and tentative assignments for DDQ, PNA and their complex.

DDQ	PNA	Complex	Assignments
3325 w	3480 s	3481s	v (N-H)
3218br	3356s, br	3416br	v (O-H),
-	3320s,br	3369br	v(C-H), aromatic
	-	3222sh	v ( <sup>1</sup> NH)
2250vw		-	v <sub>s</sub> (C-H), CH <sub>3</sub> + CH <sub>3</sub>
2231ms	3108 w	3231w	v(C-H), aromatic v ( <sup>1</sup> NH)
-	1923w	2928ms	
	1747w	2209ms	v (C?N):DDQ
1673 vs	1635ms	1633vs	v(C=O)+v(C=C)+
-	-	1606s	v (C-N): v <sub>as</sub> (NO <sub>2</sub> )
1552 vs	1591vs	1589ms	v(C=C), aromatic
	-	-	$\delta$ def (N-H), +NH <sub>2</sub> ring breathing bands
-	1474s	1498vs	$\delta$ (C-H) deformation
1451ms	1442s	1435vs	
	1398vs	1327vs	v(C=C)
1358w	1302w	1255m, sh	v <sub>as</sub> (C-N)
-		1240vs	
1267s	-	-	v(C-O)
1172 vs	1183w	1112ms	
1072w -	1110br	1110ms	v <sub>s</sub> (C-N)
1010vw	-	-	
-	998s	-	$\delta$ (C-H) in plane bending
893vs	842sharp	987mw	$\delta$ rock, +NH <sub>2</sub>
800vs		850m	v(C-Cl); DDQ, complex
	754vs	760w	C-H out of plane
720s	698vs	629mw	bending
-	534ms	563ms	
615 ms	490ms	495br	C-H wagging
428s	418sharp	420ms	CNC deformation

S, strong, w, weak, m, medium, sh, shoulder, v, very, vs, very strong, br, broad; v, stretching, vs, symmetrical stretching; v<sub>as</sub>, asymmetrical stretching

*Determination of standard free energy changes ( $\Delta G^\circ$ ) and energy ( $E_{CT}$ ) of the  $\pi$ - $\pi^*$  interaction between donor and acceptor*

The standard free energy changes of complexation ( $\Delta G^\circ$ ) were calculated from the association constants by the following equation derived by Martin, Swarbrick and Cammarata [16].

$$\Delta G^\circ = -2.303 RT \log K_{CT} \quad (6)$$

where  $\Delta G^\circ$  is the free energy change of the CT-complexes ( $KJ \text{ mol}^{-1}$ ),  $R$  is the gas constant ( $8.314 \text{ Jmol}^{-1}K$ ),  $T$  is the temperature and  $K_{CT}$  is the association constant of the complex ( $l \text{ mol}^{-1}$ ) in different solvents at different temperatures  $20^\circ\text{C}$ ,  $25^\circ\text{C}$  and  $30^\circ\text{C}$ , shown in Tables 2-4.

The energy ( $E_{CT}$ ) of the  $\pi$ - $\pi^*$  interaction between donor (PNA), and acceptor (DDQ), is calculated using the following equation derived by G. Briegleb and Z. Angew [17]:

$$E_{CT} = 1243.667 / \lambda_{CT} \quad (7)$$

where  $\lambda_{CT}$  is the wavelength of the CT band.

The calculated values of  $E_{CT}$  are given in Tables 2-4.

*Spectrophotometric study of the formation constants of the charge transfer complexes in different polar solvents*

The stoichiometries and the formation constants of the charge transfer complex of p-nitroaniline with DDQ were determined in different polar solvents, viz., carbon tetrachloride, chloroform and dichloromethane at different temperatures  $20^\circ\text{C}$ ,  $25^\circ\text{C}$  and  $30^\circ\text{C}$  using the Benesi-Hildebrand equation [18, 19]. The spectrophotometric data were employed to calculate the values of the formation constants,  $K_{CT}$  of the complexes. The changes in the absorbance upon addition of PNA to a solution of DDQ of fixed concentration follow the Benesi-Hildebrand equation [18, 19] in the form:

$$[A]_0 / A = (1 / K_{CT}\epsilon_{CT}) \times 1 / [D]_0 + 1/\epsilon_{CT} \quad (8)$$

where  $[D]_0$  and  $[A]_0$  are the concentrations of the PNA donor, and DDQ acceptor, respectively,  $A$  is the absorbance of the donor-acceptor mixture at  $\lambda_{CT}$ , against the solvents as reference,  $K_{CT}$  is the formation constant and  $\epsilon_{CT}$  is the molar extinction coefficient, different from that of the complex in eq.(8) [18,19], which is valid under the condition  $[D]_0 \gg [A]_0$  [11, 12] for 1:1 donor-acceptor complexes. The concentration of the donor PNA was changed over a wide range from 0.01M to 0.5M while the concentration of the  $\pi$  acceptor DDQ was kept fixed at 0.01M in each reaction

mixture. These produced solutions with donor: acceptor molar ratio varying from 1:1 to 50:1. The experimental data are given in Table 3.

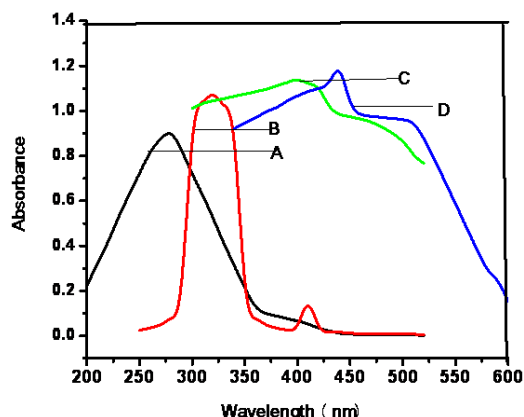


**Fig. 1.** Absorption spectra of (A) 0.01M DDQ (B) Blank solvent (dichloromethane) (C) 0.01 M p-nitro aniline (D) CT-complex of 0.01 M PNA and 0.01 M DDQ in dichloromethane.

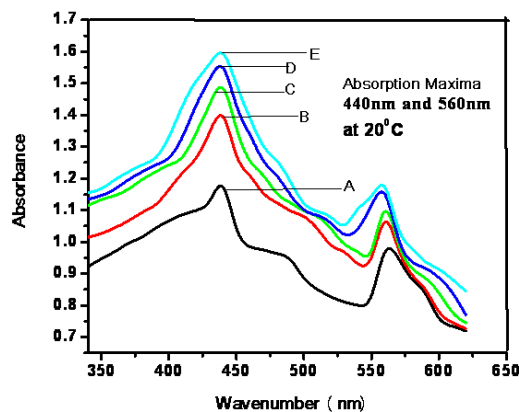


**Fig. 2.** Absorption spectra of DDQ ( $1 \times 10^{-2}M$ ) in dichloromethane at  $20^\circ\text{C}$  with addition of p-nitroaniline concentrations ranging from 0.01M to 0.05M with increasing concentrations from bottom to top.

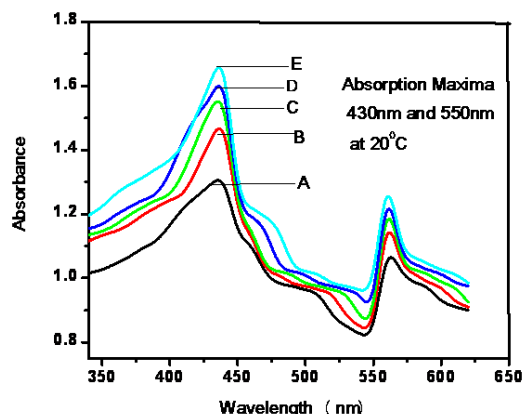


**Fig. 3.** Absorption spectra of DDQ ( $1 \times 10^{-2}M$ ) in chloroform at  $20^\circ\text{C}$  with addition of p-nitroaniline concentrations ranging from 0.01M to 0.05M with increasing concentrations from bottom to top.

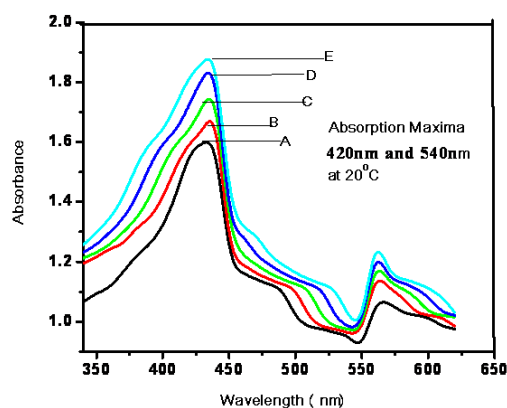


Fig. 4. Absorption spectra of DDQ ( $1 \times 10^{-2}$ M) in carbon tetrachloride at 20°C with addition of p-nitroaniline concentrations ranging from 0.01M to 0.05M with increasing concentrations from bottom to top.

The Benesi – Hildebrand [18, 19] method is an approximation that has been used many times and gives decent results. The intensity in the visible region of the absorption bands, measured against the solvent as reference, increases with the increase in the polarity and addition of PNA. The typical absorbance data for the charge transfer complexes of PNA with DDQ in different polar solvents at different temperatures 20°C, 25°C and 30°C are reported in Table 5. In all systems very good linear plots according to eq. (8) [18, 19] were obtained, as shown in Figs 5-7.

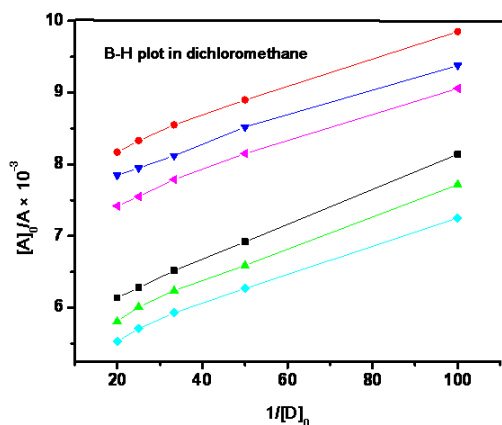


Fig. 5. Relation between  $[A]_0/A$  and  $1/[D]_0$  of DDQ+PNA in  $CH_2Cl_2$ .

Formation constants for the complexes in different polar solvents at different temperatures 20°C, 25°C and 30°C determined from the BH plots are summarized in Table 5. The correlation coefficients of all plots were above 0.99. Plots of  $[A]_0/A$  against  $1/[D]_0$  were found to be linear in all systems in Figs. 5-7 showing 1:1 charge transfer complexes, i.e. the straight lines are obtained with the slopes  $1/K_{CT}\epsilon_{CT}$ . These results are an evidence of 1:1 CT-complexes. From the slope  $1/K_{CT}\epsilon_{CT}$  and

the intercept,  $1/\epsilon_{CT}$ ,  $K_{CT}$  and  $\epsilon_{CT}$  of the CT-complex were calculated in different polar solvents

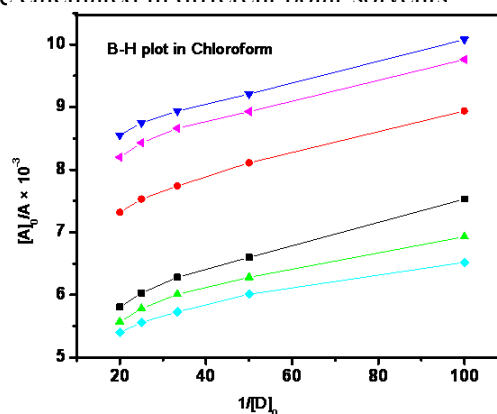


Fig. 6. Relation between  $[A]_0/A$  and  $1/[D]_0$  of DDQ+PNA in  $CHCl_3$ .

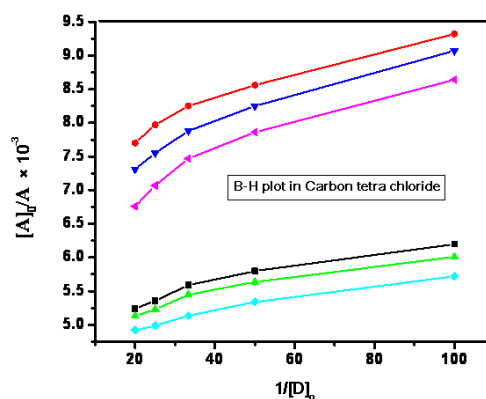


Fig. 7. Relation between  $[A]_0/A$  and  $1/[D]_0$  of DDQ+PNA in  $CCl_4$ .

#### Appearance of two CT-bands

The two absorption peaks of the CT-complex in each system and their  $\lambda_{max}$  are given in Table 5.

Well defined absorption peaks of the two CT bands were observed for the DDQ complexes with PNA. Multi-CT absorption bands have been found in the CT complexes containing strong electron acceptors such as chlorine, bromanil and TCNE [20].

The origin of the multi-CT bands observed in the case of DDQ/PNA complex can be explained by the existence of two closely located occupied orbitals of the donors [21].

#### Effect of temperature on the formation constant

Temperature affects the values of  $K_{CT}$ , generally  $K_{CT}$  for DDQ complexes increases with the increase in temperature. But in some cases, such as the complexes of DDQ with PNA at 25°C, and  $\lambda_{max}$  540 nm in  $CCl_4$ , at 30°C, and  $\lambda_{max}$  560 nm in  $CH_2Cl_2$ , at 30°C, and  $\lambda_{max}$  550 nm in  $CHCl_3$ , and at 30°C, and  $\lambda_{max}$  540 nm in  $CCl_4$ , its value decreases with the increase in temperature, as shown in Table 5. There may be a decrease in the

stability of the complex with the increase in temperature in these systems. This trend is similar to that reported in many systems, such as TCNB-benzene complexes and DDQ and acetanilide, biphenyl and naphthalene systems [21].

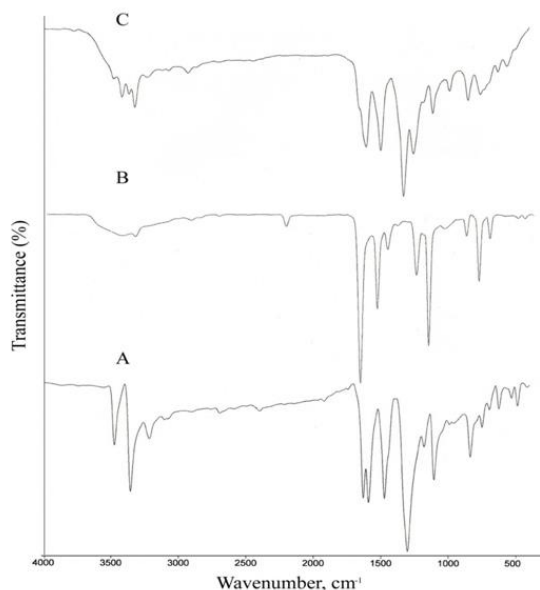


**Fig. 8.** FT-IR spectrum of (A) complex of DDQ and PNA, (B) acceptor DDQ and (C) donor (PNA).

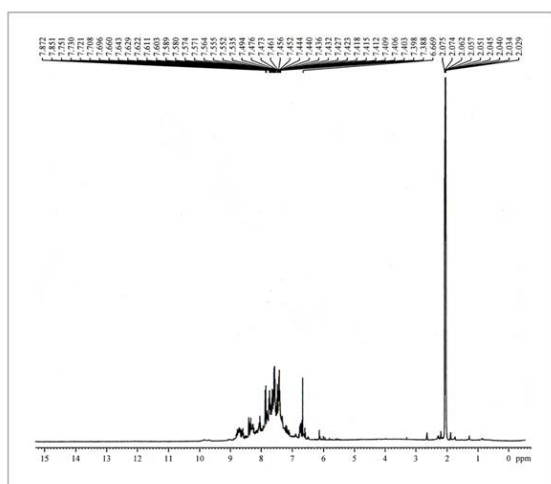


**Fig. 9.** <sup>1</sup>H NMR spectrum of the CT-complex

*Effect of solvents on the formation of CT-complexes*

The spectroscopic properties were markedly affected by varying solvent polarity. In the present investigation, the  $K_{CT}$  values increased significantly from dichloromethane to carbon tetrachloride with decreasing solvent polarity. The values of the association constant  $K_{CT}$  and the values of molar extinction coefficient are shown in Table 5. Moreover, the experimental results of the CT interaction between DDQ with PNA in different polar solvents reveal that the values of the

association constant  $K_{CT}$ , in dichloromethane at  $\lambda_{CT}$  440 nm and 560 nm are 228 ( $1 \text{ mol}^{-1}$ ), 383 ( $1 \text{ mol}^{-1}$ ) at 20°C, 234 ( $1 \text{ mol}^{-1}$ ), 393 ( $1 \text{ mol}^{-1}$ ) at 25°C and 247 ( $1 \text{ mol}^{-1}$ ) and 351 ( $1 \text{ mol}^{-1}$ ) at 30°C. In chloroform the values of the association constant  $K_{CT}$ , at  $\lambda_{CT}$  430 nm and 550 nm are 269 ( $1 \text{ mol}^{-1}$ ), 362 ( $1 \text{ mol}^{-1}$ ) at 20°C, 356 ( $1 \text{ mol}^{-1}$ ), 455 ( $1 \text{ mol}^{-1}$ ) at 25°C and 393 ( $1 \text{ mol}^{-1}$ ), 434 ( $1 \text{ mol}^{-1}$ ) at 30°C. In carbon tetrachloride the values of the association constant  $K_{CT}$ , at  $\lambda_{CT}$  420 nm and 540 nm are 453 ( $1 \text{ mol}^{-1}$ ), 399 ( $1 \text{ mol}^{-1}$ ), at 20°C 482 ( $1 \text{ mol}^{-1}$ ), 340 ( $1 \text{ mol}^{-1}$ ), at 25°C, 488 ( $1 \text{ mol}^{-1}$ ), 301 ( $1 \text{ mol}^{-1}$ ), at 30°C. The values of the molar extinction coefficients  $\epsilon_{20}$ ,  $\epsilon_{25}$ , and  $\epsilon_{30}$  in dichloromethane are 176 ( $1 \text{ mol}^{-1}\text{cm}^{-1}$ ), 127 ( $1 \text{ mol}^{-1}\text{cm}^{-1}$ ) and 184 ( $1 \text{ mol}^{-1}\text{cm}^{-1}$ ), 133 ( $1 \text{ mol}^{-1}\text{cm}^{-1}$ ) and 193 ( $1 \text{ mol}^{-1}\text{cm}^{-1}$ ), 141 ( $1 \text{ mol}^{-1}\text{cm}^{-1}$ ), respectively. The values of the molar extinction coefficients  $\epsilon_{20}$ ,  $\epsilon_{25}$ , and  $\epsilon_{30}$  in chloroform are 181 ( $1 \text{ mol}^{-1}\text{cm}^{-1}$ ), 142 ( $1 \text{ mol}^{-1}\text{cm}^{-1}$ ), 185 ( $1 \text{ mol}^{-1}\text{cm}^{-1}$ ), 120 ( $1 \text{ mol}^{-1}\text{cm}^{-1}$ ), and 191 ( $1 \text{ mol}^{-1}\text{cm}^{-1}$ ), 125 ( $1 \text{ mol}^{-1}\text{cm}^{-1}$ ), respectively, as shown in Table 5. The values of the molar extinction coefficients  $\epsilon_{20}$ ,  $\epsilon_{25}$ , and  $\epsilon_{30}$  in carbon tetrachloride are 195 ( $1 \text{ mol}^{-1}\text{cm}^{-1}$ ), 133 ( $1 \text{ mol}^{-1}\text{cm}^{-1}$ ), 199 ( $1 \text{ mol}^{-1}\text{cm}^{-1}$ ), 141 ( $1 \text{ mol}^{-1}\text{cm}^{-1}$ ), 209 ( $1 \text{ mol}^{-1}\text{cm}^{-1}$ ), 152 ( $1 \text{ mol}^{-1}\text{cm}^{-1}$ ), respectively, as represented in Table 5. The increase in the  $K_{CT}$  values with decreasing solvents polarity may also be due to the fact that the CT-complex should be stabilized in less polar solvents [22].

The influence of solvent polarity on the spectroscopic and thermodynamic properties of molecular electron-donor-acceptor (EDA) complexes is discussed. The data given in Table 5 show that DDQ interacts more strongly with PNA in carbon tetrachloride than in the other two solvents.

The experimentally determined values of oscillator strength, ( $f$ ) in dichloromethane at 20°C are  $3.63 \times 10^{-5}$  and  $3.48 \times 10^{-5}$ ; at 25°C are  $2.36 \times 10^{-5}$ , and  $1.73 \times 10^{-5}$ ; and at 30°C are  $2.64 \times 10^{-5}$  and  $6.58 \times 10^{-5}$ , as given in Table 2. The values of the oscillator strength, ( $f$ ) in chloroform at 20°C are  $2.65 \times 10^{-5}$  and  $2.42 \times 10^{-5}$ ; at 25°C are  $1.93 \times 10^{-5}$  and  $6.75 \times 10^{-5}$ ; and at 30°C are  $2.13 \times 10^{-5}$  and  $7.57 \times 10^{-5}$ , respectively, as shown in Table 3. In carbon tetrachloride the values of the oscillator strength, ( $f$ ) at 20°C are  $2.07 \times 10^{-5}$  and  $6.26 \times 10^{-5}$ ; at 25°C are  $1.87 \times 10^{-5}$  and  $1.54 \times 10^{-5}$ ; and at 30°C are  $2.27 \times 10^{-5}$  and  $1.22 \times 10^{-5}$ , respectively (Table 4).

The values of the transition dipole moment, ( $\mu_{EN}$ ) in dichloromethane are 0.892 Debyes and 0.757 Debyes at 20°C; 0.912 Debyes and 0.775 Debyes at 25°C; and 0.934 Debyes and 0.798 Debyes at 30°C (see Table 2). In chloroform the

values of the transition dipole moment, ( $\mu_{EN}$ ) are 0.905 Debyes and 0.801 Debyes at 20°C; 0.914 Debyes and 0.736 Debyes at 25°C; and 0.930 Debyes and 0.752 Debyes at 30°C (Table 3). In carbon tetrachloride the values of the transition dipole moment, ( $\mu_{EN}$ ) are 0.939 Debyes and 0.775 Debyes at 20°C; 0.949 Debyes and 0.798 Debyes at 25°C; and 0.972 Debyes and 0.829 Debyes at 30°C (Table 4), which indicate that the complex should be more stable in the less polar solvent CCl<sub>4</sub> than in the other two solvents.

The free energy change of the complexation also reveals that the CT-complex formation between the donor (PNA) and the acceptor (DDQ) is exothermic in nature. The values of  $\Delta G^\circ$  in dichloromethane: -13.408 KJmol<sup>-1</sup> and -14.721 KJmol<sup>-1</sup> at 20°C; -13.405 KJmol<sup>-1</sup> and -14.778 KJmol<sup>-1</sup> at 25°C; and -13.636 KJmol<sup>-1</sup> and -14.492 KJmol<sup>-1</sup> at 30°C are shown in Table 2. In chloroform the values of  $\Delta G^\circ$  at 20°C are -13.808 KJmol<sup>-1</sup> and -14.549 KJmol<sup>-1</sup>; at 25°C are -14.549 KJmol<sup>-1</sup> and -15.120 KJmol<sup>-1</sup>; and at 30°C -14.778 KJmol<sup>-1</sup> and -15.006 KJmol<sup>-1</sup> (Table 3). In carbon tetrachloride the values are -15.120 KJmol<sup>-1</sup> and -14.835 KJmol<sup>-1</sup> at 20°C; -15.291 KJmol<sup>-1</sup> and -14.435 KJmol<sup>-1</sup> at 25°C; and -15.291 KJmol<sup>-1</sup> and -14.093 KJmol<sup>-1</sup> at 30°C (Table 4). The values of  $\Delta G^\circ$  generally become more negative as the association constants of the molecular complex increase.

The calculated values of  $I_D$  of the DDQ/PNA system in dichloromethane at 20°C are 9.40(eV), 8.54(eV); 9.37(eV) and 8.49 (eV) at 25°C and 9.32(eV) and 8.63(eV) at 30°C (Table 2). In chloroform the values of  $I_D$  at 20°C are 9.38 (eV) and 8.47 (eV); at 25°C are 9.35 (eV) and 8.40 (eV); and at 30°C are 9.35 (eV) and 8.39 (eV) (Table 3). The calculated values of  $I_D$  in carbon tetrachloride at 20°C are 9.37 (eV) and 8.43 (eV); at 25°C are 9.38 (eV) and 8.74 (eV); and at 30°C are 9.40 (eV) and 8.72 (eV) (Table 4). The approximate constancy of the  $I_D$  values indicates that the ionization potential has a negligibly small effect on the  $K_{CT}$  value.

#### FT-IR spectra of CT-complex and reactants

FT-IR spectra of p-nitroaniline (donor), DDQ (acceptor) and their CT-complex are shown in Fig 8. while the assignments of their characteristic FT-IR spectral bands are reported in Table 6. The formation of the charge transfer complex during the reaction of DDQ with PNA is strongly evidenced by the presence of the main characteristic infrared bands of the donor and acceptor in the spectrum of the product. There are changes in their intensities compared with those of the free donor and acceptor. This shift was attributed to the charge transfer from

donor to acceptor upon complexation.

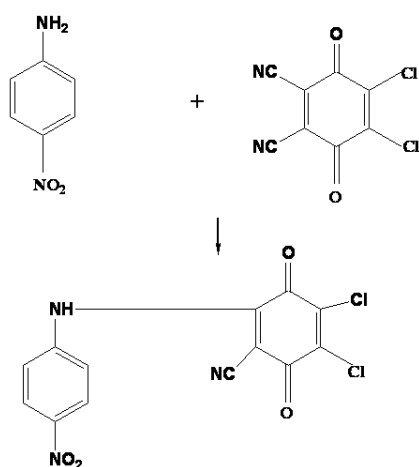
The FT-IR spectrum of the DDQ/PNA complex indicated that the band that results from the  $\nu$  (C≡N) vibration of the free DDQ acceptor changed in frequency and decreased in intensity in the complexes upon CT complexation. Free DDQ shows two  $\nu$  (C≡N) vibrations at 2250 and 2231 cm<sup>-1</sup>, while in its complex  $\nu$  (C≡N) occurs at a lower wave number value, 2209 cm<sup>-1</sup>. It is clear that  $\nu$  (C≡N) of DDQ is decreased upon complexation [23]. The characteristic band of  $\nu$  (N-H) of PNA is observed at 3480 cm<sup>-1</sup> (strong) and 3356 cm<sup>-1</sup> (strong). In the CT-complex a new band is observed at 3481 cm<sup>-1</sup>(strong). The band at 3076 cm<sup>-1</sup>(weak) is due to the aromatic C-H stretching vibration. The -NH<sub>2</sub> deformation mode is observed by the absorption at 1633 cm<sup>-1</sup> (very strong) in the CT-complex, whereas in free PNA this is observed at 1635 cm<sup>-1</sup> (medium strong). This band overlaps with the aromatic C=C stretching vibrations. The -NO<sub>2</sub> group is observed at 1606 cm<sup>-1</sup>(strong) in the CT complex, whereas in free PNA this is observed at 1591 cm<sup>-1</sup> (very strong). The group of bands assigned to  $\nu$  (C-Cl) vibrations, which appeared at 893 cm<sup>-1</sup> and 800 cm<sup>-1</sup> in the free DDQ, exhibited a shift to lower wave numbers at 862 cm<sup>-1</sup> and 780 cm<sup>-1</sup> and a decrease in intensity of the characteristic peaks [23]. These observations clearly confirm that the (C≡N) group in the DDQ acceptor participates in the complexation process. Because DDQ lacks acidic centers, the molecular complex can be assumed to form through  $\pi$ - $\pi^*$  and/or n- $\pi^*$  charge migration from the HOMO of the donor to the LUMO of the acceptor. The  $\pi$ - $\pi^*$  CT complex is formed *via* the benzene ring (electron-rich group) of the PNA and DDQ reagents (electron- acceptor).

The cyano group (C≡N) is an electron-withdrawing group that exists in DDQ in a conjugated bonding system. The 2 CN groups in DDQ withdraw electrons from the aromatic ring, and such a process will make the aromatic ring an electron-accepting region. The  $\pi^*$ -CN electron density appears to increase and more easily accept a proton from the donor because of the electron-withdrawing process and the conjugated electron system. So, the interaction mode between PNA and the DDQ acceptor also occurs through migration of an H<sup>+</sup> ion to one of the cyano groups in the DDQ acceptor to form a positive ion (-C≡N<sup>+</sup>H) that associates with the -NH<sub>2</sub> group in PNA.

#### <sup>1</sup>H- NMR spectrum of the CT- complex

The <sup>1</sup>H-NMR spectrum of the 2, 3-dichloro-5, 6-dicyano-p-benzoquinone and p-nitro aniline product in acetone is shown in Figure 9. P-nitro

aniline ring system was specified in the region  $\delta = 8.40\text{--}6.66$  ppm. The  $\text{NH}_2$  group of p-nitroaniline occurring at  $\delta = 6.71$  in the free donor was shifted to  $\delta = 6.66$ . This indicates that one of the CN groups of DDQ has been eliminated by the amino group of the p-nitroaniline donor eliminating HCN [24] (Scheme 1). The doublet peaks at  $\delta = 8.40$  ppm and the triplet peaks at  $\delta = 7.62$  ppm assigned to the rest of protons of p-nitroaniline are in the same kind in DDQ moiety in the CT-complex. The intensities and chemical shifts of the aromatic signals were significantly affected by the elimination and the accompanying changes in the structured configuration. Mechanism and structure of the CT-complex of acceptor and donor is given in Scheme 1.



**Scheme 1.** Mechanism of the interaction between p-nitroaniline and DDQ

## CONCLUSION

The UV-Vis spectrophotometric method for the study of the CT-complex of DDQ with PNA ascertains the formation of a 1:1 (A:D) complex in all three solvents, viz., carbon tetrachloride, chloroform and dichloromethane. In all systems the stoichiometry is unaltered by changing the solvent. The association constants,  $K_{CT}$  and molar extinction coefficients,  $\epsilon_{CT}$ , of all systems were evaluated by the Benesi-Hildebrand method. The spectroscopic and thermodynamic parameters of the CT-complexes were found to be dependent on the polarity of the solvents. The values of oscillator strengths, ( $f$ ) transition dipole moments, ( $\mu_{EN}$ ) resonance energies, ( $R_N$ ) and standard free energies, ( $\Delta G^\circ$ ) were estimated for the PNA/DDQ systems in different polar solvents. The results show that the investigated CT-complex is stable, exothermic and spontaneous. From the trends in the CT absorption bands, the ionization potentials of the donor molecules were estimated. The FT-IR and  $^1\text{H}$  NMR

spectra revealed that the charge transfer complex is present as an ion pair and there are few free ions in solution.

**Acknowledgements:** Authors thank Dr. Sakir Ali, Chairman of Chemistry Department, Aligarh Muslim University, India, for providing the facilities of instruments of FT-IR spectrometer, UV-Visible spectrophotometer. Financial assistance from the UGC, New Delhi extended through the Women-PDF fellowship is also gratefully acknowledged. The authors also thank the learned referee for making valuable comments.

## REFERENCES

1. L. J. Andrews, *Chem. Rev.*, **54**, 713 (1954).
2. S. P. Mc Glynn, *Chem. Rev.*, **58**, 1113 (1958).
3. R. S. Mulliken, *J. Am. Chem. Soc.*, **74**, 811 (1952).
4. R. Foster, *Organic Charge-Transfer Complexes*, New York, 1969, p.387.
5. L. E. Orgel, *J. Chem. Phys.*, **23**, 1352 (1955).
6. A.S. Amin, A.M. El-Beshbeshy, *Microchim. Acta*, **63**, 137 (2001).
7. S.M. Andrade, S.M.B. Costa, R. Pansu, *J. Colloids Interface Sci.*, **226**, 260 (2000).
8. A. Eychmuller, A.L. Rogach, *Pure Appl. Chem.*, **72**, 179 (2000).
9. M. Hayashi, T.S. Yang, J. Yu, A. Mebel, S.H. Lin, *J. Phys. Chem. A*, **101**, 4156 (1997).
10. D.A. Skoog, *Principle of analytical Chemistry*, 3<sup>rd</sup> ed. Sannder College Publishing, New York, 1985, (Chapter7).
11. M. Hasani, R. Alireza, *Spectrochim. Acta Part A*, **65**, 1093 (2006).
12. S. Bhattacharya, K. Gosh, S.C. Momas, *Spectrochim. Acta Part A*, **65**, 659 (2006).
13. R. K. Gupta, R.A. Sig, *J. App. Sci.*, **5** (1), 28 (2005).
14. G. Aloisi, S. Pignataro, *J. Chem. Soc. Faraday Trans.*, **69**, 534 (1972).
15. G. Briegleb, J. Czekalla, *Z. Physikchem. (Frankfurt)*, **24**, 237 (1960).
16. A.N. Martin, J. Swarbrick, A. Cammarata, *Physical Pharmacy*, 3<sup>rd</sup>ed, Lee & Febiger, Philadelphia, PA, 1969, p. 344.
17. G. Briegleb, *Z. Angew. Chem.* **76**, 326 (1964).
18. H.A. Benesi, J. H. Hildebrand, *J. Am. Chem. Soc.*, **71**, 2703 (1949).
19. P. Douglas, G. Waechter, A. Mills, *Photochem. Photobiol.*, **52**, 473 (1990).
20. G. Briegleb, *Electronen-Donator-Acceptor-Complex*, Springer-Verlag, Berlin, 1961.
21. M.S. Subhani, N.K. Bhatti, M. Mohammad, A.Y. Khan, *Turk J Chem.*, **24**, 223 (2000).
22. M. E. El - Zaria, *Spectrochim. Acta A*, **69**, 216 (2008).
23. H. H. Eldaroti, S. A. Gadir, M. S. Refat, A.M. A. Adam, *J. Pharm. Anal.*, **4**, 81 (2014).
24. M. S Refat, N. M. El-Metwally, *Chin. Sci. Bull.*, **56**, 19 (1993).

## СПЕКТРОСКОПСКИ ИЗСЛЕДВАНИЯ НА КОМПЛЕКСИ С ПРЕНОС НА ЗАРЯДА ОТ 2,3-ДИХЛОРО-5,6-ДИЦИАНО-р-БЕНЗОХИНОН С р-НИТРОАНИЛИН

Н. Сингх, А. Ахмад \*

Департамент по химия, Научен факултет, Мюсюлмански университет, Алигар - 202002, Индия

Постъпила на 2 август, 2015 г.; приета на 5 октомври, 2015 г.

(Резюме)

Комплекси с пренос на заряда (СТ-комплекси) с донор р-нироанилин (PNA) и акцептор 2,3-дихлоро-2,6-дициано-р-бензохинон (DDQ) са изследвани спектро-фотометрично в различни разтворители, като  $\text{CH}_2\text{Cl}_2$ ,  $\text{CHCl}_3$  и  $\text{CCl}_4$  при различни температури. Във всички случаи са наблюдавани по две линии на пренос на заряда. Резултатите показват, че образуването на СТ-комплекс в по-малко полярен разтворител сравнително високо. Стехиометрията на СТ-комплекса е 1:1. Физичните параметри на СТ-комплекса са оценени по уравнението на Benesi-Hildebrand. Данните са обсъдени в смисъла на константите на образуване ( $K_{CT}$ ), коефициента на моларна екстинкция ( $\epsilon_{CT}$ ), стандартния термодинамичен потенциал ( $\Delta G^\circ$ ), силата на осцилатора ( $f$ ), преодния диполен момент ( $\mu_{EN}$ ), рзонансната енергия ( $R_N$ ) и йонизационния потенциал ( $I_D$ ). Резултатите показват, че константата на образуване на комплекса ( $K_{CT}$ ) е зависима от природата на акцептора на електрони, на донора и от полярността на използвания разтворител. Образуването на комплекса се потвърждава чрез UV-Vis – спектроскопия, FTIR и  $^1\text{H}$ -ЯМР. Предложена е структура на СТ-комплекса между DDQ и PNA.

## Synthetic flavone derivatives. An antibacterial evaluation and structure-activity relationship study

M. Shoaib<sup>1</sup>, S. W. A. Shah<sup>1\*</sup>, N. Ali<sup>2</sup>, I. Shah<sup>1</sup>, M. N. Umar<sup>3</sup>, Shafiullah<sup>1</sup>, M. N. Tahir<sup>4</sup>, M. Ghias<sup>1</sup>.

<sup>1</sup>Department of Pharmacy, University of Malakand, Chakdara 18550, Dir Lower, Khyber Pakhtunkhwa, Pakistan

<sup>2</sup>Department of Pharmacology, Institute of Basic Medical Sciences, Khyber Medical University, Peshawar 25000, Khyber Pakhtunkhwa, Pakistan

<sup>3</sup>Department of Chemistry, University of Malakand, Chakdara 18550, Dir Lower, Khyber Pakhtunkhwa, Pakistan

<sup>4</sup>Department of Physics, University of Sargodha 40100, Punjab, Pakistan

Received September 4, 2015, Accepted December 16, 2015

Biologically active flavone derivatives with antibacterial potentials were synthesized *via* Claisen-Schmidt condensation of ketones with different aldehydes with good yields. The structures were established by different spectroscopic techniques like <sup>1</sup>H NMR, <sup>13</sup>C NMR, IR and elemental analysis. The findings showed that some of the substituted flavones possess higher antibacterial potentials than simple flavones as regards their minimum inhibitory concentration (MIC) and are potential candidates for the treatment of a wide range of infectious diseases.

**Keywords:** Flavone derivatives, antibacterial, MIC, infectious diseases.

### INTRODUCTION

Infectious diseases are among the main causes of mortality and morbidity worldwide. Advancement in the innovation of antimicrobial agents has safeguarded the way for human wellbeing. However, effectiveness of antibiotics in future is to some extent in doubtful condition due to the development of resistance to these agents in an unavoidable manner [1]. The emergence of hitherto unidentified microbes that cause infections poses a colossal health concern regarding the combat towards infectious diseases [2]. The need for new, effective and affordable drugs to treat microbial diseases in the developing world is one of the major issues facing global health today and consequently, this has created a new dimension in the search for new drugs [3]. Structural modification of anti-infective agents has confirmed to be an effective way of enhancing the lifespan of these agents [4]. Natural products have been reported to be a potential source of anti-infective agents and the prime examples are penicillin and tetracycline. Generally, polyphenolic compounds like flavonoids (natural compounds) have been reported for a wide range of pharmacological actions [5]. At present, this class of natural products is the area of interest in medical research and is known to possess pharmacological actions including antiallergic [6], anti-inflammatory [7], antiviral [8], antithrombotic [9], antimutagenic [10], antioxidant [11],

antidiabetic [12], anticancer [13], hepatoprotective [14] and antimicrobial [15-18] effects.

Most of the scientific reports are on natural flavonoids and acquire a special place in natural and heterocyclic chemistry because of their structural ornamentation in many pharmacologically active compounds. In view of the above facts regarding the significance of flavonoids in nature, it was considered worthwhile to synthesize flavonoid derivatives and to attempt to portray the structure-activity relationships (SAR).

### EXPERIMENTAL

#### *Materials and Methods*

Substituted ketones and benzaldehyde were purchased from Sigma Aldrich Chemical Company. TLC plates were Merck 60 F254, Darmstadt Germany. Solvents and chemicals like ethanol, n-hexane, ethyl acetate, DMSO of extra pure analytical grade were purchased from Merck. Mueller-Hinton agar and nutrient broth were purchased from Oxoid, UK. Ciprofloxacin and ampicillin were gifted by local pharmaceutical industries.

<sup>1</sup>H-NMR and <sup>13</sup>C NMR spectra were recorded in deuterated chloroform (CDCl<sub>3</sub>) on a Bruker SF spectrometer operating at 300 and 75 MHz frequencies, respectively. Chemical shift values are expressed in  $\delta$  (ppm) downfield relative to TMS which was used as an internal standard. Infrared spectra were recorded on Thermoscientific, USA (Nicolet 6700) infrared spectrometer by the KBr disk method. All melting points are uncorrected and

\* To whom all correspondence should be sent:  
E-mail: pharmacistsyed@gmail.com

were taken in open capillary tubes using an Electrothermal 9100 apparatus (Barnstead, UK). Reaction extents and final products purities were checked on TLC plates (Merck 60 F254) and spots were visualized under UV lamp (180-365 nm) by staining with iodine vapor.

### Synthesis and characterization

#### General procedure for the synthesis of flavone derivatives

To an ethanolic solution of substituted 2-hydroxy acetophenone (15 mM), sodium hydroxide (10 ml, 40% ethanolic) was dropwise added at room temperature. Then the corresponding benzaldehyde derivatives (15 mM) were dropwise added to this mixture and stirred for 24-48 h at room temperature ( $25 \pm 2^\circ\text{C}$ ). The reaction was monitored by TLC and upon completion, the contents were poured into crushed ice and neutralized with 1N HCl solution resulting in yellow precipitates of the corresponding chalcones. The latter were filtered and washed with water to remove the impurities.

In the next step, the respective chalcones were separately cyclized to flavone derivatives in 15 ml DMSO in the presence of iodine (375 mg) at  $140^\circ\text{C}$  for 1 h. Upon completion of the reaction, the mixtures were cooled to room temperature and poured into water followed by extraction with ethyl acetate (25 ml $\times$ 3), treated with sodium thiosulfate solution (20%), brine solution and dried over sodium sulfate. The final products (a mixture of flavone and chalcone) were subjected to column chromatography using n-hexane: ethyl acetate (9:1) to purify the flavone derivatives (Scheme 1) [19, 20].

#### 2-Phenyl-4H-chromen-4-one (F1)

The compound was obtained by stirring equimolar amounts of 2'-hydroxyacetophenone and benzaldehyde in ethanol, and adding sodium hydroxide solution with continuous stirring to get the desired chalcone. In the next step, the chalcone was cyclized to flavone by refluxing in DMSO in the presence of catalytic iodine as described above.

$^1\text{H NMR}$  (300 MHz, chloroform-*d*)  $\delta$  8.22 (dd,  $J = 8.0, 1.7$  Hz, 1H), 7.75 – 7.53 (m, 5H), 7.50 – 7.37

(m, 4H), 6.85 (s, 1H).  $^{13}\text{C NMR}$  (75 MHz,  $\text{CDCl}_3$ )  $\delta$  178.48, 163.42, 156.26, 133.79, 131.77, 131.61, 129.04, 126.66, 125.71, 125.24, 123.95, 118.09, 107.58 IR (KBr),  $\nu$ ,  $\text{cm}^{-1}$ , 1635.4, 1463.3, 1372.4, 766.0. Found, %: C 81.07; H 4.54.  $\text{C}_{15}\text{H}_{10}\text{O}_2$ . Calculated, %: C 81.19; H 4.60 [20-22].

#### 2-(4-(Dimethylamino)phenyl)-4H-chromen-4-one (F2)

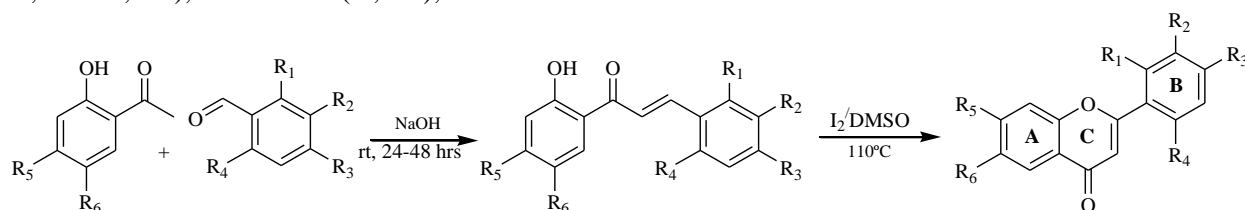
The compound was obtained by stirring equimolar amounts of 2'-hydroxyacetophenone and 4-(dimethylamino) benzaldehyde in ethanol, and adding sodium hydroxide solution under continuous stirring to get the desired chalcone. In the next step, the chalcone was cyclized to flavone by refluxing in DMSO in the presence of catalytic iodine.

$^1\text{H NMR}$  (300 MHz, chloroform-*d*)  $\delta$  8.24 (dd,  $J = 7.9, 1.7$  Hz, 1H), 7.89 – 7.81 (m, 2H), 7.68 (ddd,  $J = 8.7, 7.1, 1.7$  Hz, 1H), 7.55 (dd,  $J = 8.4, 1.3$  Hz, 1H), 7.40 (ddd,  $J = 8.1, 7.1, 1.1$  Hz, 1H), 6.80 – 6.76 (m, 2H), 6.73 (s, 1H), 3.10 (s, 6H).  $^{13}\text{C NMR}$  (75 MHz, chloroform-*d*)  $\delta$  ppm= 178.20, 163.7, 156.50, 152.60, 133.22, 127.75, 125.58, 124.81, 124.03, 117.84, 111.66, 104.39, 40.10. IR (KBr)  $\nu$ ,  $\text{cm}^{-1}$ , 2919.4 (CH) 1730.3(C=O), 1197.8 and 1363.2 (C-N), 1558.1(C=C), 3311.5 (=C-H) 1127.2 (C-O). Found, %: C 76.96; H 5.70; N 5.28.  $\text{C}_{17}\text{H}_{15}\text{NO}_2$ . Calculated, %: C 76.59; H 5.60; N 5.60 [20].

#### 2-(*p*-Tolyl)-4H-chromen-4-one (F3)

The compound was obtained by stirring equimolar amounts of 2'-hydroxyacetophenone and 4-methylbenzaldehyde (*p*-tolylaldehyde) in ethanol, and adding sodium hydroxide solution under continuous stirring to get the desired chalcone. In the next step, the chalcone was cyclized to flavone by refluxing in DMSO in the presence of catalytic iodine.

$^1\text{H NMR}$  (300 MHz, chloroform-*d*)  $\delta$  8.23 (dd,  $J = 7.9, 1.7$  Hz, 1H), 7.85 (d,  $J = 8.3$  Hz, 2H), 7.71 (td,  $J = 8.4, 7.2, 1.2$  Hz, 1H), 7.53 (d,  $J = 8.5$  Hz, 1H), 7.39 (td,  $J = 7.9, 0.8$  Hz, 1H), 7.27 (d, 2H), 6.92 (s, 1H), 2.39 (s, 3H).  $^{13}\text{C NMR}$  (75 MHz,  $\text{CDCl}_3$ )  $\delta$  178.1, 162.7, 156.2, 142.5, 134.1, 129.6, 128.4, 126.5, 125.6, 125.2, 123.5, 118.2, 106.5, 104.1, 21.5. IR (KBr)  $\nu$ ,  $\text{cm}^{-1}$ , 1640, 1465, 817 [21, 22].



Scheme 1. Synthesis of flavone derivatives.

*2-(4-Chlorophenyl)-4H-chromen-4-one (F4)*

The compound was obtained by stirring equimolar amounts of 2'-hydroxyacetophenone and 4-chlorobenzaldehyde in ethanol, and adding sodium hydroxide solution under continuous stirring to get the desired chalcone. In the next step, the chalcone was cyclized to flavone by refluxing in DMSO in the presence of catalytic iodine.

<sup>1</sup>H NMR (300 MHz, chloroform-*d*) δ 8.24 (dd, *J* = 8.0, 1.6 Hz, 1H), 7.83 (d, 2H), 7.72 (td, *J* = 8.7, 7.1, 1.7 Hz, 1H), 7.53 (d, *J* = 8.4 Hz, 1H), 7.47 (d, 2H), 7.40 (t, *J* = 7.6 Hz, 1H), 6.75 (s, 1H). <sup>13</sup>C NMR (75 MHz, CDCl<sub>3</sub>) δ 178.2, 162.1, 156.1, 137.8, 133.9, 130.2, 129.3, 127.5, 125.7, 125.3, 123.9, 118.0, 107.6. IR (KBr) *v*, cm<sup>-1</sup>, 1662, 1374, 1092, 827, 754 [21, 22].

*2-(2,4-Dichlorophenyl)-4H-chromen-4-one derivative (F5)*

The compound was obtained by stirring equimolar amounts of 2'-hydroxyacetophenone and 2,4-dichlorobenzaldehyde in ethanol and adding sodium hydroxide solution under continuous stirring to get the desired chalcone. In the next step, the chalcone was cyclized to flavone by refluxing in DMSO in the presence of catalytic iodine.

<sup>1</sup>H NMR (300 MHz, chloroform-*d*, ppm) δ 8.27 (dd, *J* = 8.0, 1.7 Hz, 1H, H-3'), 7.74 (ddd, *J* = 8.7, 7.1, 1.7 Hz, 1H, 5'-H), 7.64 – 7.56 (m, 2H, 5-H, 6'-H), 7.55 – 7.40 (m, 3H, 6-H, 7-H, 8-H), 6.68 (s, 1H, H-3). <sup>13</sup>C NMR (75 MHz, CDCl<sub>3</sub>, ppm) δ 177.98 (C-4), 161.51 (C-2), 156.54 (C-8a), 137.43 (C-2'), 134.06 (C-4'), 133.81 (C-6'), 131.42 (C-5'), 130.77 (C-3'), 130.40 (C-1'), 127.58 (C-7), 125.82 (C-6), 125.50 (C-5), 123.81 (C-4a), 118.18 (C-8), 113.16 (C-3). IR (KBr) *V*<sub>max</sub> cm<sup>-1</sup>: 3066.5, 2920.6, 1734.1, 1645.4, 1221.1, 748.2. Anal. Calcd. for C<sub>15</sub>H<sub>8</sub>Cl<sub>2</sub>O<sub>2</sub>: C, 61.88; H, 2.77. Found: C, 60.99; H, 2.28 [20].

*2-(2,3-Dichlorophenyl)-4H-chromen-4-one (F6)*

The compound was obtained by stirring equimolar amounts of 2'-hydroxyacetophenone and 2,3-dichlorobenzaldehyde in ethanol and then sodium hydroxide solution was added under continuous stirring to get the desired chalcone. In the next step, the chalcone was cyclized to flavone by refluxing in DMSO in the presence of catalytic iodine.

<sup>1</sup>H NMR (300 MHz, chloroform-*d*) δ 8.32 – 8.17 (m, 1H, H4'), 7.86 – 7.61 (m, 2H, H5', 6'), 7.56 – 7.21 (m, 4H, H-5,6,7,8), 6.67 (s, 1H, H3). <sup>13</sup>C NMR (75 MHz, CDCl<sub>3</sub>) δ 178.39(C4), 162.62(C2), 156.58(C8a), 134.60(C7), 134.26(C3'), 134.08(C1'), 132.62(C5), 129.80(C4'), 128.93(C5'), 127.65(C2'), 125.85(C6'),

125.61(C4a), 123.69(C6), 118.23(C8), 112.98(C3). IR (KBr) *V*<sub>max</sub> cm<sup>-1</sup>: 3048.9, 2918.5, 1714.7, 1659.3, 1191.3, 747.8. Anal. Calcd. for C<sub>15</sub>H<sub>8</sub>Cl<sub>2</sub>O<sub>2</sub>: C, 61.88; H, 2.77. Found: C, 62.02; H, 2.46 [20].

*2-(3,4-Dichlorophenyl)-4H-chromen-4-one (F7)*

The compound was obtained by stirring equimolar amounts of 2'-hydroxyacetophenone and 3,4-dichlorobenzaldehyde in ethanol and adding sodium hydroxide solution with continuous stirring to get the desired chalcone. In the next step, the chalcone was cyclized to flavone by refluxing in DMSO in the presence of catalytic iodine.

<sup>1</sup>H NMR (300 MHz, chloroform-*d*) δ 8.24 (dd, *J* = 8.0, 1.7 Hz, 1H), 8.04 (d, *J* = 2.1 Hz, 1H), 7.74 (tq, *J* = 7.0, 2.2 Hz, 2H), 7.65 – 7.56 (m, 2H), 7.46 (ddd, *J* = 8.2, 7.1, 1.1 Hz, 1H), 6.80 (s, 1H). <sup>13</sup>C NMR (75 MHz, CDCl<sub>3</sub>) δ 178.03, 160.82, 156.08, 135.96, 134.09, 133.70, 131.69, 131.11, 128.06, 125.78, 125.55, 125.25, 123.87, 118.06, 108.19. IR (KBr) *v*, cm<sup>-1</sup>, 1659.3, 1413.7, 1378.8, 750.04, 747.8. Found, %: C 61.92; H 2.53. C<sub>15</sub>H<sub>8</sub>Cl<sub>2</sub>O<sub>2</sub>. Calculated, %: C 61.88; H 2.77 [20].

*2-(2,6-Dichlorophenyl)-4H-chromen-4-one (F8)*

The compound was obtained by stirring equimolar amounts of 2'-hydroxyacetophenone and 2,6-dichlorobenzaldehyde in ethanol and adding sodium hydroxide solution under continuous stirring to get the desired chalcone. In the next step, the chalcone was cyclized to flavone by refluxing in DMSO in the presence of catalytic iodine.

<sup>1</sup>H NMR (300 MHz, chloroform-*d*) δ 8.30 (dd, *J* = 8.0, 1.7 Hz, 1H), 7.83 – 7.68 (m, 1H), 7.58 – 7.36 (m, 5H), 6.47 (s, 1H). <sup>13</sup>C NMR (75 MHz, CDCl<sub>3</sub>) δ 178.06, 162.03, 156.96, 133.65, 133.39, 128.48, 126.58, 125.75, 125.50, 124.89, 123.43, 120.38, 117.58. IR (KBr) *v*, cm<sup>-1</sup>, 2918.5, 1714.7, 1659.3, 1191.3, 747.8. Found, %: C 61.94; H 2.49. C<sub>15</sub>H<sub>8</sub>Cl<sub>2</sub>O<sub>2</sub>. Calculated, %: C 61.88; H 2.77.

*2-(4-(Trifluoromethyl)phenyl)-4H-chromen-4-one (F9)*

The compound was obtained by stirring equimolar amounts of 2'-hydroxyacetophenone and 4-(trifluoromethyl) benzaldehyde in ethanol and adding sodium hydroxide solution under continuous stirring to get the desired chalcone. In the next step, the chalcone was cyclized to flavone by refluxing in DMSO in the presence of catalytic iodine.

<sup>1</sup>H NMR (300 MHz, chloroform-*d*) δ 8.25 (dd, *J* = 8.0, 1.7 Hz, 1H), 8.06 (d, *J* = 8.2 Hz, 2H), 7.85 – 7.69 (m, 3H), 7.61 (dd, *J* = 8.4, 1.1 Hz, 1H), 7.47 (m, 1H), 6.88 (s, 1H). <sup>13</sup>C NMR (75 MHz, CDCl<sub>3</sub>) δ 178.14, 161.57, 156.17, 135.16, 134.10, 133.77, 132.90, 126.62, 126.02, 125.77, 125.54, 123.91, 118.11, 108.71. IR (KBr) *v*, cm<sup>-1</sup>, 3073.3 (=C-H),

1641.8 (C=O), 1316.8 (C-F), 1165.3 (C-O), 849.8 (C-F). ESI:  $m/z$  ( $C_{16}H_9F_3O_2$ )  $H^+$ : calculated, 291.0627, found: 291.0629 [23, 24].

*2-(4-(Trifluoromethyl)phenyl)-7-methoxy-4H-chromen-4-one (F10)*

The compound was obtained by stirring equimolar amounts of 2'-hydroxy-4'-methoxyacetophenone and 4-(trifluoromethyl) benzaldehyde in ethanol and adding sodium hydroxide solution under continuous stirring to get the desired chalcone. In the next step, the chalcone was cyclized to flavone by refluxing in DMSO in the presence of catalytic iodine.

$^1H$  NMR (300 MHz, chloroform-*d*)  $\delta$  8.16 (d,  $J$  = 8.7 Hz, 1H), 8.10 – 8.00 (m, 2H), 7.80 (d,  $J$  = 8.3 Hz, 2H), 7.09 – 6.97 (m, 2H), 6.83 (s, 1H), 3.97 (s, 3H).  $^{13}C$  NMR (75 MHz,  $CDCl_3$ )  $\delta$  177.56, 164.45, 161.23, 157.98, 135.27, 132.77, 127.18, 126.51, 126.08, 125.98, 125.93, 117.82, 114.76, 108.76, 55.91. IR (KBr)  $\nu$ ,  $cm^{-1}$ , 3130.4 (=C-H), 2815.3 (C-H), 1650.4 (C=O), 1381.4 (C-F), 1111.7 (C-O), 836.4 (C-F). HRMS ( $ES^+$ )  $m/z$   $C_{34}H_{22}F_6O_6Na$  requires 663.1213; Found 663.1234 [25].

*6-Bromo-2-(4-(trifluoromethyl)phenyl)-4H-chromen-4-one (F11)*

The compound was obtained by stirring equimolar amounts of 2'-hydroxy-5'-bromoacetophenone and 4-(trifluoromethyl) benzaldehyde in ethanol and adding sodium hydroxide solution under continuous stirring to get the desired chalcone. In the next step, the chalcone was cyclized to flavone by refluxing in DMSO in the presence of catalytic iodine.

$^1H$  NMR (300 MHz, chloroform-*d*)  $\delta$  8.38 (d,  $J$  = 2.5 Hz, 1H), 8.06 (d,  $J$  = 8.1 Hz, 2H), 7.88 – 7.78 (m, 3H), 7.58 – 7.45 (m, 1H), 6.90 (s, 1H).  $^{13}C$  NMR (75 MHz,  $CDCl_3$ )  $\delta$  176.88, 161.93, 154.95, 137.13, 134.13, 128.47, 126.72, 126.18, 126.13, 125.21, 124.32, 120.13, 119.07, 108.73. IR (KBr)  $\nu$ ,  $cm^{-1}$ , 3090.4 (=C-H), 1633.7 (C=O), 1316.3 (C-F), 1173.2, 828.4 (C-F), 632.1 (C-Br). HRMS ( $ES^+$ )  $m/z$   $C_{32}H_{16}Br_2F_6O_4Na$  requires 760.9212; found 760.9164 [25].

*Antibacterial Activity*

Antibacterial screening of the flavone derivatives mentioned above was performed against Gram-positive and Gram-negative bacterial strains using the agar well diffusion method. Briefly, about 20 ml of sterile Mueller-Hinton Agar was poured in sterile petri plates and allowed to solidify. The

sterile cotton swab was dipped into the bacterial culture ( $10^6$  to  $10^8$  CFU/ml) and the agar plates were evenly inoculated by swabbing followed by the wells formation using a sterile cork-borer (6 mm diameter). Each prelabeled well was filled with 100  $\mu$ l of various concentrations of flavone derivatives and allowed to diffuse by refrigerating for 30 min. The plates were then incubated at 37°C for 24 h. Triplicate plates were prepared for each treatment and the average zone of inhibition excluding well was recorded. DMSO was used as a negative control. The antibacterial potential in the form of zone of inhibition in millimeters (mm) was compared with the standard antibiotics ampicillin and ciprofloxacin [26-28].

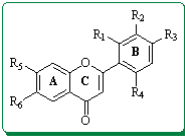
*Minimum inhibitory concentration (MIC)*

Compounds inhibiting growth of one or more of the above microorganisms were again tested for their minimum inhibitory concentration values (MIC). The MIC values were determined by the broth dilution technique. Briefly, a stock solution of each compound was prepared in dimethylsulfoxide (DMSO) and serially diluted to achieve the desired concentration range. To each of the preidentified sterile test tubes containing a specific concentration of the test compound, a standard volume of nutrient broth medium was added. The inoculum consisting of an overnight broth culture of microorganisms was added to each tube. The tubes were incubated at 37°C for 24 h and examined for turbidity. A control tube containing no antimicrobial agent was also included and ciprofloxacin was used as a standard. The lowest concentration required to stop the growth of bacteria was regarded as MIC [29].

**RESULTS AND DISCUSSION**

The general structure and physical parameters of the flavone derivatives are given in Scheme 1 and Table 1 while the spectroscopic parameters are given in the experimental section of this study. Results of the antibacterial activity of synthetic flavones in respect to their zone of inhibition are given in Table 2. It is reported that substitution in the ring A and ring B may increase or decrease the antibacterial response. Results from the study reveal that addition of halogen (Br) at ring A and trifluoromethyl at ring B enhances the antibacterial response against Gram positive and Gram negative bacteria.

**Table 1.** Physical parameters of the flavone derivatives



Flavone	R <sub>1</sub>	R <sub>2</sub>	R <sub>3</sub>	R <sub>4</sub>	R <sub>5</sub>	R <sub>6</sub>	Yield	Appearance	R <sub>f</sub>	M.P (°C)
F1	H	H	H	H	H	H	68.7%	Creamy white solid	0.58	96-98
F2	H	H	N(CH <sub>3</sub> ) <sub>2</sub>	H	H	H	73.6%	Brick red solid	0.67	107-109
F3	H	H	CH <sub>3</sub>	H	H	H	77.8%	Off white solid	0.64	154-158
F4	H	H	Cl	H	H	H	84.2%	White crystals	0.69	178-181
F5	Cl	H	Cl	H	H	H	87.0%	White solid	0.57	190-193
F6	Cl	Cl	H	H	H	H	81.0%	White solid	0.64	188-191
F7	H	Cl	Cl	H	H	H	79.3%	White solid	0.61	195-197
F8	Cl	H	H	Cl	H	H	81.6%	White solid	0.63	182-185
F9	H	H	CF <sub>3</sub>	H	H	H	85.3%	Monoclinic crystals	0.63	134-137
F10	H	H	CF <sub>3</sub>	H	OCH <sub>3</sub>	H	83.4%	Triclinic crystals	0.57	167-170
F11	H	H	CF <sub>3</sub>	H	H	Br	85.7%	Monoclinic crystals	0.71	171-173

**Table 2.** Antibacterial activity (Zone of inhibition) of compounds F1–F11.

Flavones	Concentration (µg/ml)	Zone of inhibition (mm)		
		Gram-positive bacteria		Gram-negative bacteria
		<i>B. subtilis</i>	<i>S. aureus</i>	<i>P. aeruginosa</i>
<b>F1</b>	25	19.4±1.67	25.2±1.06	23.1±0.91
	50	23.6±2.13	29.8±0.81	25.4±1.33
	100	21.1±1.28	28.3±1.27	29.2±1.72
<b>F2</b>	25	13.5±0.97	16.2±0.84	15.3±1.41
	50	15.3±1.71	16.8±1.27	16.1±2.08
	100	19.6±2.25	18.1±1.15	21.4±1.14
<b>F3</b>	25	18.0±1.67	20.3±1.31	21.1±1.47
	50	19.2±2.08	18.6±1.01	19.4±1.07
	100	21.4±1.27	19.1±2.17	23.8±1.31
<b>F4</b>	25	12.2±0.87	10.1±1.15	13.3±1.54
	50	15.8±1.19	13.5±1.52	18.1±1.73
	100	16.3±1.65	15.8±1.37	17.4±0.87
<b>F5</b>	25	10.6±1.07	6.0±1.48	7.1±2.13
	50	13.4±1.12	8.1±0.85	8.3±1.04
	100	14.7±1.89	8.4±1.14	8.8±1.26
<b>F6</b>	25	10.3±1.38	8.1±0.91	9.3±1.66
	50	13.5±1.25	10.3±1.12	11.0±0.83
	100	13.1±1.87	10.8±1.54	11.3±1.24
<b>F7</b>	25	13.2±1.09	12.3±1.76	13.1±0.88
	50	13.0±1.18	15.5±2.08	18.0±1.34
	100	17.1±1.05	17.3±1.43	16.2±1.02
<b>F8</b>	25	9.7±1.31	5.4±3.04	5.2±1.07
	50	12.5±1.14	7.1±2.14	6.3±1.51
	100	14.8±1.07	7.7±1.87	6.4±1.25
<b>F9</b>	25	20.6±1.62	28.3±2.11	25.1±1.04
	50	23.2±0.74	31.1±1.33	26.4±0.79
	100	23.1±0.93	33.5±2.05	29.3±0.94
<b>F10</b>	25	15.3±1.61	22.4±0.87	19.2±1.17
	50	17.0±0.91	15.2±1.13	17.2±0.86
	100	18.4±1.18	23.8±1.25	21.8±1.21
<b>F11</b>	25	23.6±1.37	33.1±1.38	27.4±1.02
	50	25.3±0.74	35.0±1.15	29.2±1.14
	100	25.7±1.31	34.6±1.07	29.5±0.87
Ciprofloxacin		31±1.02	35±0.93	32±1.05
Ampicillin		29±0.87	38±1.15	33±0.96

All values are taken as mean±SEM (n=3)

The replacement of the methoxy group at ring A decreases the response in comparison to other trifluoromethyl groups at ring B in the flavone derivatives. The standard antibiotics ciprofloxacin and ampicillin showed a significant response on both Gram positive and Gram negative bacteria.

On the other hand, the simple flavone and the methyl containing flavones at ring B also showed significant response in comparison to other flavone derivatives. It is also worth mentioning that a resistance was observed by *S. aureus* and *P. aeruginosa* in some of the halogenated flavones that showed the ineffectiveness of these compounds. The order of response with respect to the zone of inhibition is **F11, F9, F10, F1, F3, F2, F4, F7, F6, F5, F8**.

Table 2 illustrates the minimum inhibitory concentrations MIC ( $\mu\text{g/ml}$ ) of the synthetic flavone derivatives against Gram positive and Gram negative bacteria. It is observed that flavone substituted at both rings (F11) possesses an inhibitory potential at low concentration against all tested bacteria which is reported to be 12.5, 6.25 and 6.25 ( $\mu\text{g/ml}$ ), respectively, that is almost equal to the response of the standard ciprofloxacin. This attested that the introduction of halogen and trifluoromethyl moiety enhances the potential in comparison with simple flavones and other derivatives. The MICs in  $\mu\text{g/ml}$  of the tested flavones derivatives are given in Table 3.

The plants have an unlimited capability to produce aromatic substances. Generally, these aromatic compounds are phenols or oxygen-substituted molecules that naturally serve as a defensive tool against attacks by insects, herbivores and microorganisms [30]. An in-depth literature survey reported the significance of natural and synthetic flavonoid derivatives as regards antibacterial activity [31–35]. In the present study, the antibacterial activities of synthetic flavone derivatives were compared with respect to zone of inhibition and minimum inhibitory concentration (MIC) values. From the results it is evident that there is a significant co-relationship between the presence of functional groups and the antibacterial response of the compounds. The present study illustrates an effort to predict the SAR of flavone derivatives with good activity against Gram-positive and Gram-negative bacteria.

Based upon the findings of this study, it can be concluded that the presence of a halogen group at ring A and a trifluoromethyl group at ring B produces flavones (**F9, F10 and F11**) with potent activity.

Apart from simple flavone (**F1**), addition of methyl and dimethylamino groups at ring B (**F3 and F2**) also showed promising results against all bacteria. On the other hand, halogenated substituted flavones at ring B (**F4-F8**) showed almost minimum activity.

**Table 3.** Antibacterial activity (minimum inhibitory concentration) of compounds F1–F11.

Flavone	MIC ( $\mu\text{g/ml}$ )		
	Gram-positive bacteria		Gram-negative bacteria
	<i>B.subtilis</i>	<i>S.aureus</i>	<i>P.aeruginosa</i>
<b>F1</b>	25	37.5	25
<b>F2</b>	75	75	62.5
<b>F3</b>	62.5	50	50
<b>F4</b>	87.5	87.5	100
<b>F5</b>	100	100	100
<b>F6</b>	125	125	100
<b>F7</b>	75	87.5	87.5
<b>F8</b>	>125	>125	>125
<b>F9</b>	12.5	25	25
<b>F10</b>	50	50	37.5
<b>F11</b>	12.5	6.25	6.25
<b>Ciprofloxacin</b>	6.25	6.25	6.25

Several antibacterial mechanisms of action have been assigned to flavonoids.

Among those, the possible mechanisms of action are inhibition of nucleic acid synthesis by inhibition of the enzymes topoisomerase and DNA gyrase; causing pores in the membrane or reduction in fluidity; damage of the cytoplasmic membrane, inhibition of the cellular metabolism, resulting from the inhibition of the enzyme NADH-cytochrome C reductase; inhibition of cell membrane synthesis; inhibition of cell wall synthesis caused by D-alanine/D-alanine ligase inhibition and aggregation of bacterial cells [36-39].

## CONCLUSIONS

Researchers are constantly designing and synthesizing new anti-infective molecules

worldover. The dilemma of resistance to these agents is on the rise and there is a dire necessity for the discovery of new agents with antibiotic activity against the resistant bacterial strains. The present study is an effort to assess flavone derivatives as potential drug candidates for antibacterial activity. The SAR study of flavone derivatives with antibacterial potentials revealed a correlation between the presence of additional functional groups at different positions of the flavone ring A and B structure and the antibacterial activity. Of the compounds included in this study, **F9**, **F10** and **F11** were found to be the most active compounds. Thus, these three compounds can act as future potential candidates to develop newer synthetic antibacterial agents. These new molecules can either be used alone or in combination with other antibiotics to combat infections and would reduce the effective dose to be administered.

**Acknowledgements:** We are thankful to the Department of Pharmacy, University of Malakand Khyber Pakhtunkhwa Pakistan for Provision of laboratory facilities.

#### REFERENCES:

1. B. Ocelik, M. Kartal, & I. Orhan. *Pharmaceutical Biology*, **49**, 396 (2011).
2. M. W. Iwu, A. R. Duncan, C. O. Okunji. New antimicrobials of plant origin. In: Perspectives on new crops and new uses J. Jannick (ed). ASHS Press; 1999, p. 457.
3. P.M. Shah. *Clin. Microbiol. Infect.* **11**, 36 (2005).
4. K. Poole. *J. Pharm. Pharmacol.* **53**, 283 (2001).
5. B. Havsteen. *Biochem. Pharmacol.* **32**, 1141 (1983).
6. M. Kawai, T. Hirano, S. Higa, J. Arimitsu, M. Maruta, Y. Kuwahara, T. Ohkawara, K. Hagihara, T. Yamadori, Y. Shima, A. Ogata, I. Kawase, & T. Tanaka. *Allergol. Int.* **56**, 113 (2007).
7. A.G. Lafuente, E. Guillamon, A. Villares, M.A. Rostagno, & J.A. Martinez. *Inflamm. Res.*, **58**, 537 (2009).
8. J. Johari, A. Kianmehr, M. R. Mustafa, S. Abubakar, & K. Zandi. *Int. J. Mol. Sci.* **13**, 16785 (2012).
9. M.R. Peluso. *Exp. Biol. Med.* , **231**, 1287 (2006).
10. K.Y. Park, G.O. Jung, K.T. Lee, M.Y. Choi, G.T. Kim, H.J. Jung, & H.J. Park. *J. Ethnopharmacol.*, **90**, 73 (2004).
11. C. Kanaswami, L.T. Lee, P.P. Lee, J.J. Hwang, F.C. Ke, Y.T. Huang, & M.T. Lee. *In Vivo*, **19**, 895 (2005).
12. M. Jung, M. Park, H.C. Lee, Y.H. Kang, E.S. Kang, & S.K. Kim. *Curr. Med. Chem.*, **13**, 1203 (2006).
13. P. Batra, & A. K. Sharma. *Biotech.* **3**, 439 (2013).
14. H. Oh, D.H. Kim, J.H. Cho, & Y.C. Kim. *J. Ethnopharmacol.*, **95**, 421 (2004).
15. C. Proestos, I.S. Boziaris, J.E. Nychas, & M. Komaitis. *Food Chem.*, **95**, 664 (2006).
16. D.I. Batovska, & I.T. Todorova, *Curr. Clin. Pharmacol.*, **05**, 01 (2010).
17. G. Casano, A. Dumetre, C. Pannecouque, S. Hutter, N. Azas, & M. Robin. *Bioorg. Med. Chem.*, **18**, 6012 (2010).
18. H. L. Liu, W.B. Jiang, & M.X. Xie. *Anticancer Drug Discov.*, **5**, 152 (2010).
19. V.H.E Susanti, S. Matsjeh, T.D. Wahyuningsih, Mustofa & T. Redjeki. *Indo. J Chem*, **12**, 146 (2012).
20. M. Shoaib, S. W. A. Shah, N. Ali, I. Shah, M. N. Umar, Shafiullah, M. Ayaz, M. N. Tahir, S. Akthar. *Journal of Chemistry*, **2015**, 1 (2015).
21. K. Donghee, H. Kyungrok & H. Sungwoo. (2012). *Org. Biomol. Chem.*, **10**, 7305 (2012).
22. Z. Jie, Z. Yufen & F. Hua. *Angew. Chem. Int. Ed.*, **50**, 3769 (2011).
23. L. Klier, T. Bresser, T. A. Nigst, K. Karaghiosoff, P. Knochel, *J. Am. Chem. Soc.*, **134**, 13584, (2012).
24. D. Zhao, B. Beiring, F. Glorius, *Angew. Chem. Int. Ed.*, **52**, 8454, (2013).
25. S.B.A. Ghani, P.J. Mugisha, J.C. Wilcox, E.A.M. Gado, E.O. Medu, A.J. Lamb, & R.C.D. Brown, *Synth. Commun.*, **43**, 1549 (2013).
26. P. O. Olutiola, O. Famurewa, H.G. Sonntag, An Introduction to General Microbiology—A Practical Approach, 2nd edition, Bolabay publication, Nigeria, 1991, p. 112.
27. J. G. Colle, J. P. Duguid, A. G. Fraser, B. P. Marmion, Laboratory strategies in diagnosis. in Practical Medical Microbiology, T.J. Mackie, J.E. MacCartney (eds), Churchill Livingstone, London 1989, p. 601.
28. F. Mujeeb, P. Bajpai, & N Pathak. *Biomed. Res. Int.*, **2014**, 1 (2014).
29. A. Husain, M. Rashid, R. Mishra & D. Kumar. *Acta Pol. Pharm.*, **70**, 443 (2013).
30. T. Arif, J.D. Bhosalea, N. Kumara, T.K. Mandala, R.S. Bendreb, G.S. Lavekara, & R. Dabura. *J. Asian Nat. Prod. Res.*, **11**, 621 (2009).
31. J.C. Chukwujekwu, F.R.V. Heerden FR & J.V. Staden. *Phytother. Res.*, **25**, 46 (2011).
32. J.M. Favela-Hernandez, A. Garcia, E. Garza-Gonzalez, V.M. Rivas-Galindo, & J.M. Camacho-Corona. *Phytother. Res.*, **26**(12), 1957 (1960).
33. A.P. Mukne, V. Viswanathan, & A.G. Phadatare. *Pharmacogn. Rev*, **5**, 13 (2011).
34. M. Tomczyk, A. Wiater, M. Pleszczynska. *Phytother. Res.*, **25**, 343 (2011).
35. A. Baldisserotto, S. Vertuani, A. Bino, D. De Lucia, I. Lampronti, R. Milani, R. Gambari, S. Manfredini. *Bioorg. Med. Chem.*, **23**, 264 (2015).
36. T.P. Cushnie, A.J. Lamb. *Int. J. Antimicrob. Agents*, **27**, 181 (2006).
37. T.P. Cushnie, A.J. Lamb. *Int. J. Antimicrob. Agents*, **38**, 99 (2011).
38. N.C. Gordon & D.W. Wareham, *Int. J. Antimicrob. Agents*, **36**, 129 (2010).
39. D. Wu, Y. Kong, C. Han, J. Chen, L Hu, H. Jiang, & X. Shen, *Int. J. Antimicrob. Agents*, **32**, 421 (2008).

## СИНТЕТИЧНИ ФЛАВОНОВИ ПРОИЗВОДНИ. АНТИБАКТЕРИАЛНИ СВОЙСТВА И ВРЪЗКА МЕЖДУ АКТИВНОСТ И СТРУКТУРА

М. Шоахиб<sup>1</sup>, С.У.А. Шах<sup>1\*</sup>, Н. Али<sup>2</sup>, И. Шах<sup>1</sup>, М.Н. Умар<sup>3</sup>, Шафиула<sup>1</sup>, М.Н. Тахр<sup>4</sup>, М. Гиас<sup>1</sup>

<sup>1</sup>Департамент по фармация, Университет в Малаканд, Чакдара 18550 Дир Лоуер, Кхибер Пактункуа, Пакистан

<sup>2</sup>Департамент по фармакология, Институт по базови медицински науки, Кхибер Медицински Университет, Пешавар 25000, Кхибер Пактункуа, Пакистан

<sup>3</sup>Департамент по химия, Университет в Малаканд, Чакдара 18550 Дир Лоуер, Кхибер Пактункуа, Пакистан<sup>4</sup>  
Департамент по физика, Университет Саргодха 40100 Пунджаб, Пистан

Постъпила на 4 септември 2015 г.; приета на 16 декември 2015 г.

(Резюме)

Синтезирани са с висок добив биологично активни флавонови производни с антибактериален потенциал от кетони с различни алдехиди чрез кондензация на Claisen-Schmidt. Структурите им са установени чрез различни спектроскопски методи: <sup>1</sup>H ЯМР, <sup>13</sup>C ЯМР, ИЧ и елементарен анализ. Резултатите показват, че някои от заместените флавонови проявяват по-висока антибактериална активност от простите флавонови по отношение на тяхната минимална концентрация на инхибиране (МИС) и са потенциални кандидати за лечението на широк спектър от инфекциозни заболявания.

## Interaction studies of DNA binding with a new Cu(II) complex by spectrophotometric, spectrofluorometric, voltammetric and circular dichroism techniques

M. Bordbar<sup>1,\*</sup>, F. Khodaie<sup>2</sup>, M. Tabatabaee<sup>2</sup>, A. Yeganeh-Faal<sup>3</sup>, Z. Mehri lighvan<sup>4</sup>, S. Mohammad-Ganji<sup>5</sup>

<sup>1</sup>Department of Chemistry, Faculty of Science, University of Qom, Qom 37185-359, Iran.

<sup>2</sup>Department of Chemistry, Yazd Branch, Islamic Azad University, Yazd, Iran.

<sup>3</sup>Department of Chemistry, Faculty of Science, Payame Noor University, Tehran, Iran.

<sup>4</sup>Young Researchers and Elites Club, Department of Chemistry, Isfahan University of Technology, Isfahan, 84156/8311

<sup>5</sup>National Institute for Genetic Engineering & Biotechnology (NIGEB), P. O. Box: 14965-161 Tehran, Iran.

Received September 14, 2015, Accepted March 28, 2016

The binding ability of the water-soluble copper(II) complex with pyridine-2,6-dicarboxylate (pydc<sup>2-</sup>) and 2-aminopyrimidine (amp) with the formula [Cu(pydc)(amp)].2H<sub>2</sub>O.H<sub>2</sub>O (**1**) to calf thymus DNA (CT-DNA) was investigated. The binding ability of **1** was studied by measuring the effects on the electronic absorption spectra, thermal denaturation studies, fluorescence quenching studies using methylene blue (MB) as a fluorescent probe and circular dichroism (CD) spectra. All results suggest that the interaction mode between (**1**) and DNA takes place by intercalation with a binding constant of  $(9.51 \pm 0.2) \times 10^4 \text{ M}^{-1}$ .

**Keywords:** Intercalative Interaction, CT-DNA, Methylene Blue, Mixed Nitrogen Donor Ligands, Cu (II) Complex.

### INTRODUCTION

Cis-platine is one of the widely utilized antitumor drugs [1]. In order to decrease the toxicity of this kind of platinum complexes, many kinds of amine-substituted compounds are employed in the research of antitumor agents [2-4]. Some natural products have been used as amine-substituted ligands in this research [5], such as D-glucosamine [6], chitosan [7] and their derivatives. These are non-toxic towards the human body and the amino group in the chain has special activity. However, one disadvantage of normal chitosan is its low solubility in water. Recently there has been considerable interest in the binding of small water-soluble molecules to DNA [8]. Investigations of the interaction between small molecules and DNA are basic works in the design of new types of pharmaceutical molecules. A small molecule which can interact with DNA can be assigned to several categories: metal ions and metal complexes, such as metal bipyridyl complex [9] and metal phenanthroline complex [10]; heavy metals which cause damage of DNA, such as chromium [11], antibiotics, organic dyes and organic pesticides [12], protein molecules and nanoparticle markers [13]. Studies of the interaction between transition

metal complexes and DNA have been pursued in recent years [14]. Metal complexes are known to bind to DNA *via* both covalent and non-covalent interactions. In covalent binding, the labile ligands of the complexes are replaced by a nitrogen base of DNA such as guanine N7. On the other hand, non-covalent DNA interactions include intercalative, electrostatic and groove (surface) binding of cationic metal complexes both outside the DNA helix, and along major or minor grooves. Among these interactions, intercalation is one of the most important DNA binding modes, as it invariably leads to cellular degradation and is an enthalpically driven process resulting from the insertion of a planar aromatic ring system between ds-DNA base pairs with concomitant unwinding and lengthening of the DNA helix [15]. Copper is a cofactor essential for the tumor angiogenesis processes [16]. Among the metal complexes, copper (II) complexes containing heterocyclic bases have been developed as a result of their diverse applications following the discovery of the “chemical nuclease” activity of the [Cu(phen)<sub>2</sub>]<sup>2+</sup> complex [17]. Furthermore, copper complexes have shown strong interactions with DNA *via* surface associations or intercalation [18]. The factors that may affect their association with DNA include their size, the type of ligands, the presence and the position of small lipophilic groups. On the other hand, copper complexes having strong association with DNA are also capable of inducing a hydrolytic cleavage [19], as

\* To whom all correspondence should be sent:  
E-mail: m.bordbare@gmail.com

several copper-based synthetic nucleases have been reported [20]. Their importance is due to their capacity to cleave DNA *via* oxidative mechanisms resulting from copper's ability to adopt different oxidation states.

In this work, the Cu (II) complex of 2-aminopyrimidine (amp) and pyridine-2,6-dicarboxylate (pydc) (**1**) was synthesized [21]. Interactions of this complex with calf thymus DNA (CT-DNA) were studied by UV-Vis, fluorescence using MB as a fluorescence probe [22], depressing emission quenching of this complex by  $K_4[Fe(CN)_6]$  in presence of DNA [23], circular dichroism spectroscopic methods and cyclic voltammetry (CV) measurements in order to gain a better understanding of the binding mechanism of this complex [24].

## EXPERIMENTAL

### *Reagents*

The reagents and chemicals were purchased from commercial sources and used as received without further purification. Calf thymus DNA (CT-DNA) was obtained from Sigma. The stock solution of CT-DNA gave a ratio of UV absorbance at 260 and 280 nm ( $A_{260}/A_{280}$ ) of 1.89 to check DNA purity and making sure that the DNA was sufficiently free from protein contamination [25]. The DNA concentration was determined by UV absorbance ( $\epsilon = 6600 M^{-1} cm^{-1}$  at 260 nm) [26]. The stock solutions were stored at 4° C and used within 4 days. All experiments involving interaction of the complex with DNA were carried out in doubly distilled water buffer containing 5mM Tris-HCl [Tris(hydroxymethyl)-aminomethane] and 50 mM NaCl, adjusted to pH 7.3 with hydrochloric acid.

### *Electronic Absorption Spectra*

The UV-Vis spectra were recorded on a Varian Cary-100 UV-Vis spectrophotometer. Absorption titration experiments were conducted by fixing constant concentration of the complex at 783  $\mu M$  while varying the concentrations of CT-DNA or by fixing constant concentration of the (amino) and (pydc) ligands at 70  $\mu M$  while varying the concentration of Cu(II) metal cation ( $[Cu(II)]/[L]=0-5$ ). All experiments were conducted in a buffer containing 5 mM Tris-HCl (pH 7.3) and 50 mM NaCl. CT-DNA being an absorbing species in the absorption range of the complex, the titrations were carried out by adding the same amounts of CT-DNA solution to both reference and measuring cell to eliminate the absorbance of DNA itself.

### *Fluorescence Spectra*

The fluorescence spectra were recorded on a Varian Cary Eclipse spectrofluorometer. The complex at a fixed concentration (19.6  $\mu M$ ) was titrated by increasing amounts of CT-DNA. Excitation wavelength of the complex was 296 nm, scan speed = 100 nm/min, slit width 5/5 nm. All experiments were conducted in a buffer containing 5 mM Tris-HCl (pH 7.3) and 50 mM NaCl. The binding mode of the complex with CT-DNA was studied by using methylene blue (MB) as a fluorescence probe. Also, depressing the emission quenching of this complex by  $K_4[Fe(CN)_6]$  in the presence of DNA was studied.

### *Circular Dichroism Measurements*

Circular dichroism measurements were carried out on a Jasco-810 spectropolarimeter at room temperature. A rectangular quartz cell of 1 cm path length was used to obtain spectra from 320 to 220 nm with a scanning speed of 100 nm/min and a response time of 4 s. Each spectrum was accumulated at least three times and results were expressed as molar ellipticity (H). The optical chamber of the CD spectrometer was deoxygenated with dry nitrogen before use and kept in a nitrogen atmosphere during the experiments. Scans were accumulated and automatically averaged. CD spectrum was generated which represented the average of three scans from which the buffer background had been subtracted. In the CD spectrum the concentrations of CT-DNA and complex were 100 and 50  $\mu M$ , respectively.

### *Thermal Denaturation Experiments*

Thermal denaturation experiments were carried out on a Varian Cary-500 UV-Vis double beam spectrophotometer. The absorbance of 75  $\mu M$  DNA at 260 nm was monitored in the absence and presence of 37.5  $\mu M$  complex with temperature ranging from 55 to 100 °C.

### *Cyclic Voltammetry Experiments*

Cyclic voltammetry experiments were performed at room temperature with a conventional three-electrode electrochemical cell, using a Metrohm Autolab potentiostat/galvanostat. The three-electrode system used in this research consisted of a gold electrode as a working electrode, an Ag/AgCl reference electrode and a Pt foil auxiliary electrode. The solution was prepared by dissolving the complex in aqueous buffer containing 5 mM Tris-HCl (pH 7.3) and 50 mM NaCl.

### Viscometry Measurements

The viscosity was determined using a digital Brookfield circulating bath Ultra DV III viscometer maintained at  $25.0 \pm 0.1$  °C in a circulating water-bath. Data were analyzed as  $(\eta/\eta_0)^{1/3}$  versus the ratio of the concentration of (1) and DNA, where  $\eta$  is the viscosity of DNA in presence of the complex and  $\eta_0$  is the viscosity of DNA alone.

### Synthesis of the Complex

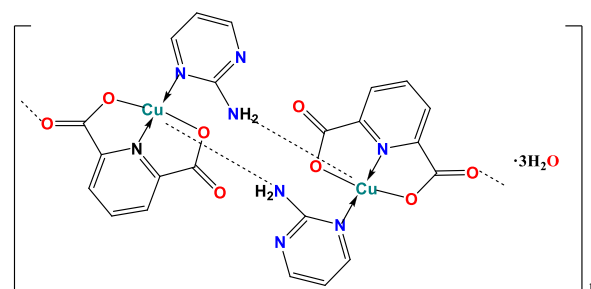
The copper complex was prepared as described by our group [27]. Pyridine-2,6-dicarboxylic acid (0.167 g, 1 mmol) was dissolved in 10 ml of deionized water containing 0.08 g (2 mmol) of NaOH and was stirred for 30 min at room temperature. An aqueous solution of 0.241 g (1 mmol) of  $\text{Cu}(\text{NO}_3)_2 \cdot 3\text{H}_2\text{O}$  and 0.095 g (1 mmol) of 2-aminopyrimidine was added to pyridine-2,6-dicarboxylic acid solution. The reaction mixture was placed in a Parr-Teflon lined stainless steel vessel, sealed and heated at 130°C for 4 h. Blue crystals of the complex were obtained upon slow cooling (yield 91%) [28].

## RESULTS AND DISCUSSION

### Characterization of the Complex

Recently, synthesis and characterization of  $\{[\text{Cu}(\text{pydc})(\text{amp})] \cdot 3\text{H}_2\text{O}\}_n$  by elemental analysis, IR spectroscopy, thermal analysis and X-ray diffraction studies have been reported by our group [28]. As reported in ref. [21], each Cu (II) ion is coordinated by an O,N,O-tridentate  $\text{pydc}^{2-}$  ligand (bound *via* pyridine nitrogen atom and two carboxylate oxygen atoms) and one heterocyclic nitrogen atom of the 2-aminopyrimidine ligand (Scheme 1). The same coordination mode was found for the nickel complex [29]. The six-coordination was completed by two water molecules in the nickel complex, while each metal ion in the copper complex is weakly connected to two neighboring ones, through two carboxylate bridging groups of dipicolinate and the amino-nitrogen of the  $\text{NH}_2$  group of 2-aminopyrimidine (Scheme 1).

The FTIR spectrum of the crystals shows broad strong bands in the region  $3275\text{--}3523\text{ cm}^{-1}$ , which could be related to the existence of  $\text{O}\text{--}\text{H}\cdots\text{O}$  hydrogen bonding between the water molecules. It must have been coupled by other indicative peaks such as N–H and O–H stretching frequencies and the stretching frequencies due to the aromatic rings which originally fall within this region.



**Scheme 1.** Structure of the Cu (II) mixed ligand complex

### Absorption Spectra

Electronic absorption spectroscopy is universally employed to examine the binding mode of DNA with metal complexes [30]. The absorption spectra of (1) in the absence and presence of CT-DNA are given in Fig.1. In the absence of DNA, the absorption spectrum of (1) has a strong  $\pi\text{--}\pi^*$  transition band at 268 nm. Increasing DNA concentration, the absorption band of the complex at 268 nm shows hypochromism of 85.5% and bathochromism of about 8 nm; at 220 nm it shows 51% hypochromism and bathochromism about 9 nm. These phenomena indicate that the complex probably interacts with CT-DNA by intercalation mode, involving strong  $\pi\text{--}\pi$ -stacking interactions between the aromatic rings of the complex and DNA base pairs.

The apparent binding constant,  $K_b$ , for the interaction between the complex and CT-DNA can be determined by analysis of the spectrophotometric titration data at room temperature using Eq. (1) [31].

$$[\text{DNA}]/(\epsilon_a - \epsilon_f) = [\text{DNA}](\epsilon_b - \epsilon_f) + 1/K_b(\epsilon_b - \epsilon_f)(1)$$

where  $[\text{DNA}]$ ,  $\epsilon_a$ ,  $\epsilon_f$  and  $\epsilon_b$  correspond to the total concentration of CT-DNA base-pair,  $A_{\text{obsd}}/[\text{Com}]$ , the extinction coefficient for the free complex and the extinction coefficient for the complex in the fully bound form, respectively. In the plot of  $[\text{DNA}]/(\epsilon_a - \epsilon_f)$  versus  $[\text{DNA}]$ ,  $K_b$  is given by the ratio of the slope to the intercept.

Until now, the binding constant reported in most papers has been calculated at a single wavelength since different parts of a compound do not have similar interaction with DNA. In this case, the absorption spectrum at different wavelengths is differently affected by this interaction and is expected to give different binding constants at different wavelengths. The calculated binding constants for DNA-(1) at some of the selected wavelengths are reported in Table 1. It can be inferred that different values for the binding constant are obtained at different wavelengths. It

seems that the comparative binding constant calculated at a single wavelength for the DNA-compound interaction may not be correct. This probably may be true if the binding constant is reckoned as an average of the binding constants at all wavelengths. Herein, we calculated the binding constant  $K_b$  for the DNA-(1) at all wavelengths in MATLAB and the mean result is  $9.51(\pm 0.2)\times 10^4$  L mol<sup>-1</sup>.

**Table 1.**  $K_b$  values at different wavelengths

Wave length (nm)	280	270	260	220	202
$K_b$ (M <sup>-1</sup> )	$5.46 \times 10^4$	$1.00 \times 10^5$	$3.21 \times 10^4$	$9.52 \times 10^5$	$4.34 \times 10^6$

The  $K_b$  value obtained for our copper(II) complex is considerably higher than those for any other known copper(II) complexes including complexes such as [Cu(phen)<sub>2</sub>Cl<sub>2</sub>] ( $K_b$ ,  $2.70 \times 10^3$  M<sup>-1</sup>) [32], [Cu(phen)(L-Thr)(H<sub>2</sub>O)]ClO<sub>4</sub> ( $K_b$ ,  $6.35 \times 10^3$  M<sup>-1</sup>) [33], [Cu(II) Schiff base complexes] ( $K_b$ ,  $3.20 \times 10^3$  and  $9.60 \times 10^3$  M<sup>-1</sup>) [34] [Cu(phen)(L-Gly)(H<sub>2</sub>O)] ( $K_b$ ,  $4.68 \times 10^3$  M<sup>-1</sup>) [35]

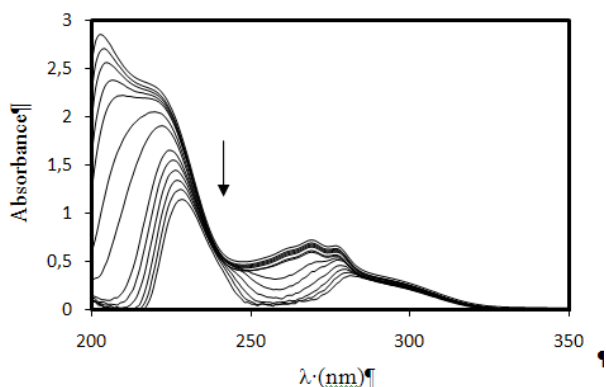


**Fig. 1.** UV-Vis absorption spectra of the complex (70 μM) in the presence of increasing amounts of CT-DNA; [DNA]=(0-950) μM The arrow shows the changes upon increasing the amount of CT-DNA.

### Fluorescence Spectra

The complex showed fluorescence emission in Tris buffer at room temperature, with a maximum at about 363 nm. As shown in Fig. 2, the fluorescence intensity of the complex was steadily quenched with the increasing concentration of CT-DNA.

The interaction mode of the complex binding to DNA can be determined according to the classical Stern-Volmer equation [36]:

$$F_0/F = 1 + K_q [Q] \quad (2)$$

where  $F_0$  and  $F$  represent the emission intensity in the absence and presence of quencher, respectively,  $K_q$  is a linear Stern-Volmer quenching constant and

$[Q]$  is the quencher concentration. The Stern-Volmer quenching plots from the fluorescence titration data are shown in the inset of Fig. 2.

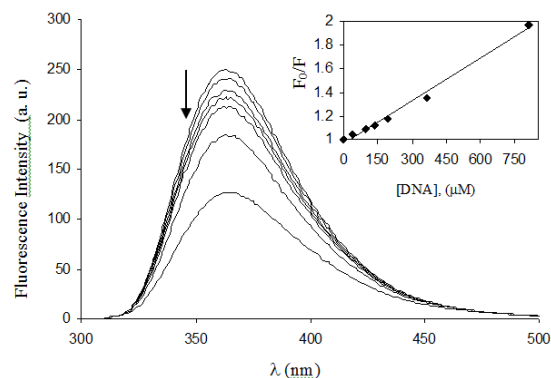


**Fig. 2.** Emission spectra of the complex (a) in Tris-HCl buffer upon addition of CT-DNA. [Complex]= 20 μM, [DNA]= (0-809) μM. Arrow shows the intensity change upon increasing CT-DNA concentration. The inset is a Stern-Volmer quenching plot of (1) with increasing concentrations of CT-DNA.

The fluorescence quenching constant ( $K_q$ ) evaluated using the Stern-Volmer equation is  $1.12 \times 10^3$  M<sup>-1</sup>. When the Stern-Volmer plot is linear, it indicates that only one type of quenching process occurs and the obtained linear relationship could be applied to determine DNA. This phenomenon of the quenching of luminescence of the complex by CT-DNA may be attributed to the photoelectron transfer from the guanine base of DNA to the excited metal-to-ligand charge-transfer (MLCT) state of the complex [37].

### DNA-MB Displacements

Further support for the binding of the complexes to DNA by intercalation mode was given by the competitive binding experiment. MB has long been used as a planar dye molecule for biological straining and diagnosis of diseases including carcinoma [38]. The interaction of methylene blue with DNA has been studied with various methods [39]. Most studies indicated that (at low ionic strength buffer and low concentration of DNA) the major binding mode of MB with DNA was through intercalation. The experiment involves the addition of the present complex CT-DNA pretreated with MB as a fluorescence probe ([DNA]/[MB]=10) and the measurement of emission intensities of DNA-bound MB. Interestingly, the emission intensity of MB is quenched on adding CT-DNA. This emission quenching phenomenon reflects the change in the excited state structure in consequence of the electronic interaction in the MB-DNA complex [40], expected from the strong stacking interaction (intercalation) between the adjacent

DNA base pairs. The emission spectra of the MB–DNA solutions in the presence of increasing amounts of (1) is shown in Fig. 3, which clearly reveals a gradual increase in the fluorescence intensity of the probe molecule (MB) by adding (1). The increase in fluorescence intensity is due to the release of free MB molecules from the DNA–MB complex. Therefore, the formation of metal complex–DNA prevents the binding of MB. The complete metal complex–DNA formation occurs when the probe fluorescence intensity is sufficiently close to the corresponding pure MB fluorescence intensity. Complete recovery of MB fluorescence intensity is indicative of an intercalative mode of binding, but in this experiment, the recovery of MB was 6% in  $[\text{complex}]/[\text{DNA}]=3$  and 37% in  $[\text{complex}]/[\text{DNA}]=92$ , which confirms that the intercalative binding strength of the Cu (II) complex to DNA is weaker than to MB.

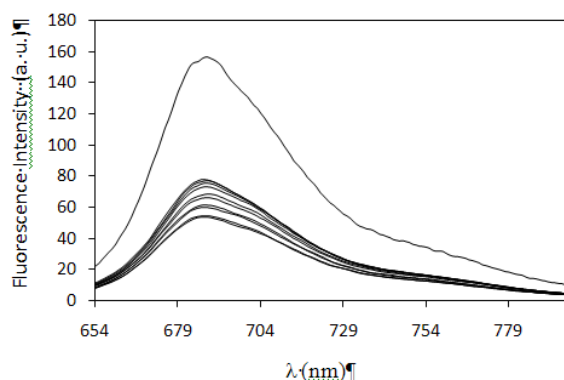


**Fig. 3.** Emission spectra of the competitive reaction between Cu (II) complex and methylene blue with DNA.  $C_{\text{complex}} = 0.0, 144.0, 283.0, 420.0, 550.0, 680.0, 1048.0, 1765.0, 2080.0,$  and  $3129.0 \mu\text{M}$ ,  $C_{\text{MB}} = 5 \mu\text{M}$  and  $C_{\text{DNA}} = 50 \mu\text{M}$  in Tris–HCl buffer (5 mM, pH 7.3) plus 50 mM NaCl.

#### Emission Quenching Titration with $K_4\text{Fe}(\text{CN})_6$

In aqueous solution, iodide and ferrocyanide anions quench the fluorescence of (1) very efficiently, so we used potassium ferrocyanide as the quencher to determine the relative accessibilities of the free and bound (1). The highly negatively charged quencher is repelled away from the negatively charged phosphate backbone of DNA, the bound copper cation should be protected from anionic quenchers, while the emission from free complexes should be readily quenched by an anionic quencher. Fig. 4 shows the linear Stern–Volmer plots with ferrocyanide anion as a quencher for (1), at  $[\text{DNA}]/[\text{Complex}] = 0$  or  $40$ , as expected for a single-component donor–acceptor system.

As illustrated in Fig. 4, the emission of (1) in the presence of DNA is difficult to be quenched. This

may be explained by the fact that the bound cations of the complex are protected from the anionic water-bound quencher by the array of negative charges along the DNA phosphate backbone [41]. The obtained quenching constants were  $3.5$  and  $2.1 \text{ M}^{-1}$  with and without CT-DNA, respectively. The quenching of (1) was in fact enhanced by a factor of  $1.6$  when (1) was bound to the DNA helix.

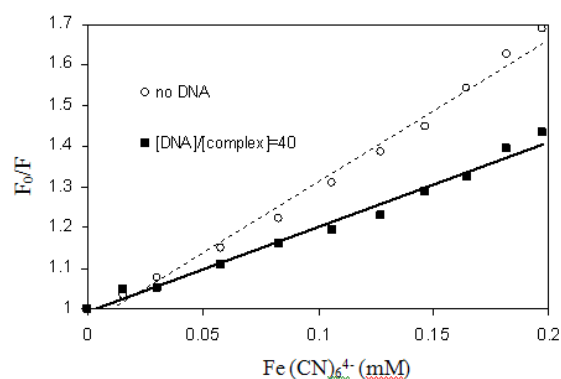


**Fig. 4.** Emission quenching with  $\text{Fe}(\text{CN})_6^{4-}$  for free and DNA-bound (1).

#### CD Spectroscopy

Circular-dichroism (CD) studies were conducted to determine the extent of change in conformation of DNA upon complexation. CD spectral variations of CT-DNA were recorded by addition of the complex to CT-DNA. The CD spectrum of CT-DNA consists of a positive band at  $277 \text{ nm}$  due to base stacking and a negative band at  $248 \text{ nm}$  due to helicity, which is characteristic of DNA in the right-hand B form and is quite sensitive to the mode of DNA interactions with small molecules [24]. Thus simple groove binding and electrostatic interaction of small molecules show less or no perturbation on the base stacking and helicity bands, while intercalation enhances the intensities of both bands, stabilizing the right-hand B conformation of CT-DNA as observed for the classical intercalator methylene blue [42]. Fig. 5 shows the CD spectra of CT-DNA which was added to the complex. In these CD data the intensities of both negative and positive bands decreased significantly similar to that induced by the other Cu (II) complex [43]. This alteration suggests that the DNA binding of the complex induces certain conformational changes, such as the conversion from a more B-like to a more Z-like structure within the DNA molecule [44]. In addition, (1) binds DNA mainly by intercalation mode and indicates an unwinding of the DNA helix upon complex formation and loss of helicity [45].

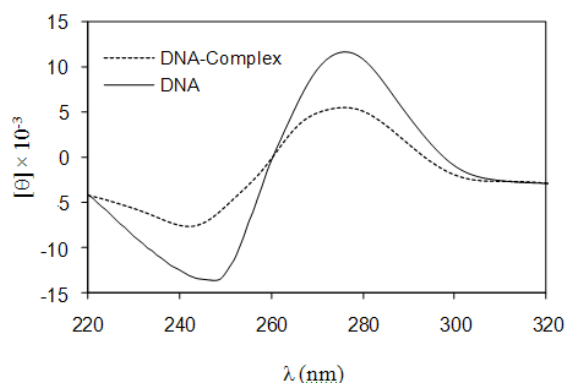


**Fig. 5.** Circular dichroism spectra of DNA (50  $\mu\text{M}$ ) in Tris-HCl (5 mM) in the presence of increasing amounts of copper complex (100  $\mu\text{M}$ ).

#### Thermal Denaturation Studies

Thermal denaturation studies of CT-DNA with the complex provide evidence for the ability of the complex to stabilize the double-stranded DNA [46]. It is well-accepted that when the temperature of the solution increases, the double-stranded DNA gradually dissociates to single strands, generating a hyperchromic effect in the absorption spectra of the DNA bases ( $\lambda_{\text{max}} = 260 \text{ nm}$ ). So the transition temperature of double strands to single strands can be determined by monitoring the absorbance of the DNA bases at 260 nm as a function of temperature [26]. According to the previous reports [47], intercalation normally facilitates base stacking in DNA and increases the melting temperature  $T_m$  of DNA.

The effect of **(1)** on the melting temperature ( $T_m$ ) of CT-DNA in the buffer is shown in Fig. 6. In this experiment, the  $T_m$  of CT-DNA alone was 81.62  $^{\circ}\text{C}$ . After adding the complex,  $\Delta T_m$  increased by 3.95  $^{\circ}\text{C}$  for the mole ratio of  $[\text{Cu}]/[\text{DNA}] = 0.5$ . It has been reported that  $\Delta T_m$  for metallointercalators ( $>10 \text{ }^{\circ}\text{C}$ ) [48] and the organic intercalator EB (13  $^{\circ}\text{C}$ ) [49] were higher than for this complex. These results indicated that the binding strength between the complex and DNA was only moderate [46]. The observed small change in the  $T_m$  of CT-DNA in the presence of **(1)** suggests that the dominating interaction of this complex with DNA is intercalative binding [50, 51].

#### DNA-Binding Study with Cyclic Voltammetry

The application of cyclic voltammetry (CV) to the study of the binding of metal complexes to DNA provides a useful complement to the above methods of investigation [12, 52].

Typical cyclic voltammetric (CV) behavior of 48  $\mu\text{M}$  **(1)** in the absence and presence of CT-DNA

is shown in Fig. 7. The cyclic voltammogram of **(1)** in the absence of DNA (Fig. 7A) featured reduction of 2+ to the 1+ form at a cathodic peak potential,  $E_{\text{PC}}$  of -0.57 V versus SCE.

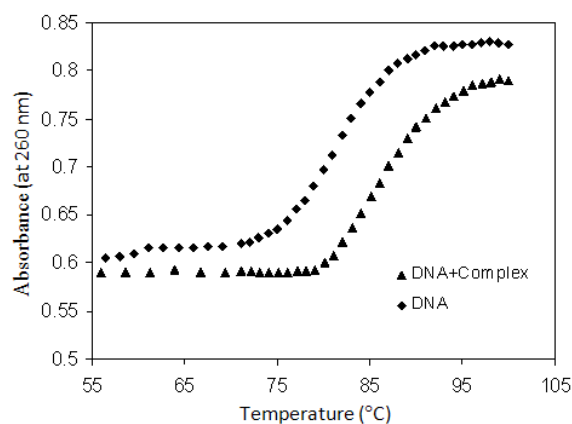


**Fig. 6.** Plots of the changes of absorbance at 260 nm of CT-DNA on heating in the absence and presence of the complex.  $C_{\text{DNA}} = 75 \mu\text{M}$  and  $C_{\text{complex}} = 37.5 \mu\text{M}$  in 50 mM Tris-HCl with 50 mM NaCl.

Reoxidation of 1+ occurred upon scan reversal, at 0.18 V. The separation of the anodic and cathodic peak potentials,  $\Delta E_p = 255 \text{ mV}$ , indicated an irreversible redox process. The formal potential  $E^0$  (or voltammetric  $E_{1/2}$ ), taken as the average of  $E_{\text{PC}}$  and  $E_{\text{PA}}$  is -195 mV, in the absence of DNA. The presence of DNA in the solution at the same concentration of **(1)** causes a decrease in the voltammetric current coupled with a slight shift in the  $E_{\text{PC}}$  (-0.59 V),  $E_{\text{PA}}$  (0.22 V) versus SCE and  $E_{1/2}$  ( $E_{1/2} = -185 \text{ mV}$ ) to a less negative potential (Fig. 7B). The drop of the voltammetric currents in the presence of CT-DNA can be attributed to diffusion of the metal complex bound to the large, slowly diffusing DNA molecule.

#### Viscosity Study

Intercalation and groove binding modes can be distinguished by using hydrodynamic methods such as viscosity, flow dichroism measurements, and NMR [53, 54]. Intercalation of the molecules to the DNA resulted in unwinding and lengthening of the DNA. This DNA elongation causes the viscosity of the solution to increase.

The effect of **(1)** on the viscosity of DNA at  $25.0 \pm 0.1 \text{ }^{\circ}\text{C}$  is shown in Fig. 8. It can be observed that the viscosity of DNA increases with increasing amounts of **(1)**. Such behavior is in accordance with that of other intercalators, which increase the relative specific viscosity for the lengthening of the DNA double helix resulting from intercalation. This result indicates that **(1)** can intercalate between

adjacent DNA base pairs, causing an extension in the helix, and thus increases the viscosity of DNA.

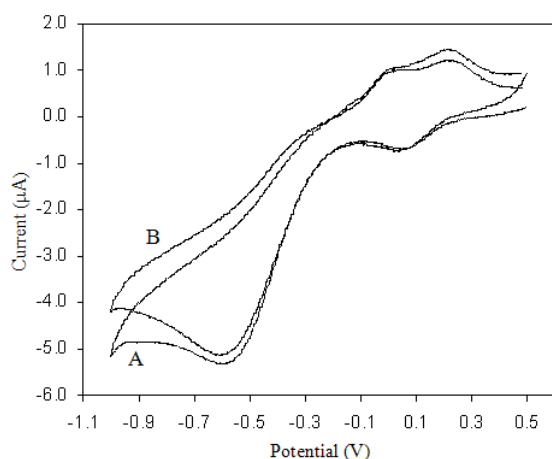


**Fig. 7.** Cyclic voltammograms of (1) in the absence (A) and presence (B) of DNA in 50 mM NaCl, 5 mM Tris, pH 7.3. [Cu]=122 µM, [DNA]/[Cu]=1, Scan rate, 50 mVs<sup>-1</sup>.

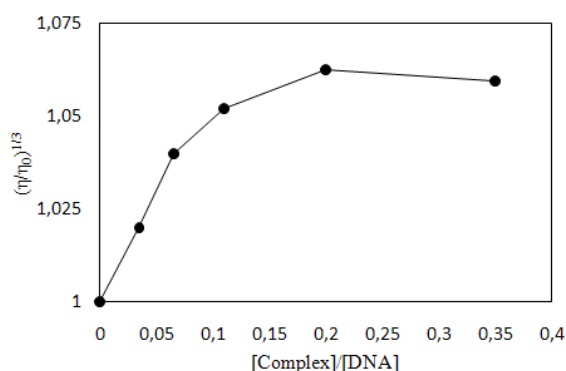


**Fig. 8.** Effect of increasing amount of (1) on the relative viscosity of CT-DNA at 25 ± 0.1 °C, [DNA]= 50 µM, pH 7.3.

## CONCLUSIONS

It is clear that transition metal complexes offer a great potential as structure-selective binding agents for nucleic acids.

In this work the interaction between (1) and calf thymus DNA was investigated using UV, fluorescence and CD spectroscopy, cyclic voltammetry and viscosity measurements. The experimental results indicate that (1) could bind to DNA molecules mainly by intercalative mode, which correlates well with the extended aromatic ring system present in the ligand.

UV-Visible spectroscopy enabled us to find the Cu complex/DNA binding constant. The  $K_b$  of this complex is  $9.51 (\pm 0.2) \times 10^4 \text{ M}^{-1}$ . The existence of hypochromicity, large red shift in the (1) spectra suggests an intercalation binding mode. Increase in DNA viscosity during its interaction with (1) is

consistent with lengthening of DNA due to intercalation. Today many researchers focus their attention on the bioactivity of Cu(II) complexes. So further studies on anticancer activities of the complex are in progress, because non-covalent binding is reversible and is typically preferred over covalent adduct formation, keeping in mind the drug metabolism and toxic side effects.

## REFERENCES

1. E. Wong, C.M. Giandomenico, *Chem. Rev.*, **99**, 2451 (1999).
2. R.N. Bose, K. Allen, M. Wangner, E. Volckova, D.W. Li, R.T. Heath, *Inorganica Chimica Acta*, **300-302**, 937 (2000).
3. I. Haiduc, C. Silvestru, *Coord. Chem. Rev.*, **124**, 55 (1986).
4. D. Kovala-Demertzi, P.N. Yadava, D.M. A., C. M., *J. Inorg. Biochem.*, **78**, 347 (2000).
5. S.A.W. Gruner, E. Locardi, E. Lohof, H. Kessler, *Chem. Rev.*, **102**, 491 (2002).
6. G. Micera, S. Deiana, A. Dessi, P. Decock, B. Dubois, H. Kozłowski, *Inorg. Chim. Acta*, **107**, 45 (1985).
7. X. Fei Liu, Y. Lin Guan, D. Zhi Yang, Z. Li, K. De Yao, *J. Appl. Polym. Sci.*, **79**, 1324 (2001).
8. M. Asadi, E. Safaei, B. Ranjbar, L. Hasani, *J. Mol. Struct.*, **754**, 116 (2005).
9. Z.S. Yang, Y.L. Wang, Y.Z. Zhang, *Electrochem. Commun.*, **6**, 158 (2004).
10. M. Carter, A. Bard, *J. Am. Chem. Soc.*, **109**, 7528 (1987).
11. S. Kawanishi, S. Inoue, S. Sano, *J. Biol. Chem.*, **261**, 5952 (1986).
12. Y.F. Li, C.Z. Huang, X.H. Huang, M. Li, *Anal. Chim. Acta*, **429**, 311 (2001).
13. J. Wang, D. Xu, A.N. Kawde, R. Polsky, *Anal. Chem.*, **73**, 5576 (2001).
14. A. Dimitrakopoulou, C. Dendrinou-Samara, A. Pantazaki, M. Alexiou, E. Nordlander, D. Kessissoglou, *J. Inorg. Biochem.*, **102**, 618 (2008).
15. A.M. Pyle, J.P. Rehmann, R. Meshoyrer, C.V. Kumar, N.J. Turro, J.K. Barton, *J. Am. Chem. Soc.*, **111**, 3051 (1989).
16. X. Zhang, C. Bi, Y. Fan, Q. Cui, D. Chen, Y. Xiao, Q.P. Dou, *Int. J. Mol. Med.*, **22**, 677 (2008).
17. A. Spassky, D.S. Sigman, *Biochemistry*, **24**, 8050 (1985).
18. D.K. Chand, H.-J. Schneider, A. Bencini, A. Bianchi, C. Giorgi, S. Ciattini, B. Valtancoli, *Chem. A Eur. J.*, **6**, 4001 (2000).
19. B.K. Santra, P.A.N. Reddy, G. Neelakanta, S. Mahadevan, M. Nethaji, A.R. Chakravarty, *J. Inorg. Biochem.*, **89**, 191 (2002).
20. M. Lainé, F. Richard, E. Tarnaud, C. Bied-Charretton, C. Verehère-Béaur, *J. Biol. Inorg. Chem.*, **9**, 550 (2004).
21. M. Tabatabaee, *Chem. Cent. J.*, **6:5**, (2012).
22. Z. Hu, C. Tong, *Anal. Chim. Acta*, **587**, 187 (2007).

23. J.Z. Wu, L. Yuan, *J. Inorg. Biochem.*, **98**, 41-45 (2004).
24. V.I. Ivanov, L.E. Minchenkova, A.K. Schyolkina, A.I. Poletayev, *Biopolymers*, **12**, 89 (1973).
25. S. Satyanarayana, J.C. Dabrowiak, J.B. Chaires, *Biochemistry*, **31**, 9319 (1992).
26. C.V. Kumar, E.H. Asuncion, *J. Am. Chem. Soc.*, **115**, 8547 (1993).
27. M. Tabatabaee, *Chem Cent J*, **6**, 5 (2012).
28. R.A. Nyquist, C.L. Putzig, R.O. Kagel, M.A. Leugers, *Infrared Spectra of Inorganic Compounds (3800-45cm<sup>-1</sup>)*, Academic press, 1971.
29. M. Tabatabaee, *Acta Crystallogr.*, **E66**, m647 (2010).
30. J.M. Kelly, M.J. Murphy, D.J. McConnell, C. Ohuigin, *Nucleic Acids Res.*, **13**, 167 (1985).
31. T. Meehan, H. Gamper, J.F. Becker, *J. Biol. Chem.*, **257**, 10479 (1982).
32. T. Gupta, S. Dhar, M. Nethaji, A.R. Chakravarty, *Dalton Trans.*, 1896 (2004).
33. S. Zhang, Y. Zhu, C. Tu, H. Wei, Z. Yang, L. Lin, J. Ding, J. Zhang, Z. Guo, *J. Inorg. Biochem.*, **98**, 2099 (2004).
34. S. Mathur, S. Tabassum, *Cent. Eur. J. Chem.*, **4**, 502 (2006).
35. S. Zhang, J. Zhou, *J. Coord. Chem.*, **61**, 2488 (2008).
36. M.R. Eftink, C.A. Ghiron, *Anal. Biochem.*, **114**, 199 (1981).
37. P.X. Xi, Z.H. Xu, X.H. Liu, F.J. Chen, L. Huang, Z.Z. Zeng, *Chem. Pharm. Bull.*, **56**, 541 (2008).
38. B. Meric, K. Kerman, D. Ozkan, P. Kara, S. Erensoy, U. Akarca, M. Mascini, M. Ozsoz, *Talanta*, **56**, 837 (2002).
39. B.S. Fujimoto, J.B. Clendenning, J.J. Delrow, P.J. Heath, M. Schurr, *J. Phys. Chem.*, **98**, 6633 (1994).
40. E. Long, J. Barton, *Acc. Chem. Res.*, **23**, 271 (1990).
41. J.K. Barton, J.M. Goldberg, C.V. Kumar, N.J. Turro, *J. Am. Chem. Soc.*, **108**, 2081 (1986).
42. B. Nordén, F. Tjerneld, *Biopolymers*, **21**, 1713 (1982).
43. S. Roy, R. Banerjee, M. Sarkar, *J. Inorg. Biochem.*, **100**, 1320 (2006).
44. A.D. Richards, A. Rodger, *Chem. Soc. Rev.*, **36**, 471 (2006).
45. K. Akdi, R.A. Vilaplana, S. Kamah, J.A.R. Navarro, J.M. Salas, F. Gonzalez-Valchez, *J. Inorg. Biochem.*, **90**, 51 (2002).
46. S. Xiao, W. Lin, C. Wang, M. Yang, *Bioorg. Med. Chem. Lett.*, **11**, 437 (2001).
47. G.A. Neyhart, N. Grover, S.R. Smith, W.A. Kalsbeck, T.A. Fairley, M. Cory, H. Holden Thorp, *J. Am. Chem. Soc.*, **115**, 4423 (1993).
48. S. Arounaguirri, B.G. Maiya, *Inorg. Chem.*, **35**, 4267 (1996).
49. M.J. Waring, *J. Mol. Biol.*, **13**, 269 (1965).
50. P.U. Maheswari, M. Palaniandavar, *Inorg. Chim. Acta*, **357**, 901 (2004).
51. R.B. Nair, E.S. Teng, S.L. Kirkland, C.J. Murphy, *Inorg. Chem.*, **37**, 139 (1998).
52. G. Psomas, *J. Inorg. Biochem.*, **102**, 1798 (2008).
53. R. Palchaudhuri, P.J. Hergenrother, *Curr. Opin. Biotechnol.*, **18**, 497 (2007).
54. L. Strekowski, B. Wilson, *Mutat. Res.-Fundam. Mol. Mech. Mutag.*, **623**, 3 (2007).

## ИЗСЛЕДВАНЕ НА ВЗАИМОДЕЙСТВИЕТО НА ДНК С НОВ Cu(II) КОМПЛЕКС ЧРЕЗ СПЕКТРОСКОПСКИ, СПЕКТРОФЛУОМЕТРИЧНИ, ВОЛТАМПЕРОМЕТРИЧНИ МЕТОДИ И С КРЪГОВ ДИХРОИЗЪМ

М. Бордбар<sup>1,\*</sup>, Ф. Ходайе<sup>2</sup>, М. Табатабае<sup>2</sup>, А. И. Фаал<sup>3</sup>, З. Мехрилихван<sup>4</sup>,  
С. Мохамад-Ганджи<sup>5</sup>

<sup>1</sup>Департамент по химия, Научен факултет, Университет в Кум, Кум, Иран

<sup>2</sup>Департамент по химия, Клон Язд, Ислямски университет „Азад“, Язд, Иран

<sup>3</sup>Департамент по химия, Университет Паяме Нур, П.К. 37185-311, Иран

<sup>4</sup>Клуб на младия изследовател, Клон Северен Техеран, Ислямски университет „Азад“, Техеран, Иран

<sup>5</sup>Национален институт за генно инженерство и биотехнология (NIGEB), П.К. 14965-161, Техеран, Иран.

Постъпила на 14 септември, 2015 г.; приета на 28 март, 2016 г.

(Резюме)

Изследвана е свързващата активност на водо-разтворими мед(II) комплекс с пиридин-2,6-диарбоацетат (pydc<sup>2-</sup>) и 2-аминопиримидин (amp) с формула [Cu(pydc)(amp)].2H<sub>2</sub>O.Н<sub>2</sub>O (**1**) с DNA (СТ-DNA) от телешки тимус. Свързващата активност на **1** е изследвана чрез ефекта ѝ върху електронните абсорбционни спектри, ефекта на термична денатурация, флуоресцентното закаляване (използвайки метиленово синьо като флуоресцентен маркер) и спектри на кръгов дихроизъм. Всички резултати внушават взаимодействие между (**1**) и ДНК чрез интеркалация с константа на свързване (9.51±0.2)×10<sup>4</sup> M<sup>-1</sup>.

## Structural, magnetic and catalytic properties of Co substituted manganite nano-perovskites

A. Gholizadeh<sup>1\*</sup>, A. Malekzadeh<sup>2</sup>, M. Ghiasi<sup>2</sup>

<sup>1</sup>*School of Physics, Damghan University (DU), Damghan, I.R. Iran*

<sup>2</sup>*School of Chemistry, Damghan University (DU), Damghan, I.R. Iran*

Received August 4, 2015, Revised October 22, 2015

In this work, structural, magnetic and catalytic properties of  $\text{LaMn}_{1-x}\text{Co}_x\text{O}_3$  ( $x = 0.00, 0.25, 0.50, 0.75, 1.00$ ) are investigated. The structural characterization of the samples by X-ray powder diffraction and using the X'Pert package and Fullprof program is evidence for a monoclinic structure (P21/n space group) with  $x = 0.5$  and a rhombohedral structure (R-3c space group) for other samples. These results have been confirmed by FTIR measurements. The magnetic characterizations of the samples have been studied by magnetization measurement versus temperature and field. The structural and magnetic results show the ferromagnetic interactions of  $\text{Co}^{2+}\text{-Mn}^{4+}$  for  $x \leq 0.5$  are being progressively replaced by the less effective  $\text{Co}^{2+}\text{-Co}^{3+}$  and  $\text{Mn}^{4+}\text{-Co}^{3+}$  interactions for  $x > 0.5$ . The catalytic activity of  $\text{LaMn}_{1-x}\text{Co}_x\text{O}_3$  was evaluated for  $\text{C}_2\text{H}_6$  combustion and CO oxidation reactions. Under similar reaction conditions, the catalytic results show that the  $\text{LaMn}_{0.5}\text{Co}_{0.5}\text{O}_3$  nano-perovskite is the best catalyst for  $\text{C}_2\text{H}_6$  combustion and CO oxidation.

**Keywords:** Nano-Perovskite; Manganite-Cobaltite; Structural and Magnetic Phase Transition;  $\text{C}_2\text{H}_6$  combustion; CO oxidation.

### INTRODUCTION

Many efforts have been made to reduce the use of precious metals in catalysts (Pt, Pd and Rh), and use new compounds which are cheaper and have a better catalytic activity. Finding a suitable replacement for expensive catalysts used in various industries, including the automotive industry, to further reduce the environmental pollutants emitted is a major research endeavor in the modern world. A high activity in the reduction-oxidation (redox) reaction, oxygen storage capability and high flexibility in including other metals in the structure, have proposed perovskite compounds  $\text{ABO}_3$  as a good candidate for this replacement. In addition, being inexpensive and having heat and mechanical resistance properties are some other advantages of these compounds. Among perovskite compounds, lanthanum manganites and cobaltites with formulas  $\text{LaMnO}_3$  and  $\text{LaCoO}_3$  are the famous compounds that are used to complete the oxidation reaction of CO and hydrocarbons [1-2].

$\text{LaMn}(\text{Co})\text{O}_3$  with a perovskite structure is an insulator-antiferromagnetic at room temperature due to the absence of ions  $\text{Mn}^{4+}$  ( $\text{Co}^{4+}$ ). With the replacement of the  $\text{La}^{3+}$  ions by bivalent elements (Sr, Ca, ...), the trivalent ions Mn (Co) are converted to a mixture of ions  $\text{Mn}^{3+}$  and  $\text{Mn}^{4+}$  ( $\text{Co}^{3+}$  and  $\text{Co}^{4+}$ ). The measurements reported on

polycrystalline samples of  $\text{La}_{1-y}\text{M}_y\text{Mn}(\text{Co})\text{O}_3$ , showed an insulator-antiferromagnetic behavior for low and high values of  $y$  and metal-ferromagnetic behavior at the concentration  $y \approx 1/3$  [3-4]. In these compounds, the ferromagnetic-paramagnetic transition associated with a metal-insulator transition below the curie temperature ( $100 < T_C$  (K)  $< 350$ ) has been attributed to the double-exchange theory between the ions  $\text{Mn}^{3+}\text{-Mn}^{4+}$  ( $\text{Co}^{3+}\text{-Co}^{4+}$ ) [5]. In manganite-cobaltite  $\text{LaMn}_{1-x}\text{Co}_x\text{O}_3$ , the origin of the metal-ferromagnetic behavior is due to ferromagnetic interaction between the ions of  $\text{Mn}^{3+}\text{-Mn}^{3+}$  and  $\text{Mn}^{4+}\text{-Co}^{2+}$  [6]. Furthermore, all the electronic, magnetic and redox properties of the samples will depend on the nature of the interaction between the Co and Mn ions via oxygen.

Several investigators [5-8] have reported that in  $\text{ABO}_3$  perovskites, the A ions in general are catalytically inactive and the active ions at the B position readily interact with the gas molecules. It should be noted that the substitution at the A-site with a bivalent cation or a tetravalent cation leads to a different behavior of the catalytic activity of manganite-cobaltite compounds. Because the B-O bond length and the bond energy depend on the lattice parameter this alters the B-O<sub>ad</sub> [5]. The Sr substitution for La in  $\text{La}_{1-y}\text{A}_y\text{CoO}_3$  leads to higher oxidation states for Co, so that the higher the amount of Sr, the higher is the concentration of  $\text{Co}^{4+}$  [8]. However, since  $\text{Co}^{4+}$  is unstable, then oxygen release can take place ending in the formation of oxygen vacancies that leads to a

\* To whom all correspondence should be sent:  
E-mail: gholizadeh@du.ac.ir; ah\_gh1359@yahoo.com

decrease of the catalytic activity. By contrast, the insertion of  $Ce^{4+}$  in  $La_{1-y}A_yCoO_3$  leads to a partial reduction of  $Co^{3+}$  to  $Co^{2+}$ , thus affording a large amount of active sites for oxygen adsorption from the gas-phase that leads to an increase in catalytic activity [5].

The changes in the  $AB_{1-x}B'_xO_3$  perovskite catalytic properties of the substituting cation B with B' can be classified in two categories: geometric and electronic structure of cation B' [6]. The effect of B' substitution on geometric and electronic factors is considered in the calculation of the structural and magnetic changes.

In this work, we prepared  $LaMn_{1-x}Co_xO_3$  ( $x = 0.00, 0.25, 0.50, 0.75, 1.00$ ) by the citrate precursor method and tried to explain the structural and magnetic properties and the influence of Co substitution on their catalytic activities for  $C_2H_6$  combustion and CO oxidation reactions by using reasonable experimental data.

## EXPERIMENTAL

The  $LaMn_{1-x}Co_xO_3$  compounds with  $x = 0.00, 0.25, 0.50, 0.75, \text{ and } 1.00$  were prepared by the citrate precursor method, similar to the recipe reported elsewhere [9]. First, a solution containing appropriate concentrations of metal nitrates  $La(NO_3)_3 \cdot 6H_2O$ ,  $Mn(NO_3)_2 \cdot 4H_2O$ ,  $Co(NO_3)_2 \cdot 6H_2O$  and citric acid, equal to the total number of moles of nitrate ions, was evaporated at  $60^\circ C$ , overnight. The homogeneous sol-like substance was subsequently dried at  $80^\circ C$ , overnight. The resulting spongy and friable materials were completely powdered and kept at  $200^\circ C$ , overnight. The resulting materials were powdered again and calcined at  $600^\circ C$  for 5 h. The samples were subsequently calcined for 5 more hours at  $900^\circ C$ .

The X-ray diffraction (XRD) patterns have been recorded using a Bruker AXS diffractometer D8 ADVANCE with  $Cu-K\alpha$  radiation in the range  $2\theta = 20-80^\circ$  at room temperature (RT). The XRD data was analyzed using a commercial X'pert package and the Fullprof program.

XRD profile analysis is a simple and powerful method to evaluate the crystallite size and lattice strain. Two factors determine the breadth of the Bragg peak including the crystallite size-dependent ( $\beta_D$ ) or strain dependent broadening ( $\beta_S$ ) effects, except for the instrument-dependent effect. To do an accurate analysis for size and strain effects, the instrumental broadening must be accounted for. Scherrer's equation is as follows:

$$D = \frac{0.94 \lambda}{\beta_{hkl} \cos \theta}, \quad (1)$$

This shows the broadening of the XRD pattern which is attributed to the crystallite size-induced broadening. Here,  $\beta_{hkl}$  is the full-width at half-maximum of the diffraction peaks. The information on strain ( $\epsilon$ ) and crystallite size ( $D$ ) of the powders have been obtained from  $\beta_{hkl}$  and the planar spacing  $d_{hkl}$  via the Halder-Wagner method [10]:

$$\left(\frac{\beta_{hkl}^*}{d_{hkl}^*}\right)^2 = \left(\frac{1}{D}\right)^2 \left(\frac{\beta_{hkl}^*}{d_{hkl}^*}\right)^2 + \left(\frac{\epsilon}{2}\right)^2, \quad (2)$$

where  $\beta_{hkl}^* = \beta_{hkl} \cos \theta / \lambda$  and  $d_{hkl}^* = 2 \sin \theta / \lambda$ . Finally, the results of the Halder-Wagner method are compared with the Scherrer method.

The FT-IR spectra were recorded in a Perkin-Elmer spectrum RXI-IR spectrometer, operating by ratio, single beam, or interferogram mode, in the range  $400-1500 \text{ cm}^{-1}$ . The samples were finely ground in an agate mortar with KBr as diluent and pelleted for the IR analysis. The morphology of the samples was studied by SEM (Philips XL30) analysis. The particle size of the samples was investigated by TEM (LEO Model 912AB) analysis.

The absorption coefficient is a suitable quantity for studying the band gap energy. Optical absorption spectra of  $LaMn_{1-x}Co_xO_3$  between 200 and 1100 nm wavelengths have been recorded at room temperature using a HP-UV-Vis system (Agilent8453, model). The band gap energies have been calculated in accordance with Ref. [11]. The following relation holds between the optical absorption coefficient,  $\alpha(\lambda)$ , and the optical band gap energy of a direct band transition [25]:

$$(3) \quad (\alpha h\nu)^2 = B(h\nu - E_g)$$

where B is an energy-independent constant and  $\alpha(\lambda) = 2.303 A(\lambda)/t$  is the optical absorption coefficient calculated from the absorption spectra ( $A(\lambda)$  is the mean particle size of the sample (t)). The band gap energy of the samples is estimated by extrapolating the linear part of  $(\alpha h\nu)^2$  vs. a  $h\nu$  plot. The hysteresis loops at 10 K and temperature dependence of magnetization between 10-400 K was carried out in a SQUID magnetometer (Quantum Design, Inc.). The magnetization curve in high fields can usually be fitted by the empirical formula; law of approach to saturation [12]:

$$M(H) = M_s [1 - (a/H) - (b/H^2) - (c/H^3)] + \chi H + EH^{1/2}, \quad (4)$$

where  $M(H)$  and  $M_S$  are the magnetization at the field  $H$  and the saturation magnetization explained by atomic theory, respectively.

Catalytic tests for  $C_2H_6$  combustion and CO oxidation reactions over  $LaMn_{1-x}Co_xO_3$  catalysts were studied in an experimental set-up using a quartz tube, filled with 200 mg of a 60-100 mesh sized catalyst supported on ceramic wool under GHSV of  $12,000\text{ h}^{-1}$ . In a typical experiment, a model exhaust gas obtaining a mixture of 6 vol% CO and 0.2 vol%  $C_2H_6$  as a hydrocarbon (HC) model compound, in Ar and air (a stoichiometric ratio with respect to oxygen) was passed through the catalyst bed with a total gas mixture flow rate of 40 mL/min at STP. Catalytic test studies were carried out by temperature rising in random intervals from  $50^\circ\text{C}$  to the complete oxidation temperature. The product stream was analyzed by a GC on a FI detector.

## RESULTS AND DISCUSSIONS

### *Structural and morphologic properties*

X-ray diffraction patterns of  $LaMn_{1-x}Co_xO_3$  ( $x = 0.00, 0.25, 0.50, 0.75, 1.00$ ), are shown in Fig. 1. The XRD data were analyzed using both the commercial X'Pert High Score package and the Fullprof program. Identification of the structure type using the X'pert package confirms the perovskite structure in all samples without a presence of impurity phases. As shown in the XRD pattern of samples  $x = 0.00, 0.25, 0.75, 1.00$  (Fig. 1), a splitting of the peaks of the perovskite at angles  $\sim 33^\circ, \sim 41^\circ, \sim 58^\circ, \sim 68^\circ$  and  $\sim 78^\circ$  is an indication of a rhombohedral system [13]. Also, for a better comparison, a peak at about  $\sim 33^\circ$  is shown in the inset of Fig. 1. For  $x = 0.00$ , the peak at  $\sim 33^\circ$  is a very intense doublet, while for other samples it is fully split. These results for  $x = 0.00$  suggest a mixture of  $LaMnO_3$  and  $LaMnO_{3+\delta}$  with cubic and rhombohedral structures, respectively. However, the XRD pattern of sample  $x = 0.50$  is different, while more broadening of the peaks mentioned above and a splitting of the peak at the angle  $\sim 47^\circ$  indicate a lower symmetry.

Results of the Rietveld analysis using the Fullprof program indicate that all the diffraction peaks of the sample at  $x = 0.50$  can be quite well indexed in the monoclinic structure (space group  $P2_1/n$ ) and for other samples in the Rhombohedral structure (space group  $R-3c$ ). Also, the results of the Rietveld analysis using the Fullprof program indicate that the best fit with the least difference was carried out (Fig. 1). To perform a Rietveld

refinement we need good initial values for the lattice parameters and the type of space group obtained from a phase analysis of the X'pert package.

The hexagonal cell is no longer primitive and has three times the volume of the rhombohedral cell. When the XRD pattern of a rhombohedral sample is indexed, i.e., with reference to hexagonal axes and the true nature of the lattice determined, we usually want to know the lattice parameters  $a_r$  and  $\alpha$  of the rhombohedral unit cell. But the dimensions of the rhombohedral cell can be determined from the dimensions of the hexagonal cell and this is an easier process than solving the rather complicated plane-spacing equation for the rhombohedral system. The first step is to analyze and index the XRD pattern on the basis of the hexagonal axes using the Fullprof program. Then, the parameters  $a_H$  and  $c$  of the hexagonal cell are calculated in the usual way. Finally, the parameters  $a_r$  and  $\alpha$  of the rhombohedral cell are determined from the refined parameters  $a_H$  and  $c$  of the hexagonal cell using the Fullprof program according to the following equations:

$$a_r = \frac{1}{3}\sqrt{3a_H^2 + c^2}, \quad \sin \frac{\alpha}{2} = \frac{3}{2\sqrt{3+(c/a_H)^2}}, \quad (5)$$

The derived lattice parameters of the samples for rhombohedral and monoclinic structures are given in Table 1. It should be noted that if the  $c/a_H$  ratio of the hexagonal cell takes on the special value of 2.45, then the angle  $\alpha$  of the rhombohedral cell will be equal to  $60^\circ$  and the bond angle  $B-O-B$  is  $180^\circ$ . Consequently, the lattice points will be face-centered cubic ( $t$  is equal to 1). Also, the magnitude of the rotation of  $BO_6$  can be evaluated from either the angle  $\alpha$  of the rhombohedral unit cell written in Table 1 or from the axial ratio  $c/a_H$  of the hexagonal cell. As a result of the rotation (tilting), the  $B-O-B$  bond angle ( $\leq 180^\circ$ ) and  $\alpha$  deviate from the ideal perovskite value. Notice, that for trigonal angles,  $\alpha$ , is less than 60 degrees, the transformation can be achieved by an expansion along the body diagonal [111] of the Rhombohedral or along the  $c$ -axis [001] of the hexagonal; while, for trigonal angles this is greater than 60 degrees, a contraction in the body diagonal [111] of the Rhombohedral or along the  $c$ -axis [001] of the hexagonal. Therefore, the obtained values of the angle  $\alpha$  are higher than  $60^\circ$  this means the  $BO_6$  octahedron is slightly compressed along the (hexagonal  $c$  axis) rhombohedral (111) axis with respect to the cubic structure.

From the X-ray diffraction patterns at about  $33^\circ$  shown in the inset of Fig. 1, two tendencies are

observed for values of  $x \leq 0.50$  and  $x > 0.50$ . For values of  $x \leq 0.50$ , the peaks shift is nearly constant upon increasing the Co-content and means a slight increase of the unit cell volume. But for values of  $x > 0.50$ , an increase of peaks shifts to larger  $2\theta$ , consequently a decrease of the unit cell volume is observed with the degree of substitution. These findings are in accordance with the refined unit cell volume obtained from the Rietveld method using the Fullprof program summarized in Table 1.

There is no apparent linear correlation between the perovskite structure, the substitution degree and that for  $x = 0.50$  when the transformation of the crystal phase occurs. This is due to the substitution of  $Mn^{x+}$  ions in the lattice by  $Co^{x+}$  ions. Therefore, all these findings should be correlated with the ionic radii of each one of the components. The presence of several ionic states ( $Mn^{3+}$ ,  $Mn^{4+}$ ,  $Co^{2+}$  and  $Co^{3+}$ ) makes it difficult to decide just from the XRD data.

**Table 1.** The structure type and unit cell parameters of  $LaMn_{1-x}Co_xO_3$ .

Sample	Structure (space group)	lattice Parameters	V ( $\text{\AA}^3$ )
x = 0.00	Rhombohedral (R-3c)	$a = b = c = 5.45866$ ( $\text{\AA}$ ) $\alpha = \beta = \gamma = 60.4735$ ( $^\circ$ )	116.243
x = 0.25	Rhombohedral (R-3c)	$a = b = c = 5.45903$ ( $\text{\AA}$ ) $\alpha = \beta = \gamma = 60.6003$ ( $^\circ$ )	116.595
x = 0.50	Monoclinic (P 21/n)	$a = 5.36332$ ( $\text{\AA}$ ) $b = 5.46978$ ( $\text{\AA}$ ) $c = 7.74353$ ( $\text{\AA}$ ) $\beta = 88.6507$ ( $^\circ$ )	227.103
x = 0.75	Rhombohedral (R-3c)	$a = b = c = 5.39213$ ( $\text{\AA}$ ) $\alpha = \beta = \gamma = 60.7529$ ( $^\circ$ )	112.741
x = 1.00	Rhombohedral (R-3c)	$a = b = c = 5.37493$ ( $\text{\AA}$ ) $\alpha = \beta = \gamma = 60.7199$ ( $^\circ$ )	111.584

**Table 2.** the values of crystallite size and strain of  $LaMn_{1-x}Co_xO_3$  obtained from Scherrer and H-W methods.

Sample	$D_{m-Sch}$ (nm)	$D_{H-W}$ (nm)	$\epsilon_{H-W} * 10^3$ (no unit)
x = 0.00	28.89	32.36	2.42
x = 0.25	28.45	29.58	2.12
x = 0.50	19.5	23.47	5.48
x = 0.75	14.48	27.55	10.56
x = 1.00	40.91	28.73	5.68

**Table 3.** Magnetic results of  $LaMn_{1-x}Co_xO_3$ .

Sample	$M_S(10\text{ K})$ (emu/g)	$H_C(10\text{ K})$ (Oe)	$M_r(10\text{ K})$ (emu/g)	$T_C$ (K)
x = 0.00	8.96	90	1.50	130
x = 0.25	7.34	2730	3.48	184
x = 0.50	4.21	4310	2.32	230
x = 0.75	1.29	5040	0.30	179
x = 1.00	0.54	4310	0.23	169

**Table 4.** Catalytic performance (%), the C<sub>2</sub>H<sub>6</sub> combustion and CO oxidation temperatures (°C) for LaMn<sub>1-x</sub>Co<sub>x</sub>O<sub>3</sub>.

Sample	Temperature of CO conversion (°C)			Temperature of C <sub>2</sub> H <sub>6</sub> conversion (°C)		
	10%	50%	90%	10%	50%	90%
x = 0.00	255	295	350	260	358	483
x = 0.25	175	195	298	237	376	404
x = 0.50	127	160	190	177	283	393
x = 0.75	160	179	213	180	374	430
x = 1.00	220	330	380	178	576	702

Several considerations can be forwarded, however, at this stage: first of all, it can be expected that for  $x \leq 0.50$ , when substituting Mn<sup>3+</sup> by cobalt ions, this ion enters as Co<sup>2+</sup>, leading to the formation of an equivalent amount of Mn<sup>4+</sup> to preserve the electro-neutrality of the lattice. In such a case, the mean ionic radius of the B cation must show an increase, with an accompanying increase of the lattice volume (Table 1). It is known that the mean ionic radius of Mn<sup>4+</sup>-Co<sup>2+</sup> is larger than that of Mn<sup>3+</sup>-Co<sup>3+</sup> [14]. Therefore, the increase in lattice volume has been attributed to the assumption of substituting Co<sup>2+</sup> by Mn<sup>3+</sup> due to the larger mean ionic radius of Mn<sup>4+</sup>-Co<sup>2+</sup> compared to Mn<sup>3+</sup>-Co<sup>3+</sup>. For  $x > 0.50$ , a large reduction of the lattice volume (Table 1) correlates well with the presence of Co ions as Co<sup>3+</sup> in a low spin (LS) state, for which the ionic radius is lower than the corresponding high spin (HS) state (Co<sup>3+</sup>: HS, 0.61 and LS, 0.545 Å). In such a case, the mean ionic radius of the B-site decreases, with an accompanying decrease of the lattice volume (Table 1). Again, this hypothesis is confirmed by the magnetic and catalytic data presented further in this work. For this, a correlation with the magnetic data is necessary, as will be discussed later in this work.

The influence of substitution on the crystal structure can be described by a tolerance factor ( $t = r_{A-O} / (\sqrt{2} r_{B-O})$ ) introduced by Goldschmidt to estimate the deviation from the ideal structure. As a result, for  $x \leq 0.50$ , as  $\langle r_{B-O} \rangle$  increases,  $t$  decrease, at first the rhombohedral structure for  $x = 0.0$  is further distorted to the rhombohedral structure for  $x = 0.25$  and then for  $x = 0.50$  the structure transforms to monoclinic in which the bending of the B-O-B bond increases and the bond angle deviates from 180°. For  $x > 0.50$  inversely, as  $\langle r_{B-O} \rangle$  decreases,  $t$  increase, the lattice structure transforms from a monoclinic to a rhombohedral structure.

The results for the crystallite sizes obtained from the mean value of 15 strongest peaks shown in Fig. 1 for both structures by using the Scherrer method are summarized in Table 2.

The Halder-Wagner method was used to study the individual contributions of crystallite size and lattice micro-strain on isotropic line broadening of 15 strongest peaks of the LaMn<sub>1-x</sub>Co<sub>x</sub>O<sub>3</sub> compounds.

In this method, the plot of  $\left(\frac{\beta_{hkl}^*}{d_{hkl}^*}\right)^2$  (axis y) versus  $\left(\frac{\beta_{hkl}^*}{d_{hkl}^*}\right)$  (axis-x) is a straight line (see Fig. 2).

The crystallite size is determined from the slope inverse of the linearly fitted data and the root of the y-intercept gives the strain, respectively. The results of crystallite size and micro-strain of LaMn<sub>1-x</sub>Co<sub>x</sub>O<sub>3</sub> ( $x = 0.00, 0.25, 0.50, 0.75, 1.00$ ) estimated by the Scherrer and H-W methods are summarized in Table 2. The values for  $x = 0.50, 0.75$  are less than for the other samples.

The H-W method supposes that the “crystallite size” profile contributes to the line broadening by a Lorentzian function and the “strain” profile by a Gaussian function. This method shows that line broadening is essentially isotropic. However, the advantage of the H-W method over the Scherrer method is that less weight is given to the data from reflections at high angles where the precision is usually lower [10].

However, the mean crystallite size obtained from the Scherrer formula and the H-W analysis (see Table 2) show a greater variation because of the difference in averaging of the particle size distribution and the results of the H-W method are more accurate, with all the data points touching the fitting line. It is noted that the crystallite size obtained from this method is a minimum at about  $x = 0.50$ .

Fig. 3 shows the FTIR spectrum of LaMn<sub>1-x</sub>Co<sub>x</sub>O<sub>3</sub> ( $x = 0.00, 0.25, 0.50, 0.75, 1.00$ ). The presence of metal oxygen bonds i.e. symmetrical lengthening of the O-B-O and asymmetrical lengthening of the B-O bond of the octahedron BO<sub>6</sub> structures could be revealed from the peaks at 410 and 600 cm<sup>-1</sup>, respectively. The widening of the 600 cm<sup>-1</sup> band and/or the appearance of a shoulder indicates a structure with a lower symmetry [6].

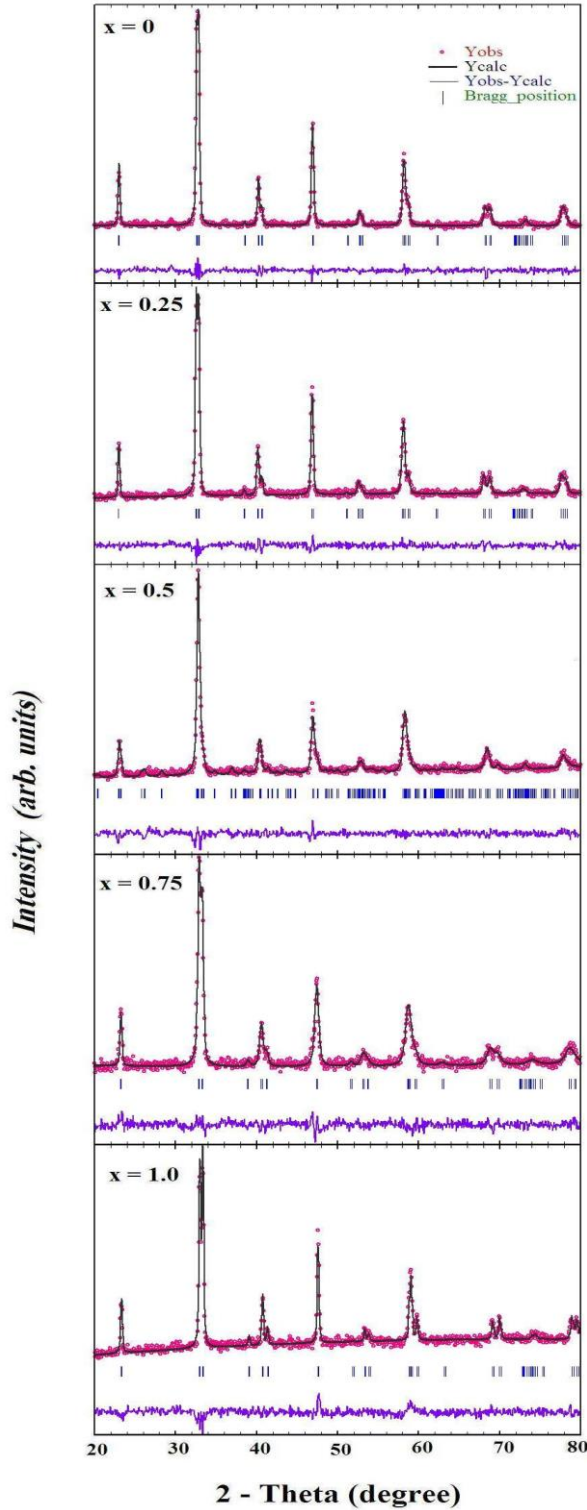


**Fig. 1.** Rietveld analysis of the X-ray diffraction patterns for  $\text{LaMn}_{1-x}\text{Co}_x\text{O}_3$  ( $x = 0.00, 0.25, 0.50, 0.75, 1.00$ ). The circle signs represent the raw data. The solid line represents the calculated profile. Vertical bars indicate the position of Bragg peaks for samples with the rhombohedral structure (Space Group  $R\bar{3}c$ ) and for the sample  $x = 0.5$  with the monoclinic structure (Space Group  $P2_1/n$ ). The lowest curve is the difference between the observed and the calculated patterns. The X-ray diffraction patterns for all samples at about  $33^\circ$  are shown in the inset of  $x = 0.75$ .

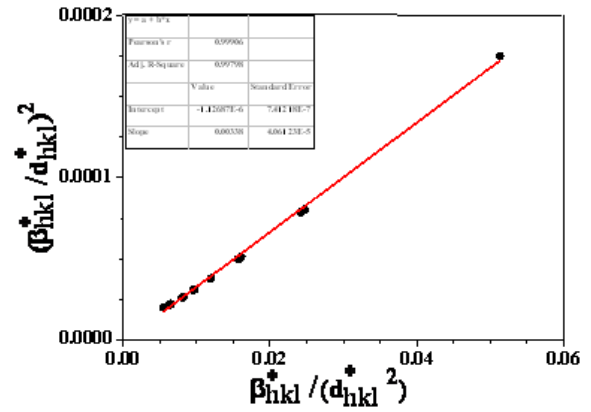


**Fig. 2.** Fitted curves of the Halder-Wagner analysis for  $x = 0$ . The y-intercept gives the mean value of the strain and the slope gives the crystallite size.

Therefore, for the perovskites with  $x < 0.50$ , the spectra corresponds to a rhombohedral structure with a great symmetry but for  $x > 0.50$ , a shoulder appears at  $550 \text{ cm}^{-1}$  and is characteristic of a rhombohedral structure with a lower symmetry. The peak at  $410 \text{ cm}^{-1}$  can be attributed to a lower symmetry in three samples  $x = 0.50, 0.75, 1.00$ . These results are in accordance with the unit cell parameter  $a$  obtained from the XRD analysis so that the larger  $a$ , shows a lower symmetry. The narrow band at  $1385 \text{ cm}^{-1}$  might correspond to the  $\text{CO}_3^{2-}$  groups.

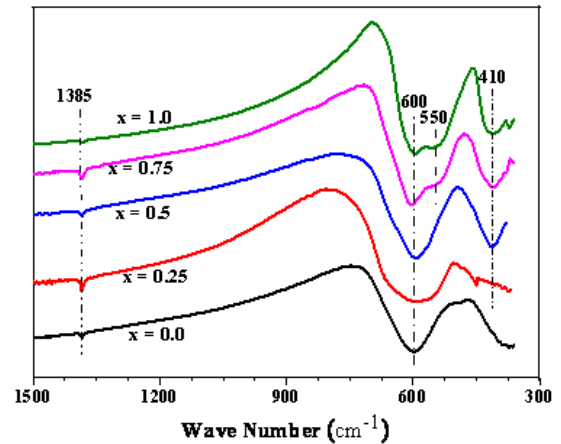


**Fig. 3.** FT-IR spectra for  $\text{LaMn}_{1-x}\text{Co}_x\text{O}_3$ .

A similar morphology is observed in SEM micrographs of the samples for  $\text{LaMn}_{1-x}\text{Co}_x\text{O}_3$  ( $x = 0.0, 1.0$ ) as shown in Fig. 4. The TEM micrographs and particle size distribution of samples at  $x = 0.0$  and  $1.0$  are shown in Fig. 4. Size distribution histograms are fitted by using a log-normal function as follow:

$$P(d) = \frac{1}{d\sigma_d\sqrt{2\pi}} \exp\left\{-\frac{1}{2\sigma_d^2} \ln^2\left(\frac{d}{d_{TEM}}\right)\right\}, \quad (6)$$

where  $\sigma_d$  is the standard deviation of the diameter and  $d_{TEM}$  is the mean diameter obtained from the

TEM results. The mean diameter was calculated to be 36 nm ( $x = 0.0$ ) and 50 nm ( $x = 1.0$ ), respectively. These results are different from the calculated crystallite sizes from the XRD line profile. The differences are related to the irregular shape of the nanoparticles with spherical and polygon morphologies which are observed in the TEM micrographs [8].

### Magnetic properties

The hysteresis loops of the  $\text{LaMn}_{1-x}\text{Co}_x\text{O}_3$  ( $x = 0.00, 0.25, 0.50, 0.75, 1.00$ ), shown in Fig. 5, are compared at 10 K, measured in a SQUID magnetometer (Quantum Design, Inc.). The curves of  $M_H$ , and S-shaped hysteresis loops show the coercivity field  $H_C$  (intersection with the x axis), remanance magnetization  $M_r$  (intersection with the y axis) and the saturation magnetization  $M_S$ . The values of  $H_C$ ,  $M_r$  and  $M_S$  as calculated are summarized in Table 3. The increase of  $H_C$  with cobalt content has been attributed to the increase of the magnetic domains. The  $M_r$  and  $M_S$  values for samples  $x \leq 0.50$  are larger than  $x > 0.50$ .

The temperature dependence of magnetization in the range 5-400 K under the applied magnetic field 0.1T for  $\text{LaMn}_{1-x}\text{Co}_x\text{O}_3$  ( $x = 0.00, 0.25, 0.50, 0.75, 1.00$ ) is shown in Fig. 6. The Curie temperature obtained from the critical point in the derivative of the M-T curves is mentioned in Table 3 that clearly displays a non-monotonic dependence of  $T_C$  with the Co doping level. In Co doped samples, the interval of  $T_C$  is about 50 K for each addition of 0.25 cobalt concentration. Firstly, the transition temperature,  $T_C$ , increases with  $x$  and then decreases as  $x$  increases. The compound  $\text{LaMn}_{0.5}\text{Co}_{0.5}\text{O}_3$  characterized by the presence of two ferromagnetic phases with  $T_C = 225$  and 150K is subject to the synthesis conditions [15]. The former magnetic phase is formed at 700 °C, whereas the latter phase can be obtained by quenching from 1300 °C. A high-spin order  $\text{Co}^{2+}$ - $\text{Mn}^{4+}$  valence state and low-spin disorder-nonmagnetic  $\text{Mn}^{3+}$ - $\text{Co}^{3+}$  ions were discovered for samples with higher and lower Curie temperatures, respectively. In addition, the  $\text{Co}^{2+}$  and  $\text{Mn}^{4+}$  ions are ferromagnetically aligned and the average ionic radii of  $\text{Mn}^{4+}$ - $\text{Co}^{2+}$  are larger than those of  $\text{Mn}^{3+}$ - $\text{Co}^{3+}$  and the high temperature samples  $\text{LaMn}_{0.5}\text{Co}_{0.5}\text{O}_3$  are characterized by a smaller volume [14].

The pure manganite  $\text{La}^{3+}\text{Mn}^{3+}\text{O}_2$  ( $x = 0$ ) is essentially antiferromagnetic [13] with an orthorhombic structure, while in our case, there is a ferromagnetic component with a low coercive field and large magnetization values. A recent study [16]

showed that stoichiometric  $\text{LaMnO}_3$  should be prepared in the absence of oxygen but sintering in ambient air results in nonstoichiometric  $\text{LaMnO}_{3+\delta}$  with the formation of  $\text{Mn}^{4+}$  ions larger than 20%.

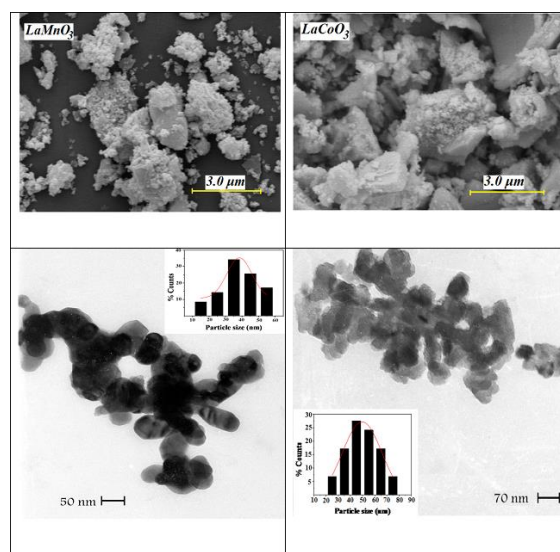


Fig. 4. SEM results, TEM micrographs and size distribution histograms for  $\text{LaMn}_{1-x}\text{Co}_x\text{O}_3$ .

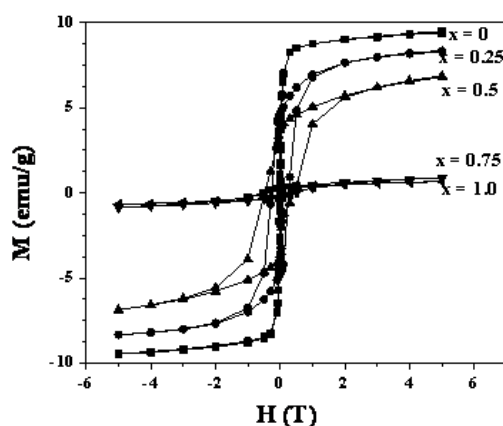


Fig. 5. The hysteresis loops (M-H) at 10 K for  $\text{LaMn}_{1-x}\text{Co}_x\text{O}_3$ .

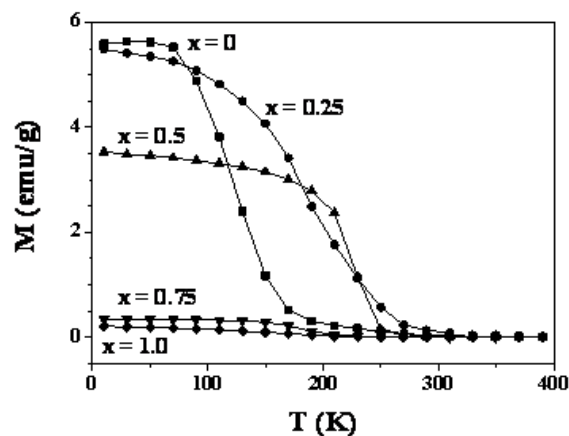


Fig. 6. The magnetization curves versus temperature measured under an applied magnetic field 0.1T for  $\text{LaMn}_{1-x}\text{Co}_x\text{O}_3$ .

For our sample  $\text{LaMnO}_3$  annealed in the presence of oxygen, the room temperature structure is rhombohedral and indicates the percentage of  $\text{Mn}^{4+}$  is larger than 20%. Therefore, the magnetization values observed in the studied  $\text{LaMnO}_3$  sample can be related to a double exchange of  $\text{Mn}^{4+}$ - $\text{Mn}^{3+}$ . In addition, all the samples are definitely ferromagnetic. The  $M_S$  values for  $x \leq 0.50$  are larger than  $x > 0.50$ . It is known that the interactions of  $\text{Co}^{2+}$ - $\text{Co}^{3+}$  and  $\text{Co}^{3+}$ - $\text{Mn}^{3+}$  are of the anti-ferromagnetic type and  $\text{Co}^{2+}$ - $\text{Mn}^{3+}$  and  $\text{Mn}^{4+}$ - $\text{Mn}^{3+}$  are ferromagnetic [6]. In accordance with the structural results, the large magnetization values for  $x \leq 0.50$  suggests a substitution of  $\text{Co}^{2+}$  with  $\text{Mn}^{3+}$  reaching a maximum at  $x = 0.50$ , for which the charge equilibrium equation is  $\text{La}^3\text{Mn}^{4+}_{0.5}\text{Co}^{2+}_{0.5}\text{O}^{2-}_3$ . While for  $x > 0.50$ , the magnetization decreases by several orders of magnitude, meaning that the ferromagnetic interactions of  $\text{Co}^{2+}$ - $\text{Mn}^{4+}$  are weaker (the quantity of Mn cations decreases), being progressively replaced by the less effective  $\text{Co}^{2+}$ - $\text{Co}^{3+}$  and  $\text{Mn}^{4+}$ - $\text{Co}^{3+}$  interactions. Therefore, again the hypothesis presented from structural calculations is confirmed by the magnetic data. Catalytic performance (%) curves of  $\text{C}_2\text{H}_6$  combustion and CO oxidation reactions for  $\text{LaMn}_{1-x}\text{Co}_x\text{O}_3$  with  $x = 0.00, 0.25, 0.50, 0.75$  and  $1.00$  are shown in Figs. 7, 8. Also, catalytic performance tests of  $\text{LaMn}_{1-x}\text{Co}_x\text{O}_3$  catalysts at 10%, 50% and 90% of  $\text{C}_2\text{H}_6$  combustion and CO oxidation are summarized in Table 4. The changes in the catalytic properties of  $\text{A}(\text{B}, \text{B}')\text{O}_3$  perovskite in substitution of cation B with B' can be classified in two categories: geometric and electronic structure of the cation B'. The effect of Co substitution on the geometric factors is considered in the calculation of factor  $t$  that should be related to the structural changes summarized in Table 1. It is suggested that

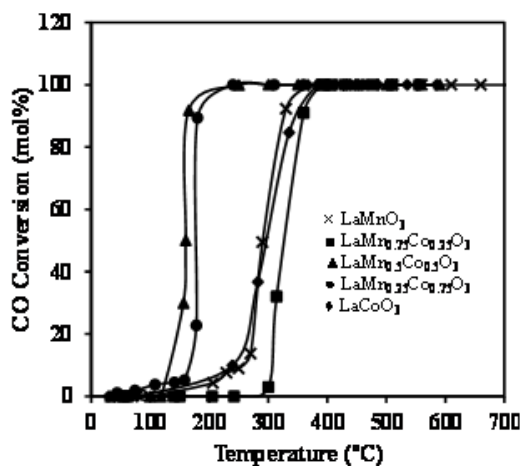


Fig. 7. Catalytic performance curves of  $\text{LaMn}_{1-x}\text{Co}_x\text{O}_3$  for CO oxidation.

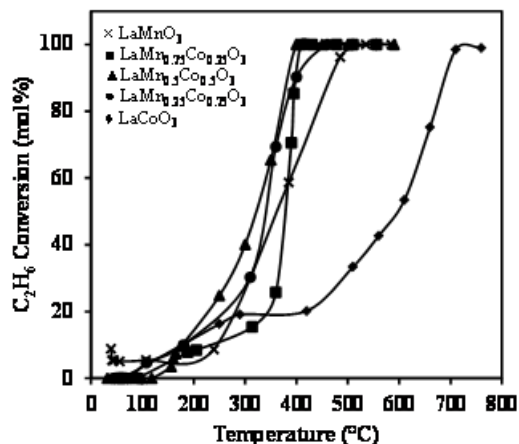


Fig. 8. Catalytic performance curves of  $\text{LaMn}_{1-x}\text{Co}_x\text{O}_3$  for the  $\text{C}_2\text{H}_6$  combustion.

### Catalytic Properties

the decrease in the tolerance factor will be lower than the  $B$ - $O$ - $B$  bond strength and promotes the formation of oxygen vacancies at the surface [7]. Therefore, it is expected that the samples  $x = 0.50, 0.75$  show a higher activity for  $\text{C}_2\text{H}_6$  combustion and CO oxidation reactions.

There is an inverse relationship between the crystallite size and the specific surface area of the samples. In addition, it is known that the higher activity should be related to the higher specific surface and lower crystallite sizes. Consequently, we can conclude that the higher activity of the samples  $x = 0.50, 0.75$  can be attributed to a lower crystallite size.

The band gap energies calculated for  $\text{LaMn}_{1-x}\text{Co}_x\text{O}_3$  compounds with  $x = 0.00, 0.25, 0.50, 0.75$ , and  $1.00$  are 1.58, 1.23, 0.98, 1.13, and 0.99, respectively. These values of the band gap energy show a semiconducting behavior of the samples. The low band gap energy of the compounds contributes to their high catalytic activities.

Also, the results of the catalytic characterization should be related to the electronic configuration which intervenes directly in the structural and magnetic changes formed. In  $\text{ABO}_3$  perovskites, a simple way of varying the oxidation state of the  $\text{B}^{3+}$  ion is by substitution of the  $\text{A}^{3+}$  ion by a different one with an oxidation state other than 3. For example, in  $(\text{La}, \text{M})\text{CoO}_3$  systems, the appearance of  $\text{Co}^{4+}$  ions by substitution with  $\text{M} = \text{Sr}$  decreases the rate, whereas the presence of  $\text{Co}^{2+}$  ions by introduction of  $\text{M} = \text{Ce}^{4+}$  enhances the rate of the oxidation reaction of CO and the hydrocarbons[5]. Therefore, the noticeable higher activity of  $x = 0.25, 0.50$  and  $0.75$  perovskites is attributed to the presence of  $\text{Co}^{2+}$ , as pointed out for hole doped  $(\text{La}, \text{M})\text{CoO}_3$  systems in reducing the atmosphere,

compared to pure cobaltite [5]. The larger  $\text{Co}^{2+}$  cation than  $\text{Co}^{3+}$  results in a shorter Co-O bond (see Fig. 3). Thus, lattice oxygens participate more easily in the redox process and therefore reduce the conversion temperature of  $\text{C}_2\text{H}_6$  combustion and CO oxidation. This behavior is explained considering that at high x values, the amount of unstable  $\text{Co}^{4+}$  ions and/or of oxygen vacancies increases, which favors the diffusion of lattice oxygen from the bulk to the surface, as charge compensators. As a consequence of the above discussions,  $\text{C}_2\text{H}_6$  combustion and CO oxidation take place at a lower temperature over the  $x = 0.50$  catalyst compared with the other samples.

Some reports have shown volcano-type dependence between the activity of  $\text{C}_2\text{H}_6$  combustion and CO oxidation and the electronic configuration of the transition metal ions B [5, 7]. According to crystal field theory, the octahedral environment of the  $\text{B}^{3+}$  ions splits into two lower and higher energy levels  $t_{2g}$  and  $e_g$ , respectively. The maximum activity in the volcano curves is attained for an occupation of the  $e_g$  levels of less than one electron whereas the  $t_{2g}$  levels remain half-filled or completely filled [5]. Also, the  $\text{Mn}^{4+}$  ion configuration in these manganites with the half filled  $t_{2g}$  orbitals and empty  $d_{z^2}$  orbitals shift the Fermi level towards the centre of the antibonding  $e_g$  orbitals at the surface, which promotes CO and  $\text{C}_2\text{H}_6$  chemisorptions at the surface leading to  $\text{C}_2\text{H}_6$  combustion and CO oxidation [7, 8]. Finally, we may conclude from the structural, magnetic, and catalytic variations of the sample at  $x = 0.50$  that the spin states of the  $\text{Co}^{2+}$  and  $\text{Mn}^{4+}$  ions may be in low spin  $t_{2g}^6 e_g^1$  and  $t_{2g}^3$ , respectively.

## CONCLUSIONS

The structural characterization of  $\text{LaMn}_{1-x}\text{Co}_x\text{O}_3$  ( $x = 0.00, 0.25, 0.50, 0.75, 1.00$ ) by X-ray powder diffraction and FTIR measurements is evidence for a monoclinic structure (P21/n space group) with  $x = 0.50$  and a rhombohedral structure (R-3c space group) for other samples without the presence of impurity phases. The unit cell volume obtained from the Rietveld method shows increasing and decreasing tendencies for the values  $x \leq 0.5$  and  $x > 0.5$ , respectively. The structural and magnetic results suggest  $\text{Co}^{2+}$  and  $\text{Co}^{3+}$  substitution with Mn ions for  $x \leq 0.50$  and  $x > 0.50$ , respectively. The results also show that the sample for  $x = 0.50$  has a lower symmetry, smaller crystallite size (bigger surface area) and a higher content of  $\text{Co}^{2+}$  than the other samples which make it the best catalyst for  $\text{C}_2\text{H}_6$  combustion and CO oxidation.

**Acknowledgment:** The authors wish to thank Frances Hellman, from the University of California-Berkeley for her help with the magnetic measurements.

## REFERENCES

1. P. Ciambelli, S. Cimino, S. De Rossi, L. Lisi, G. Minelli, P. Porta, G. Russo, *Appl. Catal. B.*, **29**, 239 (2001).
2. H. Tanaka, M. Misono, *Solid. State. Mater. Sci.*, **5**, 381 (2001).
3. C. Zener, *J. Phys. Rev.*, **81**, 440 (1951).
4. J. B. Goodenough, *J. Phys. Rev.*, **100**, 564 (1955).
5. M. A. Peña, J. L. G. Fierro, *Chem. Rev.*, **101**, 1981 (2001),
6. G. Pecchi, C. Campos, O. Peña, L. E. Cadus, *J. Mol. Catal. A: Chem.*, **282**, 158 (2008).
7. R.G. Shetkar, A.V. Salker, Electrical, *J. Mater. Sci. Technol.*, **26**, 1098 (2010).
8. E. Frozandeh-Mehr, A. Malekzadeh, M. Ghiasi, A. Gholizadeh, Y. Mortazavi, A. Khodadadi, *Catal. Commun.*, **28**, 32 (2012).
9. M. Khazaei, A. Malekzadeh, F. Amini, Y. Mortazavi, A. Khodadadi, *Cryst. Res. Technol.*, **45**, 1064 (2010).
10. A. Gholizadeh, *J. Adv. Mater. Process.*, **3**, 71 (2015).
11. A. Gholizadeh, N. Tajabor, *Mater. Sci. Semicond. Process.*, **13**, 162 (2010).
12. R. Groessinger, *Phys. Stat. Sol. (a)*, **66**, 665 (1981).
13. G. Pecchi, C. Campos, O. Peña, *Mater. Res. Bull.*, **44**, 846 (2009).
14. G.V. Bazuev, A.V. Korolyov, M.A. Melkozyorova, T.I. Chupakhina, *J. Magn. Magn. Mater.*, **322**, 494 (2010).
15. P. A. Joy, Y. B. Kholam, S. K. Date, *Phys. Rev. B*, **62**, 8608 (2000).
16. Y.D. Zhao, J. Park, R. J. Jung, H. J. Noh, S. J. Oh, *J. Magn. Magn. Mater.*, **280**, 404 (2004).

## СТРУКТУРНИ, МАГНИТНИ И КАТАЛИТИЧНИ СВОЙСТВА НА КОБАЛТ-ЗАМЕСТЕНИ МАНГАНТИНИ ПЕРОВСКИТИ

А. Голизаде<sup>1</sup>, А. Малекзаде<sup>2</sup>, М. Гиаси<sup>2</sup>

<sup>1</sup>Училище по физика, Университет Дамган, Дамган, И.Р. Иран

<sup>2</sup> Училище по химия, Университет Дамган, Дамган, И.Р. Иран

Постъпила на 4 август, 2015 г.; коригирана на 22 октомври, 2015 г.

(Резюме)

В тази работа са изследвани структурните, магнитните и каталитичните свойства на  $\text{LaMn}_{1-x}\text{Co}_x\text{O}_3$  ( $x = 0.00, 0.25, 0.50, 0.75, 1.00$ ). Структурното охарактеризиране на образците чрез прахова рентгено-структурна дифракция и с помощта на пакет от програми X<sup>Pert</sup> и Fullprof доказва моноклинна структура (P21/n пространствена група) с  $x = 0.5$  и ромбоедрична структура (R-3c пространствена група) за други проби. Тези резултати се потвърждават с FTIR-измервания. Магнитните характеристики на пробите са определени с измервания при различни температури и полета. Структурните и магнитните резултати показват, че феромагнитните взаимодействия  $\text{Co}^{2+}\text{-Mn}^{4+}$  при  $x \leq 0.5$  прогресивно се заменят с по-малко ефективните взаимодействия  $\text{Co}^{2+}\text{-Co}^{3+}$  и  $\text{Mn}^{4+}\text{-Co}^{3+}$  за  $x > 0.5$ . Каталитичната активност на  $\text{LaMn}_{1-x}\text{Co}_x\text{O}_3$  са оценени за реакциите на изгаряне на  $\text{C}_2\text{H}_6$  и окислението на CO. При сходни условия резултатите от катализата показват, че nano-перовскитът  $\text{LaMn}_{0.5}\text{Co}_{0.5}\text{O}_3$  е най-добрия катализатор за тези две реакции.

## Performance study of compartment-wise behaviour of modified anaerobic hybrid baffled (MAHB) reactor

S. R. Hassan<sup>1</sup>, N. Q. Zaman<sup>2,3</sup>, I. Dahlan<sup>3,4\*</sup>

<sup>1</sup>Faculty of Agro Based Industry, Universiti Malaysia Kelantan, Campus Jeli, 17600, Jeli, Kelantan, Malaysia

<sup>2</sup>School of Civil Engineering, Universiti Sains Malaysia, Engineering Campus, 14300 Nibong Tebal, Pulau Pinang, Malaysia.

<sup>3</sup>Solid Waste Management Cluster, Science and Engineering Research Centre, Universiti Sains Malaysia, Engineering Campus, Seri Ampangan, 14300 Nibong Tebal, Pulau Pinang, Malaysia

<sup>4</sup>School of Chemical Engineering, Universiti Sains Malaysia, Engineering Campus, 14300 Nibong Tebal, Pulau Pinang, Malaysia.

Received November 25, 2014, Revised November 2, 2015

A modified anaerobic hybrid baffled (MAHB) reactor was used to study its suitability for treatment of recycled paper mill effluent (RPME) and to establish the relationship between operational parameters and reactor design. The present study highlights the configuration of MAHB reactor, its start up, the effect of hydraulic retention time (HRT) on treatment efficiency and performance evaluation of MAHB reactor while treating RPME wastewater. The start-up process was carried out at HRT of 4 days. The MAHB reactor was run with constant feeding COD of 3000 mg L<sup>-1</sup> and HRT of 1, 3, 5 and 7 days. A start-up of 28 days was required for the MAHB reactor. Reactor performance evaluation of the compartment-wise profiles was carried out at different HRTs. Low pH of 6 – 6.2 and high volatile fatty acid concentration of 90 – 168 mg L<sup>-1</sup> were recorded in the first compartment for each HRT due to acidogenesis and acetogenesis processes. System pH and alkalinity showed an increment profile while VFA concentration decreased as it moves from compartment 1 to 5. Biogas volume was high ( 6.56 L at higher HRT) with a decreasing pattern of methane content from 96 – 35 % from compartment 1 to 5. Contrarily, at low HRT of 1 day, although the biogas volume was lower, the methane content showed an increment of 42 – 64 %. The results indicate that MAHB reactor was successfully operated in treating RPME wastewater.

**Keywords:** modified anaerobic hybrid baffled (MAHB) reactor, anaerobic digestion process, recycled paper mill effluent (RPME).

### INTRODUCTION

The application of anaerobic technology in treating industrial wastewaters highly depends on the performance of the reactor used. Thompson *et al.* [1] reported that about 80% COD removal efficiency was constantly achieved using anaerobic treatment, while Arshad and Hashim [2] obtained 58 % methane content with total organic carbon (TOC) and lignin removal efficiencies of 56 % and 51 %, respectively, at an OLR of 4.5 g TOC L<sup>-1</sup>per day and HRT of 18 h in treating the paper mill effluent. Another approach of treating paper mill effluent is by integrating two or more methods to take advantages of both processes. Shaw *et al.* [3] showed that a combination of aerobic reactor followed by anaerobic reactor is able to remove 66% of toxicity. From the survey, anaerobic baffled reactor (ABR) was one of the favorable systems in treating industrial waste. Although ABR were extensively used to treat different types of industrial waste, literature survey

shows that there is lack of data on the anaerobic treatment of recycled paper mill effluent (RPME) wastewater by a novel modified anaerobic hybrid baffled (MAHB) reactor.

This novel MAHB reactor consists of five compartments which are a combination of regular suspended growth and fixed biofilm systems. The most significant advantage of this design is the ability to nearly perfectly realize the staged multi-phase anaerobic theory, allowing different bacterial groups to develop under more favorable conditions, low costs and without the associated control problems. The MAHB bioreactor combines suspended growth and attached growth processes in a single reactor to take advantage of both biomass types [1][4].

With a less expensive, simple configuration and a background of successful performance and having been judged to perform well for industrial wastewater of conventional ABR, this hybrid novel MAHB reactor was assumed to give better performance in terms of COD removal and methane production. Keeping this as an observation, the present study was carried out to investigate the

\* To whom all correspondence should be sent:

E-mail: chirvan@usm.my

performance of the MAHB reactor treating RPME at different HRT in relationship of the compartmentalization behavior. The present study was also aimed to integrate various aspects like (a) performance of the reactor and compartment-wise variation of various parameters and (b) stable operation for a quite extended period in terms of COD removal efficiency, biogas production and performance of each different compartment of the MAHB reactor.

## METHODS

### Reactor configuration

A laboratory-scale modified anaerobic hybrid baffled (MAHB) reactor was fabricated using polypropylene. It consisted of 5 chambers (CH1–CH5) of equal size and volume, connected in series as shown in Fig 1.

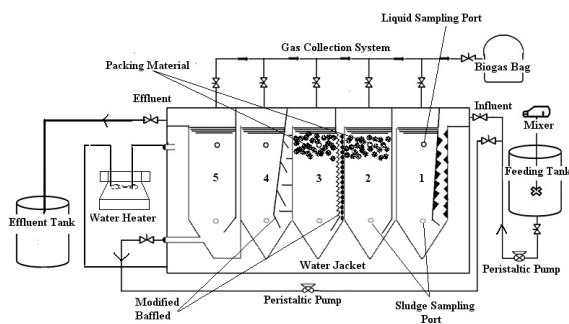


**Fig. 1.** Schematic diagram of 58 L capacity bench-scale continuous feed MAHB reactor.

The whole unit is square in shape with length to width ratio ( $l/w$ ) of 3.61 and  $l \times b \times h$  dimensions of 795 mm  $\times$  220 mm  $\times$  300 mm. To collect the biogas produced, five separate gas manifolds were provided and the biogas was finally led to the gas collection cum measurement assembly. The individual chamber was divided by a hanging baffle into five compartments, i.e., downcomer and upcomer. The volume of the downcomer was half that of the upcomer and the bottom portion of the baffle separating the two compartments was inclined at 45° and was stretched up to the center of the upcomer. The total volume of the modified anaerobic hybrid baffled (MAHB) reactor was 65 L with a net working volume of 58 L. The volume of the individual set of 5 compartments (CH1–CH5) was 11.6 L. The net volumes of the downcomer and the upcomer were 3.86 L and 7.74 L, respectively.

### Feed wastewater flow pattern

The wastewater was collected from Muda Paper Mill Bhd, Bandar Tasek Mutiara, Penang, Malaysia and refrigerated at 4°C. Prior to analysis, the

samples were warmed to room temperature ( $25 \pm 2^\circ\text{C}$ ). The collected samples were analysed for the required parameters such as pH, total dissolved solids (TDS), volatile suspended solids (VSS), total suspended solids (TSS), total solids (TS), alkalinity, ammonia, biological oxygen demand (BOD) and dissolved oxygen (DO) according to the Standard Methods of Analysis of Water and Wastewater [5] and were intermittently mixed to feed the reactor with a consistent quality.

**Table 1.** Physicochemical characteristics of recycled paper mill effluent.

Parameter	Concentration
pH	6.36
Alkalinity ( $\text{mg L}^{-1}$ as $\text{CaCO}_3$ )	94
TSS ( $\text{mg L}^{-1}$ )	645
VSS ( $\text{mg L}^{-1}$ )	850
TDS ( $\text{mg L}^{-1}$ )	3345
TS ( $\text{mg L}^{-1}$ )	5320
BOD <sub>5</sub> ( $\text{mg L}^{-1}$ )	669
COD ( $\text{mg L}^{-1}$ )	4328
VFA ( $\text{mg L}^{-1}$ )	501
Ammonia ( $\text{mg L}^{-1}$ )	0.4
DO ( $\text{mg L}^{-1}$ )	1.5

The wastewater was fed to the reactor with the help of a variable speed peristaltic pump. The MAHB reactor was operated at various hydraulic retention times (HRTs) by varying the flowrate of influent wastewater ( $Q_{inf}$ ), thereby varying the organic loading rate (OLR). The average composition of RPME wastewater is shown in Table 1. The wastewater flows from the downcomer to the upcomer, within an individual chamber through the sludge bed formed at the bottom of the individual chambers. After receiving treatment in the particular chamber, wastewater enters the next chamber from the top. Due to the specific design and positioning of the baffle, the wastewater is evenly distributed in the upcomer and the vertical upflow velocity ( $V_{up}$ ) could be significantly reduced. The treated effluent was collected from the outlet of CH5. The reactor was kept in a temperature controlled chamber maintained at 35°C.

### Sampling and Analysis

MAHB reactor was monitored every two days for COD, pH and biogas produced while volatile fatty acids (VFA) and alkalinity were measured weekly. Samples were taken for analysis from all five compartments of MAHB at HRT of 1, 3, 5 and 7 days as the system achieved its steady state. Biogas composition was determined using Shimadzu gas chromatograph with a flame ionization detector (GC-FID) with a propack N column. Carrier gas was helium set at a flow rate of 50 mL min<sup>-1</sup>, column temperature of 28°C, detector temperature of 38°C and injector temperature of 128°C. VFAs were measured using esterification methods. Triplicate samples were collected for each parameter reading to increase the precision of the results, and only the average value was reported throughout this study. Conventional parameters such as pH and alkalinity were measured according to the Standard Methods [5] while COD was measured using the spectrophotometer DR-2800 according to the reactor digestion method [6].

## RESULTS AND DISCUSSION

### Start-up of MAHB reactor

In this study, the MAHB reactor was filled with seed sludge taken from Malpom and allowed to rest for 12 days. Then, after 15 days, feeding of the RPME wastewater was resumed at a flow rate of 14.5 L per day at HRT of 4 days with a very low organic loading rate (OLR) of 0.1963 g COD L<sup>-1</sup> per day. The resumed wastewater feeding helped the development of the sludge bed at the bottom of the individual compartments of the MAHB reactor. The acclimatization curve for determination of the start-up period is shown in Fig. 2.

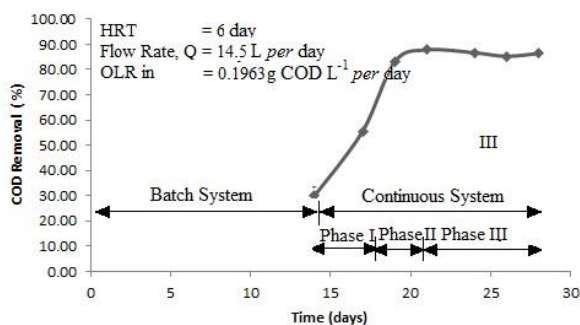


Fig. 2. Acclimatization curve for determination of the start-up period of MAHB reactor

S-shaped acclimatization curve with three distinct phases was demonstrated during the acclimatization period. During phase I of the acclimatization period of 16 days (from day 12 until day 17), the observed SS and COD removal

may be attributed to the interception of organics in the sludge bed. During the second phase of 5 days (17th – 21st day), a significant gain of up to 90% was observed in COD removal. The curve indicated that the COD reduction efficiency was related to the period of acclimatization. The steady state of increase in efficiency signified the adequate quantum of biosludge accumulation in the reactor [7]. The third phase of acclimatization lasted for 8 days (from day 21 until day 28). Last four consecutive observations revealed consistent COD removal efficiency of 85% and specific biogas yield of 0.25 L CH<sub>4</sub> per day. At this stage, the MAHB reactor was counted as matured or acclimatized. Therefore, the start-up period for the MAHB reactor was adjudicated to be 28 days. From previous studies, Lettinga *et al.* [8] took about 84 days for the start-up, whereas Kalogo *et al.* [9] required a period of 140 days of self-inoculated UASB. The anaerobic contact filter was started-up by feeding cow dung slurry and sewage sludge by Vijayaraghavan and Ramanujan [10] who needed 160 days to complete the start-up operation. The analysis of the requirements of start-up periods showed that the time consumed by the MAHB reactor was favorably comparable.

### Performance evaluation of MAHB reactor

#### Compartment-wise profile during HRT variation

Performance of MAHB reactor was subjected to four changes in HRT by increasing the feed flow rate. Figure 3 illustrates the COD removal efficiency and VFA concentration at different compartments of MAHB reactor. From the obtained results, it is seen that at each different HRT of 1, 3, 5 and 7 days, the COD removal efficiency shows an increasing pattern from compartment 1 to 5. COD removal efficiency was low at HRT of 1 day with an average of 50 – 92% from compartment 1 to 5.

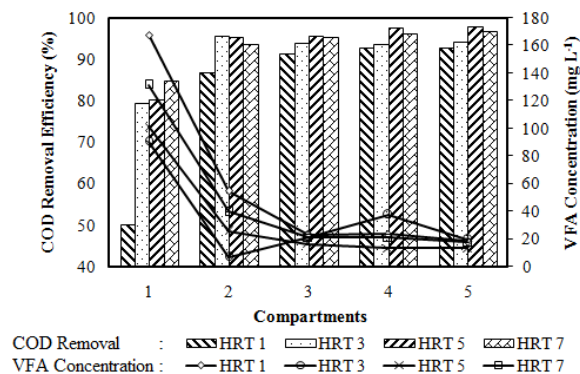


Fig. 3. COD removal and VFA concentration variation of each compartment of the MAHB reactor. Compartments are numbered in the sequence of flow pattern from compartment 1 to 5 at steady state.

From the obtained results it follows that at each different HRT of 1, 3, 5 and 7 days, the COD removal efficiency shows an increasing pattern from compartment 1 to 5. COD removal efficiency was low at HRT of 1 day with an average of 50 – 92% from compartment 1 to 5.

As the HRT was increased, the COD removal efficiency started to increase to a range of 79 – 94 %, 80 – 97 % and 84 – 96 % for HRT of 3, 5 and 7 days, respectively. This result shows that the retention times play an important role for the microbes inside to digest the substrate. Similar patterns were recorded by Krishna *et al.*[11], which indicates that COD removal efficiency of each compartment increased in the sequence of flow pattern from compartment 1 to 5. It is essential to note that as the HRT increased, the compartment-wise COD removal efficiency increased. In compartment 1, as the HRT increased, significant increase of COD removal efficiency was recorded. This shows that most of the organic matter was removed in the first compartment [12] while treating low-strength RPME wastewater using MAHB reactor.

In addition, VFA concentration tends to decrease with high HRT. The maximum VFA concentration achieved was 167 mg L<sup>-1</sup> in compartment 1 at HRT 1. As the wastewater moves from compartment 1 to 5, the concentrations of VFA decreased for all HRTs. This is a result of the conversion of VFA into final products such as hydrogen, carbon dioxide and acetate for methane production.

The VFA profile demonstrated that the main biochemical activities occurring in the first few compartments are hydrolysis and acidogenesis [13, 14]. For the last few compartments, methanogenesis appeared to be dominant. These observations implied that the MAHB reactor promoted a systematic selection in the different compartments in such a manner as to bring out phase separation. Wang *et al.* [15] also reported that the total VFA concentration decreased along the reactor from compartment 2 while treating high-strength wastewater using conventional ABR.

#### System pH and alkalinity for different compartments

The pH and alkalinity profiles for the MAHB reactor at different HRTs are shown in Figure 4. Slightly lower pH was noted in compartment 1 for each different HRT in a range of 6.1 to 6.3. As the wastewater moves towards the later compartments, a gradual increase in pH was achieved. The pH was found close to 7 (6.3 – 6.55) at the rear end of the

MAHB reactor. Similar patterns were also recorded by Dama *et al.* [16] who reported that earlier compartments had a lower pH as acidogenesis and acetogenesis take place in those compartments. It was also observed that during every shift to the next HRT, the pH in the first two chambers dropped rapidly, while other chambers (CH3–CH5) were found to be less affected.

This indicated that accumulation of fatty acids was restricted up to CH3 only, unaffacting the methanogenesis occurring in the rest of the chambers.

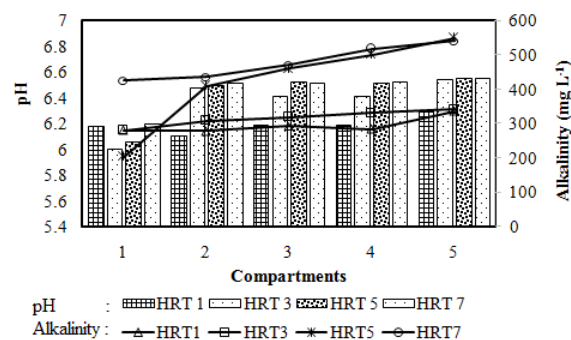


**Fig. 4.** pH and alkalinity variation of each compartment of MAHB reactor. Compartments are numbered in the sequence of flow pattern from compartment 1 to 5 at steady state.

This was due to the fact that hydrolysis, acidogenesis and acetogenesis occur in the initial chambers. Furthermore, degradation of VFA results in the increment of pH from compartment 1 to compartment 5 [17]. The distinct pH profile shows an indication of the degree of different phases created within the system. Similar alkalinity profiles were noted in the compartment-wise arrangement of the MAHB reactor.

#### Gas Production and Composition

Figure 5 illustrates the biogas volume and the methane content for each compartment at different HRTs. Overall, the biogas volume for HRT 3 was higher (range of 3 to 6.6 L per day) than for HRT 1 (range of 1.3 to 3.2 L per day) due to the longer hydraulic retention times which give enough time for the anaerobic process to take place in each compartment. For HRT 1 day, the total biogas volume increased from 2.2 to 3.2 L per day from compartment 1 to 3 but then decreased to 1.8 L per day in compartment 5 and *vice versa* for HRT 3. For longer HRTs, the travelling time to move up and down the compartment of the reactor is longer, which contributes to a larger biogas volume. However, most of the nutrients were already converted to methane in the first three

compartments. This explains the decrement of biogas volume at the last two compartments.

The methane content of the total biogas produced was determined every two days until it reached steady state. The order of the compartments from 1 to 5 shows that the methane content of the total biogas increased in sequence under HRT of 1 day (OLR = 3 g CODL<sup>-1</sup>per day) but decreased for HRT of 3 days (OLR = 1 g CODL<sup>-1</sup>per day). These results were in accordance with the conclusion of former studies by Uyanik [18] who indicated that acidogenic reactions were dominant in the earlier compartments of the MAHB reactor. However, at HRT of 3 days (with high OLR), the accumulation of VFA resulted in reduction of methane percentage through the rear of the reactor. The methane content, which can be a valuable indicator of the performance of the MAHB reactor shows a stepped up value from 42% to 64% as the HRT decreases under the average OLR of 3 g CODL<sup>-1</sup>per day. These results are in agreement with previous research by Liu *et al.* [19].

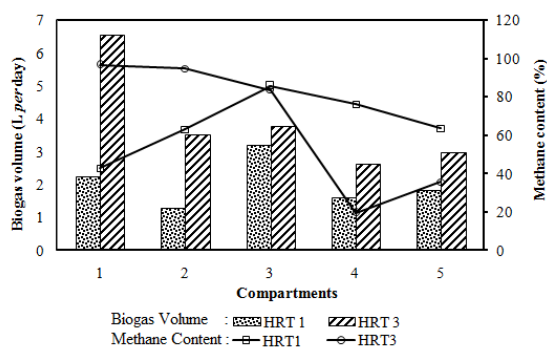


**Fig. 5.** Gas production variation of each compartment of the MAHB reactor at HRT of 1 day and 3 days.

Obviously, high methane content suggests high activity of methanogenic bacteria. The methanogenic bacteria can be divided into two main groups due to differences in substrate utilization - hydrogenotrophic and acetotrophic methanogens [20]. Hydrogenotrophic methanogens only use CO<sub>2</sub> and H<sub>2</sub> as their substrate. The partial pressure of hydrogen acts as a main indicator to describe disturbances and stability in AD. For that reason, hydrotrophic methanogens activity is crucial for the efficiency and stability of AD in processing of simple soluble types of substrates (i.e. ethanol, propionate, dextrose and acetate) and numerous types of wastewater. For acetotrophic methanogens, such as *Methanosarcinales* genus, they use simple compounds such as acetate as their substrate. More than 70% of biomethane are produced by acetate degradation. Methanogenic

bacteria that bind hydrogen are found to belong to *Methanobacteriaceae* family [21].

For cellulose (lignin) saccharification, the microbes that facilitate the process might consist of hydrolyzing and acid producing microorganisms. The primary route is the initial cleavage of ether-linked subunits followed by subsequent degradation of substituted aromatic rings where the derivatives of vanillic acid, cinnamic acid and syringic acid are the important constituents of lignin. For this AD process, fermenting bacteria (i.e., methanogenic bacteria) and acetogenic bacteria are responsible for breaking this ether-linked and aromatic ring bond [22].

## CONCLUSIONS

The present study revealed that HRT significantly influences the compartment-wise profile of MAHB reactor in terms of COD removal, VFA concentration, pH and alkalinity, methane content and biogas volume in treating RPME wastewater. The pH profile shows an increment within a range of 6.3 to 6.6 as the RPME wastewater moves towards the end of the MAHB reactor. Maximum alkalinity obtained was between 335 and 548 mg L<sup>-1</sup> in compartment 5 for each different HRT. The maximum methane content was 96.8 % with total biogas volume of 6.56 L per day at HRT of 3 days (OLR of 1 g CODL<sup>-1</sup>per day) in the MAHB reactor. High COD removal of 98.0% was achieved at HRT 5 of 0.6 g CODL<sup>-1</sup>per day. Therefore, the optimum HRT for anaerobic treatment of RPME in MAHB reactor was 5 days. Moreover, high COD removal and methane content was achieved in the MAHB reactor.

**Acknowledgement:** The authors acknowledge the financial support from the Universiti Sains Malaysia (RU-I A/C.1001/PJKIMIA/814148) and MyBrain15 Scholarship (KPM(B) 870204115782).

## REFERENCE

1. G.Thompson, J. Swain, M. Kay, C.F. Forster, *Bioresource Technology*, **77**, 275 (2001).
2. A. Arshad, N.H. Hashim. *International Journal of Environmental Research*, **6**, 1735 (2012).
3. C.B. Shaw, C.M. Carliell, A.D. Wheatley, *Water Research*, **36**, 1993 (2002).
4. S. R. Hassan, H. M. Zwain, I. Dahlan, *Journal Advance Science Research*, **4**, 07 (2013).
5. L.S. Clescerl, A.E. Greenberg, A.D. Eaton, eds. Standard methods for the examination of water and wastewater, American Public Health Association, American Water Works Association, Water Environment Federation, Washington, 1998.

6. S.R. Hassan, H. M.Zwain, N. Q. Zaman, I. Dahlan, *Environmental Technology*, **35**, 3(2013).
7. M. Hutnan, M. Drtil, L. Mrafkova, J. Derco, J. Buday, *Bioprocess Engineering*, **21**, 439 (1999).
8. G. Lettinga, J. Field, J. van Lier, G. Zeeman, L.W. HuishoffPol, *Water Science and Technology*, **35**, 5 (1997).
9. Y. Kalogo, J.H. MBouche, W. Verstraete, *Journal of Environmental Engineering*, **127**, 179 (2001).
10. K. Vijayaraghavan, T.K. Ramanujam, *Bioprocess Engineering*, **20**, 499 (1999).
11. G.V.T.G. Krishna, P. Kumar, P. Kumar, *Journal of Environmental Management*, **90**, 166 (2009).
12. C. Polprasert, P. Kemmadamrong, F.T. Tran, *Environmental Technology*, **13**, 857 (1992).
13. J.C. Akunna, M. Clark, *Bioresource Technology*, **74**, p? (2000).
14. M.I. Baloch, J.C. Akunna, *Journal of Environmental Technology*, **129**, 1015 (2003).
15. J. Wang, Y. Huang, X. Zhao, *Bioresource Technology*, **93**, 205 (2004).
16. P. Dama, J. Bell, K.M. Faxon, C.J. Brouckaert, T. Huany, C.A. Buckley, *Water Science Technology*, **26**, 263 (2002).
17. M.I. Baloch, J.C. Akunna, P.J. Collier, *Bioresource Technology*, **98**, 1849 (2007).
18. S.Uyanik, P.J. Sallis, G.K. Anderson, *Water Research*, **36**, 933 (2002).
19. X. Liu, N. Ren, Y. Yuan, *Bioresource Technology*, **100**, 104 (2009).
20. B. Demirel, P. Scherer, *Reviews in Environmental Science and Bio/Technology*, **7**, 173 (2008).
21. D.R. Boone, D.P. Chynoweth, R.A. Mah, P.H. Smith, A.C. Wilkie, *Biomass and Bioenergy*, **5**, 191 (1993).
22. J.J. Ko, Y. Shimizu, K. Ikeda, S.K. Kim, C.H. Park, S. Matsui, *Bioresource Technology*, **100**, 1622 (2009).

## ИЗСЛЕДВАНЕ НА СЕКЦИОННОТО ПОВЕДЕНИЕ НА МОДИФИЦИРАН АНАЕРОБЕН ХИБРИДЕН РЕАКТОР С ПРЕГРАДИ (МАНВ)

С.Р. Хасан<sup>1</sup>, Н.К. Заман<sup>1</sup>, И. Дахлан<sup>2\*</sup>

<sup>1</sup>Училище за строително инженерство, Саинс-университет в Малайзия, 14300 Нибонг Тебал, Пулау Пинанг, Малайзия

<sup>2</sup>Училище по химично инженерство, Саинс-университет в Малайзия 14300 Нибонг Тебал, Пулау Пинанг, Малайзия

Постъпила на 25 ноември, 2014 г.; коригирана на 2 ноември, 2015 г.

(Резюме)

Използван е модифициран анаеробен хибриден реактор с прегради (МАНВ) за изучаването на приложимостта му за третиране на отпадъчни води от рециклирането на хартия (RPME) и установяването на връзката между работните параметри и оформлението на реактора. Определени са конфигурацията на реактора, пускането му в действие и ефекта на времепребиваването (HRT) върху ефективността на пречистване и работата на реактора. Пусковият процес се зивършва прю времепребиваване от 4 дни. МАНВ-реакторът работи с постоянно захранване с ХПК от 3000 mg L<sup>-1</sup> и времепребиваване HRT от 1, 3, 5 и 7 дни. Пусковият период е 28 дни. Работата на реактора се оценява по секционните профили за различни HRT. В първото отделение се наблюдават рН от 6 – 6.2 и високи концентрации на летливи мастни киселини от 90 до 168 mg L<sup>-1</sup> при всяко времепребиваване заради ацидогенезата и ацетогенезата. рН и алкалността на системата показва нарастване на профила по дължината на реактора, докато концентрациите на мастните киселини намалява от отделение 1 до отделение 5. Обемът на биогаза е голям ( 6.56 L при високи HRT) с намаляване на съдържанието на метан от 96 до 35 % от отделение 1 до 5. Обратно, при малки HRT (1 ден), въпреки че бемът на биогаз е малък, съдържанието на метан нараства от 42 до 64 %. Резултатите показват, че МАНВ-реакторът работи успешно за пречистването на отпадъчни води от рециклирането на хартия.

## Sorption capacity of oil sorbent for the removal of thin films of oil

D.A. Baiseitov, M.I. Tulepov, L.R. Sassykova\*, Sh.E. Gabdrashova, G.A. Essen, K.K. Kudaibergenov, Z.A. Mansurov

*Al-Farabi National University, Almaty, Kazakhstan*

Received May 4, 2015, Accepted July 27, 2015

The dependence of the sorption capacity of the sorbents on the amount of sorbent, sorption time, thickness of the oil film, as well as the number of cycles of use of the sorbent was investigated. The performed studies in this work demonstrated the potential use of the synthesized sorbents as adsorbents for the removal of thin oil films.

**Keywords:** oil sorbent, sorption capacity, thin oil film.

### INTRODUCTION

At present, the pollution of surface water bodies by petroleum hydrocarbons occurs not only under accident oil spills, but also during routine maintenance. The process of operative removal of oil pollution from the water surface is topical considering the increasing technogenic impact on the ecosystem. It is therefore particularly important to solve this problem. There is search of materials suitable for collecting oil from surface water and sewage industrial water.

Cleaning of the surface of water bodies from contamination involves the removal of the oil film by mechanical and (or) physical and chemical methods. Most promising and environmentally expedient is the method of removing oil film with the help of oil sorbents [1]. The materials used for the collection of oil and petroleum products from water, are commonly called oil sorbents, as well as collectors of oil and oil absorbers. One of the main problems when cleaning the surface of water bodies from pollution is the removal of a thin oil film having the ability to spread in the shortest terms over vast distances, violating the oxygen exchange [2-3].

For the production of oil sorbents various raw materials are applied [4]. By the mechanism of oil removal are distinguished the sorbents, for which physical surface adsorption dominates. Here, the collection of oil occurs due to adhesion to the surface of the sorbent particles. In this case, the amount of oil absorbed is determined by the specific surface area of the material and its properties (hydrophobic and oleophilic). Literature data show that such a mechanism for collecting of oil and petroleum products is realized for oleophilic

powders and granular materials with closed porous structure and materials in which the pores by size are not available for the molecules of the removable substances [5].

### EXPERIMENTAL

All experiments were carried out by the methods described in [6-8]. A Petri dish was filled with water and weighed, and then an oil slick was applied to the water surface so that it didn't touch the walls of the cup, followed by the cup reweighed. Then, on the oil slick a sample of sorbent was applied to complete absorption of the oil spill and the cup was reweighed. Gain of oil weight to the weight of the sorbent gave the value of the absorption capacity of the sorbent in water.

Weight of dry cup was 134.15 g and with water - 178.93 g. The weight of the oil slick was 0.4 g and the weight of the cup became 179.33 g. After the total absorption of the oil slick by a modified carbon sorbent with weight of 0.04 grams, the weight of the cup amounted to 179.37 g, and the sorption capacity was 10.0 g/g.

The weight of the cup with water was 173.44 g and 173.90 - with the oil spill, after applying the carbon sorbent of vegetable origin of weight 0.22 g, the oil spill was absorbed by the sorbent. The sorption capacity of the sorbent was 5, i.e. 1 g of sorbent could adsorb 5 g of oil.

After repeating the experiment with stirring of oil and sorbent, the total absorption of the oil slick was achieved with 0.05 g of modified carbon sorbent, i.e. the adsorbent capacity increased to 10.9 g/g.

For creation of an oil film into a Petri dish, about 40 ml of water with a salt concentration of 17-20 g/l (seawater) was poured and a few drops of oil were added. When the oil slick was formed, its diameter and thickness were determined.

\* To whom all correspondence should be sent:  
E-mail: larissa.rav@mail.ru

## RESULTS AND DISCUSSION

In the laboratory tests the medium viscous oil of Karazhanbas was used (Figure 1).

The dependence of the sorption capacity of the obtained carbonized sorbents based on rice husk (CRH) on the amount of sorbent, the sorption time, the thickness of the oil film, as well as the number of cycles of use of the sorbent was studied.

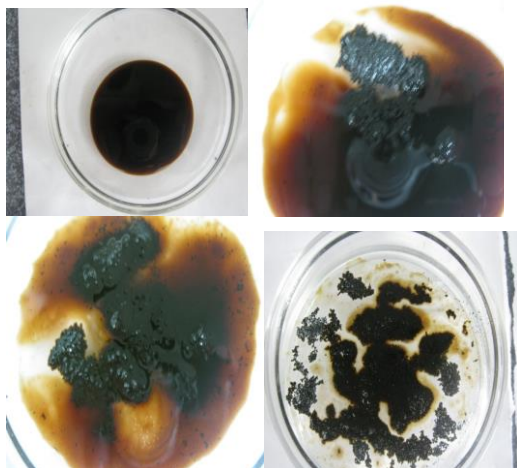


**Fig. 1.** Sorption of oil of Karazhanbas.

Figure 2 shows the sorption capacity of the sorbents on the sorption time. As can be seen from the presented data, the maximum sorption of oil is in the first minutes (~ 3-4 minutes), after which the sorbent based on foam rubber and sunflower husk carbonizate (FRCSH- 300) is able to retain the sorbed oil for two days, whereas the sorbents on the basis of polystyrene foam and carbonizate of rice husk PFCRH-400 and modified foam rubber (MFR-300) after active sorption gradually began to release it after 4 hours.

Such behavior of the sorbents may be due to the lower level of hydrophobicity and oleophilicity of the sorbents based on PFCRH-400 and MFR-300, and the different structure of the sorbents.

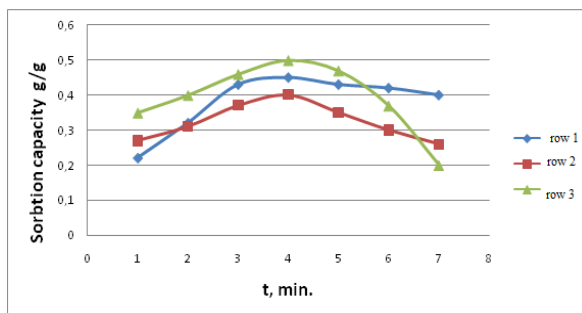


**Fig. 2.** Dependence of the sorptive capacity of the sorbents on the sorption time: 1 - Foam rubber + carbonizate of sunflower husk (FRCSH- 300) 2 - Foam polystyrene + carbonizate of rice husk (PFCRH-400) 3 - Modified foam rubber (MFR -300)

The sorption capacity of vegetable materials without polymers was studied as well. With the increase in mass of the sorbent amount, the sorbed by it oil gradually increased. After reaching the optimal sorption time (4 hours), the speed of active sorption markedly decreased, which may be explained, apparently, on the one hand by the oil saturation of the sorbents, and on the other hand, by the process of desorption (in the case of CRH-400 and -300).

The dependence of the sorption capacity of the sorbents on the thickness of the oil film was also studied (Fig.3).

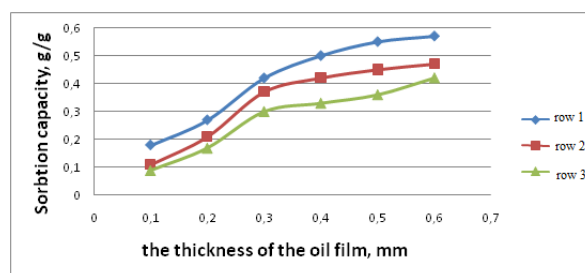


**Fig. 3.** - Dependence of the sorption capacity of the sorbent on the thickness of the oil film: row 1 - Foam rubber + carbonizate of sunflower husk (FRCRH- 300); row 2- Foam polystyrene + carbonizate of rice husk (PFCRH -400); row-3 modified foam rubber (MFR-300)

It is known that the maximum absorption capacity of the sorbent is exhibited with an excess amount of absorbed oil [9,10]. As seen in Fig.3, the increase in the thickness of oil film increases the oil absorption capacity of the sorbents.

The results of the studies of the dependence of the sorption capacity of the sorbents on the number of cycles used are shown in Table 1.

Regenerability of sorbents in one of the basic performance parameters. The obtained data illustrate the good regenerability of the sorbents and the possibility of their repeated use.

Regeneration of the sorbents was carried out by centrifugation by washing with a hydrocarbon solvent and followed air drying.

The data in Table 1 demonstrate the potential use of the sorbents synthesized by us as adsorbents for the removal of thin oil films.

We have also studied the maximum oil absorption of CKP-400, depending on the viscosity and the physical state of aggregation, i.e. the sorbed oil product was a petroleum oil, oil, gasoline and diesel fuel.

In the cases when the thickness of oil spill layer is less than the thickness of the sorbent the collection of oil from the water surface also occurs beyond the sorbent place. Table 2 shows that the sorbent absorbs oil «Mobil», to a higher extent than

gasoline and diesel. This is probably due to the higher affinity of the sorbent to the sorbed oil.

With increasing film thickness, the oil sorption capacity of the sorbent increases.

From the data of Table 2 it is clear that the collection of relatively low-viscosity products (gasoline and diesel) racking of their excesses and real-absorbing properties of the sorbent are characterized by oil absorption at the level of 30-40 g/g.

This sorbent is easily regenerated by simple squeezing of the absorbed oil. Despite of the high oil absorption of sorbent "CRH- 400" its application in dispersed form is not enough technological due to the significant time consuming

technical difficulties that arise at spraying of the sorbent on the surface oil spills and subsequent collection of the spent sorbent.

Since the performance of the sorbent heavily depends on the ambient temperature, for example, in winter conditions, we also investigated the effect of ambient temperature and volume weight of sorbents based on Apricot stone CAS-400 and rice husk CRH-400.

Table 3 represents the temperature dependence of the sorption capacity of sorbents (CAS - 400 with weight by volume of 50 g/cm<sup>3</sup> and CRH- 400 with weight by volume of 150 g/cm<sup>3</sup>) on oil and petroleum products in the temperature interval 10-50 °C.

**Table 1.** Dependence of the sorption capacity of the sorbents on the number of cycles used

Number of Cycles	Sorption Capacity, g/g		
	FRCRH-300	FPCRH-400	MFR -300
1	0.45	0.49	0.42
2	0.44	0.40	0.40
3	0.35	0.38	0.40
4	0.33	0.35	0.32

**Table 2.** Effect of the thickness of oil and oil products on the sorption capacity of the sorbent CRH-400, g/g

Collected oil product	Layer thickness, cm	Amount (g/g) of the sorbent on the collected oil product		Degree of squeezing, %
		absorbed	squeezed	
Oil field "Kumkol"	4.1	38-40	28	86
Oil "Mobil"	1.1	53-60	43	87
Motor car gasoline	3	32-33	25	78
Diesel fuel	4	24-30	19	77

**Table 3.** Influence of temperature of the medium and bulk density of sorbents on the sorption capacity on oil and petroleum products (g/g).

Weight by volume, g/cm <sup>3</sup>	Temperature of medium, °C	Sorption capacity of sorbents, g/g			
		Oil	Fuel oil	Diesel fuel	Gasoline
CAS-400 50 g/cm <sup>3</sup>	10	9.3	7.4	1.6	1.4
	15	12.4	11.5	2.4	2.1
	25	15.6	16.2	3.5	3.0
	30	17.4	17.3	3.5	2.4
	35	20.4	21.4	2.4	-
	40	22.5	24.2	1.0	-
CRH-400 150 g/cm <sup>3</sup>	10	4.0	2.2	8.3	7.2
	15	5.3	2.5	9.2	8.1
	20	5.4	2.6	10.3	9.1
	25	6.2	3.4	11.4	12.1
	30	8.1	5.2	12.5	12.1
	35	8.8	6.3	12.4	-
	40	10.2	7.2	12.0	-

Analyzing the data of Table 3, we can come to the following regularities: in the case of oil and fuel oil, temperature increase leads to a constant growth of the sorption capacity for oil and fuel oil of the sorbent CAS-400. In this case, the established temperature limit for the sorbents is not the limit of saturation of oil and fuel oil.

The maximum adsorption capacities of these sorbents are 22.5 and 24.2 g/g, respectively. In the case of gasoline and diesel fuel in the sorbent CAS-400 with weight by volume of 50 g/m<sup>3</sup> the maximum sorption of diesel fuel was achieved at a temperature of 30°C and was equal to 3.5 g/g. A further increase in the temperature of the medium causes a decrease in the sorption capacity of the sorbent on diesel fuel. This is due to the fact that the sufficiently large mesh size of the sorbent AS - 400 ensures that the forces of attraction between the sorbate molecules are higher than those between the sorbate and sorbent molecules, resulting in a liquid phase portion flowing from the cells of a solid sorbent during weighing [11].

In the same Table 3 the regularities of the changes of the sorption capacity of the sorbent CRH-400 with a bulk density of 150 g/m<sup>3</sup> with temperature are given. By analogy, in this case, regardless of the type of the sorbate, a regular increase of the temperature of sorption capacity was observed. This is due to the fact that with increasing temperature, the viscosity of oil and petroleum products is reduced, and thereby, the migration of sorbate to a diffusion region of fine-mesh macrostructure of the sorbents is accelerated. However, here, an opposite picture is observed: the sorption capacity for diesel fuel and gasoline is higher than that of oil and fuel oil. In this case, we are confronted with the specifics of selective sorption of sorbents and their ability to selectively perform the sorption of oil and petroleum products, depending on the size of the cells and bulk density. The studies revealed that the conducted studies allow to speak about potential use of the sorbents synthesized by us as adsorbents for the removal of thin oil films. On the basis of experimental data it was revealed that the maximum absorption of crude

oil is reached at equal proportions of the film thickness of dispersed sorbent and the thickness of layer of an oil spill, i.e. in the case of oil «Mobil» with a layer thickness of 1.1 cm the maximum adsorbed quantity of oil products is 53-60 g.

## CONCLUSION

It was found that irrespective of the type of oil and volume weight of the sorbent, with an increase of thickness of layer of oil from 1.0 to 7.0 mm there was a general tendency to increase the sorption capacity. It is interesting to note that the maximum sorption for each type of oil occurred on sorbents with definite values of bulk density.

## REFERENCES

1. F.A. Kamenshikov, E.I. Bogomolnii, Oil sorbents, M., Izhevsk, Institute of computer science, 2003, p. 268.
2. V. E. Ryabchikov, Modern methods of water preparing for industrial and domestic use, M., De Le print, 2004, p. 300.
3. F.A. Kamenshikov, E.I. Bogomolnii, Removal of oil products from the water surface and ground, M., Izhevsk, Institute of Computer Science, 2006, p.528.
4. G.I. Gorozhankina, L.I. Pinchukova, *Pipeline transport of oil*, **4**, 12 (2000).
5. V.V.Bordunov, E.O.Koval, I.A.Sobolev, *Oil and gas technologies*, **6**, 30 (2000).
6. J. Jandosov, Z.A. Mansurov, M.I. Tulepov, M.A. Bijsenbaev, Z.R. Ismagilov, N.V. Shikina, I.Z. Ismagilov, I.P. Andrievskaya, *Periodical of Advanced Materials Research*, **602-604**, 85 (2013).
7. K. Kudaibergenov, Y. Ongarbayev, Z. Mansurov, M. Tulepov, Y. Tileuberdi, *Applied Mechanics and Materials*, **446 – 447**, 1508 (2014).
8. K. Kudaibergenov, Y. Ongarbayev, M. Tulepov, Z. Mansurov, *Advanced Materials Research*, **893**, 478 (2014).
9. H. Luik, I. Johannes, V. Palu, L. Luik, K. Krwusement, *J. Anal. Appl. Pyrolysis*, **79**, 121 (2004).
10. R.-Q. Sun, L.-B. Sun, Y. Chun, Q.-H. Xu, *Carbon*, **46**(13), 1757 (2008).
11. Y.N. Kahramanly, *Refining and Petrochemistry*, **12**, 42 (2010).

## СОРБЦИОНЕН КАПАЦИТЕТ НА СОРБЕНТИ ЗА ОТСТРАНЯВАНЕ НА ТЪНКИ СЛОЕВЕ ОТ НЕФТ

Д.А. Байсейтов, М.И. Тулепов, Л.Р. Сасикова, Ш.Е. Габдрашова, Г.А. Есен, К.К. Кудайбергенов, З.А.  
Мансуров

*Национален университет „Ал-Фараби“, Алмати, Казахстан*

Постъпила на 4 май, 2015 г.; приета на 27 юли, 2015 г.

(Резюме)

Изследван е сорбционният капацитет на сорбенти в зависимост от количеството, времето, дебелината на нефтения филм, както и броя на циклите на употреба. Извършените изследвания демонстрират потенциалната полза от синтетични сорбенти за отстраняването на тънки филми от нефт.

## Influence of the carrier phase composition on the catalytic activity of copper-cobalt oxides deposited on slag glass-ceramics

I. K. Mihailova<sup>1\*</sup>, S. V. Dimitrova<sup>2</sup>, D. D. Stoyanova<sup>3</sup>, D. R. Mehandjiev<sup>3</sup>

<sup>1</sup> University of Chemical Technology and Metallurgy, 8, St. Kl. Ohridski Blvd., 1756 Sofia, Bulgaria

<sup>2</sup> University of Architecture, Civil Engineering and Geodesy, 1, H. Smirnenski Str. 1046 Sofia, Bulgaria

<sup>3</sup> Institute of General and Inorganic Chemistry, Bulgarian Academy of Sciences, Acad. Georgi Bonchev Str., bld. 11, 1113 Sofia, Bulgaria

Submitted May 20, 2015; Revised November 11, 2015

In order to check to what extent the slag based glass-ceramics may be used as carriers in the preparation of active supported catalysts, copper-cobalt oxide catalysts on different carriers (glass-ceramics obtained on the basis of blast furnace slag) were studied. The catalytic activity towards the complete oxidation of carbon monoxide was evaluated. The samples were characterized by X-ray diffraction (XRD), scanning electron microscopy (SEM) and BET analyses. Three main crystalline phases were present in varying proportions in the catalyst carriers: melilite, anorthite and pyroxene. The results of catalytic tests were interpreted with respect to the catalyst carrier phase composition. It was found that the catalytic activity and the formation of catalytically active complexes depend on the phase composition of the carrier. Among the crystalline phases present in the composition of the carriers, pyroxene contributes to the formation of the most efficient catalytically active complexes.

**Keywords:** Phase composition, supported catalysts, catalytic activity.

### INTRODUCTION

Regardless of its variable composition, blast furnace slag can be successfully used as an adsorbent or as a carrier for the preparation of catalysts for full oxidation. It has been found that this is possible because of the presence of crystalline phases of the melilite group. They determine the adsorption capacity of the slag to the ions of some heavy metals such as lead, copper and the like [1–8], whereas the inclusion of transition metal ions in the crystalline structure yields catalysts for the oxidation of CO and hydrocarbons [9, 10].

The preparation of catalysts, the active phase of which is deposited on a carrier, requires the synthesis to be conducted so that there are catalytically active complexes (CAC) on the surface of the carrier [11–14]. It is essential that the carrier and its chemical nature play an important role in CAC when there are deposited catalysts, since a variety of ions from the deposited phase, but also from the carrier may be involved in it [11–14]. Therefore, the same catalytically active phase deposited on different carriers has different catalytic activity in the same catalytic reaction. It is of interest to check to what extent the slag glass-ceramics obtained on the basis of blast furnace slag, may be used as carriers for the preparation of catalysts by depositing oxides of 3d-transition

metals. For slag glass-ceramics of this type, it has been shown that the crystal structure of the phases in them conditions the adsorption capacity to the ions of lead [15].

Therefore, the aim of this paper was to study the influence of phase composition of slag glass-ceramics which were used as a carrier of copper-cobalt oxides in reactions of CO oxidation.

### EXPERIMENTAL

#### *Synthesis of the carriers*

To obtain the carriers – slag glass-ceramics, kaolin, Al<sub>2</sub>O<sub>3</sub>, and TiO<sub>2</sub> were used, as well as granulated blast furnace slag with the following composition – CaO (40.5%), SiO<sub>2</sub> (35.2%), A<sub>2</sub>O<sub>3</sub> (9.3%), MgO (5.2%), BaO (3.2%), MnO (2.6%), S (1.2%), K<sub>2</sub>O (1.0%), Na<sub>2</sub>O (0.3%), FeO (1.0), Fe (0.7%). First, the parent glasses were prepared by melting at 1450–1470 °C for 60–90 min. Then the glasses were ground, pressed and heated at 1000 °C for 3 h. The method of synthesis of the samples is described in more detail in [16]. The choice of particular compositions and additives was based on our previous experimental data [17–19], which showed that high-strength glass-ceramics could be obtained from such compositions. Four sample carriers were obtained by changing the ratio of components with a view to the formation of different crystal phases. The carriers were designated as SC (a) with initial composition: 73.6% slag and kaolin 20.7%; SC (b) with initial

\* To whom all correspondence should be sent:  
E-mail: irena66@mail.bg

composition: slag 68.2%, kaolin 20.5%, Al<sub>2</sub>O<sub>3</sub> 5.7%; SC (c) with initial composition: slag 74.3% kaolin 12.0%, Al<sub>2</sub>O<sub>3</sub> 8.0% and SC (d) with initial composition: slag 79.9%, kaolin 12.2%, Al<sub>2</sub>O<sub>3</sub> 2.2%. In all batches, 5.7% of TiO<sub>2</sub> was added.

#### *Synthesis of the catalysts*

The obtained carriers were impregnated with a solution containing copper nitrate and cobalt nitrate with different concentrations, while maintaining the atomic ratio of Cu: Co = 1: 2. The procedure was carried out using a solution/carrier ratio of 5 (v/w) at a temperature of 90 °C for 1 h. Then the samples were left in the solution without heating for 24 h and the impregnation procedure was repeated once more. After impregnation and drying at 110 °C, the samples were heated in air at 350 °C for 3 h. The samples were labeled CAT (a), CAT (b), CAT (c) and CAT (d) and they were obtained from the respective carriers – SC (a), SC (b), SC (c) and SC (d).

#### *Experimental methods*

X-ray powder diffraction (XRD) analysis was applied for phase identification. An X-ray diffractometer Philips with Cu K $\alpha$  radiation ( $\lambda = 1.5418 \text{ \AA}$ ) was used in the range from 15° to 90° 2 $\theta$  (step size: 0.05°, counting time per step: 1 s). The crystalline phases were identified using the powder diffraction file cards № 35-0755, 41-1486 and 31-0249 from database JCPDS - International Centre for Diffraction Data PCPDFWIN v.2.2. (2001) ) [20].

The microstructure of the glass ceramic materials was investigated by SEM. Microscope JEOL JSM 5510 was used. The samples were coated with gold in an auto fine coater JEOL JFC-12200.

The concentration of the solutions used just after the procedure for the deposition of copper and cobalt phases was determined by ICP-OES analysis using Prodigy high-dispersion ICP-OES spectrometer from Teledyne Leeman Labs.

The measurement of the specific surface area of the samples was carried out by nitrogen adsorption at 77.4 K. Nitrogen adsorption isotherms were used to calculate the specific surface area using the BET equation.

The catalytic activity of the samples was measured in an isothermal plug-flow reactor enabling operation under steady-state conditions without any temperature gradients. The size of the catalyst particles (0.3 – 0.6 mm) was chosen taking into account the reactor diameter (6 mm) and the hourly space velocity (20 000 h<sup>-1</sup>). The gas feed

flow rate was 4.0 L/h, the catalyst bed volume was 0.2 cm<sup>3</sup>, and the mass of the charged catalyst was 0.50 – 0.55 g. The catalytic oxidation was performed within the temperature interval 200 – 400 °C, the oxidizing agent used being oxygen from the air (gas mixture: 21% O<sub>2</sub> and 79% N<sub>2</sub>). The preliminary treatment of the catalysts included heating in air flow at 120 °C for 1 h. The flow of CO was fed into the reactor by an Ismatex M62/6 pump (Switzerland). The initial concentration of carbon monoxide was 0.5 vol. %. The carrier gas was air (a mixture of 21% O<sub>2</sub> and 79% N<sub>2</sub>). A Maihak gas analyzer (O<sub>2</sub>, CO, CO<sub>2</sub>) was used to measure the CO and CO<sub>2</sub> concentrations with an accuracy of  $\pm 0.1$  ppm, whereas the oxygen measurement accuracy was  $\pm 100$  ppm.

## RESULTS AND DISCUSSION

Table 1 presents the results of the identified crystalline phases, for the given specific surface and for the deposited amounts of copper and cobalt. As seen from the Table, three main crystalline phases in varying proportions are present in the samples: melilite, anorthite and pyroxene [15, 16].

The quantification of the contents of each of these phases in the samples showed the following: the phase content of sample CAT (a) was anorthite accounting for slightly more than 50% of the crystalline phases. The compositions of CAT (b) and CAT (c) were characterized by a more significant participation of pyroxene in the phase content; 40-51% of the crystalline phases and melilite was the predominant crystal phase only in sample CAT (d).

From the data in Table 1 for specific surface area, it is obvious that the samples differ in this indicator; the highest one is that of CAT (d). The samples also differ in contents of the two metals, but the atomic ratio is preserved and is approximately equal to two. As noted before, the preparation of the catalysts was conducted so that there were CAC with ratio Co / Cu = 2 on the surface, for which it is known to have high activity in oxidation reactions [21].

The microscopic images of the samples showed that they had very suitable microstructure for carriers of catalysts. Fig. 1 shows a microscopic image of the specimen CAT (d).

Common micro-structural features were observed in all slag glass-ceramics [15, 16]. There was a good sintering of the initial powders. The obtained glass-ceramic materials had a finely dispersed crystalline structure showing microcrystals of  $\sim 3\text{-}4 \mu\text{m}$ . Amorphous phase densely envelopes the crystals. Idiomorphic crystals

with a characteristic morphology that corresponds to anorthite, melilite and pyroxene, respectively, were identified in large rounded pores measuring up to 10-20  $\mu\text{m}$ . The pores observed in our study (Fig. 1) were typical intragranular induced crystallization pores. We consider it probable that these pores were formed as a consequence of the crystallization of glass. The crystals formed in the amorphous matrix had a higher density than the density of the amorphous mass, which led to shrinking of the sample and the formation of induced porosity.

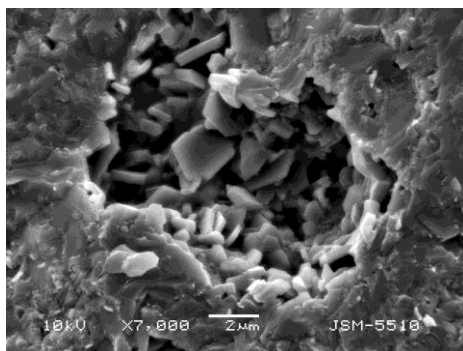


Fig. 1. SEM image of the sample CAT (d).

It was important to get information about the obtained crystalline structure containing copper and cobalt. Fig. 2 shows the X-ray-diffraction data for catalyst CAT (d), since according to chemical analysis, Table 1, this sample contains the highest amounts of the deposited phases and it is expected that this may have an impact on X-ray patterns.

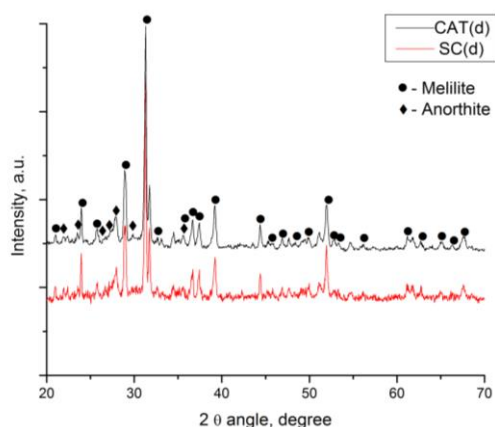


Fig. 2. X-ray diffraction data about catalyst CAT (d) and carrier SC (d)

For comparison, the X-ray pattern of the original sample used for obtaining the sample carrier SC (d) is shown. These diffraction patterns, as shown in Fig. 2, are almost identical, so unfortunately the newly formed copper- and cobalt-containing phases cannot be identified on the basis of XRD. The presence of the following crystalline phases is likely:  $\text{CuO}$ ,  $\text{Co}_3\text{O}_4$ ,  $\text{CuCo}_2\text{O}_4$ , but due to the small

quantities and the possibility of their most intense diffraction peaks to overlap with the peaks of the diffractogram of the carrier, they cannot be confirmed by XRD.

Figures 3 and 4 present the results of testing the catalytic activity of the catalysts. Fig. 3 shows data for the catalytic activity –  $\eta$  as a degree of CO oxidation in %. The catalytic activity given as an amount of oxidized CO per gram of catalyst – intensity ( $I_g$ ) is presented in Fig. 4.

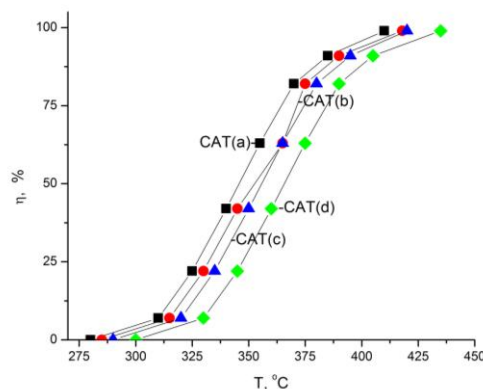


Fig. 3. Degree of conversion of CO [ $\eta$ , %] in dependence on temperature [ $T$ ,  $^{\circ}\text{C}$ ].

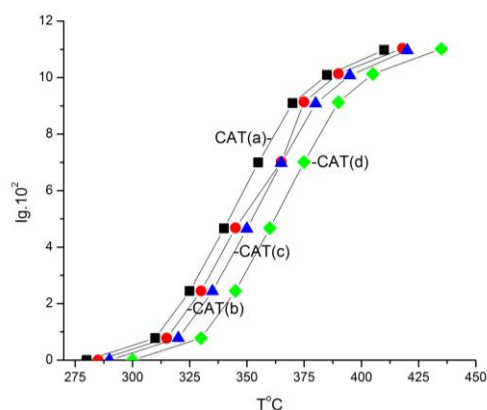
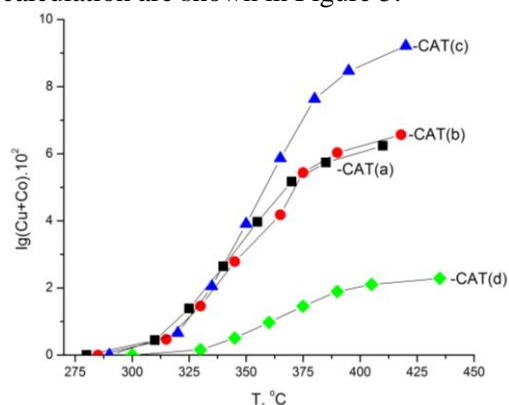


Fig. 4. Dependence of the amount of oxidized CO of 1 g catalyst for 1 hour [ $I_g$ ] on temperature [ $T$ ,  $^{\circ}\text{C}$ ]

As it can be seen from the figures, the most active catalyst regarding both indicators is the catalyst CAT (a), and the least active one is the catalyst CAT (d). The difference in the activity of the catalysts is not huge, as it can be seen from Table 2, where the values for  $\eta$  and  $I_g$  at temperatures 365  $^{\circ}\text{C}$  are given. As the Table shows, the values for the parameter  $\eta$  are grouped in the range 76-49%. The same is true for the  $I_g$ . For CAT (a)  $I_g = 8.40 \cdot 10^{-2}$ , whereas for CAT (d)  $I_g = 5.45 \cdot 10^{-2}$ , despite the fact that the latter catalyst has the highest specific surface area (Table 1). This proves that this parameter – specific surface, is not decisive. The basic indicator must be the amount of the deposited oxide phases and their activity efficiency – namely, the activity of formed CAC. In

order to clarify how effectively the oxides of copper and cobalt are used, the intensity (I<sub>g</sub>) for one gram of total content of copper and cobalt in the catalysts (I<sub>g(Cu+Co)</sub>) was estimated. The results of this calculation are shown in Figure 5.



**Fig. 5.** Dependence of the amount of oxidized CO of 1 g (Cu + Co) for 1 hour I<sub>g(Cu + Co)</sub> on temperature [T, °C]

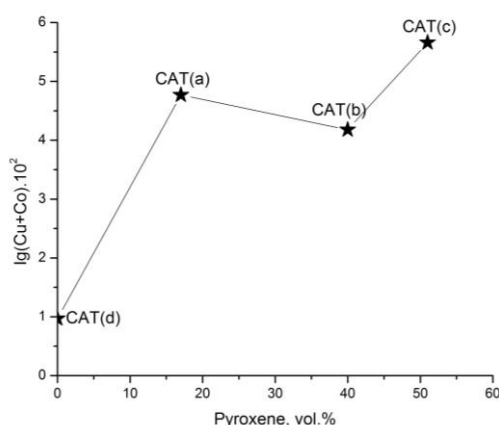


**Fig. 6.** Dependence of the intensity of the catalysts – I<sub>g(Cu + Co)</sub> at 365 °C on the content of pyroxene.

It can be seen from the figure that the sample CAT (d) again has the lowest activity. In this case the differences in activity are significant. According to this indicator, CAT (c) exhibits the highest activity, although the contents of copper and cobalt in it are the lowest (Table 1). Accordingly, not only the amount of the applied oxides, but also the phase composition is important for the formation of CAC – the amount and type of crystallized phases. If you compare the data presented in Table 1 and Table 2 it is immediately clear that in the least active

catalyst CAT (d), the phase pyroxene is missing. If we assume that this phase promotes the formation of more active CAC, i.e., it plays a significant role, it would be logical that with the increase of its amount, the activity of the catalysts would also increase. Fig. 6 presents data about I<sub>g(CuCo)</sub> depending on the content of the crystalline phase pyroxene. Activity actually increases with the increase of pyroxene in the catalysts. Therefore, this crystalline phase results in the formation of the most active CAC. Of course, the role of anorthite should not be ignored, since the catalysts are active even in the absence of pyroxene. On the basis of the obtained results, it is possible to make a conclusion that anorthite contributes to the formation of more efficient CAC than melilite. These crystal phases belong to two main structural silicate types and the CAC formed differ. These data confirm that the carrier and its nature play an important role in CAC formation.

**Table 2.** Data for the catalytic activity at 365 °C.

Samples	η, %	I <sub>g</sub> .10 <sup>2</sup>	I <sub>gCuCo</sub> .10 <sup>2</sup>
CAT(a)	75.7	8.40	4.77
CAT(b)	63.0	7.02	4.18
CAT(c)	63.0	6.97	5.66
CAT(d)	49.0	5.45	0.97

The activity of CAC depends on the generated Cu- and Co-containing phases; the formation of crystalline phases with spinel structure is desirable. The reason for the formation of more active CAC on carriers containing pyroxene is probably due to the ability of pyroxene to contribute to the heterogeneous nucleation of the spinel. An epitaxial relationship is widely observed in spinel exsolution lamellae within pyroxene [22, 23] facilitated by similar spacing and plane group symmetries of oxygen atoms of {010} pyroxene and {110} spinel. Hammer *et al.* [24], concluded that clustering and physical contact of pyroxene and spinel forming from melt develop from heterogeneous nucleation followed by epitaxial crystal growth. In the available literature we found no data on epitaxial relationships between spinel and anorthite or spinel and melilite.

**Table 1.** Phase compositions, BET surface area of the catalyst carriers and amount of copper and cobalt deposited

Sample	Crystalline phases, vol %			S <sub>0</sub> , m <sup>2</sup> /g	Content, weight %		Mol. ratio Cu/Co
	Melilite	Anorthite	Pyroxene		Cu	Co	
CAT(a)	32	51	17	17.7	0.62	1.14	1.90
CAT(b)	20	40	40	23.3	0.54	1.14	2.27
CAT(c)	26	23	51	31.2	0.40	0.79	2.13
CAT(d)	66	34	0	43.3	1.55	3.27	2.17

## CONCLUSIONS

Based on the experimentally obtained results for the catalytic activity of copper and cobalt oxides deposited on slag glass-ceramics, it can be concluded that the formation of catalytically active complexes (CAC) depends on the phase composition of the carrier. Among the crystalline phases present in the composition of slag glass-ceramics, pyroxene contributes to the formation of the most efficient CAC whereas the influence of anorthite and melilite is weaker.

## REFERENCES

1. S. V. Dimitrova, D. Mehandjiev, *Wat. Res.*, **32**, 3289 (1998).
2. S. Dimitrova, D. Mehandjiev, *Compt. rend. Acad. bulg. Sci.*, **52**, 33 (1999).
3. D. R. Mehandjiev, S. V. Dimitrova, *Bulg. Chem. Comm.*, **31**, 580 (1999).
4. S. V. Dimitrova, D. Mehandjiev, *Compt. rend. Acad. bulg. Sci.*, **53**, 49 (2000).
5. S. Dimitrova, V. Nickolov, D. Mehandjiev, *J. Mat. Sci.*, **36**, 2639 (2001).
6. E. Nehrenheim, J. P. Gustavson, *Biores. Technol.*, **99**, 1571 (2008).
7. A. Nakahira, H. Naganuma, T. Kubo, Y. Yamasaki, *J. Ceram. Soc. Jpn.*, **116**, 500 (2008).
8. Y. F. Zhou, R. J. Heines, *Water Air Soil Poll.*, **215**, 631 (2010).
9. S. Dimitrova, G. Ivanov, D. Mehandjiev, *Appl. Cat.*, **206**, 81 (2004).
10. S. Dimitrova, G. Ivanov, D. Mehandjiev, *Compt. rend. Acad. bulg. Sci.*, **55**, 79 (2002).
11. D. Mehandjiev, Proc. Inter. Symp. Heter. Cat., Varna, 2000, p. 19.
12. T. Tsoncheva, *Compt. rend. Acad. bulg. Sci.*, **53**, 49 (2000).
13. T. Tsoncheva, S. Vankova, D. Mehandjiev, *Fuel*, **82**, 755 (2003).
14. R. Nickolov, T. Tsoncheva, D. Mehandjiev, *Fuel*, **81**, 203 (2002).
15. S. V. Dimitrova, I. K. Mihailova, P. V. Vassileva, D. R. Mehandjiev, *Compt. rend. Acad. bulg. Sci.*, **65**, 1675 (2012).
16. Mihailova, I. K., P. R. Djambazki, D. Mehandjiev, *Bulg. Chem. Comm.*, **43**, 293 (2011).
17. I.T. Ivanov, I. Georgieva, F. Dipchikov, Proc. 11th Int. Conf. Glass and Ceramic, Varna, 1993, B. Samuneva. I. Gutzow, Y. Dimitriev, S. Bachvarov (eds.), Acad. Publ. House Marin Drinov, Sofia, 1994, p. 240.
18. I. Ivanov, I. Georgieva, F. Dipchikov, C. Ionchev, Proc. 12th Int. Conf. Glass Ceramics, Varna, 1996, B. Samuneva et al. (eds.), Acad. Publ. House Marin Drinov, Sofia, 1997, p. 200.
19. I. Georgieva - Mihailova, PhD Thesis, UCTM, Sofia, 1997.
20. JCPDS International Center for Diffraction Data, Powder Diffraction File, Swarthmore, PA.
21. S. Angelov, D. Mehandjiev, B. Piperov, V. Zarkov, A. Terlecki-Baricevic, D. Jovanovic, *Appl. Catalysis*, **16**, 431 (1985).
22. M. Feinberg, H.-R. Wenk, P. Renne, and G. R., Scott, *American Mineralogist*, **89**, 462 (2004).
23. F. P. Okamura, I. S., McCallum, J. M. Stroh, and S., Ghose, Proc. 7th Lunar and Planetary Science Conference, **2**, 1976, p.1889.
24. I.E. Hammer, T. G. Sharp, *P. Wessel, Geology*, **38**, 367 (2010).

## ВЛИЯНИЕ НА ФАЗОВИЯ СЪСТАВ НА НОСИТЕЛЯ ВЪРХУ КАТАЛИТИЧНАТА АКТИВНОСТ НА МЕДНО-КОБАЛТОВИ ОКСИДИ НАНЕСЕНИ ВЪРХУ ШЛАКОСИТАЛИ

Ирена К. Михайлова<sup>1</sup>, Соня В. Димитрова<sup>2</sup>, Даниела Д. Стоянова<sup>3</sup>, Д. Р. Механджиев<sup>3</sup>

<sup>1</sup> Химикотехнологичен и металургичен университет, бул. „Св. Климент Охридски“ № 8, София 1756, България

<sup>2</sup> Университет по архитектура, строителство и геодезия, бул. „Христо Смирненски“ № 1, София 1046, България

<sup>3</sup> Институт по обща и неорганична химия – Българска академия на науките, ул. „Акад. Георги Бончев“ блок 11, София 1113, България

Постъпила на 20 май 2015 г.; коригирана на 11 ноември 2016 г.

(Резюме)

За да се провери доколко шлакоситали могат да се използват като носители за получаване на активни нанесени катализатори, са изследвани катализатори, получени чрез нанасяне на медно-кобалтови оксиди на различни шлакоситали. Каталитичната активност е изследвана по отношение окислението на въглероден оксид. Образците са охарактеризирани с помощта на рентгенодифракционен анализ, сканираща електронна микроскопия и ВЕТ-анализ. Установено е, че мелилит, пироксен и анортит в различни съотношения са основните кристални фази в тях. Резултатите от каталитичните тестове са интерпретирани във връзка с фазовия състав на носителите на катализаторите. Установено е, че каталитичната активност и формирането на каталитично активни комплекси зависят от фазовия състав на носителите. От кристалните фази в състава на носителите пироксенът допринася за образуване на най-ефективни каталитично активни комплекси.

## Validation of a TLC-densitometric method for quality control of Estradiol valerate in drug combinations

S. Ivanova, D. Tsvetkova\*

*Department of Pharmaceutical Chemistry, Faculty of Pharmacy, Medical University-Sofia*

Received January 28, 2016; Accepted February 25, 2016

The aim of the current study was the validation of a TLC-densitometric method for quality control of Estradiol valerate in drug combination dosage forms. The TLC conditions were: glass plates with silicagel G<sub>60</sub>F<sub>254</sub>; mobile phase: chloroform : water = 90 : 10 v/v. The TLC-densitometric method was validated with respect to the analytical parameters: linearity, LOD, LOQ, accuracy and precision (repeatability). Linear regression analysis was performed. The regression calibration curve was built. Linearity accordance between the concentration and spot area in range:  $5.10^{-4}$  g/ml ÷  $3.10^{-3}$  g/ml was proved by the regression equation:  $y = 28874286.x + 14290$ . LOD =  $3.15.10^{-4}$  mg/ml; LOQ =  $9.54.10^{-3}$  mg/ml.

For estimating the accuracy the recovery is presented in R [%] ± RSD [%] with the respective confidence interval: R[1.5 mg]: 95.92 % ÷ 103.98 %; R[2 mg]: 93.35 % ÷ 108.89 %; R[2.5 mg]: 95.37 % ÷ 103.77 %. Precision is estimated by standard deviation, relative standard deviation and confidence interval. All data for the obtained quantity correspond to the confidence interval: 1.88 mg ÷ 2.17 mg. The proposed validated TLC-densitometric method is appropriate for quality control of Estradiol valerate in commercially available tablets.

**Key words:** TLC-densitometry, Estradiol valerate, validation, linearity, accuracy.

### INTRODUCTION

Osteoporosis is a systemic skeletal disease, characterized by decreased bone mass and altered bone microarchitecture, leading to increased bone fragility and fracture risk in women [1] and men [2]. Estradiol valerate is used for treatment of symptoms of menopause (hot flashes, burning, irritation) and types of prostate cancer (androgen-dependent), for prevention of osteoporosis in postmenopausal women, replacement of estrogen in women with ovarian failure or other conditions that cause a lack of natural estrogen in the body. The risk of osteoporosis is increased in estrogen deficiency [3].

Estradiol valerate is included in combined dosage forms for contraception with Cyproterone acetate (Femilar) [4] and Dienogest [5, 6]. On the pharmaceutical market drug products are available for treatment of climacteric symptoms in postmenopausal women, containing Estradiol valerate 2 mg in combination with: Ciproterone acetate 1 mg (Climen tabl.) [4]; Dienogest 2 mg (Climodien tabl.) [7], Medroxyprogesterone acetate 10 mg (Divina, Farlutes) [8]; Levonogestrel 0.15 mg (Climonorm tabl.) [9].

The following methods for determination of Estradiol valerate in tablets are described: I) UV-spectrophotometry at  $\lambda = 280$  nm [10]; II) UV-

spectrophotometry - first derivative at  $\lambda = 270$  nm [11] and  $\lambda = 292$  nm [10]; III) fluorimetry after derivatization reaction with dansyl chloride [12]. For determination of Estradiol valerate in drug combinations containing other components in the tablets the following methods are developed:

I) UV-derivative spectrophotometry:

1) Estradiol valerate and Cyproterone acetate [13]

2) 2nd derivative spectrophotometry: at  $\lambda = 297.4$  nm for Estradiol valerate and at  $\lambda = 273.4$  for Medroxyprogesterone acetate [14]

II) chemiluminescence method: inhibition of luminol luminescence by Estradiol valerate [15]

III) HPLC with UV-detection:

1) Estradiol valerate/Dienogest: stationary phase: ACE C<sub>8</sub>, mobile phase: ammonium nitrate: acetonitrile = 30 : 70 v/v, flow rate: 2 ml/min,  $\lambda = 280$  nm, internal standard: Cyproterone acetate [16]

2) Estradiol valerate/Medroxyprogesterone acetate: stationary phase: C<sub>18</sub>, mobile phase: ammonium nitrate: acetonitrile = 30 : 70 v/v,  $\lambda = 280$  nm [17]

IV) GC/MS: Estradiol valerate and Medroxyprogesterone acetate [18]

V) electrochemical method: carbon electrode modified with iron tetrapyridinoporphyrazine: 17 $\beta$ -Estradiol valerate in injections [19].

The aim of the current study is to validate the TLC-densitometric method for quality control of Estradiol valerate with respect to the analytical

\* To whom all correspondence should be sent:  
E-mail: dobrinka30@abv.bg

parameters: selectivity, linearity, accuracy, precision.

## MATERIALS AND METHODS

### Materials

I) Reference standard: Estradiol valerate

II) Reagents with analytical grade quality: chloroform (Sigma Aldrich, N: SZBD 074SV UN 1888); 99.98 % ethanol (Sigma Aldrich, N: SZBD 0500V UN 1170), distilled water

III) TLC glass plates precoated with silicagel G<sub>60</sub>F<sub>254</sub>, 20 cm × 20 cm (Sigma Aldrich, N: 2364681).

### Method: TLC-densitometry.

I) Instrumentation: densitometer VILBER LOURMAT CN-15.LC Serial:16263; sample applicator 10 µl micropipette (Hamilton, Bonaduz, Switzerland, N:18005701); TLC chamber (22 cm × 12 cm × 22 cm); stationary phase: Silicagel G<sub>60</sub>F<sub>254</sub>; mobile phase: chloroform : distilled water = 90 : 10 v/v, detection at λ = 254 nm.

II) Preparation of solution of RS for linearity check.

Accurately weighed quantities of the reference standard Estradiol valerate: 0.005 g, 0.01 g, 0.015 g, 0.02 g, 0.025 g, 0.03 g were dissolved in separate volumetric flasks of 10.0 ml in 99.98 % ethanol to obtain solutions with concentrations correspondingly:  $5.10^{-4}$  g/ml;  $1.10^{-3}$  g/ml;  $1.5.10^{-3}$  g/ml,  $2.10^{-3}$  g/ml,  $2.5.10^{-3}$  g/ml,  $3.10^{-3}$  g/ml.

III) Preparation of model mixtures for accuracy check.

Accurately weighed quantities equivalent to 0.015 g, 0.020 g, 0.025 g of the reference standard Estradiol valerate were dissolved in separate volumetric flasks of 10.0 ml in 99.98 % ethanol to obtain 3 samples from 3 different model mixtures with contents equivalent to 80 % (1.5 mg/ml, I), 100 % (2 mg/ml, II) and 120 % (2.5 mg/ml, III) of the theoretical concentration in the tablets (2 mg).

IV) Preparation of model mixtures for precision (repeatability) check.

Accurately weighed quantities equivalent to 0.02 g of the reference standard Estradiol valerate were dissolved in 6 separate volumetric flasks of 10.0 ml in 99.98 % ethanol to obtain 6 model mixtures with Estradiol valerate content equivalent to 100 % (2 mg/ml) of the theoretical concentration in the tablets (2 mg).

## RESULTS AND DISCUSSION

The TLC-densitometric method was validated for the analytical parameters: selectivity, linearity, accuracy and precision.

### 1) Selectivity

A "placebo" solution without the active substance Estradiol valerate was prepared in the same manner like the solution of the reference standard. The selectivity of the applied TLC-densitometric method was proved by the fact, that on the chromatograms with "placebo" solutions there were no spots with R<sub>f</sub>, corresponding to the R<sub>f</sub> of Estradiol valerate (0.92).

### 2) Linearity

Linearity accordance between the concentration and spot area in the range:  $5.10^{-4}$  g/ml ÷  $3.10^{-3}$  g/ml was proved by the regression equation:  $y = 28874286.x + 14290$ . (Fig. 1.). LOD =  $3.15.10^{-4}$  mg/ml; LOQ =  $9.54.10^{-3}$  mg/ml.

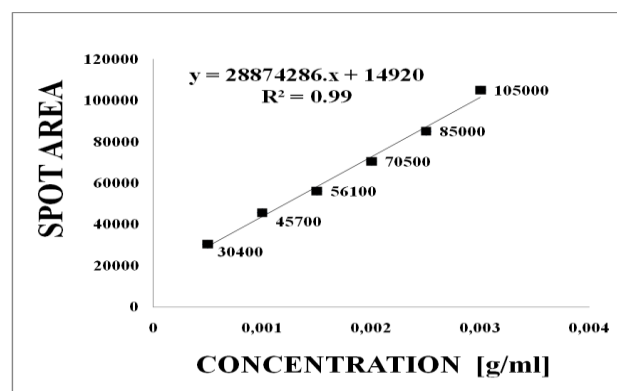


Fig. 1. Linearity for Estradiol valerate

### 3) Test for system suitability

The suitability of the system was confirmed by the lack of a statistically significant difference between the values of the chromatographic mobility parameter relative to the front (R<sub>f</sub>) in the analysis of 6 samples of Estradiol valerate: R<sub>f</sub>: 0.43, 0.43, 0.43, 0.43, 0.44, 0.44 ( $0.43 \div 0.005$ , SD = 1.4).

### 4) Accuracy

For the estimation of accuracy, in Table 1 are summarized data for the spot area (A), obtained by the method of calibration curve for model mixtures, the quantity [C] and the recovery [RC] of Estradiol

valerate, arithmetical mean ( $\bar{X}$ ); standard deviation (SD) and relative standard deviation (RSD) (%);

$S\bar{X}$  – mean quadratic error; P – confidence possibility (%) ;

$\bar{X} \div t.S\bar{X}$  – confidence interval; E – relative error. Accuracy is presented by the recovery R (%) and RSD [20].

**Table 1.** Data for spot area (A), quantity [C] and degree of recovery [RC] for Estradiol valerate in model mixtures – estimation of accuracy.

N:	A	[C <sub>1.5</sub> ] [mg]	R [C <sub>1.5</sub> ] [%]	A	[C <sub>2</sub> ] [mg]	R [C <sub>2</sub> ] [%]	A	[C <sub>2.5</sub> ] [mg]	R [C <sub>2.5</sub> ] [%]
1.	56000	1.42	97.73	68000	1.84	96.84	84000	2.39	97.55
2.	57900	1.49	99.33	71500	1.96	100.51	86200	2.47	98.80
3.	60700	1.59	102.58	76200	2.12	106.0	90300	2.61	102.35
$\bar{X} \pm SD$	58200	1.5 ± 0.09		71900	1.97 ± 0.14		86833	2.49 ± 0.11	
$\bar{R} [\%] \pm$ RSD[%]			99.95 ± 2.39			101.12 ± 4.56	3197		99.57 ± 2.5
SD	2364	0.09	2.39	4115	0.14	4.61	3.68	0.11	2.49
RSD [%]	4.06	6.0	2.39	5.72	7.11	4.56		4.42	2.5
$S \bar{X}$		0.05	1.38		0.08	2.66		0.06	1.44
P [%]		90.0	90.0		90.0	90.0		90.0	90.0
t		2.92	2.92		2.92	2.92		2.92	2.92
t.S $\bar{X}$		0.15	4.03		0.23	7.77		0.18	4.2
$\bar{X} \pm$ t.S $\bar{X}$		1.35 ÷ 1.65	95.92 ÷ 103.98		1.74 ÷ 2.2	93.35 ÷ 108.89		2.31 ÷ 2.67	95.37 ÷ 103.77
E [%]		3.33	1.38		4.06	2.63		2.41	1.45

**Table 2.** Data for spot area (A), quantity [C] and degree of recovery [RC] for Estradiol valerate in model mixtures – estimation of precision.

N:	C	A	U A	[C]	R [C] [mg/l]	U [C]
1.	1.95	69900	1.14	1.90	97.44	1.22
2.	1.95	70300	0.99	1.92	98.46	1.00
3.	2.00	71900	0.36	1.97	98.50	0.44
4.	2.00	73500	0.27	2.03	101.50	0.22
5.	2.05	75200	0.93	2.09	101.95	0.89
6.	2.05	76100	1.29	2.12	103.41	1.22
$\bar{X} \pm SD$		72817 ± 2584		2.01 ± 0.09		
$\bar{R} [\%] \pm$ RSD[%]					100.21 ± 2.39	
SD		2584		0.09	2.38	
RSD [%]		3.51		4.48	2.39	
$S \bar{X}$				0.04	0.98	
P [%]				98.0	98.0	
t				3.37	3.37	
t.S $\bar{X}$				0.13	3.30	
$\bar{X} - t.S \bar{X} \div$ $\bar{X} + t.S \bar{X}$				1.88 ÷ 2.17	96.91 ÷ 103.51	
E [%]				1.99	0.98	

All results are within the respective confidence interval: R[1.5 mg]: 95.92 % ÷ 103.98 %; R[2 mg]: 93.35 % ÷ 108.89 %; R[2.5 mg]: 95.37 % ÷ 103.77 %.

#### 5) Precision (repeatability)

Precision is estimated by the uncertainty of the result, determined by standard deviation (SD), relative standard deviation (RSD) and confidence

interval ( $\bar{X} \div t.S \bar{X}$ ). Table 2 presents: C – added content of Estradiol valerate in model mixtures, [C] – content obtained by the method of the calibration curve, [RC] – degree of recovery, U[A] – Chauvenet criterion for area, U[C] – Chauvenet criterion for the obtained content. All data for the obtained quantity of Estradiol valerate correspond to the con-fidence interval: 1.88 mg ÷ 2.17 mg (SD = 0.05).

### CONCLUSIONS

Estradiol valerate is available on the market in drug combinations with: Ciproterone acetate, Dienogest, Medroxyprogesterone acetate, Levonogestrel. The obtained quantities by the applied method correspond to the relevant confidence interval: 1.88 mg ÷ 2.17 mg. The proposed validated TLC-densitometric method is appropriate for quality control of Estradiol valerate in commercially available tablets.

**Acknowledgements:** This article was prepared with the financial support from DP N:13/2015, Medical University-Plovdiv, Bulgaria.

### REFERENCES

1. S. Sanders, S. A. Geraci, *South Med. J.*, **106**(12), 698 (2013).
2. S. Khosla, S. Amin, E. Orwoll *Endocr. Rev.*, **9**(4), 441 (2008).
3. V. B. Popat, K. A. Calis, V. H. Vanderhoof, G. Cizza, J. C. Reynolds, N. Sebring, J. F. Troendle, L. M. Nelson, *J. Clin. Endocrinol. Metab.*, **94**(7), 2277 (2009).
4. J. T. Jensen, J. Bitzer, M. Serrani, *J. Contracept.*, **4**(1), 39 (2013).
5. A. Graziottin, *Minerva Ginecol.*, **66**, (5), 479 (2014).
6. J. W. Kiley L. P. Shulman, *Int. J. Womens Health.*, **3**(1), 281 (2011).
7. T. Gräser T. Römer, K. D. Wiedey, A. Janaud, *Climacteric.*, **4**(4), 332 (2001).
8. C. Egarter P. Geurts, E. Boschitsch, P. Speiser, J. Huber, *Acta Obstet. Gynecol. Scand.*, **75**(4), 386 (1996).
9. D. B. Georgiev, S. Golbs, A. Goudev, *Methods Find. Exp. Clin. Pharmacol.*, **23**(4), 197(2001).
10. B. Yilmaz, *Int. J. Pharm. Sci. Rev. Res.*, **1**(2), 112 (2010).
11. A. S. L. Mendez, L. Deconto, C. V. Garcia, *Química nova São Paulo*, **33**(4), 981 (2010).
12. S. Fishman, *J. Pharm. Sci.*, **64**(4), 674 (1975).
13. E. Dinç, C. Yücesoy, I. M. Palabiyik, O. Ustündağ, F. Onur, *J. Pharm. Biomed. Anal.*, **32**(3), 539 (2003).
14. M. I. Toral, C. Soto, P. Richter, A. E Tapia, *J AOAC Int.*, **85**(4), 883 (2002).
15. W. Liu L. Xie, H. Liu, S. Xu, B. Hu, W. Cao, *Luminescence*, **28**(3), 407 (2013).
16. M. G. Çağlayan I. M. Palabiyik, F. Onur, *J. AOAC Int.*, **93**(3), 862 (2010).
17. A. Segall, F. Hormaechea, M. Vitale, V. Perez, M. T. Pizzorno, *J. Pharm. Biomed. Anal.*, **19**(5), 803 (1999).
18. B. Yilmaz, *Anal. Sci.*, **26**(3), 391 (2010).
19. I. V. Batista, M. R. Lanza, I. L. Dias, S. M. Tanaka, A. A. Tanaka, M. D. Sotomayor, *Analyst*, **133**(12), 1692 (2008).
20. N. P. Dimov, In: Chromatography in Pharmaceutical Analysis Dimov (ed. N. P. Dimov), Sofia, Chemical Pharmaceutical Research Institute (NIHFI), 1999, p. 205.

## ВАЛИДИРАНЕ НА TLC-ДЕНЗИТОМЕТРИЧЕН МЕТОД ЗА КОНТРОЛ НА КАЧЕСТВОТО НА ESTRADIOL VALERATE В ЛЕКАРСТВЕНИ КОМБИНАЦИИ

С. Иванова, Д. Цветкова\*

*Катедра по фармацевтична химия, Фармацевтичен факултет, Медицински университет-София*

Получена 28 януари, 2016 г., приета 25 февруари, 2016 г.

(Резюме)

Целта на настоящото изследване е валидирането на TLC-дензитометричен метод за контрол на качеството на Estradiol valerate в комбинирани дозирани лекарствени форми. Условието на TLC са: стъклени плаки: Silicagel G<sub>60</sub>F<sub>254</sub>; подвижна фаза: хлороформ : вода = 90 : 10 v/v. TLC-дензитометричният метод е валидиран по отношение на аналитичните параметри: линейност, LOD, LOQ, точност и прецизност (повторяемост). Проведен е линеен регресионен анализ. Построена е калибрационна права. Линеината зависимост между концентрацията и площта на петната в интервала:  $5 \cdot 10^{-4} \text{ g/ml} \div 3 \cdot 10^{-3} \text{ g/ml}$  се доказва от уравнението на регресия:  $y = 28874286 \cdot x + 14290$ .  $\text{LOD} = 3.15 \cdot 10^{-4} \text{ mg/ml}$ ;  $\text{LOQ} = 9.54 \cdot 10^{-3} \text{ mg/ml}$ .

За оценка на аналитичния параметър точност, е представен аналитичният добив в  $R [\%] \pm \text{RSD} [\%]$ , като резултатите отговарят на съответния доверителен интервал:  $R[1.5 \text{ mg}]$ : 95.92 %  $\div$  103.98 %;  $R[2 \text{ mg}]$ : 93.35 %  $\div$  108.89 %;  $R[2.5 \text{ mg}]$ : 95.37 %  $\div$  103.77 %. Прецизността е оценена чрез изчисляване на стандартно отклонение, относително стандартно отклонение и доверителен интервал. Всички данни за получените количества съответстват на доверителния интервал: 1.88 mg  $\div$  2.17 mg. Предложеният валидиран TLC-дензитометричен метод е подходящ за контрол на качеството на Estradiol valerate valetate в таблетки.

## Synthetic cannabimimetics detected in smoking blends on the Bulgarian territory – toxicological significance

P. A. Gateva<sup>1\*</sup>, V. T. Angelova<sup>2</sup>, R. T. Georgieva-Nikolova<sup>3</sup>, T. R. Veselinov<sup>4</sup>, V. H. Nankova<sup>4</sup>,  
M. M. Nikolova<sup>5</sup>, R. K. Hadjiolova<sup>6</sup>, M. P. Slavova<sup>7</sup>

<sup>1</sup> - Department of Pharmacology and Toxicology, Faculty of Medicine, Medical University of Sofia, Sofia, Bulgaria

<sup>2</sup> - Department of Chemistry, Faculty of Pharmacy, Medical University of Sofia, Sofia, Bulgaria

<sup>3</sup> - Department of Chemistry and Biochemistry, Faculty of Medicine, Medical University of Sofia, Sofia, Bulgaria

<sup>4</sup> - Research Institute of Forensic Science and Criminology, Sofia, Bulgaria

<sup>5</sup> - Middlesex University, School of Health and Education – London, United Kingdom

<sup>6</sup> - Department of Pathophysiology, Faculty of Medicine, Medical University of Sofia, Sofia, Bulgaria

<sup>7</sup> - Department of Biotechnologies, University of Chemical Technology and Metallurgy, Sofia, Bulgaria

Submitted June 10, 2015; Accepted July 15, 2015

Synthetic cannabimimetics are some of the most aggressively marketed narcotic drugs. Most often they are added to herbal incenses or are sold in powder as “bath salts”, “research chemicals/not intended for human consumption”, “plant foods”, etc. In our country for the period of 2010-2013 in herbal incenses were identified JWH-018, JWH-073, MAM-2201, UR-144и STS-135. Analysis of the information about their effects after human’s consumption reveals that they are psychoactive substances often with stronger effects than the marijuana itself. The time of their appearance on the market coincides with their worldwide distribution and almost always precedes their inclusion into the List of forbidden substances. Our legislative system attempts to include the new designer drugs under regulation as quickly as possible.

**Keywords:** cannabimimetics, JWH-018, JWH-073, MAM-2201, UR-144, STS-135

### INTRODUCTION

Synthetic cannabinoids and cannabimimetics are amongst the most aggressively marketed narcotic drugs. To this day, more than a hundred substances of this kind have been synthesized. Synthetic cannabinoids are substances structurally similar to  $\Delta^9$ -tetrahydrocannabinol (THC) – the active component of marijuana. The chemical structure of cannabimimetics does not bear any resemblance to THC, but produces similar pharmacological/physiological effects on the body. Although the two terms are often used as synonyms, it is important from a judicial point of view to distinguish them; as, according to the legislation of many countries cannabinoids are illegal from the moment of their production, unlike cannabimimetics, the regulation of which comes into effect months, and sometimes years, after they have been synthesized.

Around 2004, herbal smoking blends (‘herbal incense’ or ‘spice’) appeared in Europe as an alternative to cannabis. At first it was thought that their cannabis-like effects were herb-induced; however, it was soon rightly suspected that they also had synthetic substances added to them. Synthetic cannabinoids and cannabimimetics are

commonly added to dried narcotic herbs that, when smoked, produce psychopharmacological effects: *Salvia divinorum*, *Mitragyna speciosa* (Kratom), *Turnera aphrodisiaca* (Damiana), *Leonotis leonurus* (Lion’s ear), *Pedicularis densiflora* (Indian Warrior), *Rosa canina* (Dog Rose, rosehip), *Althaea officinalis* (marshmallow), etc. to produce the so called ‘synthetic marijuana’. Synthetic cannabimimetics are first dissolved in acetone or ethanol, which the herbs are sprayed with and dried, producing various concentrations of these potentially toxic substances [1]. They usually come in small packages, wrapped in foil, with attractive labels.

According to our country’s *National Focal Point for Narcotics and Addiction*, during the last few years there has been a steady trend in the use of synthetic cannabinoids and cannabimimetics.

We present our experience with newly-discovered cannabimimetics in our country – the subject of forensic medicine reports for the period 2010-2013. The subjects for analysis are dried herbal blends, reported to the Center for Expert Forensic Analysis and Trials – Research Institute of Forensic Science and Criminology – Ministry of Interior, Sofia, for the purpose of determining their significance in forensic toxicology.

\* To whom all correspondence should be sent:  
E-mail: pandreevagateva@yahoo.com

## METHODS

The following techniques were used for analysis:

1. Visual and microscopic analysis, weighing analysis – conducted on a Sartorius MC 210-S weighing balance, class I accuracy according to The Bulgarian Institute for Standardization (BDS) EN 45501:2001, max – 210 g; min-0.02 g, scale interval (d) 0.0001. The balance has a calibrating certificate from the accredited calibration laboratory Kalibra Bulgaria ltd.

2. Thin-layer chromatography (TLC): TLC plate with adsorbent: silica gel; solvent: chloroform:methanol (9:1); solvent front: 10 cm; developing material: iodine platinate.

3. The following analytical methods were used for measuring the respective proportion of each of the components in the analyzed blends:

a) Gas chromatography: Thermo Finnigan GC Ultra Gas Chromatograph, quartz capillary column EC-5 (30 m × 0.32 mm × 0.25 μm), injector at 270 °C, flame ionization detector at 300 °C, with temperature programming from 160 °C to 290 °C (10 min) with a heating rate of 30°C/min, carrier gas: nitrogen 1.3 ml/min.

b) Gas chromatography: Hewlett Packard 6890 Gas Chromatograph, injector at temperature of 270 °C, quartz capillary column EC™ 20 /15 m × 0.25 mm/ with temperature programming from 100 °C to 290 °C with a heating rate of 15 °C/min, carrier gas: nitrogen 1.5 ml/min. Flame ionization detector with hydrogen 35 ml/min at 300 °C.

4. Gas chromatography was used for identifying the substances in the analyzed samples – mass spectrometry (GC-MS) – Thermo Finnigan Trace GC/MS Gas Chromatograph – column: AT-5MS (30 m × 0.25 mm × 0.25 μm) by Alltech. Temperature programming: 60 °C/4min/ - 15 °C – 290 °C /10min/. Carrier gas: helium at flow rate: 1.0 ml/min. Split injector at split ratio: 1:20 at 270 °C. Interface at 280 °C and ionization chamber at 250 °C. Scan range: 40-460 amu. Ionization mode: electron ionization (EI).

Identification of the obtained mass spectra was done by their comparison with two mass spectral libraries by using computer software.

## RESULTS AND DISCUSSION

The active components were isolated from the vegetal matter using methanol. The procedure is easy to perform and gives fixed results, which is most likely due to the substances being added to the vegetal matter, and therefore not having to be isolated from cell components.

As expected, none of the extracts cross-reacted with the cannabinoid panel of our immunological screening laboratory test (Randox Evidence).

By using the above-described analytical methods and by doing comparison with a database and the existing body of literature, we identified the following compounds: JWH-018, JWH-073, MAM-2201, UR-144 and STS-135. As Bulgarian legislation forbids the use of narcotics, regardless of their effects and the level of impact, the precise concentrations were not further discussed.

### *JWH-018 and JWH-073*

In samples analyzed in 2010 and 2011, JWH-018 (see Table 1), and its butyric analog - JWH-073 (see Table 2) were determined. The literature search revealed that these substances were synthesized at the end of the past century [2], with a high affinity for the endocannabinoid receptors CB1 and CB2. In December 2008, two laboratories – THC Pharma (Germany) and AGES PharmMed (Austria), independently determined the presence of JWH-018 in smoking blends [3]. The same results were obtained in other laboratories across Europe and Japan [4, 5]. A direct link was discovered between JWH-018 and the psychotropic effects of smoking blends in which it was present [6].

Before JWH-018 was made illegal in Western Europe at the beginning of 2009, JWH-073 was found in predominantly low concentrations in smoking blends. Blends that possessed it were mostly regarded as impure [7].

However, after the ban, JWH-073 fully replaced JWH-018 (before its ban in 2011).

The effects of JWH-018 and JWH-073 were tested on animals, and it was found that they are similar to those produced by THC – the classic ‘cannabinoid tetrad’ was observed, which includes hypothermia, analgesia, catalepsy, and locomotion suppression [8, 9]. Moreover, the effects of JWH-073 and, to a greater degree those of JWH-018, were much more clearly expressed than the ones produced by THC.

No systemic research has been done on the effects of JWH-018 and JWH-073 on humans. Information about them is mostly found on Internet forums. The most common mode of use of synthetic cannabinoids is smoking, although peroral use is also possible. The contents of JWH-018 and JWH-073 in smoking blends vary between 2.3 mg/g and 35.9 mg/g, and between 5.8 and 22.9 mg/g, respectively [4, 7].

In humans, the effects usually occur either instantaneously, or in 1 to 10 min after smoking. In different individuals, these last 20 min to 4-6 h, and

they resemble those produced by marijuana: high spirits and euphoria; antistressor effect; creative, philosophical, abstract mental activity; increased sense of hearing, smell, taste, vision; altered body sensations; altered perception of time; analgesia; reduced nausea and increased appetite. Adverse effects: increased heart rate (palpitations); eye redness; dry mouth; impaired short term memory; impaired motor coordination; delayed reactions. Although not well documented, excessive use has been found to produce effects not typically observed in marijuana users – agitation and vomiting [10]. There is a reported case of addiction to Spice Gold (a smoking blend containing JWH-018) (after daily consumption of 3 g for several months, followed by the development of withdrawal syndrome, similar to the one produced by hard drugs [11]). There is also a reported case of acute intoxication with seizures and tachycardia, leading to hospitalization [12]. A recently published systematic literature review on psychopathological events resulting from the use of synthetic cannabimimetics summarized the results of 223 trials, leading to its authors coining the term ‘spicephrenia’ [13]. Although there is currently no scientific evidence, these substances have been

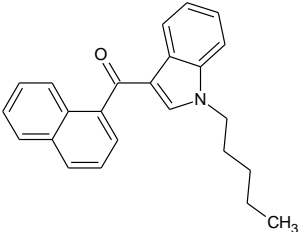
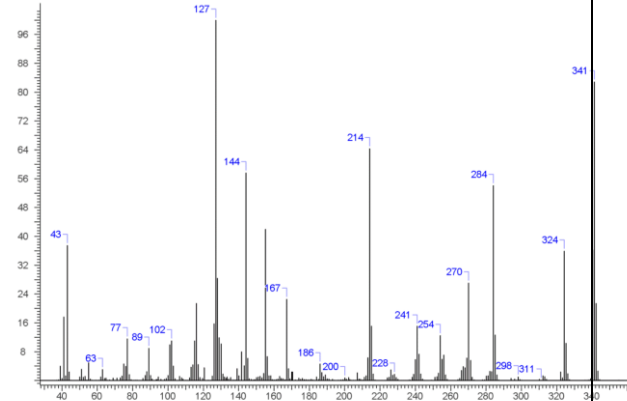
found to trigger acute psychosis in susceptible individuals, and/or exacerbate psychotic episodes in individuals with established psychosis.

A literature search revealed that in February 2011, JWH-018 and JWH-073 were included in the list of “Plants and chemicals with high degree of risk for social health because of the harmful effect of their abuse, prohibited for putting in practice in human and veterinary medicine”.

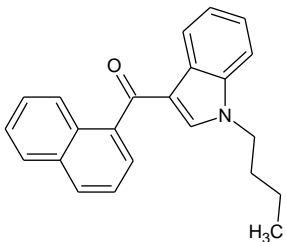
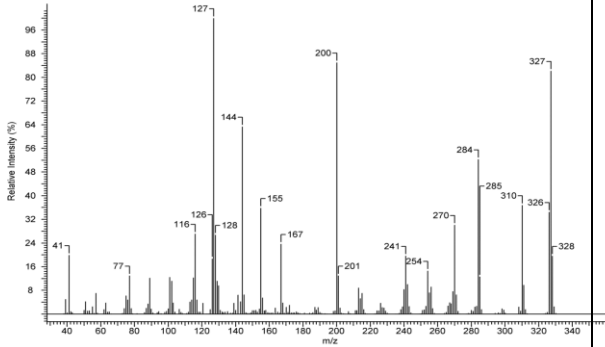
#### MAM-2201

In samples we analyzed in 2012, we established the presence of a substance called MAM-2201 (see Table 3), which is thought to act as a powerful agonist of the cannabinoid receptors. It was first isolated in laboratories in Germany and Netherlands in June 2011, as a component of synthetic cannabimimetic smoking products [14]. MAM-2201 is a new substance developed by ‘research chemical’ suppliers of grey-market recreational drugs. Structurally, MAM-2201 is a hybrid of two known cannabinoids, JWH-122 and AM-2201, which were used as active components of cannabinoid smoking blends, before being internationally banned. MAM-2201 was banned in New Zealand in July 2012.

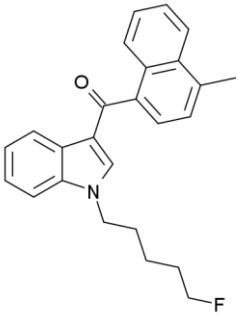
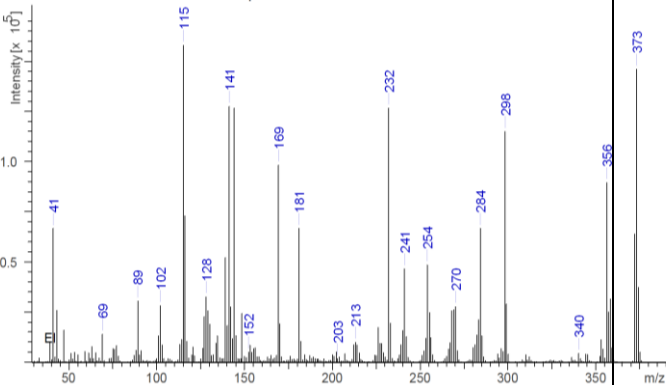
**Table 1.** JWH-018 – general, physical and analytical data

 <p style="text-align: center;">JWH-018</p>	<p>IUPAC name</p> <p>Synonyms</p> <p>Molecular weight</p> <p>Chemical formula</p> <p>Appearance</p> <p>Melting point (°C)</p> <p>GC-MS spectral data</p>	<p>Naphthalen-1-yl-(1-pentylindol-3-yl)methanone</p> <p>AM678, pentyl-3-(1-naphthoyl)indole</p> <p>341.189 g/mol</p> <p>C<sub>24</sub>H<sub>23</sub>NO</p> <p>White to grey powder</p> <p>51.9</p> <p>(Principal GC-MS ions)</p> <p>127.1, 214.2, 270.2, 284.2, 324.3, (341.3 [M<sup>+</sup>])</p> 
--	--	---

**Table 2.** JWH-073 – general, physical and analytical data.

 <p style="text-align: center;">JWH-073</p>	<p>IUPAC name Synonyms Molecular weight Chemical formula Appearance Melting point (°C) GC-MS spectral data</p>	<p>Naphthalen-1-yl-(1-butylindol-3-yl)methanon - 327.16 g/mol C<sub>23</sub>H<sub>21</sub>NO White powder 99.8</p> <p style="text-align: center;">(Principal GC-MS ions) 127.1, 144.1, 200.2, 284.2, 310.3, (327.3 [M<sup>+</sup>])</p> 
--	--	--

**Table 3.** MAM 2201 – general, physical and analytical data.

 <p style="text-align: center;">MAM 2201</p>	<p>IUPAC name Synonyms Molecular weight Chemical formula Appearance Melting point (°C) GC-MS spectral data</p>	<p>(1-(5-Fluoropentyl)-1H-indol-3-yl)(4-methyl-1-naphthalenyl)-methanone AM 2201 4-methylnaphthyl analog; JWH-122 N-(5-fluoropentyl) analog 373.462 g/mol C<sub>25</sub>H<sub>24</sub>FNO White powder 109.4</p> <p style="text-align: center;">(Principal GC-MS ions) 115.2, 141.1, 169.3, 181.1, 232.2, 284.2, 298.1, 356.2, 373.1 [M<sup>+</sup>]</p> 
---	--	---

Internet forum testimonies of herbal incense smokers claim that MAM-2201 does not cause chest tightness, its taste is not very appealing but its effect is stronger and longer-lasting than that of cannabinoids. The minimal effective dose is 500 µg, and the dose-response curve is very steep. In

some cases, panic attacks and vomiting are observed. There is a lack of clinical data for MAM-2201.

In medical literature, several cases of MAM-2201 intoxication can be found. One of them is that of a 31 year-old man of Japanese origin who, after

smoking 300 mg smoking incense through a bong, falls into a transitory acute psychotic state with agitation, aggression, anxiety and vomiting, with a comorbid sympathomimetic syndrome (arterial hypertension, tachycardia, hyperglycemia) [15]. His condition required immediate hospitalization. One hour after smoking, his blood contained 49 mg/ml MAM-2201. His psychological state recovered 1.5 hours after smoking.

Another case is that of a 59 year-old man, with a fatal outcome [16]. The forensic medical report, done on the 4<sup>th</sup> day *post mortem*, established the presence of MAM-2201 in the blood and in a number of tissues; its concentration in the adipose tissue being 124 times higher than that in the blood.

There is also a case of an intranasal ingestion of the powdered substance, paired with the local anesthetic benzocaine, by a 20 year-old individual; who was urgently admitted to the emergency room 6 hours later with agitation, xerostomia, chest pain, severe dyspnea, tachycardia, and hypertonia. These effects are thought to be due to the noradrenalin secretion – one of the supposed mechanisms of the cannabinoid receptor agonists [12].

There is a reported case of seizures and death of a 36 year-old man after a simultaneous intake of several synthetic cannabinoids through smoking blends, including MAM-2201 and UR-144, and amphetamines [17].

At the time we identified MAM-2201 in smoking blends (2012), it was not included in the list of “Plants and chemicals with high degree of risk for social health because of the harmful effect of their abuse, prohibited for putting in practice in human and veterinary medicine”. However, its analog AM-2201 was included, which justified the undertaking of legal action.

#### *UR-144*

In smoking blends analyzed in 2012-2013, the substance UR-144 or KM-X1 (see Table 4) was also identified. Apart from the compound itself, its main pyrolysis product-artefact was also found in the samples; which is due to the molecular rearrangement caused by the high temperature in the GC injector port.

The chemical structure of UR-144 is very similar to that of JWH-018, the first synthetic cannabinoid. The presence of UR-144 in herbal incense was first reported in Korea in 2012, and it quickly spread throughout Europe and New Zealand [18]. The substance was found in Russia, Croatia, Sweden, Germany, Finland, Norway, Hungary, Japan, and the USA.

UR-144 is a clinical candidate developed by Abbott Laboratories, which acts as a full agonist of the peripheral cannabinoid receptors CB2, but with a much lower affinity for the psychoactive CB1 receptors [19]. The CB2 receptors play a role in the perception of pain, and therefore similar compounds are of medical interest. Despite the relatively low affinity of UR-144 to the CB1 receptors, Internet forum reviews of users of this substance show that it is popularly sought-after for its psychoactive activity.

UR-144 is mainly distributed as a research chemical, in quantities of 0.25 to 100 g. Although it is labeled as ‘unfit for human consumption’, UR-144 is usually smoked like a joint (mixed with tobacco, St. John’s worth, and other herbs). New UR-144-smokers usually start with doses of 0.5-2 mg, and often reach doses of up to 2.5-20 mg (its contents in cigarettes is 0.05%-0.4%). Some users take several doses at a time in order to prolong the effect, which leads to the intake of several tens of mg of the substance in one smoke.

The effect occurs 0.5-2 min after smoking, reaches its peak 3-5 min later, and wears off after 1-2 hours (after 4 hours at high doses). Its users compare its effect to the ones produced by JWH-122, AM-2201, and marijuana. At inhaling, it produces a cocaine-like euphoric and aphrodisiacal effect that comes with an opiate-like tidal feeling, which slowly subsides after 35-40 minutes. During the effect, euphoria, uplifted mood, relaxation, drowsiness, hallucinations, and increased appetite are observed. Most commonly reported adverse effects include anxiety, paranoia, attention deficit, depression and hallucinations, which can last for several days. At high doses, especially during the first few minutes, the hallucinogen effect is very intensive. Overdosing causes tachycardia, nausea, disorientation, dysphoria, blurred vision, inability to communicate, extreme hallucinations, and loss of consciousness. UR-144 tolerance can be developed, compelling the users to increase the doses they take over time. There is one reported case of an epileptic fit after smoking UR-144 [3].

In 2012, UR-144 was the most commonly found synthetic cannabinoid in laboratories in Russia and Poland. It was the most popular synthetic cannabinoid for 2012. In 2013, two UR-144 analogs were released to the market. In many countries, including the UK, Russia and New Zealand, UR-144 was banned in 2012. At the time we discovered this substance in smoking blends, it was not yet banned in Bulgaria. In 2013, it was included in the list of “Plants and chemicals with high degree of risk for social health because of the

harmful effect of their abuse, prohibited for putting in practice in human and veterinary medicine”.

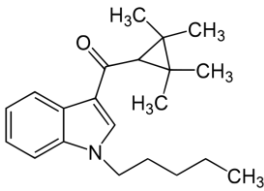
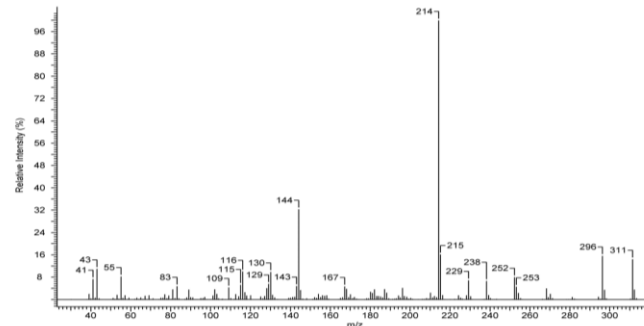
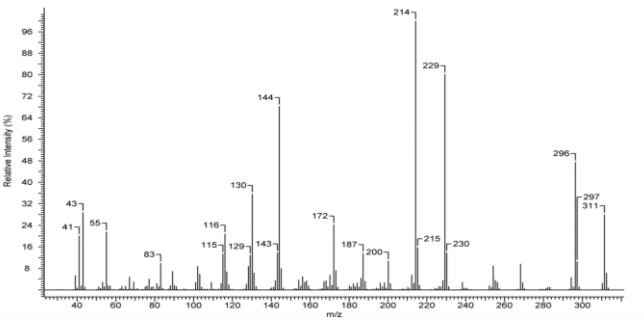
### STS-135

STS-135 is a designer synthetic cannabinoid, which acts as a full powerful agonist to the CB1 and CB2 receptors (see Table 5).

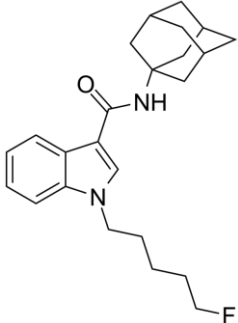
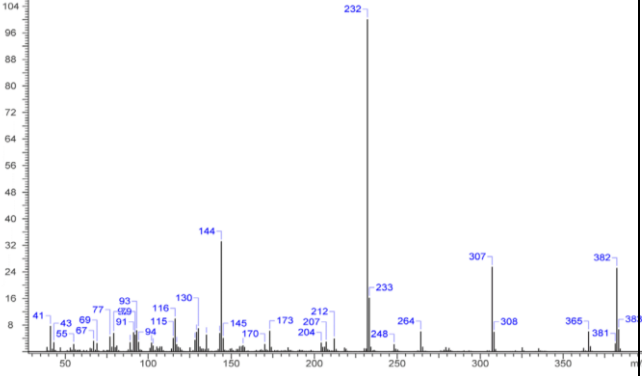
This compound has a unique carboxamide bond between the adamantyl side chain and the indole ring, which allows for it to circumvent regulation. STS-135 has a 5-fluoropentyl side chain, which is a commonly found modification in the aminoalkylindole series of designer drugs. It is known that the adamantoyl group is a selective CB1 agonist; the adamantyl carboxamide group is

described in literature and may possess higher affinity for CB2 receptors in the periphery. Similar compounds include AB-001 (1-pentyl-3-(1-adamantoyl) indole), JWH-018 adamantyl carboxamide, AM1248, AKB48, and AKB48-N-(5-fluoropentyl) analogs. The origins of the name of STS-135 are unknown, but it is thought that it is derived from the name of the last US space mission; a metaphor for the psychoactive activity of the substance. There are reported cases of abuse of compounds with the adamantoyl structure, and unpublished reports about the presence of STS-135 in synthetic cannabinoid samples.

**Table 4.** UR-144 – general, physical and analytical data of the compound (A) and its main pyrolysis product (B)

 <p style="text-align: center;">UR-144</p>	<p>IUPAC name</p> <p>Synonyms</p> <p>Molecular weight</p> <p>Chemical formula</p> <p>Appearance</p> <p>Melting point (°C)</p> <p>GC-MS spectral data of UR-144 (A) and its main pyrolysis product (B)</p>	<p>(1-Pentylindol-3-yl)-(2,2,3,3-tetramethylcyclopropyl)methanone</p> <p>KM-X1</p> <p>311.461 g/mol</p> <p>C<sub>21</sub>H<sub>29</sub>NO</p> <p>White powder</p> <p>68.0</p> <p style="text-align: center;">(Principal GC-MS ions)</p> <p style="text-align: center;">116.2, 130.1, 144.1, 214, 229.1, 296.0, 311.1[M<sup>+</sup>]</p> <p>(A)</p>  <p>(B)</p> 
--	---	---

**Table 5.** General, physical and analytical properties of STS-135

 <p>STS-135</p>	<p>IUPAC name N-adamantyl-1-fluoropentylindole-3-carboxamide</p> <p>Synonyms 5F-APICA 5-fluoro-APICA</p> <p>Molecular weight 382.51 g/mol</p> <p>Chemical formula C<sub>24</sub>H<sub>31</sub>FN<sub>2</sub>O</p> <p>Appearance White powder</p> <p>Melting point (°C) 138.6</p> <p>GC-MS spectral data (Principal GC-MS ions)</p>	<p>116.2, 130.1, 144.1, 173.1, 232.1, 307.0, 365.1, 382.3[M<sup>+</sup>]</p> 
--	--	--

There are no official statements on the pharmacological profile of STS-135 as of yet. The only information available is on Internet forums, provided by users of the substance: there are short-term panic attacks of 10-15 minutes. During smoking and evaporating, the substance gives off an unpleasant smell. The effect is pleasant, but less euphoric than that of cannabis. Some report a ‘bipolar effect’ – exaltation, followed by depression. It also causes a certain hallucinogenic effect.

### CONCLUSION

The manufacturing, distribution and use of illegal drugs and chemical substances has seen dynamic changes over the last few years, as, together with the wide distribution of explosives, the so-called ‘designer drugs’ or ‘legal highs’ have had an unprecedented success. These are uncontrolled substances whose effects are similar to the controlled ones. Manufactured in semi-legal or illegal laboratories, widely marketed on the Internet, and with misleading labels such as ‘research chemicals/unfit for human consumption’, or as ‘smoking blends’, ‘bath salts’, ‘plant food’, etc., they are either structural analogs of controlled substances, or have different structure but similar effects. Laws for the regulation of these substances are too slow to come into effect, compared to the

speed with which the substances are distributed on the market. Since 2010, designer synthetic cannabinimimetics are categorized by the World Anti-Doping Agency as ‘banned substances prohibited in sport’.

Most of these substances were originally developed by scientists researching the CB1 and CB2 receptors in the human body. Often, the newly-synthesized cannabinoids and cannabinimimetics prove to be more powerful than THC. Therefore it is difficult, and in the case of the cannabinimimetics – downright impossible, to be detected by standard marijuana screening tests. That and the uncontrolled status of synthetic cannabinimimetics at their initial release to the market, is the reason behind the mass consumption of ‘synthetic marijuana’.

### REFERENCES

1. W. E. Fantegrossi, J. H. Moran, A. Radominska-Pandya, P. L. Prather, *Life Sci.*, **97**, 45, (2014).
2. J. L. Wiley, D. R. Compton, D. Dai, J. A. Lainton, M. Phillips, J. W. Huffman, B. R. Martin, *J. Pharmacol. Exp. Ther.* **285**, 995, (1998).
3. A. Grigoryev, P. Kavanagh, A. Melnik, S. Savchuk, A. Simonov, *J. Anal. Toxicol.*, **37**, 265, (2013).
4. N. Uchiyama, R. Kikura-Hanajiri, J. Ogata, Y. Goda, *Forensic Sci Int.*, **198**, 31, (2010).

5. V. Auwärter, S. Dresen, W. Weinmann, M. Müller, M. Pütz, N. Ferreirós, *J. Mass Spectrom.*, **44**, 832, (2009).
6. K. Atwood, J. W. Huffman, A. Straiker, K. Mackie., *Br. J. Pharmacol.*, **260**, 585, (2010).
7. R. Lindigkeit, A. Boehme, I. Eiserloh, M. Luebbecke, M. Wiggermann, L. Ernst, T. Beuerle, *Forensic Sci. Int.*, **191**, 58, (2009).
8. J. L. Poklis, D. Amira, L. E. Wise, J. M. Wiebelhaus, B. J. Haggerty, A. Poklis, *Forensic Sci. Int.*, **220**, 91, (2012).
9. R. Marshall, T. Kearney-Ramos, L. K. Brents, W. S. Hyatt, S. Tai, P. L. Prather, W. E. Fantegrossi, *Pharmacol Biochem Beha.*, **124C**, 40, (2014).
10. A.Y. Hopkins, B. L. Gilchrist, *J. Emerg. Med.*, **45**, 544, (2013).
11. U. S. Zimmermann, P. R. Winkelmann, M. Pilhatsch, J. A. Nees, R. Spanage, K. Schulz, *Dtsch. Arztebl. Int.*, **106**, 464, (2009).
12. J. Lapoint, L. P. James, C. L. Moran, L. S. Nelson, R. S. Hoffman, J. H. Moran, *Clin. Toxicol. (Phila)*, **49**, 760, (2011).
13. D. Papanti, F. Schifano, G. Botteon, F. Bertossi, J. Mannix, D. Vidoni, M. Impagnatiello, E. Pascolo-Fabrizi, T. Bonavigo, *Hum. Psychopharmacol.*, **28**, 379, (2013).
14. K Simolka, R Lindigkeit, HM Schiebel, U Papke, L Ernst, T Beuerle, *Anal. Bioanal. Chem.*, **404**, 157, (2012).
15. A. Derungs, A. E. Schwaninger, G. Mansella, R. Bingisser, R. Kraemer, M. E., Liechti *Forensic Toxicol.* **31**, 164, (2013).
16. T. Saito, A. Namera, N. Miura, S. Ohta, S. Miyazaki, M. Osawa, S. Inokuchi, *Forensic Toxicol.*, **31**, 333, (2013).
17. N. Schaefer, B. Peters, D. Bregel, S. Kneisel, V. Auwärter, V. Schmidt, A. H. Ewald, *Toxicchem. Krimtech.*, **80**, 248, (2013).
18. H. Choi, S. Heo, E. Kim, B. Y. Hwang, C. Lee, J. Lee, *Forensic Toxicol.*, **31**, 86, (2013).
19. J. M. Frost, M. J. Dart, K. R. Tietje, T. R. Garrison, G. K. Grayson, A. V. Daza, O. F. El-Kouhen, L. N. Miller, L. Li, B. B. Yao, G. C. Hsieh, M. Pai, C. Z. Zhu, P. Chandran, M. D. Meyer, *J. Med. Chem.*, **51**, 1904, (2008).

## СИНТЕТИЧНИ КАНАБИМИМЕТИЦИ, УСТАНОВЯВАНИ В СМЕСКИ ЗА ПУШЕНЕ НА ТЕРИТОРИЯТА НА БЪЛГАРИЯ– ТОКСИКОЛОГИЧНО ЗНАЧЕНИЕ

П. А. Гатева<sup>1\*</sup>, В. Т. Ангелова<sup>2</sup>, Р. Т. Георгиева-Николова<sup>3</sup>, Ц. Р. Веселинов<sup>4</sup>, В. Х. Нанкова<sup>4</sup>, М. М. Николова<sup>5</sup>, Р. К. Хаджиолова<sup>6</sup>, М. П. Славова<sup>7</sup>

<sup>1</sup>Катедра по фармакология и токсикология, Медицински факултет, Медицински университет - София България

<sup>2</sup>Катедра по химия, Фармацевтичен факултет, Медицински университет-София, София България

<sup>3</sup>Катедра по химия и биохимия, Медицински факултет, Медицински университет – София, София, България

<sup>4</sup>Научен институт по съдебна медицина и криминология, София, България

<sup>5</sup>Middlesex University, School of Health and Education – London, United Kingdom

<sup>6</sup>Катедра по патофизиология, Медицински факултет, Медицински университет - София България

<sup>7</sup>Катедра по биотехнологии, Химикотехнологичен и металургичен университет, София, България

Получена на 10 юни 2015 г., приета на 15 юли 2015 г.

(Резюме)

Синтетичните канабимиметици са едни от най-агресивно налагащите се на пазара наркотични вещества. Най-често те се добавят към растителни смеси за пушене или се продават под формата на прах като „соли за вана“, „химикали за анализ, непредназначени за употреба от хора“, „растителни храни“ и др. В нашата страна за периода от 2010 до 2013 г. в смеси за пушени са идентифицирани JWH-018, JWH-073, MAM-2201, UR-144 и STS-135. Анализът на информацията относно ефектите им след консумирането им от хора показва, че те са психоактивни субстанции, често с по-силни ефекти от самата марихуана. Времето на тяхната поява на пазара съвпада със световното им разпространение и почти винаги предшества включването им в Списъка със забранени вещества. Нашата правна система се стреми да включва колкото се може по-бързо новите дизайнерски дроги в регулация.

## Hydrogen sorption of magnesium plates deformed by surface mechanical attrition treatment

Á. Révész<sup>1\*</sup>, C. Szilágyi<sup>1</sup>, T. Spassov<sup>2</sup>

<sup>1</sup>Department of Materials Physics, Eötvös University, Budapest, H-1518, P.O.B. 32, Budapest, Hungary

<sup>2</sup>Faculty of Chemistry and Pharmacy, University of Sofia “St. Kl. Ohridski”, 1 J. Bourchier Str., 1164 Sofia, Bulgaria

Received June 26, 2015; Revised December 1, 2015

Surface modification attrition treatment was carried out on commercial magnesium disks in a SPEX 8000 shaker mill. Morphological and microstructural evolution during the severe plastic deformation process have been investigated by scanning electron-microscopy and X-ray diffraction line profile analysis, respectively. Complementary hydrogen absorption experiments in a Sieverts'-type apparatus revealed that hydrogen kinetics and the microstructural parameters exhibit correlation.

**Keywords:** Hydrogen storage; Mg-based; Microstructure; Severe plastic deformation; Surface modification by attrition treatment.

### INTRODUCTION

Magnesium attracts high interest in solid state hydrogen storage due to its remarkable gravimetric storage capacity, lightness and moderate cost [1, 2]. Unfortunately, the relatively high stability of the hydride phase and the poor  $\text{Mg} \leftrightarrow \text{MgH}_2$  kinetics retain the wide-spread application of commercial  $\text{MgH}_2$  [3]. In order to overcome these obstacles, magnesium is extensively subjected to severe plastic deformation (SPD) by different technical routes [4, 5]. Among them high energy ball milling (HEBM) is applied, since this technique leads to the most effective particle-size and crystallite-size reduction [3, 6-8], which significantly enhance the hydrogen sorption kinetics due to the increased volumetric density of grain boundaries and lattice defects [9, 10]. Moreover, the addition of metal or metal-oxides catalyst powders to magnesium [9, 11, 12] results in the thermo-dynamical destabilization of  $\text{MgH}_2$  [8]. Notwithstanding that HEBM exhibits several advantages, drawbacks are also present due to powder processing, i.e. surface oxidation, large energy consumption, the necessity of an inert atmosphere, a potential fire risk and the difficulty of industrial level production.

These disadvantages of HEBM have extensively been eliminated very recently by novel bulk SPD techniques, including high-pressure torsion (HPT) [13-16], cold rolling [17-19] and equal-channel angular pressing [20-23]. These bulk methods have numerous benefits, i.e. the process is less intensive than HEBM, scaling up to larger quantities at a lower cost has a larger potential, impurity

concentration is lower and causes less safety concerns [20].

Recently, an alternative SPD method was invented by Lu and coworkers by modifying the surface layer of a bulk material by mechanical attrition [24, 25]. Conventional surface-modified techniques usually involve chemical reactions resulting in an optimized mechanical, tribological or chemical structure of the surface layer in order to improve the general performance of the end-product. Nevertheless, the change of the surface microstructure by decreasing the grain size of the top-most layer of the bulk material can also accelerate the different reactions. Namely, the surface mechanical attrition treatment (SMAT) technique involves repeated multidirectional impacts by flying balls to induce severe plastic deformation in the surface layer of a target sample accompanied with large grain boundary misorientation, formation of dislocation blocks and surface nanocrystallization [26]. This nanocrystalline surface layer becomes chemically active, promoting the effectiveness of subsequent treatments such as nitriding [24] and chromizing [27]. Examination of the Mg alloy subjected to SMAT indicated an improved wear resistance of the surface nanocrystalline layer with an average grain size of  $30 \pm 5$  nm [28, 29]. As a result of the SMAT process, the micro-hardness of a biodegradable Mg-alloy has increased considerably in the near-surface region, however, the high dislocation density and abundant grain boundaries have severely weakened the corrosion resistance [30]. Cross sectional structural investigations revealed that the SMAT affected layer can be subdivided into three zones, i.e. an ultrafine grain zone at the top surface, a subsurface transition zone and

\* To whom all correspondence should be sent:  
E-mail: reveszadam@ludens.elte.hu

a deformed zone where the initial grains are only plastically deformed [31]. The enhanced hardening achieved by the non-uniform deformation and grain-size gradient microstructure during the SMAT technique can satisfactorily be correlated by the physical model of Li et al. [32].

In the present experiment, we applied the SMAT technique on commercial Mg disks for different treatment times to generate a different microstructure in the severely deformed top layer. We demonstrate the correlation of hydrogen absorption kinetics and the microstructure obtained by applying the Convolutional Whole Profile Fitting (CMWP) algorithm of X-ray line profiles.

## EXPERIMENTAL

### *SMAT processing*

The mechanical treatment by the SMAT technique was carried out on commercial magnesium specimens (Goodfellow #MG007918) in a SPEX 8000 mixer mill. The conventional end cap of the container was replaced by a well-attached Mg disk target (50 mm in diameter and 5 mm in thickness). In order to ensure an approximately homogeneous distribution of the impacts, the stainless steel vial was filled with plenty hardened steel balls. Based on preliminary experiments [33], we applied 40 balls with a diameter of 6.35 mm and 12 balls with a diameter of 12.5 mm for different treatment times (15 min, 30 min and 90 min). The whole SMAT process was carried out in air. It is noted that the use of a few balls can lead to a non-uniform distribution of the impact points, while too many balls result in many ball-to-ball collisions and a reduced impact velocity.

### *Microstructural characterization*

Microstructural characterization of the surface of the SMATed disks was performed by X-ray powder diffraction (XRD) with Cu-K $\alpha$  radiation on a Philips X'pert powder diffractometer in  $\theta$ -2 $\theta$  geometry. The instrumental pattern was measured on NIST SRM660a LaB6 peak profile standard material.

The recorded X-ray diffraction patterns have been evaluated by the CMWP fitting procedure developed by prof. T. Ungár and co-workers [34]. Briefly, the CMWP analysis incorporates the direct fit of the whole of the X-ray diffractogram as measured by summing up the background, theoretically constructed profile functions and measured instrumental profile. These profile functions are calculated for each Bragg-reflection

as the inverse Fourier transform of the product of the size and strain of Fourier coefficients and the Fourier coefficients of the corresponding measured instrumental profile [35]. In the simplest version of the CMWP analysis it is assumed that the crystallites are spherical and obey lognormal size distribution:

$$G(x) = (2\pi)^{-1/2} \sigma^{-1} x^{-1} \exp[-(\ln(x/m))^2/2\sigma^2], \quad (1)$$

where  $\sigma$  and  $m$  are the variance and median of the distribution, respectively. Besides the microstructure size parameters, the line profile analysis provides the strain parameters, the average dislocation density ( $\rho$ ) and effective outer cut-off radius of dislocations ( $R_e$ ). From the available data, the average coherently scattering crystallite size can be determined [34] as:

$$\langle D \rangle = m \exp(2.5\sigma^2), \quad (2)$$

More details of the fitting algorithm and its systematic application to ball-milled Mg-based powders can be found elsewhere [10, 35, 36].

The morphology was studied on a FEI QUANTA 3D dual beam scanning electron microscope (SEM). The local composition was quantitatively determined by energy dispersive X-ray (EDX) analysis.

### *Hydrogen sorption kinetics*

Hydrogenation kinetic curves of the SMAT processed Mg samples were measured by a Sieverts'-type apparatus (PCT) at 573 K. The initial hydrogen pressure was set as 1 MPa. For details, see [15].

## RESULTS AND DISCUSSION

The microstructural variations associated with the SMAT process of commercial Mg disks can be monitored in Fig. 1. The diffractograms carried out on the topmost surface of all treated states are evidently characterized by the peaks of hexagonal Mg (JCPDS 35-0821). As the milling commences, the breadth of the Bragg-peaks changes slightly, indicating a variation of lattice strain and average grain-size induced by the severe plastic deformation during the surface modification. In addition, faint diffraction peaks corresponding to the MgO phase emerge at the end of the treatment process. As a result of the surface treatment, one might expect some evolving anisotropy, nevertheless the relative intensities of the Mg-peaks change only negligibly, contrary to other different SPD-processed Mg-alloys [15, 23]. An example of the CMWP fitting procedure is presented in Fig. 2, where the measured diffractogram corresponding to

the sample SMATed for 15 min, the fitted pattern and the difference plot between the measured and fitted patterns are presented. An obvious correlation between the measured and fitted pattern is clear, however slight differences occur at the high intensity peak centers.

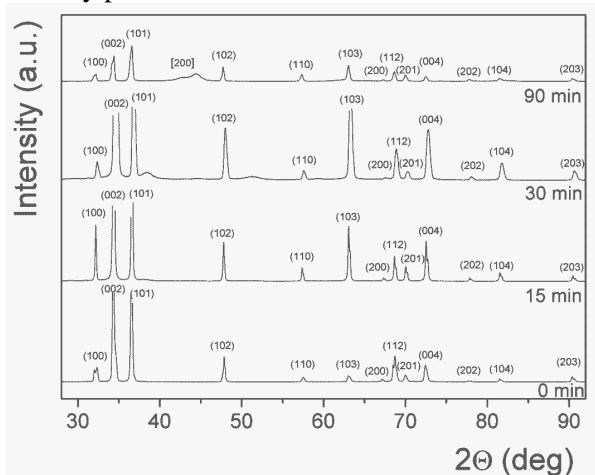


**Fig. 1.** XRD patterns taken from the surface of the Mg plates treated for different times. The brackets (...) and [...] denote the Bragg-peaks of hexagonal Mg and MgO, respectively.

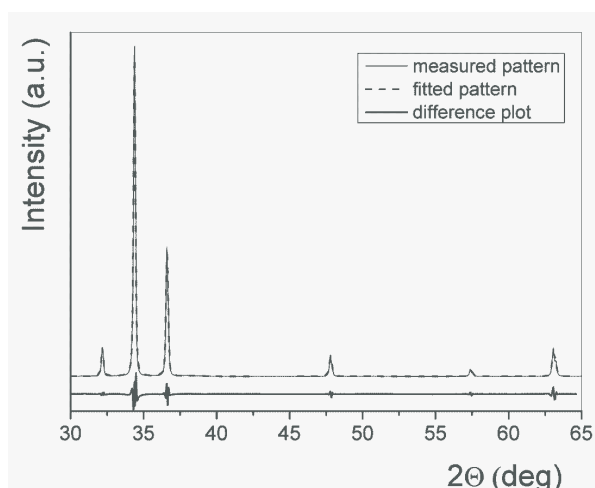


**Fig. 2.** Measured XRD pattern of the Mg disk SMATed for 15 min, the function fitted by the CMWP method and the difference between the measured and fitted data.

The median and the variance of the magnesium crystallite-size distribution as a function of the SMAT procedure time determined by the CMWP procedure can be realized in Fig. 3. As seen, the  $m$  value decreases continuously from the initial value of 29 nm to 18.5 nm at the early stages of the treatment time, however, a remarkable increase up to 32.4 nm is noticed after 90 min. At the same time,  $\sigma$  gradually decreases for up to 30 min from 0.74 to 0.58 and then obeys a subsequent increase (0.81) at the end of the SMAT treatment. From the calculated data of  $m$  and  $\sigma$ , the corresponding

normalized log-normal distribution functions can be plotted, see Fig. 4. A simultaneous shift of the distribution maxima to lower values and a significant narrowing of the histograms up to 30 min of SMAT treatment are evidenced from the curves, indicating that not only a crystallite-size reduction occurs in the uppermost layers of the Mg disks, but a homogenization on the nanoscale also takes place. Surprisingly, these phenomena do not continue until the end of the SMAT process, on the contrary, longer treatment time exhibits a wider distribution of the crystallite size referring to a relatively more inhomogeneous microstructure. Moreover, the right-hand sidetail of the distribution function becomes more pronounced, corresponding to the formation of larger crystallites.

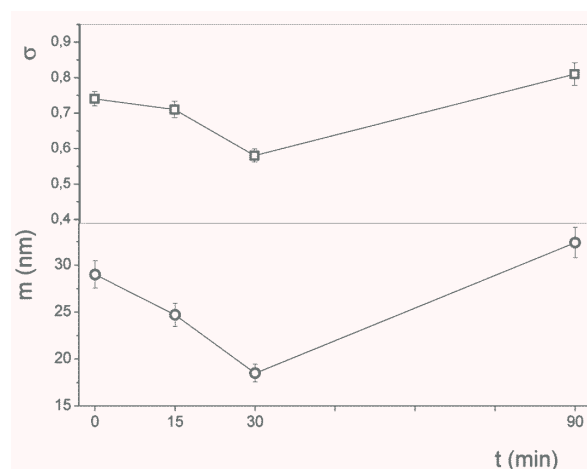


**Fig. 3.** Variation of the median ( $m$ ) and the variance ( $\sigma$ ) as a function of treatment time.

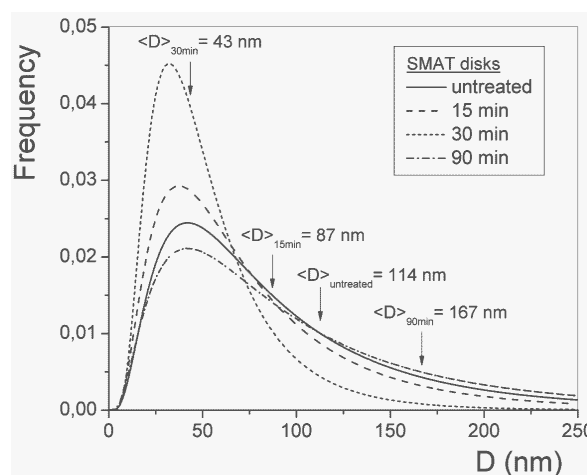


**Fig. 4.** Crystallite size distribution functions of the Mg disks. The volume averaged crystallite size ( $\langle D \rangle = m \exp(2.5\sigma^2)$ ) for each treatment time is also denoted.

The calculated volume averaged crystallite size values ( $\langle D \rangle$ ) are plotted in Fig. 5. As one can conclude, the SMAT process changes the microstructure of the top deformed layer considerably,  $\langle D \rangle$  decreases by a factor of 3 (to 43

nm) after 30 min of treatment. Thereafter some kind of recrystallization takes place, reaching a final value of  $\langle D \rangle = 167$  nm. As described above, the CMWP analysis provides also the strain parameters, in our case the average lattice defect density, i.e. the dislocation density plays a crucial role. Fig. 5 also presents the variation of  $\rho$  as a function of the surface treatment time. A roughly linear increase can be noticed reaching a maximum value of  $\rho = 2.5 \cdot 10^{13} \text{ m}^{-2}$  after finishing the SMAT process. This value is slightly lower than that as found for ball-milled Mg powder [35] and an Mg-alloy processed by equal channel angular pressing [37]. Despite the large defect density, the obtained average defect distance  $L \geq 200$  nm ( $L = \rho^{-1/2}$ ) exceeds the average crystallite size  $\langle D \rangle$  at any treated state. Consequently, a significant portion of the crystallites can be considered as defect-free. In addition, as obtained from the analysis, the severe plastic deformation during SMAT favors the formation of  $\langle a \rangle$ -type dislocations with a Burgers' vector  $b = \frac{1}{3} \langle \bar{2}110 \rangle$ , exhibiting the lowest formation energy among the possible types of dislocations. The relative fraction of  $\langle a+c \rangle$  and  $\langle c \rangle$ -type of dislocations is negligible.

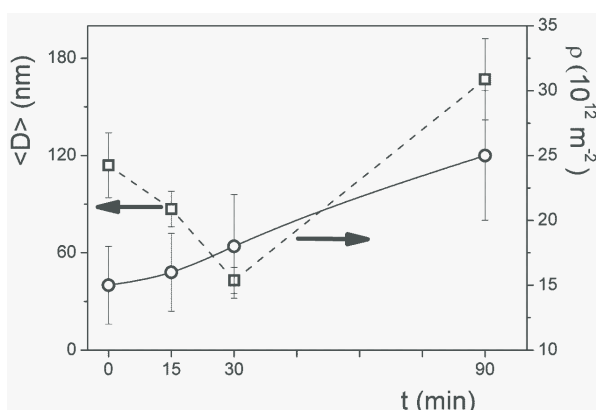


**Fig. 5.** Variation of the average crystallite size ( $\langle D \rangle$ ) and the average dislocation density ( $\rho$ ) as a function of the SMAT treatment time.

SEM images taken on the cross-section of the sample SMATed for the longest treatment time (90 min) explain some aspects of the relevant XRD pattern and exhibit several interesting features concerning the morphology of the severely deformed top layer (Fig. 6). As the low magnification micrograph (250x) indicates, the surface of the treated sample is uneven, clear signs of surface shearing and folding are visible and can be divided up into well-separated areas of different contrast. In some areas the formation of a non-contiguous bright surface layer is observed. One might also notice that cracks perpendicular to the surface, which are favorable for accelerated

hydrogen diffusion, penetrate into the bulk regions. At higher magnification (1000x) it is clear that the surface layer is not uniform, its thickness spans over a wide range with an average value of 22  $\mu\text{m}$ . The results of the EDS elemental analysis carried out on three different regions (denoted by rectangles) can be found in Table 1.

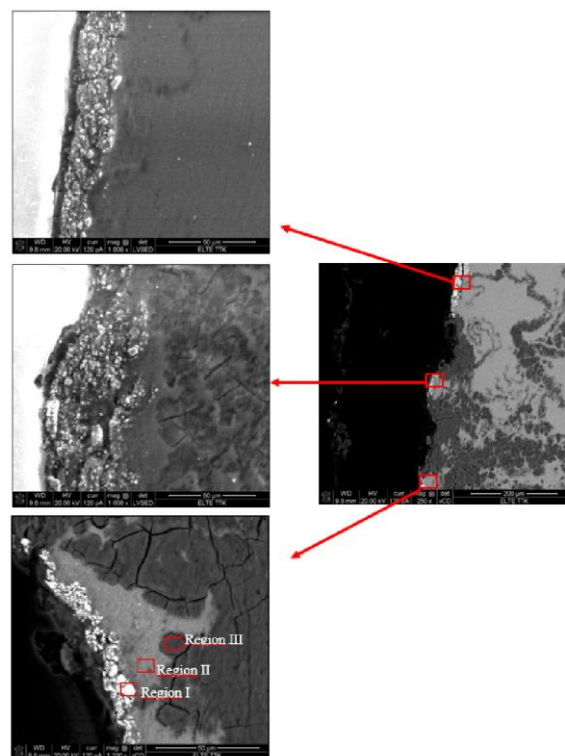


**Fig. 6.** SEM images taken on different parts of the cross section of the disk treated for 90 min.

**Table 1.** Elemental concentrations of the three different regions obtained on the cross section of the Mg disk treated for 90 min of SMAT.

Element	Region I	Region II	Region III
	Atomic percent		
Mg	76,41	99,10	99,75
Fe	20,93	0,33	0,14
Ni	1,85	0,10	0,04
Nb	0,66	0,23	0,07
Al	0,15	0,24	0,00

Concentrations averaged for the brightest white area (Region I) are significantly enriched in iron. Regions II and III are abundant in magnesium, the contrast difference may originate from the different iron and trace element content. At first glance, the detected high iron content at some positions of the surface layer is surprising, since no elemental Fe could be identified on the corresponding XRD pattern (see Fig. 1). Henceforth, it is assumed that iron is dissolved in the Mg-lattice and on the grain boundaries among the individual crystallites, even though Fe is immiscible in Mg according to the

equilibrium phase diagram [38]. Nevertheless, the extreme severe plastic deformation occurring at the contact points between the target and the balls may result in highly non-equilibrium processes that can promote some solubility of iron in Mg. The detected significant amount of iron presumably originates from the milling media, i.e. the steel vial and the balls. During the initial stages of the SMAT process the bombarded Mg-targets become harder and physically active. After a certain amount of processing time, the abundant ball-to-target collisions can induce some removal of hardened Mg particles (chips) from the top layer. Later on these particles are mixed with iron debris in the milling container due to the ball-to-ball collisions. As a final step, this powder mixture is re-deposited onto some parts of the fresh and active surface of the target disk forming the observed non-contiguous iron-rich top surface layer.

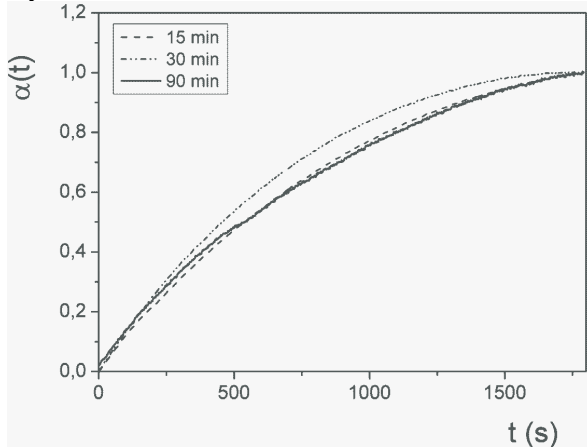


**Fig. 7.** Normalized hydrogen kinetic absorption curves of the Mg plates, treated for different SMAT times.

Normalized hydrogen absorption kinetic data ( $\alpha$ ) for the different Mg plates obtained at 573 K are presented in Fig. 7. All the specimens absorb hydrogen almost without activation, as the maximum capacity is reached after the first full absorption-desorption cycle. The detectable maximum capacity of the disks increases gradually with the SMAT treatment time, confirming the fact that Mg or Mg-based alloys processed by SPD under air are able to absorb hydrogen [39]. As one will also notice, the initial absorption kinetics is fast for all samples, reaching 50% of hydriding within 500s. As the CMWP results indicate (see Figs. 4 and 5), the specimen treated for the longest time (90 min) suffers a recrystallization of the nanocrystalline Mg-grains, however, it exhibits the largest defect density. Henceforth, the observed increase in the maximum H-capacity can be attributed mainly to the lattice defects (dislocations)

generated during the heavy shear deformation during the SMAT process which can act as hydrogen absorption sites in the grain interiors by enhancing the diffusion of the H atoms, while the role of the grain boundaries and particle surfaces is remarkably less important. In a recent paper we have shown that abundant lattice defects have a crucial role in the creation of new and easily accessible hydrogen sites in Mg-Ni alloys produced by HPT [15]. Moreover, Horita and co-workers demonstrated noticeable hydrogen storage performance in coarse-grained MgNi<sub>2</sub> processed by HPT due to the intense anisotropic strain, although this compound possesses no measurable capacity under equilibrium conditions [13].

The normalized absorption curves for all treatment times can satisfactorily be fitted by the contracting volume function (CV) [40]. In brief, this model is valid when the nucleation starts at the surface of the particle and growth takes place from the surface into the bulk and the growth of the new phase occurs with a constant interface velocity. The kinetics can then be described by:

$$\alpha_{CV}(t, R) = 1 - (1 - k_{CV}t)^n, \quad (3)$$

where  $k_{CV}$  is a reaction constant and can be given as  $k_{CV} = u/R$ , where  $u$  is the velocity of the hydride metal interface motion and  $R$  is the average crystallite radius.  $n$  depends on the dimensionality of the growth, with  $n = 3$  for three-dimensional and  $n = 2$  for two-dimensional growth. The parameters obtained from the CV fits are listed in Table 2. As realized, the dimensionality parameter increases monotonously with the treatment time referring to a more isotropic hydride formation. The  $u$  value is significantly the greatest for the disk processed for 90 min of SMAT, indicating that the growth velocity of the hydride phase is the largest for this specimen, in accordance with the above findings, i.e. despite the larger average crystallite size, the abundant lattice defects account for the observed H-storage performance. In addition, we can further assume that iron as a catalyst can also influence the hydrogenation of the Mg-disks processed by the SMAT technique.

**Table 2.** Fitting parameters of the CV-model for different times.

Treatment time (min)	$k_{CV} \left(\frac{1}{s}\right)$	$n$	$u \left(\frac{nm}{s}\right)$
15	$(4,686 \pm 0,010) \cdot 10^{-4}$	$2,378 \pm 0,007$	$0,020 \pm 0,024$
30	$(4,997 \pm 0,009) \cdot 10^{-4}$	$2,669 \pm 0,006$	$0,003 \pm 0,014$
90	$(4,112 \pm 0,033) \cdot 10^{-4}$	$2,798 \pm 0,029$	$0,082 \pm 0,027$

## CONCLUSIONS

In this study commercial Mg disks were subjected to intense plastic deformation by SMAT. The CMWP analysis of X-ray line profiles revealed that the uppermost layer of the disks undergoes significant microstructural changes, i.e. the volume averaged coherent crystallite size reaches a minimum of  $\langle D \rangle = 43$  nm after 30 min of SMAT treatment, while a significant recrystallization takes place after that ( $\langle D \rangle = 167$  nm). During this process, the removal of hardened Mg particles from the top layer occurs which are mixed with iron debris in the milling container later on. As a final step, this powder mixture is re-deposited onto the target disk forming a non-contiguous iron-rich top surface layer. Combined XRD and SEM experiments confirmed that iron forms a non-equilibrium solid solution in the Mg-lattice. At the same time the average lattice defect obeys a roughly linear increase up to a final value of  $\rho = 2.5 \cdot 10^{13} \text{ m}^{-2}$ . The hydrogen absorption curves of all the SMAT processed samples can satisfactorily be fitted by the CV function. By analyzing the fitting parameters, we found that the growth velocity of the hydride phase is the largest for the disk treated for 90 min, indicating that lattice defects (dislocations) generated during the SMAT process can act as hydrogen absorption sites in the grain interiors, while the role of the grain boundaries and particle surfaces is remarkably less important.

**Acknowledgements:** Á.R. is indebted for the János Bolyai Research Scholarship of the Hungarian Academy of Sciences. T.S. is grateful to the FP7 project Beyond Everest. The authors appreciate the support of G. Varga in the SEM experiments. We acknowledge the support of the COST Action MP1103.

## REFERENCES

1. E.C.E. Rönnebro, E.H. Majzoub, *MRS Bull.*, **38**, 452(2013).
2. L. Schlapbach, A. Züttel, *Nature*, **414**, 353(2001).
3. R.A. Varin, T. Czujko, Z.S. Wronski, *Nanomaterials for Solid State Hydrogen Storage*, Springer Science, New York, 2009.
4. R.Z. Valiev, R.K. Ishlamgaliev, I.V. Alexandrov, *Prog. Mater. Sci.*, **45**, 103(2000).
5. Y. Estrin, A. Vinogradov, *Acta Mater.*, **61**, 782 (2013).
6. L. Zaluski, A. Zaluska, P. Tessier, J.O. Ström-Olsen, R. Schulz, *Mater. Sci. Forum*, **225**, 853 (1996).
7. D. Fátay, Á. Révész, T. Spassov, *J. Alloys Compd.*, **399**, 237(2005).
8. W. Oelerich, T. Klassen, R. Bormann, *J. Alloys Compd.*, **315**, 237 (2001).
9. Á. Révész, D. Fátay, T. Spassov, *J. Alloys Compd.*, **434-435**, 725(2007).
10. D. Fátay, T. Spassov, P. Delchev, G. Ribárik, Á. Révész, *Int. J. Hydrogen Energy*, **32**, 2914 (2007).
11. X. Zhao, S. Han, Y. Zhu, X. Chen, D. Ke, Z. Wang, T. Liu, Y. Ma, *J. Solid State Chem.*, **221**, 441 (2015).
12. X. Zhu, L. Pei, Z. Zhao, B. Liu, S. Han, R. Wang, *J. Alloys Compd.*, **577**, 64 (2013).
13. Y. Kusadome, K. Ikeda, Y. Nakamori, S. Orimo, Z. Horita, *Scripta Mater.*, **57**, 751(2007).
14. K. Edalati, A. Yamamoto, Z. Horita, T. Ishihara, *Scripta Mater.*, **64**, 880 (2011).
15. Á. Révész, Zs. Kánya, T. Verebélyi, P.J. Szabó, A.P. Zhilyaev, T. Spassov, *J. Alloys Compd.*, **504**, 83 (2010).
16. T. Hongo, K. Edalati, H. Iwaoka, M. Arita, J. Matsuda, E. Akiba, Z. Horita, *Mater. Sci. Engineering A*, **618**, 1 (2014).
17. S.D. Vincent, J. Lang, J. Huot, *J. Alloys Compd.*, **512**, 290 (2012).
18. J. Bellemare, J. Huot, *J. Alloys Compd.*, **512**, 33 (2012).
19. D.R. Leiva, H.C. de Almeida Costa, J. Huot, T.S. Pinheiro, A.M. Jorge, T.T. Ishikawa, W.J. Botta, *Mater. Res.*, **15**, 813 (2012).
20. V.M. Skripnyuk, E. Rabkin, Y. Estrin, R. Lapovok, *Acta Mater.*, **52**, 405 (2004).
21. V.M. Skripnyuk, E. Rabkin, Y. Estrin, R. Lapovok, *Int. J. Hydrogen Energy*, **34**, 6320 (2009).
22. A.M. Jorge, E. Prokofiev, G.F. de Lima, E. Rauch, M. Veron, W.J. Botta, M. Kawasaki, T.G. Langdon, *Int. J. Hydrogen Energy*, **38**, 8306 (2013).
23. Á. Révész, M. Gajdics, L.K. Varga, Gy. Krállics, T. Spassov, *Int. J. Hydrogen Energy*, **39**, 9911 (2014).
24. W.P. Tong, N.R. Tao, Z.B. Wang, J. Lu, K. Lu, *Science*, **299**, 686 (2003).
25. X. Wu, N. Tao, Y. Hong, G. Liu, B. Xu, J. Lu, K. Lu, *Acta Mater.*, **53**, 681(2005).
26. N.R. Tao, Z.B. Wang, W.P. Tong, M.L. Sui, J. Lu, K. Lu, *Acta Mater.*, **50**, 4603 (2002).
27. Z.B. Wang, J. Lu, K. Lu, *Acta Mater.*, **53**, 2081 (2005).
28. H.Q. Sun, Y.N. Shi, M.X. Zhang, *Surf. Coat. Technol.*, **202**, 2859 (2008).
29. H.Q. Sun, Y.N. Shi, M.X. Zhang, K. Lu, *Surf. Coat. Technol.*, **202**, 3947 (2008).
30. N. Li, Y.D. Li, Y.X. Li, Y.H. Wu, Y.F. Zheng, Y. Han, *Mater. Sci. Engineering C*, **35**, 314 (2014).
31. Y. Samih, B. Beausir, B. Bolle, T. Grosdidier, *Mater. Charact.*, **83**, 129 (2013).
32. J. Li, S. Chen, X. Wu, A.K. Soh, *Mater. Sci. Engineering A*, **620**, 16 (2015).
33. Á. Révész, L. Takacs, *J. Alloys Compd.*, **441**, 111 (2007).
34. G. Ribárik, J. Gubicza, T. Ungár, *Mater. Sci. Engineering A*, **387-389**, 343 (2004).
35. Á. Révész, D. Fátay, *J. Power Sources*, **195**, 6997 (2010).
36. Á. Révész, M. Gajdics, T. Spassov, *Int. J. Hydrogen Energy*, **38**, 8342 (2013).
36. J. Gubicza, K. Máthis, Z. Hegedús, G. Ribárik, A.L. Tóth, *J. Alloys Compd.*, **492**, 166 (2010).

37. A. A. Nayeb-Hashemi, J. B. Clark, L. J. Swartzendruber, *Bulletin of Alloy Phase Diagrams*, **6**, 235 (1985).
38. J. Huot, S.D. Vincent, *J. Alloys Compd.*, **509**, L175 (2011).
39. P.W.M Jacobs and F.C Tompkins: Classification and theory of solid reactions, in *Chemistry of the Solid State*, W.E. Garner (ed.), Butterworth, London, 1955, p.184..

## СОРБЦИЯ НА ВОДОРОД В МАГНЕЗИЕВИ ПЛАСТИНИ ДЕФОРМИРАНИ ЧРЕЗ ПОВЪРХНОСТНО МЕХАНИЧНО ИЗТРИВАНЕ

А. Ревеш<sup>1</sup>, Ц. Силаги<sup>1</sup>, Т. Спасов<sup>2</sup>

<sup>1</sup>Факултет по физика на материалите, Йотвош университет, Будапеща, Н-1518, Р.О.В. 32, Унгария

<sup>2</sup>Факултет по химия и фармация, Софийски университет "Св. Кл. Охридски", 1 Дж. Баучер, 1164 София, България

Получена на 26 юни 2015 г., коригирана на 1 декември 2015 г.

(Резюме)

Търговски магнезиеви дискове са модифицирани чрез повърхностно механично изтриване в мелница тип SPEX 8000. Морфологичните и микроструктурни промени по време на процеса на пластична деформация са изследвани с помощта съответно на сканираща електронна микроскопия и рентгеново дифракционен линеен профилен анализ. Водородно-абсорбционни експерименти с апарат на Сиверт показват наличие на корелация между кинетиката на водородна сорбция и микроструктурните параметри на материала.

## Chemical composition of *Limonium thouinii* (viv.) kuntze (Plumbaginaceae) and the DPPH free radical scavenging activity

M. Lefahal<sup>1</sup>, M. Benahmed<sup>2</sup>, L. Djarri, N. Zaabat<sup>1</sup>, A. E Hay<sup>3</sup>, M. Kamel<sup>1</sup>, M.G. Dijoux Franca<sup>3</sup>, H. Laouer<sup>4</sup>, S. Akkal<sup>1\*</sup>

<sup>1</sup>Université de Constantine1, Unité de Recherche Valorisation des ressources naturelles Molécules bioactives et Analyses Physico-Chimiques et Biologiques, Département de Chimie, Facultés des Sciences exactes, Algérie.

<sup>2</sup>Université Larbi Tébessi Tébessa Laboratoire des molécules et applications, Algérie.

<sup>3</sup>UMR 5557 CNRS-UCBL – Ecologie Microbienne, CESN, ISPB, 8 Avenue Rockefeller, F69373 Lyon cedex, France

<sup>4</sup>Université Ferhat Abbas Sétif 1, laboratoire de valorisation des ressources naturelles biologiques. le département de biologie et d'écologie végétales, Algérie.

Received July 8, 2015, Accepted October 2, 2015

The present work considers the phytochemical investigation and DPPH free radical-scavenging activity of the aerial parts of *Limonium thouinii* (Viv.) Kuntze (Plumbaginaceae). The aerial parts of *Limonium thouinii* (Viv.) Kuntze allow the isolation of four flavonoids: Quercetin, Vitexin, Isoorientin and Cannabiscitrin. Their structures were elucidated on the basis of spectroscopic analysis, including UV, MS and NMR techniques. The DPPH free radical-scavenging activity was evaluated on crude extracts (MeOH, EtOAc and n-BuOH extracts).

**Keywords:** Plumbaginaceae; *Limonium thouinii*; Flavonoids; Free DPPH radical scavenging activity.

### INTRODUCTION

The genus *Limonium* Miller belongs to the Plumbaginaceae family [1]. This genus is represented by 350 species which are growing throughout the world [2]. The flora of Algeria contains 20 species of *Limonium* among which 8 are endemic [3]. Many *Limonium* species were well known in folk medicine for their cure proprieties, such as *L. wrightii* species which is used for the treatment of fever or arthritis [4], the roots of *L. gmelinii* are used in folk medicine as an astringent and for acute gastrointestinal diseases [5]. Furthermore, *L. brasiliense* are employed as an antioxidant medicinal herb [6], whereas *L. sinense* exhibits antiviral activity [7]. Previous phytochemical studies of *Limonium* revealed the presence of different classes of flavonoids such as flavanes, aurones, flavonols and flavonol glycosides [8-14]. Furthermore, it is observed that *Limonium thouinii* has been tested as an inhibitor of corrosion [15]. The present study was aimed to investigate, for the first time, the constituent aerial parts of *L. thouinii*. The fractionation, isolation and structural elucidation yielded four compounds, which are shown in Fig. 1. The crude extracts were evaluated for their DPPH free radical-scavenging activity. Flavonoids are a group of polyphenolic compounds with known properties which include free radical scavenging, due to the presence of the

hydroxyl group in their chemical structures [16].

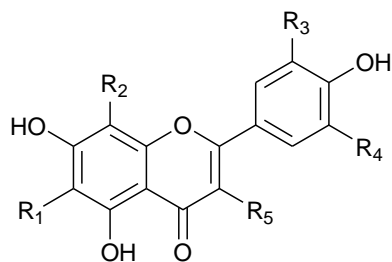
### RESULTS AND DISCUSSION

Structures elucidation compounds 1-4 (fig.1) were identified by means of spectral data as quercetin (**1**), Apigenin 8-C-glucoside (**2**), Luteolin 6-C-glucoside (**3**) and Myricetin-3'-O-glucoside (**4**). These compounds are identified by spectral data, co-chromatography with authentic sampling when possible and confirmed by comparison with data from the literature [16-20]. Compound 1 was identified by spectroscopic techniques (UV-visible and mass spectroscopy), while 2, 3 and 4 were identified by UV-visible and <sup>1</sup>H, <sup>13</sup>C NMR spectra and mass spectroscopy.

Quercetin **1**. UV ( $\lambda_{max}$ , nm), MeOH: 255-368. Mass spectrum (IE) m/z: 302 [M]<sup>+</sup>, 153 [A1 + H], 137 [B2]. [17].

Vitexin (Apigenin 8-C-glucoside) **2**. UV ( $\lambda_{max}$ , nm), MeOH: 266-336. Mass spectrum (ES) m/z : 433 [M+H].  $\delta$  <sup>1</sup>H NMR (300 MHz, DMSO-d<sub>6</sub>): 6.71 (1H, s, H-3), 6.21(1H, s, H-6), 8 (2H, d, J= 8.6 Hz, H-2', H-6'), 6.9 (2H, d, J= 8.6 Hz, H-5', H-3'), 4.75 (1H, d, J= 9.9 Hz, H-1''), sugar protons (3.5- 4), 13.13 (1H, s, OH-5).  $\delta$  <sup>13</sup>C NMR (75 MHz, DMSO-d<sub>6</sub>): 163.8 (C-2), 102.4 (C-3), 182.0 (C-4), 161.2 (C-5), 98.3 (C-6), 163.2 (C-7), 104.6 (C-8), 156.0 (C-9), 104.6 (C-10), 121.6 (C-1'), 128.9 (C-2'), 115.8 (C-3'), 160.4 (C-4'), 115.8 (C-5'), 128.9 (C-6'), 73.4 (C-1''), 70.9 (C-2''), 78.7 (C-3''), 70.5 (C-4''), 81.8 (C-5''), 61.3 (C-6''). [18].

\* To whom all correspondence should be sent:  
E-mail: salah4dz@yahoo.fr



	R1	R2	R3	R4	R5
1	H	H	OH	H	OH
2	H	Glu	H	H	H
3	Glu	H	OH	H	H
4	H	H	OH	O-glu	OH

Fig. 1. Chemical structures of compounds 1-4.

Isoorientin (*Luteolin 6-C-glucoside*) 3. UV ( $\lambda_{max}$ , nm), MeOH: 266-336. Mass spectrum (ES)  $m/z$ : 447 [M-H].

$\delta$   $^1H$  NMR (300 MHz, CD3OD): 6.57 (1H, s, H-3), 6.52(1H, s, H-8), 7.39(1H, d, J= 2.2 Hz, H-2'), 7.41 (1H, dd, J= 2.2; 8.6 Hz, H-6'), 6.93(1H, d, J= 8.6 Hz H-5'), 4.92 (1H, d, J= 9.9 Hz ,H-1"). Sugar protons (3.5- 3.9).  $\delta$   $^{13}C$  NMR (75 MHz, CD3OD): 166.3 (C-2), 103.9 (C-3), 184.0 (C-4), 162.0 (C-5), 109.2 (C-6), 165.0 (C-7), 95.2 (C-8), 158.7 (C-9), 105.2 (C-10), 123.5 (C-1'), 114.1 (C-2'), 147.0 (C-3'), 151.0 (C-4'), 116.8 (C-5'), 120.3 (C-6'), 72.5 (C-1"), 75.3 (C-2"), 80.1 (C-3"), 71.7 (C-4"), 82.6 (C-5"), 62.8 (C-6"). [19].

Cannabiscitrin (*Myricetin-3'-O-glucoside*) 4, UV ( $\lambda_{max}$ , nm), MeOH: 254-371. Mass spectrum (ES)  $m/z$ : 479 [M-H], 317[M-H-162].  $\delta$   $^1H$  NMR (300 MHz, CD3OD): 6.18 (1H, d, J= 2.2Hz, H-6), 6.44 (1H, d, J= 2.2Hz, H-8), 7.57 (1H, d, J= 2.2 Hz, H-2'), 7.73 (1H, d, J= 2.2 Hz, H-6'), 4.93 (1H, H1"). Sugar protons (3.5- 3.96).  $\delta$   $^{13}C$  NMR (75 MHz, CD3OD): 147.2 (C-2), 138.6 (C-3), 177.3 (C-4), 162.0 (C-5), 99.3 (C-6), 165.7 (C-7), 94.5 (C-8), 158.0 (C-9), 104.4 (C-10), 123.3 (C-1'), 109.9 (C2'), 146.9 (C-3', C-5'), 138.6 (C-4'), 111.6 (C-6'), 104.4 (C1"), 74.8 (C-2"), 77.6 (C-3"), 71.2 (C-4"), 78.4 (C-5"), 62.4 (C-6"). [20, 21].

#### DPPH free radical-scavenging activity

The anti-radical activity extracts of *L. thouinii* was evaluated through the ability to scavenge DPPH radicals. The results are represented in Table 1.

The results shown in table1 indicate that all extracts present a weak DPPH free radical-scavenging activity compared to Trolox (TEAC  $_{MeOH}$  = 0.119, TEAC  $_{n-BuOH}$  = 0.081, TEAC  $_{EtOAc}$  = 0.037).

Table 1. DPPH free radical-scavenging activity of *L. thouinii* extracts

	IC <sub>50</sub> ( $\mu$ g/ml)	ARP	TEAC
Trolox	0.106	9.43	1
MeOH	0.89	1.13	0.119
EtOAc	2.87	0.354	0.037
n-BuOH	1.30	0.77	0.081

#### CONCLUSIONS

The phytochemical investigation of *Limonium thouinii* (Viv.) Kuntze revealed the presence of flavonol (Quercetin), two C-glucoside flavones (Vitexin, Isoorientin) and one O-glucoside flavonol (Cannabiscitrin), these four flavonoids are identified for the first time in this species, but Cannabiscitrin is a new compound in the Plumbaginaceae family. The tested extracts of the plant showed a weak DPPH free radical scavenging activity. We have also found the relationship of total flavonoids contents in these extracts with antioxidant activity, may be the hydroxyl group in these chemical structures.

#### EXPERIMENTAL SECTION

The aerial parts of *Limonium thouinii* (Viv.) Kuntze (Plumbaginaceae) was collected during the flowering period, from Setif in the east of Algeria and identified by Prof. H. Laouer (biology and plant ecology department, University of Setif, Algeria). A voucher specimen was deposited in the Herbarium of our laboratory. Voucher specimens of the plant material are deposited in the Herbarium at the department of biology and ecology vegetal, University of Setif (UFAS).

#### Extraction and isolation

Air dried aerial parts of *L. thouinii* (300 g) were soaked in methanol solvent (70%) at room temperature for 72 hours. The residue was filtered and concentrated under reduced pressure to dryness and the residue was dissolved in hot water and kept in the cold overnight. After filtration the aqueous solution was successively extracted with ethyl acetate and n-BuOH. The n-BuOH extract (5g) was subjected to a column polyamide MN SC6 and eluted with a gradient of Toluene-MeOH with increasing polarity to give ten fractions (F1-F10). The fractions F5 and F6 were applied to a preparative PC on Watman n<sup>o</sup>3 paper using acetic acid 15%, then by preparative TLC on polyamide DC6 to yield compounds: 1 (10mg), 2 (8mg), 3 (30mg) and 4 (11mg).The structures of the isolated compounds were elucidated by spectral analysis

mainly MS, UV, H 1 NMR and C 13 NMR as well as by comparing their spectroscopic data with those reported in the literature.

#### DPPH free radical-scavenging activity

The free radical scavenging capacity of the *L. thouinii* extracts were determined by using DPPH• (1, 1-diphenyl-2-picryl-hydrazyl), according to the method of Brand-Williams [22]. Five concentrations of each extract were prepared from the stock solution, added in equal volume, to the methanolic solution of DPPH on 96 well micro plates. After an incubation of 30 min at room temperature, the absorbance was determined at 515 nm. Trolox was used as a standard control.

The percentage inhibition of the DPPH free radical was calculated as per the following formula:

$$\% \text{ inhibition of DPPH radical} = \frac{(\text{DO control} - \text{DO sample})}{\text{DO control}} \times 100$$

The IC50 value was defined as the concentration of antioxidant necessary to decrease the initial DPPH concentration by 50% [23] and determined from the results by linear regression analysis. The lower IC50 values designate the greater antiradical activity. The antiradical power (ARP) was calculated as 1/IC50: the highest ARP values indicate the greater DPPH scavenging effect. The evaluation of free radical-scavenging activity was performed by the Trolox Equivalent Antioxidant Capacity (TEAC). The TEAC value is based on the ability of the antioxidant to scavenge the DPPH radical and was calculated by the following formula:

$$\text{TEAC} = \frac{\text{ARP (compound)}}{\text{ARP (Trolox)}}$$

**Acknowledgments:** This work was supported by the National Basic Research Program of Algeria Project (E00920120008).

#### REFERENCES

1. T.G. Tutin, V.H. Heywood, N.A. Burges, D. M. Moore, D. H. Valentine, S. M. Walter, D. A. Webb, *Flora Europaea*, 3rd ed. Cambridge University Press, 1972, p. 29.
2. M. Dolores Liedo, M. Erben, M. B. Crespo, Myriolepis, *Taxon*, **52**, 67 (2003).
3. P. Quezel, S. Santa, *New flora of Algeria and the southern régions*. 2nd ed., Paris : CNRS, 1963, p. 731.
4. F. Medini, R. Ksouri, H. Falleh, W. Megdiche, N. Trabelsi, C. Abdelly, *Journal of Medicinal Plants Research*, **5**(31), 6719 (2011).
5. L. M. Korul'kina, G. E. Zhusupova, E. E. Shul'ts, K. B. Erzhanov, *Chemistry of Natural Compounds*, **40**(5), 417 (2004).
6. D. Saidana, S. Mahjoub, O. Boussaada, J. Chriaa, A. Mahjoub, I. Chéraif, M. Daami, Z. Mighri, A. N. Helal, *J Am Oil Chem Soc.*, **85**(9), 817 (2008).
7. K. Yuh-Chi, L. Lie-Chwen, T. Wei-Jern, C. Cheng-Jen, K. Szu-Hao, H. Yen-Hui, *Antimicrob Agents Chemother*, **46**(9), 2854 (2002).
8. G. E. Zhusupova, S. A. Abilkaeva, *Chemistry of Natural Compounds*, **42**(1), 112 (2006).
9. L. Zhang, G.Zou, *Chemistry of Natural Compounds*, **40**(6), 602 (2004).
10. S. Asen, J. R. Plimmer, *Phytochemistry*, **11**, 2601 (1972).
11. J. I. Lee, C. Kong, M. E. Jung, S. Y. Lim, Y. Seo, *Biotechnology and Bioprocess Engineering*, **16**, 992 (2011).
12. L. M. Korul'kina. E. E. Shul'ts, G. E. Zhusupova, Zh. A. Abilov, K. B. Erzhanov, M. I. Chaudri, *Chemistry of Natural Compounds*, **40**(5), 465 (2004).
13. F. E. Kandil, Kh. M. Ahmed, H. A. Hussieny, A. M. Soliman, *Chemistry of Natural Compounds*, **41**(3), 417 (2005).
14. I. S. Movsumov, E. A. Garaev, *Chemistry of Natural Compounds*, **41**(3), 417 (2005).
15. M. Benahmed, M. Lafhal, N. Djeddi, H. Laouer, S. Akkal, *Advances in Environmental Biology*, **12**(6), 4052 (2012).
16. F. Pourmorad, S. J. Hosseinimehr, N. Shahabimajd. *African Journal of Biotechnology*, **5**(11), 1142 (2006).
17. M. A. Aderogba, A. O. Ogundaini, J. N. Eloff, *Afr J Trad CAM*, **3**(4), 59 (2006).
18. L. Yun-Lian, K. Yueh-Hsiung, S. Ming-Shi, C. Chien-Chih, O. Jun-Chih, *Journal of the Chinese Chemical Society*, **47**(1), 253 (2000).
19. R. N. Yadava, S. Khan, *Int J Pharm Sci Res.*, **3**(10), 3932 (2012).
20. L. Xian-yin, Z. Yu-ying, H. Liang, *China Journal of Chinese Materia Medica*, **31**(19), 1597 (2006).
21. L. Chun-mei, W. Tao, Z. Yi, G. Xiu-mei, L. Tianxiang, *Journal of Shenyang Pharmaceutical University*, **27**(9), 711 (2010).
22. W. Brand-Williams, M. E. Cuvelier, C. Berset, *LW T- Food Sci Control*, **28**(1), 25 (1995).
23. S. Azzouzi, N. Zaabat, K. Medjroubi, S. Akkal, K. Benlabed, F. Smati, M.G. Dijoux-Franca, *Asian Pac J trop med.*, **7**(1), S481 (2014).

## ХИМИЧЕН СЪСТАВ НА *Limonium thouinii* (viv.) kuntze (Plumbaginaceae) и DPPH-АКТИВНОСТТА ЗА ОТСТРАНЯВАНЕ НА СВОБОДНИ РАДИКАЛИ

М. Лефахал<sup>1</sup>, М. Бенахмед<sup>2</sup>, Л. Джари, Н. Заабат<sup>1</sup>, А.Е. Хай<sup>3</sup>, М. Камел<sup>1</sup>, М.-Г. Дижу Франка<sup>3</sup>, Х. Лауе<sup>4</sup>, С. Аккал<sup>1</sup>

<sup>1</sup>Университет в Константин, Група по изследване на оползотворяването на природни ресурси, биоактивни молекули, физико-химични и биологични анализи, Департамент по химия, Факултет по точни науки, Алжир

<sup>2</sup>Университет Ларби Тебеси, Алжир

<sup>3</sup>Университет в Лион 1, Департамент по микробиология, Вийорбан, Франция

<sup>4</sup> Университет Ферхат Абас Сетиф 1, Лаборатория по оползотворяване на биологични ресурси, Департамент по биология и екология на растителните ресурси, Алжир.

Постъпила на 8 юли, 2015 г.; приета на 2 октомври, 2015 г.

(Резюме)

Настоящата работа разглежда фитохимичните изследвания и DPPH-отстраняващата активност към свободните радикали на надземните части на растението *Limonium thouinii* (Viv.) kuntze (Plumbaginaceae). Надземните части на това растение позволяват да се изолират четири флавоноида: кверцетин, витексин, изо-ориентин и канабисцитрин. Тяхната структура се определя на базата на спектроскопски анализи, включващи УВ, МС и ЯМР – техники. Способността им да отстраняват DPPH свободни радикали е определяна върху сурови екстракти в метанол, етилацетат и n-бутанол.

## Evaluation of the drying methods and conditions with respect to drying kinetics, colour quality and specific energy consumption of thin layer pumpkins

O. İsmail<sup>1\*</sup>, Ö. G. Kocabay<sup>1,2</sup>

<sup>1</sup>*Department of Chemical Engineering, Faculty of Chemical and Metallurgical Engineering, Yildiz Technical University, Davutpaşa Campus, 34210 İstanbul, Turkey*

<sup>2</sup>*T.R. Ministry of Culture and Tourism, Directorate of Central and Laboratory for Restoration and Conservation, İstanbul, Turkey*

Received August 3, 2015, Revised September 21, 2015

In this study, the effects of dry air temperature and power levels when drying pumpkin (*Cucurbita pepo* L.) slices by five different methods was investigated experimentally. Pumpkin slices were dehydrated by five different drying methods: open-sun, vacuum, microwave, infrared and hot air drying. In particular, the experiments were carried out at two different microwave power levels (90 and 180 W), infrared power levels (83 and 125 W) and hot air temperatures (50 and 70 °C) to investigate the effects of these factors on the microwave, infrared and hot-air drying, respectively. The vacuum drying experiment was carried out in one vacuum oven dryer at a constant temperature of 50 °C and a pressure of 0.1 kPa. The experimental moisture data was fitted to some models (namely Lewis, Henderson and Pabis, Page, Logarithmic, Aghbashlo et al., Verma et al. and Midilli et al. models) available in the literature and according to the results, the Midilli et al. model is superior to the others in explaining the drying behavior of pumpkin slices. The energy efficiency and diffusion coefficients increased with the increase in microwave power. In terms of colour criteria the best values were obtained by the hot-air and open-sun drying methods.

**Keywords:** colour, drying models, mathematical models.

### INTRODUCTION

In accordance with the botanical classification Cucurbitaceae is part of the Dicotyledoneae class, Cucurbitales team, Cucurbitaceae genus. Approximate 118 kinds and 825 species are present in the Cucurbitaceae genus. In the genus of Cucurbitaceae, *Cucurbita pepo* L. is a species with a high economic value [1].

Pumpkin (*Cucurbita pepo* L.) is one of the most important vegetables grown in Turkey. In 2012, pumpkin's world production reached 24616115 tons meanwhile in Turkey its production was 395986 tons. The five major pumpkin producing countries in the world are China, India, Ukraine, Egypt and the United States [2].

Pumpkins, which grow in the different regions of Turkey, are a seasonal crop and for this reason a processing step is often used to preserve pumpkin products. Depending upon the processing possibilities, inadequateness of seasonal fresh vegetables and fruits, Turkey as well as in many countries are experiencing big economic losses. It was reported that in the developing countries approximately 30 to 40 percent of the seasonal fresh vegetables and fruits are cast away due to spoilage [3].

The excess quantity of agricultural produce can't be consumed immediately and its life span is too short. These products can be kept fresh after special processing. Great numbers of preserving techniques such as freezing, heat treatment, drying etc. are used to increase the endurance of foodstuffs. In food products with respect to protection of the vitamin value, maintenance of a good outward appearance, taste preservation, the emergence of a decreasing mass advantage, the improvement of storage and transportation facilities, drying is the most appropriate method [4, 5].

The most common drying method used for drying fruits and vegetables in the world and in Turkey is open-sun and outdoors drying. Because the solar energy is renewable, clean and cheap, open-sun drying is carried out commonly in the tropical countries. As there are no energy requirements and a maintenance expense, open-sun drying is a cost-effective method. The only disadvantages of drying under the sun in accordance with other processes are that the drying rate is slow and the time is prolonged [6].

Convective drying by hot air is a widely used drying method in the literature. In these kinds of dryers specific, air speed is practiced by product, the product has a short drying time. Having a simple design, manufactured locally, having a small maintenance and operational cost, drying different

\* To whom all correspondence should be sent:  
E-mail: ismail@yildiz.edu.tr

products according to the season, are among the advantages of these drying systems [7, 8]. During both conventional drying processes, considerable loss in food content takes place. To reduce the food content losses, to preserve the quality of the dried food and to shorten the drying time at low temperatures, the vacuum drying process is successfully applied instead of the conventional methods [9].

Microwave and infrared technology, which has become common in recent years, takes its place in the food industry by shortening the drying time associated with providing quality food. Using microwave driers in combination with hot air live driers increases product quality and energy efficiency [10]. The fundamental principle of microwave heating is provided with the conversion of electromagnetic energy to thermal energy by affecting the polar molecules in the material [11]. Microwave heating systems are successful drying systems for fruits, cereal crops and many food products which have a high moisture content. In brief, drying with microwaves has the characteristics of 4 important properties; fast processing, energy efficiency, low cost and a high quality of the dried product [12].

As stated in [13], various infrared heat sources could be used for drying applications. IR energy is a form of electromagnetic energy or heat energy. The penetration properties of IR radiation into a given material directly increases the energy flux without burning the material's surface and so the required heating time of the conventional heating method decreases. The advantages of infrared heating by conventional heating can be listed as follows: providing regular heating in a short time, decreasing deterioration and nutritional loss, the equipment has simple and flexible usage areas and considerably economizes the energy consumption.

Drying is also the most energy consuming process in the food industry. New drying methods and dryers must be designed and investigated to minimise the energy cost of the drying process [14].

Although there are some investigations focused on the drying characteristic of the pumpkin, there is too much information on the drying characteristics of the *Cucurbita pepo* L., which is a subgroup of pumpkin. The objectives of this study are to evaluate and compare the drying kinetics, product quality and specific energy consumption during the drying of pumpkin slices (*Cucurbita pepo* L.) by five drying methods: (1) hot-air convection drying, (2) open-sun drying (3) the vacuum drying process, (4) IR drying and (5) microwave drying. Two different drying conditions were applied for the

microwave, IR and hot-air drying methods. In addition to this, to obtain the best model for the drying kinetics of pumpkin slices; Lewis, Henderson & Pabis, Page, Logarithmic, Aghbashlo et al., Verma et al. and Midilli et al. models were fitted to the experimental data. Also effective moisture diffusivity values were calculated.

## MATERIALS AND METHODS

### *Material*

Fresh pumpkin (*Cucurbita pepo* L.) samples were obtained from a local supermarket in İstanbul, Turkey and stored in a chamber at 15–20 °C until processing. The initial moisture content of the fresh pumpkin samples was determined using the drying oven (Memmert UM-400, Germany) at 105 °C for 24 h [15]. These experiments were run thrice to obtain a reasonable average. The average initial moisture content of the pumpkins was found to be 92 % w.b. Before the drying process the pumpkin samples were washed, their top and bottom parts were cut and then the pumpkin samples were cut into  $0.5 \pm 0.03$  cm sized cylindrical slices using a knife.

### *Drying equipment and IR drying procedure*

Drying experiments were carried out in a moisture analyzer with a 250 W halogen lamp (Snijders Moisture Balance, Snijders b.v., Tilburg, Holland). During the infrared drying process, a sample was separated over the entire pan evenly and homogeneously. The power level was set in the control unit of the equipment. The drying experiment was performed at the infrared power levels of 83 W and 125 W. The pumpkin samples (approximately  $40 \pm 0.2$  g) were taken from the dryer at 30 min time intervals during the drying process and their weights were measured with a digital balance (Precisa, model XB220A, Precisa Instruments AG, Dietikon, Switzerland) with an accuracy of 0.001 g. When the samples' moisture content reached approximately 0.08 g water/g of dry matter (dry basis) the drying process was terminated.

### *MW*

The drying experiments were carried out in a Robert Bosch Hausgerate GmbH (Germany) model microwave oven which has a maximum output power of 800 W at 2450 MHz. The microwave oven has the capability of operating at different microwave stages while its power range is 90 to 800 W. The area subjected to microwave drying is 530 mm x 500 mm x 322 mm in size and consists

of a rotating glass plate which is 300 mm in diameter at the base of the oven.

The adjustment of the microwave output power and processing time was done with the aid of a digital control apparatus located on the microwave oven. The drying experiments were set at two different microwave power levels of 90 W and 125 W. During drying, the experiments were carried out using the sliced pumpkins known weight of approximately  $34 \pm 2$  g with the thin layer placed on the rotatable plate fitted inside the microwave oven cabin. The rotating glass plate was removed from the oven every 2 min during the drying period and the moisture loss was determined by weighing the plate using a digital balance. The microwave drying process continued until the moisture content reduced to approximately 0.09 g water/g of dry basis of the initial moisture content.

#### *Cabinet dryer*

The drying experiments were performed in a cabinet type dryer (APV & PASILAC Limited of Carlisle, Cumbria, UK). It was made up of stainless steel sheets and it consisted of a rectangular tunnel 0.54 m x 1.4 m x 1.02 m in size. The dryer consisted of a centrifugal fan to supply the air flow, an electrical heater and an air filter. The dryer is operated at dry bulb temperatures of 0–200 °C. The desired drying air temperature was attained by electrical resistance and controlled by the heating control unit. The velocity of the air passed through the system was measured by an anemometer in the range of 0.4–30  $\text{ms}^{-1}$  (model AM-4201, Lutron Electronic, Taipei, Taiwan). The air flow was measured directly in the drying chamber. The samples were dried in the perforated square chamber, which had a flow cross-section of 30 cm x 30 cm. Weight loss of the samples was recorded by using a digital balance (Mettler-Toledo AG, Grefensee, Switzerland, model BB3000) with a sensitivity of 0.01 g.

The pumpkin slices of about 100g were distributed uniformly as a single layer at the sample tray and then were dried in the hot air dryer. The hot air drying was carried out by drying the pumpkin samples at 50°C and 70°C air temperatures and with a constant air velocity of 1 m/s. Pumpkin samples' moisture loss was measured by a balance and recorded at 30 min intervals. The drying process was finished when the moisture content of the samples achieved approximately 0.07 g water/g of dry matter.

#### *Open air-sun drying*

To clean the samples from dust and foreign materials, the selected pumpkin samples were

washed with tap water. Open air - sun drying experiments were carried out during the month of August 2014 (from 08.00 a.m. to 20.00 p.m.) in Greece. The pumpkin slices of about 50 g were distributed uniformly as a single layer on the sample tray and then were exposed to sunlight for 12 hours daily. Moisture loss and the ambient air's temperature was measured by a portable digital balance during the drying process at 30 min intervals (Alfais, I2000-1, which has 0–300 g measurement range with an accuracy of  $\pm 0.1$  g). When the drying time took more than 12 h to reduce the effect of the increase in moisture content, samples were packed overnight. The ambient air's temperature during the drying experiments was between 36 to 49 °C. The highest air temperature was reached between 10:30 a.m. and 14:30 p.m. The drying process continued until the sample reached the desired moisture level of 9 % (w.b.). The dried samples were packed in low density polyethylene bags.

#### *Vacuum drying oven*

Vacuum drying treatment was performed in the laboratory type vacuum oven (Nuve EV 0180, Turkey) with the technical features ~220 V, 50 Hz, 3.5 A and 800 W. The vacuum oven's temperature, which has a sensitivity of 1°C, is a maximum of 250°C. The area of vacuum drying was 30 cm x 20 cm x 25 cm in size. A laboratory type vacuum pump (Carpanelli MMDE80B4, Italy) was used in the vacuum drying operation. Its operating conditions were ~220/240 V, 50/60 Hz and 5.1/4.8 A. The adjustment of the vacuum value and processing temperature was done with the aid of a digital control facility located on the vacuum drying oven. In the drying experiments pumpkin slices' with a weight approximately of  $30 \pm 2$  g and a constant temperature of 50 °C and pressure of 0.1 kPa were used in the vacuum oven dryer. The moisture loss in the pumpkin slices was measured with a balance and it was recorded at 30 min intervals. Good results as a consequence of drying of the pumpkin slices by vacuum drying were not achieved.

#### *Mathematical modelling*

##### *Moisture ratio*

The moisture ratio (*MR*) and drying rate were calculated using the following equations:

$$MR = \frac{M_t - M_e}{M_o - M_e}, \quad (1)$$

where *MR* is the moisture ratio,  $M_t$ ,  $M_o$  and  $M_e$  are the moisture content (g water/g dry matter) on a dry

basis at any time, initial and equilibrium, respectively. The equilibrium moisture content ( $M_e$ ) was assumed to be zero for microwave, infrared drying etc. and the  $MR$  equation (Equation 1) was simplified as Equation 2 [16]:

$$MR = \frac{M_t}{M_o}, \quad (2)$$

#### Drying Rate

The drying rate during the experiments was calculated using the following formula:

$$\frac{dM}{dt} = \frac{M_{t+dt} - M_t}{dt}, \quad (3)$$

where  $t$  is the drying time (min),  $M_t$  and  $M_{t+dt}$  are the moisture content at  $t$  and  $t + dt$  (g water/g dry matter) respectively.

#### Effective moisture diffusivity

The effective moisture diffusivity is therefore calculated by the following equation [17]:

$$MR = \frac{M_t - M_e}{M_o - M_e} = \frac{8}{\pi^2} \sum_{n=0}^{\infty} \frac{1}{(2n+1)^2} \exp\left[-\frac{(2n+1)^2 \cdot \pi^2 \cdot D_{eff}}{4L^2} t\right] \quad (4)$$

where,  $D_{eff}$  is the effective moisture diffusivity ( $m^2/s$ );  $L$  is the half-thickness of the slab in the samples (m); and  $n$  is a positive integer. In practice, only the first term of Eq. (4) is used to yield [18]:

$$MR = \frac{M_t - M_e}{M_o - M_e} = \frac{8}{\pi^2} \exp\left[-\frac{\pi^2 D_{eff} t}{4L^2}\right] \quad (5)$$

The effective moisture diffusivity ( $D_{eff}$ ) was also typically calculated by using the slope of Eq. (5). A straight line with a slope of  $k_o$  was obtained when  $\ln(MR)$  was plotted versus the time:

$$k_o = \frac{\pi^2 D_{eff}}{4L^2} \quad (6)$$

Using the slope value of (Eq. 6), the effective moisture diffusivity could be determined.

#### The statistical modelling procedure

In order to determine the moisture ratio as a function of drying time, seven different thin-layer drying models, namely Lewis, Henderson & Pabis, Page, Logarithmic, Aghbashlo et al., Verma et al. and Midilli et al. models were used (Table 1).

#### Statistical analysis

The statistical analysis of the experimental data was determined using the STATISTICA computer program. Three criteria of statistical analysis were used to evaluate the adjustment of the experimental data to the different models; the coefficient of determination ( $R^2$ ), reduced chi-square ( $\chi^2$ ) and root – mean-square error (RMSE). The parameters can be calculated as follow:

$$\chi^2 = \frac{\sum_{i=1}^N \left( MR_{exp,i} - MR_{pre,i} \right)^2}{N - z} \quad (7)$$

$$RMSE = \left[ \frac{1}{N} \sum_{i=1}^N \left( MR_{pre,i} - MR_{exp,i} \right)^2 \right]^{1/2} \quad (8)$$

where  $MR_{exp,i}$  and  $MR_{pre,i}$  are the experimental and predicted dimensionless MR, respectively,  $N$  is the number of the data values and  $z$  is the number of constants of the models. Higher  $R^2$ , smaller  $\chi^2$  and RMSE values indicated a better fit of the experimental data to the model [26].

**Table 1.** List of models.

Model name	Model	Reference
Lewis	$MR = \exp(-kt)$	[19]
Henderson and Pabis	$MR = a \exp(-kt)$	[20]
Page	$MR = \exp(-kt^n)$	[21]
Logarithmic	$MR = a \exp(-kt) + c$	[22]
Aghbashlo et al.	$MR = \exp\left(-\frac{k_1 t}{1 + k_2 t}\right)$	[23]
Verma et al.	$MR = a \exp(-kt) + (1-a) \exp(-gt)$	[24]
Midilli et al.	$MR = a \exp(-kt^n) + bt$	[25]

*Colour measurement*

The sample colour before and after the drying process was measured using a Chromameter CR - 400 (Minolta, Japan). For the dried samples three parameters L, a and b, which indicate the brightness (on a lightness–darkness scale), greenness-redness and blueness-yellowness respectively, were used to study the changes in colour. The Chroma was determined using the following equation [27].

$$C^* = \sqrt{a^2 + b^2} \quad , (9)$$

*Energy consumption*

*Energy consumption in the infrared*

In the IR dryer, sum of the energy was consumed by the IR lamp to dry the pumpkin samples.

$E_t$  is the total energy consumption during the infrared drying that is calculated using the following equation (10).

$$E_t = P * t \quad , (10)$$

where  $E_t$  is the total energy consumption (kWh), P is the infrared power level (kW), t is the drying time (h).

*Energy consumption in the microwaves*

The energy consumption value required for drying pumpkin slices in the microwaves was calculated with Equation (11) [28].

$$E_t = P * t \quad , (11)$$

where  $E_t$  is the total energy consumption (kWh), P is the microwave power output (kW), t is the drying time (h).

*Energy consumption in the hot air*

In hot air drying, the total energy consumption was due to the drying and blowing of air by an electric heater and fan, respectively. The total energy consumption value was calculated from Equation (12) [29]:

$$E_t = \rho_a A v c_p \Delta T * D_t \quad , (12)$$

where  $E_t$  is the total energy consumption (kWh),  $\rho_a$  is the air density ( $\text{kg/m}^3$ ), A is the cross sectional area of the container ( $\text{m}^2$ ), herein a sample is placed, v is the air velocity (m/sec),  $c_p$  is the specific heat ( $\text{kJ/kg } ^\circ\text{C}$ ),  $\Delta T$  is a temperature difference between the air inlet and outlet of the

dryer ( $^\circ\text{C}$ ),  $D_t$  is the total drying time of each sample (h).

*Calculation of the specific energy consumption*

The total energy consumption of the drying process was evaluated through the Specific Energy Consumption (SEC). Electrical energy was consumed during the drying process. The specific energy consumption, which is a measure of the energy needed to evaporate a unit mass of water from the product, was calculated using the following equation [30]:

$$Q_s = \frac{Q_t}{m_w} \quad , (13)$$

where  $Q_s$  is the specific energy consumption in  $\text{kWh *kg}^{-1}[\text{H}_2\text{O}]$ ,  $Q_t$  is the consumed energy in kWh,  $m_w$  is the mass of vaporized water in kg  $[\text{H}_2\text{O}]$ .

RESULTS AND DISCUSSION

*Drying curves*

Figure 1 shows the moisture ratio as a function of drying time for the different drying methods and conditions.

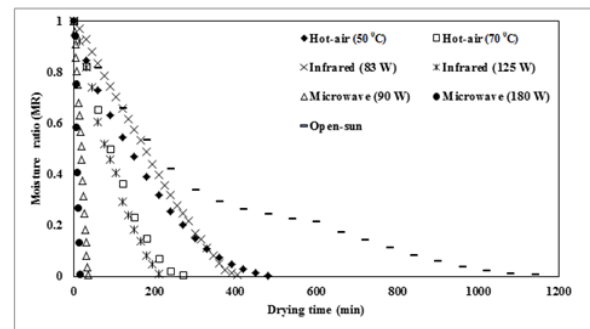


**Fig. 1.** Drying curves of pumpkin slices at different drying methods and conditions.

As seen from Figure 1, the drying time was quite different for four drying methods to reach the final moisture ratio. The drying time of the dried pumpkin slices with different drying methods ranged from 14 to 1140 minutes. The drying curves are typical and similar to fruits and vegetables. In Fig. 1 it is discerned that the increase in the microwave power level [31, 32], air temperature [33, 34] and infrared power level [35] shortened the drying period in microwave drying, air-drying and infrared drying, respectively. The moisture ratio decreases gradually with the increases in drying time, exhibiting a downward curve. The figure also indicates that the drying time for microwave drying is much shorter than the hot air, infrared and open-sun drying. The time required to reduce the

moisture ratio from 1 to 0.006 ranged between 14 and 36 min at two power levels with microwave drying, while it ranged between 270 and 480 min at two temperatures with hot air drying, while it ranged between 210 and 405 min at two power levels with infrared drying. To reach the desired final moisture content, 14 minutes drying time indicated the high efficiency of the microwave drying method (180 W), which was about 82 times faster than open-sun drying. The drying time of pumpkin slices dried under the sun was determined as 19 h.

The drying time was much faster than for the other drying methods as compared to the conditions by microwave drying of pumpkin slices. For this reason, the drying rate (g water)/(g dry matter\*min) curves are shown in the two different figures as Figure 1 and 2 in order to clearly see the drying rate curves.

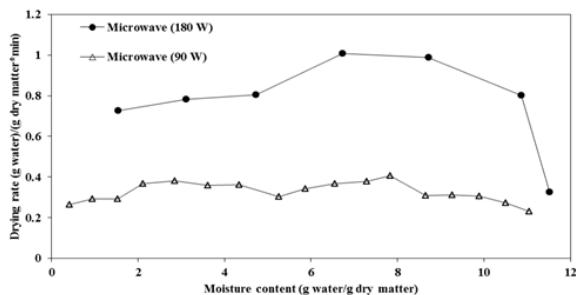


**Fig. 2.** Drying rate versus moisture content of pumpkin slices at two different microwave power levels.

Since the initial moisture content of the pumpkin slices was relatively constant (11.5 g water/g dry matter), the difference in the drying time requirements was considered mainly due to the difference in the drying rates. The drying rate curves for pumpkin slices dried at two microwave output power levels (90 to 180 W) are given in Figure 2. Depending on the drying conditions, the

average drying rates of pumpkin slices ranged from 0.407 to 1.008 (g water)/(g dry matter\*min) for the output power between 90 and 180 W, respectively. The moisture content of the pumpkin (92% w.b.) was very high during the initial phase of the drying process which resulted in a higher absorption of microwave power level and higher drying rates due to the higher moisture diffusion. As the drying time progressed, the moisture loss in the product caused a decrease in the absorption of microwave power and resulted in a fall in the drying rate. Higher drying rates were determined at higher microwave output power levels. Thus, the microwave output power level had a crucial effect on the drying rate. The variation of drying rate with moisture content for the different drying conditions of hot air, infrared and open-sun drying are shown in Figure 3.

As expected, the drying rate would decrease as the moisture content decreases. As can be seen from these figures, no constant rate period exists. All the drying processes occurred in the falling rate period. In the infrared drying experiments (83 and 125 W) initially rising but after a while falling the drying rate period is present. The experiment, in which the infrared power level is 125 W, the rising drying rate period is clear by far. During the falling drying rate period, the predominant mechanism is the internal mass transfer. The open sun drying experiment lasted for approximately 19 h. Consequently, a small rising drying rate period formed in the figure that originated as a result of the drying process continued the next day. Similar results were reported by [36, 14, 37].

#### Mathematical Modelling of Drying Data

The values of  $R^2$ ,  $\chi^2$  and RMSE were calculated and given in Table 2.

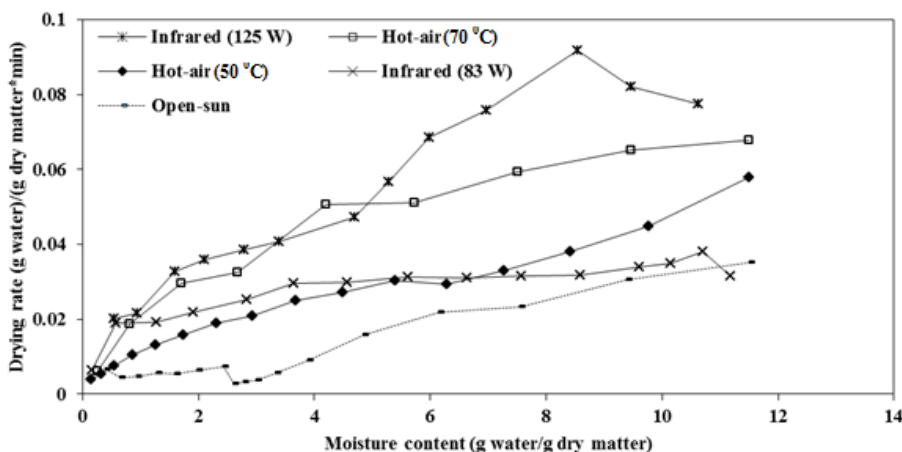


**Fig. 3.** Drying rate versus moisture content of pumpkin slices at different drying methods and conditions.

**Table 2.** Statistical results obtained from the selected models.

Models	Drying methods	Drying conditions	R <sup>2</sup>	χ <sup>2</sup>	RMSE
Lewis	Infrared	83 W	0.9304	0.007238	0.083527
	Infrared	125 W	0.9563	0.004683	0.066081
	Microwave	90 W	0.8991	0.010951	0.101825
	Microwave	180 W	0.8982	0.013873	0.110176
	Sun	36 to 49 °C	0.9864	0.001048	0.031551
	Hot - air	50 °C	0.9826	0.001724	0.040277
	Hot - air	70 °C	0.9673	0.004022	0.060163
Henderson & Pabis	Infrared	83 W	0.9803	0.005327	0.070318
	Infrared	125 W	0.9676	0.003731	0.056838
	Microwave	90 W	0.9247	0.008652	0.087956
	Microwave	180 W	0.9211	0.012548	0.097011
	Sun	36 to 49 °C	0.9876	0.001007	0.030106
	Hot - air	50 °C	0.9846	0.001626	0.037867
	Hot - air	70 °C	0.9728	0.003757	0.054825
Page	Infrared	83 W	0.9912	0.000947	0.029651
	Infrared	125 W	0.9937	0.000719	0.024955
	Microwave	90 W	0.9907	0.000754	0.025974
	Microwave	180 W	0.9946	0.000854	0.025309
	Sun	36 to 49 °C	0.9904	0.000780	0.026491
	Hot - air	50 °C	0.9937	0.000664	0.024207
	Hot - air	70 °C	0.9959	0.000562	0.021209
Logarithmic	Infrared	83 W	0.9982	0.000193	0.013117
	Infrared	125 W	0.9974	0.000318	0.015943
	Microwave	90 W	0.9973	0.000324	0.016517
	Microwave	180 W	0.9932	0.001284	0.028329
	Sun	36 to 49 °C	0.9878	0.001048	0.029848
	Hot - air	50 °C	0.9989	0.000118	0.009865
	Hot - air	70 °C	0.9970	0.000474	0.018212
Aghbashlo et al.	Infrared	83 W	0.9304	0.007516	0.083527
	Infrared	125 W	0.9563	0.005044	0.066081
	Microwave	90 W	0.8991	0.011595	0.101825
	Microwave	180 W	0.8982	0.016185	0.110176
	Sun	36 to 49 °C	0.9903	0.000785	0.026586
	Hot - air	50 °C	0.9825	0.001839	0.040277
	Hot - air	70 °C	0.9673	0.004524	0.060163
Verma et al.	Infrared	83 W	0.9583	0.004685	0.064667
	Infrared	125 W	0.9780	0.002743	0.046818
	Microwave	90 W	0.9758	0.002956	0.049879
	Microwave	180 W	0.9868	0.002509	0.039598
	Sun	36 to 49 °C	0.9890	0.000944	0.028327
	Hot - air	50 °C	0.9866	0.001510	0.035258
	Hot - air	70 °C	0.9847	0.002419	0.041154
Midilli at al.	Infrared	83 W	0.9994	0.000070	0.00775
	Infrared	125 W	0.9984	0.000216	0.012588
	Microwave	90 W	0.9991	0.000113	0.009452
	Microwave	180 W	0.9986	0.000315	0.012555
	Sun	36 to 49 °C	0.9924	0.000692	0.023526
	Hot - air	50 °C	0.9987	0.000151	0.010758
	Hot - air	70 °C	0.9990	0.000170	0.010089

**Table 3.** Colour parameters of fresh and dried pumpkin slices.

Drying methods	Drying conditions	Colour parameters			C*
		L	a	b	
	Fresh	67.75	11.06	21.77	24.41
Infrared	83 W	49.73	12.80	10.66	16.65
	125 W	47.75	14.42	10.74	17.98
Microwave	90 W	67.19	0.59	27.28	27.28
	180 W	57.11	3.89	26.31	26.59
Hot - air	50 °C	68.95	11.91	25.65	28.28
	70 °C	68.68	11.58	26.75	29.15
Open - sun	31 - 46 °C	70.63	11.12	24.2	26.63

**Table 4.** Effective moisture diffusivity values for the various drying methods.

Drying methods	Drying conditions	D <sub>eff</sub> (m <sup>2</sup> s <sup>-1</sup> )
Infrared	83 W	3.24 x 10 <sup>-10</sup>
	125 W	6.09 x 10 <sup>-10</sup>
Microwave	90 W	0.85 x 10 <sup>-7</sup>
	180 W	2.48 x 10 <sup>-7</sup>
Hot - air	50 °C	2.78 x 10 <sup>-10</sup>
	70 °C	9.38 x 10 <sup>-10</sup>
Open - sun	31 – 46 °C	2.96 x 10 <sup>-11</sup>

Thin-layer drying models, in other words the Lewis, Henderson and Pabis, Page, Logarithmic, Aghbashlo et al., Verma et al. and Midilli et al. were used to describe the drying process during the drying of pumpkin slices.

In order to describe the moisture ratio as a function of drying time with different drying methods, 7 different drying models were fitted to the experimental data and their coefficient of determination (R<sup>2</sup>), reduced chi-square (χ<sup>2</sup>) and root-mean-square error (RMSE) were calculated. R<sup>2</sup>, RMSE and χ<sup>2</sup> statistical data with respect to 7 different drying models are given in the Table 2. The grade of fitting was determined by the lowest χ<sup>2</sup> and RMSE and the highest R<sup>2</sup> values.

From Table 2, the statistical data with respect to 7 different drying models used for explaining the drying circumstance occurred in the falling rate drying period was examined individually and using the Midilli et al. model and provided the minimum error for a separable moisture rate. At drying the process of pumpkin slices' standard error (RMSE) of prediction conducted by this model ranged from 0.00775 to 0.023526. In addition to this as seen from the table, the chi-square (χ<sup>2</sup>) values ranged from 0.000070 to 0.000692 which are close to zero.

Adequacy of modelling ranged from 0.9994 to 0.9924.

*Effect of drying methods and conditions on the colour of pumpkin slices*

Before and after the drying process, the L (lightness), a (greenness), b (yellowness) and C\* (Chroma) values of pumpkin slices were measured and these results are given in Table 3.

One of the quality of the parameters of food and agricultural product is the colour parameter. Too much colour changes influence the marketing negatively by affecting the quality of the product. It is an index of the inherent good qualities of a food and the association of colour with the acceptability of a food is universal. Among the several basic quality characteristics of dried pumpkin slices the colour is an important one which indicates the effect levels of different drying methods or conditions. As stated previously, the L term stands for brightness, the a term is for a green-red balance, the b term is for a blue-yellow balance, the Hunter colour ratio and the chroma are measures for the colour purity. Values for the L, a, b and chroma (C\*) coordinates of the fresh pumpkin slices were 67.75, 11.06, 21.77 and 24.41, respectively.

In general, the infrared drying at 83 and 125 W produced no remarkable changes in the colour parameters of the pumpkin slices as compared with the fresh pumpkin. However, the increase of power level from 83 W to 125 W caused an increase of the a and b values and a decrease of the L value. The microwave irradiation drying at 90 W allowed the obtaining of a product which was more similar to the fresh sample when the lightness was considered since the L value varied only from 67.75 to 67.19. When comparing the values obtained for the opposing colour parameters between the fresh sample and the pumpkin slices dried at 90 W, the a decreased from 11.06 to 0.59, showing that the red colour decreased with the drying process. As for the b, it increased slightly from 21.77 to 27.28, the dried samples were more yellow. These observations are corroborated with the increase from 24.41 to 27.28 in the value of the chroma. The dried pumpkin at 180 W turns into the final product as much lighter, much less red and more yellow with L, a and b values for which the values are 57.11, 3.89 and 26.31, respectively. The colour criteria obtained from the air drying experiments using 50 and 70 °C temperatures are given in Table 3. According to this the colour is closest to the fresh product when the air drying process's temperature is 50°C and 75°C. When the drying air temperature increased from 50 to 75 °C; the L, a values decreased and b values increased. These results were consistent with the observations made by different authors on the drying of pumpkin (*Cucurbita pepo* L.) slices [38, 39]. As seen from Table 3, the best colour values were achieved during the open sun drying and these values are the closest to the fresh material. This is followed by hot air-drying, microwave drying and infrared drying successively. Similar findings are also available in the literature [40, 41].

#### *Determination of Effective Moisture Diffusivity*

The effective moisture diffusivity was calculated using the method of slopes. Effective diffusivities are typically determined by plotting the experimental drying data in terms of  $\ln(MR)$  versus time. From the Eq. (6), a plot of  $\ln(MR)$  versus time gives a straight line with a slope ( $k_0$ ). This slope is the measure of the diffusivity. The effective diffusivity values for various drying methods and conditions are presented in Table 4.

Among the four drying methods, microwave drying offered the highest values of  $D_{\text{eff}}$  for microwave power levels of 90 and 180 W. In microwave drying, the  $D_{\text{eff}}$  values increased with

the increasing drying microwave power. If samples were dried at higher microwave power, increased heating energy would increase the activity of the water molecules leading to a higher moisture diffusivity. The value of  $D_{\text{eff}}$  for infrared and hot-air drying was slightly higher than the open sun drying. In drying pumpkin slices by the infrared and hot-air drying methods, the effective moisture diffusivity value increases with increasing power and temperature. In foods the effective moisture diffusivity values are in the range of  $10^{-12}$  to  $10^{-6}$   $\text{m}^2/\text{s}$  and the accumulation of values is in the region  $10^{-10}$  to  $10^{-8}$   $\text{m}^2/\text{s}$  (75%) [42, 43]. In the literature there is no study associated with the drying of pumpkin slices (*Cucurbita pepo* L.) with infrared and open sun drying. Some studies dealing with the drying of pumpkin slices with microwaves are available in the literature but data about the effectiveness of moisture diffusivity does not exist.

The  $D_{\text{eff}}$  value of pumpkin slices (*Cucurbita pepo* L.) [8] undergoing hot-air drying at 50 and 60 °C was in the range of  $3.38 \times 10^{-10}$  to  $9.38 \times 10^{-10}$   $\text{m}^2/\text{s}$ , respectively.

#### *Energy consumption*

The energy consumption values obtained in the drying trials carried out with three different drying methods are given in Figure 4.

When three different drying methods were compared with the energy consumption values, the lowest energy consumption occurred in the microwave drying method and this was followed by the infrared and hot-air drying methods. Energy consumption is zero for the open sun drying so this drying method isn't accounted for in Figure 4. As seen in Figure 4, the total energy consumption decreases with the increasing air temperature and power level. The best result with regard to energy consumption was obtained for microwave drying at the 180 W power level. The energy consumption at this level was 0.042 kWh. Among all the drying methods the highest value with respect to the energy consumption was obtained for the hot-air drying process at a temperature of 50°C and 1.35 kWh. The energy consumption was 0.042–0.054, 0.44–0.56 and 0.75–1.35 kWh for microwave, infrared and hot-air drying, respectively. As a result, the energy consumption in the drying processes carried out at low temperature and power levels which yielded a longer drying period was determined to be at higher rates. These results agree with the observations of previous researchers [44, 45].

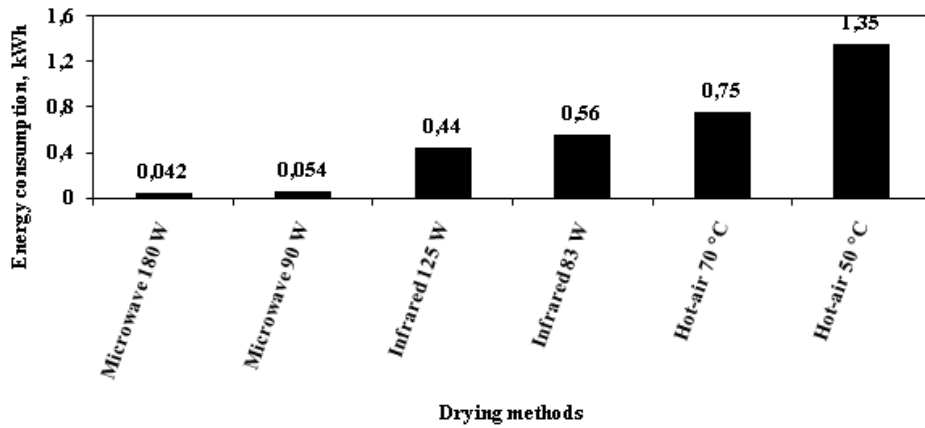


Fig. 4. Energy consumption versus different drying methods of pumpkin slices during the drying process.

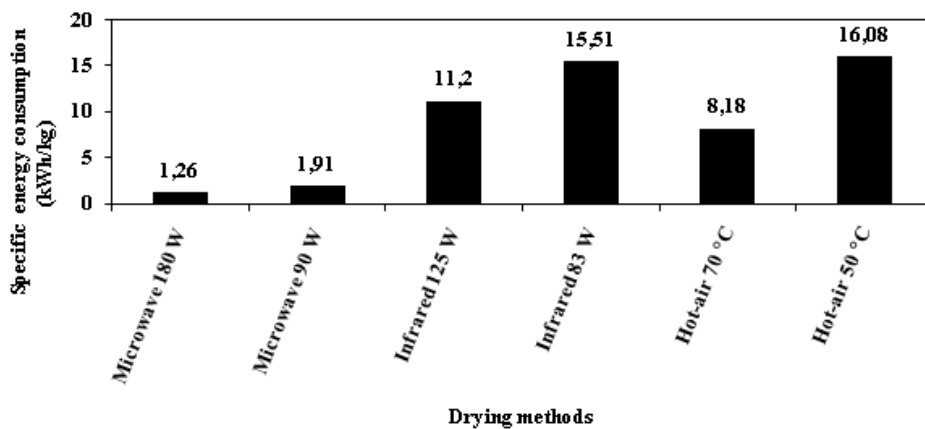


Fig. 5. Specific energy consumption versus different drying methods and conditions for drying of 1 kg wet product.

#### Specific energy consumption

The specific energy consumption was determined by considering the total energy supplied to dry pumpkin samples from an initial moisture content of about 11.5 g water/g dry matter to a final moisture content of approximately 0.05 to 0.10 g water/g dry matter in all three dryers.

The specific energy consumption of the drying process under the different drying methods and conditions was calculated by Equation (13) and this graph is given in Figure 5.

As can be understood from Figure 5, a minimum heat energy (1.26 kWh/kg) is needed by the microwave drying method to dry 1 kg of pumpkin slices. The maximum energy (16.08 kWh/kg) is needed for the hot-air drying method. Because of a minimum of heat energy consumption (1.26 kWh/kg) and less drying time (14 min) it can be said from Figure 5 that the microwave drying method must be selected for drying the fresh pumpkin samples. Again as seen from Figure 5, reducing the specific energy consumption was observed by the increase in power level and

temperature. These results are similar to those reported by the researchers for the other products [46, 47, 28, 48].

#### CONCLUSION

The pumpkin (*Cucurbita pepo* L.) has an important place for our country's vegetable production. Obtaining new products by drying pumpkin slices will increase the income gained from pumpkin production/processing and this situation will allow for the consumption of pumpkin all the year round. Researchers were motivated to prospect using different combinations of drying technologies because of the increasing trends in energy cost, product quality and product quantity.

Based on the conducted experiments, we can draw the following conclusions. The vacuum drying process is not suitable for the drying of pumpkin slices. The best result based on the drying period, coefficient of diffusion and specific energy consumption was obtained by the microwave drying method at the 180 W output power level.

In drying pumpkin slices by this method, the drying period was found to be 14 min, the coefficient of diffusion was  $2.48 \times 10^{-7} \text{ m}^2\text{s}^{-1}$ , the energy consumption was found to be 0.042 kWh and the specific energy consumption was found to be 1.26 kWh/kg.

For the foodstuffs high “L”, “b” and low “a” values are important parameters.

The measured colour parameters of the dried samples compared to fresh, the best colour quality was obtained in the pumpkin slices dried by the hot-air and open-sun drying methods.

The experimental data was obtained as a consequence of drying pumpkin slices by five different drying methods and the conditions were modelled with seven different thin layer drying models available in the literature. The Midilli et al. model, which will be used for determining the changing of the product’s moisture content, has a high modelling efficiency. Therefore it is possible to obtain results very close to the experimental values.

The opinion is that the microwave drying method can be easily applied industrially and offers uniform high quality products to the consumer.

#### REFERENCES

1. R.W. Robinson, D.S. Decker-Walters, Cucurbits, CAB International, New York, NY, (1997).
2. FAO, FAO Statistical Database (2012), available from: <http://www.fao.org>
3. M.A. Karim, M.N.A. Hawlader, *Int. J. Heat Mass Transfer.*, **48**, 4914 (2005).
4. D. Arslan, M.M. Ozcan, *LWT-Food Sci and Technol.*, **43**, 1121 (2010).
5. M. Zielinska, M. Markowski, *Chem Eng Process.*, **49**, 212 (2010).
6. D.B. Jadhav, G.L. Visavale, N. Sutar, *Drying Technol.*, **28**, 600 (2010).
7. F.M. Berruti, M. Klaas, C. Briens, F. Berruti, *J Food Eng.*, **92**, 196 (2009).
8. İ. Doymaz, *J Food Eng.*, **79**, 243 (2007).
9. A. Arevalo-Pinedo, F.E.X. Murr, *J Food Eng.*, **80**, 152 (2007).
10. G.P. Sharma, S. Prasad, *J Food Eng.*, **50**, 99 (2001).
11. R. Vadivambal, D.S. Jayas, *Biosyst Eng*, **98**, 1 (2007).
12. M. Zhangz, J. Tang, A. J. Majumdar, S. Wang, *Trends Food Sci Tech.*, **17**, 524 (2006).
13. C. Strumillo, T. Kudra, *Drying: Principles, Applications and Design.*, Topics in Chemical Engineering. R.Hughes (ed.), Vol. 3. New York; Gordon and Breach Science Publishers, p. 371, (1986).
14. H. Kocabiyik, D. Tezer, *Int J Food Sci Tech.*, **44**, 953 (2009).
15. AOAC., Official method of analysis, Arlington, USA, (1990).
16. R.A. Chayjan, M. Kaveh, S. Khayati, *J Food Process Preserv.*, **1745**, 4549 (2014).
17. J. Crank, *The Mathematics of Diffusion*, second ed. Oxford University Press, London, UK, (1975).
18. K. Sacilik, *J. Food Eng.*, **79**(1), 23 (2007).
19. J.S. Roberts, D.R. Kidd, O. Padilla-Zakour, *J. Food Eng.*, **89**, 460 (2008).
20. S.M. Henderson, S. Pabis, *J Agr Eng Res.*, **6**, 169 (1961).
21. G. Page, [M.S. thesis], Factors influencing the maximum rates of air-drying shelled corn in thin layer, Department of Mechanical Engineering, Purdue University, West Lafayette, IN. 1949.
22. R.P. Kingsly, R. K. Goyal, M. Manikantan, S. M. Ilyas, *Int J Food Sci Tech.*, **42**, 65 (2007).
23. M. Aghbashlo, M.H. Kianmehr, S. Khani, M. Ghasemi, *Int Agrophys.*, **23**, 313 (2009).
24. L.R. Verma, R.A. Bucklin, J.B. Endan, F.T. Wratten, *TASAE*, **28**, 296 (1985).
25. A. Midilli, H. Kucuk, Z. Yapar, *Drying Technol.*, **20**(7), 1503 (2002).
26. K.O. Falade, O.S. Ogunwolu, *J. Food Process.*, **38**, 373 (2014).
27. S. Phoungchandang, S. Saentaweek, *Food Bioprod Process.*, **89** (4), 429 (2011).
28. A. Motevali, S. Minaei, M. H. Khoshtagaza, *Energ Convers Manage.*, **52**(2), 1192 (2011).
29. M. Aghbashlo, M.H. Kianmehr, H. Samimi-Akhijahani, *Energ Convers Manage.*, **49**, 2865 (2008).
30. W. Jindarat, P. Rattanadecho, S. Vongpradubcha, *Exp Therm Fluid Sci.*, **35**(4), 728 (2011).
31. L.V. Mana, T. Orikasa, Y. Muramatsu, A. Tagawa, *J Food Process Technol.*, **3**, 10 (2012).
32. J. Wang, J.S. Wang, Y. Yu, *Int J Food Sci Tech.*, **42**, 148 (2007).
33. T.Y. Tunde-Akintunde, G. O. Ogunlakin, *J Food Sci Tech.*, **50** (4), 705 (2013).
34. P.K. Wankhade, R.S. Sapkal, V. S. Sapkal, *Procedia Eng.*, **51**, 371 (2013).
35. İ. Doymaz, *J. Agric. Sci.*, **19**, 44 (2013).
36. D. Evin, *Food Bioprod Process.*, **90**, 323 (2012).
37. J. Wang, K. Sheng, *LWT.*, **39**, 247 (2006).
38. T. Rakcejeva, R. Galoburda, L. Cude, E. Strautniece, *Procedia Food Sci.*, **1**, 441 (2011).
39. M. Shafafi Zenoozians, H. Feng, S. M. A. Razavi, F. Shahidi, H.R. Pourreza, *J Food Process Pres*, **32**, 88 (2008).
40. I. Alibas, *LWT.*, **40**, 1445 (2007).
41. R.P.F. Guine, S. Pinho, M. J. Barroca, *Food Bioprod Process.*, **89**, 422 (2011).
42. Z. Erbay, F. Icier, *Crit Rev Food Sci Nutr.*, **50** (5), 441 (2010).
43. P.S. Madamba, R.H. Driscoll, K. A. Buckle, *J. Food Eng.*, **29**(1), 75 (1996).
44. I. Alibas, *Biosystems Eng.*, **96**(4), 495 (2007).
45. H.S. El-Mesery, G. Mwithiga, *Afr. J. Agric. Res.*, **7**(31), 4440 (2012).
46. A.R. Celma, F.L. Rodriguez, F. C. Blazquez, *Food Bioprod Process.*, **87**, 247 (2009).
47. I. Das, S.K. Das, S. Bal, *J Food Eng.*, **62**, 9 (2004).
48. G.P. Sharma, S. Prasad, *Energy.*, **31**, 1921 (2006).

## ОЦЕНЯВАНЕ НА МЕТОДИТЕ И УСЛОВИЯТА НА СУШЕНЕ СПОРЕД КИНЕТИКАТА, КАЧЕСТВАТА НА ЦВЕТОВЕТЕ И СПЕЦИФИЧНАТА ЕНЕРГИЯ НА СУШЕНЕ НА ТЪНКИ СЛОЕВЕ ОТ ТИКВА

О. Исмаил<sup>1</sup>, Й.Г. Коджабай<sup>1,2</sup>

<sup>1</sup>*Департамент по химично инженерство, Факултет по химично и металургично инженерство, Кампус „Давут паша“, Технически университет „Йилдиз“, 34210 Истанбул, Турция*

<sup>2</sup>*Регионална лаборатория по възстановяване и консервация в Истанбул, Турция*

Постъпила на 3 август 2015 г.; коригирана на 21 септември 2015 г.

(Резюме)

В тази работа са изследвани експериментално температурата на сушене на резени от тиква (*Cucurbita pepo* L.) и нивата на мощността. Образците са дехидратирани по пет различни метода: на открито, под вакуум, микровълни, инфрачервени лъчи и горещ въздух. Две нива на мощността са изпитани както следва: микровълни (90 и 180 W), инфрачервени лъчи (83 и 125 W) и горещ въздух (50 и 70 °C), за да се изследва ефекта на тези методи. Вакуумното сушене е изследвано при постоянна температура от 50 °C и налягане от 0.1 kPa. Опитните данни за влагата са обработени по различни модели, известни в литературата (на Lewis, Henderson & Pabis, Page, логаритмичен, Aghbashlo и др., Verma и др. и Midilli и др.). Според тези резултати моделът на Midilli и др. превъзхожда останалите в хода на сушенето на образците. Енергийната ефективност и дифузионните коефициенти нарастват с нарастване на мощността на микровълните. От цвetoва гледна точка най-добри резултати се получават при сушене с горещ въздух и на открито.

## Preparation, characterization and fluorescence of two cadmium compounds with different extended structures

Z.-L. Yao<sup>2</sup>, Y.-P. Pei<sup>1</sup>, Z.-Y. Luo<sup>1</sup>, R.-H. Hu<sup>1</sup>, Y.-X. Yang<sup>1</sup>, Wen-Tong Chen<sup>1\*</sup>

<sup>1</sup>*Institute of Applied Chemistry, School of Chemistry and Chemical Engineering, Jiangxi Province Key Laboratory of Coordination Chemistry, Jingtangshan University, Ji'an, Jiangxi 343009, China*

<sup>2</sup>*Biology and Chemistry Engineering Department, Fuqing Branch of Fujian Normal University, Fuqing, Fujian 350300, P.R. China*

Received August 6, 2015, Revised August 19, 2015

Two cadmium compounds,  $[\text{Cd}_2\text{Cl}_4(2,2'\text{-bipy})]_n$  (**1**) and  $[\text{CdCl}_2(2,2'\text{-bipy})]_n$  (**2**) (bipy = bipyridine) with different extended structures, have been obtained from hydrothermal reactions and structurally characterized by X-ray single-crystal diffraction. Compound **1** is characterized by a three-dimensional (3D) structure and the cadmium ion is coordinated by three chloride ions and one nitrogen atom to yield a tetrahedron. Differently, compound **2** features a one-dimensional (1D) structure and the cadmium ion is coordinated by four chloride ions and two nitrogen atoms to yield an octahedron. Fluorescence investigation shows that compound **1** displays an emission in the ultraviolet region, while compound **2** exhibits an emission in the green region.

**Keywords:** crystal, cadmium, extended structure, fluorescence, hydrothermal reaction

### INTRODUCTION

Because of the intrinsic aesthetic appeal and the various applications, metal halide bipyridine compounds have recently gained more and more interest [1-23]. The pyridyl rings of the bipyridine are characteristic of a delocalized  $\pi$ -system. Therefore, bipyridine is a useful ligand for preparing light emitting compounds which can be applied in many fields such as organic light emitting diodes, chemical sensors and solar energy conversion. To our knowledge, a large amount of metal halide bipyridine compounds have been reported so far [1]. However, the group-12 (IIB) metal halide bipyridine compounds are still relatively rare. Actually, the IIB metal halide bipyridine compounds can usually exhibit useful fluorescence and photoelectric properties. Furthermore, 2,2'-bipyridine is a bifunctional ligand and it can act as a bidentate ligand to coordinate the metal ions. Our recent efforts in synthesizing IIB metal halide bipyridine compounds are mainly aimed at the systems containing the 2,2'-bipyridine. In this paper, we report the preparation, crystal structures and fluorescence of two cadmium compounds  $[\text{Cd}_2\text{Cl}_4(2,2'\text{-bipy})]_n$  (**1**) and  $[\text{CdCl}_2(2,2'\text{-bipy})]_n$  (**2**) (bipy = bipyridine) which are synthesized from hydrothermal reactions. It is noteworthy that both compounds show totally different extended structures, although they have similar molecular formula.

### EXPERIMENTAL

#### Materials and instrumentation

All chemicals and reagents employed are purchased and used as received without purification. Fluorescence studies are performed with solid state samples at room temperature on a computer-controlled JY FluoroMax-3 spectrometer.

#### Synthesis of $[\text{Cd}_2\text{Cl}_4(2,2'\text{-bipy})]_n$ (**1**).

A mixture of  $\text{CdCl}_2$  (1 mmol, 183 mg) and 2,2'-bipy (0.5 mmol, 78 mg) are stirred and dissolved in 1 mL ethanol and 9 mL distilled water at an ambient temperature. Then, the mixture is heated at 180 °C for 10 days in a 25 mL teflon-lined stainless steel autoclave. Colorless block crystals of compound **1** are obtained and dried in air.

#### Synthesis of $[\text{CdCl}_2(2,2'\text{-bipy})]_n$ (**2**).

This compound is prepared by mixing  $\text{CdCl}_2$  (1 mmol, 183 mg), 2,2'-bipy (1 mmol, 156 mg), 3 mL ethanol and 7 mL distilled water in a 25 mL Teflon-lined stainless steel autoclave and heated at 180 °C for 10 days. After being slowly cooled down to room temperature at 6 K/h, colorless crystals are collected.

#### X-ray structure determination.

The X-ray single-crystal data set of both compounds are measured on a Rigaku Mercury CCD X-ray area detector with graphite monochromatic Mo- $K\alpha$  radiation ( $\lambda = 0.71073 \text{ \AA}$ ). Their data reduction and empirical correction

\* To whom all correspondence should be sent:  
E-mail: cwtqq@aliyun.com

absorption are performed with the CrystalClear software. Crystal structures for both compounds are solved by the direct methods and refined by full-matrix least-squares techniques against  $F^2$  with the Siemens SHELXTL™ Version 5 crystallographic software package. Non-hydrogen atoms are found based on the difference Fourier maps, while the hydrogen atoms are symmetrically generated and allowed to ride on the parent atoms. The crystal data and structural refinement parameters are presented in Table 1. Selected bond lengths and angles are given in Table 2. CCDC No. 1416689 (**1**) and 1416690 (**2**).

## RESULTS AND DISCUSSION

The ORTEP figure displaying the molecular structure of compound **1** is shown in Figure 1.

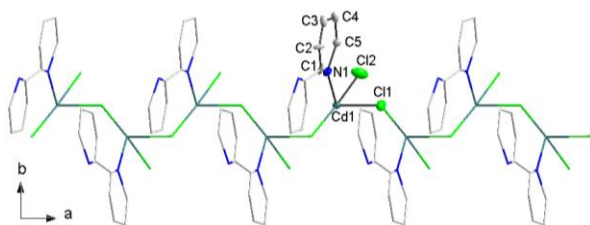


**Fig. 1.** An ORTEP figure showing the molecular structure of compound **1** (hydrogen atoms were omitted for clarity)

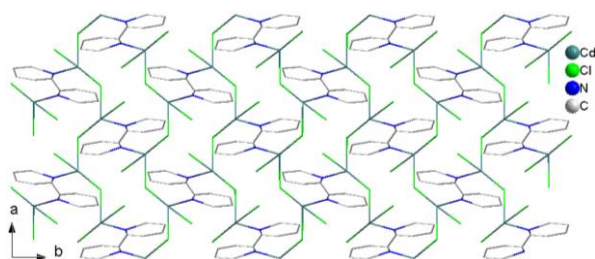
The X-ray single-crystal diffraction results reveal that the molecular structure of compound **1** is characterized by a three-dimensional (3D) structure. All of the crystallographically independent atoms are located on the general positions. The cadmium ion is coordinated by three chloride ions and one nitrogen atom to yield a tetrahedron. The bond length of Cd-N is 2.208(2) Å, while the Cd-Cl bond lengths are between 2.5185(16) Å and 2.6722(13) Å. These bond lengths are normal and comparable with those previously reported [1-8]. The bond angle of N-Cd-N is 69.18(7)°. The bond angles of N-Cd-Cl and Cl-Cd-Cl are in the wide range of 85.70(6)°–160.069(12)° and 84.35(8)°–178.694(2)°, respectively. The result of the bond valence calculation reveals that the cadmium ion is in the +2 oxidation state (Cd1: 1.7) [1]. The pyridyl rings of 2,2'-bipy are perfectly coplanar with the nitrogen atoms pointing in opposite directions. The 2,2'-bipy of compound **1** acts as a bidentate ligand binding to two cadmium(II) ions. The deviation of the atoms of the pyridyl rings is -0.099 Å – +0.081 Å apart from their average ring plane. The molecules of compound **1** interlink two neighboring ones via the chloride ions to form an infinite chain running along the *a* axis (Figure 1). The chains further interconnect together to yield a three-dimensional (3D) framework, as given in Figure 2.

**Table 1.** Crystallographic data and structural refinement parameters for **1** and **2**

Compound	<b>1</b>	<b>2</b>
Empirical formula	C10 H8 Cd2 Cl4 N2	C10 H8 Cd Cl2 N2
Color and Habit	colorless block	colorless block
Crystal Size (mm)	0.14 0.10 0.08	0.12 0.08 0.05
Crystal system	monoclinic	monoclinic
Space group	<i>I</i> 2/ <i>a</i>	<i>C</i> 2/ <i>c</i>
<i>a</i> (Å)	7.1691(4)	17.52(2)
<i>b</i> (Å)	9.3087(5)	9.290(10)
<i>c</i> (Å)	16.4175(12)	7.165(9)
$\beta$ (°)	93.1810(10)	110.897(14)
<i>V</i> (Å <sup>3</sup> )	1093.93(12)	1090(2)
Formula weight	522.78	339.48
<i>Z</i>	4	4
Theta range (°)	5.41 – 25.02	4.98 – 25.00
Reflections collected	1734	3455
Independent, observed reflections ( $R_{int}$ )	526, 513 (0.0196)	884, 433 (0.0577)
Density(cal.) (g/cm <sup>3</sup> )	3.174	2.665
Absorption coefficient (mm <sup>-1</sup> )	4.838	5.405
Temperature(K)	296(2)	296(2)
<i>F</i> (000)	984	790
<i>R</i> 1, <i>wR</i> 2	0.0695, 0.1642	0.0866, 0.1353
Goodness-of-fit	1.018	0.645
Largest and Mean Delta/Sigma	0, 0	0.004, 0
$\Delta\rho$ (max, min) (e/Å <sup>3</sup> )	1.265, -0.858	1.779, -0.872

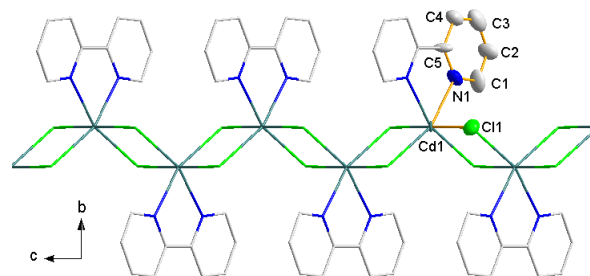
**Table 2.** Some bond lengths (Å) and angles (°)

Compound 1			
Cd(1)-N(1)	2.208(2)	N(1)-Cd(1)-Cl(1)	89.56(7)
Cd(1)-Cl(1)	2.5877(13)	Cl(2)-Cd(1)-Cl(1)	177.39(5)
Cd(1)-Cl(1)#1	2.6722(13)	N(1)-Cd(1)-Cl(1)#1	82.65(7)
Cd(1)-Cl(2)	2.5185(16)	Cl(2)-Cd(1)-Cl(1)#1	84.91(6)
N(1)-Cd(1)-Cl(2)	88.21(7)	Cl(1)-Cd(1)-Cl(1)#1	96.15(4)
Symmetry codes: #1 $x-1/2, -y+2, z$ .			
Compound 2			
Cd(1)-N(1)	2.3220(18)	Cl(1)-Cd(1)-Cl(1)#1	103.40(8)
Cd(1)-N(1)#1	2.3220(18)	N(1)-Cd(1)-Cl(1)#2	95.38(6)
Cd(1)-Cl(1)	2.5422(17)	N(1)#1-Cd(1)-Cl(1)#2	85.70(6)
Cd(1)-Cl(1)#1	2.5422(17)	Cl(1)-Cd(1)-Cl(1)#2	94.83(8)
Cd(1)-Cl(1)#2	2.752(2)	Cl(1)#1-Cd(1)-Cl(1)#2	84.35(8)
Cd(1)-Cl(1)#3	2.752(2)	N(1)-Cd(1)-Cl(1)#3	85.70(6)
N(1)-Cd(1)-N(1)#1	69.18(7)	N(1)#1-Cd(1)-Cl(1)#3	95.38(6)
N(1)-Cd(1)-Cl(1)	160.069(12)	Cl(1)-Cd(1)-Cl(1)#3	84.35(8)
N(1)#1-Cd(1)-Cl(1)	94.61(7)	Cl(1)#1-Cd(1)-Cl(1)#3	94.83(8)
N(1)-Cd(1)-Cl(1)#1	94.61(7)	Cl(1)#2-Cd(1)-Cl(1)#3	178.694(2)
Symmetry codes: #1 $-x+1, y, -z+3/2$ ; #2 $x, -y+1, z+1/2$ ; #3 $-x+1, -y+1, -z+1$ .			

**Fig. 2.** A packing figure of compound 1 viewed down along the  $c$  axis.

Compound 2 crystallizes in the space group  $C2/c$  of the monoclinic system, while compound 1 crystallizes in the monoclinic  $I2/a$  space group. The Cd(II) ion of compound 2 is located in a special position, while other crystallographically independent atoms reside at general positions. The crystal structure of compound 2 is characteristic of a one-dimensional (1D) chain-like motif comprising of  $\text{CdCl}_2(2,2'\text{-bipy})$  building blocks. As depicted in Figure 3, the cadmium ion of compound 2 is coordinated by four chloride ions and two nitrogen atoms to yield an octahedron. The equatorial plane of this octahedron yields two nitrogen atoms and two chloride ions, while both apical positions are occupied by another two chloride ions. The result of the bond valence calculation reveals that the cadmium ion is in the +2 oxidation state (Cd1: 2.1). Different from compound 1, both nitrogen atoms of the pyridyl rings of compound 2 point in the same direction and both of them are coordinated to the same cadmium ion. The bond lengths of Cd–N and Cd–Cl in the equatorial plane are 2.3220(18) Å and 2.5422(17) Å, respectively. The bond lengths of the apical Cd–Cl are 2.752(2) Å. The bond distances of Cd–N and Cd–Cl in the coordination sphere of the

cadmium ion are normal and comparable with those reported in the references [1, 2, 3, 4]. Each cadmium(II) ion interconnects two neighboring ones through two  $\mu_2$ -chloride ions to form an infinite 1-D chain-like motif, as displayed in Figure 3. The 2,2'-bipy of compound 2 is a bidentate ligand chelating one cadmium(II) ion, while that of compound 1 acts as a bidentate ligand binding to two cadmium(II) ions. The dihedral angle between the pyridyl rings of the 2,2'-bipy molecule of compound 2 is 7.024(23)°. The 1-D chains stack together via the van der Waals interaction to give a 3-D packing figure, as shown in Figure 4. The reason for the 3D structure and 1D chain in compounds 1 and 2, respectively, should be ascribed to different coordination modes of the 2,2'-bipy ligand. In compound 1, two nitrogen atoms of one 2,2'-bipy point to opposite directions that allow the 2,2'-bipy to bind to two different cadmium(II) ions and yield a 3D structure. However, in compound 2, both nitrogen atoms of one 2,2'-bipy point to the same direction and both of them are coordinated to one same cadmium ion and only form a 1D chain.

**Fig. 3.** An ORTEP figure showing the molecular structure of compound 2 (hydrogen atoms were omitted for clarity).

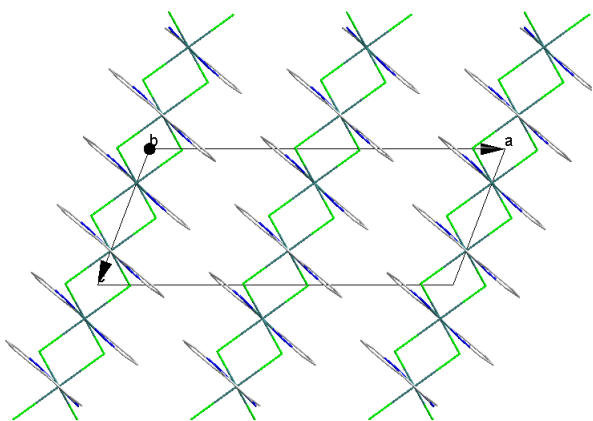


**Fig. 4.** A packing figure of compound **2** viewed down along the *b* axis

To our knowledge, the 2,2'-bipy and the cadmium ion can generally display fluorescence [5, 6, 7]. Based on this consideration, we deduced the fluorescence spectra for both compounds by using solid-state samples at an ambient temperature. As presented in Figure 5, the excitation spectra of compound **1** shows that the effective energy absorption is dominantly found in the ultraviolet region of 300–350 nm.

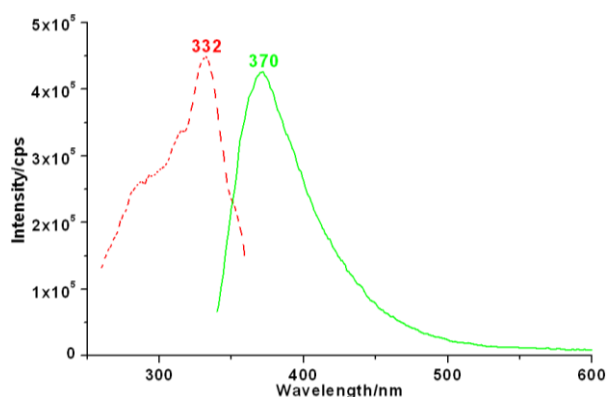


**Fig. 5.** Solid-state fluorescence spectra of compound **1** under room temperature with the dashed and solid lines representing excitation and emission spectra, respectively.

Excitation at 370 nm yields a strong band at 332 nm. The peak at 332 nm, is an intensive emission in the ultraviolet region. As for compound **2**, we also measured its fluorescence spectra and the result is shown in Figure 6. As depicted in Figure 6, the excitation spectra of compound **2**, exhibits the effective energy absorption mainly in the ultraviolet region of 350–400 nm. The excitation spectra under the emission of 522 nm display a strong band at 391 nm. By virtue of the excitation peak of 391 nm, we also measured the emission spectra of compound **2** and the result shows an intensive emission peak in the green region with a maximum value of 522 nm.

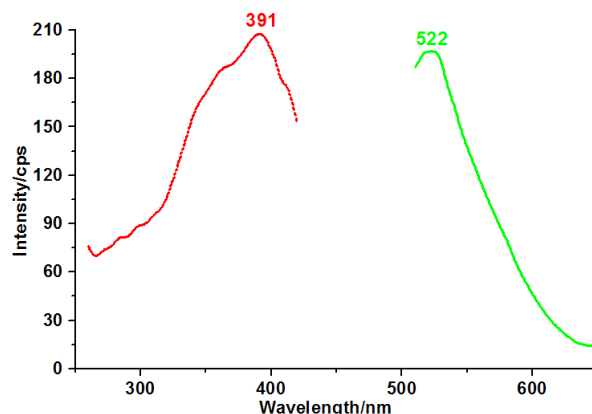


**Fig. 6.** Solid-state fluorescence spectra of compound **2** under room temperature with the dashed and solid lines representing excitation and emission spectra, respectively.

In summary, two cadmium compounds with different extended structures have been synthesized through hydrothermal reactions and structurally characterized by X-ray single-crystal diffraction. Compound **1** features a 3D structure, while compound **2** is characterized by a 1D motif. The coordination environments of the cadmium ions and the binding modes of the 2,2'-bipy ligand in both compounds are different, which yields different extended structures of the title compounds. Fluorescence investigation shows that the compounds display different fluorescence spectra.

**Acknowledgements:** We acknowledge the financial support of the NSF of China (21361013), the science and technology project of Jiangxi Provincial Department of Education (GJJ14554), the NSF of Jiangxi Province (20132BAB203010), and the open foundation (No. 20150019) of the State Key Laboratory of Structural Chemistry, Fujian Institute of Research on the Structure of Matter, Chinese Academy of Sciences.

## REFERENCES

1. C. K. Prier, D. A. Rankic, D. W. C. MacMillan. *Chem. Rev.*, **113**, 5322 (2013).
2. C. Riplinger, M. D. Sampson, A. M. Ritzmann, C. P. Kubiak, E. A. Carter. *J. Am. Chem. Soc.*, **136**, 16285 (2014).
3. T. R. Cook, Y.-R. Zheng, P. J. Stang. *Chem. Rev.*, **113**, 734 (2013).
4. A. O. Surov, A. A. Simagina, N. G. Manin, L. G. Kuzmina, A. V. Churakov, G. L. Perlovich. *Crystal Growth Des.*, **15**, 228 (2015).
5. Z. Yao, W. Chen, R. Hu. *Indian J Chem, Sec A*, **54**, 489 (2015).
6. H. F. Chen, M. J. Zhang, M. S. Wang, W. B. Yang, X. G. Guo, C. Z. Lu. *Inorg. Chem. Commun.*, **23**, 123 (2012).
7. R. Hu, W. Chen, Q. Y. Luo, Y. Xu, X. Zhang. *Asian J.*

- Chem.*, **27**, 2339 (2015).
8. W. Chen. *Journal of Jingtangshan University (Natural Science)*, **35**(5), 38 (2014).
9. Z. H. Lei, X. Li. *J. Coord. Chem.*, **64**, 2450 (2011).
10. W.-T. Chen, Z.-L. Yao, H.-M. Kuang, H.-L. Chen, Z.-G. Luo. *Synth. React. Inorg. M.*, **45**, 952 (2015).
11. Z. Ma, B. Liu, H. Yang, Y. Xiang, M. Hu, J. Sun. *J. Coord. Chem.*, **62**, 3314 (2009).
12. B. Machura, I. Nawrot, K. Michalik. *Polyhedron*, **31**, 548 (2012).
13. W. Chen. *Synth. React. Inorg. M.*, **45**, 315 (2015).
14. I. D. Brown, D. Altermat. *Acta Crystallogr. B.*, **41**, 244 (1985).
15. X.-H. Jin, J.-K. Sun, L.-X. Cai, J. Zhang. *Chem. Commun.*, **47**, 2667 (2011).
16. W. Chen, R. Hu, X. Yi, Y. Wang, Z. Luo, H. Fu, J. Liu, H. Chen. *Asian J. Chem.*, **26**, 4865 (2014).
17. C. Hu, Q. Li, U. Englert. *CrystEngComm.*, **5**, 519 (2003).
18. W. Chen, R. Hu, Z. Luo, H. Chen, X. Zhang, J. Liu. *Indian J Chem, Sec A*, **53**, 294 (2014).
19. M. S. Henry, M. Z. Hoffman. *J. Am. Chem. Soc.*, **99**, 5201 (1977).
20. M. S. Henry, M. Z. Hoffman. *J. Phys. Chem.*, **83**, 618 (1979).
21. H. J. Zhao, D. Jia, J. H. Li, G. J. Moxey, C. Zhang. *Inorg. Chim. Acta*, **432**, 1 (2015).

## ПРИГОТВЯНЕ, ОХАРАКТЕРИЗИРАНЕ И ФЛУОРЕСЦЕНЦИЯ НА ДВЕ КАДМИЕВИ СЪЕДИНЕНИЯ С РАЗЛИЧНИ РАЗГЪНАТИ СТРУКТУРИ

Ж.-Л. Яо<sup>2</sup>, И.-П. Пей<sup>1</sup>, Ж.-И. Луо<sup>1</sup>, Р.-Х. Ху<sup>1</sup>, И.-С. Яанг<sup>1</sup>, Уен-Тонг Чен<sup>1\*</sup>

<sup>1</sup>Институт по приложна химия, Колеж по химия и химично инженерство, Ключова лаборатория по координационна химия в провинция Янгси, Университет Джингангшан, Джсиан, Янгси 343009, Китай  
<sup>2</sup>Департамент по химично и биоинженерство, Клон Фуджин на Университета във Фуджиян, Фуджиян 350300, Китай

Постъпила на 6 август 2015 г.; коригирана на 19 август 2015 г.

(Резюме)

Две кадмиеви съединения  $[\text{Cd}_2\text{Cl}_4(2,2'\text{-bipy})]_n$  (**1**) и  $[\text{CdCl}_2(2,2'\text{-bipy})]_n$  (**2**) (bipy = бипиридил) с различни разгънати структури са получени при хидротермални реакции и са структурно охарактеризирани с рентгеноструктурен анализ чрез дифракция на един кристал. Съединение **1** се характеризира с три-измерна (3D) структура, а кадмиевият йон се координира от три хлоридни йона и един азотен атом с получаването на тетраедър. Съединение **2** се характеризира с едно-измерна (1D) структура, а кадмиевият йон се координира с четири хлоридни йона и та азотни атома с получаването на октаедър. Флуоресцентните изследвания показват, че съединение **1** дава емисии в ултравиолетовата област, докато съединение **2** проявява емисии в зелената област на спектъра.

## Non-Darcy effect on non-Newtonian Bingham fluid with heat transfer between two parallel plates

W. Abbas<sup>1</sup>, Hazem Ali Attia<sup>2</sup>, Mostafa A. M. Abdeen<sup>3\*</sup>

<sup>1</sup>Basic and Applied Science Department, College of Engineering and Technology, Arab Academy for Science, Technology, and Maritime Transport, Cairo, Egypt

<sup>2</sup>Department of Engineering Mathematics and Physics, Faculty of Engineering, El-Fayoum University, El-Fayoum-63514, Egypt

<sup>3</sup>Department of Engineering Mathematics and Physics, Faculty of Engineering, Cairo University, Giza-12211, Egypt

Submitted August 13, 2015; Accepted September 15, 2015

The non-Darcy model for the Bingham fluid has a wide range of applications in energy systems and magnetic material processing. This work investigated the effect of unsteady non-Darcy flow on the velocity and temperature distributions for non-Newtonian Bingham fluid between two infinite parallel porous plates with heat transfer considering the Hall Effect. A constant pressure gradient is applied in the main axial direction and an external uniform magnetic field and uniform suction and injection are applied in the direction perpendicular to the plates. The dimensionless governing coupled momentum and energy equations taking the Joule and viscous dissipations into consideration are derived and solved numerically using the finite difference approach. The effect of porosity of the medium, Hartmann, and Hall current parameters on the velocity and temperature distributions with a Reynolds number fixed at 10 (For  $R_e \geq 10$ , non-Darcy model is sufficient) is investigated. It is found that the porosity and inertial effects have a marked effect on decreasing the velocity distribution in an inverse proportionality manner. Furthermore, increasing the non-Darcian parameter decreases the temperature values for each value of the porosity.

**Keywords:** Non-Newtonian fluid, Bingham model, Non-Darcyflow, Heat transfer, Hall current.

### INTRODUCTION

Recently, Researchers have considerable interest in the study of flow phenomenon between two parallel plates because of its possible applications in many branches of science and technology, as its occurrence in rheumatic experiments to determine the constitutive properties of the fluid, in lubrication engineering, and in transportation and processing encountered in chemical engineering, etc. [1]. On the other hand, Couette flow of an electrically conducting viscous incompressible fluid under the action of a transverse magnetic field has many applications in magneto-hydrodynamic (MHD) power generators, aerodynamics heating, pumps, polymer technology, petroleum industry, and fluid droplets-sprays [2]. Bharali and Borkakati [3], studied the effect of Hall currents on magneto hydrodynamic (MHD) flow of an incompressible viscous electrically conducting fluid between two non-conducting porous plates in the presence of a strong uniform magnetic field. The steady flow of an electrically conducting, viscous, incompressible fluid bounded by two parallel infinite insulated horizontal plates and the heat transfer was studied

by Attia and Kotb [4]. Joaquín et al. [5], studied numerically the variations with velocity of suction, hall effect, Reynolds and Hartmann number, particle concentration and Eckert number on the unsteady MHD Couette Flow and heat transfer of a dusty and electrically conducting fluid between parallel plates in the presence of an external uniform magnetic field and uniform suction and injection. The transient hydromagnetic flow through a porous medium between two infinite parallel porous plates with heat transfer considering the Hall effect and the temperature dependent physical properties under constant pressure gradient was studied by Attia et al. [6]. Also, other research work concerning the flow between two parallel plates has been obtained under different physical effects [7-12].

A non-Newtonian fluid is a fluid that does not obey Newton's law of viscosity (viscosity is variable based on applied stress or force). The non-Newtonian fluid is a classical problem that has many industrial applications such as cement, drilling mud, sludge, grease, granular suspensions, aqueous foams, slurries, paints, food products, plastics and paper pulp exhibit a yield stress  $\tau_0$  to allow for the motion of the fluid. Many non-Newtonian fluids, encountered in chemical engineering processes, are known to follow the so-

---

\* To whom all correspondence should be sent:  
E-mail: [mostafa\\_a\\_m\\_abdeen@hotmail.com](mailto:mostafa_a_m_abdeen@hotmail.com)

called ‘‘Bingham model’’ which have a linear shear stress/shear strain relationship and require a finite yield stress before they begin to flow (the plot of shear stress against shear strain does not pass through the origin). Several examples are clay suspensions, drilling mud, toothpaste, mayonnaise, chocolate and mustard. Many authors have studied the flow of a Bingham fluid under different physical effects and geometries, Walton and Bittleston [13], described analytical and numerical solutions for the flow of a Bingham plastic in an eccentric annulus. The magneto-hydrodynamic unsteady flow of an electrically conducting viscous incompressible non-Newtonian Bingham fluid bounded by two parallel non-conducting porous plates was studied with heat transfer considering the Hall effect by Yang and Zuh [14]. Rees and Bassom [15], presented an unsteady free convection flow of a Bingham fluid when it saturates a porous medium and the flows was induced by suddenly raising the constant temperature of a vertical bounding surface.

Fluid flow in porous media is important in many areas of reservoir engineering, such as petroleum, environmental and ground water hydrology[16]. According to previous work, Darcy’s law depicts fluid flow behavior in porous media. The Darcy law is sufficient in studying small rate flows where the Reynolds number is very small ( $Re < 10$ ) [17]. For larger Reynolds numbers the Darcy law is insufficient and several models have been adopted to correct the Darcy law. Based on a review of previous work, the Darcy-Forchheimer model is probably the most popular modification to Darcy flows. In 1901, Philippe Forchheimer assumed that Darcy’s law is still valid, but an additional term must be added to account for the increased pressure drop and represent the microscopic inertial effect [18]. Recent contributions are the interesting studies considered in the references [19-24].

In the present paper, an extension has been made to the study in [25], to assess the influence of Non-Darcy porous media on unsteady non-Newtonian Bingham fluid between two infinite horizontal porous plates, by heat transfer and the Hall Effect. The fluid is acted upon by a constant pressure gradient, a uniform suction from above and a uniform injection from below while it is subjected to a uniform magnetic field perpendicular to the plates. The inclusion of the porosity effect and inertial effects as well as the velocity of suction or injection leads to some interesting effects, on both the velocity and temperature distributions to be investigated.

### MATHEMATICAL MODEL

In the present model, two infinite horizontal plates located at the  $y = \pm h$  planes and extended from  $x = 0$  to  $\infty$  and from  $z = 0$  to  $\infty$  have been considered and filled with incompressible, non-Newtonian fluid obeying the Bingham model and electrically conducting fluid through a porous medium. The characteristics of the porous medium in this study obey the Darcy-Forchheimer model. The fluid flows between the two plates under the influence of a pressure gradient  $dp/dx$  in the  $x$ -direction which is constant with time. The two plates are porous, insulated and kept at two constant but different temperatures  $T_1$  for the lower plate and  $T_2$  for the upper plate ( $T_2 > T_1$ ). The upper plate moves with a uniform velocity  $U_0$  whereas the lower plate is kept stationary. A uniform suction from above and injection from below, with velocity  $v_0$ , are applied impulsively at  $t = 0$ . A uniform magnetic field  $B = (0, B_0, 0)$  is applied parallel to the  $y$ -axis which is normal to the planes of the plates in the positive direction. The effect of the Hall current is considered which results in a new component for the velocity in the  $z$ -direction.

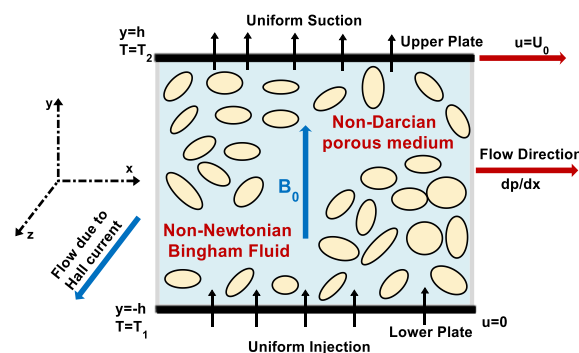


Fig. 1. Schematic diagram of the problem

From the geometry of the problem and due to the infinite dimensions in the  $x$  and  $z$  directions, it is evident that the physical quantities do not change in these directions ( $\partial/\partial x = \partial/\partial z = 0$  for all quantities). The flow in the porous medium deals with the analysis in which the differential equation governing the fluid motion is based on the Darcy-Forchheimer law which considers the drag exerted by the porous medium. The fluid motion starts from rest at  $t = 0$ , and the no-slip condition at the plates implies that the fluid velocity has neither a  $z$  nor an  $x$ -component at  $y = \pm h$ . The initial temperature of the fluid is assumed to be equal to  $T_1$  as the temperature of the lower plate. Figure 1 represents a schematic diagram of the proposed problem.

The governing equations of this study are based on the conservation laws of mass, linear momentum and energy for both phases.

The generalized Ohm's law including the Hall current is given in the form [26]:

$$\vec{j} = \sigma \left[ \vec{E} + \vec{v} \times \vec{B} - \frac{1}{en_e} (\vec{j} \times \vec{B}) \right], \quad (1)$$

Where  $\vec{j}$  is the electric current density vector,  $\sigma$  is the electric conductivity of the fluid,  $\vec{v}$  is the velocity vector,  $\vec{E}$  is the intensity vector of the electric field,  $\vec{B}$  is the induced magnetic vector,  $e$  is the charge of an electron and  $n_e$  is the number density of electrons.

The fluid velocity vector is given by:

$$\vec{v}(y, t) = u(y, t)\vec{i} + v_0\vec{j} + w(y, t)\vec{k}, \quad (2)$$

By neglecting the polarization effect, we get the electric field vector equal to zero ( $\vec{E}=0$ ). The generalized Ohm's law equation (1) gives  $J_y = 0$  everywhere in the flow. The current density components  $J_x$  and  $J_z$  are given as:

$$J_x = \frac{\sigma B_0}{1+m^2} (mu - w), \quad (3a)$$

$$J_z = \frac{\sigma B_0}{1+m^2} (u + mw), \quad (3b)$$

where,  $m$  is the Hall parameter,  $m = \frac{\sigma B_0}{en_e}$ .

The vector equation of motion for the fluid is governed by the momentum equation together with the generalized Ohm's law and non-Darcy's resistance and can be written as:

$$\rho \frac{D\vec{v}}{Dt} = -\nabla p + \nabla \cdot (\mu \nabla \vec{v}) + \vec{j} \times \vec{B} - \frac{\mu}{K} \vec{v} - \frac{\lambda \rho}{K} |\vec{v}| \vec{v}, \quad (4)$$

where,  $\rho$  is the density of the fluid,  $D/Dt$  is a differential operator,  $t$  is the time,  $K$  is the Darcy permeability,  $\lambda$  is the inertial coefficient, and  $\mu$  is the apparent viscosity.

The two components of the momentum equation (4) in the x and z-direction become:

$$\rho \frac{\partial u}{\partial t} + \rho v_0 \frac{\partial u}{\partial y} = \frac{-\partial p}{\partial x} + \frac{\partial}{\partial y} \left( \mu \frac{\partial u}{\partial y} \right) - \frac{\sigma B_0^2}{1+m^2} (u + mw) - \frac{\mu}{K} u - \frac{\lambda \rho}{K} u^2, \quad (5)$$

$$\rho \frac{\partial w}{\partial t} + \rho v_0 \frac{\partial w}{\partial y} = \frac{\partial}{\partial y} \left( \mu \frac{\partial w}{\partial y} \right) - \frac{\sigma B_0^2}{1+m^2} (w - mu) - \frac{\mu}{K} w - \frac{\lambda \rho}{K} w^2, \quad (6)$$

where,  $u$  and  $v$  are velocity components in the x- and z-directions.

The energy equation describing the temperature distribution for the fluid and Joule dissipations is given by Attia et al.[25]:

$$\rho c_p \frac{\partial T}{\partial t} + \rho c_p v_0 \frac{\partial T}{\partial y} = k \frac{\partial^2 T}{\partial y^2} + \mu \left[ \left( \frac{\partial u}{\partial y} \right)^2 + \left( \frac{\partial w}{\partial y} \right)^2 \right] + \frac{\sigma B_0^2}{1+m^2} (u^2 + w^2) \quad (7)$$

where,  $c_p$  and  $k$  are the specific heat capacity and the thermal conductivity of the fluid, respectively and  $T$  denotes the temperature. The second and third terms on the right side represent, respectively, the viscous and Joule dissipations. We notice that each of these terms has two components. This is because the Hall effect leads to an additional velocity component  $w$  in the z-direction.

The shear stress  $\tau$  of the Bingham fluid model can be written as follows[25]:

$$\tau = \tau_0 + K_B \dot{\gamma} \quad \text{for } |\tau| > \tau_0 \\ \dot{\gamma} = 0 \quad \text{for } |\tau| \leq \tau_0$$

where,  $\dot{\gamma} = \sqrt{\left( \frac{\partial u}{\partial y} \right)^2 + \left( \frac{\partial w}{\partial y} \right)^2}$  is the shear rate,  $\tau_0$  is the yield stress,  $K_B$  is the plastic viscosity of the Bingham fluid. Thus, the apparent viscosity is given by:

$$\mu = K_B + \frac{\tau_0}{|\dot{\gamma}|}, \quad (8)$$

Owing to provides no information about the stress field whenever  $\tau < \tau_0$ , and is discontinuous. In order to avoid this discontinuity, Papanastasiou [27] proposed a modified model with a growth rate parameter  $m$  which controls the exponential growth of stress. Thus the Bingham model can be rewritten by using Papanastasiou modification as follows:

$$\tau = \tau_0 [1 - e^{-\delta \dot{\gamma}}] + K_B \dot{\gamma} \quad \text{for all } \dot{\gamma}, \quad (9)$$

The parameter  $m$  controls the stress growth, such that the yield stress  $\tau_0$  a finite stress is allowed to vanish, therefore this model is valid for all regions [28]. For sufficiently the parameter  $\delta > 100$  in the above equation mimics the Bingham plastic model [28]. Thus, the scalar viscosity is given by:

$$\mu = K_B + \frac{\tau_0 [1 - e^{-\delta |\dot{\gamma}|}]}{|\dot{\gamma}|}, \quad (10)$$

The initial and boundary conditions of both the flow and heat problems are, respectively, given by:

$$\text{At } t \leq 0: u = w = 0; T = T_1, \quad (11a)$$

$$\text{At } t > 0: u = w = 0; T = T_1 \\ \text{at } y = -h, \quad (11b)$$

$$\text{At } t > 0: u = U_0; w = 0; T = T_2 \\ \text{at } y = h. \quad (11c)$$

The following non-dimensional variables will be introduced into equations (5)-(7) and (10)-(11):

$$x^* = \frac{x}{h}, y^* = \frac{y}{h}, z^* = \frac{z}{h}, t^* = \frac{t U_0}{h}, \\ u^* = \frac{u}{U_0}, w^* = \frac{w}{U_0}, p^* = \frac{p}{\rho U_0^2}, \\ T^* = \frac{T - T_1}{T_2 - T_1}, \mu^* = \frac{\mu}{K_B}$$

The non-dimensional conservation equations will be in the following forms:

Momentum conservation in the x-direction:

$$\frac{\partial u^*}{\partial t^*} + s \frac{\partial u^*}{\partial y^*} = \frac{-\partial p^*}{\partial x^*} + \frac{1}{R_g} \frac{\partial}{\partial y^*} \left( \mu^* \frac{\partial u^*}{\partial y^*} \right) - \frac{Ha^2}{R_g(1+m^2)} (u^* + mw^*) - \beta \mu^* u^* - \gamma u^{*2} \quad (12)$$

Momentum conservation in the z-direction:

$$\frac{\partial w^*}{\partial t^*} + s \frac{\partial w^*}{\partial y^*} = \frac{1}{R_g} \frac{\partial}{\partial y^*} \left( \mu^* \frac{\partial w^*}{\partial y^*} \right) - \frac{Ha^2}{R_g(1+m^2)} (w^* - mu^*) - \beta \mu^* w^* - \gamma w^{*2} \quad (13)$$

Energy conservation:

$$\frac{\partial T^*}{\partial t^*} + s \frac{\partial T^*}{\partial y^*} = \frac{1}{R_g Pr} \frac{\partial^2 T^*}{\partial y^{*2}} + \frac{E_c \mu^*}{R_g} \left[ \left( \frac{\partial u^*}{\partial y^*} \right)^2 + \left( \frac{\partial w^*}{\partial y^*} \right)^2 \right] + \frac{E_c Ha^2}{R_g(1+m^2)} (u^{*2} + w^{*2}) \quad (14)$$

The apparent viscosity:

$$\mu^* = 1 + \frac{\tau_D \left[ 1 - \eta \sqrt{\left( \frac{\partial u^*}{\partial y^*} \right)^2 + \left( \frac{\partial w^*}{\partial y^*} \right)^2} \right]}{\sqrt{\left( \frac{\partial u^*}{\partial y^*} \right)^2 + \left( \frac{\partial w^*}{\partial y^*} \right)^2}}, \quad (15)$$

The dimensionless initial and boundary conditions of both the flow and heat problems are, respectively, given by:

$$\text{At } t^* \leq 0: u^* = w^* = 0; T^* = 0, \quad (16a)$$

$$\text{At } t^* > 0: u^* = w^* = 0; T^* = 0$$

$$\text{at } y = -1, \quad (16b)$$

$$\text{At } t^* > 0: u^* = 1; w^* = 0; T^* = 1$$

$$\text{at } y = 1, \quad (16c)$$

where,  $R_g = \frac{\rho U_0 h}{K_B}$  is the Reynolds number representing the ratio of inertial forces to viscous forces,  $Ha^2 = \frac{\sigma B_0^2 h^2}{K_B}$  is the Hartmann number squared which represents the ratio of electromagnetic force to the viscous force,  $Pr = \frac{\mu C_p}{k}$  is the Prandtl number which dimensionless number defines the ratio of the momentum diffusivity (kinematic viscosity) to thermal diffusivity,  $\tau_D = \frac{\tau_0 h}{K_B U_0}$  is the dimensionless yield stress,  $S = \frac{V_0}{U_0}$  is the suction parameter representing the mass of the fluid passing through the lower plate and exiting through the upper plate (when  $S > 0$  the suction at the upper plate and injection at the lower plate),  $E_c = \frac{U_0^2}{c_p (T_2 - T_1)}$  is the Eckert number which defines the ratio of the kinetic energy of the flow to the enthalpy difference,  $\beta = \frac{h^2}{R_g K}$  is the porosity parameter,  $\gamma = \frac{\lambda h}{K}$  is the dimensionless non-Darcy parameter, and  $\eta = \frac{\delta U_0}{h}$  is the dimensionless growth parameter.

## NUMERICAL SOLUTION

There are many numerous methods available for the solution of the differential equation system. In the present work the finite difference method is used to solve the coupled non-linear partial differential equation systems (12)–(15) under conditions (16a), (16-b), and (16-c). The computational domain is discretized with a uniform grid of dimension  $\Delta t$  and  $\Delta y$  in time and space respectively as shown in Figure 2. A finite difference scheme for coupled partial differential equation systems (12)–(15) is created using the Crank-Nicolson implicit method which can be achieved by doing an average of the central difference schemes at time levels  $n$  and  $n+1$ .

To solve for the  $n+1$ <sup>th</sup> time step, where we know already the  $n$ <sup>th</sup> time step, we consider our scheme as if we were standing at the  $n+0.5$  time step and then take the average of the forward half time step and backward half time step. So the discretized equations would be of the form:

x-direction momentum equation:

$$\begin{aligned} & \frac{u_i^{n+1} - u_i^n}{\Delta t} + s \left( \frac{u_{i+1}^{n+1} - u_{i-1}^{n+1} + u_{i+1}^n - u_{i-1}^n}{4\Delta y} \right) = -C + \\ & \frac{1}{R_g} \left( \frac{\mu_{i+1}^{n+1} - \mu_{i-1}^{n+1} + \mu_{i+1}^n - \mu_{i-1}^n}{4\Delta y} \right) \left( \frac{u_{i+1}^{n+1} - u_{i-1}^{n+1} + u_{i+1}^n - u_{i-1}^n}{4\Delta y} \right) + \\ & \frac{1}{R_g} \left( \frac{\mu_i^{n+1} + \mu_i^n}{2} \right) \left( \frac{u_{i+1}^{n+1} - 2u_i^{n+1} + u_{i-1}^{n+1}}{2\Delta y^2} + \right. \\ & \left. \frac{u_{i+1}^n - 2u_i^n + u_{i-1}^n}{2\Delta y^2} \right) - \\ & \frac{Ha^2}{R_g(1+m^2)} \left( \frac{u_i^{n+1} + u_i^n}{2} + m \frac{w_i^{n+1} + w_i^n}{2} \right) - \\ & \beta \left( \frac{\mu_i^{n+1} + \mu_i^n}{2} \right) \left( \frac{u_i^{n+1} + u_i^n}{2} \right) - \gamma \left( \frac{u_i^{n+1} + u_i^n}{2} \right)^2 \end{aligned} \quad (17)$$

y-direction momentum equation:

$$\begin{aligned} & \frac{w_i^{n+1} - w_i^n}{\Delta t} + s \left( \frac{w_{i+1}^{n+1} - w_{i-1}^{n+1} + w_{i+1}^n - w_{i-1}^n}{4\Delta y} \right) = \\ & \frac{1}{R_g} \left( \frac{\mu_{i+1}^{n+1} - \mu_{i-1}^{n+1} + \mu_{i+1}^n - \mu_{i-1}^n}{4\Delta y} \right) \left( \frac{w_{i+1}^{n+1} - w_{i-1}^{n+1} + w_{i+1}^n - w_{i-1}^n}{4\Delta y} \right) + \\ & \frac{1}{R_g} \left( \frac{\mu_i^{n+1} + \mu_i^n}{2} \right) \left( \frac{w_{i+1}^{n+1} - 2w_i^{n+1} + w_{i-1}^{n+1}}{2\Delta y^2} + \right. \\ & \left. \frac{w_{i+1}^n - 2w_i^n + w_{i-1}^n}{2\Delta y^2} \right) - \\ & \frac{Ha^2}{R_g(1+m^2)} \left( \frac{w_i^{n+1} + w_i^n}{2} - m \frac{u_i^{n+1} + u_i^n}{2} \right) - \\ & \beta \left( \frac{\mu_i^{n+1} + \mu_i^n}{2} \right) \left( \frac{w_i^{n+1} + w_i^n}{2} \right) - \gamma \left( \frac{w_i^{n+1} + w_i^n}{2} \right)^2 \end{aligned} \quad (18)$$

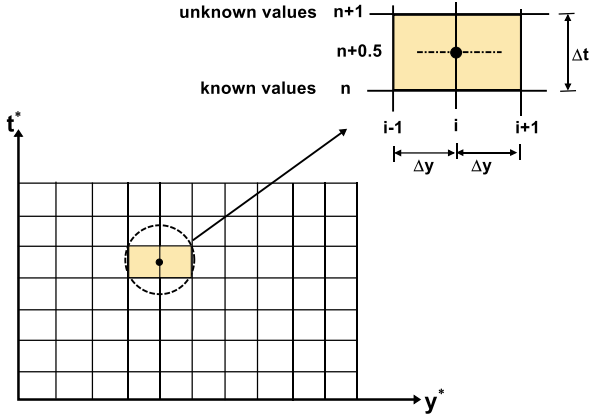


Fig. 2. Mesh layout for the Crank-Nicolson implicit method.

Similarly, the Crank-Nicolson approximation to the Energy equation is:

$$\begin{aligned} & \frac{T_i^{n+1} - T_i^n}{\Delta t} + S \left( \frac{T_{i+1}^{n+1} - T_{i-1}^{n+1} + T_{i+1}^n - T_{i-1}^n}{4\Delta y} \right) = \\ & \frac{1}{Pr Re} \left( \frac{T_{i+1}^{n+1} - 2T_i^{n+1} + T_{i-1}^{n+1}}{2\Delta y^2} + \frac{T_{i+1}^n - 2T_i^n + T_{i-1}^n}{2\Delta y^2} \right) + \\ & \frac{Ec}{Re} \left( \frac{\mu_i^{n+1} + \mu_i^n}{2} \right) \left( \left( \frac{u_{i+1}^{n+1} - u_{i-1}^{n+1} + u_{i+1}^n - u_{i-1}^n}{4\Delta y} \right)^2 + \right. \\ & \left. \left( \frac{w_{i+1}^{n+1} - w_{i-1}^{n+1} + w_{i+1}^n - w_{i-1}^n}{4\Delta y} \right)^2 \right) + \\ & \frac{Ec Ha^2}{Re(1+m^2)} \left( \left( \frac{u_i^{n+1} + u_i^n}{2} \right)^2 + \left( \frac{w_i^{n+1} + w_i^n}{2} \right)^2 \right) \end{aligned} \quad (19)$$

Finally, the resulting block tri-diagonal system is solved using the generalized Thomas-algorithm. All calculations are carried out for the non-dimensional variables and parameters given by,  $\frac{\partial p^*}{\partial x^*} = C = -5$ . Grid-independence studies show that the computational domain  $0 < t < \infty$  and  $1 < y < 1$  is divided into intervals with step sizes  $\Delta t = 0.0001$  and  $\Delta y = 0.005$  for time and space respectively.

## RESULTS AND DISCUSSION

Figures 3-5 show the evolution of dimensionless velocities  $u^*$  and  $w^*$  and temperature distribution  $T^*$  with time  $t^*$  for various Darcy and non-Darcy parameters ( $\beta$  and  $\gamma$ ) at  $Ha=3$ ,  $m=3$ ,  $S=1$ ,  $Re=10$ ,  $Pr=1$ ,  $Ec=0.2$  and  $\tau_D = 0.1$ . Figures 3 and 4 show the effect of Darcy and non-Darcy parameters ( $\beta$  and  $\gamma$ ) on the time development of  $u^*$  and  $w^*$ . It is obvious that increasing the Darcy parameter  $\beta$  decreases  $u^*$  and  $w^*$  and its steady state time as a result of increasing the resistive damping porosity force on  $u^*$  and  $w^*$ . On the other hand, increasing the non-Darcy parameter  $\gamma$  for each value of  $\beta$  decreases the velocity  $u^*$  and  $w^*$  and its steady state

time which reflects the expected resistance because of the inertial effects.

Also, it is observed that the charts of the velocity  $u^*$  are asymmetric about the  $y = 0$  plane because of the suction. Figure 5 shows the effect of Darcy and non-Darcy parameters on the time progression of the temperature  $T^*$ . It is observed that the increase of the Darcy parameter  $\beta$  and non-Darcy parameter  $\gamma$  decreases  $T^*$  and its steady state time. The increasing  $\beta$  and  $\gamma$  decreases  $u^*$  which in turn decreases the viscous dissipation and  $T^*$ . Also, increasing the non-Darcy parameter  $\gamma$  for each value of  $\beta$  further decreases the temperature and its steady time because of the additional resistive inertial effects. Figures 3-a, 4-a, and 5-a, indicate the unsteady non-Newtonian Bingham fluid case where the plates and medium are non-porous ( $\beta=0$  and  $\gamma=0$ ) obtaining the highest velocity and temperature distributions, which were considered earlier by Attia [25]. In addition, we mean a flow without additional inertial effects and the Darcy case where  $\beta=1$  and  $\gamma=0$  as shown in figures 3-b, 4-b and 5-b, obtained to provide an easier quick path for the fluid flow and temperature values.

Figure 6 presents the profiles of the velocity component  $u^*$  and  $w^*$  and temperature distribution  $T^*$  at the center of the channel ( $y^* = 0$ ) with time  $t^*$  for various non-Darcy parameters  $\gamma$  and for  $\tau_D = 0.01$  and  $0.1$  at  $Ha=3$ ,  $m=3$ ,  $S=1$ ,  $Re=10$ ,  $Pr=1$ ,  $Ec=0.2$ . The figures show that, with increasing the yield stress  $\tau_D$  decreases the velocity components  $u^*$  and  $w^*$  and temperature profile  $T^*$ , the time at which they reach their steady state values also decreases as a result of increasing the viscosity. It is obvious that increasing the non-Darcy parameter  $\gamma$  decreases  $u^*$ ,  $w^*$ ,  $T^*$  and its steady state time as a result of increasing the resistive damping porosity force on  $u^*$  and  $w^*$ . Also, it observed that the velocity component  $u^*$  reaches the steady state faster than  $w^*$  which, in turn, reaches the steady state faster than  $T^*$ . This is expected as  $u^*$  is the source of  $w^*$ , while both  $u^*$  and  $w^*$  act as sources for the temperature.

The influence of the non-Darcy parameter  $\gamma$  on the velocity components  $u^*$ ,  $w^*$  and temperature distribution  $T^*$  with time  $t^*$  for various Hartmann numbers  $Ha$  are shown in figure 7 at the center of the channel ( $y^* = 0$ ). It is clear that, with increasing the value of the non-Darcy parameter  $\gamma$  ( $\gamma = 0.1, 2$ ), there is a marked decrease in the velocity components  $u^*$  and  $w^*$ , i.e. the flow is accelerated strongly with the decrease in the non-Darcy parameter, owing to a simultaneous increase in the inertial force in equation (12)  $-\gamma u^{*2}$  and in equation (13)  $-\gamma w^{*2}$ .

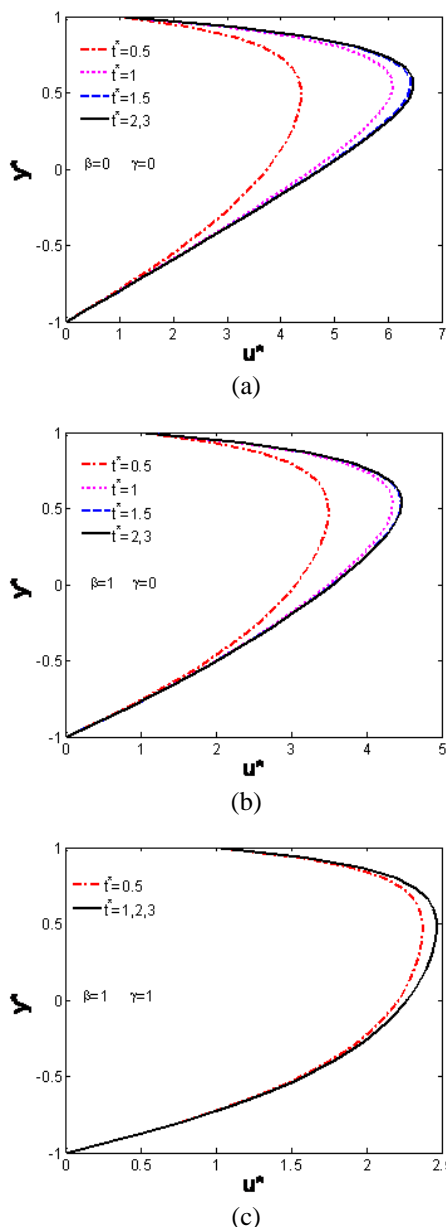


**Fig. 3.** Time variation of the profile of  $u^*$  for various values of  $\gamma$  and  $\beta$ . (a)  $\beta=0$  and  $\gamma=0$ ; (b)  $\beta=1$  and  $\gamma=0$ ; (c)  $\beta=1$  and  $\gamma=1$ .

Figure 7-a shows that, with an increase of the Hartmann number  $Ha$ , the magnitude of the velocity component  $u^*$  is reduced because the hydromagnetic drag force in equation (12),  $\frac{-Ha^2}{R_2(1+m^2)}(u^* + mw^*)$  is proportional to the square of  $Ha$  and remains with a negative sign. Therefore, by increasing the Hartmann number  $Ha$  creates a larger negative force. On the other hand, figure 7-b indicates the increase in the velocity component  $w^*$  with a rise in the Hartmann number because the hydromagnetic force in (13)  $\left(\frac{-Ha^2}{R_2(1+m^2)}(w^* - mu^*)\right)$  has two components, positive

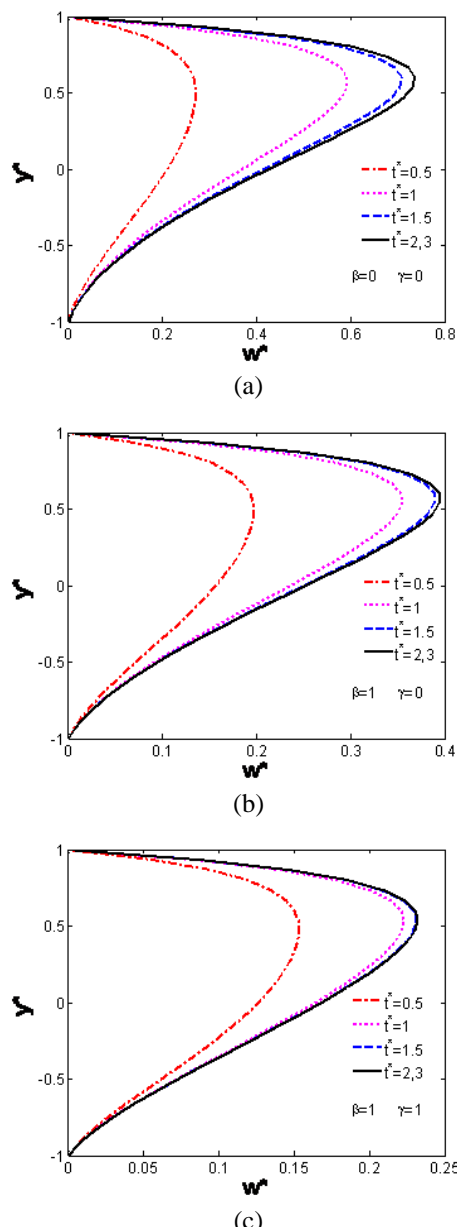


**Fig. 4.** Time variation of the profile of  $w^*$  for various values of  $\gamma$  and  $\beta$ . (a)  $\beta=0$  and  $\gamma=0$ ; (b)  $\beta=1$  and  $\gamma=0$ ; (c)  $\beta=1$  and  $\gamma=1$ .

$u^* \left(\frac{Ha^2}{R_2(1+m^2)} mu^*\right)$  and negative  $w^* \left(\frac{-Ha^2}{R_2(1+m^2)} w^*\right)$ , so the collective effect is markedly boosted with a rise in the Hartmann number. The temperature  $T^*$  is also increasing substantially with increasing the Hartmann number  $Ha$  indicating that the regime is cooled by stronger magnetic fields.

Figure 8 presents the influence of the non-Darcy parameter  $\gamma$  on the velocity components  $u^*$ ,  $w^*$  and the temperature distribution  $T^*$  with time  $t^*$  for the Hall parameter  $m$  at  $\beta = 1, S=1, Ha=3, R_e=10, P_r=1, E_c=0.2, \tau_D=0.1$ . It is clear that by increasing the non-Darcy parameter  $\gamma$  (inertial effect),  $u^*$ ,  $w^*$  and  $T^*$  decrease. Figure 8-a, indicates that the velocity of component  $u^*$  increases by increasing the Hall

parameter  $m$  which can be attributed to the fact that an increment in  $m$  decreases the resistive force. Figure 8-b shows that the velocity component  $w^*$  decreases with the increasing Hall parameter  $m$  which can be attributed to the fact that an increment in  $m$  increases the resistive force. Figure 8-c shows that  $T^*$  decreases with the increasing Hall parameter  $m$  for all values of time as a result of an increase in the Hall current parameter  $m$ , will decrease the contribution from the Joule dissipation term.

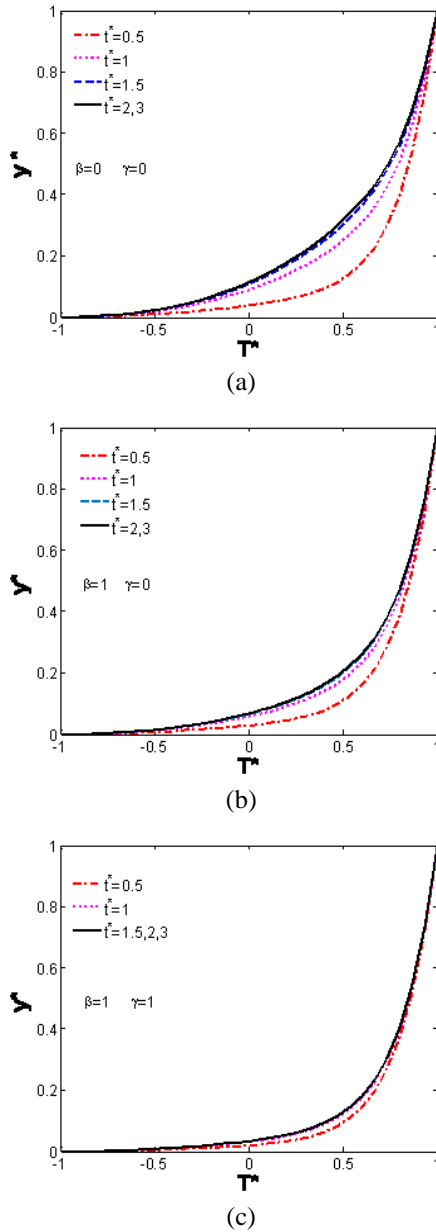


**Fig. 5.** Time variation of the profile of  $T^*$  for various values of  $\gamma$  and  $\beta$ . (a)  $\beta=0$  and  $\gamma=0$ ; (b)  $\beta=1$  and  $\gamma=0$ ; (c)  $\beta=1$  and  $\gamma=1$ .

### CONCLUSIONS

The unsteady couette flow of non-Newtonian Bingham fluid between two parallel porous plates containing a non-Darcy porous medium has been

studied with heat transfer and the Hall effect in the presence of uniform suction and injection.

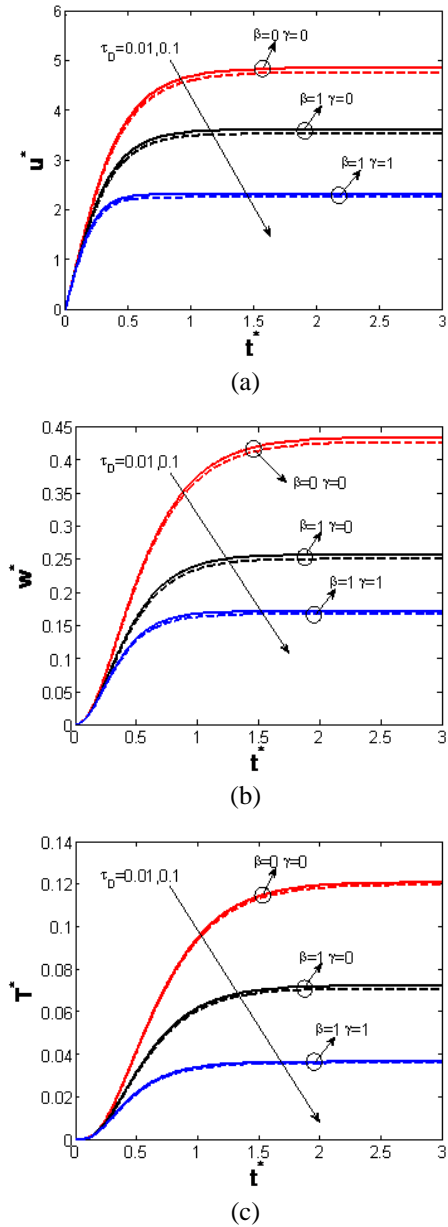


**Fig. 6.**  $u^*$ ,  $w^*$ , and  $T^*$  versus  $t^*$  at channel center ( $y^* = 0$ ) for various values of  $\gamma$  and  $\beta$  and various values  $\tau_D$ . (a)  $u^*$ ; (b)  $w^*$ ; (c)  $T^*$  Profile.

The governing momentum and energy equations are solved numerically using the finite difference approximations. Through the numerical results the following can be concluded:

- The effects of the resistive porosity force and the inertial force (Darcy and non-Darcy parameters  $\beta$  and  $\gamma$ ) on the velocity components and temperature distribution have been investigated. The increase in  $\beta$  and  $\gamma$  will decrease the velocity and temperature.
- The yield stress  $\tau_D$  has a remarkable effect on the velocity components and temperature distribution. An increase occurred in  $\tau_D$

accompanied by a decrease in the velocity and temperature as well as their steady state time.

- The effects of the Hartmann number  $Ha$  on the velocity components and temperature distribution have been studied. By increasing  $Ha$  the x-component of the velocity will decrease, while the z-component of the velocity and temperature will increase.
- The effect of the Hall parameter  $m$  on the velocity components and temperature distributions has been assessed. The Hall parameter  $m$  is directly proportional to the x-component of the velocity while it is inversely proportional to the z-component of the velocity and temperature distribution.

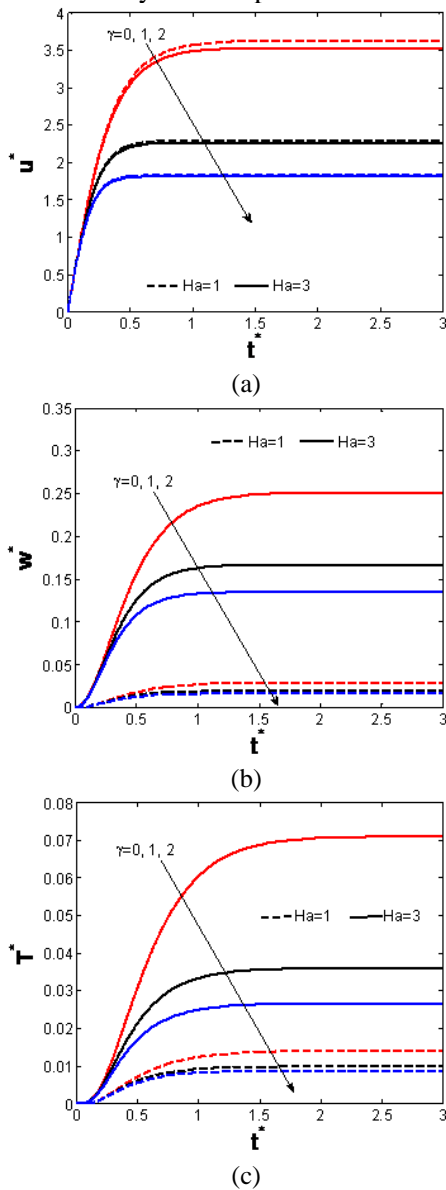


**Fig. 7.** Effect of the non-Darcian parameter  $\gamma$  on  $u^*$ ,  $w^*$ , and  $T^*$  profiles at the channel center for low and high Hartmann number  $Ha$ . (a)  $u^*$ ; (b)  $w^*$ ; (c)  $T^*$  Profile

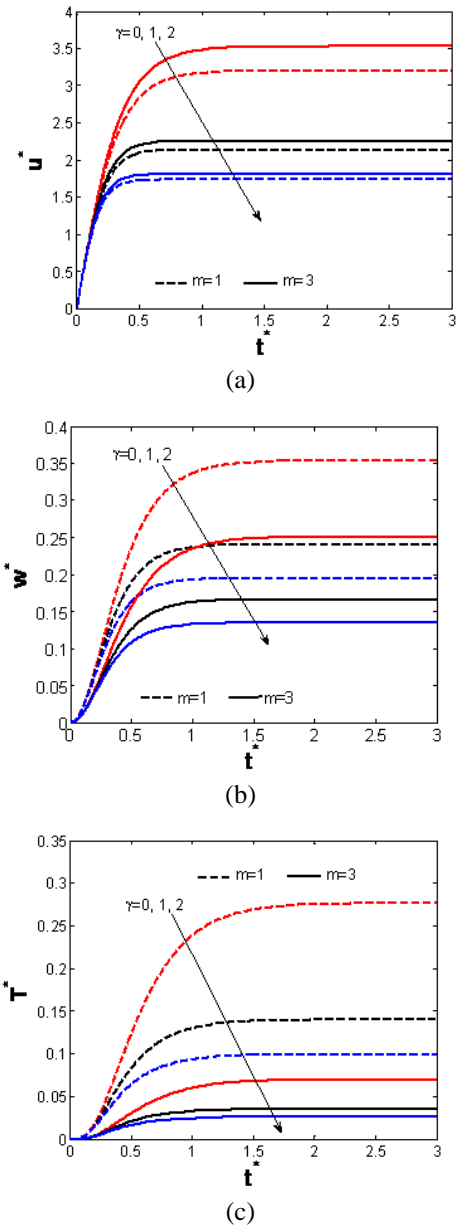


**Fig. 8.** Effect of the non-Darcian parameter  $\gamma$  on  $u^*$ ,  $w^*$ , and  $T^*$  profiles at channel center for various values of the Hall parameter  $m$ . (a)  $u^*$ ; (b)  $w^*$ ; (c)  $T^*$  Profile

## REFERENCES

1. B. Devika, P. V. Narayana, S. Venkataramana, *International Journal of Engineering Science Invention*, **2**, 26(2013).
2. H. A. Attia, W. Abd El-Meged, W. Abbas, M. A. M. Abdeen, *International Journal of Civil Engineering*, **12**, 277 (2014).
3. A. Bharali and A. K. Borkakati, *Applied Scientific Research*, **39**, 155 (1982).
4. H. A. Attia, N. A. Kotb, *Actamechanica*, **117**, 215 (1996).
5. Z. Joaquín, E. Pablo, G. Enrique, L. M. José, A. B. Osman, *Int. Comm. Heat and Mass Trans.*, **37**, 1432 (2010).
6. H. A. Attia, W. Abbas, M. A. M. Abdeen, A. E.-D. Abdin, *Blug. Chem. Commun.*, **46**, 535 (2014).

7. E. Sweet, K. Vajravelu, R. A. Van Gorder, I. Pop, *Commun Nonlinear Sci Numer Simulat*, **16**, 266 (2011).
8. H. A. Attia, W. Abbas, M. A. M. Abdeen, M. S. Emam, *European Journal of Environmental and Civil Engineering*, **18**, 241 (2014).
9. H. A. Attia, W. Abbas, M. A. M. Abdeen, A. A. M. Said, *Sadhana*, **40**(1), 183 (2015).
10. H. A. Attia, W. Abbas, A. El-Din Abdin, M. A. M. Abdeen, *High Temperature*, **53**, 891 (2015).
11. C-C. Liu, C-Y. Lo, *International Communications in Heat and Mass Transfer*, **39**, 1354 (2012).
12. H. A. Attia, W. Abbas, M. A. M. Abdeen, *Journal of the Brazilian Society of Mechanical Sciences and Engineering*, in press, Available online 11 February, 2015.
13. I. C. Walton, S. H. Bittleston, *J. Fluid Mech.*, **222**, 39 (1991).
14. S. Yang, K. Zhu, *J. Non-Newtonian Fluid Mech.*, **138**, 73 (2006).
15. D. A. S. Rees, A. P. Bassom, *International Journal of Heat and Mass Transfer*, **82**, 460 (2015).
16. Z. Zeng, R. Grigg, *Transport In Porous Media*, **63**, 57 (2006).
17. O.A. Bég, J. Zueco, H.S. Takhar, *Communications in Nonlinear Science and Numerical Simulation*, **14**, 1082 (2009).
18. A. Matthew, M. Sc. Thesis, Texas Tech University, Lubbock, Texas, United States, 2006.
19. Y. J. Kim, *International Journal of Engineering sciences*, **38**, 833 (2000).
20. D. Pal, B. Talukdar, *International Journal of Appl. Math. and Mech.*, **7**, 58 (2011).
21. S. S. Das, M. Maity, J. K. Das, *International Journal of Energy and Environment*, **1**, 109 (2012).
22. A.A. Moniem, W. S. Hassanin, *Applied Mathematics*, **4**, 694 (2013).
23. A. Afify, *Transport in Porous Media*, **66**, 391 (2007).
24. O. A. Bég, J. Zueco, R. Bhargava, H. S. Takhar, *International Journal of Thermal Sciences*, **48**, 913 (2009).
25. H. A. Attia, M. E. Sayed-Ahmed, *Applied Mathematical Modelling*, **28**, 1027 (2004).
26. Abdeen M. A. M., Attia H A, Abbas W, Abd El-Meged W, *Indian Journal of Physics*, **87**, 767 (2013).
27. T. C. Papanastasiou, *J. Rheol.*, **31**, 385 (1987).
28. E. Mitsoulis, *The British Society of Rheology*, **135**, 135 (2007).

## ОТКЛОНЕНИЯ ОТ ЗАКОНА НА ДАРСИ ПРИ НЕНЬУТОНОВИ БИНГАМОВИ ФЛУИДА С ТОПЛОПРЕНАСЯНЕ МЕЖДУ ДВЕ УСПОРЕДНИ ПЛОСКОСТИ

У. Аббас<sup>1</sup>, Х. Али Атия<sup>2</sup>, М.А.М. Абдийн<sup>3</sup>

<sup>1</sup>Департамент по основни и приложни науки, Колеж по инженерство и технологии, Арабска академия за наука, технологии и морски транспорт, Кайро, Египет

<sup>2</sup>Департамент по инженерство, математика и физика, Инженерен факултет, Университет Ел-Фаюм, Ел-Фаюм - 63514, Египет

<sup>3</sup>Департамент по инженерство, математика и физика, Инженерен факултет, Университет в Кайро, Гиза-12211, Египет

Постъпила на 13 август 2015 г.; приета на 15 септември 2015 г.

(Резюме)

Моделът на не-Дарси'ев поток за Бингамови флуиди има широк кръг от приложения в енергийните системи и обработката на магнитни материали. Тази работа изследва ефекта на не-Дарси'ево течение върху разпределението на скоростите и температурата за не-нютонув Бингамов флуид между две безкрайни успоредни порьозни плоскости с топлопренасяне отчитайки ефекта на Хол. По главното надлъжно направление се прилага постоянен градиент на налягането, перпендикулярно на плоскостите се прилага постоянно външно магнитно поле, както и равномерно всмукване и впръскване в същото направление. Изведение са и числено са решени безизмерните уравнения на движението и енергията, отчитащи механичната и вискозната дисипация на енергията. Изследвани са ефектите на порьозността на средата, на Хартман и Хол, на скоростта и разпределението на температурата за число на Рейнолдс равно на 10 (за  $Re_e \geq 10$  не-Дарси'евият модел е достатъчен). Намерено е, че порьозността и инерционните ефекти имат забележимо влияние върху разпределението на скоростите. Освен това, нарастването на не-Дарси'евия параметър понижава температурата при всяка порьозност.

## Convective heat transfer of viscous fluid over a stretching sheet embedded in a thermally stratified medium

T. Mahmood<sup>1</sup>, J. Ahmed<sup>2\*</sup>, A. Shahzad<sup>2</sup>, R. Ali<sup>3</sup>, Z. Iqbal<sup>1</sup>

<sup>1</sup>Department of Mathematics, Faculty of Sciences, HITEC University, Taxila Cantt, Pakistan

<sup>2</sup>Department of Basic Sciences, University of Engineering and Technology, Taxila 47050, Pakistan

<sup>3</sup>University of Central Asia, 722920, Naryn, Kyrgyzstan

Received August 17, 2015; Accepted September 7, 2015

In this article we have investigated the heat transfer of an electrically conducting viscous fluid over a porous stretching sheet in a thermally stratified medium. The governing non-linear partial differential equations are reduced to ordinary differential equations using appropriate similarity transformations. The resulting ordinary differential equations are then solved in the form of a confluent hyper-geometric function for an exact solution. The developed exact solutions of the velocity and temperature fields are graphically sketched and examined for various values of pertinent parameters including the Prandtl number, stratification parameter, suction/injection parameter and the magnetic parameter. The skin friction coefficient and the local Nusselt number are tabulated and thoroughly discussed.

**Keywords:** Convective heat transfer; Suction/Injection; Exact solution

### INTRODUCTION

The study of the boundary layer flow on a stretching sheet has been done by a large number of researchers during the last few decades with the aid of significant applications of industrial and technological processes. To name a few; these applications include manufacturing of glass fiber, drawing plastic films and wires, the condensation process, crystal growing polymer extrusion and others. These processes are highly dependent on the subject of heat transfer of stretching surfaces. In his ground breaking work, Sakiadis [1] presented the studies on the boundary flow layer over continuously moving surfaces and obtained the numerical solution. Natarjaet al. [2] obtained the closed form solution for the boundary layer flow of walters' B-type fluid, over a stretching sheet for the heat transfer and obtained the coefficients of skin friction. Meanwhile, Crane [3] provided the closed form solution for the boundary layer flow of a stretching sheet. The heat transfer in hydrodynamic flow of viscoelastic fluid over a stretching sheet was analyzed by Char [4]. Liao [5] studied the analytic solution of unsteady boundary layer flows caused by an impulsively stretching plate. Khan and Sanjayanand [6] presented the analytic solution for the heat transfer of visco-elastic boundary layer flow with viscous dissipation. Devi and Ganga [7] bring into account the non-linear MHD flow in a porous medium over a stretching porous surface including the effects of viscous dissipation. Abel et al. [8] have

investigated the heat transfer over a stretching surface for second grade fluid through porous medium with viscous dissipation and a non-uniform heat source/sink. Cortell [9] investigated the flow and heat transfer through a porous medium over a stretching surface with heat generation/absorption and suction/blowing. Hayat et al. [10] provided the analytic solution for the axi-symmetric flow and heat transfer of second grade fluid past over a stretching sheet. Xu and Liao [11] considered the unsteady MHD flows of non-Newtonian fluids over impulsively a stretching plate. In another related article Cortell [12] studied MHD flow heat transfer of visco-elastic fluid by considering the effects of viscous dissipation.

Thermally stratified flows are of significant interest because of their importance in thermo-hydraulics, volcanic flows, geothermal systems and also in industrial thermal processes. Stratification of a medium arises due to temperature variation which results in density variation of the medium. Stratification may also arise due to the presence of different fluids so that a stable situation arises when the lighter fluid lies over the denser one. Keeping in view these applications of stratified mediums several studies have been carried out. Hayat et al. [13] studied the thermally stratified flow of third grade fluid over a stretching sheet including radiation. Kandasamy and Khamis [14] discussed the effect of thermal stratification on heat transfer across a porous vertical stretching sheet. Ishak et al. [15] studied the mixed convection flow to a vertical plate in a thermally stratified medium. Mukhopadhyay and Ishak [16] examined mixed convection flow along a stretching cylinder in a

\* To whom all correspondence should be sent:  
E-mail: j.ahmedqau@gmail.com

thermally stratified medium. MHD boundary layer flow and heat transfer over an exponentially stretching sheet in a thermally stratified medium have also been investigated by the same author Mukhopadhyay [17].

It is clear that the suction/injection of fluid can play a significant role in changing the flow field. Roughly speaking, suction tends to enhance the skin friction, whereas injection acts in the opposite manner. These processes have great importance in many engineering activities like the design of thrust bearing and radial diffusers, thermal oil recovery and many more.

In manufacturing processes the properties of the final product highly depend on the rate of cooling. In this scenario, an electrically conducting fluid proves to be beneficial for industrial application. The applied magnetic field may play a key role in heat transfer and momentum of the boundary layer flow. Keeping all these facts in view, recently Chen [18] examined the analytic solution of MHD flow and heat transfer for two types of visco-elastic fluid over a stretching sheet, also bring under consideration the energy dissipation, internal heat source and thermal radiation. Liu [19] presented an analytic solution for heat transfer of second grade MHD flow subject to the transverse magnetic field across a stretching sheet with power law surface heat flux. Shahzad and Ali [20, 21] contributed a couple of articles on an approximate solution for MHD flow of a non-Newtonian Power law fluid over a vertical stretching sheet with convective boundary conditions and radiation effects, respectively. Kar et al. [22] studied the heat and mass transfer effects on dissipative and radiative visco-elastic MHD flow over a stretching porous sheet.

The exact solution for the flow problem with heat transfer is highly demanding in many research areas. The exact solutions are handy to compare with the numerical counter parts in the study of several flow problems. The purpose of the present study is, to give the exact solution of fluid flow and heat transfer of an electrically conducting viscous fluid over a stretching sheet in a thermally stratified medium with suction/injection. We derived a closed form analytic solution in the form of a confluent hyper-geometric function for non-dimensional velocity and temperature profiles. The skin friction coefficient and heat flux at the wall with a constant wall temperature are brought into account. The influence of different non-dimensional parameters like the Prandtl number, magnetic number, stratification parameter and the surface suction/injection are graphically discussed with respect to velocity and temperature profiles.

### MATHEMATICAL FORMULATION

We consider the steady two-dimensional boundary layer flow of an incompressible electrically conducting viscous fluid, which is passed over a stretching sheet in the presence of a magnetic field coinciding with the plane  $y = 0$ . The flow is generated due to linearly stretching of sheet by applying two equal and opposite forces along the  $x$ -axis keeping the origin fixed as observed in figure (1). A variable magnetic field  $B_o$  is applied normal to the sheet. It is assumed that the surface temperature of the sheet is  $T_w(x) = T_0 + a(\frac{x}{l})^2$  and is embedded in a thermally stratified medium of a variable ambient fluid temperatures  $T_\infty = T_0 + b(\frac{x}{l})^2$  where  $T_w > T_\infty$ ,  $T_0$  is the reference temperature,  $a > 0$ ,  $b \geq 0$  are constants.

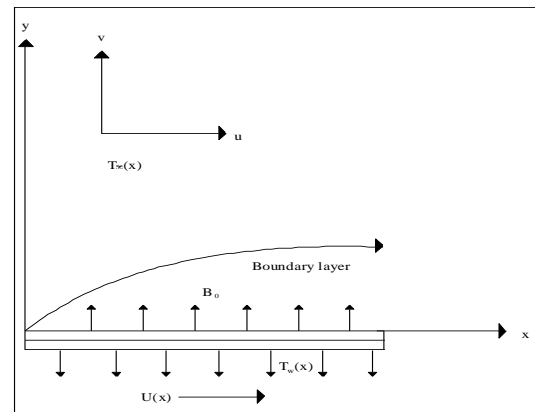


Fig. 1. Sketch of the physical problem.

Under these assumptions the steady state boundary layer equations governing the flow and heat transfer of viscous fluid are

$$\frac{\partial u}{\partial x} + \frac{\partial v}{\partial y} = 0, \quad (1)$$

$$u \frac{\partial u}{\partial x} + v \frac{\partial u}{\partial y} = \nu \frac{\partial^2 u}{\partial y^2} - \frac{\sigma B_o^2 u}{\rho}, \quad (2)$$

$$u \frac{\partial T}{\partial x} + v \frac{\partial T}{\partial y} = \frac{k}{\rho c_p} \frac{\partial^2 T}{\partial y^2}, \quad (3)$$

where  $x$  and  $y$  are the directions along and perpendicular to the sheet respectively, with  $u$  and  $v$  the velocity components along the  $x$  and  $y$  directions, respectively,  $T$  the temperature of the fluid,  $\nu$  the kinematic viscosity,  $\rho$  the density of the fluid,  $\sigma$  the electrical conductivity,  $B_o$  the applied magnetic field and  $c_p$  is the specific heat at constant pressure. The corresponding boundary conditions for the momentum equation are

$$u = U = Ex \quad v = -v_0 \quad \text{at } y = 0, \quad (4)$$

$$u \rightarrow 0 \text{ as } y \rightarrow \infty,$$

where  $E > 0$  is called stretching rate,  $v_0 > 0$  is the velocity of suction and  $v_0 < 0$  is the velocity of injection. To facilitate the analysis we introduce the following transformations:

$$u = Uf'(\eta), \quad v = -\sqrt{Ev}f(\eta), \quad \eta = \sqrt{\frac{E}{\nu}}y, \quad (5)$$

clearly  $u$  and  $v$  satisfy Eq. (1), here  $f(\eta)$  is the dimensionless stream function,  $\eta$  is the similarity variable and denote the differentiation with respect to  $\eta$ . Making use of Eq. (5) in Eq. (2) the following third order non-linear differential equation is obtained:

$$f''' - f'^2 + ff'' - M_n f' = 0, \quad (6)$$

where  $M_n = \frac{\sigma B_0^2}{\rho E}$ , is the Magnetic parameter.

Similarly the boundary conditions in Eq. (4) can be written as:

$$f'(\eta) = 1, \quad f(\eta) = S \quad \text{at } \eta = 0, \quad (7)$$

$$f'(\eta) \rightarrow 0 \text{ as } \eta \rightarrow \infty,$$

where  $S = \frac{v_0}{\sqrt{Ev}} > 0$  ( or  $< 0$ ) is the suction (or injection) parameter.

Lawrence and Rao [23] presented a general method and obtained an all non-unique solution of the modified Eq. (6). Recently Taha et al. [24] have discussed a unified compatibility method for the exact solutions of non-linear flow models of Newtonian and non-Newtonian fluids, we consider the following solution:

$$f(\eta) = S + \frac{1}{\beta}(1 - \exp[-\beta\eta]), \quad (8)$$

where  $\beta = \frac{S + \sqrt{S^2 + 4(1 + M_n)}}{2}$  with  $S^2 + 4(1 + M_n) \geq 0$ .

The physical quantities of interest are the skin friction coefficient  $C_f$  and the local Nusselt number  $N_u$  defined as:

$$C_f = \frac{\tau_w}{\frac{\rho}{2}U^2}, \quad N_u = \frac{xq_w}{k(T_w - T_0)}, \quad (9)$$

where  $\tau_w = \mu\left(\frac{\partial u}{\partial y}\right)_{y=0}$  is the wall shear stress and  $q_w = -k\left(\frac{\partial T}{\partial y}\right)_{y=0}$  the wall heat flux. In terms of dimensionless variables defined in Eq. (5), we can write:

$$\text{Re}^{1/2} C_f = f''(0), \quad \text{Re}^{-1/2} N_u = -\theta'(0), \quad (10)$$

where  $\text{Re} = \frac{xU}{\nu}$  is the local Reynolds number.

## SOLUTION OF THE HEAT TRANSFER EQUATION

In order to solve the governing heat transport Eq. (3), we consider the boundary with a prescribed surface temperature (PST). In this case we employ the following surface boundary conditions on temperature:

$$T = T_w(x) = T_0 + a\left(\frac{x}{l}\right)^2 \quad \text{at } y = 0, \quad (11)$$

$$T = T_\infty(x) = T_0 + b\left(\frac{x}{l}\right)^2 \quad \text{as } y \rightarrow \infty,$$

where  $T_w$  and  $T_\infty$  are the temperatures at the wall and far away from the wall, respectively and  $T_0$  is the reference temperature. In order to obtain the similarity solution we define the non-dimensional temperature variables as:

$$\theta(\eta) = \frac{T - T_0}{T_w - T_0}. \quad (12)$$

Making use of the transformations (5) and (12), we obtain the following non-dimensional form of temperature Eq. (3) as:

$$\theta'' + \text{Pr}(f\theta' - 2f'\theta) = 2St \text{Pr} f', \quad (13)$$

where in the non-dimensional parameters  $\text{Pr} = \frac{\rho C_p \nu}{k}$  the Prandtl number and  $St = \frac{b}{a}$  is the stratification parameter. We note that  $St > 0$  for a stably stratified environment and  $St = 0$  corresponds to an unstratified environment.

The non-dimensional form of the boundary conditions in Eq. (11) is:

$$\theta = 1 - St \quad \text{at } \eta = 0, \quad (14)$$

$$\theta \rightarrow 0 \quad \text{as } \eta \rightarrow \infty.$$

Following the introduction of a new variable  $\xi = -\frac{\text{Pr}}{\beta^2} \exp(-\beta\eta)$ , Eq. (13) becomes:

$$\xi \frac{d^2\theta}{d\xi^2} + (1 - \text{Pr}^* - \xi) \frac{d\theta}{d\xi} + 2\theta = -2St, \quad (15)$$

and the boundary conditions presented in Eq. (14) reduce to:

$$\theta(\xi) = 1 - St \quad \text{at } \xi = -\text{Pr}^*, \quad (16)$$

$$\theta(\xi) = 0 \quad \text{at } \xi = 0,$$

where  $\text{Pr}^* = \frac{\text{Pr}}{\beta^2}$  is the modified Prandtl number.

Equations (15) and (16) constitute a non-homogenous boundary value problem. Let us decompose the temperature  $\theta(\xi)$  into two parts:

$$\theta(\xi) = \theta_c(\xi) + \theta_p(\xi), \quad (17)$$

where  $\theta_c(\xi)$  stands for the complementary solution and  $\theta_p(\xi)$  is a particular solution. The closed form particular solution is given by:

$$\theta_p(\xi) = -St. \tag{18}$$

The complementary factor  $\theta_c(\xi)$  can be written in the form of a confluent hyper-geometric function [25] as:

$$\theta_c(\xi) = AM[-2, 1 - Pr^*, \xi] + B\xi^{Pr^*} M[-2 + Pr^*, 1 + Pr^*, \xi] \tag{19}$$

where  $M$  is the Kummer's function defined as:

$$M(a_o, b_o, z) = 1 + \sum_{n=1}^{\infty} \frac{(a_o)_n z^n}{(b_o)_n n!}, \tag{20}$$

$$(a_o)_n = a_o(a_o + 1)(a_o + 2) \cdots (a_o + n - 1),$$

$$(b_o)_n = b_o(b_o + 1)(b_o + 2) \cdots (b_o + n - 1).$$

The solution of Eq. (15), subject to the boundary conditions of Eq. (16) is determined to be:

$$\theta(\xi) = StM[-2, 1 - Pr^*, \xi] + \left\{ \frac{1 - StM[-2, 1 - Pr^*, -Pr^*]}{(-Pr^*)^{Pr^*} M[-2 + Pr^*, 1 + Pr^*, -Pr^*]} \right\} \xi^{Pr^*} M[-2 + Pr^*, 1 + Pr^*, \xi] - St. \tag{21}$$

The temperature profile in term of  $\eta$  is given by

$$\theta(\eta) = StM[-2, 1 - Pr^*, -Pr^* \exp(-\beta\eta)] + \left\{ \frac{1 - StM[-2, 1 - Pr^*, -Pr^*]}{M[-2 + Pr^*, 1 + Pr^*, -Pr^*]} \right\} \times \exp(-\beta Pr^* \eta) M[-2 + Pr^*, 1 + Pr^*, -Pr^* \exp(-\beta\eta)] - St. \tag{22}$$

The derivative of the Kummer's function  $M(a_o, b_o, z)$  with respect to  $z$  is given by:

$$\frac{d^n}{dz^n} M[a_o, b_o, z] = \frac{(a_o)_n}{(b_o)_n} M[a_o + n, b_o + n, z].$$

The dimensionless wall temperature gradient is obtained from Eq. (22)

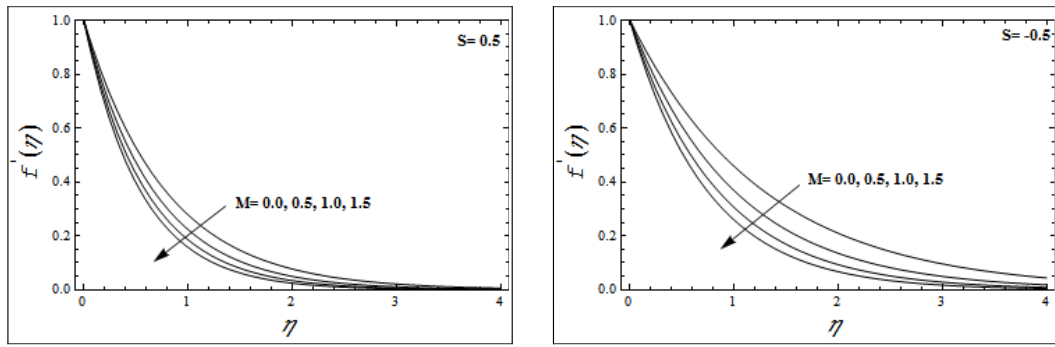
$$\theta'(0) = \frac{-2St\beta Pr^*}{1 - Pr^*} M[-1, 2 - Pr^*, -Pr^*] - \left\{ \frac{1 - StM[-2, 1 - Pr^*, -Pr^*]}{M[-2 + Pr^*, 1 + Pr^*, -Pr^*]} \right\} \times \left\{ -\frac{\beta Pr^* (-2 + Pr^*)}{1 + Pr^*} M[-1 + Pr^*, 2 + Pr^*, -Pr^*] + \beta Pr^* M[-2 + Pr^*, 1 + Pr^*, -Pr^*] \right\}. \tag{23}$$

### GRAPHICAL RESULTS AND DISCUSSION

Momentum and heat transfer in a boundary layer flow of a viscous fluid over a stretching sheet in a thermally stratified medium have been discussed in

this article. The governing non-linear partial differential equations have been reduced to a set of non-linear ordinary differential equations. The exact solutions are developed for the reduced problem in terms of the Kummer's function. In order to have a clear insight of a physical problem, the influence of various pertinent parameters on velocity and temperature profiles are shown graphically through figures (2–9). Figures (2a, 2b) depict the influence of the magnetic parameter  $M$  on the velocity profile  $f'(\eta)$  for both suction/injection  $S$  cases. It is observed that the velocity profile  $f'(\eta)$  decreases with an increase in the values of the magnetic parameter  $M$  for both suction/injection parameters  $S$ . The boundary layer thickness also decreases here. The variation of suction/injection parameter  $S$  on the velocity profile  $f'(\eta)$  is shown in figures (3a, 3b). The velocity profile  $f'(\eta)$  decreases in the case of the suction parameter ( $S > 0$ ), while the opposite behavior is noticed in case of injection ( $S < 0$ ). Figures (4a, 4b) are plotted to see the effects of the Prandtl number  $Pr$  on the temperature profile  $\theta(\eta)$  in the presence of suction/injection parameter  $S$ . It is obvious from these figures that an increase in the Prandtl number  $Pr$  results in a decrease in the temperature profile  $\theta(\eta)$  for both cases suction ( $S > 0$ ) and injection ( $S < 0$ ), however this decrease in the temperature profile  $\theta(\eta)$  is more prominent in the case of suction ( $S > 0$ ). The influence of the suction /injection parameter  $S$  on the temperature profile  $\theta(\eta)$  is displayed in figures (5a, 5b). These figures show that by increasing the suction parameter ( $S > 0$ ) the temperature profile  $\theta(\eta)$  increases while an adverse behavior is observed in the case of injection ( $S < 0$ ).

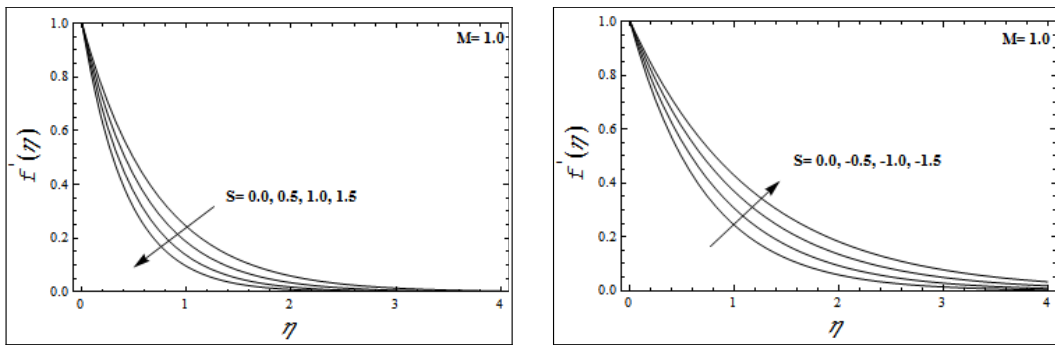
In order to see the effects of the stratified medium  $St$  on the temperature profile  $\theta(\eta)$  in the presence of the suction/injection parameter  $S$  figures (6a, 6b) are plotted. These figures illustrate that the temperature profile  $\theta(\eta)$  decreases as the stratification parameter  $St$  increases for both suction/injection parameters  $S$ . As the increase in the stratification medium  $St$  implies an increase in ambient fluid temperature or a decrease in the surface temperature, which results in a decrease of the thermal boundary layer thickness.



2a

2b

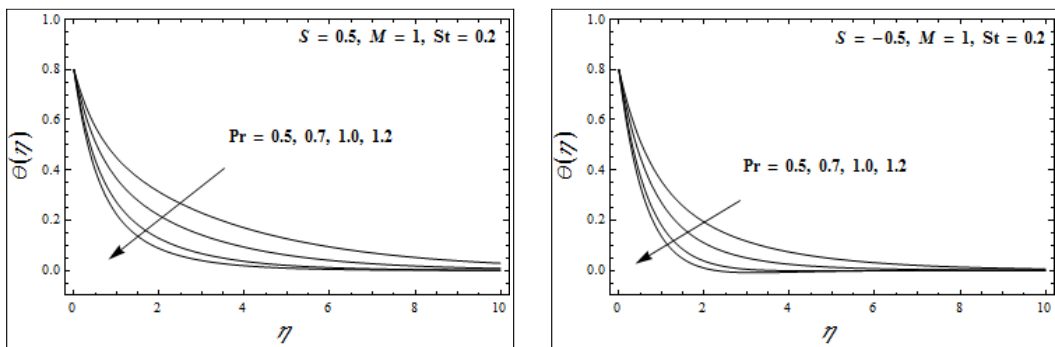
**Fig.2.** Variation of velocity profile  $f'(\eta)$  with  $\eta$  for several values of magnetic parameter  $M$  in the presence of the suction/injection parameter  $S$ .



3a

3b

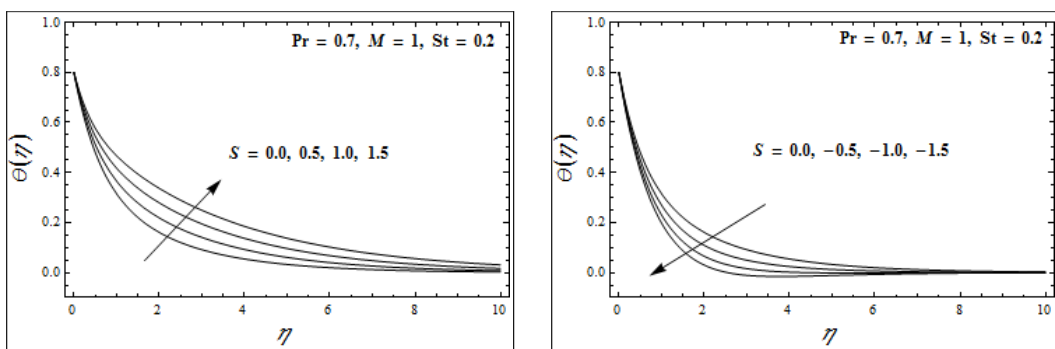
**Fig. 3.** Variation of the velocity profile  $f'(\eta)$  with  $\eta$  for several values of the suction/injection parameter  $S$ .



4a

4b

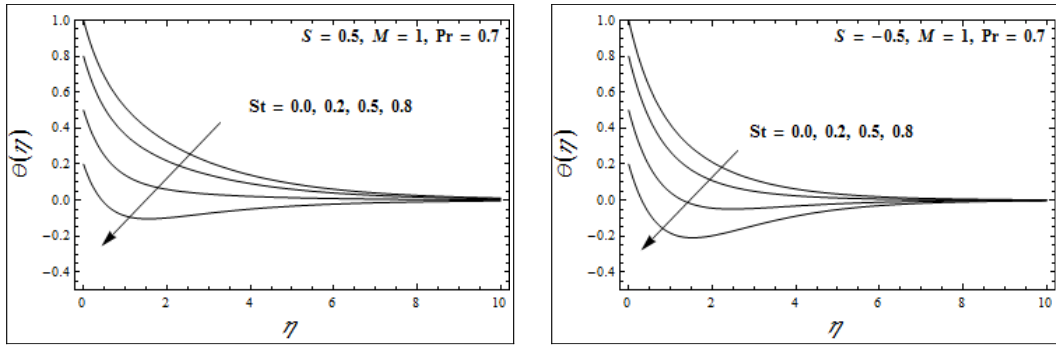
**Fig. 4.** Variation of the temperature profile  $\theta(\eta)$  with  $\eta$  for several values of the Prandtl number  $Pr$ .



5a

5b

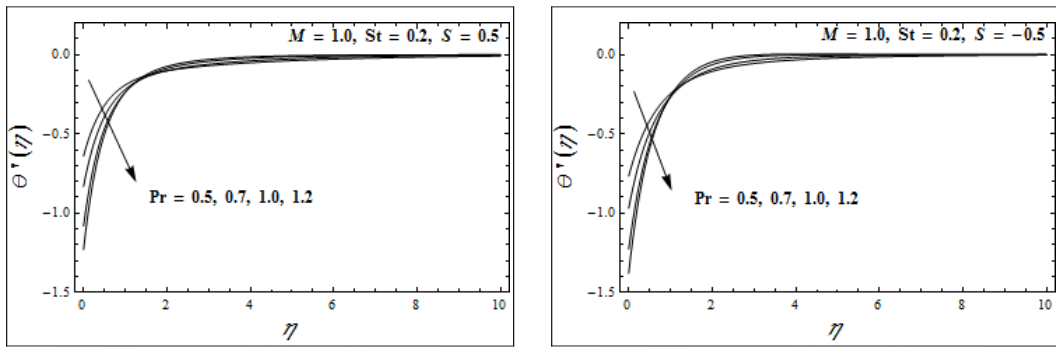
**Fig. 5.** Variation of the temperature profile  $\theta(\eta)$  with  $\eta$  for several values of the suction parameter  $S$ .



6a

6b

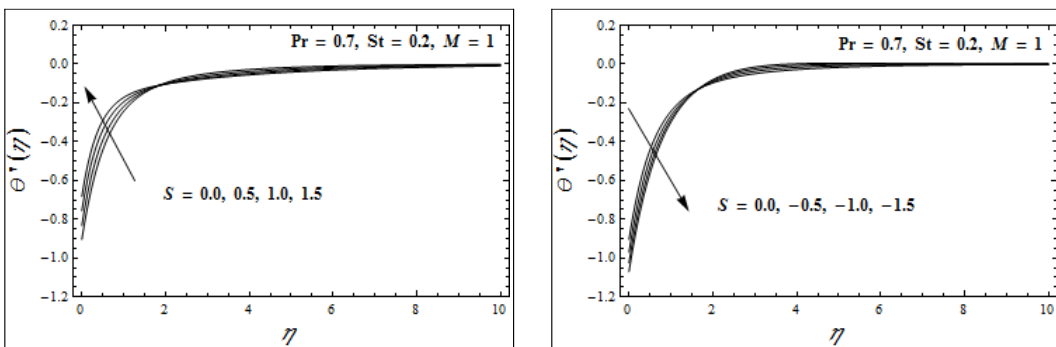
**Fig. 6.** Variation of the temperature profile  $\theta(\eta)$  with  $\eta$  for several values of the thermal stratification parameter  $St$  in the presence of suction/injection  $S$ .



7a

7b

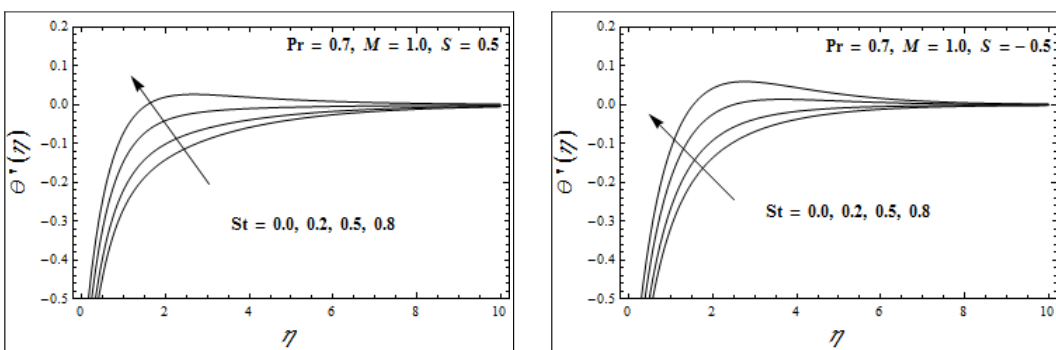
**Fig. 7.** Variation of the temperature gradient  $\theta'(\eta)$  with  $\eta$  for several values of the Prandtl number  $Pr$ .



8a

8b

**Fig. 8.** Variation of the temperature gradient  $\theta'(\eta)$  with  $\eta$  for several values of the suction/injection parameter  $S$ .



9a

9b

**Fig. 9.** Variation of the temperature gradient  $\theta'(\eta)$  with  $\eta$  for several values of the thermal stratification parameter  $St$ .

The influence of the Prandtl number  $Pr$  on the temperature gradient  $\theta'(\eta)$  in the presence of suction/injection  $S$  is displayed in figures (7a,7b).

From these figures it is observed that initially an increase in the Prandtl number  $Pr$  results in a decrease in the temperature gradient  $\theta'(\eta)$ . It is also observed that the temperature gradient  $\theta'(\eta)$  starts increasing after a certain distance  $\eta$  from the surface. Moreover this effect is more prominent in the case of injection ( $S < 0$ ). From figures (8a,8b) it can be seen that by increasing the suction parameter ( $S > 0$ ) the temperature gradient  $\theta'(\eta)$  increases up to a certain distance from the surface and then decreases. Quite the opposite behavior is observed in the case of injection ( $S < 0$ ). To analyze the effect of the stratification parameter  $St$  on the temperature gradient the figures (9a,9b) are plotted. It is noticed that the temperature gradient  $\theta'(\eta)$  increases with an increase in the stratification parameter  $St$  for both suction and the injection parameter  $S$ . Furthermore, it is also observed that this increase is more prominent in the case of injection ( $S < 0$ ).

**Table 1.** Values of the skin friction coefficient  $C_f$   $Re^{1/2} = f''(0)$  for several values of the material parameters.

$M$	$S$	$-f''(0)$
0.0	0.5	1.28078
0.5		1.50000
1.0		1.68614
0.5	-1.0	0.822876
	-0.5	1.00000
	0.0	1.22474
	0.5	1.50000
	1.0	1.82288

Table 1 is displayed in order to see the effect of the magnetic parameter  $M$  and the suction/injection parameter  $S$  on the skin friction coefficient. We can see that by increasing the values of the magnetic parameter  $M$  and the suction/injection parameter  $S$ , the values of the skin friction coefficient increase. Table 2 shows the effect of the Prandtl number  $Pr$ , suction/injection  $S$  and stratification parameter  $St$  on the dimensionless heat transfer rate at the wall. It has been observed that the increase in the Prandtl number

$Pr$  and stratification parameter,  $St$  results, an increase in the dimensionless heat transfer rate at the wall. While increasing values of suction/injection parameter  $S$  decreases the dimensionless heat transfer rate at the wall.

**Table 2.** Values of the Nusselt number  $N_u$   $Re^{-1/2} = -\theta'(0)$  for several values of the material parameters for  $M = 1$ .

$Pr$	$S$	$St$	$-\theta'(0)$
0.5	0.5	0.2	0.640382
0.7			0.831958
1.0			1.08195
0.7	0.5	0.0	0.87966
		0.2	0.831958
		0.5	0.760405
0.7	-1.0	0.2	1.02462
	-0.5		0.969256
	0.0		0.904259
	0.5		0.831958
	1.0		0.756596

### CONCLUDING REMARKS

In this contribution, we have articulated the exact solutions of a viscous fluid over a stretching sheet in a thermally stratified medium in the presence of a magnetic field. The modeled non-linear partial equations were transformed into a system of non-dimensional ordinary differential equations using appropriate transformations. The exact solutions were found in the form of confluent hyper-geometric functions (Kummer's function). The influence of pertinent parameters on the velocity and temperature profiles were shown graphically and discussed in details. Numerical values concerning the skin friction coefficient and Nusselt numbers with several respective parameters were provided in tabular form.

### REFERENCES

1. B. C. Sakiadis, *AICHE J.*, **7**, 26 (1961).
2. H. R. Natarja, M. S. Sarma, B. N. Rao, *Acta Mech.*, **128**, 259 (1998).
3. L. J. Crane, *Z. Angew. Math. Phys.*, **21**, 645 (1970).
4. M. I. Char, *J. Math. Anal. Appl.*, **186**, 674 (1994).
5. S. J. Liao, *Commun. Nonlin. Sci. Numer. Simul.*, **11**, 326 (2006).
6. S. K. Khan, E. Sanjayanand, *Int. J. Heat Mass Transf.*, **48**, 1534 (2005).
7. S. P. A. Devi, B. Ganga, *Ind. J. Appl. Math.*, **5**, 45 (2009).

8. M. S. Abel, M. M. Nandeppanavar, S. B. Malipatla, *Int. J. Heat Mass Transf.*, **53**, 1788 (2010).
9. R. Cortell, *Fluid dyn. Res.*, **37**, 231 (2005).
10. T. Hayat, M. Sajid, *Int. J. Heat Mass Transf.*, **50**, 75 (2007).
11. H. Xu, S. J. Liao, *J. Non-Newton. Fluid Mech.*, **159**, 46 (2005).
12. R. Cortell, *Phys. Lett. A.*, **357**, 298 (2006).
13. T. Hayat, S. A. Shehzad, M. Qasim, S. Asghar, A. Alsaedi, *J. Thermophys. Heat Transf.*, **28**, 155 (2014).
14. R. Kandasamy and A. Khamis, *Int. J. Appl. Mech. Eng.*, **12**, 47 (2007).
15. A. Ishak, R. Nazar, I. Pop, *Int. J. Heat Mass Transf.*, **51**, 3693 (2008).
16. S. Mukhopadhyay, A. Ishak, *J. Appl. Math.* (2012), Article ID 491695.
17. S. Mukhopadhyay, *MHD Alex. Eng. J.*, **52**, 259 (2013).
18. C. H. Chen, *Int. J. Heat Mass Transf.*, **53**, 4264 (2010).
19. I. C. Liu, *Int. J. Heat Mass Transf.*, **47**, 4427 (2004).
20. A. Shahzad, R. Ali, *Walailak J. Sci. Tech.*, **10**, 43, (2013).
21. A. Shahzad, R. Ali, *Canad. J. Appl. Sci.*, **2**, 202 (2012).
22. M. Kar, S. N. Sahoo, P. K. Rath, G. C. Dash, *Arab. J. Sci. Eng.*, **39**, 3393 (2014).
23. P. S. Lawrence, B. N. Rao, *Acta Mech.*, **112**, 223, (1995).
24. T. Aziz, F. M. Mahomed, D. P. Mason, *Int. J. Non-linear Mech.*, **78**, 142 (2016).
25. Abramowitz, L. A. Stegun, *Handbook of mathematical functions*, National Bureau of standards/Amer. Math. Soc. Providence, RI., 1972, p.55.

## КОНВЕКТИВНО ТОПЛОПРЕНАСЯНЕ ВЪВ ВИСКОЗЕН ФЛУИД НАД РАЗТЕГНАТ ЛИСТ, ПОСТАВЕН В ТЕРМИЧНО ЕДНОРОДНА СРЕДА

Т. Махмуд<sup>1</sup>, Дж. Ахмед<sup>2\*</sup>, А. Шахзад<sup>2</sup>, Р. Али<sup>3</sup>, З. Икбал<sup>1</sup>

<sup>1</sup>Департамент по математика, Научен факултет, Университет НИТЕС, Таксила Кант, Пакистан

<sup>2b</sup>Департамент по основни науки, Технологично-инженерен университет, Таксила 47050, Пакистан

<sup>3</sup>Централно-азиатски университет, Бишкек, Киргизстан

Постъпила на 19 август, 2015 г.; приета на 7 септември, 2015 г.

(Резюме)

В тази статия ние изследвахме топлопренасянето в електропроводящ вискозен флуид над разтегнат поръзен лист в термично еднородна среда. Не-линейните частни диференциални уравнения на преноса са сведени до обикновени с помощта на автомоделни трансформации. Получените обикновени диференциални уравнения са решени точно във вид на изродени хипергеометрични функции. Получените точни решения за скоростното и температурното поле са представени графично и са изследвани за различни съществени параметри на течението, включвайки числото на Прандтл, параметъра на стратификация, параметъра за всмукване/впръскване и за магнитните свойства. Табулирани са и подробно са обсъдени коефициента на триене и числото на Нуселт.

## IR spectral and structural changes caused by the conversion of acetanilide into azanion

E .A. Velcheva\*, Z. I. Glavcheva, B.A. Stamboliyska

Department of Structural Organic Analysis, Institute of Organic Chemistry with Centre of Phytochemistry, Bulgarian Academy of Sciences, Acad. G. Bonchev St., Block 9, 1113 Sofia, Bulgaria

Received June 26, 2015, Revised September 10, 2015

The structures of acetanilide azanion and of its  $^{15}\text{N}$  labelled analogue have been studied by means of both IR spectra and DFT calculation, employing the B3LYP functional and 6-311+G(2df,p) basis set. A good agreement has been found between the theoretical and experimental vibrational characteristic of the particles studied. The conversion of acetanilide molecule into the azanion causes  $150\text{ cm}^{-1}$  decrease in the carbonyl stretching frequency, threefold increase in the integrated intensity of the corresponding IR band and other essential spectral changes. According to the calculations, the structural changes in the steric structure caused by this conversion take place *at* and *next* to the azanionic center. The new (azanionic) charge is distributed as follows:  $-0.304\text{ e}^-$  and  $-0.346\text{ e}^-$  are delocalized over the phenyl and acetyl groups and  $-0.349\text{ e}^-$  of its remained localized at the azanionic centre.

**Keywords:** N-phenylacetamide, anion, DFT

### INTRODUCTION

The structure of organic anions is of general interest, as in living organisms part of bioactive molecules are dissociated in the body liquids, so that certain physiological actions are assumed to be due to its solvated anions. However, the highly reactive nature of anionic species has limited their structural characterization. The conversions of neutral molecule into radical-anions, carbanions, azanion, *etc.* are accompanied by essential changes in the vibration spectra. So, these changes are very informative for the structural variations caused by the same conversions [1]. The structure of large series of organic molecules and their anions have been successfully studied recently on the basis of experimental IR spectra combined with DFT computations [2-6]. The title compound is an interesting and convenient object of the molecule  $\rightarrow$  anion conversions investigations, as it contains the (-CO-NH-) characteristic group and can be easily converted into a stable azanion.

Acetanilide, (N-phenylacetamide) was the first analgesic and antipyretic synthetic drug and was introduced into medical practice under the name of Antifebrin by Cahn and Hepp in 1886 [7]. The discovery of acetanilide as effective therapeutic agent was leading to the development of many new drugs, structural analogues, with similar or different pharmacological properties [8]. In the body acetanilide is mostly converted to p-hydroxyacetanilide [9], which has replaced

acetanilide in therapy because it is less likely to induce blood disorders.

The early work on infrared (IR) spectra of acetanilide was reviewed by Crooks [10], Mann and Thompson [11], Abbott *et al.* [12]. A detailed empirical assignment of IR and Raman bands of acetanilide was reported about 50 years ago [13]. The complete IR band assignment of the acetanilide molecule was recently performed using ab initio Hartree-Fock (HF) [9] and DFT calculations [14,15]. The carbonyl C=O stretching frequencies and intensities of IR bands in series of substituted acetanilides were found to correlate with both Hammett's substituent constants and certain indices computed within ab initio and DFT methods [16-18]. IR spectra of a series of various carboxamide azanions were studied by Ognyanova and coworkers [19]. The authors reported that the stretching vibration frequencies of the amide C=O shifts downward depending on the substituents. Neither the detailed IR spectra nor structure of acetanilide azanion have been studied theoretically or experimentally. The purpose of the present investigation is to follow the spectral and structural changes, caused by the conversion of acetanilide molecule into the corresponding azanion on the basis of both DFT computations and spectroscopic experiments.

### EXPERIMENTAL AND COMPUTATIONS

Acetanilide (Aldrich, 99%) was used without additional purification. We prepared acetanilide- $^{15}\text{N}$  from aniline- $^{15}\text{N}$  (VEB-Berlin-Chemie, 97.2% at. Enrichment) and acetic anhydride. The

\* To whom all correspondence should be sent:  
E-mail: ev@orgchm.bas.bg

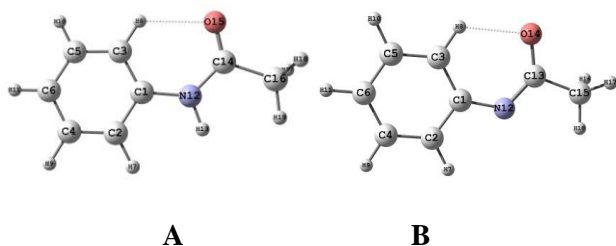
corresponding acetanilide azanion (counter ion  $\text{Na}^+$ ) and its isotope-labeled derivative were prepared by adding dimethyl sulfoxide (DMSO/DMSO- $d_6$ ) solutions of acetanilide and acetanilide  $^{-15}\text{N}$  to excess of dry sodium methoxide  $-d_0$  and  $-d_3$ , and filtration of the reaction mixture by a syringe filter. The conversion of the parent isotopomeric compounds into azanions under these conditions (solvent, concentrations, counter ion) is practically complete: no bands of the parent compounds can be seen in the spectra after metalation. IR spectra were measured on Bruker Tensor 27 Fourier transform infrared (FTIR) spectrophotometer in a  $\text{CaF}_2$  cell of 0.13 mm (0.10 – 0.15 mol  $\text{l}^{-1}$  DMSO/DMSO- $d_6$  solutions), at a resolution of  $1\text{ cm}^{-1}$  and 64 scans.

The quantum chemical calculations were performed using the Gaussian 09 package [20]. The geometry optimizations of the structures investigated were done without symmetry restrictions, using density functional theory (DFT). We employed B3LYP hybrid functional, which combines Becke's three-parameter nonlocal exchange with the correlation functional of Lee and coworkers [21,22], adopting 6-311+G(2df,p) basis sets. The stationary points found on the molecular potential energy hypersurfaces were characterized using standard harmonic vibrational analysis. The theoretical vibrational spectra were interpreted by means of potential energy distributions (PEDs) using VEDA 4 program [23]. For a better correspondence between experimental and calculated values, we modified the results using the empirical scaling factors [24].

## RESULTS AND DISCUSSIONS

### Energy analysis

All conformers of acetanilides and its deprotonated form have determined from rotation about Ph-N and N-C bonds. The structures of the most stable conformers are shown in Scheme 1.



**Scheme 1.** B3LYP/6311+G(2df,p) optimized structures of the most stable conformers of acetanilide molecule A and its azanion B.

Both structures of molecule and azanion correspond to *trans*-type conformers (with respect to the phenyl and methyl groups). According to the B3LYP/6-311+G(2df,p) calculations the *cis* conformers of molecule are less stable than the *trans* form by  $11.6\text{ kJmol}^{-1}$ . This result is with agreement with the theoretical study of Ilieva *at al.*[17]. The presence of the same conformer was also established by crystallographic analysis[25,26] and experimental and IR spectral data in solution [16]. According to the theoretical data, the *trans* conformer of the azanion is the more stable by the  $21.6\text{ kJmol}^{-1}$ .

The calculated total energies of the studied species are as follow:

$$E_{\text{tot}} = -440.299988561\text{ H for the acetanilide}$$

$$E_{\text{tot}} = -439.7337264\text{ H for the acetanilide azanion}$$

The energy difference  $\text{ED} = E(\text{anion}) - E(\text{molecule})$  can be used as an approximate measure of  $\text{pK}_a$  of a given compound in the gas phase [27]. Georgieva and Velcheva [28] have found that ED values of series of C-H, N-H and O-H acids correlate fairly well (correlation coefficient  $R = 0.94$ ) with the corresponding  $\text{pK}_a$  values, measured in DMSO. Having in mind  $\text{ED} = 1489.06\text{ H}$  and the correlation equation:

$$\text{pK}_a(\text{DMSO}) = 0.11507\text{ED} - 150.04\text{ kJ mol}^{-1}$$

we estimated a "theoretical"  $\text{pK}_a$  value of acetanilide at 21.0 in excellent agreement with the experimental value of 21.5 in DMSO [29].

### Infrared spectra

Organic anions are not soluble in common spectroscopic solvents and usually react with them. So, polar aprotic solvents, most frequently DMSO, are used to study the IR spectra of organic anionic derivatives [2-6,30].

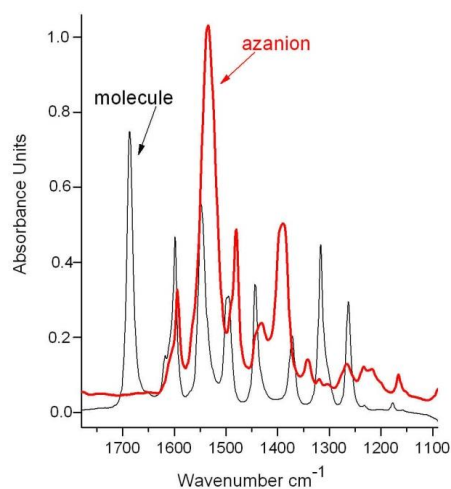


**Fig. 1.** IR spectra (0.12 mol  $\text{l}^{-1}$  in DMSO- $d_6$ ) of acetanilide molecule and its azanion.

Acetanilide azanion (e.g., acetanilide itself) is highly soluble and very stable in DMSO. To perform a correct comparison of the IR spectra of acetanilide isotopomers with those of their azanions, we shall consider their DMSO solution spectra. As in the preceding subsection, we shall now use theoretical data for the most stable conformers of the species studied. The fragment of the infrared spectrum of acetanilide in DMSO- $d_6$  solution is shown in Figure. 1.

The numerical values of the experimental IR data are compared with the theoretical ones in Table 1.

Fairly good agreement between the scaled theoretical and measured IR frequencies is observed. The mean deviation between them is 10  $\text{cm}^{-1}$ . The largest differences between theoretical and experimental IR data correspond to the N-H stretching vibrations. They form a multiplet in the interval 3300 – 3080  $\text{cm}^{-1}$ , because of the formation of strong hydrogen bonds mainly with DMSO solvent. The assignment of the experimental bands to the calculated normal modes in the C–H stretching region (3040–2800  $\text{cm}^{-1}$ ) is not obvious because there are fewer bands in the experimental spectrum than predicted by the calculations

**Table 1.** Theoretical (B3LYP/6-311+G(2df,p) and experimental (solvent DMSO- $d_6$ ) vibrational frequencies ( $\text{cm}^{-1}$ ) and IR integrated intensities ( $A$  in  $\text{km}\cdot\text{mol}^{-1}$ ) of acetanilide

$\nu_{\text{calc.}}$	$\nu_{\text{calc.}}^a$	$A_{\text{calc}}$	Approximative description <sup>b</sup>	$\nu_{\text{exp.}}$	$A_{\text{exp.}}$
3622	3574	19.2	100 $\nu(\text{N-H})$	3301-3070	
3243	3200	5.5	99 $\nu(\text{Ph-H})$		
3189	3147	15.1	91 $\nu(\text{Ph-H})$		
3174	3133	20.1	86 $\nu(\text{Ph-H})$	3041	10.2
3165	3123	0.2	90 $\nu(\text{Ph-H})$		
3146	3104	12.7	100 $\nu(\text{Ph-H})$	3010	14.1
3114	3072	3.6	100 $\nu^{\text{as}}(\text{CH}_3)$	2977	8.8
3113	3072	15.7	100 $\nu^{\text{as}}(\text{CH}_3)$	2934	10.5
3042	3002	9.5	100 $\nu^s(\text{CH}_3)$	2855	4.2
1750	1715	246.7	81 $\nu(\text{C=O})$	1686	127.5
1643	1610	43.6	53 $\nu^{\text{Ph}}(\text{CC})$ , 10 $\delta^{\text{Ph}}(\text{CCH})$	1617	45.7
1634	1601	37.7	55 $\nu^{\text{Ph}}(\text{CC})$ , 10 $\delta(\text{HNC})$	1599	34.3
1555	1524	292.3	42 $\delta(\text{HNC})$ , 15 $\nu(\text{N-C})$ , 10 $\delta^{\text{Ph}}(\text{CCH})$	1547	118.6
1531	1501	63.7	71 $\delta^{\text{Ph}}(\text{CCH})$	1495	51.3
1489	1460	12.5	95 $\delta(\text{CH}_3)$		
1470	1441	7.2	93 $\delta(\text{CH}_3)$		
1468	1439	125.0	58 $\nu(\text{Ph-H})$ , 15 $\delta(\text{HNC})$	1443	50.1
1400	1372	34.8	88 $\delta(\text{CH}_3)$	1372	32.1
1360	1333	8.3	76 $\nu(\text{Ph-H})$		
1338	1321	120.5	43 $\nu^{\text{Ph}}(\text{CC})$ , 35 $\nu(\text{N-C})$	1317	60.2
1265	1249	92.7	17 $\delta(\text{HNC})$ , 17 $\nu(\text{Ph-N})$	1263	35.9
1236	1219	37.0	18 $\nu(\text{C-CH}_3)$ , 17 $\nu(\text{N-C})$ , 15 $\nu(\text{Ph-N})$		
1206	1182	19.5	90 $\nu(\text{Ph-H})$	1177	20.4
1185	1169	0.9	79 $\nu(\text{Ph-H})$		
1114	1099	9.0	40 $\nu^{\text{Ph}}(\text{CC})$ , 33 $\nu(\text{Ph-H})$		
1054	1040	5.4	56 $\nu^{\text{Ph}}(\text{CC})$		
1053	1039	5.8	95 $\delta(\text{CH}_3)$		
1019	1006	9.1	77 $\delta^{\text{Ph}}(\text{CCC})$		
1013 <sup>c</sup>	1000	11.4	90 $\delta(\text{CH}_3)$		

<sup>a</sup>Scaled by 0.985[24]. <sup>b</sup>Vibrational modes:  $\nu$ , stretching;  $\delta$ , bendings. The numbers before the mode symbols indicate % contribution (10 or more) of a given mode to the corresponding normal vibration, according to the potential energy distribution. <sup>c</sup> Followed by 22 lower-frequency normal vibrations.

**Table 2.** Theoretical (B3LYP/6-311+G(2df,p) and experimental (solvent DMSO-d<sub>6</sub>) vibrational frequencies (cm<sup>-1</sup>) and IR integrated intensities (a in km mol<sup>-1</sup>) of acetanilide anion.

$\nu_{\text{calc.}}$	$\nu_{\text{calc.}}^{\text{a}}$	$A_{\text{calc}}$	Approximative description <sup>b</sup>	$\nu_{\text{exp.}}$	$A_{\text{exp.}}$
3221	3175	4	99 $\nu(\text{Ph-H})$		
3159	3114	35	100 $\nu(\text{Ph-H})$		
3149	3104	73	99 $\nu(\text{Ph-H})$	3048	18.1
3119	3074	53	99 $\nu(\text{Ph-H})$	3008	16.2
3111	3067	17	99 $\nu(\text{Ph-H})$		
3101	3057	36	89 $\nu^{\text{as}}(\text{CH}_3)$		
3055	3012	42	100 $\nu^{\text{as}}(\text{CH}_3)$	2960	17.3
3008	2965	80	100 $\nu^{\text{s}}(\text{CH}_3)$	2915	14.5
1628	1603	63	59 $\nu^{\text{Ph}}(\text{CC})$ , 22 $\delta^{\text{Ph}}(\text{CCH})$	1594	49.1
1576	1552	16	61 $\nu^{\text{Ph}}(\text{CC})$ , 15 $\delta^{\text{Ph}}(\text{CCH})$ , 13 $\delta^{\text{Ph}}(\text{CCC})$		
1570	1545	815	67 $\nu(\text{C=O})$ , 16 $\nu(\text{N-C})$	1533	388.2
1508	1485	212	63 $\delta^{\text{Ph}}(\text{CCH})$ , 10 $\nu(\text{Ph-N})$	1480	99.3
1478	1455	4	88 $\delta(\text{CH}_3)$		
1472	1449	1	44 $\delta^{\text{Ph}}(\text{CCH})$ , 21 $\nu^{\text{Ph}}(\text{CC})$		
1465	1443	30	67 $\delta(\text{CH}_3)$	1430	51.6
1398	1378	696	36 $\nu(\text{N-C})$ , 23 $\nu(\text{Ph-N})$	1385	219.7
1354	1335	1	92 $\delta(\text{CH}_3)$	1339	37.8
1339	1320	57	50 $\delta^{\text{Ph}}(\text{CCH})$ , 11 $\nu^{\text{Ph}}(\text{CC})$		
1299	1280	59	54 $\nu^{\text{Ph}}(\text{CC})$ , 10 $\delta^{\text{Ph}}(\text{CCH})$	1266	30.5
1238	1220	3	26 $\nu(\text{Ph-N})$ , 16 $\nu(\text{N-C})$	1216	32.7
1176	1159	36	60 $\delta^{\text{Ph}}(\text{CCH})$	1165	19.1
1165	1148	3	78 $\delta^{\text{Ph}}(\text{CCH})$	1129	2.2
1087	1072	9	50 $\delta^{\text{Ph}}(\text{CCH})$ , 23 $\nu^{\text{Ph}}(\text{CC})$		
1048 <sup>c</sup>	1033	1	92 $\delta(\text{CH}_3)$ , $\delta(\text{OCN})$		

<sup>a</sup>Scaled by 0.9858 [24]. <sup>b</sup>Vibrational modes:  $\nu$ , stretching;  $\delta$ , bendings. The numbers before the mode symbols indicate % contribution (10 or more) of a given mode to the corresponding normal vibration, according to the potential energy distribution matrix. <sup>c</sup> Followed by 24 lower-frequency normal vibrations.

The highest frequency experimental bands observed in the IR spectrum (3040–3000 cm<sup>-1</sup>) are assigned to the aromatic C-H stretches, while the lower frequency bands are attributed to the methyl group motions. The  $\nu(\text{C-H})$  bands are of low intensity in both the experimental and theoretical spectra.

DFT calculations reproduce well the IR frequencies measured in DMSO of the Amide-I, Amide-II, Amide-III vibrations. The Amide-I mode ( $\nu(\text{CO})$ ) is predicted to appear at 1715 cm<sup>-1</sup> as a very intense band. Experimentally, a very strong band was detected at 1686 cm<sup>-1</sup> in DMSO. In KBr pellet this band is downshifted strongly to 1665 cm<sup>-1</sup> due to intermolecular hydrogen N–H...C=O bonding in the crystal [14]. The strong IR band observed at 1544 cm<sup>-1</sup> was identified as Amide-II (the scissoring deformation  $\delta(\text{HNC})$ ) in accordance with its scaled theoretical value of 1524 cm<sup>-1</sup>. The stretching  $\nu(\text{N-C})$  strongly coupled with CC,

denoted as Amide-III was predicted as a high intensity band at 1321 cm<sup>-1</sup> and measured at 1317 cm<sup>-1</sup> in the experimental spectra. The theoretical and experimental IR data for the acetanilide azanion are compared in Table 2.

As above we can find there a good agreement between experimental and scaled theoretical frequencies. The mean deviation between them is 9.1 cm<sup>-1</sup> within the corresponding interval of 9–25 cm<sup>-1</sup>, typical for DFT calculations of frequencies for series of anions [2-6]. The frequency isotopic shifts, resulting from the <sup>15</sup>N substitution, are also well reproduced (Table 3).

The conversion of acetanilide into the azanion results in very essential changes in the IR spectrum (Tables 1 and 2; Figure 1), e.g.:

- Essential decrease in the carbonyl stretching frequency  $\nu(\text{CO})$ . There is no longer carbonyl band at the usual place. Its frequency decreases by: predicted 170 cm<sup>-1</sup>, measured

153 cm<sup>-1</sup>. The appearance of  $\nu(\text{CO})$  bands of acetanilide azanion at 1533 cm<sup>-1</sup> corroborated the assignment reported by Ognyanova and coworkers [19] and agree qualitatively with assigned of the very strong band at 1549 cm<sup>-1</sup> in IR spectrum of paracetamol dianion [30]. Incorrectly Liu *et al.* [31] assumed that the band at 1594 cm<sup>-1</sup> in the IR spectrum of the complex containing deprotonated acetanilide ligand originates from  $\nu_{\text{C=O}}$  in analogy to the spectrum of the acetanilides. A -8 cm<sup>-1</sup> <sup>15</sup>N isotopic shift has been measured in DMSO for this band; the theory gives a -2 cm<sup>-1</sup> value of the same shifts.

- Essential increase in the integrated intensity of the carbonyl band  $A_{\text{CO}}$ : predicted 3.3fold, measured 3 fold.

- Increase in C-N stretching frequency  $\nu(\text{C-N})$ : predicted 57 cm<sup>-1</sup>, measured 68 cm<sup>-1</sup>. The shift of this the coordinate to higher frequency is obviously due to the significant shortening of the C-N bond, caused by the conversion of the acetanilide molecule into the azanion.

- Essential increase in the corresponding intensity  $A_{\text{C-N}}$ : predicted 5.8fold, measured 3.6 fold.

- Strong enhancement of the intensity of the aromatic skeletal bands of the phenylene ring 19 (Wilson's notation): predicted 3.3-fold, measured 2-fold.

**Table 4.** Theoretical (B3LYP/6-311+G(2df,p)) and experimental bond lengths R (Å) and bond angles A (°) in the acetanilide molecule and its azanion.

	Molecule		$\Delta^b$	Anion	
	Experimental <sup>a</sup>	Theoretical		Theoretical	$\Delta^c$
<i>Bond lengths</i>					
R(C <sup>1</sup> ,C <sup>2</sup> )	1.394	1.397	0.003	1.421	0.024
R(C <sup>2</sup> ,C <sup>3</sup> )	1.385	1.390	0.005	1.390	0.000
R(C <sup>3</sup> ,C <sup>4</sup> )	1.383	1.389	0.006	1.393	0.004
R(C <sup>4</sup> ,C <sup>5</sup> )	1.390	1.390	0.000	1.396	0.006
R(C <sup>5</sup> ,C <sup>6</sup> )	1.378	1.385	0.007	1.384	-0.001
R(C <sup>1</sup> ,N <sup>12</sup> )	1.409	1.409	0.000	1.376	-0.033
R(N <sup>12</sup> ,C <sup>14</sup> )	1.348	1.374	0.026	1.338	-0.036
R(C <sup>14</sup> ,O <sup>15</sup> )	1.222	1.216	-0.006	1.252	0.036
R(C <sup>14</sup> ,C <sup>16</sup> )	1.505	1.516	0.011	1.534	0.018
<i>Bond angles</i>					
A(C <sup>1</sup> ,C <sup>2</sup> ,C <sup>3</sup> )	119.6	119.3	-0.3	121.1	1.7
A(C <sup>4</sup> ,C <sup>3</sup> ,C <sup>2</sup> )	121.2	121.4	0.2	121.8	0.5
A(C <sup>5</sup> ,C <sup>4</sup> ,C <sup>3</sup> )	120.4	119.1	-1.3	118.1	-1.0
A(C <sup>6</sup> ,C <sup>5</sup> ,C <sup>4</sup> )	120.5	120.2	-0.3	120.7	0.5
A(N <sup>12</sup> ,C <sup>1</sup> ,C <sup>6</sup> )	116.9	117.1	0.2	116.3	-0.9
A(C <sup>14</sup> ,N <sup>12</sup> ,C <sup>1</sup> )	127.5	129.5	2.0	122.6	-6.9
A(N <sup>12</sup> ,C <sup>14</sup> ,O <sup>15</sup> )	123.3	124.0	0.7	130.2	6.2
A(C <sup>16</sup> ,C <sup>14</sup> ,N <sup>12</sup> )	115.5	114.6	-0.9	113.4	-1.3

<sup>a</sup>See Ref. [26]. <sup>b</sup>Algebraic deviations (Å, degrees) between experimental and theoretical values. <sup>c</sup>Algebraic deviations (Å, degrees) between theoretical values of the anion and molecule.

**Table 3.** Theoretical (B3LYP/6-311+G(2df,p)) end experimental (in DMSO) vibrational frequencies (cm<sup>-1</sup>) of acetanilide azanion-<sup>15</sup>N and corresponding isotopic shifts.

Azanion		Azanion- <sup>15</sup> N		$\Delta_{\text{calc.}}$	$\Delta_{\text{exp.}}$
$\nu_{\text{calc.}}$	$\nu_{\text{exp.}}$	$\nu_{\text{calc.}}$	$\nu_{\text{exp.}}$		
1603	1594	1602	1592	-1	-2
1552		1552		0	
1545	1533	1543	1525	-2	-8
1485	1480	1484	1478	-1	-2
1455		1455		0	
1449		1449		0	
1443	1430	1442	1430	0	0
1378	1385	1362	1373	-16	-12
1335	1339	1332	1334	-2	-5

### Structural analysis of the species studied

According to X-ray diffraction experimental data the dihedral angle between the phenyl ring and amide group planes in the monoclinic crystal of acetanilide is 43.4° [26]. According to the calculations in the most stable conformers of the isolated molecule these groups are planar. The same groups in the isolated azanion have been predicted to be again planar. The theoretical and experimental bond lengths and angles in the acetanilide and its azanion are listed in Table 4.

As seen, there is a good agreement between the experimental and the theoretical values. The largest deviation from 0.026 Å is in bond N<sup>12</sup>-C<sup>14</sup> and can be associated with the formation of hydrogen bonds in the solid state. The mean absolute deviations (m.a.d.) between theoretical and experimental bond lengths and angles of acetanilide molecule are 0.006 Å and 0.07, respectively. This result leads us to believe that the theoretical bonds lengths and angle for the acetanilide anion are also reliable. The most significant changes caused by the conversion molecule azanion take place both at the azanionic center and next to it, with agrees the data for other azanions [2,4]. They are strong shortening of the Ph-N and N-C and bonds, strong lengthening of the C=O and C-CH<sub>3</sub> bonds.

The net electronic charges q of the fragments of the species studied are as follows:

	C <sub>6</sub> H <sub>5</sub>	NH/N <sup>-</sup>	COCH <sub>3</sub>
q in the molecule	0.098	0.012	-0.110
q in the azanion	-0.206	-0.339	-0.455

The charge change values  $\Delta q_i = q_i(\text{anion}) - q_i(\text{molecule})$  are usually quite informative in showing the distributions of the new charges in anions [2-4,30]. According to the present calculations, the new (azanionic) charge is distributed as follows: -0.304 e<sup>-</sup> and -0.346 e<sup>-</sup> are delocalized over the phenyl and acetyl groups and -0.349 e<sup>-</sup> of its remained localized at the azanionic centre.

## CONCLUSION

The spectral and structural changes, caused by the conversion of the acetanilide molecule into the corresponding azanion have been studied by IR spectra DFT method at B3LYP/6-311+G(2df,p) level.

A comparison of calculated with measured infrared data can be used as a test for the reliability of the structural predictions for various molecules and anions of this and similar types. These predictions can be very useful in cases of molecules and ions for which experimental structural parameters are inaccessible or unknown. IR spectral changes, which take place as a result of the conversion of molecule into azanion, were adequate predicted by same theoretical method.

**Acknowledgements:** Financial support of National Science Fund, Bulgaria (RNF01/0110) is gratefully acknowledged.

## REFERENCES

1. I. N. Juchnovski, I. G. Binev, in: S. Patai, Z. Rappoport (Ed.): The chemistry of functional groups, Suppl. C., Wiley, New York, 1983, p. 107.
2. A. D. Popova, E. A. Velcheva, B. A. Stamboliyska, *J. Mol. Struct.*, **1009**, 23 (2012).
3. E. A. Velcheva, B. A. Stamboliyska, P. J. Boyadjieva, *J. Mol. Struct.*, **963**, 57 (2010).
4. A. D. Popova, M. K. Georgieva, O. I. Petrov, K. V. Petrova, E. A. Velcheva, *Int. J. Quant. Chem.*, **107**, 1752 (2007).
5. S. Stoyanov, J. A. Tsenov, D. Y. Yancheva, *J. Mol. Struct.*, **1009**, 42 (2012).
6. S. Stoyanov, *J. Phys. Chem.*, **114**, 5149 (2010).
7. A. Cahn, P. Hepp, *Centralbl. Klein. Med.*, **7**, 561 (1886).
8. The Merck Index, 8th ed. Rahway, NY, Merck & Co., Inc., 1968, electronic version, 1998.
9. B. B. Brodie, A. E. Axelrod, *J. Pharmacol. Exp. Ther.*, **94**, 22 (1948).
10. D. A. Crooks, *Nature, Lond. A*, **160**, 17 (1947).
11. J. Mann, H. W. Thompson, *Proc. Royal Soc. Lond. A*, **192**, 489 (1948).
12. N. B. Abbott, A. Elliott, *Proc. Royal Soc. Lond. A*, **234**, 247 (1956).
13. V. V. Chalapathi, K. V. Ramiah, *Proc. Indian Acad. Sci. Sec A*, **67**, 184 (1968).
14. J. Binoy, N. B. Prathima, C. M. Krishna, C. Santhosh, I. H. Joe, V. S. Jayakumar, *Laser Phys.*, **16**, 1253 (2006).
15. H. Q. Liang, Y. P. Tao, L. G. Han, Y. X. Han, Y. J. Mo, *Guang Pu Xue Yu Guang Pu Fen Xi*, **32**, 2706 (2012).
16. S. Ilieva, B. Hadjieva, B. Galabov, *J. Mol. Struct.*, **508**, 73 (1999).
17. S. Ilieva, B. Hadjieva, B. Galabov, *J. Org. Chem.*, **67**, 6210 (2002).
18. D. Cheshmedzhieva, V. Dimitrova, B. Hadjieva, S. Ilieva, *J. Mol. Struct.*, **1009**, 69 (2012).
19. V. Ognyanova, J. Petrov, G. N. Andreev, *Spectrosc. Lett.*, **30**, 933 (1997).
20. M. J. Frisch, G. W. Trucks, H. B. Schlegel, G. E. Scuseria, M. A. Robb, J. R. Cheeseman, G. Scalmani, V. Barone, B. Mennucci, G. A. Petersson, H. Nakatsuji, M. Caricato, X. Li, H. P. Hratchian, A. F. Izmaylov, J. Bloino, G. Zheng, J. L. Sonnenberg, M. Hada, M. Ehara, K. Toyota, R. Fukuda, J. Hasegawa, M. Ishida, T. Nakajima, Y. Honda, O. Kitao, H. Nakai, T. Vreven, J. A. Montgomery, Jr., J. E. Peralta, F. Ogliaro, M. Bearpark, J. J. Heyd, E. Brothers, K. N. Kudin, V. N. Staroverov, R. Kobayashi, J. Normand, K. Raghavachari, A. Rendell, J. C. Burant, S. S. Iyengar, J. Tomasi, M. Cossi, N. Rega, J. M. Millam, M. Klene, J. E. Knox, J. B. Cross, V. Bakken, C. Adamo, J. Jaramillo, R. Gomperts, R. E. Stratmann, O. Yazyev, A. J. Austin, R. Cammi, C. Pomelli, J. W. Ochterski, R. L. Martin, K. Morokuma, V. G. Zakrzewski, G. A. Voth, P. Salvador, J. J. Dannenberg, S. Dapprich, A. D. Daniels, Ö. Farkas, J. B. Foresman, J. V. Ortiz, J. Cioslowski, D. J. Fox,

- Gaussian 09, Revision A1, Gaussian Inc., Wallingford CT, 2009.
21. A. D. Becke, *J. Chem. Phys.*, **98**, 5648 (1993).
22. C. Lee, W. Yang, G. R. Parr, *Phys. Rev.*, **B37**, 785 (1998).
23. M. H. Jamroz, *Vibrational Energy Distribution Analysis VEDA 4*, Warsaw, 2004-2010.
24. J. P. Merrick, D. Moran, L. Radom, *J. Phys. Chem.*, **A111**, 11683 (2007).
25. C. J. Brown, *Acta Crystallogr.*, **21**, 442 (1966).
26. H. J. Wasserman, R. R. Ryan, S. P. Layne, *Acta Crystallogr.*, **C41**, 783 (1985).
27. V. M. Vlasov, L. A. Oshkina, *Org. React.*, **28**, 47 (1993).
28. M. K. Georgieva, E. A. Velcheva, *Int. J. Quantum. Chem.*, **106**, 1316 (2006).
29. F. G. Bordwell, G. Z. J. Ji, *Am. Chem. Soc.*, **113**, 8398 (1991).
30. I. G. Binev, P. J. Boyadjieva, Y. I. Binev, *J. Mol. Struct.*, **447**, 235 (1998).
31. X. Liu, S. Zhang, Y. Ding, *J. Mol. Struct.*, **1018**, 185 (2012).

## ИЧ СПЕКТРАЛНИ И СТРУКТУРНИ ПРОМЕНИ ПРИЧИНЕНИ ОТ ПРЕВРЪЩАНЕТО НА АЦЕТАНИЛИДА В АЗАНИОН

Е. А. Велчева\*, З. И. Главчева, Б. А. Стамболийска

*Лаборатория „Структурен органичен анализ“, Институт по органична химия с център по фитохимия, Българска академия на науките, ул. „Акад. Г. Бончев“, бл.9, 113 София*

Постъпила на 26 юни 2015 г., Преработена на 10 септември 2015 г.

Структурите на азаниона на ацетанилида и на неговия  $^{15}\text{N}$  белязан аналог са изследвани с помощта на ИЧ спектри и ТФП изчисления, използвайки V3LYP функционал и 6-311+G(2df,p) базисен набор. Намерено е добро съответствие между теоретичните и експерименталните вибрационни характеристики на изследваните частици. Превръщането на молекулата ацетанилид в азанион предизвиква  $150\text{ cm}^{-1}$  понижение на карбонилната валентна честота, трикратно увеличение на интегралната интензивност на съответната ИЧ ивица и други съществени спектрални промени. Според изчисленията, структурните промени в пространствената структура, причинени от това превръщане, са *при* и *непосредствено до* азанионния център. Новият (азанионен) заряд се разпределя както следва:  $-0.304\text{ e}^-$  и  $-0.346\text{ e}^-$  са делокализирани върху фенилната и ацетилната групи и  $0.349\text{ e}^-$  от него остават локализирани при азанионния център.

## Kinetics of laser-induced photodissociation of oxyhemoglobin and its biomedical applications

A.I. Gisbrecht<sup>1\*</sup>, M.M. Asimov<sup>2</sup>

<sup>1</sup>*Institute of Electronics, Bulgarian Academy of Sciences,  
72 Tzarigradsko Chaussee Blvd., Sofia, Bulgaria*

<sup>2</sup>*Institute of Physics, National Academy of Sciences of Belarus,  
68 Nezavisimost Ave., Minsk, Belarus*

Submitted September 9, 2015; Revised October 6, 2015

In this study we investigate the kinetics of oxygen tension ( $pO_2$ ) in skin tissue under the influence of the transcutaneous laser irradiation. The results of *in vivo* experimental measurements of  $pO_2$  by a method of transcutaneous oxygen monitoring (TcOM) are presented. The results show that under laser irradiation the value of tissue oxygenation increases and after approximately 10 minutes of exposure exceeds its initial level up to 1.6 times. The observed increase in  $pO_2$  indicates the process of photodissociation of oxyhemoglobin ( $HbO_2$ ) in skin blood vessels, which results in local  $O_2$  increase in the tissue. Such laser-induced enrichment of tissue oxygenation can be used in phototherapy of pathologies, where the elimination of local tissue hypoxia is critical.

**Keywords:** oxyhemoglobin photo-dissociation; tissue oxygenation; oxygen tension.

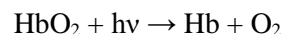
### INTRODUCTION

Tissue oxygenation plays a key role in the cell metabolism, energy supply and life activity of an organism. Many diseases such as diabetes, burns, bedsores and wounds are accompanied with an insufficient supply of oxygen to the tissues [1,2]. Also, the deficit of oxygen in cancer tissue is a major problem limiting the efficiency of photodynamic therapy [3,4]. The wound healing process directly depends on the oxygen pressure in skin tissue (Tc $PO_2$ ). For example, the additional supply of oxygen leads to an increase in the rate of collagen synthesis and an improvement of the protective functions of the skin. It is currently accepted that the adequate tissue oxygen concentration for normal cell metabolism should exceed 40 mmHg. Injuries, infections, and diseases can reduce this vital tissue oxygen level down to almost zero, which indicates tissue hypoxia. Optimal tissue healing occurs when the  $pO_2$  rises to between 50 and 80 mmHg. Consequently, the value of  $pO_2$  is an objective indicator for evaluating the local state of the tissue and the efficiency of cell metabolism. Controlling this mechanism provides the possibility for biological stimulation with a therapeutic effect.

In clinical practice the commonly used method for elimination of tissue hypoxia is ventilation of the lungs by pure  $O_2$  at normal and hyperbaric pressure. Sustained periods at such  $pO_2$  levels can

only be realized through the use of hyperbaric oxygen therapy [5], but it leads to the risk of oxygen intoxication. Moreover, this approach has not had a broad clinic application for local treatment due to technical difficulties. Thus the problem of local hypoxia elimination in biological tissues remains significant and the methods of influencing the delivery of oxygen to the tissue are of considerable interest. One of these methods is the light radiation in the optical spectral range.

A new approach for the optically induced increase in the local oxygen concentration due to photodissociation of oxyhemoglobin in cutaneous blood vessels has been proposed in [6]. The absorption of light by blood  $HbO_2$  is connected with the following photochemical and photophysical processes. It is known [7] that absorption of a photon with the activation energy leads to the dissociation of a part of the molecules, resulting in the release of molecular oxygen and the formation of deoxyhemoglobin. Photodissociation is one of the simplest chemical reactions when a compound dissociates under the action of radiation.



The quantum efficiency of the photodissociation of oxyhemoglobin is high and reaches 10 % in a wide visible spectral range [7].

The photophysical process is connected with the non-radiative dissipation of the absorbed excitation energy, as the heat generated in this process is transferred to the blood capillaries with a characteristic thermal relaxation time of ~ 0.05-1.2 msec. Estimates show that in the typical case a local increase in temperature of only 0.1 - 0.5 °C

\* To whom all correspondence should be sent:  
E-mail: aigiz@abv.bg

may be expected [8]. Such a small rise in the local temperature may produce little improvement in the capillary microcirculation of the blood and can hardly stimulate the cell metabolism [9].

We suppose that in the case of low energy irradiation the most important process is the photodissociation of HbO<sub>2</sub>. Experimental proof of the suggested concept has been demonstrated in [10,11]. The observed local decrease in the level of arterial blood saturation during laser irradiation clearly proves the induced photodissociation of HbO<sub>2</sub> in blood capillary vessels. The efficiency of this process depends on the wavelength and the output power of the laser radiation, the blood vessels density in the irradiation area, the optical properties of the skin and the depth of the blood vessels in the tissue.

It is interesting but still unclear what fraction of O<sub>2</sub> molecules released by photodissociation can escape from the heme pocket and diffuse through the cell membranes and capillary walls, thereby increasing the tissue oxygen pressure. However, relevant studies mainly refer to *in vitro* experiments or studies of individual cases [12-15]. No investigations have been carried out as yet into whether an immediate improvement in the oxygen saturation occurs *in vivo*, which would be a key to wound healing.

In this paper, we present an experimental study *in vivo* of the pO<sub>2</sub> rate in skin under the influence of local transcutaneous He-Ne laser (628 nm) irradiation.

## METHODS

The transcutaneous oximeter method, based on the principle of measuring the oxygen tension pO<sub>2</sub> in arterial blood, is a method for direct registration of gases that dissolve in the blood plasma. The choice of this method is determined by the fact that the TcOM allows the direct determination of the oxygen pressure in the skin tissue, in units of mmHg. Measurements were carried out using a transcutaneous oxygen monitor "Radiometer" TCM-4 with a Clark-type polarographic sensor with a diameter of 2.5 mm (TcPO<sub>2</sub> electrode) that consists of a platinum cathode and silver anode, electrolyte and an oxygen permeable membrane; a heating section and an electronic system for measuring and controlling the sensor temperature. (Fig.1 a).

The measurements were carried out on three volunteers, in the conditions of an absence of physical and emotional stress, in a seated position and at room temperature. All the procedures performed in the study were in accordance with the

ethical standards. Human studies in the article were approved by the relevant Institutional Review Board. During an individual measurement, all conditions were identical for all the subjects and remained constant throughout the measurement.

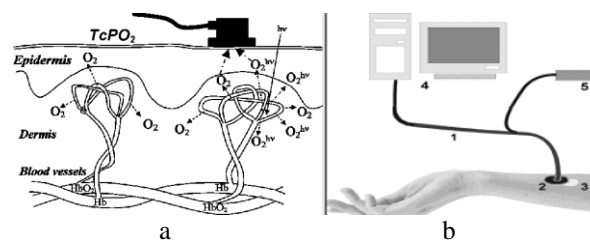


**Fig. 1.** Model of oxygen diffusion in tissue (a) and measurement (b) of tissue oxygen tensions: 1 - Clark sensor, 2 - electrolytic cell, 3 - irradiating zone, 4 - monitor TCM, 5 - He- Ne laser.

The measurement procedure is as follows. The sensor is placed on the skin of the forearm, an area with high capillary pressure then it is heated to 43°C (Fig. 1 b). Under the influence of temperature, oxygen diffuses from the capillaries into the epidermis and then into the electrolytic cell, where it is measured. The value of oxygen tension, measured transcutaneously (TcPO<sub>2</sub>), corresponds to the value of pO<sub>2</sub> measured in the arterial blood plasma. The errors in the determination of TcPO<sub>2</sub> come from the skin thickness, the subcutaneous blood flow and the physiological factors influencing O<sub>2</sub> delivery to the skin surface (decrease in the blood flow, the arterial blood pressure, the vasoconstriction occurrence). Since oxygenation depends on a number of factors, the laser radiation was only used once and the measurements were carried out immediately, in order to obtain direct observation of the effect of radiation.

## RESULTS

For local irradiation of cutaneous blood vessels, a He-Ne (632,8 nm) laser was chosen. As shown in the model calculations of the absorption spectra at the tissue depth [6], this wavelength lies in the effective absorption band of HbO<sub>2</sub> and penetrates deep into the skin issue. The laser output is 1 mW, and the beam diameter – 2,5 mm, providing a laser power density of ~ 20 mW/cm<sup>2</sup>. First, after thermostabilization, the initial oxygen pressure in the tissue is measured, then the laser radiation is applied. In Fig.2 the measured values of pO<sub>2</sub> in dependence on the irradiation time are presented. The obtained results are normalized to the initial oxygen pressure value.

As can be seen, the tissue oxygen tension increases for all three patients (although with different rates) and reaches saturation levels after

approximately 10 minutes of exposure. The value of  $TcPO_2$  in the irradiation zone depends on the time of exposure and the properties of the tissue that differ considerably for all three cases. It is significant to note that this growth of  $TcPO_2$  is due to the additional  $O_2$  in the tissue as a result of the laser-induced photodissociation of  $HbO_2$ . The oxygen released from  $HbO_2$  first increases the  $pO_2$  in the blood plasma and then diffuses into the surrounding tissue. The value of the  $TcPO_2$  measured transcutaneously increases about 1.6 times compared with its initial value. Generally, the diffusion occurs in three directions: toward the skin surface, inward to the muscle tissues and some is carried away by the blood flow. If we assume that the same amount of oxygen is carried away in all these directions, we should expect an increase in  $pO_2$  in the arterial blood plasma by about a factor of 4.8.

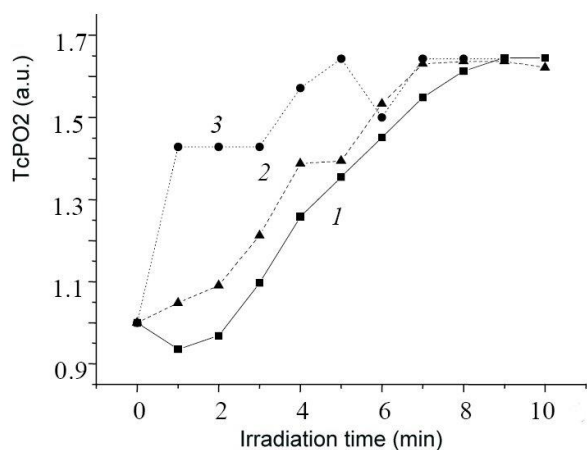


Fig. 2. Kinetics of laser-induced tissue oxygenation.

It is interesting to note that the obtained value of  $pO_2$  realized by laser-induced photodissociation of  $HbO_2$  is comparable with the one typically reachable by the conventional method of hyperbaric oxygen therapy [5].

## DISCUSSION

In contrast to other (in vitro) studies, this study was carried out under in vivo conditions, so it is possible to make statements about the feasibility of the measurement effect.

Thus, we demonstrate that after prolonged irradiation (several minutes), a certain fraction of oxygen molecules released due to photodissociation of  $HbO_2$  diffuses in the surrounding tissue and increases the oxygen partial pressure. Since the values of oxygenation depend on a number of factors, the results of this study cannot identify any immediate effect of the radiation on the oxygenation in tissue in vivo. Thus, it would be reasonable if further studies on the immediate

effects on oxygen saturation would take into account additional parameters, such as a variation in the wavelength radiation. The results obtained should correlate with the characteristics of light propagation in blood-filled tissues. The visible light in the blue and green spectral range has a small penetration depth into skin tissue, because of their proximity to the absorption bands of some basic skin chromophores such as  $HbO_2$  and melanin. Red and especially near infrared radiation penetrates much deeper into the soft tissues and plays a dominant role in the absorption of laser radiation by oxyhemoglobin in the deeper layers of tissue blood vessels. Such possibility to increase the free oxygen content in tissues can be applied in clinical practice for treatment of a number of diseases related to problems with the microcirculation and oxygen supply and therefore requires further investigations.

It is very important to note that photodissociation of  $HbO_2$  produces only molecular oxygen as a by-product and not singlet oxygen. Lepeshkevich in [16] uses time-resolved luminescence spectroscopy in the near-infrared region and does not measure detectable quantities of singlet oxygen during the photodissociation of  $O_2$  from myoglobin and hemoglobin.

## CONCLUSION

The obtained results demonstrate that the laser-induced photodissociation of oxyhemoglobin, whose main biological function is the transport of molecular oxygen, gives the possibility for an additional oxygen supply and allows the development of optical methods for tissue hypoxia elimination. Monitoring the kinetics of tissue oxygenation gives the possibility to control the normal aerobic cell metabolism.

It is shown that the efficiency of laser-induced oxygenation is comparable with the method of hyperbaric oxygenation, at the same time providing advantages by the local action. Advances in technology can lead to further improvement in the management of patients with wounds.

**Acknowledgement:** This work is partially supported by the project DFNI B02/9 /2014 of the Bulgarian Science Fund.

## REFERENCES

1. D. Leaper, *Int. Wound. J.*, **3**, 4 (2007).
2. H.W.Hopf, M.D.Rollins, *Antioxidants and redox signaling*, **9**, 1183 (2007).
3. H. Lui, R. R. Anderson, *Dermatol. Clin.*, **11**, 1 (1993).
4. H. I. Pass, *J Natl. Cancer Inst.*, **85**, 443 (1993).

5. P. M. Tibbles, J. S. Edelsberg, *N. Engl. J. Med.*, **334**, 1642 (1996).
6. M. M. Asimov, R. M. Asimov, A.N. Rubinov, *J. Appl. Spectrosc.*, **65**, 877 (1998).
7. W. Saffran, Q. Gibson, *J. Biol. Chem.*, **252**, 7955 (1977).
8. J. R. Basford, *Lasers Surg. Med.*, **9**, 1 (1989).
9. D.A. Rogatkin, A.V. Dunaev, *Journal of Medical Research and Development*, **3**, 100 (2014).
10. M. Asimov, R. Asimov, M. Mirshahi, A. Gisbrecht, *Proc. SPIE.*, **4397**, 390 (2001).
11. I. Yabushita, T. Kobayashi, *Spectroscopy*, **24**, 333 (2010).
12. P. Liu, Z. Zhu, *J. Biomed. Optics*, **17**, 125002 (2012).
13. F. Heu, C. Forster, B. Namer, A. Dragu, *Laser Ther.*, **22**, 21 (2013).
14. H. Matsuo, Y. Morimoto, T. Arai, R. Wada, *Lasers Med. Sci.*, **15**, 181 (2000).
15. A. Stratonnikov, N. Ermishova, V. Loshchenov, *Quantum. Electron.*, **32**, 917 (2002).
16. S. Lepeshkevich, A. Stasheuski, *J. Photochem. Photobiol. B.*, **120**, 130 (2013).

## КИНЕТИКА НА ЛАЗЕРНО-ИНДУЦИРАНАТА ФОТОДИСОЦИАЦИЯ НА ОКСИХЕМОГЛОБИНА В КРЪВТА ЗА БИОМЕДИЦИНСКИ ПРИЛОЖЕНИЯ

А.И. Гизбрехт<sup>1</sup>, М.М. Асимов<sup>2</sup>

<sup>1</sup>Институт по електроника, БАН, София, бул. Цариградско шосе 72.

<sup>2</sup>Физически Институт на Академия на науките на Беларус.

Постъпила на 9 септември 2015 г., коригирана на 6 октомври 2015 г.

(Резюме)

В тази статия ние изследваме кинетиката на напрежение на кислорода ( $pO_2$ ) в кожната тъкан под въздействието на транскутанно лазерно облъчване. Експериментални измервания на оксигенацията са направени с помоща на метода на полярографски презкожен мониторинг на кислорода (ТсОМ). Резултатите показват, че при облъчване с He-Ne лазер (632 nm) степента на тъканната оксигенация се увеличава в зависимост от продължителността на облъчването и след около 10 минути достига стационарно ниво, като максималното измерено увеличение е 1,6 пъти. Трябва да отбележим, че кинетиката на растежа на  $PO_2$  е пряко обусловена от допълнителното освобождаване на  $O_2$  в тъканта като резултат на лазерно-индуцираната фотодисоциация на  $HbO_2$  в кръвоносните съдове на кожата, което води до локално увеличаване на  $O_2$  в тъканта. Това лазерно-индуцирано обогатяване на тъканите с кислород може да се използва в фототерапия на патологии, в зони с нарушена микроциркулация на кръв и тъкани в състояние на хипоксия, например в тумори, изгаряния, рани и язви.

## Determination of trace amounts of manganese in water samples by flame atomic absorption spectrometry after dispersive liquid-liquid microextraction

A. Mirabi<sup>1\*</sup>, M. R. Jamali<sup>2</sup>, Q. Kazemi<sup>1</sup>

<sup>1</sup>Department of Chemistry, Qaemshahr Branch, Islamic Azad University, Qaemshahr, Iran

<sup>2</sup> Department of Chemistry, Payam Noor University, Behshahr, Iran

Received April 20, 2015, Revised December 28, 2015

Dispersive liquid-liquid microextraction was combined with flame atomic absorption spectrometry for the determination of manganese in water samples. 1-(2-Pyridylazo)-2-naphthol (PAN), chloroform and ethanol were used as chelating agent, extraction solvent and disperser solvent, respectively. In this extraction method, a mixture of 500  $\mu\text{L}$  ethanol (disperser solvent) and 100  $\mu\text{L}$  chloroform (extraction solvent) was rapidly injected by syringe into the water sample containing manganese ions and  $4 \times 10^{-4}$  mol  $\text{L}^{-1}$  1-(2-pyridylazo)-2-naphthol (PAN) (chelating agent). Thereby, a cloudy solution was formed. After centrifugation (5 min at 4000 rpm), the droplets of the cloud were settled at the bottom of the conical test tube ( $70 \pm 2$   $\mu\text{L}$ ). The settled phase was separated using a micro-syringe and diluted to 100  $\mu\text{L}$  with ethanol. A microsample introduction system was employed for the nebulization of a micro-volume of the diluted solution into FAAS. Some effective parameters on extraction and complex formation, such as extraction and disperser solvent type and their volume, extraction time, salt effect, pH and concentration of the chelating agent, were optimized. Under the optimum conditions, an enrichment factor (EF) of 50 was obtained from only 5 mL of water sample. The calibration graph was linear in the range of 10–200 ng  $\text{mL}^{-1}$  with limit of detection (LOD) of 3.0 ng  $\text{mL}^{-1}$ . The relative standard deviation (R.S.D.) for ten replicate measurements of 50 ng  $\text{mL}^{-1}$  of manganese was 3.3 %. The method was successfully applied for the extraction and determination of manganese in some natural water samples.

**Keywords:** Dispersive liquid-liquid microextraction, Preconcentration, Manganese, Water sample, FAAS.

### INTRODUCTION

Manganese is a necessity for the proper function of several enzymes and is an essential micro-nutrient for the function of the brain, nervous system and normal bone growth. It is present in large quantities in various steel materials as a hardening agent. It also finds application in pharmaceutical preparations. However, excessive intake can cause lesions, headache, psychotic behavior, drowsiness and other related symptoms and/or diseases. Thus manganese is an important element from the environmental perspective [1]. In general, concentrations of manganese in fresh waters [2] are within the range from 0.02 to 130 ng  $\text{mL}^{-1}$ . Therefore, the determination of this metal as  $\text{Mn}^{2+}$  ion often requires a method offering low detection limits. Although atomic spectrometric methods are powerful analytical tools for the determination of trace elements in environmental samples, preconcentration techniques combined with AAS are still necessary [3]. Liquid-liquid extraction (LLE) [4-6], solid phase extraction (SPE) [7-17] and cloud point extraction (CPE) [18-21] have been widely used for the preconcentration of manganese from water samples prior to its determination by flame atomic absorption spectrometry. However, that technique is rather

time-consuming and requires a large amount of sample. Separation and preconcentration based on dispersive liquid-liquid microextraction (DLLME) offer a convenient alternative to more conventional extraction methods [22]. This is a modified solvent extraction method and its acceptor-to-donor phase ratio is greatly reduced comparing with other extraction methods. In this method, the appropriate mixture of extraction solvent and disperser solvent is rapidly injected by syringe into aqueous samples containing the analytes. Thereby, a cloudy solution is formed. In fact, the cloudy state is due to the formation of fine droplets of extraction solvent dispersed in the sample solution. Then, this cloudy solution is centrifuged and the fine droplets are settled at the bottom of a conical test tube. The determination of the analytes in the settled phase can be performed by instrumental analysis. In this extraction method, any component originally present in the solution that interacts with the fine droplets of extraction solvent directly or after previous derivatization reaction can be extracted from the initial solution and concentrated in the small volume of the settled phase. The advantages of DLLME method are simplicity of operation, rapidity, low cost, high recovery and enrichment factor. The dispersive liquid-liquid extraction methodology has been used to separate and preconcentrate organic compounds prior to their

\* To whom all correspondence should be sent:

determination with chromatographic methods [23-25]. The DLLME has also been used for the extraction and preconcentration of metal ions after the formation of sparingly water-soluble complexes [26-27].

In the present work we report on the results obtained in a study of the dispersive liquid-liquid microextraction of manganese after the formation of a complex with PAN, with subsequent analysis by flame atomic absorption spectrometry using microsample introduction. The proposed method was also applied to the determination of manganese in water samples.

## EXPERIMENTAL

### *Apparatus*

A Thermo M series (Model: M5) flame atomic absorption spectrometer was utilized, equipped with a 50 mm burner head, deuterium background correction and air-acetylene flame. A manganese hollow cathode lamp (Thermo Scientific S51214) was used as radiation source, operated at 15 mA with a monochromator spectral bandpass of 0.1 nm. For manganese detection, the wavelength was set at the 232.0 nm resonance line. The acetylene and the air-flow rates were 0.8 and 10.0 L min<sup>-1</sup>, respectively. The Centurion Scientific centrifuge (Model K240R, Arundel, UK) was used to accelerate the phase separation. The pH values were measured with a Metrohm pH-meter (Model: 691, Herisau, Switzerland), supplied with a glass-combined electrode.

### *Reagents and solutions*

All reagents used were of analytical grade. All solutions were prepared with ultra pure water. The manganese stock solution (1000.0 mg L<sup>-1</sup>) was prepared by dissolving appropriate amounts of Mn (NO<sub>3</sub>)<sub>2</sub> in ultra pure water. Working solutions were prepared from the stock solution by serial dilutions with ultra pure water. Chloroform, carbon tetrachloride, chlorobenzene, acetone, methanol and ethanol were of analytical grade from Merck (Darmstadt, Germany). A 1 × 10<sup>-2</sup> mol L<sup>-1</sup> solution of 1-(2-pyridylazo)-2-naphthol (PAN) (Merck, Darmstadt, Germany) was prepared by dissolving an appropriate amount of PAN in acetone. This solution was kept in a dark place at room temperature. A stock standard ammonia/ammonium chloride buffer solution (0.1 mol L<sup>-1</sup>, pH 10.0) was prepared by dissolving an appropriate amount of ammonia in ultra pure water and neutralizing to pH 10.0 with hydrochloric acid. The pipettes and vessels used for trace analysis were kept in 10%

nitric acid for at least 24 h and subsequently washed four times with ultra pure water before use.

### *Dispersive Liquid-Liquid Microextraction Procedure*

5.0 mL of ultra pure water was placed in a 10 mL screw cap glass test tube with conical bottom and spiked at levels of 10-200 ng mL<sup>-1</sup> of manganese. Then 0.2 mL of 1.0 × 10<sup>-2</sup> mol L<sup>-1</sup> of PAN (as chelating agent) was added to this solution and the pH of the solution was adjusted by adding ammonia / ammonium chloride buffer solution (1.0 × 10<sup>-3</sup> mol L<sup>-1</sup>, pH 10.0). Then a mixture of 500 µL of ethanol (as disperser solvent) and 100 µL of chloroform (as extraction solvent) was injected rapidly into the sample solution by using 1.0-mL syringe, and the mixture was gently shaken. A cloudy solution (water, ethanol and chloroform) was formed in the test tube. In this step, manganese ions were extracted into the fine droplets of chloroform. The mixture was then centrifuged for 5 min at 4000 rpm. After this process, the dispersed fine droplets of chloroform were settled at the bottom of the conical test tube (70 ± 2 µL). The settled phase was separated using a micro-syringe, diluted to 100 µl with ethanol and then injected into the microsample introduction (discrete nebulization) system of FAAS.

## RESULTS AND DISCUSSION

In this research, DLLME combined with FAAS was developed for determination of manganese in water samples. In order to obtain a high recovery and a high enrichment factor, the effects of different parameters on the complexation and extraction conditions such as pH, concentration of buffer and chelating agent, kind of extraction and disperser solvent and their volumes, extraction time and salt addition, were optimized. In order to study the mentioned parameters, extraction recovery and enrichment factor were calculated by equations (1) and (2), respectively.

$$EF = C_{\text{sed}} / C_0 \quad (1)$$

where EF, C<sub>sed</sub> and C<sub>0</sub> are the enrichment factor, concentration of analyte in the sedimented phase and initial concentration of analyte in the aqueous sample, respectively.

$$R \% = [(C_{\text{sed}} \times V_{\text{sed}}) / (C_0 \times V_{\text{aq}})] \times 100 = [(EF \times V_{\text{sed}}) / V_{\text{aq}}] \times 100 \quad (2)$$

where R %, V<sub>sed</sub> and V<sub>aq</sub> are the extraction recovery, volume of sedimented phase and volume of aqueous sample, respectively. These parameters are known except C<sub>sed</sub>. Calculation of C<sub>sed</sub> was done by direct injection of a standard solution of Mn-

PAN complex in chloroform with concentration in the range of 0.5-10  $\mu\text{g mL}^{-1}$  to FAAS.

#### Effect of pH

The separation of metal ions by dispersive liquid-liquid microextraction involves prior formation of a complex with sufficient hydrophobicity to be extracted into the small volume of sedimented phase, thus achieving the desired preconcentration. The pH value plays a unique role in metal-chelate formation and subsequent extraction. The effect of pH on the complex formation and extraction of manganese from water samples was studied within the pH range of 2-12 by addition of NaOH or HCl. The results are illustrated in Figure 1. According to these results, the pH of 10.0 was chosen for the extraction.

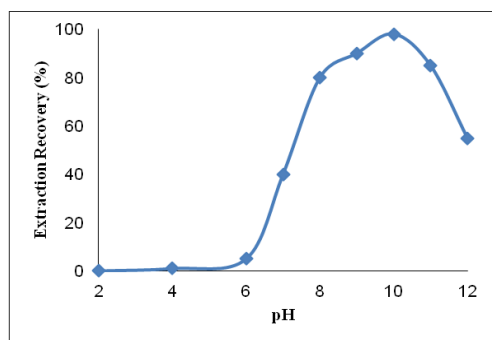


**Fig. 1.** Effect of pH on the extraction recovery of manganese by DLLME. Extraction conditions: water sample volume, 5.0 mL; disperser solvent (ethanol) volume, 500  $\mu\text{L}$ ; extraction solvent ( $\text{CHCl}_3$ ), 100  $\mu\text{L}$ ; PAN concentration,  $4.0 \times 10^{-4} \text{ mol L}^{-1}$ , concentration of manganese,  $50 \mu\text{g L}^{-1}$ .

#### Effect of PAN concentration

Dispersive liquid-liquid microextraction of 0.25  $\mu\text{g}$  of manganese using PAN from 5.0 mL sample solutions was conducted by varying the concentration of PAN. The extraction recovery for Mn (II) as a function of the concentration of chelating agent is shown in Figure 2. The recovery increases up to a PAN concentration of  $1.0 \times 10^{-4} \text{ mol L}^{-1}$  and reaches near quantitative extraction efficiency. A concentration of  $4.0 \times 10^{-4} \text{ mol L}^{-1}$  of PAN was chosen to account for other extractable species that might potentially interfere with the assaying of Mn (II).

#### Effect of Type and Volume of Extraction Solvent

Careful attention should be paid to the selection of the extraction solvent. It should have higher density than water, extraction capability for the compounds of interest and low solubility in water. Chloroform, carbon tetrachloride and

chlorobenzene were compared in the extraction of manganese. A series of sample solutions were studied by using 500  $\mu\text{L}$  ethanol and different volumes of extraction solvent to achieve 70  $\mu\text{L}$  volume of sedimented phase. Thereby, 100, 80 and 80  $\mu\text{L}$  of chloroform, carbon tetrachloride and chlorobenzene, respectively, were used. The results revealed that chloroform has the highest extraction efficiency (98.5 %) in comparison with carbon tetrachloride (32.0 %) and chlorobenzene (76.0 %). Hence, chloroform was chosen as extraction solvent.

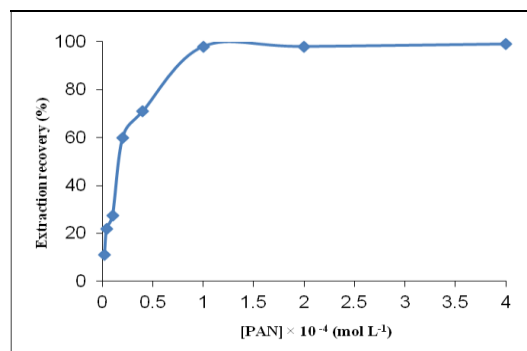


**Fig. 2.** Effect of PAN concentration on the extraction recovery of manganese by DLLME. Extraction conditions: water sample volume, 5.0 mL; disperser solvent (ethanol) volume, 500  $\mu\text{L}$ ; extraction solvent ( $\text{CHCl}_3$ ), 100  $\mu\text{L}$ ; concentration of manganese,  $50 \mu\text{g L}^{-1}$ ; pH = 10.0.

To examine the effect of the extraction solvent volume, solutions containing different volumes of chloroform were subjected to the same DLLME procedure. The experimental conditions were fixed and included the use of 500  $\mu\text{L}$  ethanol containing different volumes of chloroform. Figure 3 shows the curve of extraction recovery *versus* volume of the extraction solvent (chloroform). According to Figure 3, the extraction recovery increases up to

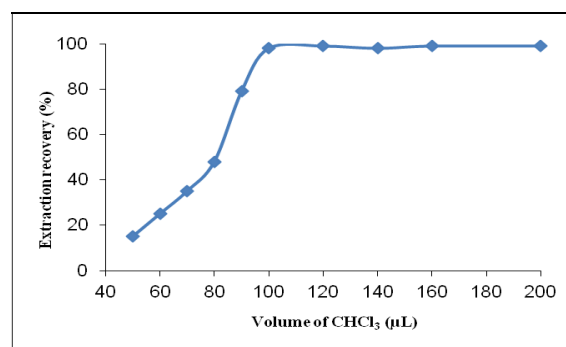


**Fig. 3.** Effect of the volume of extraction solvent ( $\text{CHCl}_3$ ) on the extraction recovery of manganese by DLLME. Extraction conditions: water sample volume, 5.0 mL; disperser solvent (ethanol) volume, 500  $\mu\text{L}$ ; PAN concentration,  $4.0 \times 10^{-4} \text{ mol L}^{-1}$ ; concentration of manganese,  $50 \mu\text{g L}^{-1}$ ; pH = 10.0.

100  $\mu\text{L}$  of chloroform and then remains constant. Thus, 100  $\mu\text{L}$  of chloroform was chosen as the optimum amount.

#### Effect of Type and Volume of Disperser Solvent

The main criterion for selection of the disperser solvent is its miscibility in both the extraction solvent and the aqueous sample. For this purpose, different solvents such as acetone, ethanol and methanol were tested. A series of sample solutions were studied by using 500  $\mu\text{L}$  of each disperser solvent containing 100  $\mu\text{L}$  of chloroform (extraction solvent). The results showed the best extraction recovery when ethanol was used. Thus, ethanol was selected as a disperser solvent.

Investigation of the effect of different volumes of ethanol (disperser solvent) on the extraction recovery would be very rough, because the variation of the volume of ethanol makes change in the volume of settled phase at constant volume of chloroform (extraction solvent). Thereby, to achieve a constant volume of the settled phase (70  $\mu\text{L}$ ) the volumes of ethanol and chloroform were changed simultaneously. The experimental conditions were fixed and included the use of different volumes of ethanol, 300, 400, 500, 600, 700, 800, 900, 1000, 1200 and 1500  $\mu\text{L}$  containing 90, 95, 100, 105, 110, 115, 120, 125, 135 and 150  $\mu\text{L}$  of chloroform, respectively. Under these conditions, the volume of the sedimented phase was constant ( $70 \pm 2 \mu\text{L}$ ). Figure 4 shows the curve of extraction recovery *versus* volume of the disperser solvent (ethanol). The results show that there was no considerable variation of the extraction recovery between 400 and 800  $\mu\text{L}$  of ethanol and the extraction recovery was high and then decreased by increasing the volume of ethanol. It is clear that by increasing the volume of ethanol, the solubility of

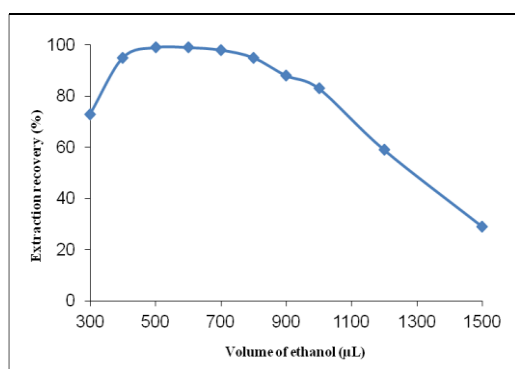


**Fig. 4.** Effect of the volume of disperser solvent (ethanol) on the extraction recovery of manganese by DLLME. Extraction conditions: water sample volume, 5.0 mL; extraction solvent ( $\text{CHCl}_3$ ), 100  $\mu\text{L}$ ; PAN concentration,  $4.0 \times 10^{-4} \text{ mol L}^{-1}$ ; concentration of manganese, 50  $\mu\text{g L}^{-1}$ ; pH = 10.0.

the complex in water increases. Therefore, the extraction recovery decreases. Thus, 500  $\mu\text{L}$  of ethanol was selected as the optimum volume in order to achieve a better and more stable cloudy solution.

#### Effect of Extraction Time

Extraction time is one of the most important factors in most extraction procedures. In DLLME, the extraction time is defined as the interval of time between injecting the mixture of disperser and extraction solvent, and starting centrifugation. The effect of extraction time was examined in the range of 0-45 min under constant experimental conditions. The results showed that the extraction time has no significant effect on the extraction efficiency. It was revealed that after the formation of the cloudy solution, the surface area between the extraction solvent and the aqueous phase is essentially infinitely large. Thereby, transfer of Mn-PAN complex from the aqueous phase to the extraction solvent is fast. This is one of the considerable advantages demonstrated by the DLLME technique, i.e., short extraction time.

#### Effect of Buffer Concentration

The influence of buffer amounts was studied by maintaining the other experimental variables constant. The results showed that above  $0.5 \times 10^{-3} \text{ mol L}^{-1}$  of buffer solution, no obvious variation of the extraction yield took place. Thus,  $1.0 \times 10^{-3} \text{ mol L}^{-1}$  of buffer solution was chosen as the optimal to achieve higher buffering capacity.

#### Effect of Salt

For investigating the influence of ionic strength on the performance of DLLME, experiments were carried out by adding different amounts of NaCl ( $0.0 - 1.0 \text{ mol L}^{-1}$ ). The other experimental conditions were kept constant. The results showed that the ionic strength has no appreciable effect upon extraction efficiency up to  $1.0 \text{ mol L}^{-1}$  of NaCl. These observations showed the possibility of using this method to separation of manganese from highly saline solutions.

#### Effect of Other Ions

The effects of common ions in natural water samples on the recovery of manganese were studied. In these experiments, 5.0 mL of solutions containing 50  $\text{ng mL}^{-1}$  of manganese and various amounts of interfering ions were treated according to the recommended procedure. An ion was considered to interfere when its presence produced a variation of more than 5% in the extraction

recovery of the sample. The results (Table 1) indicate that the Mn (II) recoveries are almost quantitative in the presence of interfering ions.

**Table 1.** Effect of foreign ions on the preconcentration and determination of manganese.

Ion	Ion/Mn(II) (w/w)	Recovery (%)
Li <sup>+</sup>	1000	96.4
Na <sup>+</sup>	1000	101.5
Cu <sup>2+</sup>	500	98.7
Ni <sup>2+</sup>	500	95.8
Al <sup>3+</sup>	500	99.3
Zn <sup>2+</sup>	500	104.2
Pb <sup>2+</sup>	250	103.7
Cd <sup>2+</sup>	250	97.5
Co <sup>2+</sup>	100	99.5
Cr <sup>3+</sup>	100	102.6
Fe <sup>2+</sup>	50	104.3
NO <sub>3</sub> <sup>-</sup>	1000	100.9
Cl <sup>-</sup>	500	96.6
SO <sub>4</sub> <sup>2-</sup>	250	95.8

*Figures of Merit*

Table 2 summarizes the analytical characteristics of the optimized method, including linear range, limit of detection, repeatability, and enrichment factor. The calibration graph was linear within the range of 10-200 ng mL<sup>-1</sup> of manganese. The limit of detection, defined as C<sub>L</sub> = 3S<sub>B</sub> / m (where C<sub>L</sub>, S<sub>B</sub> and m are the limit of detection, standard deviation of the blank and slope of the

calibration graph, respectively), was 3.0 ng mL<sup>-1</sup>. The relative standard deviation (RSD) for ten replicate measurements of 50 ng mL<sup>-1</sup> Mn (II) was 3.3 %. The enrichment factor was 50.

*Application to Samples*

The proposed DLLME-FAAS methodology was applied to the determination of Mn in several water samples. Water samples (i.e. tap water, sea water, river water and mineral water) were filtered through a 0.45 μm pore size membrane filter to remove suspended particulate matter and aliquots of water (5.0 mL) were subjected to DLLME. According to the results, the concentration of manganese in the analyzed water samples was below the LOD of the method. Moreover, the robustness of the proposed method was checked by performing recovery test on a synthetic sample (no certified reference material was available). Each type of water was spiked with variable amounts of Mn (II) to assess matrix effects. The results are shown in Table 3.

**Table 2.** Analytical characteristics of the proposed method.

Parameter	Analytical feature
Linear range (ng mL <sup>-1</sup> )	10-200
Limit of detection (ng mL <sup>-1</sup> ) (n =10)	3.0
Repeatability (RSD, %) (n =10)	3.3
Enrichment factor	50

**Table 3.** Determination of Mn (II) in different water samples.

Sample	Mn <sup>2+</sup> spiked (ng mL <sup>-1</sup> )	Mn <sup>2+</sup> detected (ng mL <sup>-1</sup> )	Recovery (%)
Tap water	0.00	n.d. <sup>a</sup>	—
(From the drinking water system of Tehran, Iran)	0.10	0.098 (3.6) <sup>b</sup>	98
	0.20	0.198 (3.5)	99
Sea water	0.00	n.d.	—
(Caspian sea water, Iran)	0.10	0.102 (3.7)	102
	0.20	0.192 (3.8)	96
River water	0.00	n.d.	—
(Ziarat River, Gorgan, Iran)	0.10	0.101 (3.6)	101
	0.20	0.190 (3.5)	95
Mineral water	0.00	n.d.	—
(From Abali mineral water, Tehran, Iran)	0.10	0.097 (3.4)	97
	0.20	0.206 (3.5)	103

<sup>a</sup> Not detected; <sup>b</sup> RSD of three replicate experiments

**Table 4.** Comparison of the present method with other methods for pre-concentration and determination of manganese(II).

Method	LOD ng mL <sup>-1</sup>	RSD (%)	EF	Reference
CPE-FAAS	2.9	1.3	17	19
CPE-FAAS	5.0	—	20	20
DLLME-UV-Vis	4.0	3.8	5.9	28
CPE-FAAS	33	—	96	29
SPE-UV-Vis	17	—	60	30
DLLME-FAAS	3.0	3.3	50	Present work

The relative recoveries of manganese from the mentioned water samples at various spiking levels were between 95.0 and 103.0 %. These results demonstrated that the matrices of these water samples had little effect on DLLME of manganese.

#### Comparison with other methods

A comparison of the present method with other reported methods for manganese preconcentration and determination is given in Table 4. The present method has low LOD, good enrichment factor and good RSD and these characteristics are comparable or even better than most of the other methods named in Table 4. All these results indicate that the present method is a reproducible, simple, and low-cost technique that can be used for the preconcentration and determination of manganese (II) in real samples.

#### CONCLUSION

Dispersive liquid-liquid microextraction combined with flame atomic absorption spectrometry allows tackling the determination of manganese in natural waters in a simple way. The method is efficient, rapid and economical. High preconcentration factor was obtained easily through this method and a detection limit at the sub ng mL<sup>-1</sup> level was achieved with only 5.0 mL of sample. In this method preparation time, as well as consumption of toxic organic solvents was minimized without affecting the sensitivity of the method.

**Acknowledgements:** The author thanks the research council at the Qaemshahr Branch of Islamic Azad University for financial support.

#### REFERENCES

1. K. C. Teo, J. Chen, *Analyst*, **126**, 534 (2001).
2. H. J. M. Bowen, *Environmental Chemistry of the Elements*, Academic Press, London, UK, 1979, p. 15.
3. A. Mizuike, *Enrichment Techniques for Inorganic Trace Analysis*, Springer-Verlag, Berlin, 1983.
4. P.K. Tarafder, R.K. Mondal, L. Kunkal, P. Murugan, D.P.S. Rathore, *Chem. Anal. (Warsaw)*, **49**, 251 (2004).
5. S.A. Barakat, *Anal. Chim. Acta*, **393**, 223 (1999).
6. D.T. Burns, S.A. Barakat, M. Harriott, M.S. El-Shahawi, *Anal. Chim. Acta*, **270**, 213 (1992).
7. C. Cui, M. He, B. Hu, *J. Hazard. Mater.* **187**, 379 (2011).
8. S.G. Ozcan, N. Satiroglu, M. Soylak, *Food Chem. Toxicol.*, **48**, 2401 (2010).
9. M. Ghaedi, K. Niknam, K. Taheri, H. Hossainian, M. Soylak, *Food Chem. Toxicol.*, **48**, 891 (2010).
10. A. Baysal, S. Akman, *Environ. Monit. Assess.*, **160**, 199 (2010).
11. S. Tokalioglu, V. Yilmaz, S. Kartal, *Environ. Monit. Assess.*, **152**, 369 (2009).
12. D. Rekha, K. Suvardhan, J.D. Kumar, P. Subramanyam, P.R. Prasad, Y. Lingappa, P. Chiranjeevi, *J. Hazard. Mater.*, **146**, 131 (2007).
13. P. Pohl, B. Prusisz, *Food Chem.* **102**, 1415 (2007).
14. A.P. dos Anjos, L. Cornejo-Ponce, S. Cadore, N. Baccan, *Talanta*, **71**, 1252 (2007).
15. M. Knap, K. Kilian, K. Pyrzynska, *Talanta*, **71**, 406 (2007).
16. M. Soylak, M. Tuzen, *J. Hazard. Mater. B.* **137**, 1496 (2006).
17. M. Grotti, M.L. Abemoschi, F. Soggia, R. Frache, *Anal. Bioanal. Chem.*, **375**, 242 (2003).
18. H. Cesur, *Turk. J. Chem.*, **27**, 307 (2003).
19. Z. Sun, P. Liang, Q. Ding, Jing Cao, *Anal. Sci.*, **22**, 911 (2006).
20. V.O. Doroschuk, S.O. Lelyushok, V.B. Ishchenko, S.A. Kulichenko, *Talanta*, **64**, 853 (2004).
21. A.R. Rod, Sh. Borhani, F. Shemirani, *Eur. Food Res. Technol.*, **223**, 649 (2006).
22. M. Rezaee, Y. Assadi, M. R. Milani Hosseini, E. Aghaee, F. Ahmadi, S. Berijani, *J. Chromatogr. A.*, **1116**, 1 (2006).
23. R. R. Kozani, Y. Assadi, F. Shemirani, M. R. Milani Hosseini, M. R. Jamali, *Talanta*, **72**, 387 (2007).
24. R. R. Kozani, Y. Assadi, F. Shemirani, M. R. Milani Hosseini, M. R. Jamali, *Chromatographia*, **66**, 81 (2007).
25. S. Berijani, Y. Assadi, M. Anbia, M. R. Milani Hosseini, E. Aghaee, *J. Chromatogr. A.*, **1123**, 1 (2006).
26. E. Zeini Jahromi, A. Bidari, Y. Assadi, M. R. Milani Hosseini, M. R. Jamali, *Anal. Chim. Acta.* **585**, 305 (2007).
27. P. Liang, H. Sang, *Anal. Biochem.*, **380**, 21 (2008).
28. I.S. Balogha, L. Rusnakova, J.S. Krlikova, L. Kocurova, M. Torokc, V. Andruch, *Intern. J. Environ. Anal. Chem.*, **92**, 1059 (2012).
29. M.A. Farajzadeh, M.R. Fallahi, *Anal. Sci.*, **22**, 635 (2006).
30. M. Dogutan, H. Filik, *Analytica Chimica Acta*, **485**, 205 (2003).

## ОПРЕДЕЛЯНЕ НА СЛЕДИ ОТ МАНГАН ВЪВ ВОДНИ ПРОБИ ЧРЕЗ ПЛАМЪКОВА АТОМНО-АБСОРБЦИОННА СПЕКТРОФОТОМЕТРИЯ СЛЕД ДИСПЕРСИОННА ТЕЧНО-ТЕЧНА МИКРО-ЕКСТРАКЦИЯ

А. Мираби<sup>1\*</sup>, М.Р. Джамали<sup>2</sup>, К. Каземи<sup>1</sup>

<sup>1</sup> Департамент по химия, Клон Кхаемшахр, Ислямски университет „Азад“, Кхаемшахр, Иран

<sup>2</sup> Департамент по химия, Университет Паяме Нур, Бехшахр, Иран

Постъпила на 20 април, 2015 г.; приета на 28 декември, 2015 г.

(Резюме)

Дисперсионната течна-течна микро-екстракция е комбинирана с чрез пламъкова атомно-абсорбционна спектрофотометрия за определянето на манган във водни проби. Използвани са 1-(2-пиридиазо)-2-нафтол (PAN), хлороформ и етанол като хелатни агенти, екстрагент и диспергиращ разтворител. По този екстракционен метод смес от 500  $\mu\text{L}$  етанол и 100  $\mu\text{L}$  хлороформ (екстрагент) се инжектира бързо във водна проба, съдържаща манганови йони и  $4 \times 10^{-4} \text{ mol L}^{-1}$  1-(2-пиридиазо)-2-нафтол (PAN) (хелатообразуващ агент). Получава се мътна дисперсия. След центрофугиране (5 мин. при 4000 об./мин.) става утаяване на капки от дисперсията в конична епруветка ( $70 \pm 2 \mu\text{L}$ ). Утаената фаза се отделя с помощта на микро-спринцовка и се разрежда до 100  $\mu\text{l}$  д етанол. Тази система за въвеждане микро-проби се използва за анализ на разредени разтвори в чрез пламъкова атомно-абсорбционна спектрофотометрия. Оптимизирани са някои ефективни параметри на екстрагента и типът на диспергиращия разтворител и техния, времето за екстракция, солевият ефект, рН и концентрацията на хелатообразуващия агент. При оптималните условия факторът на обогатяване (EF) е 50 и е получен от водна проба само от 5 mL. Калибрационната линия е права в интервала 10–200  $\text{ng mL}^{-1}$  с граница на откриване 50  $\text{ng mL}^{-1}$  манган и 3.3 %. Методът е приложен успешно за екстракцията и определянето на манган в проби от някои природни води.

## A new synthesis method and photophysical properties of Ir(C<sup>^</sup>N)<sub>3</sub> cyclometalated iridium phosphorescent complexes

Q.-W. Chang<sup>1,2</sup>, J. Li<sup>2</sup>, C.-X. Yan<sup>2</sup>, J. Jiang<sup>2</sup>, J.-L. Chen<sup>2</sup>, Q.-S. Ye<sup>2</sup>, J. Yu<sup>2</sup>, W.-P. Liu<sup>1,2\*</sup>

<sup>1</sup>Faculty of Material Science and Engineering, Kunming University of Science and Technology, Kunming 650093, Yunnan, People's Republic of China

<sup>2</sup>State Key Laboratory of Advanced Technologies for Comprehensive Utilization of Platinum Group Metals, Kunming Institute of Precious Metals, Kunming 650106, Yunnan, People's Republic of China

Received September 25, 2015, Revised October 13, 2015

A new convenient synthesis method with excellent yields for Ir(ppy)<sub>3</sub> and Ir(piq)<sub>3</sub> is developed using [(acac-O,O)<sub>2</sub>(acac-C<sup>3</sup>)Ir(H<sub>2</sub>O)] as an efficient starting material. Their structures are fully characterized by elemental analysis, <sup>1</sup>H-NMR and ESI-MS. The photophysical properties of both compounds are studied by UV-visible spectra and photoluminescence spectra.

**Keyword:** iridium, cyclometalated complexes, synthesis, phosphorescent, Ir(C<sup>^</sup>N)<sub>3</sub>.

### INTRODUCTION

Neutral cyclometalated iridium phosphorescent complexes with Ir(C<sup>^</sup>N)<sub>3</sub> and Ir(C<sup>^</sup>N)<sub>2</sub>(LL) types are the most promising phosphorescent materials in organic light-emitting devices (OLEDs)[1-4]. Tris-cyclometalated iridium complexes have attracted considerable attention due to a potential application in OLED [5]. Several experimental procedures[5-6] have been developed for their synthesis using IrCl<sub>3</sub>·nH<sub>2</sub>O, Ir(acac)<sub>3</sub>, [Ir(acac)(coe)<sub>2</sub>] or the chlorinated bridged dimer as a precursor, their synthesis often requires harsh reaction conditions to proceed so that they can not be widely be applied in OLED. Therefore, developing the new synthesis route for Ir(C<sup>^</sup>N)<sub>3</sub> type phosphorescent complexes is very worthy and interesting. [(acac-O,O)<sub>2</sub>(acac-C<sup>3</sup>)Ir(H<sub>2</sub>O)] has a rich coordination and reaction chemistry due to the presence of a coordinated water ligand [7-9], which has a better reaction activity than Ir(acac)<sub>3</sub> for preparing Ir(C<sup>^</sup>N)<sub>3</sub> type phosphorescent complexes. In this contribution, a new convenient synthesis method with excellent yields for Ir(ppy)<sub>3</sub> and Ir(piq)<sub>3</sub> is developed using [(acac-O,O)<sub>2</sub>(acac-C<sup>3</sup>)Ir(H<sub>2</sub>O)] as a new precursor.

### EXPERIMENTAL

#### General considerations

All manipulations were performed in an atmosphere of high purity argon using conventional Schlenk techniques. All reagents and solvents in this study were used without further purification. [(acac-O,O)<sub>2</sub>(acac-C<sup>3</sup>)Ir(H<sub>2</sub>O)] was synthesized

from IrCl<sub>3</sub>·nH<sub>2</sub>O and NaHCO<sub>3</sub> in refluxing acetylacetone according to the literature[10]. NMR spectra were obtained on a Bruker AV400 using tetramethylsilane as an internal reference. Mass spectrometry studies were carried out on an Autospec 3000 Instrument. Elemental analyses for C, H, and N were performed using a Carlo-Ebra Instrument. UV-visible absorption spectra were measured on a Cary 50Bio spectrophotometer. The photoluminescence (PL) spectra were recorded on an F-7000 spectrometer in CH<sub>2</sub>Cl<sub>2</sub>.

#### Synthesis of Fac-Ir(ppy)<sub>3</sub>

[(acac-O,O)<sub>2</sub>(acac-C<sup>3</sup>)Ir(H<sub>2</sub>O)] (2 g, 3.94 mmol) and 2-phenylpyridine (3.67 g, 23.66 mmol) were refluxed under an inert gas atmosphere in 50 mL of glycerol for 24 h. After the mixture was cooled to room temperature, 50 mL of 1M HCl solution and 50 ml of methanol were added and stirred for 30 min and then filtered to yield the crude product. The crude product was flash chromatographed on a silica column using dichloromethane to yield 80% (2.06 g) product. <sup>1</sup>H-NMR (400 MHz, CDCl<sub>3</sub>), ppm: 8.52(d, 1H), 7.84(d, 1H), 7.72(t, 1H), 7.52(d, 1H), 7.13(t, 1H), 6.77(t, 1H), 6.63(t, 1H), 6.27(d, 1H). ESI-MS: m/z = 655(M+1), 501(Ir(ppy)<sub>2</sub>+1) Anal. Found: C 60.45, H 3.62, N 6.45. Calcd: C 60.53, H 3.69, N 6.42.

#### Synthesis of Ir(piq)<sub>3</sub>

The synthesis procedure of Ir(piq)<sub>3</sub> was the same for Ir(ppy)<sub>3</sub> except that 1-phenylisoquinoline was used in place of 2-phenylpyridine in the same molar amount: yield 72% (2.28 g). Anal. Found: C 67.12, H 3.74, N 5.20. Calcd: C 67.15, H 3.76, N 5.22. <sup>1</sup>H-NMR (400 MHz, DMSO-*d*<sub>6</sub>), ppm: 8.92(d, 1H), 8.16(d, 1H), 7.93(t, 1H), 7.78(t, 2H), 7.48(d, 1H),

\* To whom all correspondence should be sent:  
E-mail: liuweiping0917@126.com

7.36(d, 1H), 6.90(t, 1H), 6.79(d, 1H), 6.72(t, 1H).  
ESI-MS: m/z = 827(M+23), 425(M/2+23).

## RESULTS AND DISCUSSION

### Synthesis and characterization of Ir(ppy)<sub>3</sub> and Ir(piq)<sub>3</sub>

Ir(ppy)<sub>3</sub> and Ir(piq)<sub>3</sub> were synthesized by reacting [(acac-O,O)<sub>2</sub>(acac-C<sup>3</sup>)Ir(H<sub>2</sub>O)] with corresponding cyclometalated ligands (see scheme 1). And their structures were confirmed by element analysis, ESI-MS (see experiment section) and <sup>1</sup>H-NMR (see Figure 1). The results match those reported for Ir(ppy)<sub>3</sub> and Ir(piq)<sub>3</sub>[11-12] and the molecule structures shown in Figure 2.

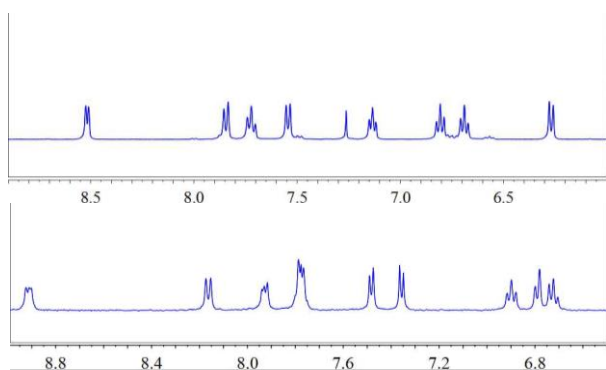


**Fig. 1.** <sup>1</sup>H-NMR of Ir(ppy)<sub>3</sub> in CDCl<sub>3</sub> (above) and Ir(piq)<sub>3</sub> in DMSO-*d*<sub>6</sub> (below).

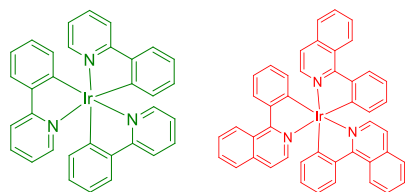


**Fig. 2.** Molecular structures of Ir(ppy)<sub>3</sub> and Ir(piq)<sub>3</sub>.

### Photophysical properties of Ir(ppy)<sub>3</sub> and Ir(piq)<sub>3</sub>

The absorption and emission spectroscopic behaviors of Ir(ppy)<sub>3</sub> and Ir(piq)<sub>3</sub> are studied at room temperature in CH<sub>2</sub>Cl<sub>2</sub>. Figure 3 shows the UV-vis absorption and photoluminescence spectra of Ir(ppy)<sub>3</sub>. The absorption band observed at 273 nm is related to spin-allowed  $\pi$ - $\pi^*$  transitions (corresponding to ligand centered states, <sup>1</sup>LC) of the cyclometalated ppy ligands. The broad and unresolved absorption band at lower energy,

peaking at 367nm, is assigned to spin-allowed d- $\pi^*$  transitions (corresponding to metal-to-ligand charge transfer states, <sup>1</sup>MLCT), whereas absorptions at wavelengths between at 430 nm and 500 nm involve <sup>3</sup>MLCT states. The emission at ambient temperature shows a maximum peak at 512 nm. The UV-vis absorption and photoluminescence spectra of Ir(piq)<sub>3</sub> are also given in Figure 4. In the range below about 350 nm, the band is related to spin-allowed  $\pi$ - $\pi^*$  transitions (<sup>1</sup>LC), and the two lower-energy bands appear in the region of about 370-550 nm are tentatively assigned to the <sup>1</sup>MLCT and <sup>3</sup>MLCT transitions. The maximum emission peak of Ir(piq)<sub>3</sub> is at 619 nm.

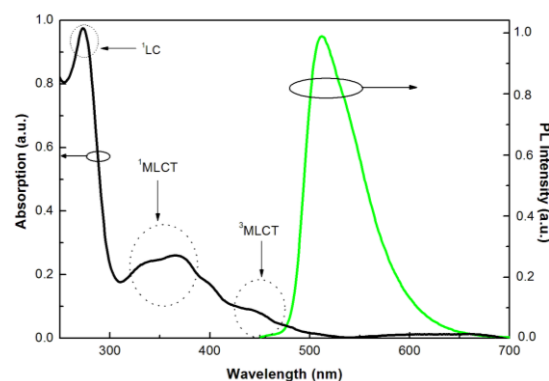


**Fig. 3.** Absorption and photoluminescence spectra of Ir(ppy)<sub>3</sub> in CH<sub>2</sub>Cl<sub>2</sub> at ambient temperature.

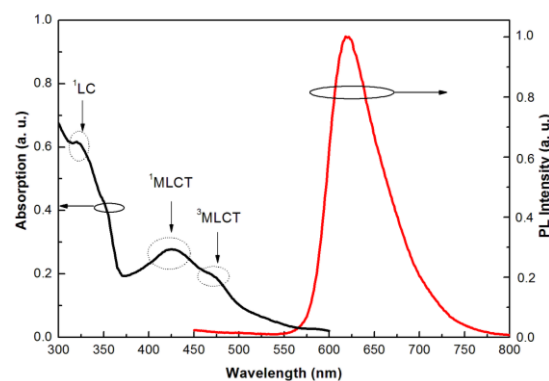
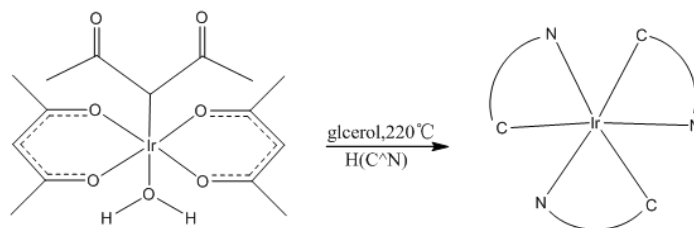


**Fig. 4.** Absorption and photoluminescence spectra of Ir(piq)<sub>3</sub> in CH<sub>2</sub>Cl<sub>2</sub> at ambient temperature.



**Scheme 1.** Synthesis route of Ir(C<sup>N</sup>)<sub>3</sub> type phosphorescent complexes.



Comparing the absorption and emission spectra of Ir(ppy)<sub>3</sub> and Ir(piq)<sub>3</sub>, both compounds show similar spectral features which agree with the reports in the literature [12-15]. Differently, the absorption and emission peaks of Ir(piq)<sub>3</sub> have a red shift due to the bigger conjugation degree of piq than that of ppy.

## CONCLUSION

In conclusion, The advantages of the herein described synthetic procedures are that the complexes Ir(ppy)<sub>3</sub> and Ir(piq)<sub>3</sub> can be obtained in high yields by a convenient method starting from [(acac-O,O)<sub>2</sub>(acac-C<sup>3</sup>)Ir(H<sub>2</sub>O)]. The general usefulness of the described procedures for the synthesis of closely related cyclometalated iridium complexes will be examined by us in the near future.

**Acknowledgments:** The authors are grateful to Yunnan Provincial Science Foundation (Grant No. 2015IB019) and Kunming Science Foundation (Grant No.2016KJH059) P.R.China for the financial support.

## REFERENCES

1. S. Lamansky, P. Djurovich, D. Murphy, F. Abdel-Razzaq, H. E. Lee, C. Adachi, P. E. Burrows, S. R. Forrest, M. E. Thompson, *J. Am. Chem. Soc.*, **123**, 4304 (2001).
2. M. A. Baldo, D. F. O'Brien, Y. You, A. Shoustikov, S. Sibley, M. E. Thompson, S. R. Forrest, *Nature*, **395**,151 (1998).
3. M. G. Helander, Z. B. Wang, J. Qiu, M. T. Greiner, D. P. Puzzo, Z. W. Liu, Z. H. Lu, *Science*, **332**, 944 (2011).
4. A. B. Tamayo, B. D. Alleyne, P. I. Djurovich, S. Lamansky, I. Tsyba, N. N. Ho, R. Bau, M. E. Thompson, *J. Am. Chem. Soc.*, **125**, 7377 (2003).
5. S. Lamansky, P. Djurovich, D. Murphy, F. Abdel-Razzaq, R. Kwong, I. Tsyba, M. Bortz, B. Mui, R. Bau, M. E. Thompson, *Inorg. Chem.*, **40**, 1704 (2001).
6. H. C. Böttcher, M. Graf, K. Sünkel, P. Maver, H. Krüger, *Inorganica Chimica Acta*, **365**,103 (2011).
7. Q. Chang, J. Chen, M. Xie, W. Liu, Y. Yu, Q. Ye, X. Chen, *J. Struct. Chem.*, **52**, 824 (2011).
8. Q. W. Chang, C. Y. Hu, J. L. Chen, M. J. Xie, W. P. Liu, Q. S. Ye, Y. Yu, X. Z. Chen, L. Q. Chen, *Transit. Met. Chem.*, **36**, 337 (2011).
9. Q. W. Chang, G. F. Chen, C. Y. Hu, J. L. Chen, Q. S. Ye, X. Z. Chen, J. Jiang, W. P. Liu, *Res. Chem. Intermed.*, **38**, 1571 (2012)..
10. R. A. Periana, X. Y. Liu, G. Bhalla, *Chem. Commun.*, **24**, 3000 (2002).
11. M. Lepeltier, F. Dumur, J. Marrot, E. Contal, D. Bertin, D. Gigmes, C. R. Mayer Dalton, *Trans.*, **42**, 4479 (2013).
12. M. G. Colombo, T. C. Brunold, T. Riedener, H. U. Güdel, *Inorg. Chem.*, **33**, 545 (1994).
13. W. Holzer, A. Penzkofer, T. Tsuboi, *Chemical Physics Letters*, **308**, 93 (2005).
14. H. Yersin, T. Hofbeck, *Inorg. Chem.*, **49**, 9290 (2010).
15. J. Brey, P. Stössel, S. Schrader, A. Starukhin, W. J. Finkenzeller, H. Yersin, *Chem. Mater.*, **15**, 1745 (2005).
16. K. Dedeian, P. I. Djurovich, F. O. Garces, G. Carlson, R. J. Watts, *Inorg. Chem.*, **29**, (1990).

## НОВ МЕТОД ЗА СИНТЕЗАТА И ФОТО-ФИЗИЧНИ СВОЙСТВА НА Ir(C<sup>N</sup>)<sub>3</sub> ЦИКЛОМЕТАЛИРАНИ ИРИДИЕВИ ФОСФОРЕСЦЕНТНИ КОМПЛЕКСИ

К.-У. Чанг<sup>1,2</sup>, Дж. Ли<sup>2</sup>, Ц.-С. Ян<sup>2</sup>, Дж. Джианг<sup>2</sup>, Дж.-Л. Чен<sup>2</sup>, К.-С. Йе<sup>2</sup>, Дж. Ю, У.-П. Лю<sup>1,2\*</sup>

<sup>1</sup>Факултет по материалознание и инженерство, Кунминг'ски университет за наука и технология, Кунминг 650093, Юнан, КНР

<sup>2</sup>Държавна ключова лаборатория по нови технологии за пълно оползотворяване на метали от платиновата група, Кунминг'ска лаборатория за благородни метали, Кунминг 650106, Юнан, КНР

Постъпила на 25 септември 2015 г.; коригирана на 13 октомври 2015 г.

(Резюме)

Създаден е нов удобен метод за синтеза на Ir(ppy)<sub>3</sub> и Ir(piq)<sub>3</sub> с отличен добив. Като изходен материал е използван [(acac-O,O)<sub>2</sub>(acac-C<sup>3</sup>)Ir(H<sub>2</sub>O)]. Тяхната структура е напълно охарактеризирана чрез елементен анализ, <sup>1</sup>H-NMR и ESI-MS. Фотофизичните свойства на двете съединения са изучени чрез UV-Vis спектри и фотолуминисцентни спектри.

## Preparation and modification of peanut shells and their application for heavy metals adsorption

Z. Yang<sup>1</sup>, Y. G. Wang<sup>1,3,4</sup>, Y. J. Jing<sup>3,4</sup>, Q. W. Wei<sup>3,4</sup>, F. F. Leng<sup>3,4</sup>, H. Ma<sup>3,4</sup>, Y. L. Wang<sup>3,4</sup>, J. X. Chen<sup>1,2\*</sup>

<sup>1</sup> School of Energy and Power Engineering, Lanzhou University of Technology, Lanzhou 730050, China

<sup>2</sup> School of Petrochemical Engineering, Lanzhou University of Technology, Lanzhou 730050, China

<sup>3</sup> School of Life Science and Engineering, Lanzhou University of Technology, Lanzhou 730050, China

<sup>4</sup> The Key Lab of Screening, Evaluation and Advanced Processing of TCM and Tibetan Medicine, Gansu Educational Department, Lanzhou 730050, China

Received June 13, 2016, Accepted July 26, 2016

Peanut shells are a test adsorption material, the influences of key factors (pH, reaction duration, initial concentration and adsorption dosage) on its adsorption of heavy metal ions including  $Pb^{2+}$ ,  $Cu^{2+}$  and  $Zn^{2+}$  were studied. The results showed that: the adsorption rate of the above mentioned heavy metal ions increased gradually with the pH increase. We also noticed that the adsorption of heavy metal ions by unmodified peanut shells performed well under acidic conditions, while the best results for modified peanut shells were obtained under alkaline conditions. Meanwhile, the adsorption rate reached about 88% of the maximum adsorption rate after treatment for a 15 min reaction and tended to balance after 50 min; with increasing initial ion concentration, the adsorption rate increased gradually, and reached the maximum adsorption rate at 30 mg/L. However, it was gradually reduced when over 30 mg/L. The results revealed that adsorption rate increased with the adsorbent dosage. The dynamic behaviors of both modified and unmodified peanut shells well fit the Lagergren (II) order chemical reaction kinetics model. Additionally, compared with unmodified peanut shells, the adsorption effect for modified shells was significant.

**Keywords:** Peanut Shell, Adsorption, Heavy Metals, Modification, Dynamics.

### INTRODUCTION

The heavy metals,  $Pb^{2+}$ ,  $Cu^{2+}$ ,  $Zn^{2+}$ , are harmful to the environment. They accumulate in the living organisms by adsorption and thus pose a serious threat to public health. Excessive accumulation of copper *in vivo* could lead to many diseases like diarrhea, skin diseases and even death [1, 2]. Lead is a cumulative poison acting on various systems and organs of the human being [3], such as the hematopoietic and cardiovascular system, the central nervous systems and the reproductive organs [4]. There are many technical methods used to treat contamination by heavy metals, such as ion exchange resin, activated carbon adsorption, chemical precipitation and electrochemical treatment [5]. These methods have some effect, but their cost compared with biotechnology, is much larger and may cause secondary pollution.

In recent years, the biomass material, as an adsorbent applied for controlling heavy metals contamination, is becoming a hot research topic. Biomass materials have the advantage of widespread-sources, convenience, low-cost, directly-treated and thus greatly reduce the cost of

the treatment of heavy metals. Therefore biomass materials find good application prospects [6, 7]. Different from the traditional process, the biological assay has the following advantages: metal ions can be selectively removed with low concentrations of heavy metals; energy-efficiency, cost-effectiveness; easy separation and recovery of heavy metals; the sustainability-adsorbent is easily regenerated and recycled.

As the increasing lack of non-renewable resources such oil and coal, the preparation of new industrial products with agricultural and forestry waste together with other renewable resources as raw materials gradually draws attention from all over the world. The common agricultural and sideline products include bark, cotton shells, peanut shells, sawdust, orange peel and others. A large number of peanut shells are discarded in the natural environment or burned, which not only cause serious environmental pollution, but also are a waste of resources. Peanut hull carbide (PHC), commonly used as a bio-adsorbent produced from piles of peanut shells, is similar to the activated carbon structure in appearance. According to the research, PHC may contain polar functional groups such as aldehydes, ketones, acids and phenolic compounds, which can be involved in the formation

\* To whom all correspondence should be sent:  
E-mail: 412316788@163.com

of chemical bonds and can adsorb heavy metal ions [9]. In China, peanut shells are cheap and have a wide range of sources. In this paper, peanut shells are used as an adsorbent and therefore the mechanism of heavy metal ions in solution adsorption laws are discussed.

Peanut shells are an abundant inexpensive adsorbent and can be applied to govern heavy metal pollution after modifying its structural characteristics [10]. Up until now, many researchers [11, 12] have removed heavy metal ions from the wastewater using peanut shells as an adsorbent or using peanut shells as a raw material for activated carbon preparation [13], which had a great practical significance for recycling and application of such a large quantity of cheap agricultural and forestry waste in environmental pollution. However, these studies only focus on the effects of polluted water following the adsorption of heavy metals together with characteristics, such as the adsorption temperature, pH, amount of adsorbent and the initial ion concentration. However, these do not fully explore the best adsorption conditions of modified peanut shells. This paper mainly studied the optimum conditions of adsorption. In this paper, we modified peanut shells with 0.1 mol/L of hydrochloric acid and applied modified peanut shells to process the simulated industrial wastewater containing copper, lead and zinc ions, which provided a new thought as regards the utilization of peanut shells and the treatment for heavy metal ions.

## MATERIALS AND METHODS

### *Preparation of solutions and samples*

The peanut shells used in this study were derived from fresh peanuts. All the chemical reagents used were analytical grade. A stock solution with 100 mg/L  $\text{Pb}^{2+}$ ,  $\text{Cu}^{2+}$ ,  $\text{Zn}^{2+}$  respectively was prepared by deionized water,  $\text{Pb}(\text{NO}_3)_2$ ,  $\text{Cu}(\text{NO}_3)_2$  and  $\text{Zn}(\text{NO}_3)_2$ . Working solutions were obtained by appropriate dilution. Peanut shells were smashed and screened through a mesh of size 80. Then the samples were soaked with deionized water for 24 hours and the fine suspended material was removed as well as the soluble matter. The samples were stored in a desiccator after being dried at 80°C the modified peanut shells were prepared as follows: 200 g of peanut shells were placed in a 2.5 L beaker, 500mL 1 mol/L hydrochloric acid was added in the beaker. After being stirred for 1 h, the liquid portion was removed by filtration. The solid fraction was washed with deionized water until neutral and dried at 80°C. Infrared spectrum samples were prepared by

potassium bromide tableting. Unmodified or modified peanut shells powder and potassium bromide powder were thoroughly ground. The mixed powder was made into a transparent sheet with about 1 mm thickness by a pneumatic tableting machine. Then the samples were analyzed by a Fourier transform infrared spectrometer at 400 - 4000  $\text{cm}^{-1}$ .

### *Peanut shells adsorption of simulated industrial wastewater*

The ion mixed solution was made from 50 mg/L  $\text{Pb}^{2+}$ ,  $\text{Cu}^{2+}$ ,  $\text{Zn}^{2+}$ . 60 mL of ion mixed solution was added in an 100 mL Erlenmeyer flask, the pH of which was adjusted. The initial concentration of  $\text{Pb}^{2+}$ ,  $\text{Cu}^{2+}$ ,  $\text{Zn}^{2+}$  was measured by an atomic absorption spectrophotometer. Unmodified or modified peanut shells were placed in an Erlenmeyer flask and cultured in the constant temperature incubator shaker with an oscillation rate of 120 r/min at 32°C. Thereafter, 10 mL of solution in a centrifugal tube was centrifuged to remove the impurities in the solution. The concentration of  $\text{Pb}^{2+}$ ,  $\text{Cu}^{2+}$ ,  $\text{Zn}^{2+}$  after adsorption was measured by an atomic absorption spectrophotometer. The adsorption rate was used to determine the optimum adsorption conditions.

### *Single factor experiment and orthogonal test*

The adsorption rate is an evaluation index, four factors including the adsorption reaction duration (A), the initial ion concentration (B), dosage of the samples (C), pH value (D) were selected to be the testing factors of the adsorption efficiency of the peanut shells. According to the results of the single factor experiment, an orthogonal test with four-factors and three-levels was applied to optimize the adsorption condition of the peanut shells.

### *Kinetics experiments*

50 mL, 40 mg/L or a 50 mg/L mixed ion solution was added into a 100 mL Erlenmeyer flask with a pH adjusted to  $5.00 \pm 0.01$ . 0.50 g unmodified peanut shells powder was added in the solution. Then the solution was shaken for 10, 20, 30, 40, 60, 80 min, separately at 32°C. The concentration of  $\text{Pb}^{2+}$ ,  $\text{Cu}^{2+}$ ,  $\text{Zn}^{2+}$  were assayed and plotted after being filtered and centrifuged. Characterization of the dynamic mechanism of the data in the figure was analyzed using the following two models.

### *Lagergren apparent first-order kinetic model*

$$\ln(1-q/q_e) = -k_1 t \quad (1)$$

In which:  $q_t$ ,  $q_e$  (mg/g) are the  $\text{Cu}^{2+}$  adsorption at  $t$  (min) time,  $\text{Cu}^{2+}$  equilibrium adsorption. Respectively;  $k_1$  (g/(mg·min)) is the adsorption rate constant of first order which can be obtained by a plot using  $\ln(1 - q_t/q_e)$  and  $t$ .

Lagergren apparent second-order kinetic model

$$t/q_t = (1/k_2q_e^2) + (t/q_e) \quad (2)$$

In which:  $k_2$  (g/(mg·min)) is the adsorption rate constant of apparent second order which can be obtained by a plot using  $t/q_t$  and  $t$ ;  $k_2q_e^2$  (mg/(g·min)) is the initial adsorption rate.

## RESULTS AND DISCUSSION

### Effect of pH on the adsorption

As shown in Fig. 1, the metal ions adsorption rate of peanut shells increased gradually with the increase of pH at a range of 3-5. Unmodified peanut shells reached a maximum value when the pH was 5 and reduced when the pH was 7. However, modified peanut shells continued to increase gradually under given alkaline conditions. Thus, the optimum pH of unmodified peanut shells was acidic and the optimum pH of modified peanut shells was alkaline. Moreover, the maximum adsorption rate of modified peanut shells was higher than that of unmodified peanut shells. The maximum adsorption rates of unmodified peanut shells for  $\text{Pb}^{2+}$ ,  $\text{Cu}^{2+}$ ,  $\text{Zn}^{2+}$  were 93.3%, 77.6%, 71.5%, respectively, while the adsorption maximum of modified peanut shells for  $\text{Pb}^{2+}$ ,  $\text{Cu}^{2+}$ ,  $\text{Zn}^{2+}$  were 96.2%, 87.0%, 74.0%, respectively. Generally, the absorption efficiency of modified peanut shells was better than the unmodified one and the adsorption of peanut shells on  $\text{Pb}^{2+}$  was the most obvious.

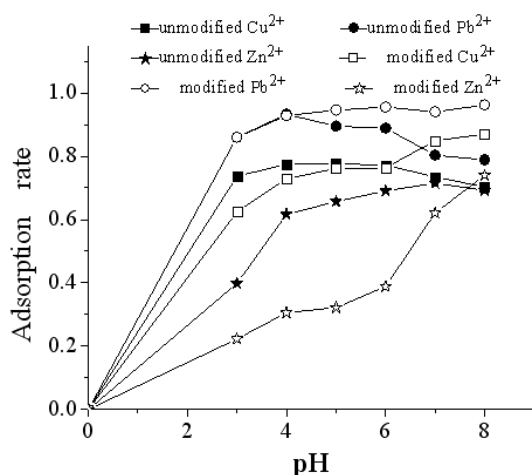


Fig. 1. The influence of pH on adsorption

### Effect of the adsorption reaction duration on adsorption

Fig. 2 showed that the adsorption rate of peanut shells for metal ions increased with time and reached a balance after a reaction duration of 50 minutes. The adsorption rate reached 88% of the maximum adsorption rate after 15 min, which showed that the adsorption by peanut shells of metal ions was terminated in a short space of time. The adsorption of modified and unmodified peanut shells and metal ions at the interface between the liquid and solid was mainly physical adsorption. In theory, the longer the reaction duration the more the adsorbent dosage, the more thorough the adsorption removal is. The maximum adsorption rates of unmodified peanut shells for  $\text{Pb}^{2+}$ ,  $\text{Cu}^{2+}$ ,  $\text{Zn}^{2+}$  were 94.3%, 69.3%, 16.7%, respectively, while the adsorption maximums of modified peanut shells for  $\text{Pb}^{2+}$ ,  $\text{Cu}^{2+}$ ,  $\text{Zn}^{2+}$  were 68.9%, 48.9%, 16.4%, respectively. Overall, the absorption efficiency of unmodified peanut shells was better than the modified one and the adsorption of peanut shells on  $\text{Pb}^{2+}$  was the most obvious.

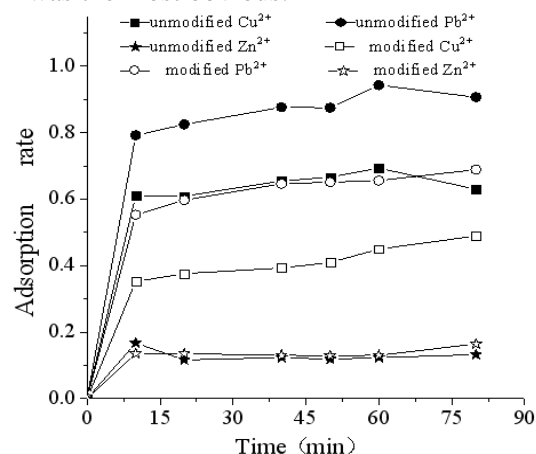


Fig. 2 The influence of reaction duration on adsorption

### Effect of the initial ion concentration on adsorption

The absorption rate increased with the initial ion concentration and reached a maximum with the initial ion concentration being 30 mg/L and then reduced gradually. When the initial ion concentration in the solution was much higher, the adsorption sites of the peanut shells for metal ions on the surface were saturated so the adsorption rate gradually decreased. In Fig. 3, when the concentration of metal ions was low, the adsorption rate was relatively high, while the adsorption rate became lower with the higher metal ion concentration, which indicated that the peanut shells were suitable for the adsorption of low metal ion concentrations. The maximum adsorption rates of unmodified peanut shells for  $\text{Pb}^{2+}$ ,  $\text{Cu}^{2+}$ ,  $\text{Zn}^{2+}$

were 90.1%, 69.9%, 69.1%, respectively, while the adsorption maximums of modified peanut shells for  $Pb^{2+}$ ,  $Cu^{2+}$ ,  $Zn^{2+}$  were 85.9%, 77.6%, 78.1%. In total, the absorption efficiency of modified peanut shells was better than the unmodified one and the adsorption of peanut shells on  $Pb^{2+}$  was the most obvious.

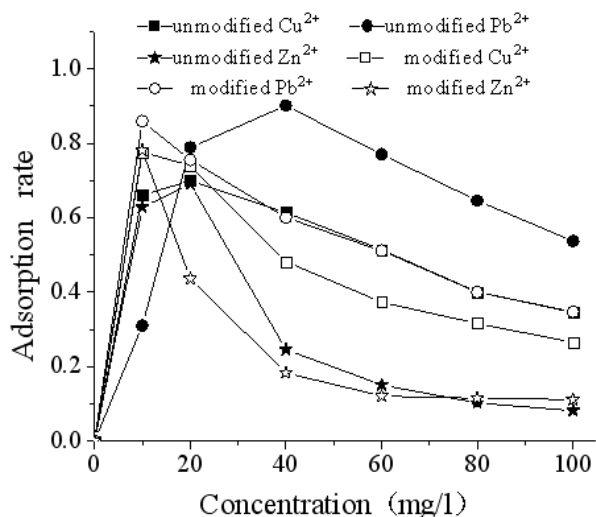


Fig. 3 The effect of the initial concentration on adsorption

#### Effect of the pH value on the adsorption

As manifested in Fig. 4, the metal adsorption range of unmodified peanut shells were 0.2-0.6g and the adsorption rate increased with the adsorbent dosage.

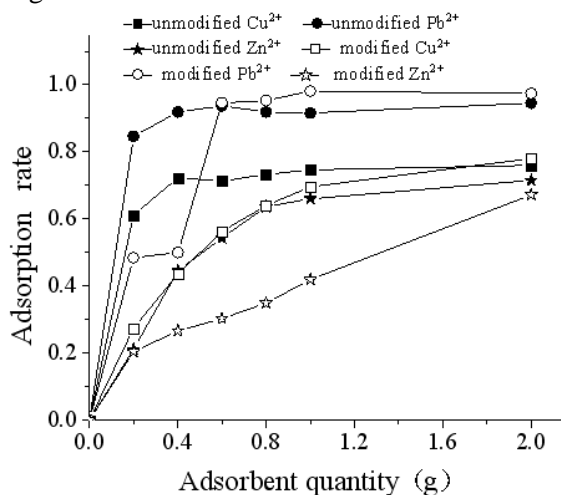


Fig. 4 The effect of the adsorbent dosage on adsorption

The maximum adsorption rates of unmodified peanut shells for  $Pb^{2+}$ ,  $Cu^{2+}$ ,  $Zn^{2+}$  were 94.5%, 76.0%, 71.5%, respectively. The adsorption rate of modified peanut shells was also increased with the adsorbent dosage and reached the maximum when the dosage of samples was 2.0 g. The adsorption maximums of modified peanut shells for  $Pb^{2+}$ ,  $Cu^{2+}$ ,

$Zn^{2+}$  were 98.1%, 78.0%, 67.2%. Increasing the amount of peanut shells increases the surface area of the peanut shells in the metal solution and the effective adsorption sites, therefore the adsorption rate increases. But when the adsorption rate of the heavy metal ions reach an equilibrium, the increasing adsorbent dosage would reduce the adsorption capacity of the per unit mass adsorbent which means non-saturation of the adsorption capacity and results in a waste of adsorbent. In total, the absorption efficiency of the modified peanut shells was better than that of the ones unmodified and the adsorption efficiency on  $Pb^{2+}$  was more obvious.

#### Analysis of the orthogonal results

##### Orthogonal results assay of the unmodified peanut shells

The most obvious factor was the initial ion concentration for  $Cu^{2+}$  and  $Zn^{2+}$  while the most significant factor was the pH value of  $Pb^{2+}$  by the Anova and range analysis in Table 1 and Table 2. Based on the K value, the best combinations of  $Cu^{2+}$ ,  $Zn^{2+}$  and  $Pb^{2+}$  were  $A_2B_3C_1D_1$ ,  $A_3B_3C_3D_2$  and  $A_1B_2C_1D_3$  respectively, which meant that the optimum condition for  $Cu^{2+}$  was the reaction duration for 60min, the initial ion concentration being 40 mg/L, the 0.5 g of adsorbent at pH 5; the optimum condition for  $Pb^{2+}$  lasted for 80min, the initial ion concentration being 40 mg/L, the 0.7 g of adsorbent at pH 6; the optimum condition for  $Zn^{2+}$  lasted for 40min, the initial ion concentration being 30 mg/L, the 0.5 g of adsorbent at pH 7.

##### Orthogonal results analysis of modified peanut shells

According to the Anova and range analysis in Table 3 and Table 4, the most obvious factor was the adsorption reaction duration for  $Pb^{2+}$  and  $Zn^{2+}$ , while the most significant factor was the initial ion concentration for  $Cu^{2+}$ . Based on the K value, the best combination of  $Cu^{2+}$ ,  $Zn^{2+}$  and  $Pb^{2+}$  were  $A_3B_3C_2D_1$ ,  $A_3B_3C_3D_3$  and  $A_1B_2C_3D_3$ , respectively, which, in detail, means that the optimum condition for  $Cu^{2+}$  was a reaction lasting for 80 min, the initial ion concentration being 30 mg/L, the 1.5 g adsorbent at pH 6; the optimum condition for  $Pb^{2+}$  was a reaction lasting for 80 min, the initial ion concentration was 30 mg/L, the 2.0 g adsorbent at pH 8; besides, the optimum condition for  $Zn^{2+}$  was a reaction lasting for 60 min, the initial ion concentration was 20 mg/L, the 2.0 g adsorbent at pH 8.

**Table 1.** Orthogonal experimental results of unmodified peanut shells.

Factors	Adsorption Rate								
	K1			K2			K3		
A	Cu <sup>2+</sup>	Pb <sup>2+</sup>	Zn <sup>2+</sup>	Cu <sup>2+</sup>	Pb <sup>2+</sup>	Zn <sup>2+</sup>	Cu <sup>2+</sup>	Pb <sup>2+</sup>	Zn <sup>2+</sup>
	0.700	0.966	0.709	0.711	0.965	0.695	0.704	0.969	0.691
B	Cu <sup>2+</sup>	Pb <sup>2+</sup>	Zn <sup>2+</sup>	Cu <sup>2+</sup>	Pb <sup>2+</sup>	Zn <sup>2+</sup>	Cu <sup>2+</sup>	Pb <sup>2+</sup>	Zn <sup>2+</sup>
	0.653	0.953	0.711	0.710	0.955	0.715	0.753	0.992	0.669
C	Cu <sup>2+</sup>	Pb <sup>2+</sup>	Zn <sup>2+</sup>	Cu <sup>2+</sup>	Pb <sup>2+</sup>	Zn <sup>2+</sup>	Cu <sup>2+</sup>	Pb <sup>2+</sup>	Zn <sup>2+</sup>
	0.719	0.957	0.704	0.681	0.954	0.681	0.715	0.988	0.703
D	Cu <sup>2+</sup>	Pb <sup>2+</sup>	Zn <sup>2+</sup>	Cu <sup>2+</sup>	Pb <sup>2+</sup>	Zn <sup>2+</sup>	Cu <sup>2+</sup>	Pb <sup>2+</sup>	Zn <sup>2+</sup>
	0.733	0.981	0.689	0.708	0.983	0.698	0.675	0.935	0.708
Best Group	Cu <sup>2+</sup>			Pb <sup>2+</sup>			Zn <sup>2+</sup>		
	A <sub>2</sub> B <sub>3</sub> C <sub>1</sub> D <sub>1</sub>			A <sub>3</sub> B <sub>3</sub> C <sub>3</sub> D <sub>2</sub>			A <sub>1</sub> B <sub>2</sub> C <sub>1</sub> D <sub>3</sub>		

**Table 2.** Anova table of unmodified peanut shells.

Variance Source	Factors											
	A			B			C			D		
SS	Cu <sup>2+</sup>	Pb <sup>2+</sup>	Zn <sup>2+</sup>	Cu <sup>2+</sup>	Pb <sup>2+</sup>	Zn <sup>2+</sup>	Cu <sup>2+</sup>	Pb <sup>2+</sup>	Zn <sup>2+</sup>	Cu <sup>2+</sup>	Pb <sup>2+</sup>	Zn <sup>2+</sup>
	0.000	0.000	0.001	0.015	0.003	0.004	0.003	0.002	0.001	0.005	0.005	0.001
Df	Cu <sup>2+</sup>	Pb <sup>2+</sup>	Zn <sup>2+</sup>	Cu <sup>2+</sup>	Pb <sup>2+</sup>	Zn <sup>2+</sup>	Cu <sup>2+</sup>	Pb <sup>2+</sup>	Zn <sup>2+</sup>	Cu <sup>2+</sup>	Pb <sup>2+</sup>	Zn <sup>2+</sup>
	2	2	2	2	2	2	2	2	2	2	2	2
MS	Cu <sup>2+</sup>	Pb <sup>2+</sup>	Zn <sup>2+</sup>	Cu <sup>2+</sup>	Pb <sup>2+</sup>	Zn <sup>2+</sup>	Cu <sup>2+</sup>	Pb <sup>2+</sup>	Zn <sup>2+</sup>	Cu <sup>2+</sup>	Pb <sup>2+</sup>	Zn <sup>2+</sup>
	0.000	0.000	0.571	2.609	1.200	2.286	0.522	0.800	0.571	0.870	2.000	0.571
F-value	Cu <sup>2+</sup>	Pb <sup>2+</sup>	Zn <sup>2+</sup>	Cu <sup>2+</sup>	Pb <sup>2+</sup>	Zn <sup>2+</sup>	Cu <sup>2+</sup>	Pb <sup>2+</sup>	Zn <sup>2+</sup>	Cu <sup>2+</sup>	Pb <sup>2+</sup>	Zn <sup>2+</sup>
	4.460	4.460	4.460	4.460	4.460	4.460	4.460	4.460	4.460	4.460	4.460	4.460
Significance	Cu <sup>2+</sup>	Pb <sup>2+</sup>	Zn <sup>2+</sup>	Cu <sup>2+</sup>	Pb <sup>2+</sup>	Zn <sup>2+</sup>	Cu <sup>2+</sup>	Pb <sup>2+</sup>	Zn <sup>2+</sup>	Cu <sup>2+</sup>	Pb <sup>2+</sup>	Zn <sup>2+</sup>
	\	\	\	\	\	\	\	\	\	\	\	\
Note	Error: Cu <sup>2+</sup> : 0.02, 8; Pb <sup>2+</sup> & Zn <sup>2+</sup> : 0.01, 8; \—non-significance.											

**Table 3.** Orthogonal experiment results of modified peanut shells

Factors	Adsorption Rate								
	K1			K2			K3		
A	Cu <sup>2+</sup>	Pb <sup>2+</sup>	Zn <sup>2+</sup>	Cu <sup>2+</sup>	Pb <sup>2+</sup>	Zn <sup>2+</sup>	Cu <sup>2+</sup>	Pb <sup>2+</sup>	Zn <sup>2+</sup>
	0.602	0.595	0.731	0.646	0.847	0.702	0.651	0.906	0.655
B	Cu <sup>2+</sup>	Pb <sup>2+</sup>	Zn <sup>2+</sup>	Cu <sup>2+</sup>	Pb <sup>2+</sup>	Zn <sup>2+</sup>	Cu <sup>2+</sup>	Pb <sup>2+</sup>	Zn <sup>2+</sup>
	0.418	0.633	0.665	0.738	0.792	0.731	0.744	0.923	0.692
C	Cu <sup>2+</sup>	Pb <sup>2+</sup>	Zn <sup>2+</sup>	Cu <sup>2+</sup>	Pb <sup>2+</sup>	Zn <sup>2+</sup>	Cu <sup>2+</sup>	Pb <sup>2+</sup>	Zn <sup>2+</sup>
	0.599	0.783	0.704	0.659	0.769	0.675	0.642	0.873	0.708
D	Cu <sup>2+</sup>	Pb <sup>2+</sup>	Zn <sup>2+</sup>	Cu <sup>2+</sup>	Pb <sup>2+</sup>	Zn <sup>2+</sup>	Cu <sup>2+</sup>	Pb <sup>2+</sup>	Zn <sup>2+</sup>
	0.649	0.736	0.689	0.611	0.769	0.671	0.639	0.843	0.728
Best Group	Cu <sup>2+</sup>			Pb <sup>2+</sup>			Zn <sup>2+</sup>		
	A <sub>3</sub> B <sub>3</sub> C <sub>2</sub> D <sub>1</sub>			A <sub>3</sub> B <sub>3</sub> C <sub>3</sub> D <sub>3</sub>			A <sub>1</sub> B <sub>2</sub> C <sub>3</sub> D <sub>3</sub>		

**Table 4.** Anova table of modified peanut shells

Variance Source	Factors											
	A			B			C			D		
SS	Cu <sup>2+</sup>	Pb <sup>2+</sup>	Zn <sup>2+</sup>	Cu <sup>2+</sup>	Pb <sup>2+</sup>	Zn <sup>2+</sup>	Cu <sup>2+</sup>	Pb <sup>2+</sup>	Zn <sup>2+</sup>	Cu <sup>2+</sup>	Pb <sup>2+</sup>	Zn <sup>2+</sup>
	0.004	0.164	0.009	0.209	0.127	0.007	0.006	0.049	0.002	0.002	0.018	0.005
Df	Cu <sup>2+</sup>	Pb <sup>2+</sup>	Zn <sup>2+</sup>	Cu <sup>2+</sup>	Pb <sup>2+</sup>	Zn <sup>2+</sup>	Cu <sup>2+</sup>	Pb <sup>2+</sup>	Zn <sup>2+</sup>	Cu <sup>2+</sup>	Pb <sup>2+</sup>	Zn <sup>2+</sup>
	2	2	2	2	2	2	2	2	2	2	2	2
MS	Cu <sup>2+</sup>	Pb <sup>2+</sup>	Zn <sup>2+</sup>	Cu <sup>2+</sup>	Pb <sup>2+</sup>	Zn <sup>2+</sup>	Cu <sup>2+</sup>	Pb <sup>2+</sup>	Zn <sup>2+</sup>	Cu <sup>2+</sup>	Pb <sup>2+</sup>	Zn <sup>2+</sup>
	0.072	1.832	1.565	3.783	1.419	1.217	0.109	0.547	0.348	0.036	0.201	0.870
F-value	Cu <sup>2+</sup>	Pb <sup>2+</sup>	Zn <sup>2+</sup>	Cu <sup>2+</sup>	Pb <sup>2+</sup>	Zn <sup>2+</sup>	Cu <sup>2+</sup>	Pb <sup>2+</sup>	Zn <sup>2+</sup>	Cu <sup>2+</sup>	Pb <sup>2+</sup>	Zn <sup>2+</sup>
	4.460	4.460	4.460	4.460	4.460	4.460	4.460	4.460	4.460	4.460	4.460	4.460
Significance	Cu <sup>2+</sup>	Pb <sup>2+</sup>	Zn <sup>2+</sup>	Cu <sup>2+</sup>	Pb <sup>2+</sup>	Zn <sup>2+</sup>	Cu <sup>2+</sup>	Pb <sup>2+</sup>	Zn <sup>2+</sup>	Cu <sup>2+</sup>	Pb <sup>2+</sup>	Zn <sup>2+</sup>
Note	Error: Cu <sup>2+</sup> : 0.22, 8; Pb <sup>2+</sup> : 0.36, 8; Zn <sup>2+</sup> : 0.02, 8; \ —non-significance.											

**Table 5.** Reaction kinetics parameters of unmodified peanut shells

Adsorbent	Initial ion concentration	Apparent first order		Apparent second order	
		k1	r1	k2	r <sup>2</sup>
Unmodified peanut shells	Pb <sup>2+</sup> (40mg/L)	0.0257	0.3769	0.4277	0.9947
	Cu <sup>2+</sup> (40mg/L)	0.0397	0.6709	0.4630	0.9987
	Zn <sup>2+</sup> (40mg/L)	0.0319	0.2885	0.1145	0.9976
	Pb <sup>2+</sup> (50mg/L)	0.0527	0.7279	0.1304	0.9993
	Cu <sup>2+</sup> (50mg/L)	0.0524	0.3590	0.4402	0.9932
	Zn <sup>2+</sup> (50mg/L)	0.0234	0.2510	0.3375	0.9867

**Table 6.** Reaction kinetics parameters of modified peanut shells

Adsorbent	Initial ion concentration	Apparent first order		Apparent second order	
		k1	r1	k2	r <sup>2</sup>
Modified peanut shells	Pb <sup>2+</sup> (30mg/L)	0.0361	0.7412	0.1264	0.9707
	Cu <sup>2+</sup> (30mg/L)	0.0289	0.7508	0.0423	0.9715
	Zn <sup>2+</sup> (30mg/L)	0.0321	0.5385	0.1465	0.8934
	Pb <sup>2+</sup> (50mg/L)	0.0922	0.9178	0.0613	0.9961
	Cu <sup>2+</sup> (50mg/L)	0.0423	0.8610	0.1645	0.9863
	Zn <sup>2+</sup> (50mg/L)	0.0276	0.5499	0.1096	0.9615

*Dynamics analysis*

The process and dynamical behavior of adsorption of metal ions (Pb<sup>2+</sup>, Cu<sup>2+</sup>, Zn<sup>2+</sup>) by peanut shells was consistent with the Lagergren apparent second-order kinetic model as shown in Table 5 and Table 6, which indicated that the physical adsorption and the biological adsorption of heavy metals happened simultaneously which coincided with many previous reports. Under the optimum condition, the average absolute deviation rate of the equilibrium adsorption amount from the Lagergren apparent first-order kinetic model (q<sub>e, cal</sub>) and experiments (q<sub>e, exp</sub>) was relatively large, while the one from Lagergren apparent second-order kinetic model (q<sub>e, cal</sub>) and experiments (q<sub>e, exp</sub>) was much smaller. Therefore, the apparent second-order adsorption dynamics model better

describes the adsorption process under the optimum condition. Moreover, the apparent second-order adsorption dynamics model was more suitable for the system when reached equilibrium after a much longer time with q<sub>e</sub> unknown.

*Infrared spectrum (IR) analysis*

As stated in Fig. 5 and Fig. 6, the infrared absorption spectra of unmodified and modified peanut shells is similar, which indicates that the hydrochloric acid modification does not have a great influence on the chemical properties of peanut shells.

The absorption peak of modified peanut shells broadened at 3420 cm<sup>-1</sup> and 1050 cm<sup>-1</sup> and the absorption intensity increased at 1640 cm<sup>-1</sup> and 1510 cm<sup>-1</sup>.

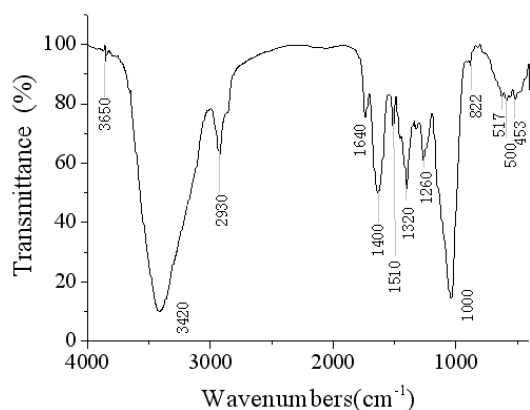


Fig. 5. Infrared spectrum of unmodified peanut shells

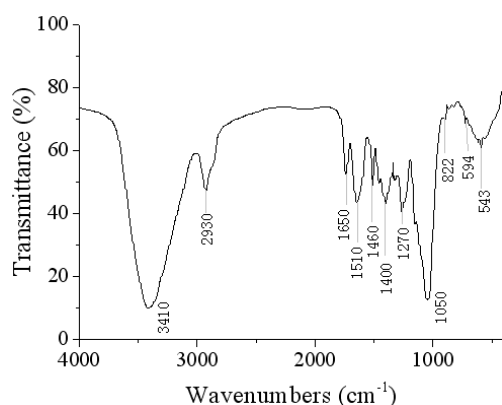


Fig. 6. Infrared spectrum of modified peanut shells.

A strong absorption peak at  $3420\text{ cm}^{-1}$  was stretching the vibration absorption peak of unsaturated hydrocarbon together with a small amount of the amino group; the peak at  $2930\text{ cm}^{-1}$  was an asymmetric stretching vibration of methylene; the peak at  $1640\text{ cm}^{-1}$  was a stretching vibration absorption peak of carbonyl; the peak at  $1510\text{ cm}^{-1}$  was likely to be an anti-symmetric stretching vibration absorption peak of the ester group from carboxylate; the peak at  $1270\text{ cm}^{-1}$  was a plane vibration absorption peak of hydroxy from cellulose; the peak at  $1050\text{ cm}^{-1}$  was a vibration absorption peak of polysaccharide backbone, which is mainly caused by stretching the vibration of C-OH from sugars or P-O-C.

## CONCLUSION

Peanut shells have the ability to adsorb  $\text{Pb}^{2+}$ ,  $\text{Cu}^{2+}$  and  $\text{Zn}^{2+}$  ions which could be influenced by factors such as the adsorption reaction duration, the initial ion concentration, dosage of the samples and the pH value. The adsorption rate grew with the increase of the pH value, the reaction duration and the adsorbent dosage, while the adsorption rate decreased with the initial rise in ion concentration. The study indicated that the adsorption of metal ions by peanut shells is completed within a short time. The effect of the recommended factors on the

adsorption was not obvious and the dynamical behavior of unmodified and modified peanut shells was more suitable for the Lagergren second-order kinetic model. The maximum adsorption rates of unmodified peanut shells for  $\text{Pb}^{2+}$ ,  $\text{Cu}^{2+}$ ,  $\text{Zn}^{2+}$  were 99.8%, 77.6%, 72.3%, respectively, while the maximum adsorption rates of modified peanut shells for  $\text{Pb}^{2+}$ ,  $\text{Cu}^{2+}$ ,  $\text{Zn}^{2+}$  were 97.6%, 80.3%, 77.1%, respectively. In a word, the absorption efficiency of modified peanut shells was higher than that of unmodified shells. Meanwhile, the adsorption efficiency of modified peanut shells was increased and further optimized.

So far, enormous progress has been made in the study of the adsorption of heavy metal ions. The experiments showed that the adsorption by agricultural and forestry waste is an effective method for removing heavy metals from wastewater, but its industrial introduction was slow and the study and development of the adsorption carriers need more hard work. There were various factors affecting the adsorption efficiency which should be further discussed, such as the modification methods and characteristics of the absorbing materials, desorption conditions of the adsorption materials and the recycling of heavy metal ions together with the regeneration and repeated utilization of the adsorbent. The influence of the coexisting cations on the adsorption process should be taken into consideration if the solution is a mixture of metals. In order to put adsorption of heavy metals into applications more efficiently, we should focus on the adsorption mechanism, the regeneration of biological adsorbent, reuse of industrial sewage, and establishment of a better adsorption technical process in the next stage.

**Acknowledgments:** This research was supported by the Special Scientific Research Fund of the Agricultural Public Welfare Profession of China (No. 201203042, 201403048-8), Science and Technology Innovation Projects of CAAS (No. CAAS-ASTIP-2014-LIHPS-08), Chinese National Natural Science Foundation (No. 31460032), Natural Science Foundation of Gansu Province (No. 1212RJYA008, 1308RJZA287), and the Foundation of Excellent Young Teachers of LUT (No. 10-061406).

## REFERENCES

1. C.S. Zhu, L.P. Wang, W.B. Chen, *Journal of Hazardous Materials*, **168**(2-3), 739 (2009).
2. C.X. Wu, Q.H. Wu, C. Wang, Z. Wang, *Chinese Chemical Letters*, **22**, 473 (2011).

3. A. Schutz, M. Olsson, A. Jensen, L. Gerhardsson, J. Borjesson, S. Mattsson, S. Skerfving, *Int Arch Occup Environ Health*, **78**, 35 (2005).
4. M. Sallmén, M.L. Lindbohm, Anttila A, Taskinen H, Hemminki K, *Epidemiology*, **11**(2), 141 (2000).
5. Y.H. Huang, C.L. Hsueh, H.P. Cheng, L.C. Su, C.Y. Cheng, *Journal of Hazardous Materials*, **144**(1-2), 406 (2007).
6. S. Dhiraj, M. Garima, M.P. Kaur, *Bioresource Technology*, **99**(14), 6017 (2008)
7. W.S.W. Ngah, M.A. Hanafiah, *Bioresource Technology*, **99**(10), 3935 (2008).
8. A.W. Krowiak, R.G. Szafran, S. Modelski, *Desalination*, **265**, 126 (2011).
9. S. Ricordel, S. Taha, I. Cisse, G. Dorange, *Separation and Purification Technology*, **24**(3), 389 (2001).
10. S.H. Zhao, Z.L. Chen, T.P. Zhang, W.B. Pan, X.C. Peng, R. Che, Y.J. Ou, G.J. Lei, D. Zhou, *Huan Jing Ke Xue*, **35**(4), 1548 (2014).
11. P.D. Johnson, M.A. Watson, J. Brown, I.A. Jefcoat, *Waste Management*, **22**(5), 471 (2002).
12. Q. Li, J.P. Zhai, W.Y. Zhang, M.M. Wang, J. Zhou, *Journal of Hazardous Materials*, **141**(1), 163 (2007).
13. S.B. Deng, B.Y. Hu, T. Chen, B. Wang, J. Huang, Y.J. Wang, G. Yu, *Adsorption*, **21**, 125 (2015).

## МОДИФИЦИРАНЕ НА ШЛЮПКИ ОТ ФЪСТЪЦИ И ТЯХНОТО ПРИЛОЖЕНИЕ ЗА АДСОРБЦИЯ НА ТЕЖКИ МЕТАЛИ

З. Янг<sup>1</sup>, И.Г. Уанг<sup>1,3,4</sup>, И.Дж. Джинг<sup>3,4</sup>, К.У. Уей<sup>3,4</sup>, Ф.Ф. Ленг<sup>3,4</sup>, Х. Ма<sup>3,4</sup>, И.Л. Уанг<sup>3,4</sup>, Дж. Кс. Чен<sup>1,2</sup>

<sup>1</sup>Училище по енергия и енергетика, Ланджоу университет по технологии, Ланджоу 730050, Китай

<sup>2</sup>Училище по нефтохимическо инженерство, Ланджоу Университет по технологии, Ланджоу 730050, Китай

<sup>3</sup>Училище по инженерство и науки за живота, Технологичен университет Ланджоу, Ланджоу 730050, Китай

<sup>4</sup>Стопански институт за фармация в Ланджоу, Китайска академия за селскостопански науки, Ланджоу 730050, Китай

Постъпила на 13 юни, 2016 г.; приета на 26 юли, 2016 г.

(Резюме)

Шлюпките от фъстъци са пробен материал за адсорбция. Изследвана е способността им да адсорбират тежки метали ( $Pb^{2+}$ ,  $Cu^{2+}$  и  $Zn^{2+}$ ) в зависимост от различни фактори (рН, времетраене на пиролизата, начална концентрация, доза). Резултатите показват, че адсорбцията на тежките метали расте с повишаването на рН. Беше установено, че адсорбцията на йоните на тежки метали върху не-модифицирани шлюпки протича добре в кисела среда, докато при модифицираните това е в алкална среда. Степента на адсорбция достига 88% от максималната след 15 минути с тенденция към равновесие след 50 мин. Степента на адсорбция расте с нарастване на концентрацията на металните йони, като максимумът се достига при 30 mg/L, а след това тя намалява.

Динамичното отнасяне както на модифицираните, така и на не-модифицираните шлюпки добре се описват от модела на Lagergren за химична кинетика на реакция от 2-ри порядък. Адсорбционният ефект на модифицираните шлюпки е много по-добър от не-модифицираните.

## Generalized atom-bond connectivity analysis of several chemical molecular graphs

W. Gao<sup>1\*</sup>, W. F. Wang<sup>2</sup>, M. K. Jamil<sup>3</sup>, R. Farooq<sup>4</sup>, M. R. Farahani<sup>5</sup>

<sup>1</sup> School of Information Science and Technology, Yunnan Normal University, Kunming 650500, China

<sup>2</sup> Department of Mathematics, Zhejiang Normal University, Jinhua 321004, China

<sup>3</sup> Department of Mathematics, Riphah Institute of Computing and Applied Sciences, Riphah International University, 14 Ali Road, Lahore, Pakistan

<sup>4</sup> School of Natural Sciences, National University of Sciences and Technology, H-12 Islamabad, Pakistan

<sup>5</sup> Department of Applied Mathematics of Iran University of Science and Technology, Narmak, Tehran 16844, Iran

Received June 15, 2016; Accepted July 10, 2015

Lots of drug tests show strong inner relationships between the bio-medical and pharmacological characteristics of the drugs and their molecular structures. Due to the effectiveness for pharmaceutical and medical scientists of their ability to grasp the biological and chemical characteristics of new drugs, the generalized atom-bond connectivity index was defined to analyze the drug molecular structures. The analysis should find widespread application prospects in developing countries, especially in poor places without the adequate financial ability and affordability of much needed chemical reagents and equipment. In this paper, based on the drug molecular structure analysis and driving edge technology, we propose the generalized atom-bond connectivity index of several popular chemical structures which is quite common in drug molecular graphs.

**Keywords** Computational chemical; Generalized atom-bond connectivity index; dendrimer stars; bridge graph; benzenoid series

### INTRODUCTION

A wide range of new drugs emerge each year with the rapid development of the manufacture of medicines. Therefore, lots of work is needed to determine the pharmacological, chemical and biological characteristics of these new drugs. The relevant reagent equipment and lab assistants are in demand in order to test the performance and side effects of these new drugs. However, in some poor areas (such as the countries in South America, Africa and Southeast Asia), they are not rich enough to afford the reagents and equipment necessary to assess the biochemical properties. Luckily, we can refer to the contributions of relevant previous studies, for example, the chemical and pharmacodynamics characteristics of the drugs and their molecular structures as these are closely linked. Once the indicators of these drug molecular structures are calculated in view of defining their topological indices, these can be used to understand their medical properties and help to repair and make up for all the defects of the medicine following the chemical experiments. From this point of view, we can appreciate the effectiveness of the methods on the topological index of computation especially for developing countries, where the available biological and medical infor-

mation about new drugs may be easily obtained without the need to carry out chemical experiments and purchase expensive hardware.

Traditionally, we look upon the structure of a drug as an undirected graph in the mathematical model of a given medicine. Each vertex represents an atom in the graph and the chemical bond between these atoms is represented by each edge. We consider  $G$  as a simple graph corresponding to a drug structure with an atom (vertex) set as  $V(G)$  and a chemical bond (edge) set as  $E(G)$ . A topological index defined on the molecule structure  $G$  can be regarded as a real-valued function  $f: G \rightarrow R^+$  which maps each drug molecular structure to certain real numbers. Decades ago, scientists introduced significant indices, including the Wiener index, the PI index, the Zagreb index and the eccentric index, to measure the characters of the drug molecules. Some reports help to determine these topological indices of special molecular graphs in chemical, nanomaterials and pharmaceutical engineering (See Yan et al. [1], Gao et al. [2-3], Gao and Farahani [4-5], Gao and Shi [6], and Gao and Wang [7-10] for more detail). The referred notations and terminologies without clear explanations can be found in Bondy and Murty [11].

Furtula et al. [12] defined the generalized version of the atom-bond connectivity index which was defined as:

\* To whom all correspondence should be sent:

E-mail: gaowei@ynnu.edu.cn

$$ABC_{\lambda}(G) = \sum_{uv \in E(G)} \left( \frac{d(u) + d(v) - 2}{d(u)d(v)} \right)^{-\lambda},$$

where  $\lambda < 0$ . Clearly, taking  $\lambda = -\frac{1}{2}$ , it becomes

the atom-bond connectivity index defined by Estrada et al. [13]. Also, Furtula et al. [12] introduced the augmented Zagreb index which was denoted as:

$$AZI(G) = \sum_{uv \in E(G)} \left( \frac{d(u)d(v)}{d(u) + d(v) - 2} \right)^3.$$

Obviously, the augmented Zagreb index is a special case of the generalized atom-bond connectivity index when  $\lambda=3$ .

Despite the contributions to the distance-based indices and degree-based molecular structures, the researches of the generalized atom-bond connectivity index for certain special drug structures still await further studies. As a consequence, the research on the generalized atom-bond connectivity index of the drug molecular structure from a mathematical point of view are becoming more and more heated with the years with more and more academic and industrial interest drawn from a variety of fields.

Respectively, we designate  $\delta(G)$  and  $\Delta(G)$  to be the minimum and maximum degrees of  $G$ . The edge set  $E(G)$  can be categorized into different parts: for any  $i$  and  $j$ ,  $\delta(G) \leq i, j \leq \Delta(G)$ , let  $E_{ij} = \{e=uv \in E(G) \mid d(v)=i, d(u)=j\}$  and  $n_{ij} = |E_{ij}|$ .

In this paper, we obtain the generalized atom-bond connectivity index of several important chemical structures with a high frequency in drug structures.

### MAIN RESULTS

#### The generalized atom-bond connectivity index of graphene $G(m, n)$

Graphene, a two-dimensional material, is a planar sheet of carbon atoms. It is usually densely packed in a honeycomb crystal lattice and also the main element of certain carbon allotropes including charcoal, fullerenes and graphite, please refer to Figure 1.

**Theorem 1.** Let  $G(m, n)$  be a graphene sheet with  $n$  rows and  $m$  columns. We obtain:

$$ABC_{\lambda}(G(m, n)) =$$

$$\begin{cases} (4m+3n)\left(\frac{1}{2}\right)^{-\lambda} + \left\lfloor \frac{n}{2} \right\rfloor (5m+1) + \left\lfloor \frac{n}{2} \right\rfloor (m+3) \left(\frac{4}{9}\right)^{-\lambda}, & n \equiv 1(\text{mod } 2) \\ (4m+3n)\left(\frac{1}{2}\right)^{-\lambda} + \left\lfloor \frac{n}{2} \right\rfloor (5m+1) + \left\lfloor \frac{n}{2} \right\rfloor (m+3) + 2m-1 \left(\frac{4}{9}\right)^{-\lambda}, & n \equiv 0(\text{mod } 2) \end{cases}$$

**Proof.** Based on the structure analysis, we obtain:

$$\begin{aligned} |E(G(m, n))| &= \\ \begin{cases} \left\lfloor \frac{n}{2} \right\rfloor (5m+1) + \left\lfloor \frac{n}{2} \right\rfloor (m+3), & n \equiv 1(\text{mod } 2) \\ \left\lfloor \frac{n}{2} \right\rfloor (5m+1) + \left\lfloor \frac{n}{2} \right\rfloor (m+3) + 2m-1, & n \equiv 0(\text{mod } 2) \end{cases} \end{aligned}$$

After further calculation, we get  $n_{22} = n + 4$ ,  $n_{23} = 4m + 2n - 4$ , and

$$n_{33} = |E(G(m, n))| - 4m - 3n.$$

As a result, according to the definition of the generalized atom-bond connectivity index, we obtain the expected result.

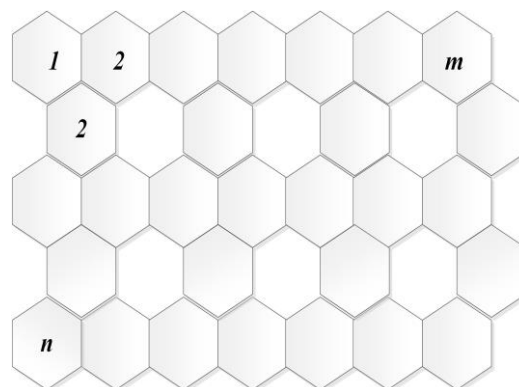


**Fig. 1.** 2-Dimensional graph of a graphene sheet

#### Generalized atom-bond connectivity index of three family of dendrimer stars

In this section, three famous infinite classes  $NS_1[n]$ ,  $NS_2[n]$  and  $NS_3[n]$  of dendrimer stars are defined and they are common in the drug structures.

**Theorem 2.** Let  $n$  be the number of steps of growth in this type of dendrimer stars. We indicate

$$\begin{aligned} ABC_{\lambda}(NS_1[n]) &= (27 \cdot 2^n - 9) \left(\frac{1}{2}\right)^{-\lambda} \\ &\quad + \left(\frac{2}{3}\right)^{-\lambda} + 3 \left(\frac{5}{12}\right)^{-\lambda}, \\ ABC_{\lambda}(NS_2[n]) &= (36 \cdot 2^n - 6) \left(\frac{1}{2}\right)^{-\lambda} + \left(\frac{4}{9}\right)^{-\lambda}, \\ ABC_{\lambda}(NS_3[n]) &= \\ &= (50 \cdot 2^n - 13) \left(\frac{1}{2}\right)^{-\lambda} + 2^{n+1} \left(\frac{2}{3}\right)^{-\lambda} + 6 \cdot 2^n \left(\frac{4}{9}\right)^{-\lambda}. \end{aligned}$$

**Proof.** After the observation to the structures

of these three dendrimer stars, we present its edge dividing below:

- for  $NS_1[n]$  :  $n_{23} = 18 \cdot 2^n - 12$  ,  
 $n_{22} = 9 \cdot 2^n + 3$ ,  $n_{13} = 1$  and  $n_{34} = 3$ ;
- for  $NS_2[n]$  :  $n_{23} = 24 \cdot 2^n - 8$  ,  
 $n_{22} = 12 \cdot 2^n + 2$  and  $n_{33} = 1$ ;
- for  $NS_3[n]$  :  $n_{23} = 28 \cdot 2^n - 6$  ,  
 $n_{22} = 22 \cdot 2^n - 7$ ,  $n_{33} = 6 \cdot 2^n$  and  $n_{13} = 2^{n+1}$ .

Hence, with the reference to the definition of the generalized atom-bond connectivity index, we obtain the expected result.

*Generalized atom-bond connectivity index of polyomino chains of n-cycles and triangular benzenoid*

In the field of mathematics, a polyomino system, an edge-connected union of cells, is a finite 2-connected plane graph where each interior face (i.e. cell) is encircled by a  $C_4$ . More details can be found in Klarner [14] and Ghorbani and Ghazi [15]. For instance, the polyomino chains of 8-cycles can be represented in Figure 2.

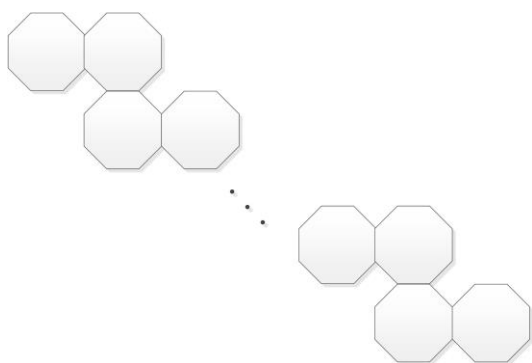


Fig. 2. The zig-zag chain of 8-cycles.

**Theorem 3.** Let  $G$  be a molecular graph as described above. We have

$$ABC_\lambda(G) = (20n + 4)\left(\frac{1}{2}\right)^{-\lambda} + (8n - 3)\left(\frac{4}{9}\right)^{-\lambda}.$$

**Proof.** Based on the structure analysis, we infer  $n_{22} = 12n + 4$ ,  $n_{23} = 8n$ , and  $n_{33} = 8n - 3$ .

Therefore, considering the definition of the generalized atom-bond connectivity index, we get the expected result.

Next, the generalized atom-bond connectivity index of a triangular benzenoid molecular graph  $T(n)$  is computed and the structure is described in Figure 3.

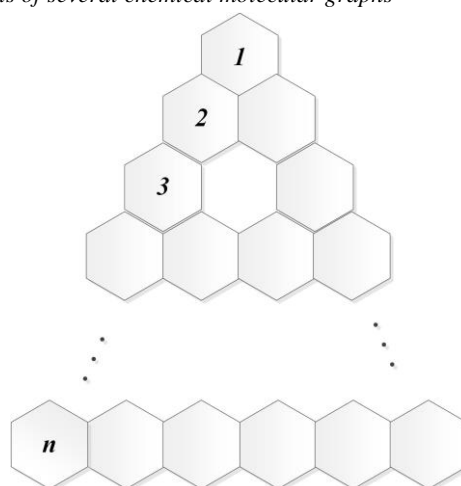


Fig. 3. Molecular graph of a triangular benzenoid  $T(n)$

**Theorem 4.** Let  $T(n)$  denote a triangular benzenoid. We get

$$ABC_\lambda(T(n)) = \frac{3n^2 - 3n + 12}{2} \left(\frac{1}{2}\right)^{-\lambda} + (6n - 6) \left(\frac{4}{9}\right)^{-\lambda}.$$

**Proof.** Based on the edge dividing technology, we get  $n_{22} = 6$ ,  $n_{23} = \frac{3n(n-1)}{2}$ , and  $n_{33} = 6(n-1)$ . Hence, concerning the definition of the generalized atom-bond connectivity index, we obtain the result.

*Generalized atom-bond connectivity index of bridge molecular structures*

Let's consider  $\{G_i\}_{i=1}^d$  a set of finite pairwise disjoint molecular graphs with  $v_i \in V(G_i)$ . The bridge molecular graph  $B(G_1, \dots, G_d) = B(G_1, \dots, G_d; v_1, \dots, v_d)$  of  $\{G_i\}_{i=1}^d$  regarding the vertices  $\{v_i\}_{i=1}^d$  is acquired from the molecular graphs  $G_1, \dots, G_d$  where the vertices  $v_i$  and  $v_{i+1}$  are linked through an edge for  $i=1, 2, \dots, d-1$ . As a result, this section helps to determine the formulas of some degree based indices for the infinite family of drug structures of the bridge molecular graph with  $G_1, \dots, G_d$  (see Figure 4). Then we define  $G_d(H, v) = B(H, \dots, H, v, \dots, v)$  for special situations of the bridge molecular graphs.

We analyze the bridge graphs as follows and the main parts of the graphs are path, cycle and complete molecular graph, respectively.

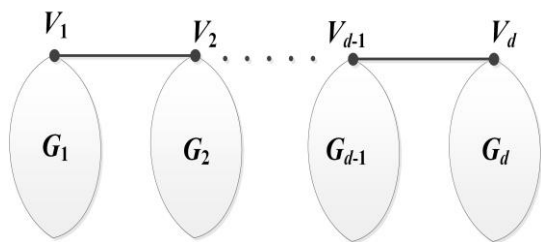


Fig. 4. The bridge molecular graph.

- Let  $P_n$  be the path with  $n$  vertices. We have  $dn$  vertices and  $dn-1$  edges for the bridge molecular graph  $G_d(P_n, v)$  (see Figure 5 for more details). Moreover, the edge set of the bridge graph  $G_d(P_n, v)$  can be categorized into four parts:  $n_{22} = d(n-3) + 2$ ,  $n_{23} = n_{12} = d$ , and  $n_{33} = d-3$ .

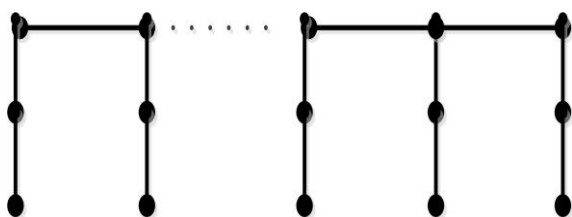


Fig. 5. The bridge molecular graph  $G_d(P_n, v)$ .

- Let  $C_n$  be the cycle with  $n$  vertices. We get  $dn$  vertices and  $dn+d-1$  edges for the bridge molecular graph  $G_d(C_n, v)$  (see Figure 6 for more details). Moreover, the edge set of the bridge molecular graph  $G_d(C_n, v)$  can be categorized into five parts:  $n_{22} = d(n-2)$ ,  $n_{23} = 4$ ,  $n_{24} = 2d-4$ ,  $n_{34} = 2$  and  $n_{44} = d-3$ .

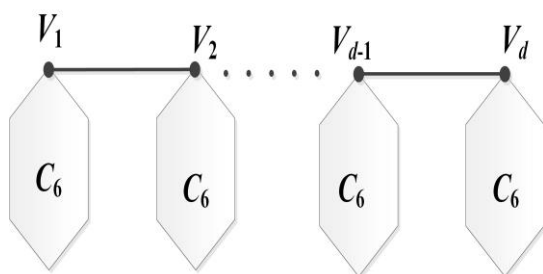


Fig. 6. The bridge molecular graph  $G_d(C_n, v)$ .

- Let  $K_n$  be a complete molecular graph with  $n$  vertices. We get  $dn$  vertices and  $\frac{dn(n-1)}{2} + d-1$  edges for the bridge molecular graph  $G_d(K_n, v)$  (see Figure 7,  $G_d(K_3, v)$  as an example). Moreover, the edge set of the bridge

molecular graph  $G_d(K_n, v)$  can be categorized into five partitions:  $n_{55} = n_{5(n-1)} = d-2$ ,  $n_{45} = n_{4(n-1)} = 2$  and  $n_{(n-1)(n-1)} = \frac{d(n-1)(n-2)}{3}$ .

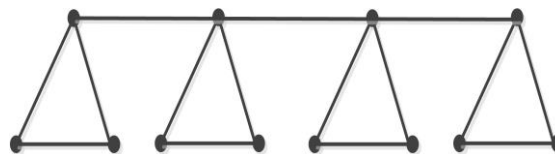


Fig. 7. The bridge molecular graph  $G_d(K_3, v)$ .

In view of the definition of the generalized atom-bond connectivity index, the main result of this section is obtained and represented below. The detailed proofs are omitted here.

**Theorem 5.**

$$\begin{aligned}
 ABC_\lambda(G_d(P_n, v)) &= d(n-1)\left(\frac{1}{2}\right)^{-\lambda} + (d-3)\left(\frac{4}{9}\right)^{-\lambda}, \\
 ABC_\lambda(G_d(C_n, v)) &= \\
 &dn\left(\frac{1}{2}\right)^{-\lambda} + (d-3)\left(\frac{3}{8}\right)^{-\lambda} + 2\left(\frac{5}{12}\right)^{-\lambda}, \\
 ABC_\lambda(G_d(K_n, v)) &= (d-2)\left(\frac{8}{25}\right)^{-\lambda} + 2\left(\frac{7}{20}\right)^{-\lambda} \\
 &+ 2\left(\frac{1}{4}\right)^{-\lambda} + (d-2)\left(\frac{n+2}{5(n-1)}\right)^{-\lambda} \\
 &+ \frac{d(n-1)(n-2)}{3} \left(\frac{2n-4}{(n-1)^2}\right)^{-\lambda}.
 \end{aligned}$$

*Generalized atom-bond connectivity index of the carbon tube networks*

In this section, we place emphasis on the  $m \times n$  quadrilateral section  $P_m^n$  with  $m \geq 2$  hexagons on the top and bottom sides and  $n \geq 2$  hexagons on the lateral sides cut from the regular hexagonal lattice  $L$ , refer to Figure 8 to observe the detailed chemical structure.

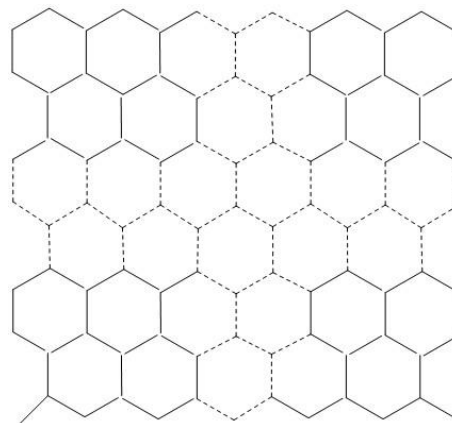


Fig. 8 Quadrilateral section  $P_m^n$  cuts from the regular hexagonal lattice.

The tube  $NA_m^n$  with  $2m(n+1)$  vertices and  $(3n+2)m$  edges is obtained by identifying two lateral sides of  $P_m^n$  by identifying the vertices  $u_i^j$  and  $u_m^j$  ( $j=0,1,\dots,n$ ).

Let  $n \in \mathbb{N}$  be even so that  $n, m \geq 2$ . The tube  $NC_m^n$  of order  $n(2m+1)$  with size  $n(3m + \frac{1}{2})$  can be obtained if we identify the top and bottom sides of the quadrilateral section  $P_m^n$  in a similarly way in which the vertices  $u_i^0$  and  $u_i^n$  for  $i=0,1,\dots,m$  and vertices  $v_i^0$  and  $v_i^n$  for  $i=0,1,\dots,m$  are identified. See Baca et al. [16] for more details.

**Theorem 6.**

$$ABC_\lambda(NA_m^n) = 4m(\frac{1}{2})^{-\lambda} + m(3n-2)(\frac{4}{9})^{-\lambda},$$

$$ABC_\lambda(NC_m^n) = 3n(\frac{1}{2})^{-\lambda} + n(3m - \frac{5}{2})(\frac{4}{9})^{-\lambda}.$$

**Proof.** For tube  $NA_m^n$ , we derive  $n_{23} = 4m$ , and  $n_{33} = m(3n-2)$ . For tube  $NC_m^n$ , we derive  $n_{22} = n$ ,  $n_{23} = 2n$ , and  $n_{33} = n(3m - \frac{5}{2})$ . Hence, in accordance with the definition of the for the generalized atom-bond connectivity index, we obtain the desired result.

*Generalized atom-bond connectivity index of dendrimer stars  $D_3[n]$*

In this section, an essential chemical structure  $D_3[n]$  is analyzed. It describes the  $n$ -th growth of star dendrimer for  $\forall n \in \mathbb{N} \cup \{0\}$ . Refer to Figure 9 for more details on the structure of this chemical molecular graph which is quite common in drug structures.

Based on the analysis in Farahani [17], we know that  $E(D_3[n])$  can be divided into four parts:  $n_{13} = 3 \cdot 2^n$ ,  $n_{22} = 6(2^{n+1} - 1)$ ,  $n_{23} = 12(2^{n+1} - 1)$ , and  $n_{33} = 9 \cdot 2^n - 6$ . Hence, we get the conclusion described below for these molecular structures.

**Theorem 7.**  $ABC_\lambda(D_3[n]) = 3 \cdot 2^n (\frac{2}{3})^{-\lambda} + 18(2^{n+1} - 1)(\frac{1}{2})^{-\lambda} + (9 \cdot 2^n - 6)(\frac{4}{9})^{-\lambda}.$

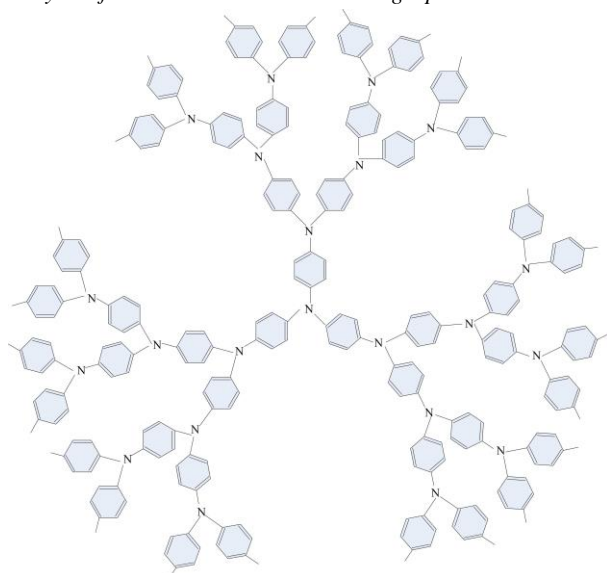


**Fig. 9.** The 2-Dimensional of the  $n$ -th growth of star dendrimer  $D_3[n]$ .

*Generalized atom-bond connectivity index of two classes of benzenoid series*

In this section, we plan to determine the generalized atom-bond connectivity index of two classes of benzenoid series.

First, the circumcoronene series of benzenoid  $H_k$  is concerned. While  $k=1, 2, 3$ , the structures are presented in Figure 10.

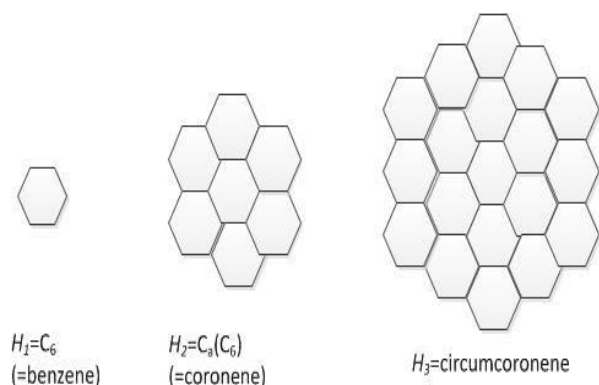


**Fig. 10.** The first, second and third molecular graphs  $H_1, H_2$  and  $H_3$  from the circumcoronene series of benzenoid.

Hence, the family of circumcoronene homologous series of benzenoid is made up of some copies of benzene  $C_6$  on circumference, for more details of this structure, please refer to Figure 11.

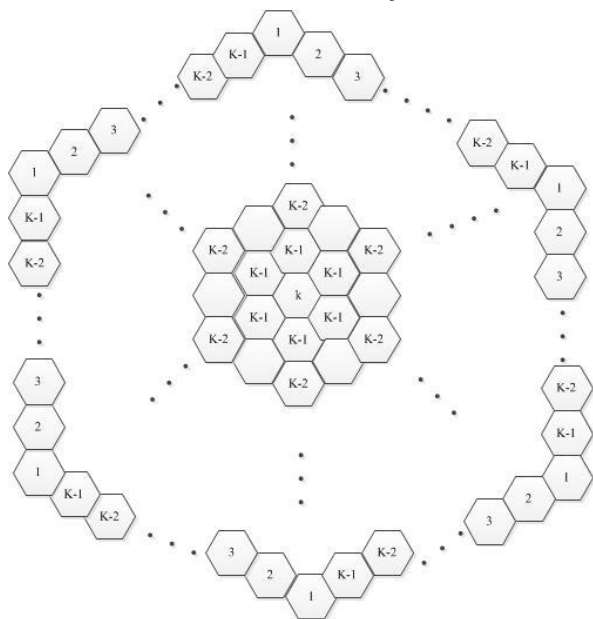


**Fig. 11.** The circumcoronene series of benzenoid  $H_k$  for  $k \geq 1$ .

**Theorem 8.**

$$ABC_\lambda(H_k) = (12k - 6)\left(\frac{1}{2}\right)^{-\lambda} + (9k^2 - 15k + 6)\left(\frac{4}{9}\right)^{-\lambda}.$$

**Proof.** Consider the circumcoronene series of benzenoid  $H_k$  for  $k \geq 1$ . It is not hard to check that  $|V(H_k)| = 6k^2$  and  $|E(H_k)| = 9k^2 - 3k$ . Moreover, we deduce  $n_{33} = 9k^2 - 15k + 6$ ,  $n_{23} = 12(k - 1)$ , and  $n_{22} = 6$ . Thus, regarding the definition of the generalized atom-bond connectivity index, we indicate the result.

Next, the capra-designed planar benzenoid series  $Ca_k(C_6)$  (the structure can be referred to Farahani and Vlad [18] for more details) is considered. By means of the intermediate results presented in Farahani and Vlad [18], we present the generalized atom-bond connectivity index of  $Ca_k(C_6)$  which is stated as follows.

**Theorem 9.**

$$ABC_\lambda(Ca_k(C_6)) = (5 \cdot 3^k + 3)\left(\frac{1}{2}\right)^{-\lambda} + (3 \cdot 7^k - 2 \cdot 3^k - 3)\left(\frac{4}{9}\right)^{-\lambda}.$$

**Proof.** Based on the analysis of the molecular structure of  $Ca_k(C_6)$ , we check that the edge set of  $Ca_k(C_6)$  can be divided into three partitions:  $n_{22} = 3^k + 3$ ,  $n_{23} = 4 \cdot 3^k$ , and  $n_{33} = 3 \cdot 7^k - 2 \cdot 3^k - 3$ . Thus, using the definition of the generalized atom-bond connectivity index, we infer the desired result.

OTHER CONCLUSIONS

Finally, we present the generalized atom-bond connectivity index for the chemical structures discussed in Gao et al. [2].

**Theorem 10.** Let  $SP[n]$  be the Dox-loaded micelle comprising a PEG-PAsp block copolymer with a chemically conjugated Dox. We obtain

$$ABC_\lambda(SP[n]) = (27n + 4)\left(\frac{1}{2}\right)^{-\lambda} + (9n + 1)\left(\frac{2}{3}\right)^{-\lambda} + n\left(\frac{3}{4}\right)^{-\lambda} + 16n\left(\frac{4}{9}\right)^{-\lambda} + n\left(\frac{5}{12}\right)^{-\lambda}.$$

**Theorem 11.** Let  $D_2[n]$  and  $D_4[n]$  be polyphenylene dendrimers with  $n$  stages. We have

$$ABC_\lambda(D_2[n]) = (104 \cdot 2^n - 92)\left(\frac{1}{2}\right)^{-\lambda} + (36 \cdot 2^n - 35)\left(\frac{4}{9}\right)^{-\lambda},$$

$$ABC_\lambda(D_4[n]) = (104 \cdot 2^n - 80)\left(\frac{1}{2}\right)^{-\lambda} + (36 \cdot 2^n - 36)\left(\frac{4}{9}\right)^{-\lambda} + 4\left(\frac{5}{12}\right)^{-\lambda}.$$

**Theorem 12.** Let  $S$  be a benzenoid system with  $n$  vertices,  $h$  hexagons and  $r$  inlets. We infer

$$ABC_\lambda(S) = (n - 2h + r + 2)\left(\frac{1}{2}\right)^{-\lambda} + (3h - r - 3)\left(\frac{4}{9}\right)^{-\lambda}.$$

**Theorem 13.** Let PH be phenylene. We deduce

$$ABC_\lambda(PH) = (2h + r + 4)\left(\frac{1}{2}\right)^{-\lambda} + (6h - r - 6)\left(\frac{4}{9}\right)^{-\lambda}.$$

**Theorem 14.** Let  $PAH_n$  be the Polycyclic Aromatic Hydrocarbons

$$ABC_\lambda(PAH_n) = 6n\left(\frac{2}{3}\right)^{-\lambda} + (9n^2 - 3n)\left(\frac{4}{9}\right)^{-\lambda}.$$

CONCLUSIONS

Accompanied by the contentiously emerging viruses, more and more unnamed diseases are found in the world at a high speed each year. This demands the development of more new drugs to treat them. The generalized atom-bond connectivity index was introduced to measure the medicinal properties of new drugs and it is quite welcome and popular in poor areas. In our paper, based on the detailed drug structure analysis and

edge dividing, we defined the generalized atom-bond connectivity index of certain molecular graphs which frequently appear in drug structures. As a result, the conclusions obtained in our paper show the promising prospects of these applications in pharmacy engineering.

**Acknowledgements:** We thank the reviewers for their constructive comments in improving the quality of this paper. This work was supported in part by NSFC (Nos.11401519 and 61262070).

#### REFERENCES

1. L. Yan, W. Gao, J. S. Li, *J. Comput. Theor. Nanosci.*, **12**(10), 3940 (2015).
2. W. Gao, M. R. Farahani, L. Shi, *Acta Med. Medit.*, **32**, 579 (2016).
3. W. Gao, M. K. Siddiqui, M. Imran, M. K. Jamil, M. R. Farahani, *Saudi Pharm. J.*, **24**(3), 258 (2016).
4. W. Gao, W. F. Wang, *Chaos Solitons Fract.*, **89**, 290 (2016).
5. W. Gao, M. R. Farahani, *Appl. Math. Nonlinear Sci.*, **1**(1), 94 (2016).
6. W. Gao, L. Shi, *IAENG Int. J. Appl. Math.*, **45**(2), 138 (2015).
7. W. Gao, W. F. Wang, *J. Diff. Eqs. Appl.*, ID:1197214, DOI:10.1080/10236198.2016.1197214
8. W. Gao, W. F. Wang, *J. Chem.*, Volume 2014, Article ID 906254, 8 pages, <http://dx.doi.org/10.1155/2014/906254>.
9. W. Gao, W. F. Wang, *Comput. Math. Meth. Med.*, Volume 2015, Article ID 418106, 10 pages, <http://dx.doi.org/10.1155/2015/418106>.
10. W. Gao, M. R. Farahani, *J. Nanotechnol.*, 2016, Article ID 3129561, 6 pages. <http://dx.doi.org/10.1155/2016/3129561>.
11. J. A. Bondy, U. S. R. Murty, *Graph Theory*, Springer, Berlin, 2008.
12. B. Furtula, A. Graovac, et al., *J. Math. Chem.*, **48**, 370 (2010).
13. E. Estrada, L. Torres, L. Rodriguez, I. Gutman, *Indian J. Chem.*, **37**(10), 849 (1998).
14. D. A. Klarner, Polyominoes. In: J. E. Goodman, J. O'Rourke, (eds.) *Handbook of Discrete and Computational Geometry*, 225-242. CRC Press, Boca Raton, 1997, Chapter 12.
15. M. Ghorbani, M. Ghazi, *Digest J. Nanomater. Biostruct.*, **5**(4), 1107 (2010).
16. M. Baca, J. Horvathova, et al., *Can. J. Chem.*, **93**(10), 1157 (2015).
17. M. R. Farahani, *Chem. Phys. Res. J.*, **6**(1), 27 (2013).
18. M. R. Farahani, M. P. Vlad, *Studia Ubb Chemia*, **LVIII**, 133 (2013).

## ОБОБЩЕН АНАЛИЗ НА СВЪРЗАНАТА АТОМНА ВРЪЗКА С НЯКОЛКО МОЛЕКУЛНИ ГРАФИ

У. Гао<sup>1\*</sup>, У.Ф. Уанг<sup>2</sup>, М.К. Джамил<sup>3</sup>, Р. Фарук<sup>4</sup>, М.Р. Фарахани<sup>5</sup>

<sup>1</sup> Училище по информатика и технология, Университет в Юнан, Кунминг 650500, Китай

<sup>2</sup> Департамент по математика, Университет в Жейджанг, Джинхуа 321004, Китай

<sup>3</sup> Департамент по математика, Институт по компютърни и приложни науки „Рифа“, Международен университет „Рифа“, Лахор, Пакистан

<sup>4</sup> Училище по естествени науки, Национален университет за наука и технологии, Исламабад, Пакистан

<sup>5</sup> Департамент по приложна математика, Ирански университет за наука и технологии, Нармак, Техеран 16844, Иран

Постъпила на 15 юни, 2015 г.; приета на 28 юли, 2015 г.

(Резюме)

Много тестове върху лекарства показват силна взаимовръзка между био-медицинските и фармакологичните им характеристики с тяхна молекулна структура. С цел да се подобри възможността на изследователите в медицината и фармацията да оценят характеристиките на нови лекарства е дефиниран обобщен индекс на свързаната атомна връзка за анализа на молекулната структура на лекарствата. В тази работа се предлага обобщен индекс на атомните връзки на няколко известни структури, които са твърде сходни с молекулните графи на лекарствата.

## Organic matter removal performance and mechanism in the constructed rapid infiltration system

W.L. Xu, Y.N. Yang\*, J.Wang, M. Tang, Y.Jian, X.J. Pei

*State Key Laboratory of Geohazard Prevention and Geoenvironment Protection, Chengdu University of Technology, Chengdu 610059, China*

Received June 15, 2015; Accepted July 26, 2015

The Constructed Rapid Infiltration System (CRI system) finds application in engineering, however, the pollutant removal mechanism is still not clear, which limits its further promotion and application. The experiment of processing wastewater by building a CRI simulation column while studying the pollutant removal mechanism and performance showed: after the CRI system operated steadily, under operation mode 1, that the CRI system had a higher removal rate of Chemical Oxygen Demand (COD) and COD had been removed effectively in a CRI filter tank 0-100cm segment, with a removal rate of up to 77.8%, under operation mode 2, the CRI system has a relatively low removal rate of COD, with an average removal rate of only 59.1%. Filtration and adsorption was the first step in the removal of organic pollutants by the CRI system; organic matter was accumulated during the flooding period and oxidized and decomposed during the drying period in the CRI system, degradation of aerobe mater played an important role in the removal of organic matter by the CRI system; alternation of the wetting and drying operation mode facilitated COD removal. The study results enrich our theoretical knowledge of the CRI system and promote the application of the CRI system.

**Key words:** Organic matter; Removal performance; Mechanism; Constructed rapid infiltration system

### INTRODUCTION

The Constructed Rapid Infiltration system (CRI system) employs a new biological wastewater treatment method, which is now becoming a hot spot of research and application in China. The CRI system finds application in engineering, however, its pollutant removal capacity and fundamentals are still insufficiently studied and limit further promotion. Therefore it is necessary to further study the migration, transformation and degradation rules and master the degradation mechanism of various pollutants in the CRI system [1-4]. This study will provide a theoretical basis to further promote and apply the CRI system by conducting the experimental processing of domestic wastewater by building a CRI simulation column in the laboratory as well as by analysis of the organic matter and removal performance.

### MATERIALS AND METHODS

#### *Building a CRI Simulation Column*

A CRI simulation column was built in the laboratory. The main part of the CRI simulation column reactor consists of an organic glass column, the column height is 200cm, the internal diameter is 21cm, the filtering material consists of 90% of

natural sand + 5% of sand marble + 5% of zeolite sand, with at a height of 150cm, the 7 sampling ports are set 25cm from the top filtering material layer to the bottom filtering material layer: 1# sampling port, 2# sampling port, 3# sampling port, 4# sampling port, 5# sampling port, 6# sampling port and 7# sampling port were set at 0cm, 25cm, 50cm, 75cm, 100cm, 125cm and 150cm from the top filtering material layer, respectively. A water distribution pipe was fixed on the top of the filtering material of the CRI system, the wastewater enters the water distribution pipe and feeds the water to the CRI system after extraction by a water pump, the wastewater quantity is controlled with a flowmeter and the wastewater flows straight down in the CRI system where it is purified by trickling through the filtering material from top to bottom. Fig.1 shows the schematic diagram of the filter tank of the CRI simulation column.

#### *Operation and Management of the CRI Simulation Column*

The CRI simulation column was operated on July 10, 2009, the experimental water was domestic wastewater from the sewer of a student apartment. The experimental design hydraulic load was 1m/d; two intermittent water distribution modes were adopted, an operational mode 1: 4 times of waterdistribution per day, 0.5h for each time, every time the water distribution quantity was 0.25m, the water was distributed once every 6h; the

\* To whom all correspondence should be sent:  
E-mail: xuwenlai1983@163.com

operational mode was 2: the water was distributed once every day, for 2h every time, every time the water distribution quantity was 1m, the water was distributed once every 24h. The CRI simulation column was started with fresh water and the COD test yielded effluent every 3d.

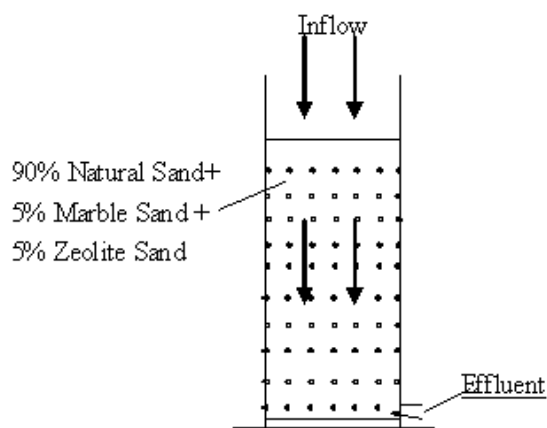


Fig.1. CRI simulation column.

*Experimental Monitoring Items*

The experimental monitoring items included CODCr, NH3-N, NO3-N, TN and TP. Table 1 shows the experimental monitoring method [5].

EXPERIMENTAL RESULTS AND ANALYSES

*Experimental Results of COD Removal by the Cri System*

Table 2 shows the COD concentration and removal rate of influent and effluent by the CRI simulation column under operational mode 1 (Notes: sampling times 1-13 are the natural bio-film colonization stage of the CRI system, and the sampling time 14 is the stable operational stage of the CRI system, Table 2 starts from sampling time 14) and Table 3 shows the COD concentration and

removal rate of influent and effluent of the CRI simulation column under operational mode 2. Table 4 shows the removal effect of COD by filtering materials of different heights in the CRI simulation column under operational mode 1.

To investigate the degradation rule of COD along with flow in the CRI simulation column, a wastewater sample at each sampling port along the flow in the CRI simulation column under operational mode 1 was taken, Table 4 displays the specific experimental results.

*Rule Analyses of COD Removal by the Cri System*

It can be seen from Table 2 that after the CRI system was operated steadily following successful natural bio-film colonization, the CRI system manifest a high COD removal rate under operational mode 1 (the hydraulic load cycle was 6h): after 7 tests (sampling numbers 14-32), after 12 tests the effluent COD concentration in the CRI system was less than 20mg/L, after 19 tests the effluent COD concentration in the CRI system was less than 30mg/L, after 19 tests the effluent COD concentration in the CRI system was less than 20.39 mg/L, in terms of the COD index, the effluent COD concentration in the CRI system under operational mode 1 reached the A-level standard or the first class standard of the Pollutant Discharge Standard for the Town and Country Sewage Treatment Project (GB18918-2002).

The influent COD concentration in the CRI system had a larger fluctuation range, whose minimum COD concentration was 90.36 mg/L and the maximum COD concentration was 189.61 mg/L, however, the effluent COD concentration in the CRI system had a small fluctuation range, which was maintained at 14-25 mg/L, suggesting that the CRI system had a stronger capacity for resisting the impact load for COD.

Table 1. Experimental methods of pollutant indexes.

Index	Experimental method
Water temperature	Thermometer method
Ph	Glass-electrodes method
COD	Potassium dichromate method
NH3-N	Nessler's reagent colorimetry
TN	Alkaline potassium per sulfate digestion-uv spectrophotometric method
TP	Ammonium molybdate spectrophotometric method

**Table 2.** COD Concentration and Removal Rate of Influent and Effluent of the CRI Simulation Column under Operational Mode 1.

Sampling times	Influent concentration (mg/L)	Effluent concentration (mg/L)	Removal rate (%)
14.	159.64	23.31	85.4
15	136.48	20.47	85
16	126.31	19.33	84.7
17	104.34	14.50	86.1
18	97.34	15.67	83.9
19	112.32	17.18	84.7
20	159.69	24.59	84.6
21	178.34	22.47	87.4
22	189.61	21.05	88.9
23	104.35	18.57	82.2
24	90.36	15.45	82.9
25	94.58	17.59	81.4
26	147.35	21.07	85.7
27	163.24	22.69	86.1
28	158.31	22.64	85.7
29	146.36	23.56	83.9
30	165.65	23.36	85.9
31	115.43	20.66	82.1
32	151.23	23.29	84.6

It can be seen from Table 3 that the removal effect of COD when the hydraulic load cycle was 24h declined dramatically compared with that when the hydraulic load cycle was 6h, with an average removal rate of only 59.1%, after 10 sampling tests (sampling numbers 33-42), after 7 sampling tests the final effluent COD concentration in the CRI system was greater than 60mg/L, after 3 tests the effluent COD concentration in the CRI system was greater than 50mg/L, after 10 tests the effluent average COD concentration in the CRI system was 60.77 mg/L, in terms of COD index, the effluent COD concentration in the CRI system exceeded the A-level standard of the first class standard of the

Pollutant Discharge Standard of the Town and Country Sewage Treatment Project (GB18918-2002).

Table 4 shows the change in COD concentration along the flow in the CRI system under operational mode 1 (the hydraulic load cycle is 6h). The average removal rate of COD by the CRI system in the 5 experiments was 84.9%, the removal rate of COD in the CRI filter tank 0-75cm segment reached 71.9%, accounting for 84.6% out of the total removal rate of COD by the CRI system, the removal rate of COD in the CRI filter tank 0-100cm segment reached 77.8%, accounting for 91.6% out of the total COD removal rate by the CRI system, suggesting that COD had been effectively removed

in the CRI filter tank 0-100cm segment and removed less effectively (only about 6%) in the CRI filter tank 0-100cm below the segment.

#### *Mechanism Analyses of COD Removal by the Cri System*

The following conclusions can be reached from the analysis of the COD removal mechanism by the laboratory simulation column[6-10]:

(1) Filtration and adsorption was the first step of organic pollutant removal by the CRI system.

It took a long time for the organic matter in the wastewater to be decomposed completely in the CRI system, more especially, some of the macromolecular organic matter can continue to be decomposed aided by the microorganisms surrounding the filtering material in the CRI system only by being first decomposed into a dissolved state through hydrolytic processes, which needed to take a relatively long period of time, in the CRI system, the filtering material and bio-film first managed the interception and adsorption of organic matter to allow sufficient contact time with the microorganisms, during which they started the biochemical reaction to let the organic matter to be completely decomposed, absorbed and utilized by the microorganisms. The filtration and adsorption was the first step of organic pollutant removal by the CRI system, providing a basis for further degradation and removal of the organic matter.

(2) The organic matter accumulates during the flooding period and is oxidized and decomposed during the drying period in the CRI system.

When the wastewater flows through the filtering material of the CRI system, the organic matter becomes detached from the aqueous phase due to adsorption, interception and flocculation. By filtering the material and bio-film, among which a portion of low molecular weight and dissolved organic matter can be quickly decomposed, absorbed and utilized by the microorganisms in the CRI system and wastewater, but the macromolecular or granular organic matter can continue to be completely decomposed by the microorganisms in the CRI system only by first being decomposed by the hydrolytic process. This involves a process where the macromolecular and granular organic matter is decomposed and dissolved to organic matter that can be absorbed and utilized by the microorganisms following the action of the hydrolytic enzyme released by the microorganisms. This process needs a relatively long period of time, so the macromolecular organic matter absorbed by the filtering material of the CRI system cannot be decomposed by the

microorganisms in a timely fashion. The matter accumulates in the CRI system, if the CRI system is fed with water all the time, then more and more organic matter accumulates in the CRI system and this will easily result in a blockage of the CRI system. In order to operate normally, the CRI system adopted an alternate wetting and drying operational mode, during the flooding period, the organic matter accumulates in the CRI system, only a small portion of low molecular weight and dissolved organic matter can be decomposed by the microorganisms, in the drying period, because no new organic matter enters the CRI system, so the microorganisms in the CRI system have plenty of time to conduct biodegradation of organic matter accumulated during the flooding period, the assimilative capacity of the CRI system was restored in the drying period, allowing continued effective adsorption and accumulation of organic matter during the next wastewater feed. The alternate wetting and drying operational modes were the safeguard for a normal operation of the CRI system, while limiting the hydraulic load of the CRI system because it took a certain time for the macromolecular organic matter to be hydrolyzed, absorbed and utilized by the microorganisms, so the drying period should not be too short. Therefore, such alternate wetting and drying operational modes limit the increase of the hydraulic load of the CRI system.

(3) The aerobic degradation played an important role in the removal of organic matter by the CRI system.

The study showed that because the CRI system adopted the alternate wetting and drying operational mode and characteristics of the CRI system itself, the CRI filter tank upper segment (0-100cm) belongs to the aerobic/anaerobic alternating segment, which has a wide range of microorganisms, very complex, including obligate aerobes, facultative microorganisms and obligate anaerobes, a relatively rich content. The obligate anaerobes required a much stricter living environment than the obligate aerobes, since the CRI system had a longer drying period and shorter flooding period, which means that the aerobic/anaerobic alternating segment had a longer aerobic state and a shorter anaerobic state, thus this segment was advantageous to the growth and reproduction of aerobes and inhibits the growth of anaerobes. Therefore, the degradation of aerobes played an important role in organic matter removal by the CRI system in the aerobic/anaerobic alternating segment (CRI filter tank 0-100cm segment).

**Table 3.** COD Concentration and Removal Rate of Influent and Effluent of the CRI Simulation Column under Operational Mode 2.

Sampling times	Influent concentration (mg/L)	Effluent concentration	Removal rate
		(mg/L)	(%)
33	163.4	47.39	71.4
34	158.6	65.03	59.6
35	148.3	63.32	57.3
36	167.5	68.34	59.2
37	159.1	61.73	61.2
38	146.8	64.45	56.1
39	152.4	59.89	60.7
40	154.7	65.75	57.5
41	146.2	58.77	59.8
42	136.7	53.04	61.2

**Table 4.** COD Concentration (mg/L) along the Flow in the CRI Simulation Column under Operation Mode 1.

Sampling times	CRI filter tank depth (cm)						
	0	25	50	75	100	125	150
43	168.6	105.8	66.6	46.6	34.6	28.2	25.3
44	171.3	105.6	63.9	44.0	37.6	26.3	25.1
45	159.6	103.7	66	48.3	39.7	28.7	25.1
46	163.2	103.9	65.5	47.2	35.1	27.0	24.2
47	160.8	101.7	63.7	45.2	35.7	26.8	24.2
Average removal rate (%)	0	37.2	60.4	72.4	79.5	83.3	85

The CRI filter tank lower segment (100-150cm) was in an anaerobic state, but it made a small contribution to organic matter removal, there were two main reasons:

1. The decomposition capacity of anaerobes was far less than that of aerobes and the decomposition of organic matter was not complete.

2. The anaerobic reaction rate of the microorganisms related to the initial concentration of nutrients, the higher the initial concentration of organic pollutants, the faster the anaerobic decomposition reaction, which is otherwise slower.

3. Because the CRI filter tank 0-100cm segment had a high removal rate of the organic matter, with an average removal rate of around 80%, by producing a small quantity of organic matter entering the anaerobic zone of the CRI filter tank the lower segment had a low anaerobic biodegradation rate of organic matter.

In conclusion, the organic matter removal by the CRI system depended mainly on aerobic biodegradation.

4. The alternation of wetting and drying operational mode facilitated COD removal.

It can be seen from Table 2 and Table 3 that under the conditions of different wet-to-dry rates, the CRI system had a remarkably different removal efficiency for organic matter, which was mainly caused by a change in the hydraulic load cycle of the CRI system due to a different wet-to-dry rate. The organic matter removal by the CRI system depended mainly on aerobic biodegradation, so the reaeration state and hydraulic retention time of the CRI system will have a great influence on organic matter removal. The main reasons for the large difference in the removal rate of COD under the conditions of two different wet-to-dry rates in this experiment are mainly as follows:

1) Differences of the reaeration effect of the CRI system.

The CRI system is a technology for wastewater treatment using a natural system without the need for aeration and its reaeration process relies mainly on air convection and diffusion. At the time of infiltration of the residual water on the surface layer of the CRI system, the air inside and outside the CRI system initiates air convection due to infiltration and inhalation by the water and air convection carried through once within one hydraulic load cycle, the volume of air convected is equal to the volume of all the water coming out of the CRI system during the time from drying of the residual water on the surface layer of the CRI system to the next wastewater feeding of the CRI system. When the CRI system was in the drying period, its reaeration mainly relied on the air diffusion. The study conducted by Zhang Jinbing [7] suggests that even when the CRI system is in the drying period, the amount of reaeration through air diffusion is still low and it is difficult for oxygen to reach deeper into the CRI system. To allow for better reaeration of the CRI system, the hydraulic load cycle of the CRI system needed to be shortened, the wastewater feeding and drying frequencies needed to be increased, and air the convection times of the air inside and outside the CRI system needed to be increased, thus allowing for an increase of the reaeration efficiency of the CRI system, which will be favorable for the decomposition of organic matter by the aerobes inside the CRI system.

The operational mode for sampling numbers 14-32 required a one time wastewater dosing every 6h, 4 times per day and the CRI system completed the whole process of one time drying and flooding every 6h. Under such an operational mode, the CRI system had a higher drying frequency and less time and it conducted air convection 4 times every day, such an operational mode strengthened the

reaeration of the CRI system, while for sampling numbers 33-42, the infiltration column only conducted air convection once every day. Thus it can be seen that the hydraulic load cycle will directly affect the reaeration way and reaeration efficiency of the CRI system. Under these experimental conditions, the reaeration way of sampling numbers 14-32 relied mainly on the air convection, while the reaeration way of sampling numbers 33-42 relied mainly on the air diffusion. Therefore, the reaeration efficiency of sampling numbers 14-32 was much higher than that of sampling numbers 33-42, it was more favorable for the decomposition of organic pollutants by aerobes under the conditions of sampling numbers 14-32, so the CRI system had better removal efficiency for organic pollutants under the operational mode of 4 times of wastewater dosing per day and one time every 6h.

2) Hydraulic retention time.

The organic matter removal by the CRI system mainly relied on the degradation by aerobes, so the length of time of contact between the organic pollutants with the bio-film in the CRI system will have a great influence on the removal effect of the organic pollutants. Because the hydraulic load of the CRI system was relatively high in the CRI system, the hydraulic retention time (HRT) had a much greater influence on the removal effect of organic pollutants [8,9].

This experiment adopted two obviously different hydraulic load cycles and the HRT had a major difference under the conditions for two different hydraulic load cycles [10-13]. When the sampling numbers 14-32 adopted 4 times of wastewater dosing per day, once every 6h and the sampling numbers 33-42 adopted the hydraulic load cycle of 24h, under such different conditions the hydraulic load was the same, however, the wastewater quantity flowing through the CRI system of each time of wastewater distribution of sampling numbers 33-42 was equal to the total wastewater quantity flowing through the CRI system of 4 times of wastewater distribution for sampling numbers 14-32, so the actual flow rate of wastewater for sampling numbers 33-42 was significantly greater than that for sampling numbers 14-32. Therefore, the wastewater had longer HRT for sampling numbers 14-32, such an operational mode was more favorable for the degradation and removal of organic matter by microorganisms in the CRI system [14, 15].

## CONCLUSIONS

The following conclusions were reached through the wastewater processing experiment by building a CRI simulation column:

(1) After the CRI system operated stably following the successful natural bio-film colonization, the CRI system had a high COD removal rate under operational mode 1: COD had been effectively removed in the CRI filter tank 0-100cm segment, with a removal rate reaching 77.8%, the effluent COD concentration in the CRI system under operational mode 1 reached the A-level standard for the first class standard of the Pollutant Discharge Standard of the Town and Country Sewage Treatment Project (GB18918-2002). The CRI system had a stronger capacity of resisting impact load for COD. The CRI system had a relatively ineffective removal effect of COD under operational mode 2, with an average removal rate of only 59.1%.

(2) Filtration and adsorption were the first steps in organic pollutant removal by the CRI system; organic matter in the CRI system was accumulated during the flooding period and oxidized and decomposed during the drying period; the aerobic degradation played an important role in organic matter removal by the CRI system; the alternate wetting and drying operational mode facilitated COD removal.

**Acknowledgements:** The research was funded by the Natural Science Foundation of China (No. 41502333), the State Key Laboratory of Geohazard Prevention and Geoenvironment Protection Foundation (No. SKLGP2015Z012, SKLGP2014Z001), the specialized research fund for the doctoral program of colleges and universities (No. 20135122120020), the scientific research plan of education department of Sichuan Province (No. 14ZB0073).

## REFERENCES

1. W.L. Xu, Y.N. Yang, C. Cheng, *Journal of Coastal Research*, **73**, 386 (2015).
2. W.L. Xu, G. Liu, G.Y. Cui, *Journal of Pure and Applied Microbiology*, **7**(2), 1227 (2013).
3. Y. Xie, A. Kang, M. Li, *Chinese Journal of Environmental Engineering*, **4**(6), 1272 (2010).
4. W. Xu, J. Zhang, Y. Liu, *Fresenius environmental bulletin*, **20**(6A), 1487 (2011).
5. State Environmental Protection Administration, *Methods of Water and Wastewater Monitoring and Analysis* (Edition 4), Beijing, 2002.
6. J.B. Liu, PhD. Dissertation, China University of Geosciences, Beijing, 2006.
7. J. Zhang, PhD. Dissertation, China University of Geosciences, Beijing, 2010.
8. F. Zhao, PhD. Dissertation, China University of Geosciences, Beijing, 2010.
9. W. Xu, PhD. Dissertation, Southwest Jiaotong University, Chengdu, 2011.
10. R. Yao, PhD. Dissertation, Chongqing University, Chongqing, 2006.
11. J. Chen, PhD. Dissertation, Southwest Jiaotong University, Chengdu, 2008.
12. H. C. Qi, W. X. Peng, Y. Q. Wu, S. B. Wu, G. J. Xu, *Journal of Computational and Theoretical Nanoscience*, **9**(9), 1525 (2012).
13. Z. L. Liu, *Information Technology Journals*, **12**(17), 4158 (2013).
14. Z. L. Liu, *Journal of Applied Sciences*, **13**(21), 4702 (2012).

## ОТСТРАНЯВАНЕ НА ОРГАНИЧНА МАТЕРИЯ И МЕХАНИЗЪМ НА ДЕЙСТВИЕ НА СИСТЕМАТА ЗА БЪРЗА ИНФИЛТРАЦИЯ

У.Л. Ксу, И.Н. Янг, Дж. Уанг, М. Танг, И. Джиан, С.Дж. Пей

*Държавна ключова лаборатория за предотвратяване на геологични опасности и опазване на околната среда, Технологичен университет в Ченгду, 610059, Китай*

Постъпила на 15 юни, 2015 г.; приета на 26 юли, 2015 г.

(Резюме)

Конструирана е бърза инфилтрационна система (CRI), която намира приложение в отстраняването на замърсители от водите. Механизмът на този процес още не е ясен, което пречатства на неговото разпространение и приложение. Експериментите по третиране на води в колона на базата на CRI-системата показват следното. При стационарен режим по способ 1 се постига висока степен на отстраняване на ХПК (до 77%) в слой от 0 до 100 cm. При способ 2 се постига средно само 59,1 % отстраняване на ХПК. При CRI-системата първите степени са филтруването и адсорбцията. Органичната материя се натрупва през периода на омокряне, а се окислява и се разлага в периода на сушене. Деграцията на аеробната материя изграе важна роля за отстраняване на органиката. Редуването на заливане и сушене благоприятства отстраняването на ХПК. Тези резултати обогатяват теоретичните знания за CRI-системата и насърчават приложението ѝ.

## Performance, synthesis and removal of vanadium on ferruginous manganese composite material

Y. B. Huang<sup>1</sup>, Q. Qiu<sup>1,\*</sup>, C. Y. Niu<sup>1</sup>, H. Q. Gao<sup>1</sup>, C. Huang<sup>1</sup>, S. X. Tu<sup>2</sup>

<sup>1</sup>School of Resources and Environmental Engineering, Wuhan University of Technology, Wuhan 430070, China;

<sup>2</sup>College of Resource and Environment, Huazhong Agricultural University, Wuhan 430070, China

Received May 10, 2015, Revised June 2, 2015

Through the processes of precipitation, filtration, drying and calcination, Fe-Mn compounds were synthesized artificially. The performance of these processes is accessed. By using X-ray fluorescence, testing the specific surface area, analyzing the X-ray diffraction, infrared spectroscopy, scanning electron microscopy testing technology to characterize this material, in order to investigate its mechanism of arsenate adsorption and the factors that influence. The results of the experiment showed that when the initial concentration of vanadium was 50mg/L, 0.1g of ferruginous manganese composite material was used, the reaction time reached 2 hours. The best absorption efficiency was obtained at the temperature 30°C and pH value of 4. Adsorption of ferruginous and manganese complexes of vanadium (V) are in accord with the Langmuir adsorption model ( $R^2=0.9682$ ), the kinetic data are consistent with the two order kinetic models ( $R^2=0.9999$ ), the maximum adsorption capacity is 14.16mg/g.

**Key words:** Fe-Mn compounds; Vanadium (V); influencing factors; adsorption mechanism; kinetics

### INTRODUCTION

Vanadium is one of the main trace elements in fossil fuels, the vanadium compounds are usually toxic and their toxicity is enhanced by the increase vanadium content. Vanadium compounds have the highest toxicity. The vanadium smelt factory and vanadium alloy plant produce the chemical dust and aerosols which cause the high concentration of vanadium pollution in the neighboring area. The oil refineries, fuel and coal fired plants and chemical plants, also cause high toxicity and vanadium pollution of the water body. In the process of vanadium industry development the high concentration of vanadium industrial waste water has the characteristics of large and harmful emissions, heavy-toxicity, not easy to biodegrade. Therefore, finding an effective treatment to the vanadium containing wastewater and restoring the vanadium (V) polluted soil has become one of the most important research subject in the field of environmental science and technology.

Currently, the research on the treatment methods of industrial wastewater containing vanadium (V) at home and abroad mainly include chemical precipitates (including iron precipitation, lime neutralization precipitation and SO<sub>2</sub> precipitation), the ion exchange method and the adsorption method. The adsorption method is renewable and widely used. The previous reports in the literature on vanadium adsorbents, such as

natural mineral water talc [5], manganese acid leaching residues [6], modified iron-chips [7], modified ferrous ion zeolite [8], that have the good adsorption capacity of vanadium (V) ions. At the same time, the pilot study of the experiment [2] proved that natural iron manganese ore has the adsorption capacity of vanadium (V) up to 522 $\mu$ g·g<sup>-1</sup> and the contrast experiment resulted that the proportion of different iron ore and ferro-manganese has a great influence on the removal of vanadium (V). Due to the above study, this experiment will compound the oxide iron that has a high surface charge, large specific surface area and strong adsorption ability for many inorganic contaminants [9] with manganese that has a strong oxidation ability. In the experiment, an effort to obtain more efficient vanadium (V) adsorption materials as well as the absorption performance and the functional mechanism of the oxide ferro-manganese compound surface on the absorption of vanadium (V).

#### *Introduction to the experiment*

#### *The main reagents and equipment*

The equipment used in the experiments is comprised of ASAP 2020M an automatic specific surface area and porosity analyzer (American Micromeritics), an Axios advanced X-ray fluorescence spectrometer (Netherland PANalytical B.V), D/MAX-RB a target X-ray diffractometer (Japan RIGAKU), JSM-5610LV a scanning electron microscope (JEOL), UV-1100 an ultraviolet and visible spectrophotometer (Shanghai MAPADA) and others.

\* To whom all correspondence should be sent:  
E-mail: 364957055@qq.com

The main reagents used in this experiment were  $\text{NaVO}_3$ , carbamide, BPHA,  $\text{FeSO}_4 \cdot 7\text{H}_2\text{O}$ ,  $\text{MnSO}_4 \cdot \text{H}_2\text{O}$ , with a high purity, the water was deionized.

#### Introduction of the experimental methods

##### The preparation of ferruginous manganese composite material

To prepare the compound a series of different concentrations of Fe/Mn solutions, through the mixture of  $\text{FeSO}_4 \cdot 7\text{H}_2\text{O}$  and  $\text{MnSO}_4 \cdot \text{H}_2\text{O}$  in water and drop the precipitation saturated solution respectively in the series solutions. In the process of dropping, the stirring of solution need be done until it no longer produces new precipitation, the solution be put standing, and pour out the supernatant liquid. Following suction and filtering the lower metal oxide hydrate precipitate in the solution and after repeatedly washing the precipitate with deionized water, until the adding of  $\text{BaCl}_2$  no longer produces a white precipitate in the filtrate. The metal oxide is dried under  $105^\circ\text{C}$  for 2 hours at a constant weight then put in a muffle furnace and calcinated for 2 hours under  $450^\circ\text{C}$ . After cooling, grinding and sieving with a 100 ~ 190 mesh, it is stored for further use.

##### Introduction of the characterization experiment

The Fe-Mn compounds are experimentally characterized by using XRF, BET, XRD, FTIR and SEM.

##### Introduction of the static adsorption experiment

Using a sodium metavanadate simulated compound 500 mg/L of vanadium (V) contained in wastewater reserve liquid (in this paper, the vanadium in the solution is measured as  $\text{V}_2\text{O}_5$ ). Accurately weigh a 0.1g adsorbent and put it in a 100mL conical flask, 30.00mL certain a concentration simulated  $\text{V}_2\text{O}_5$  solution, reacting after 1 hour in the thermostat oscillator under  $30^\circ\text{C}$ , then subjected to a high speed centrifugal spin for 30 min, BPHA and the extraction spectrophotometric method are used to analyze the residual  $\text{V}_2\text{O}_5$  concentrations in the supernatant.

##### Introduction to the adsorption and adsorption kinetics experiment

By changing the pH value (2.0~12.0) and temperature ( $25\sim 50^\circ\text{C}$ ) for different water quality conditions of the vanadium solution the adsorptive characteristics of vanadium (V) by the Fe-Mn compound is explored. Weighing another 0.1g of adsorbent and putting it in a 100mL conical flask, with 30.00mL of the concentration of 50mg/l  $\text{V}_2\text{O}_5$  solution is placed in a thermostat oscillator under

$30^\circ\text{C}$ , the samples were taken at different time intervals, the vanadium (V) concentrations were measured and calculate the adsorption quantity for different periods.

## THE RESULTS AND ANALYSIS

### The best Fe/Mn mole ratio in the preparation of composite material

#### The selection of precipitant

In the preparation of a series of solutions where the Fe/Mn mole ratios are 5:1, 3:1, 1:1, 1:3, 1:5, NaOH and  $\text{Na}_2\text{CO}_3$  are used as the precipitants, to prepare the compound oxides, the removal efficiency of vanadium (V) is compared, the results are shown in figure1. When the  $\text{Na}_2\text{CO}_3$  is used as the precipitant, the removal rate of vanadium (V) is obviously higher than the NaOH precipitant, the reason is that  $\text{Na}_2\text{CO}_3$  reacts with iron, manganese and generates the carbonate precipitation, in the subsequent calcination process, the carbonate decomposition releases large amounts of  $\text{CO}_2$ , and the porosity of the Fe-Mn compound is increased. Due to the higher porosity, a better removal will result for vanadium (V), therefore, when  $\text{Na}_2\text{CO}_3$  is used as the precipitant the Fe-Mn composite compound removal of vanadium (V) is better than when NaOH is the precipitant. In the subsequent experiments,  $\text{Na}_2\text{CO}_3$  will be used as the precipitant to prepare the Fe-Mn compound and the precipitation sequence of different precipitants can be analyzed.

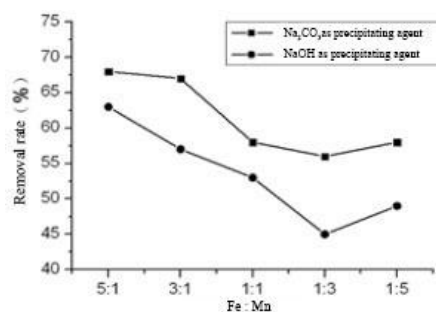
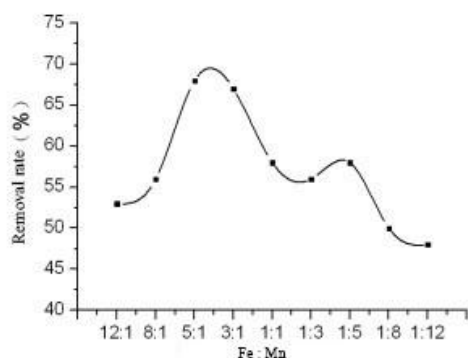


Fig.1. Comparison of the removal efficiency of the Fe-Mn compound when NaOH and  $\text{Na}_2\text{CO}_3$  are used as precipitants.

#### Selection of the Fe/Mn mole ratio

Preparation of a series of solutions with Fe/Mn mole ratios (in this study refer to the mole ratio) are 12:1, 8:1, 5:1, 3:1, 1:1, 1:3, 1:5, 1:8, 1:12, the  $\text{Na}_2\text{CO}_3$  is used as the precipitant to prepare the Fe-Mn compounds, by comparing the best Fe/Mn ratio for the removal efficiency of vanadium (V), the results are shown in figure 2.



**Fig. 2.** Different Fe/Mn ratios (mole ratio) of Fe-Mn compounds with respect to the changes in the removal rate of vanadium (V).

As evident from figure 2 the removal efficiency increases quickly with the smaller ratio of Fe/Mn, when the Fe/Mn ratio was 5:1, the maximum removal rate reached 67.8%, and then showed a decrease trend. Therefore, the subsequent experiments will choose the 5:1 Fe/Mn ratio as the best ratio for the removal of vanadium (V).

*The influence of water quality on Fe-Mn compound removal performance for vanadium*

*The influence of the pH value on the removal performance of vanadium*

Under the same reaction conditions, the initial pH value of the vanadium solution is changed in turn to explore the adsorption effects, the results are shown in figure 3. It can be seen from the figure 3 that in the pH value range of 2.0 ~ 12.0, the removal rate of the Fe-Mn compound of vanadium (V) first increases with the increase of the pH then decreases. Under the acidic reacting conditions the adsorption efficiency of vanadium (V) is higher, when the pH value reaches around 4.0, the best adsorption efficiency is achieved, the reason is that the colloid of the Fe-Mn compound is positively charged; when the experiment deals with the adsorption of positive and negative charges the pH value is close to 2, vanadium exists as  $VO_2^+$ , where the positive charge is not conducive to adsorption. When the pH value is between 3.8 ~ 3.8, the vanadium acid radical ion is  $V_{10}O_{28}^{6-}$ ,  $HV_{10}O_{28}^{5-}$  when the removal rate achieves a maximum [1]. The reason is that the acidic condition can enhance the protonation effect of the manganese ore surface, thus increasing the positive charge on the manganese ore surface [10] and plenty of  $H^+$  will dissolve the ore into some metal, making it appear more porous increasing the specific surface area, thereby increasing the removal efficiency of vanadium (V) [11]. The adsorption efficiency obviously decreases with the increasing pH value, the reason is that the vanadium anion is

under an alkaline environment and for the  $OH^-$  there is a competition for adsorption sites on the surface of the manganese ore. Therefore, the best pH value for vanadium (V) adsorption of the Fe-Mn compound is 4.0.

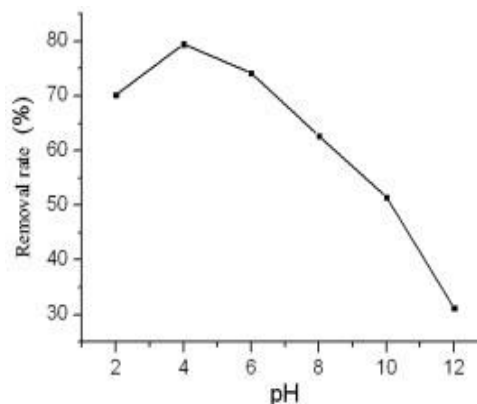


**Fig. 3.** The influence of the change in pH value on the removal performance of vanadium (V).

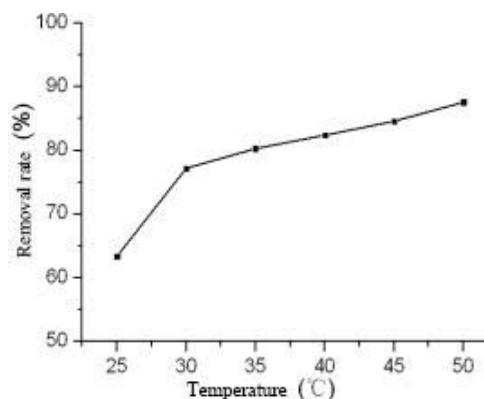


**Fig. 4.** The influence of the change reaction temperature on the removal performance of vanadium (V)

*The influence of the reaction temperature on the removal performance of vanadium (V)*

*The characterization and functional mechanism of the Fe-Mn compound*

*The analysis of the Fe-Mn compound's composition*

The composition of the adsorbent is the key factor that decides the adsorption performance of the material. In this study, the best Fe-Mn mole ratio of three mixture preparations are chosen as the adsorbents and the adsorbents are processed by grinding, drying and calcination, so the preparation of the adsorbent will not only contain iron, manganese ions, but could still contain a variety of other elements. In order to fully and accurately research the removal mechanism of compounds of the vanadium (V), XRF technology is used to obtain the composition elements of the Fe-Mn compound is shown in table 1. From table 1, it can be seen that there are 10 kinds of elements for Fe-

Mn compounds and according to the calculation the mole ratio is 5.04:1. In addition to iron and manganese oxide together with the Fe-Mn compound, due to cleaning that produce only residues of sodium oxide content that are more than 1%, the rest of the elemental contents are negligible. The removal efficiency in elimination of other elements' rather than vanadium (V) is high.

**Table 1.** The weight percentage of each oxide in the Fe-Mn compound.

Name	Percentage (%)
Na <sub>2</sub> O	2.76
MgO	0.06
Al <sub>2</sub> O <sub>3</sub>	0.02
SiO <sub>2</sub>	0.05
P <sub>2</sub> O <sub>5</sub>	0.01
SO <sub>3</sub>	0.74
CaO	0.10
MnO	7.53
Fe <sub>2</sub> O <sub>3</sub>	85.47
Cl	0.02
Initial weight	3.14

#### The analysis by SEM and BET

The methods of SEM and BET are used to analyze and measure the surface topography and specific surface area of the Fe-Mn compound. Presented in Figure 5 is a photo taken by a scanning electron microscopy that shows the morphology at an Fe/Mn ratio of 5:1. The Fe-Mn composite material before and after the removal of vanadium (V) are observed. It can be seen from figure 5 that the most of particles of the Fe-Mn compound are uneven in size although some are spherical, these particles adhere to each other and form a network structure, this natural phenomenon reflects the inherent adsorption properties of the Fe-Mn compound. The vanadium (V) ions are absorbed by water surface particles, with the help of a mesh structure bridge connection, the vanadium (V) ions form a large film that separates and removes the water. In the photo of after absorption that the space between spherical particles are significantly reduced, and large amounts of vanadium particles is absorbed by the surface of spherical particles. This photo further illustrates the reasons why the Fe-Mn compound has a good removal performance. Meanwhile, in the method of nitrogen adsorption - stripping characteristics are used to measure the specific surface area of the Fe-Mn compound that is 69.2m<sup>2</sup>/g. The result shows that the Fe-Mn

compound particles have a large specific surface area and high a surface free energy, which increases the chances that the particles react with the vanadium in the water and has a strong ability to remove the vanadium in the waste water.

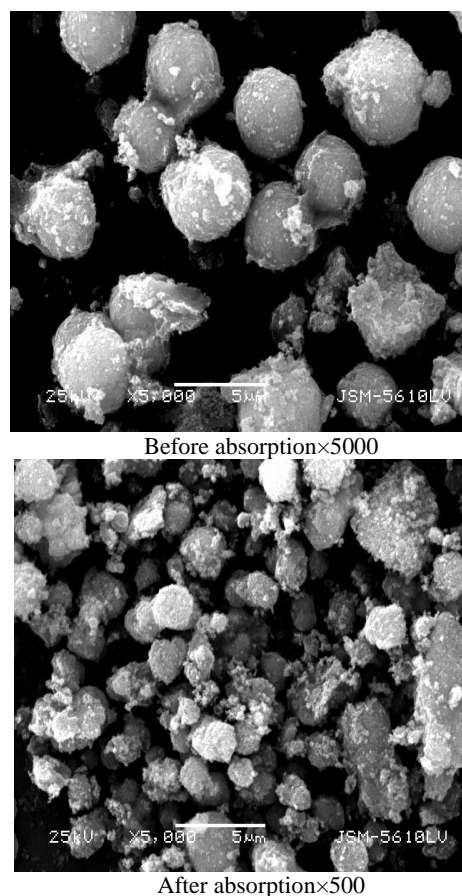


**Fig. 5.** The SEM pictures before and after the Fe-Mn compound adsorbs vanadium (V)

#### The analysis by XRD

The XRD technology is used to analyze the phase compositions of the Fe-Mn compound before and after adsorption of vanadium (V). It can be seen from figure 6 that before adsorption the composition of the Fe-Mn compound, appears similar to the magnetite and Mn<sub>2</sub>O<sub>3</sub> characteristics of the diffraction peak, the main phase compositions are Fe<sub>3</sub>O<sub>4</sub> (JCPDS 01-1111) and Mn<sub>2</sub>O<sub>3</sub> (JCPDS 02-0902). There are some serious wide and diffuse peaks in the Fe-Mn compound XRD figure showing that the Fe-Mn compound is not crystalline but porous, most of the Fe-Mn compound is amorphous in form. Compared with the XRD figures presenting the material before and after adsorption, it can be argued that the graphics have large changes before and after adsorption. The material presented in figure 7 after the reaction appears similar to the V<sub>2</sub>O<sub>3</sub>, Fe<sub>2</sub>O<sub>3</sub> and Mn<sub>2</sub>O<sub>3</sub> characteristics of the diffraction peak in the Fe-Mn

compound, the main phase compositions are V<sub>2</sub>O<sub>3</sub>(JCPDS 01-1293), Fe<sub>2</sub>O<sub>3</sub>(JCPDS 03-0800), O<sub>3</sub>(JCPDS 02-0902). These show that the chemical reaction occurs in the process of surface adsorption, partial vanadium acid radical ions are generate V<sub>2</sub>O<sub>3</sub> and Fe<sub>3</sub>O<sub>4</sub> is oxidized to Fe<sub>2</sub>O<sub>3</sub>.

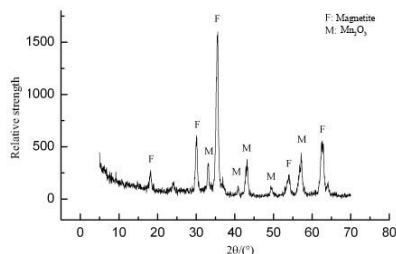


**Fig. 6** The XRD figure before the Fe-Mn compound adsorbs vanadium (V).

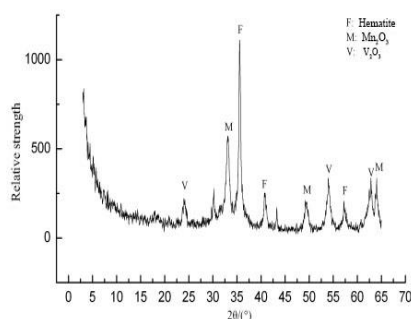


**Fig. 7.** The XRD figure after the Fe-Mn compound adsorbs vanadium (V).

#### The analysis by FTIR

In the study by an FTIR test to determine whether M-OH exist in the Fe-Mn compound, the FTIR figure of the process before and after adsorption is shown in figure 8.

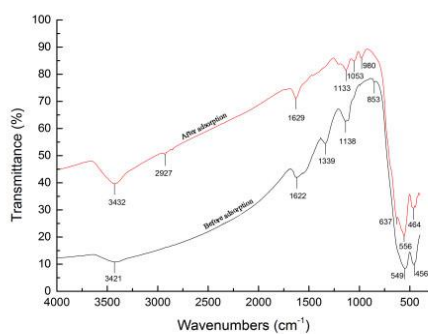


**Fig. 8.** The FTIR figure of the process before and after adsorption.

As shown in figure 8, the Fe-Mn compound there has the characteristic stretch vibration absorption peak of water and -OH (3421cm<sup>-1</sup>~3432cm<sup>-1</sup>) and -OH bending and vibration absorption peaks (1629cm<sup>-1</sup>-1622cm<sup>-1</sup>). The

absorption peak and the corresponding hydrated MnO<sub>2</sub> surface hydroxyl of the Mn-OH functional groups appear around 1138cm<sup>-1</sup>. The characteristic peaks appear at around 1200cm<sup>-1</sup> both figures, which can explain the presence of Mn-OH. The absorption peak appearing at 1400cm<sup>-1</sup> is caused by the MnO<sub>2</sub> hydration component of the hydroxyl groups and water molecules. The stretching and vibration absorption peaks of the hydroxyl groups in Fe(OH)<sub>3</sub> and water molecules appear at 3421cm<sup>-1</sup> and 3432cm<sup>-1</sup>; the bending and vibration peaks of the hydroxyl groups in Fe(OH)<sub>3</sub> and water molecules appear at 1622 cm<sup>-1</sup>, 1629 cm<sup>-1</sup>; the absorption peaks of α-FeOOH appear at 1162 cm<sup>-1</sup> and 460 cm<sup>-1</sup>. Therefore, the iron compounds and hydroxyls play an important role in the process of the Fe-Mn compound removal of vanadium (V). It can result in adsorption of the Fe-Mn compound and removal of vanadium (V) and the complexation of the surface of material and hydroxyl of iron compounds. In figure 8, the vibration and absorption band at 980cm<sup>-1</sup> is caused by the V=O bond in the partial vanadium acid radical and the absorption band at 547cm<sup>-1</sup> corresponds to the vibration of the V-O-V bond in the aggregation of partial vanadium acid radicals[14].

#### The isotherm and kinetics of adsorption

##### The adsorption isotherm

Using the isothermal adsorption models of Langmuir and Freundlich and fitting the results show that the correlation of the former ( $R^2=0.9682$ ) is bigger than the latter ( $R^2=0.9056$ ), which shows that the removal of vanadium from the Fe-Mn compound is applicable in the Langmuir adsorption isothermal adsorption equation. The related model equation is shown below.

The Langmuir equation:

$$qe = 21.786 \frac{1 + 0.513p_e}{0.513p_e}$$

The model of the Langmuir isothermal curves fit well and illustrate the adsorption process of vanadium by the Fe-Mn compound, when the concentration is low the adsorption rate is fast and the adsorption quantity of growth is slow with the increase in concentration while the adsorption is gradually in balance, which also illustrates the removal of vanadium (V) which is directly adsorbed.

##### The adsorption kinetics

Figure 9 shows the vanadium (V) adsorption kinetics process for the Fe-Mn compound. It can be seen that the adsorption rate of vanadium (V) by the Fe-Mn compound is very fast, the adsorption

capacity reached in 2-hours' is 13.19 mg/g, after 4-hours' the adsorption is gradually balanced.

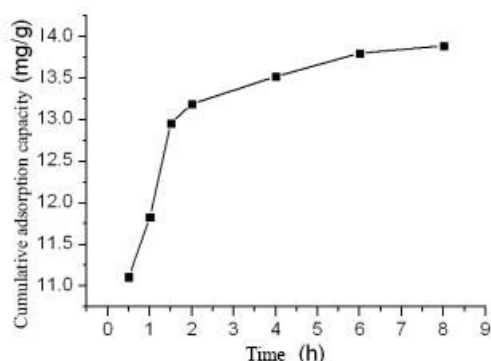


Fig.9. Curve of the adsorption rate of vanadium (V)

By using the kinetics adsorption model the specific fitting involved is shown in table 2, the adsorption model of the secondary kinetics ( $R^2=0.9999$ ) has the greatest correlation and the Lagergren adsorption model of first order kinetics ( $R^2=0.9765$ ) is greater than the fixed Elovich kinetics model ( $R^2=0.9066$ ), so the adsorption kinetics of the Fe-Mn compound with vanadium is a better fit to the adsorption model of the secondary kinetics. Therefore, the adsorption process of vanadium (V) by the Fe-Mn compound is the chemical adsorption process. According to the calculation by this model, the maximum adsorption capacity of vanadium (V) by the Fe-Mn compound is 14.16 mg/g.

### CONCLUSIONS

This paper presents a study on the removal performance of vanadium (V) through the co-precipitation preparation of the Fe-Mn compound; the conclusions obtained are as follows:

(1) The best conditions for preparation of the Fe-Mn compound are: the  $\text{FeSO}_4 \cdot 7\text{H}_2\text{O}$  is chosen

as the ferrous salt, the  $\text{MnSO}_4 \cdot \text{H}_2\text{O}$  is chosen as the manganese salt and  $\text{Na}_2\text{CO}_3$  is used as the precipitate agent, when the calcination temperature is  $450^\circ\text{C}$  and a Fe/Mn ratio of 5:1 the best removal ability of vanadium (V) is achieved.

(2) In this paper, the chosen removal agent has a good performance and the metal elements are distributed evenly in the Fe/Mn compound (the mole ratio Fe-Mn is 5:1), its specific surface area is  $69.2\text{m}^2/\text{g}$ . Besides, the Fe-Mn compound particles attach to each other and form a mesh structure that arrange loosely, which has a good adsorption of the colloidal particles in the water that have a bridge connection and a trap function.

(3) Through the analysis of the controlling variables method the best water quality conditions are achieved: 0.1g of the Fe-Mn compound are used to process 50 mg/L of simulated wastewater that contain vanadium (V), oscillation under a constant temperature of  $35^\circ\text{C}$  for 120 min, when the pH value is 4.0 the highest removal efficiency of vanadium (V) is realized.

(4) The model of secondary kinetics and isothermal adsorption models of Langmuir can better fit the adsorption process of vanadium (V) respectively by using the Fe-Mn compound, in accordance with fitting the equation calculation of the Fe-Mn compound removal efficiency of vanadium (V), the maximum adsorption capacity is 14.16 mg/g.

The analysis of the mechanism of removal of vanadium (V) from the Fe-Mn compound contains the physical adsorption, electrical adsorption and co-precipitation, dependant on the pH value. The combination of multiple adsorption methods make the co-precipitation preparation of the Fe-Mn compound has a higher removal ability of vanadium (V).

Table 2. The fitting results of the stimulated kinetics data for the Fe-Mn compound adsorption of vanadium (V)

Lagergren first order kinetics	$q_e / \text{mg} \cdot \text{g}^{-1}$	13.89	Secondary kinetics	$q_e / \text{mg} \cdot \text{g}^{-1}$	14.16	Elovich Revised absorption kinetics	a	12.09
	$k_1 / \text{min}^{-1}$	-0.5321		$k_2 / \text{mg} \cdot \text{g}^{-1} \text{min}^{-1}$	0.448		b	1.0007
	$R^2$	0.9765		$R^2$	0.9999		$R^2$	0.9066

**Acknowledgments:** This research was supported by the national natural science foundation of China (Grant No. 41471407, 2015-2018), Major Projects on the Control and Management of the Water Body Pollution of China (2009ZX07104-001), China's rural environmental special fund, Program of Science and Technology in Wuhan, China (201060723315), and Innovation funds of postgraduate in Wuhan University of Technology, China (2010-24-ZH-010). The authors would like to thank Professor Y. Lin, X.Y. Long, L. Q. Qin et al for their assistance with the XRF and FTIR.

#### REFERENCES

1. B. Donald., *Cli. Tox.*, **37** (2), 273 (1999).
2. Y. B. Huang, C. Huang, Q. X. Yang. *Jou. of wuh. uni. (sci. edi.)*, **4**(1), 6 (2014)..
3. A. Bhatnagar, A. K. Minocha, D. Pudasainee. *Chem. Eng. Jou.*, **144**(2), 5 (2008).
4. F. Kaczala, M. Marques, W. Hogland. *Wat., Air & Soil Pol.*, **223**(5): 238 (2012).
5. A. Naeem, P. Wsterhoff. *Wat. Res.*, **41** (7), 1596 (2007).
6. H. R. Li, Y. L. Feng, J. L. Liang. *Rare met.*, **27** (2), 118 (2008).
7. C. Bioconjugate. *Env. Sci and Tec.*, **19** (3), 748 (2008)..
8. C. L. Peacock, D. M. Sherman. *Geo. et Cos. Acta*, **68** (8), 1727 (2004).
9. T. Kohn, K. J. T. Livi, A. L. Roberts. *Env. sci. & tec.*, **39**(8), 2875 (2005).
10. A. Astruc, C. Cochon, S. Dessources. *App. Cat. A-gen.*, **453**(2), 24 (2013).
11. Johanssonl. *Wat. Sci Te.* 35(5), 90 (1997).
12. K. Nakamoto. N. Y., Lon., J. W., **1**, 35 (2006).
13. M. Ding. *Geo. et Cos. Acta*, **64**(5), 1216 (2000).
14. Beg S., A. Al-Alas, N. A. S. Al-Areqi. *Mat. Chem.*, **124**(1), 309 (2010).

## СВОЙСТВА, СИНТЕЗА И ОТСТРАНЯВАНЕ НА ВАНАДИЙ ОТ ФЕРО-МАНГАНОВИ КОМПОЗИТНИ МАТЕРИАЛИ

И.В. Хуанг<sup>1</sup>, К. Кю<sup>1,\*</sup>, К.И. Ню<sup>1</sup>, Х.К. Гао<sup>1</sup>, К. Хуанг<sup>1</sup>, С.С. Ту<sup>2</sup>

<sup>1</sup>Училище по околна среда и ресурси, Технологичен университет в Ухан, 430070, Китай

<sup>2</sup>Училище по околна среда и ресурси, Селскостопански университет Хуажонг, Ухан 430070, Китай

Постъпила на 10 май, 2015 г.; приета на 2 юни, 2015 г.

(Резюме)

Изкуствено са синтезирани Fe-Mn-съединения чрез утаяване, филтруване, сушене и калциниране. Изследвани са свойствата им с помощта на рентгенова флуоресценция, инфрачервена спектроскопия, сканираща електронна микроскопия. Резултатите показват, когато началната концентрация на ванадия е 50 mg/L и са използвани 0.1 g от композитния материал реакционното време достига 2 часа. Най-добра абсорбция се постига при 30°C и рН 4. Адсорбцията на ванадий (V) върху композитите е в съгласие с изотермата на Лангмюир с висок коефициент на корелация ( $R^2=0.9682$ ), а кинетичните данни се описват от кинетикана реакция от 2-ри порядък ( $R^2=0.9999$ ). Максималният адсорбионен капацитет е 14.16mg/g.

## Synthesis, structural and biological studies of cobalt ferrite nanoparticles

M.W. Mushtaq<sup>1</sup>, M. Imran<sup>1</sup>, S. Bashir<sup>2</sup>, F. Kanwal<sup>1</sup>, L. Mitu<sup>3\*</sup>

<sup>1</sup>Institute of Chemistry, University of the Punjab, Lahore-54890, Pakistan

<sup>2</sup>Centre of Ionics, Department of Physics, Faculty of Science, University of Malaya-50603, Kuala Lumpur, Malaysia

<sup>3</sup>Department of Chemistry, University of Pitesti, Pitesti-110040, Romania

Received May 31, 2015; Accepted December 16, 2015

Cobalt ferrite's nanoparticles,  $\text{CoFe}_2\text{O}_4$  (CF) were synthesized via the co-precipitation method using a new monomeric surfactant called sorbitol. Fourier Transform Infrared (FTIR) spectroscopy, X-ray powder Diffraction (XRD), a Vibrating Sample Magnetometer (VSM) and Scanning Electron Microscope (SEM) were used for their characterization. The presence of an (M–O) bond was confirmed by the absorption band at  $589\text{ cm}^{-1}$  in the FTIR spectrum. VSM studies revealed the super paramagnetic nature of cobalt ferrite nanoparticles having a saturation magnetization value of  $62.55\text{ emu/g}$  and  $59.89\text{ emu/g}$  for cobalt ferrite NPs prepared without and with surfactant assistance respectively. The hysteresis loops showed negligible hysteresis, remanence and coercivity at 300 K. The powder X-ray Diffraction (XRD) pattern confirmed a single phase spinel cubic structure. SEM micrographs have been used to confirm the particle size which is found to be 28 nm with the surfactant and 60 nm without the surfactant and to analyse the distribution of NPs. Thermogravimetric measurements have also been studied to measure the presence of surfactant. The synthesized nanoparticles via the surfactant method were screened for their antibacterial activity against *Escherichia Coli* and *Staphylococcus Aureus* and demonstrated an appreciable activity. Furthermore, the interaction of cobalt ferrite nanoparticles with calf-thymus DNA was also investigated.

**Keywords:** Cobalt ferrite, Nanoparticles, Antibacterial activity, Calf-thymus DNA.

### INTRODUCTION

In the past decade, nano-sized ferrite particles gained an attraction as a new emerging class of inorganic compounds because of their comprehensive applications in applied chemistry, high-density data storage, biochemistry, MRI and targeted drug delivery [1-3]. The paramount features about ferrite nanoparticles (NPs) established in the literature are that these compounds are non-toxic, biofriendly and exhibit strong antibacterial potential and magnetic capability [4,5]. Among these compounds, some notable examples of ferrites are iron Oxide ( $\text{Fe}_3\text{O}_4$ ), nickel ferrite ( $\text{NiFe}_2\text{O}_4$ ), manganese ferrite ( $\text{MnFe}_2\text{O}_4$ ) and cobalt ferrite ( $\text{CoFe}_2\text{O}_4$ ) nanoparticles that possess biocompatibility, small size, minimum toxicity and superparamagnetic properties enabling them as suitable candidates in the biomedical sciences. Ferrites are a family of metal oxides having a spinel structure  $\text{MFe}_2\text{O}_4$  ( $\text{M} = \text{Fe}^{+2}, \text{Co}^{+2}, \text{Ni}^{+2}, \text{Zn}^{+2}, \text{Mg}^{+2}, \text{etc.}$ ). The distribution of metal ions in ferrite NPs  $[\text{M}^{+2}]_{\text{tetra}}[\text{Fe}^{+3}]_{\text{octa}}\text{O}_4$ , modifies their magnetic behaviour.

One of the important type of nanoferrites is cobalt ferrite (CF) which exhibits an inverse spinel structure, a high curie temperature, superior chemical and mechanical stability and a large magnetic spin magnitude [6,7]. Cobalt ferrites ( $\text{CoFe}_2\text{O}_4$ ) NPs have been synthesized by various physico-chemical methods such as hydrothermal reaction, micro-emulsion, sol-gel and co-precipitation techniques [8-10]. Relative co-precipitation is found to be the most used [11]. It is established in the literature that the nanostructure of cobalt ferrite possess  $\text{Co}^{+2}$  ions in octahedral sites (B) while  $\text{Fe}^{+3}$  ions are equally distributed between tetrahedral (A) and octahedral sites (B) [12].

To apply ferrite NPs in the engineering and biomedical fields, it is crucial to control the size, morphology and surface properties. During the genesis and growth of the primary nanoparticles, the surface chemistry of the primary nanoparticles is an important factor to control the final structure of the secondary nanoparticles by a process called Ostwald ripening, aggregation and coarsening [13]. The introduction of surfactants as a capping agent during synthesis of NPs, has been widely applied to control the size as well as the mechanical stability of ferrites as reported in the literature [14]. Various capping agents were applied to control the growth of building blocks of NPs including monomeric surfactants (ethylene glycol, glycerol, etc.) [15] and polymeric surfactants (PEG<sub>300</sub>, PEG<sub>600</sub>, PEG<sub>1000</sub>,

\* To whom all correspondence should be sent:  
E-mail: ktm7ro@yahoo.com

PEG<sub>10000</sub>, PVP<sub>40000</sub>, etc.)[16]. However, post treatment of NPs with monomeric surfactant is more beneficial because the polymeric surfactant may decrease the surface area by increasing the particle size. With monomeric surfactant, the particle size of the ferrites is easily controllable and a uniform distribution of metal ions is observed in octahedral and tetrahedral sites.

Keeping in view the literature and interesting features of cobalt ferrite nanoparticles, we have synthesized them by using a wet chemical route following the addition of a novel monomeric surfactant called sorbitol to explore their characteristic aspects as well as their biological properties.

## EXPERIMENTAL

Materials: Iron chloride FeCl<sub>3</sub>·6H<sub>2</sub>O (98%), cobalt chloride CoCl<sub>2</sub>·6H<sub>2</sub>O (98%) were purchased from Uni-chem. Sodium hydroxide (99%) was procured from Riedel-de Haen while sorbitol and calf thymus DNA from BDH-England and Sigma Aldrich respectively. All these purchased chemicals were used without further purification.

The preparation of cobalt ferrite (CoFe<sub>2</sub>O<sub>4</sub>) nanoparticles: FeCl<sub>3</sub>·6H<sub>2</sub>O (0.03 mol, 8.109 g) and CoCl<sub>2</sub>·6H<sub>2</sub>O (0.015 mol, 3.567 g) were dissolved together in 100ml of double de-ionized water. Then sodium hydroxide solution (0.3 mol, 12g/100 ml) was added slowly until a pH of 11–12 was reached. The resulting reaction mixture was subsequently stirred at 80°C for 1h. Upon stirring a black coloured precipitate started to settle down. Finally, the formed precipitates were cooled, filtered, washed with de-ionized water and then by ethanol. The resulting solid was then dried at 100°C for 1h [17]. We also synthesized CoFe<sub>2</sub>O<sub>4</sub> NPs by adding 2-3 drops of sorbitol (0.01 mol, 1.82 g) as a monomeric surfactant or capping agent while keeping all other parameters constant as mentioned above. The corresponding nanopowders obtained without and with a surfactant assisted approach are called product a and b respectively.

Characterization: Powder X-ray diffraction (PXRD) analysis was conducted on a Philips analytical X-ray diffractometer using CuK $\alpha$  radiation ( $\lambda = 0.154$  nm). Fourier transform infrared (FTIR) absorption spectra were recorded using a Cary 630 FTIR spectrometer in the wave number range of 4000–400 cm<sup>-1</sup> with potassium bromide (KBr) pellets. UV–Vis spectra of pure cobalt ferrite NPs were obtained by using a UV–Vis spectrophotometer (UV-2600, Shimadzu). The magnetic behavior was studied by using a

Lakeshore-7404 vibrating sample magnetometer (VSM) at room temperature, 27°C up to a maximum applied magnetic field of 10 KOe.

## Biological Studies

Antimicrobial studies; CoFe<sub>2</sub>O<sub>4</sub> were screened for their antibacterial potential against Staphylococcus aureus and Escherichia coli strains by the Kirby-Bauer technique [18]. The antibacterial activity was determined by measuring the clear zone of inhibition after incubation for 24 h at 37°C.

Interaction between DNA and cobalt ferrite nanoparticles; the nanocomposite DNA/CoFe<sub>2</sub>O<sub>4</sub> was prepared by mixing 0.1 mg/ml of calf-thymus DNA (0.308 mM for the Phosphate group) and 0.5 mg/ml of cobalt ferrite NPs in a Tris-Hcl buffer (10 mM, pH = 7.5). The resulting bionanocomposite was isolated from the solution using magnetic separation and washed with double distilled water. The concentration of DNA was recorded by a UV-Vis Spectrophotometer at 260 nm. The amount of adsorbed DNA was calculated by the following formula:

$$A = [(C_0 - C_i)v/m] \times 100\%$$

where C<sub>0</sub> is the initial concentration (mg/ml) of DNA in the solution, C<sub>i</sub> is the concentration (mg/ml) of unbound DNA molecules, V is the volume of the reaction medium in ml and m is the mass of CF nanopowder. The adsorption capacity was expressed in mol/g and mol/m<sup>2</sup> taking into account that 1 mg/ml of DNA concentration corresponded to a 3.08 mmol/l concentration of the DNA phosphate group.

## RESULTS AND DISCUSSION

The UV-Visible spectrum of CoFe<sub>2</sub>O<sub>4</sub> NPs synthesized by the surfactant assisted method is shown in Fig.(1). It displays a characteristic band in the range 330–450 nm, which developed particularly from the dispersion and absorption phenomenon of CoFe<sub>2</sub>O<sub>4</sub> magnetic nanoparticles and is in agreement with previous relations [18].

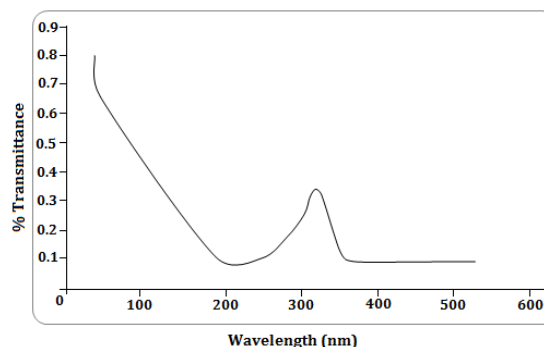
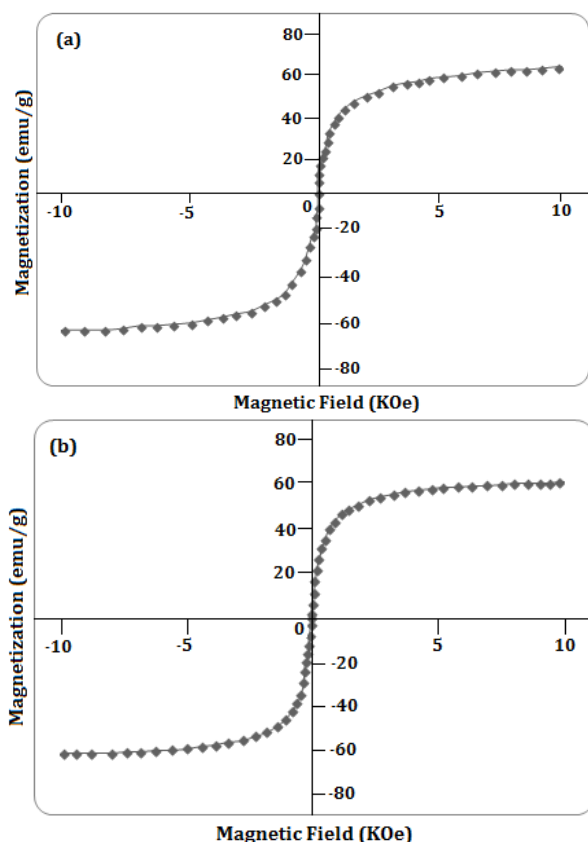


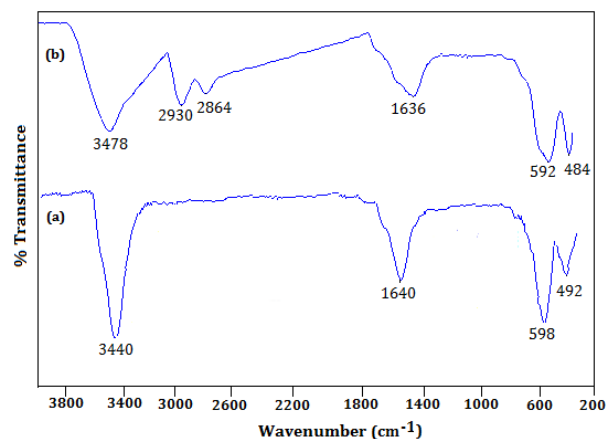
Fig. 1. UV-Visible spectrum of cobalt ferrite NPs.

Fig. 2 shows the effect of an applied magnetic field on the magnetization (emu/g) value of prepared cobalt ferrite NPs without and with the assistance of surfactant called product a and b respectively at room temperature. The M–H curves of both products (a, b) indicate types of hysteresis loop formation for soft magnetic materials with negligible coercivity,  $H_c \sim 17.62$  and  $\sim 16.94$ . It was also observed that by increasing the strength of the applied field, the value of saturation magnetization ( $M_s$ ) for product a and b sharply increases and becomes nearly saturated at about 62.55 (emu/g) and 59.89 (emu/g) respectively, suggesting the presence of small magnetic particles exhibiting superparamagnetic behaviour of CF nanoparticles [18]. Fig.(2b) affirms that the magnetic feedback is not significantly altered by applying a sorbitol coating as a surfactant on the cobalt ferrite nanoparticles. However, the small decrease in the  $M_s$  value of the surfactant assisted prepared cobalt ferrite NPs is due to the small size of the magnetic core than the uncoated cobalt ferrite NPs. In addition to this, the non-magnetic coating layer of sorbitol can behave as a magnetic dead layer on the surface of cobalt ferrite NPs, thus reducing their saturation magnetization potential [19].



**Fig. 2.** (a) Effect of an applied field on the magnetization value of cobalt ferrite NPs prepared without surfactant (b) with surfactant.

FT-IR spectra of pure cobalt ferrite NPs synthesized without and with the sorbitol assisted method at room temperature are shown in Fig.(3). Two characteristic bands at  $\sim 598$ ,  $\sim 592$  and  $\sim 492$ ,  $\sim 484$   $\text{cm}^{-1}$  were observed in both products a and b which may correspond to intrinsic stretching vibrations of the metal at a tetrahedral site ( $M_{\text{tetra}}-\text{O}$ ) bond and at an octahedral site ( $M_{\text{octa}}-\text{O}$ ) respectively [20,21]. The other important peaks of products a and b at  $\sim 3440$ ,  $\sim 3478$  and  $\sim 1640$ ,  $\sim 1636$   $\text{cm}^{-1}$  can be attributed to H–O–H stretching and bending vibrations of the absorbed water molecules on the surface of cobalt ferrite NPs respectively [22]. The additional peaks observed in Fig.(3b) at 2930 and 2864  $\text{cm}^{-1}$  correspond to  $\nu_{\text{as}}(\text{C-H})$  and  $\nu_{\text{s}}(\text{C-H})$  respectively and confirm the coated layer of sorbitol surfactant.



**Fig. 3.** (a) FT-IR spectra of  $\text{CoFe}_2\text{O}_4$  nanoparticles synthesized without surfactant (b) with surfactant assistance.

DSC/TGA was carried out in the temperature range  $25^\circ\text{C}$  to  $650^\circ\text{C}$  and the curves of the product b prepared with surfactant are shown in Fig.(4). The TGA curve in Fig.(4) exhibits two steps attributed to individual weight loss. The first loss was observed in the range  $25^\circ\text{C}$  to  $150^\circ\text{C}$  while the second loss appeared in the range  $300^\circ\text{C}$  to  $450^\circ\text{C}$ . The DSC curve shows a broad endothermic peak at  $150^\circ\text{C}$ . This might be due to desorption of water molecules from the surface of the surfactant and cobalt ferrite. The exothermic peak in the DSC curve was observed at  $350^\circ\text{C}$ . The exothermic peak can be referred to the combustion of coated surfactant. Above  $450^\circ\text{C}$ , no weight loss was found indicating the presence of only cobalt ferrite nanoparticles in the temperature range  $450^\circ\text{C}$  to  $650^\circ\text{C}$  [23,24].

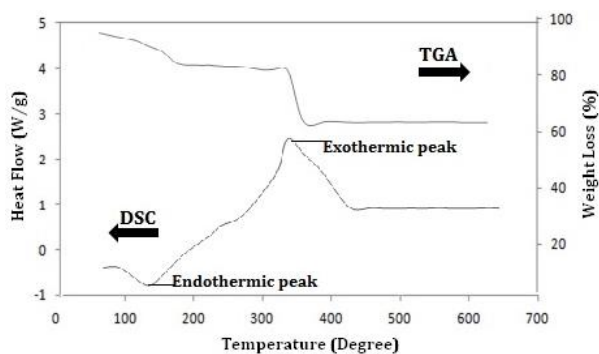


**Fig. 4.** DSC/TGA curves of cobalt ferrite nanopowder.

The X-ray diffraction pattern of  $\text{CoFe}_2\text{O}_4$  nanoparticles prepared in the form of product a and b is presented in Fig.(5). All the characteristic peaks in both products at angles  $18.29^\circ$ ,  $30.08^\circ$ ,  $35.44^\circ$ ,  $37.06^\circ$ ,  $43.06^\circ$ ,  $53.45^\circ$ ,  $56.98^\circ$  and  $62.59^\circ$  are indexed as the reflection planes of (111), (220), (311), (222), (400), (422), (511) and (440) respectively. These peaks exactly match the JCPDS (22-1086) data and confirm the single phase inverse spinel structure of the  $\text{CoFe}_2\text{O}_4$  nanocrystals [25,26]. However, product a shows an improvement of the crystalline phase of cobalt ferrite NPs as compared to product b which was prepared in the presence of the surfactant. The particle size has been determined by the Debye Sherrer equation ( $D = 0.9\lambda/\beta\cos\theta$ , where D is the crystalline size,  $\lambda$  is the wavelength of the X rays,  $\beta$  is the full width at half maximum of the diffraction peak and  $\theta$  is Bragg's angle) which is 65 nm and 32 nm for product a and b respectively. In product b the presence of a broad diffraction plane (311) justifies the smaller  $\text{CoFe}_2\text{O}_4$  NPs formed in the presence of a capping agent. This fact may be due to the performance of a monomeric surfactant in the reduction of clustering of the nanoparticles[15].

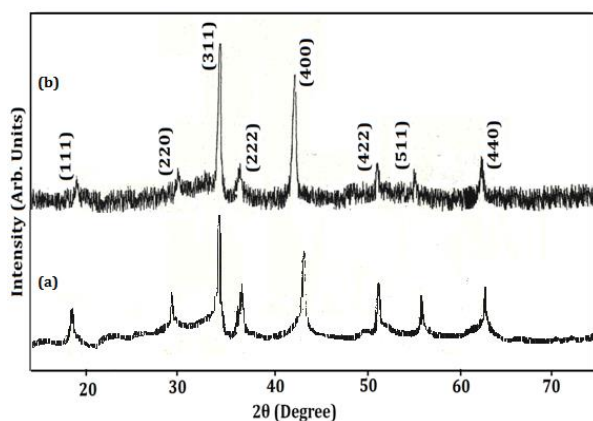


**Fig. 5.** X-ray diffraction pattern of  $\text{CoFe}_2\text{O}_4$  nanoparticles prepared (a) without a surfactant (b) with an additional surfactant.

SEM analysis of the cobalt ferrite NPs prepared without and with a surfactant are shown in Fig.(6). The average size of the cobalt ferrite NPs was about 60 nm and 28 nm for products a and b respectively which nearly matches the crystallite sizes calculated by XRD. The morphology of the cobalt ferrite NPs in product a is comprised of spherical nanocrystallites and has a uniform distribution of nanoparticles which defines the effectiveness of the surfactant. However, a slight compactness and clustering of NPs were observed in the case of product b.

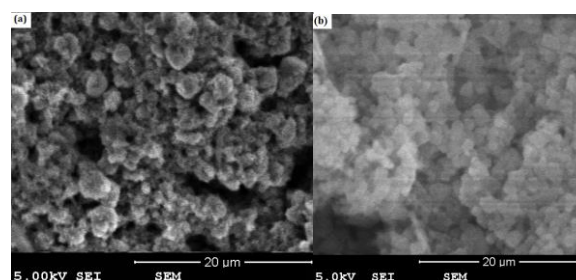


**Fig. 6.** (a) SEM images of Cobalt ferrite NPs prepared without a surfactant (b) with a surfactant.

The antibacterial potential of  $\text{CoFe}_2\text{O}_4$  NPs prepared by the surfactant method (product b) was screened against two common bacterial pathogens, *Escherichia coli* and *Staphylococcus aureus*. Generally, it was found that Gram negative strain *E.coli* is more sensitive to  $\text{CoFe}_2\text{O}_4$  as compared to Gram positive strain *S.aureus*[27] Fig.(7) and (8) demonstrate that with increasing the  $\text{CoFe}_2\text{O}_4$  concentration, the zone of inhibition also increases. The zone of inhibition was also determined for tetracycline and streptomycin as reference antibiotics. The antibacterial activity of cobalt ferrite NPs is due to their particularly small size which makes a perfect attachment to the membrane of the micro-organism [28-30].

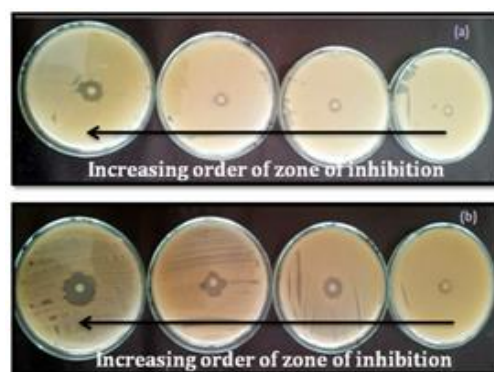


**Fig. 7.** Zone of inhibition measured for (a) *Staphylococcus aureus* (b) *Escherichia coli* in the presence of different concentrations of  $\text{CoFe}_2\text{O}_4$ .

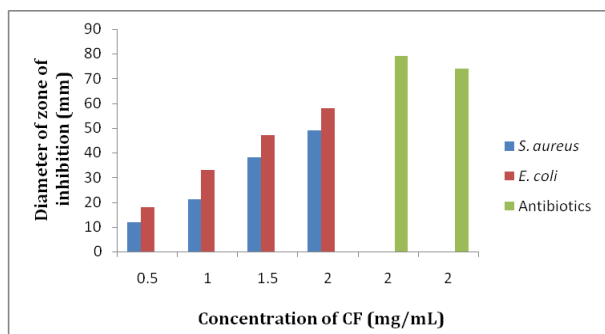


**Fig. 8.** Comparison of the zone of inhibition as measured in different concentrations of  $\text{CoFe}_2\text{O}_4$  NPs and antibiotics.

The interaction behaviour of cobalt ferrite NPs (product b) with calf-thymus DNA was also investigated. The IR spectral features of pure  $\text{CoFe}_2\text{O}_4$  NPs (product b), pure calf-thymus DNA and  $\text{CoFe}_2\text{O}_4$ /calf-thymus DNA nanocomposites are shown in Fig.(9). In Fig.(9a), the spectrum shows an absorption at  $585\text{cm}^{-1}$  for the M–O bond of  $\text{CoFe}_2\text{O}_4$ [31]. Fig.(9b) presents the characteristics peaks of calf-thymus DNA with the interesting region  $1800\text{--}700\text{ cm}^{-1}$  describing the deoxyribose stretching of DNA, oscillation of the groups in the heterocyclic nitrogenous bases and stretching vibrations (asymmetric and symmetric) of the phosphate group ( $\text{PO}_2^{-1}$ ). Two feature bands at  $1225$  and  $1085\text{ cm}^{-1}$  depict the asymmetric and symmetric vibrations of  $\text{PO}_2^{-1}$  respectively [32]. The absorption band at  $1054\text{ cm}^{-1}$  appears as a sugar band in the IR spectrum. In Fig.(9c), the spectrum exhibits the presence of a (M–O) bond at  $587\text{ cm}^{-1}$  confirming the formation of the CF/calf-thymus DNA nanocomposite. The changes in the intensity ratios of the symmetric and asymmetric vibrations ( $v_s/v_{as}$ ) of the phosphate group  $\text{PO}_2^{-1}$  indicate the participation of the  $\text{PO}_2^{-1}$  group in the synthesis of the bio-nanocomposite [33,34]. The shifting of the guanine (G) band from  $1717$  to  $1708\text{ cm}^{-1}$  and the increase in intensity of the thymine (T) band at  $1667\text{ cm}^{-1}$  indicate that the heterocyclic bases are interacting with cobalt ferrite NPs. The shift of the asymmetric and symmetric peaks of the phosphate group ( $\text{PO}_2^{-1}$ ) from  $1225$  to  $1219\text{cm}^{-1}$  and  $1085$  to  $1088\text{cm}^{-1}$  also indicate the interaction of the phosphate group ( $\text{PO}_2^{-1}$ ) with the surface of the ferrites nanoparticles [35]. The interaction of the CF/DNA bio-nanocomposite occurs due to the formation of coordination bonds between cobalt and iron ions on the particle surface and the oxygen atoms in the DNA (phosphate group, O6 in guanine and O4 in thymine) as already explained in the literature [36].

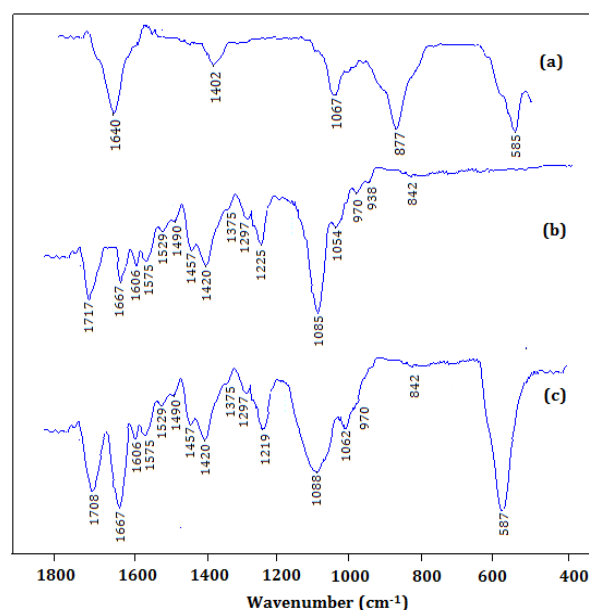


**Fig. 9.** (a) FT-IR spectra of pure  $\text{CoFe}_2\text{O}_4$  nanopowder (b) Calf-thymus DNA (c) CF/DNA.

## CONCLUSIONS

The present study demonstrates the synthesis of cobalt ferrite nanoparticles using a novel surfactant assisted co-precipitation method. The XRD pattern exhibits the presence of a cubic spinel phase in cobalt ferrite NPs. The size of the cobalt ferrite NPs was effectively reduced by applying a surfactant as measured by the XRD pattern which is in agreement with the SEM images. The outstanding magnetic response of cobalt ferrite NPs in the presence of an applied magnetic field may direct them as an efficient nanocarrier for targeted drug delivery. TGA/DSC studies are affirming the presence of a capping agent on the surface of cobalt ferrite NPs. The prepared cobalt ferrite nanoparticles also have an antibacterial potential against *E.coli* and *S.aureus* and are capable to develop interactions with nitrogenous bases of DNA. Finally, we can say that the cobalt ferrite NPs prepared by the surfactant assistant method have the potential to be applied as a biomaterial in numerous fields of material engineering, biomedical and biotechnology systems.

## REFERENCES

1. O. Yamamoto, *Int. J. Inorg. Mater.*, **3**, 643 (2001).
2. L. Zhang, Y. Jiang, Y. Ding, M. Povey, D. York, *J. Nanopart. Res.*, **9**, 479 (2007).
3. O. Seven, B. Dindar, S. Aydemir, D. Metin, M.A. Ozinel and S. Icli, *J. Photochem. Photobiol. A: Chemistry*, **165**, 103 (2004).
4. R. Brayner, R. Ferrari-Iliou, N. Brivois, S. Djediat, M.F. Benedetti, F. Fiévet, *Nano Lett.*, **6**, 866 (2006).
5. J. Sawai, *J. Microbiol. Methods*, **54**, 177 (2003).

6. X. Meng, H. Li, J. Chen, L. Mei, K. Wang, X. Li, *J. Magn. Magn. Mater.*, **321**, 1155 (2009).
7. L. Phua, F. Xu, Y. Ma, C. Ong, *Thin Solid Films*, **517**, 5858 (2009).
8. S. Sun, H. Zeng and D.B. Robinson, *J. Am. Chem. Soc.*, **126**, 273 (2004).
9. D.N. Williams, S.H. Ehrman, T.R.P. Holoman, *J. Nanobiotechnol.*, **4**, 3, doi:10.1186/1477-3155-4-3 (2006).
10. P. Gong, H. Li, X. He, *Nanotechnology*, **18**, 285604, doi:10.1088/0957-4484/18/28/285604 (2007).
11. M. Banoee, S. Seif, Z.E. Nazari, *J. Biomed. Mater. Res. B: Appl. Biomater.*, **93**, 557 (2010).
12. P. Gajjar, B. Pettee, D.W. Britt, W. Huang, W.P. Johnson, A.J. Anderson, *J. Biol. Engg.*, **3**, 1 (2009).
13. R.L. Penn, K. Tanaka, J. Erbs, *J. Cryst. Growth*, **309**, 97 (2007).
14. M. Niederberger, H. Colfen, *Phys. Chem. Chem. Phys.*, **8**, 3271 (2006).
15. K. Nejati and R. Zabihi, *Chem. Cent. J.*, **6**, 1 (2012).
16. T.R. Bastami, M.H. Entezari, Q.H. Hu, S.B. Hartono, S.Z. Qiao, *Chem. Eng. J.*, **210**, 157 (2012).
17. Y. Zhang, G.K. Das, R. Xu, T.T.Y. Tan, *J. Mater. Chem.*, **19**, 3696 (2009).
18. R. Mehta, P. Goyal, B. Dasannacharya, R. Upadhyay, V. Aswal, G. Sutariya, *J. Magn. Magn. Mater.*, **149**, 47 (1995).
19. O. Ur Rahman, S.C. Mohapatra, S. Ahmad, *Mater. Chem. Phys.*, **132**, 196 (2012).
20. S. Kumar, V. Singh, S. Aggarwal, U.K. Mandal and R.K. Kotnala, *J. Phys. Chem. C*, **114**, 6272 (2010).
21. S. Ahmad, U. Riaz, A. Kaushik, *J. Alam, J. Inorg. Organomet. Polym. Mater.*, **19**, 355 (2009).
22. R. Raveendra, P. Prashanth, B. Daruka Prasad, *Int. J. Sci. Res.*, **1**, 543 (2012).
23. G. Allaedini, S.M. Tasirin, P. Aminayi, *Int. Nano Lett.*, doi:10.1007/S40089-015-0153-8 (2015).
24. A.C.F. Costa, M.R. Morelli, R.H. Kiminami, *J. Mater. Sci.*, **42**, 779 (2007).
25. K. Maaz, S. Karim, A. Mumtaz, S. Hasanain, J. Liu, J. Duan, *J. Magn. Magn. Mater.*, **321**, 1838 (2009).
26. N. Sanpo, J. Wang and C.C. Berndt, *J. Nano Res.*, **25**, 110 (2013).
27. S.S. Mukhopadhyay, *Nanotechnol. Sci. Appl.*, **7**, 63 (2014).
28. L.L. Radke, B.L. Hahn, D.K. Wagner, P.G. Sohnle, *Clin. Immun. Immunopathol.*, **73**, 344 (1994).
29. R.M. Wang, B.Y. Wang, Y.F. He, W.H. Lv, J.F. Wang, *Polym. Advan. Technol.*, **21**, 331 (2010).
30. A. Baykal, N. Kasapoglu, Y. Koseoglu, A. C. Basaran, H. Kavas, M.S. Toprak, *Cent. Eur. J. Chem.*, **6**, 125 (2008).
31. D.K. Jangir, G. Tyagi, R. Mehrotra, S. Kundu, *J. Mol. Struct.*, **969**, 126 (2010).
32. H. Tajmir-Riahi, R. Ahmad, M. Naoui, S. Diamantoglou, *Biopolymers*, **35**, 493 (1995).
33. A.U. Metzger, T. Schindler, D. Willbold, *FEBS Lett.*, **384**, 255 (1996).
34. H. Malonga, J. Neault, H. Arakawa, H. Tajmir-Riahi, *DNA Cell Biol.*, **25**, 63 (2006).
35. J. Anastassopoulou, *J. Mol. Struct.*, 651,19 (2003).
36. K. Maaz, A. Mumtaz, S. Hasanain, A. Ceylan, *J. Magn. Magn. Mater.*, **308**, 289 (2007).

## СИНТЕЗА, СТРУКТУРНИ И БИОЛОГИЧНИ ИЗСЛЕДВАНИЯ НА НАНОЧАСТИЦИ ОТ КОБАЛТОВИ ФЕРИТИ

М.У. Муштак<sup>1</sup>, М. Имран<sup>1</sup>, С. Башир<sup>2</sup>, Ф. Канвал<sup>1</sup>, Л. Миту<sup>3\*</sup>

<sup>1</sup>Институт по химия, Университет в Пунджаб, Лахор-54890, Пакистан

<sup>2</sup>Департамент по физика, Научен факултет, Университет в Малая-50603, Куала Лумпур, Малайзия

<sup>3</sup>Департамент по химия, Университет в Питещ, Питещ-110040, Румъния

Постъпила на 31 май 2015 г.; приета на 16 декември 2015 г.

(Резюме)

Синтезирани са наночастици от кобалтови ферити,  $\text{CoFe}_2\text{O}_4$  (CF) по метода на съутаяване с използването на нов мономерен сърфактант (сорбитол). За охарактеризирането им са използвани Фуриерова инфрачервена спектроскопия (FTIR), прахов рентгеноструктурен анализ (XRD), магнетометър с вибрираща проба. Потвърдено е наличието на (M–O) - връзка по абсорбционната линия при  $589\text{ cm}^{-1}$  в FTIR-спектъра. VSM-изследвания разкриват свръх-парамагнитни свойства на наночастиците от кобалтови ферити, имащи наситена магнетизация съответно  $62.55\text{ emu/g}$  и  $59.89\text{ emu/g}$  за кобалтовите ферити, приготвени без и със сърфактант. Хистерезисните контури показват пренебрежим хистерезис, остатъчен магнетизъм и коерцитивност при 300 K. Рентгеноструктурният анализ (XRD) потвърждава като единствена фаза шпинелна кубична структура. Електронно-микроскопски (SEM) микрографии са използвани за определянето на размерите на частиците като 28 nm с използването на сърфактант и 60 nm без сърфактант. Микрографиите са използвани и за анализ на разпределението по размери. Съдържанието на сърфактант е изследвано чрез термогравиметрични измервания. Направен е скрийнинг на приготвените частици за антибактериална активност срещу *Escherichia coli* and *Staphylococcus aureus*, който показва значителна активност. Освен това е изследвано взаимодействието на наночастиците с ДНК от телешки тимус.

## The most stable transition state complexes of the aminotoluene molecule

B. Eren<sup>1</sup>, Y. Y. Gurkan<sup>2\*</sup>

<sup>1</sup>Namik Kemal University, Faculty of Agriculture, Tekirdag / Turkey

<sup>2</sup>Namik Kemal University, Department of Chemistry, Tekirdag / Turkey

Received January 15, 2015, Revised February 8, 2015

In this study the most probable reaction paths of ATnm, OATnm, MATnm, PATnm, NMATo and NMATm transition states with OH radicals have been analyzed. The optimized geometry was calculated via Gauss View 5. Subsequently, the lowest energy level was found by geometric optimization via the Gaussian 09 programme. The geometrical structure analysis and bond lengths were also calculated. This study aims to determine the most probable path for the product distribution of transition state complexes and OH radical interaction in the gas phase and aqueous media. Quantum mechanical methods were used to indicate the impact of the reaction rate over the primary intermediate, hydroxylated intermediate and finally the impact of water solvent. With the aim to determine the intermediates occurring at the reaction of transition state complexes degradation, the geometric optimization of the reactant and transition state complexes were realized through semiempirical AM1 and PM3, ab initio Hartree-Fock HF/3-21G, HF/6-31G\* and Density Functional Theory (DFT) methods. Determining the most appropriate method and the reliability of the method are compared and evaluated theoretically. Based on the Quantum mechanical calculation, all the probable rate constants of reaction paths were calculated by using Transition State Theory (TST). In order to determine the transition state of the reaction, C-O bonds were taken as a reference. Activation energy for probable reaction paths of all transition state complexes, and their most stable state were calculated from the thermodynamic perspective for the gas phase and aqueous media. The impact of water solvent was investigated by using COSMO as the solvation model.

**Keywords:** Aminotoluene, AM1, PM3, HF, TST.

### INTRODUCTION

Volatile aromatic compounds constitute a major part of air and water contaminants. They are mainly emitted into the environment from anthropogenic sources such as combustion processes, vehicle emissions and industrial sources, as well as from biogenic processes [1,2]. Organic contaminants exist at very low concentrations in the water [3]. Therefore, it is essential that the organic contaminants be removed from the drinking water [4]. Natural purification of water systems such as rivers, creeks, lakes, and pools is realized by the solar light falling on the earth. Sunbeams initiate the degradation reaction of big organic molecules into smaller and basic molecules, finally providing for the formation of CO<sub>2</sub>, H<sub>2</sub>O and other molecules [5,6].

In its reactions with organic molecules, OH behaves as an electrophile whereas O is a nucleophile. Thus, OH readily adds to unsaturated bonds while O does not. Both forms of the radical abstract H from C-H bonds and this can result in the formation of different products when the pH is raised to a range where O rather than OH is the reactant. For example, if an aromatic molecule

carries an aliphatic side chain, O attacks there by radical abstract H whilst OH adds preferentially to the aromatic ring [7]. The hydroxyl radical which is the most reactive type known in biological systems reacts with every biomolecule it encounters, including water. Potentially, every biomolecule is a hydroxyl radical scavenger at different speeds [8]. Aromatic compounds are good detectors since they hydroxylate. In addition, the position of attack to the ring depends on the electron withdrawal and the repulsion of previously present substituents. The attack of any hydroxyl radical to an aromatic compound results in the formation of a hydroxylated product [9]. Ortho-toluidine used as an intermediate in large volumes of herbicides can be solved little in water, yet can be solved in alcohol, ether, and diluted acids. Toluidine is a synthetic chemical that is normally a light yellow liquid, but turns to a reddish brown when exposed to air and light [10]. The chemical properties of toluidine are very similar to aniline and it has common features with other aromatic amines. It is a weak basic due to the amino group that is attached to the aromatic ring. At room temperature and pressure, ortho-and-meta-toluidines are viscous liquids; however the molecules in para-toluidine are more symmetrical and fit the crystal structures [11, 12].

\* To whom all correspondence should be sent:

E-mail: yyalcin@nku.edu.tr

While an intermediate in aminotoluene herbicide synthesis is used in the production of more than 90 paints and pigments, rubber, chemicals and pesticides, it is also used as a hardening agent for epoxy resin systems, a reactive material for glucose analysis and fibre dyeing in clinical laboratories [13]. Due to the damaging effects of living organisms emitting resistant foul smell and because of their solubility, aminotoluenes and their derivatives constitute an important water contaminant group. Although many methods are available for the removal of these molecules from water, every method has its own inconvenience [13-18].

In the study of Eren et al.[18] the most probable reaction paths of the aminotoluene (o-toluidine) molecule with OH radicals have been analyzed. The optimized geometry was calculated via Gauss View 5. Subsequently, the lowest energy level was found through geometric optimization via the Gaussian 09 programme. The geometrical structure analysis and bond lengths were also calculated. According to the DFT method the constant  $k$  and the entropy were found to be the highest, the enthalpy and Gibbs free energy values were the lowest, the transition states of ATnm, OATnm, MATnm, PATnm, NMATo and NMATm were concluded to be the most stable and had the lowest energy transition complexes [18].

In this study, the kinetics of the degradation reaction of the transition states of ATnm, OATnm, MATnm, PATnm, NMATo and NMATm and the hydroxyl derivatives were analyzed theoretically. With the aim to determine the intermediates obtained from the reaction of aminotoluene degradation, geometric optimization of the reactant and the transition state complexes were realized through AM1 and PM3, HF/3-21G, HF/6-31G\* and DFT methods. Based on the quantum mechanical calculation, all the probable rate constants of the reaction paths were calculated by using TST.

## COMPUTATIONAL SET-UP AND METHODOLOGY

### *Computational models*

The molecular models were created by using the mean bond distances, the geometric parameters of the benzene ring, the tetrahedral angles for sp<sup>3</sup>-hybridized carbon and oxygen atoms and 1200 for the sp<sup>2</sup>-hybridized carbon atoms. In the calculation of the hydroxylated radicals, the aromatic ring was left planar except for the position of attack. The attacking •OH radical was assumed to form a tetrahedral angle with the C–H bond due to the

change in the hybridization state of the carbon at the addition centre from sp<sup>2</sup> to sp<sup>3</sup> [2,18].

### *Molecular Orbital Calculations*

It is possible that in the photocatalytic degradation reactions of organic contaminants, more harmful products may occur than in the original material. Therefore, before experimentally realizing a photocatalytic degradation reaction, it is essential to know what the primary intermediate products are. The most reliable and accurate information is gathered through calculations carried out with quantum mechanical methods. Thus, since the yield produced is the same, the photocatalytic degradation reaction of transition state complexes and their hydroxy derivatives is based on the direct reaction of these molecules with the OH radical. With this aim, the kinetics of the reactions of the complexes and complexes derivatives with OH radicals was theoretically analyzed. The study was initiated with complexes and then exposed to an OH radical reaction and the reaction of the yield was modelled at the gas phase. The experimental findings in the scientific literature show that OH radicals detach a hydrogen atom from the saturated hydrocarbons and OH is added to the unsaturated hydrocarbons and materials of the aromatic structure [18,19]. For this purpose, all the possible reaction paths for the analyzed reactions were determined, for every reaction path molecular orbital calculations of the reactant, yield and transition state complexes were carried out with the AM1, PM3, HF and DFT methods, their molecular orbital calculations were realized and their geometries were optimized.

### *Kinetic Data Treatment*

The aim of this study was to develop a model providing the outcome of the yield distribution of the photocatalytic degradation reactions. The vibration frequencies, the thermodynamic and electronic features of every structure were calculated using the obtained optimum geometric parameters. Afterwards, the rate constant and activation energy of every reaction was calculated using the Transition State Theory for a temperature of 25°C based on the quantum mechanical calculation results.

In order to find out the reaction rate, it is necessary to calculate the equilibrium constant. The equilibrium constant is calculated using the partition functions in accordance with the mechanical methods. If the equilibrium constant  $K_{\neq}$  is written in terms of partition functions, it is as follows:

$$K^\ddagger = \frac{q^\ddagger}{q_A' q_B'} \quad (1)$$

$q^\ddagger$ ,  $q_A$ ,  $q_B$ : partition functions belonging to the transition state complex and reactants. The molecular partition function is as given below:

$$q' = q e^{-E_a(RT)^{-1}} \quad (2)$$

$E_a$  represents the activation energy, the difference between the zero point energies of the transition state complex and the reactants [18,20].

$$k = \frac{k_B T}{h} \frac{q^\ddagger}{q_A q_B} e^{-E_a(RT)^{-1}} \quad (3)$$

$k_B$  : Boltzmann constant

$h$  : Planck constant

$T$  : absolute temperature

In order to be able to calculate the rate constant, it is necessary to initially calculate the partition function of the activated complex. To realize this calculation, it is essential to know the geometry of the complex and moments of inertia. In addition,  $E_a$  should be known in order to find out the rate constant. The activation energy like the vibration frequency can only be calculated quantum mechanically.

The most probable reaction path and yield distribution of the OH radical of every molecule was determined by comparing the obtained results. The optimized geometric structures were drawn via GaussView 5 and the calculations were done via the Gaussian 09 packet programme [18,21].

### Methodology

Experimental studies were carried out recently for oxidative degradation mechanisms of aromatic pollutants and monitoring the intermediate products formed during degradation. Rapidly evolving computer technology has entered into the workspace of the chemist and it has become inevitable to support the experimental results with theoretical calculations. Methods widely used today for chemical purposes can be made more practical utilizing calculations in package software. Both methods for calculating molecular and electronic structures use the same calculations; namely they calculate the energy of a particular molecular structure and make the geometric optimization (find the lowest energy molecular structure and equilibrium geometry). Geometry optimizations are fundamentally based on the energy gradient that is the first derivative of the energy according to its position [22].

The reaction system under consideration consists of  $\bullet$ OH radicals that are open-shell species. It is well-known that open-shell molecules pose

severe problems in quantum mechanical calculations. Therefore, the geometry optimization of the reactants, the product radicals, pre-reactive and transition state complexes were performed by the AM1, PM3, HF and DFT methods with the Gaussian 09 package [18,21].

Electronic structure methods use the laws of quantum mechanics rather than the laws of classical physics. These methods are characterized by different approaches to the mathematical methods. The electronic structure methods, semiempirical methods and ab-initio methods are parts of two main groups. The AM1 and PM3 method are semiempirical methods that we use in this study. Ab-initio methods do not use experimental data except for the basic physical constants (speed of light, Planck's constant, the mass of the electron, ... etc) of the molecules of interest unlike the molecular mechanics and the semiempirical method. Only the valence electrons are taken into account in the calculation and the basic functions are defined by Slater-type orbitals [23].

DFT methods use the exact electron density to calculate the molecular properties and energies, taking the electron correlation into account. They do not suffer from spin contamination and this feature makes them suitable for calculations involving open-shell systems. The DFT calculations were carried out by the hybrid B3LYP functional, which combines HF and Becke exchange terms with the Lee–Yang–Parr correlation functional.

The choice of the basis set is very important in such calculations. Based on these results, optimizations in the present study were performed at the B3LYP/6-31G(d) level. Forming C–O bonds in the addition paths and the H–O bond in the abstraction path were chosen as the reaction coordinates in the determination of the transition states. Ground-state and transition-state structures were confirmed by frequency analyses at the same level. Transition structures were characterized by having one imaginary frequency that belonged to the reaction coordinate, corresponding to a first-order saddle point. Zero-point vibrational energies (ZPEs) were calculated at the B3LYP/6-31G(d) level [2,18].

In recent years, the density functional theory (DFT) based on these methods has become very popular. The best DFT method requires less computing power than the conventional correlation method. This method is widely preferred for systems with too many atoms and makes calculations for a shorter time compared to other ab-initio methods. Generally, such ab-initio or DFT

is used to create the initial structure for the optimization in large systems. It used to obtain the qualitative information such as molecular orbitals, atomic loads and vibrational modes of a molecule and to predict the energy on conformation and substituent effects [22].

### Solvent effect model

In aqueous media, water molecules affect the energetics of the degradation reactions of all organic compounds. Moreover, H<sub>2</sub>O induces geometry relaxation on the solutes. The latter effect becomes more important when hydrogen-bonded complexes are present. However, the results obtained in earlier studies indicate that geometry changes have a negligible effect on the energy of the solute in water for both open- and closed-shell structures [18,24,25]. In this study, to take into account the effect of H<sub>2</sub>O on the energetics and the kinetics of the aminotoluene + •OH reactions, DFT/B3LYP/6-31+G(d) calculations were carried out for the optimized structures of the reactants, the pre-reactive and the transition state complexes and the product radicals, by using COSMO (conductor-like screening solvation model) [18,25] as the solvation model, implemented in the Gaussian 09 package. The solvent was water at 25°C, with a dielectric constant  $\epsilon = 78.39$  [18,22].

COSMO is one of the polarizable continuum methods (PCMs). In PCMs, the solute molecule is placed in a cavity surrounded by a polarizable continuum, whose reaction field modifies the energy and the properties of the solute [18,26]. The geometry of the cavity is determined by the shape of the solute. The reaction field is described in terms of the apparent polarization charges or reaction field factors included in the solute Hamiltonian, so that it is possible to perform iterative procedures leading to self-consistence between the solute wave-function and the solvent polarization. The COSMO method describes the solvent reaction field by means of apparent polarization charges distributed on the cavity surface, which are determined by assuming that the total electrostatic potential cancels out at the surface. This condition can describe the solvation in polar liquids. Hence, it is the method of choice in this study [2,18].

## RESULTS AND DISCUSSION

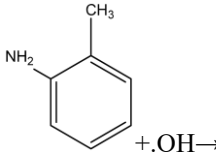
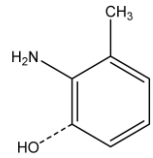
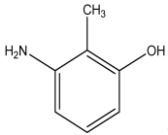
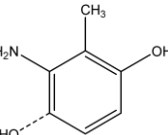
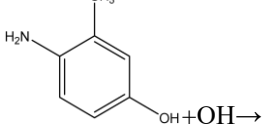
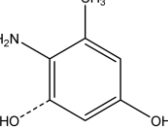
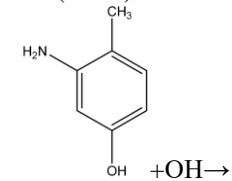
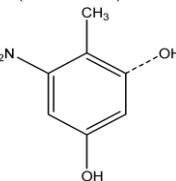
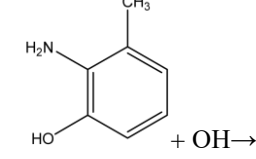
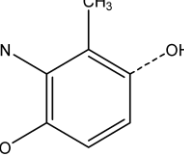
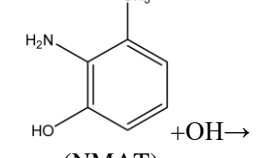
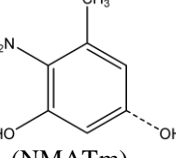
### Computational modelling

#### Reaction paths

The hydroxyl radical is a very active species and has a strong electrophilic character. [18,27]. Once

formed, it can readily attack the aminotoluene molecule and produce the reaction intermediates. •OH radical reactions with aromatic compounds proceed through the following reaction pathway: H-atom abstraction from C–H bonds and addition to aromatic rings. [18,28] Based on previous results the 6,7,8,9,18,19,29 path for the reaction of aminotoluene(AT) with •OH was determined.

**Table 1.** The reaction paths of the most stable TST complexes of AT with •OH.

	OH addition	TST
(4)		
(5)		
(6)		
(7)		
(8)		
(9)		

The path m- addition to NH<sub>2</sub> (ATnm) with TS to the AT molecule is shown in table 1.[4]. Based on previous results the path for the reaction of 3-hydroxy-2- methyl aniline (OAT) with •OH was determined. The path m- addition to NH<sub>2</sub> (OATnm) with TS to a OAT molecule is shown

table 1.(5). Based on previous results the path for the reaction of 4-hydroxy-2- methyl aniline (MAT) with  $\bullet\text{OH}$  was determined. The path m-addition to  $\text{NH}_2$  (MATnm) with TS to a MAT molecule is shown in table 1.[6].

Based on previous results the path for the reaction of 5-hydroxy-2- methyl aniline (PAT) with  $\bullet\text{OH}$  was determined. The path m- addition to  $\text{NH}_2$  (PATnm) with TS to a PAT molecule is shown in table 1.(7). Based on previous results two different paths for the reaction of 2-hydroxy-6- methyl aniline (NMAT) with  $\bullet\text{OH}$  were determined. The first two paths, o-addition (NMATo) and m-addition (NMATm) with TS to a NMAT molecule are shown in table 1. [8.9].

#### Transition State Complexes

In this study, reactants were used to find out the transition state complexes. An estimation of the initial geometry was done according to the type of reaction path using the optimum geometric parameters of the reactants. A C-O bond was chosen as the reaction coordinate while modelling the transition state complexes for the reactions realized with OH addition and the bond length was changed as 1.850-2.500 Å during calculation. The emerging OH bond length was chosen as the reaction path, and in order to determine the position of the OH radical according to the molecule, the dihedral angles belonging to this group were changed during the calculations. The activation energies and their most determined state in

thermodynamic terms for the gas phase and aqueous media were calculated for the probable reaction paths of all transition state complexes [18].

According to Fig.1, the C-O bond lengths at four probable transition states of the OH radical were taken as precise measurements. The bond lengths were calculated as (a) ATnm (3.63 Å), (b) OATnm (2.70 Å), (c) MATnm (2.64 Å), (d) PATnm (2.91 Å), (e) NMATo (2.06 Å), (f) NMATm (2.14 Å) relatively. The longest C-O bond belongs to the ATnm TS molecule and it is found that it occurs later compared to the others. Therefore, it is the most probable transition state.

#### CONCLUSIONS

It is possible that much more harmful intermediates than the ones at the beginning may occur given photocatalytic reactions of organic pollutants. The primary substances of such organic pollutants are polyaromatic substances. Thus, before realizing the photocatalytic degradation reaction experimentally, it is essential to know what the primary intermediates are. This information gives the most reliable and accurate calculations made by the quantum mechanical methods. Therefore, since the final product is the same, the photocatalytic degradation reaction of the transition state complexes and hydroxy derivatives are both based on the direct reaction with the OH radical of the transition state complexes.

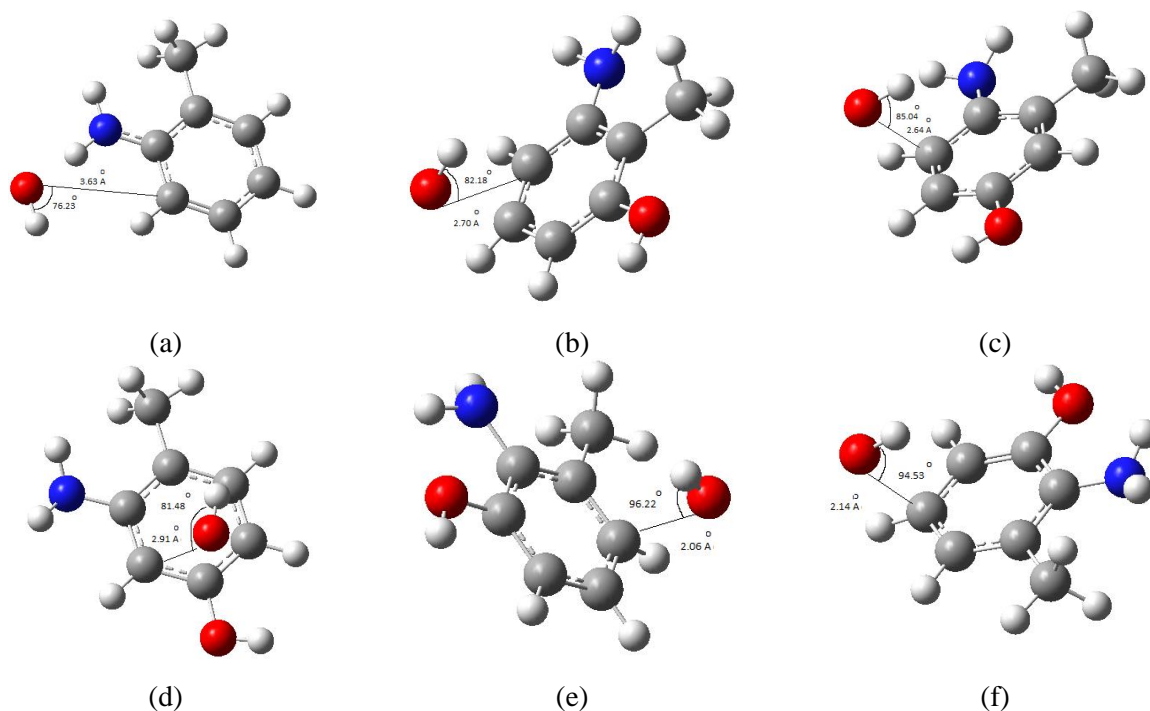


**Fig. 1.** Optimized structures of the transition state complexes of probable reaction paths (4-9): (a) ATnm, (b) OATnm, (c) MATnm, (d) PATnm, (e) NMATo, (f) NMATm

**Table2.** According to the DFT method the constant k, entropy, enthalpy and Gibbs free energy values.[18].

DFT	$\Delta H(10^2)$ (kcal mol <sup>-1</sup> )	$\Delta G(10^2)$ (kcal mol <sup>-1</sup> )	$\Delta S$ (kcal mol <sup>-1</sup> K <sup>-1</sup> )	k	$\Delta E (10^2)$ (kcal mol <sup>-1</sup> )
AT	0.964	0.718	0.082	-----	0.958
ATo	1.047	0.765	0.095	1.145x10 <sup>11</sup>	1.041
ATm	1.042	0.749	0.098	3.738x10 <sup>8</sup>	1.036
ATp	1.046	0.764	0.094	1.568x10 <sup>9</sup>	1.040
ATnm	1.033	0.747	0.096	2.257x10 <sup>12</sup>	1.028
OAT	0.998	0.735	0.088	-----	0.992
OATm	1.084	0.798	0.096	6.028x10 <sup>15</sup>	1.078
OATp	1.079	0.779	0.101	1.376x10 <sup>9</sup>	1.073
OATnm	1.079	0.778	0.101	1.005x10 <sup>9</sup>	1.073
MAT	0.997	0.733	0.089	-----	0.991
MATo	1.078	0.777	0.101	2.386x10 <sup>10</sup>	1.072
MATp	1.079	0.779	0.101	1.905x10 <sup>10</sup>	1.073
MATnm	1.076	0.772	0.102	9.504x10 <sup>4</sup>	1.070
PAT	0.997	0.735	0.088	-----	0.991
PATo	1.072	0.775	0.100	0.000	1.066
PATm	1.083	0.798	0.096	4.015x10 <sup>15</sup>	1.077
PATnm	1.075	0.769	0.103	1.139x10 <sup>10</sup>	1.069
NMAT	0.998	0.735	0.088	-----	0.992
NMATo	1.080	0.781	0.101	5.070x10 <sup>10</sup>	1.074
NMATm	1.080	0.778	0.101	2.505x10 <sup>11</sup>	1.074

In Table 2, according to the DFT method, the constant k and entropy have the highest values, the enthalpy and Gibbs free energy values are the lowest, the transition state of ATnm, OATnm, MATnm, PATnm, NMATo and NMATm are concluded to be the most stable and have the lowest energy transition of the complexes [18].

In this study, the analysis of the reaction kinetics of the most stable transition state complexes of the aminotoluene molecule by the theoretical methods was calculated. The DFT method is the most appropriate method of the theoretical methods used. The basic principle of DFT, is that the total electronic energy of the molecule is formed in connection with the total electronic density. Compared to other methods, this gives more accurate results that account for all the properties of the nucleus and electrons.

In Table 3, the activation energy levels of Ea in the gas phase of the TS molecules having the lowest energy for the DFT method for every transition state complex are given below:

-7.404 kcal mol<sup>-1</sup> of ATnm for AT, -3.077 kcal mol<sup>-1</sup> of OATm for OAT, -5.131 kcal mol<sup>-1</sup> of MATnm for MAT, -4.049 kcal mol<sup>-1</sup> of PATnm for PAT, -5.402 kcal mol<sup>-1</sup> of NMATo for NMAT and -6.359 kcal mol<sup>-1</sup> of NMATm for NMAT are the transition state complexes with the lowest energy. These

reveal the most probable transition state complexes in the gas phase. The most rapid occurring transition state complex in the gas phase has the highest values of the k rate constant. Ea<sub>ecosmo</sub> aqueous media activation energy levels for the DFT method at 1.927x10<sup>1</sup> kcal mol<sup>-1</sup> of ATnm for AT, 1.856x10<sup>2</sup> kcal mol<sup>-1</sup> of OATnm for OAT, 0.673x10<sup>1</sup> kcal mol<sup>-1</sup> of MATnm for MAT, 0.763x10<sup>1</sup> kcal mol<sup>-1</sup> of PATnm for PAT, 0.210x10<sup>1</sup> kcal mol<sup>-1</sup> of NMATo for NMAT and 0.607x10<sup>1</sup> kcal mol<sup>-1</sup> of NMATm for NMAT are the transition state complexes with the lowest energy.

This reveals that it is the most probable transition state at aqueous media. Hydroxyl radicals are used in order to remove the organic contaminants from water. In this study, the most probable reaction paths were determined to be OH radicals added to the aromatic ring.

Organic contaminants exist at very low concentrations in water [3,18]. Therefore, it is essential to remove the organic contaminants from the drinking water [4,18]. The hydroxyl radical, which is the most reactive type known in biological systems, reacts with every biomolecule it encounters including water. Potentially, every biomolecule is a hydroxyl radical scavenger at a different speed [8,18].

**Table 3.** Constant k, for gas phase and aqueous media activation energy levels calculated via AM1, PM3, HF, DFT methods

ATnm	Ea(kcal mol <sup>-1</sup> )	k	Ea <sub>ecosmo</sub> (kcal mol <sup>-1</sup> )
AM1	-1.671	1.280x10 <sup>8</sup>	2.146x10 <sup>1</sup>
PM3	1.634	2.729x10 <sup>5</sup>	2.770x10 <sup>1</sup>
HF3	5.833	1.227x10 <sup>2</sup>	3.749x10 <sup>1</sup>
HF6	8.494	1.794	4.493x10 <sup>1</sup>
DFT	-7.404	2.257x10 <sup>12</sup>	1.927x10 <sup>1</sup>
OATnm	Ea(kcal mol <sup>-1</sup> )	k	Ea <sub>ecosmo</sub> (kcal mol <sup>-1</sup> )
AM1	0.337	6.805x10 <sup>6</sup>	2.165x10 <sup>2</sup>
PM3	2.922	4.969x10 <sup>4</sup>	1.835x10 <sup>2</sup>
HF3	1.055x10 <sup>1</sup>	0.070	2.196x10 <sup>2</sup>
HF6	1.251x10 <sup>1</sup>	2.687x10 <sup>-3</sup>	2.140x10 <sup>2</sup>
DFT	-3.077	1.005x10 <sup>9</sup>	1.856x10 <sup>2</sup>
MATnm	Ea(kcal mol <sup>-1</sup> )	k	Ea <sub>ecosmo</sub> (kcal mol <sup>-1</sup> )
AM1	0.808	1.742x10 <sup>6</sup>	0.864x10 <sup>1</sup>
PM3	2.200	2.607x10 <sup>5</sup>	1.039x10 <sup>1</sup>
HF3	5.522	6.091x10	1.921x10 <sup>1</sup>
HF6	9.463	0.401	2.499x10 <sup>1</sup>
DFT	-5.131	9.504x10 <sup>4</sup>	0.673x10 <sup>1</sup>
PATnm	Ea(kcal mol <sup>-1</sup> )	k	Ea <sub>ecosmo</sub> (kcal mol <sup>-1</sup> )
AM1	-2.015	2.246x10 <sup>8</sup>	0.962x10 <sup>1</sup>
PM3	2.304	2.116x10 <sup>5</sup>	1.132x10 <sup>1</sup>
HF3	8.631	1.438	2.078x10 <sup>1</sup>
HF6	1.016x10 <sup>1</sup>	0.117	2.634x10 <sup>1</sup>
DFT	-4.049	1.139x10 <sup>10</sup>	0.763x10 <sup>1</sup>
NMATo	Ea(kcal mol <sup>-1</sup> )	k	Ea <sub>ecosmo</sub> (kcal mol <sup>-1</sup> )
AM1	-0.605	2.707x10 <sup>7</sup>	0.731x10 <sup>1</sup>
PM3	2.619	1.171x10 <sup>5</sup>	0.702x10 <sup>1</sup>
HF3	-2.222	1.075x10 <sup>9</sup>	1.298x10 <sup>1</sup>
HF6	1.059x10 <sup>1</sup>	0.072	1.840x10 <sup>1</sup>
DFT	-5.402	5.070x10 <sup>10</sup>	0.210x10 <sup>1</sup>
NMATm	Ea(kcal mol <sup>-1</sup> )	k	Ea <sub>ecosmo</sub> (kcal mol <sup>-1</sup> )
AM1	-1.698	1.954x10 <sup>8</sup>	0.413x10 <sup>1</sup>
PM3	2.475	1.744x10 <sup>5</sup>	0.665x10 <sup>1</sup>
HF3	7.262	1.165x10 <sup>1</sup>	1.867x10 <sup>1</sup>
HF6	1.015x10 <sup>1</sup>	0.110	2.365x10 <sup>1</sup>
DFT	-6.359	2.505x10 <sup>11</sup>	0.607x10 <sup>1</sup>

**Table 4.** Mulliken loads of the heavy atoms of the studied molecules.<sup>18</sup>

AT	ATnm	OAT	OAT nm
11 C -0.079158	11 C -0.063830	10 C -0.062126	10 C -0.041225
15 N -0.152651	15 N -0.068889	14 N -0.151131	14 N -0.145082
	18 O -0.231787	17 O -0.246327	17 O -0.240589
			19 O -0.211082
MAT	MATnm	PAT	PATnm
10 O -0.253210	10 O -0.243592	10 C -0.086504	10 C -0.074263
12 N -0.160178	12 N -0.150491	14 N -0.152124	14 N -0.144674
15 C -0.074152	15 C -0.063696	17 O -0.245155	17 O -0.229721
	19 O -0.097024		19 O -0.097927
NMAT	NMATo	NMATm	
10 C -0.076104	10 C -0.050241	10 C -0.066739	
14 O -0.262806	14 O -0.239830	14 O -0.256092	
16 N -0.141021	16 N -0.133101	16 N -0.114022	
	19 O -0.220675	19 O -0.223159	

Aromatic compounds are good detectors since they hydroxylate. In addition, the position of attack to the ring depends on the electron withdrawal and repulsion of the previously present substituents [9,18]. When the Mulliken loads in table 4 are analyzed, the electronegativities of the N and O atoms yield information about the bonding state of the OH radical.

**Acknowledgements:** The authors greatly appreciate the financial support of the Namik Kemal University Research Foundation. Project number: NKUBAP.00.10.AR.12.05.

#### REFERENCES

1. B.J. Finlayson-Pitts, J.N. Pitts Jr., Chemistry of the Upper and Lower Atmosphere, Academic Press, San Diego, 2000.
2. A. Hatipoglu, D. Vione, Y. Yalçın, C. Minero, Z. Çınar, *Journal of Photochemistry and Photobiology A: Chemistry*, **215**, 59 (2010).
3. K. Verschuere, "Handbook of Environmental Data on Organic Chemicals" Second Ed., Van Nostrand Reinhold Company, New York, 1983.
4. J. C. English, V. S. Bhat, G. L. Ball, C. J. McLellan, *Original Research Article Regulatory Toxicology and Pharmacology*, **64**, 2, 269 (2012).
5. R.W. Matthews, D.F. Ollis, H. Al-Ekabi, Photocatalytic Purification and Treatment of Water and Air, Elsevier Science Publishers, 1993, p. 121.
6. A. Taicheng, L. Sun, G. Li, S. Wan, *Journal of Molecular Catalysis A: Chemical*, **333**(1–2), 128 (2010).
7. V.G. Buxton, L.C. Greenstock, P.W. Helman, B.A. Ross, *Journal of Physical and Chemical Reference Data*, **17**, 513 (1988).
8. M. Anbar, P. Neta, *Int. J. Radiat Isot*, **18**, 495 (1965).
9. B. Halliwell, M. Grootveld, J.M.C. Gutteridge, 1988, *Methods of Biochemical Analysis*, 33, 59. Laidler K.J and Meiser, J.H, Physical Chemistry, The Benjamin/Cummings Publishing Company Inc., California, 1982.
10. M. J. O'Neil, Whitehouse Station, NJ: Merck & Co. Inc.: The Merck Index, 14<sup>th</sup> ed.; Editor, O'Neil M J., 2006, p. 1639.
11. C. Alba-Simionesco, J. Fan, C.A. Angell, *J. Chem. Phys.* **110**, 5262, (1999).
12. G. Pratesi, P. Bartolini, D. Senatra, M. Ricci, R. Righini, F. Barocchi, R. Torre. *Physical Review E* : **67**, 021505 (2003).
13. *IARC Monogr Eval Carcinog Risks Hum*, **99**, 1 (2010). PMID:21528837
14. *IARC Monogr Eval Carcinog Risk Chem Man*, **16**, 1 (1978).
15. *IARC Monogr Eval Carcinog Risks Chem Hum*, **27**, 1 (1982). PMID:6955259
16. *IARC Monogr Eval Carcinog Risks Hum Suppl*, **7**, 1 (1987). PMID:3482203
17. *IARC Monogr Eval Carcinog Risks Hum*, **77**, 1 (2000). PMID:11236796
18. B. Eren, Y.Yalçın Gurkan, *Bulg. Chem. Commun.* **47**(3), 849, (2015).
19. P.W. Atkins, Physical Chemistry, 6th edition, Oxford University Press, 1998, P.W. Atkins, R.S. Friedman, Molecular Quantum Mechanics, 3rd Ed., Oxford University Press Inc., New York, 1997.
20. I.N. Levine Quantum Chemistry, Allyn and Bacon Inc., Boston 1983, I.N. Levine, Quantum Chemistry i, Allyn and Bacon, Boston MA, 1991, J.P. Lowe, Quantum Chemistry, 2nd Ed., Academic Press, USA 1993.
21. M.J. Frisch, G.W. Trucks, H.B. Schlegel, G.E. Scuseria, M.A. Robb, J.R. Cheeseman, J.A. Montgomery Jr., T. Vreven, K.N. Kudin, J.C. Burant, J.M. Millam, S.S. Iyengar, J. Tomasi, V. Barone, B. Mennucci, M. Cossi, G. Scalmani, N. Rega, G.A. Petersson, H. Nakatsuji, M. Hada, M. Ehara, K. Toyota, R. Fukuda, J. Hasegawa, M. Ishida, T. Nakajima, Y. Honda, O. Kitao, H. Nakai, M. Klene, X. Li, J.E. Knox, H.P. Hratchian, J.B. Cross, C. Adamo, J. Jaramillo, R. Gomperts, R.E. Stratmann, O. Yazyev, A.J. Austin, R. Cammi, C. Pomelli, J.W. Ochterski, P.Y. Ayala, K. Morokuma, G.A. Voth, P. Salvador, J.J. Dannenberg, V.G. Zakrzewski, S. Dapprich, A.D. Daniels, M.C. Strain, O. Farkas, D.K. Malick, A.D. Rabuck, K. Raghavachari, J.B. Foresman, J.V. Ortiz, Q. Cui, A.G. Baboul, S. Clifford, J. Cioslowski, B.B. Stefanov, G. Liu, A. Liashenko, P. Piskorz, I. Komaromi, R.L. Martin, D.J. Fox, T. Keith, M.A. Al-Laham, C.Y. Peng, A. Nanayakkara, M. Challacombe, P.M.W. Gill, B. Johnson, W. Chen, M.W. Wong, C. Gonzalez, J.A. Pople, Gaussian 09, Revision B.04, Gaussian, Inc., Pittsburgh, PA, 2009.
22. J.B. Foresman, M.J. Frisch, Exploring Chemistry with Electronic Structure Methods, Gaussian Inc., Pittsburgh, PA, 1996.
23. P. Popelier, Pearson Education: Atom in Molecules, USA, 2000.
24. J. Andzelm, C. Kölmel, A. Klamt, *J. Chem. Phys.* **103**, 9312 (1995).
25. V. Barone, M. Cossi, *J. Phys. Chem. A.*, **102**, 11 (1998).
26. N.S. Hush, J. Schamberger, G.B. Bacskay, *Coord. Chem. Rev.* **249**, 299, (2005).
27. V. Brezová, M. Ceppan, E. Brandsteterova, M. Breza, L. Lapcik, *J. Photochem. Photobiol. A: Chem.* **59**, 3 (1991).
28. M. Kılıç, G. Koçturk, N. San, Z. Çınar, *Chemosphere*, **69**, 9, 1396 (2007).
29. I. Suh, D. Zhang, R. Zhang, L.T. Molina, M.J. Molina, *Chem. Phys. Lett.* **364**, 454 (2002).

## НАЙ-СТАБИЛНИТЕ ПРЕХОДНИ СЪСТОЯНИЯ НА МОЛЕКУЛАТА НА АМИНО-ТОЛУЕНА

Б. Ерен<sup>1</sup>, Й.Й. Гуркан<sup>2\*</sup>

<sup>1</sup>Университет „Намик Кемал“, Факултет по земеделие, Текирдаг, Турция

<sup>2</sup>Университет „Намик Кемал“, Департамент по химия, Текирдаг, Турция

Постъпила на 15 януари, 2016 г.; коригирана на 8 февруари, 2016 г.

(Резюме)

В тази работа са анализирани най-вероятните маршрути за преходните състояния АТnm, ОАТnm, МАТnm, РАТnm, NМАТо и NМАТm с ОН-радикали. Оптимизираната геометрия на комплексите е определена чрез геометрична оптимизация с помощта на софтуера Gaussian 09. Анализът на геометричната структура и дължината на връзките също са изчислени. Тази работа има за цел да се определят най-вероятните пътища за разпределението на преходните комплекси и взаимодействията с ОН-радикали в газова фаза и във водна среда. Използвани са квантово-механични методи за посочването на влиянието на скоростта на реакцията върху първичните, хидроксилираните междинни съединения и накрая – въздействието на разтворителя (водата). За определянето на междинните съединения при разлагането на преходните комплекси е използвана геометрична оптимизация с полу-емпирични методи (AM1 и PM3), *ab initio* Hartree-Fock HF/3-21G, HF/6-31G\* и Density Functional Theory (DFT). Сравнени са и теоретично са оценени най-подходящия метод и неговата надеждност. Най-вероятните скоростни константи на реакционните пътища са изчислени с помощта на терията на преходните състояния (TST). За определянето на преходното състояние на реакцията е взета връзката С-О за база. Изчислена е активиращата енергия на вероятните реакции за всички преходни комплекси и най-стабилните им състояния от термодинамична гледна точка за газова фаза и течна среда. Изследвано е влиянието на водата като разтворител при използването на COSMO като солватационен модел.

## BULGARIAN CHEMICAL COMMUNICATIONS

### Instructions about Preparation of Manuscripts

**General remarks:** Manuscripts are submitted in English by e-mail or by mail (in duplicate). The text must be typed double-spaced, on A4 format paper using Times New Roman font size 12, normal character spacing. The manuscript should not exceed 15 pages (about 3500 words), including photographs, tables, drawings, formulae, etc. Authors are requested to use margins of 3 cm on all sides. For mail submission hard copies, made by a clearly legible duplication process, are requested. Manuscripts should be subdivided into labelled sections, e.g. **Introduction, Experimental, Results and Discussion**, etc.

**The title page** comprises headline, author's names and affiliations, abstract and key words.

Attention is drawn to the following:

a) **The title** of the manuscript should reflect concisely the purpose and findings of the work. Abbreviations, symbols, chemical formulas, references and footnotes should be avoided. If indispensable, abbreviations and formulas should be given in parentheses immediately after the respective full form.

b) **The author's** first and middle name initials, and family name in full should be given, followed by the address (or addresses) of the contributing laboratory (laboratories). **The affiliation** of the author(s) should be listed in detail (no abbreviations!). The author to whom correspondence and/or inquiries should be sent should be indicated by asterisk (\*).

**The abstract** should be self-explanatory and intelligible without any references to the text and containing not more than 250 words. It should be followed by key words (not more than six).

**References** should be numbered sequentially in the order, in which they are cited in the text. The numbers in the text should be enclosed in brackets [2], [5, 6], [9–12], etc., set on the text line. References, typed with double spacing, are to be listed in numerical order on a separate sheet. All references are to be given in Latin letters. The names of the authors are given without inversion. Titles of journals must be abbreviated according to Chemical Abstracts and given in italics, the volume is typed in bold, the initial page is given and the year in parentheses. Attention is drawn to the following conventions:

a) The names of all authors of a certain publications should be given. The use of “*et al.*” in

the list of references is not acceptable.

b) Only the initials of the first and middle names should be given.

In the manuscripts, the reference to author(s) of cited works should be made without giving initials, e.g. “Bush and Smith [7] pioneered...”. If the reference carries the names of three or more authors it should be quoted as “Bush *et al.* [7]”, if Bush is the first author, or as “Bush and co-workers [7]”, if Bush is the senior author.

**Footnotes** should be reduced to a minimum. Each footnote should be typed double-spaced at the bottom of the page, on which its subject is first mentioned.

**Tables** are numbered with Arabic numerals on the left-hand top. Each table should be referred to in the text. Column headings should be as short as possible but they must define units unambiguously. The units are to be separated from the preceding symbols by a comma or brackets.

Note: The following format should be used when figures, equations, etc. are referred to the text (followed by the respective numbers): Fig., Eqns., Table, Scheme.

**Schemes and figures.** Each manuscript (hard copy) should contain or be accompanied by the respective illustrative material as well as by the respective figure captions in a separate file (sheet). As far as presentation of units is concerned, SI units are to be used. However, some non-SI units are also acceptable, such as °C, ml, l, etc.

The author(s) name(s), the title of the manuscript, the number of drawings, photographs, diagrams, etc., should be written in black pencil on the back of the illustrative material (hard copies) in accordance with the list enclosed. Avoid using more than 6 (12 for reviews, respectively) figures in the manuscript. Since most of the illustrative materials are to be presented as 8-cm wide pictures, attention should be paid that all axis titles, numerals, legend(s) and texts are legible.

The authors are asked to submit **the final text** (after the manuscript has been accepted for publication) in electronic form either by e-mail or mail on a 3.5” diskette (CD) using a PC Word-processor. The main text, list of references, tables and figure captions should be saved in separate files (as \*.rtf or \*.doc) with clearly identifiable file names. It is essential that the name and version of

the word-processing program and the format of the text files is clearly indicated. It is recommended that the pictures are presented in \*.tif, \*.jpg, \*.cdr or \*.bmp format, the equations are written using "Equation Editor" and chemical reaction schemes are written using ISIS Draw or ChemDraw programme.

The authors are required to submit the final text with a list of three individuals and their e-mail addresses that can be considered by the Editors as potential reviewers. Please, note that the reviewers should be outside the authors' own institution or organization. The Editorial Board of the journal is not obliged to accept these proposals.

## EXAMPLES FOR PRESENTATION OF REFERENCES

### REFERENCES

1. D. S. Newsome, *Catal. Rev.–Sci. Eng.*, **21**, 275 (1980).
2. C.-H. Lin, C.-Y. Hsu, *J. Chem. Soc. Chem. Commun.*, 1479 (1992).
3. R. G. Parr, W. Yang, *Density Functional Theory of Atoms and Molecules*, Oxford Univ. Press, New York, 1989.
4. V. Ponec, G. C. Bond, *Catalysis by Metals and Alloys* (Stud. Surf. Sci. Catal., vol. 95), Elsevier, Amsterdam, 1995.
5. G. Kadinov, S. Todorova, A. Palazov, in: *New Frontiers in Catalysis* (Proc. 10th Int. Congr. Catal., Budapest, 1992), L. Guzzi, F. Solymosi, P. Tetenyi (eds.), Akademiai Kiado, Budapest, 1993, Part C, p. 2817.
6. G. L. C. Maire, F. Garin, in: *Catalysis. Science and Technology*, J. R. Anderson, M. Boudart (eds), vol. 6, Springer-Verlag, Berlin, 1984, p. 161.
7. D. Pocknell, *GB Patent 2 207 355* (1949).
8. G. Angelov, PhD Thesis, UCTM, Sofia, 2001.
9. JCPDS International Center for Diffraction Data, Power Diffraction File, Swarthmore, PA, 1991.
10. *CA* **127**, 184 762q (1998).
11. P. Hou, H. Wise, *J. Catal.*, in press.
12. M. Sinev, private communication.
13. <http://www.chemweb.com/alchem/articles/1051611477211.html>.

## CONTENTS

S. Zhou, H. Kuai, Y. Gu, W. Zhou, A. Li, Mechanism of hydrogen transfer from 1-methylbutyl peroxide to hydroxyl radical .....	359
S. Salahi, M. T. Maghsoodlou, N. Hazeri, M. Lashkari, R. Doostmohammadi, A. Kanipour, F. Farhadpour, A. Shojaei, Two ammonium ionic liquids as efficient catalysts for the one-pot green synthesis of 3,4,5-substituted furan-2(5H)-ones .....	364
M. T. Maghsoodlou, M. Karima, M. Lashkari, B. Adrom, N. Hazeri, Convenient approach for the one-pot, three-component synthesis of 1-(benzothiazolylamino)methyl-2-naphthol using fumaric acid as a green catalyst .....	369
M. Alikarami, M. Ghasemian, BTPPC-catalyzed one-pot synthesis of 1,4-dihydropyridine derivatives via Hantzsch condensation under solvent-free conditions .....	373
F. Kanwal, R. Rehman, S. Rasul, K. Liaqat, Chromium(VI) removal from water by using polyaniline biocomposites with <i>Madhuca longifolia</i> and <i>Szygium cumini</i> leaves .....	379
M. L. Valcheva-Traykova, G. S. Bocheva, Effect of ultraviolet radiation on the free radicals formation in hypothyroid rat's liver .....	384
R. Fazaeli, H <sub>3</sub> PW <sub>12</sub> O <sub>40</sub> (PW <sub>12</sub> ) encapsulated on cotton-like mesoporous (CLM) silica as an efficient, reusable nano photocatalyst for the decolorization of Rhodamine B.....	389
A. M. Amani, H. Sepehrian, A novel eco-friendly method for the synthesis of 2,3-dihydroquinazolin-4(1H)-ones in aqueous media under ultrasonication using ZrOCl <sub>2</sub> -MCM-41 as a highly efficient nanocatalyst/nanoreactor .....	395
N. Singh, A. Ahmad, Spectroscopic studies of charge-transfer complexes of 2,3-dichloro-5,6-dicyano-p-benzoquinone with p-nitroaniline.....	403
M. Shoaib, S. W. A. Shah, N. Ali, I. Shah, M. N. Umar, Shafiullah, M. N. Tahir, M. Ghias, Synthetic flavone derivatives. An antibacterial evaluation and structure-activity relationship study .....	414
M. Bordbar, F. Khodaie, M. Tabatabaee, A.Y. Faal, Z. Mehrilighvan, S. M. Ganji, Interaction studies of DNA binding with a new Cu(II) complex by spectrophotometric, spectrofluorometric, voltammetric and circular dichroism techniques .....	422
A. Gholizadeh, A. Malekzadeh, M. Ghiasi, Structural, magnetic and catalytic properties of Co substituted manganite nano-perovskites .....	430
S. R. Hassan, N. Q. Zaman, I. Dahlan, Performance study of compartment-wise behaviour of modified anaerobic hybrid baffled (MAHB) reactor.....	440
D.A. Baiseitov, M.I. Tulepov, L.R. Sassykova, Sh.E. Gabdrashova, G.A. Essen, K.K. Kudaibergenov, Z.A. Mansurov, Sorption capacity of oil sorbent for the removal of thin films of oil .....	446
I. K. Mihailova, S. V. Dimitrova, D. D. Stoyanova, D. R. Mehandjiev, Influence of the carrier phase composition on the catalytic activity of copper-cobalt oxides deposited on slag glass-ceramics.....	451
S. Ivanova, D. Tsvetkova, Validation of a TLC-densitometric method for quality control in drug combinations .....	456
P. A. Gateva, V. T. Angelova, R. T. Georgieva-Nikolova, T. R. Veselinov, V. H. Nankova, M. M. Nikolova <sup>5</sup> , R. K. Hadjiolova, M. P. Slavova, Synthetic cannabimimetics detected in smoking blends on the Bulgarian territory – toxicological significance.....	461
Á. Révész, C. Szilágyi, T. Spassov, Hydrogen sorption of magnesium plates deformed by surface mechanical attrition treatment .....	469
M. Lefahal, M. Benahmed, L. Djarri, N. Zaabat, E. H. Anne, M. Kamel, M.-G. D. Franca, H. Laouer, S. Akkal, Chemical composition of <i>Limonium thouinii</i> (viv.) kuntze (plumbaginaceae) and the DPPH free radical scavenging activity .....	476
O. İsmail, Ö. G. Kocabay, Evaluation of the drying methods and conditions with respect to drying kinetics, colour quality and specific energy consumption of thin layer pumpkins .....	480
Z.-L. Yao, Y.-P. Pei, Z.-Y. Luo, R.-H. Hu, Y.-X. Yang, Wen-Tong Chen, Preparation, characterization and fluorescence of two cadmium compounds with different extended structures .....	492
W. Abbas, Hazem Ali Attia, Mostafa A. M. Abdeen, Non-darcy effect on non-newtonian Bingham fluid with heat transfer between two parallel plates .....	497
T. Mahmood <sup>1</sup> , J. Ahmed <sup>2*</sup> , A. Shahzad <sup>2</sup> , R. Ali <sup>3</sup> , Z. Iqbal, Convective heat transfer of viscous fluid over a stretching sheet embedded in a thermally stratified medium.....	506
E. A. Velcheva, Z. I. Glavcheva, B.A. Stamboliyska, IR spectral and structural changes caused by the conversion of acetanilide into azanion .....	514
A.I. Gisbrecht, M.M. Asimov, Kinetics of laser-induced photodissociation of oxyhemoglobin and its biomedical applications .....	521
A. Mirabi, M. R. Jamali, Q. Kazemi, Determination of trace amounts of manganese in water samples by flame atomic absorption spectrometry after dispersive liquid-liquid microextraction .....	525
Q.-W. Chang, J. Li, C.-X. Yan, J. Jiang, J.-L. Chen, Q.-S. Ye, J. Yu, W.-P. Liu, A new synthesis method and photophysical properties of Ir(C <sup>^</sup> N) <sub>3</sub> cyclometalated iridium phosphorescent complexes.....	532

<i>Y. G. Wang, Y. J. Jing, Q. W. Wei, H. Ma, Y. L. Wang, X. L. Wang, F. F. Leng, Preparation and modification of peanut shells and their application for heavy metals adsorption .....</i>	535
<i>W. Gao, W. F. Wang, M. K. Jamil, R. Farooq, M. R. Farahani, Generalized atom-bond connectivity analysis of several chemical molecular graphs .....</i>	543
<i>W.L. Xu, Y.N. Yang, J.Wang, M. Tang, Y.Jian, X.J. Pei, Organic matter removal performance and mechanism in the Constructed Rapid Infiltration System.....</i>	550
<i>Y. B. Huang, Q. Qiu, C. Y. Niu, H. Q. Gao, C. Huang, S. X. Tu, Performance, synthesis and removal of Vanadium on Ferruginous Manganese composite material .....</i>	558
<i>M.W. Mushtaq, M. Imran, S. Bashir, F. Kanwal, L. Mitu, Synthesis, structural and biological studies of cobalt ferrite nanoparticles.....</i>	565
<i>B. Eren, Y. Y. Gurkan, The most stable transition state complexes of the aminotoluene molecule .....</i>	571
<i>INSTRUCTIONS TO THE AUTHORS .....</i>	580

## СЪДЪРЖАНИЕ

С.К. Жоу, Х.В. Куай, И.Х. Гу, В. Зоу, А.Р. Ли, Механизъм на преноса на водород от 1-метил-бутилов пероксид към хидроксилен радикал .....	363
С. Салахи, М.Т. Максудлу, Н. Хазери, М. Лашкари, Р. Дустмохамади, А. Канитур, Ф. Фархадпур, А. Шоджаеи, Две амониесви йонни течности като ефективни катализатори за едностадийна зелена синтеза на 3,4,5-заместени фуран-2(5h)-они .....	368
М.Т. Максудлу, М. Карима, М. Лашкари, Б. Адром, Н. Хазери, Удобен подход за едностадийна трикомпонентна синтеза на 1-(бензотиазоламино) метил-2-нафтол с фумарова киселина като зелен катализатор .....	372
М. Аликарами, М. Гасемян, ВТРС- катализирана едностадийна синтеза на 1,4-дихидропиридинови производни чрез кондензация на hantzsh без разтворител .....	378
Ф. Канвал, Р. Рехман, С. Расул, К. Лиакат, Отстраняване на хром (VI) от води с използването на полианилинови биокомпозици с листа от <i>Madhusca longifolia</i> и <i>Szygium cumini</i> .....	383
М. Л. Вълчева-Трайкова, Г. С. Бочева, Ефект на ултравиолетовото облучване върху образуването на свободни радикали в черен дроб на плъхове с хипотиреоидизъм .....	388
Р. Фазаели, $\text{H}_3\text{PW}_{12}\text{O}_{40}$ ( $\text{PW}_{12}$ ) капсулиран в памуко-подобен мезопорьозен силициев диоксид (CLM) като ефективен и многократно употребяван нано-фотокатализатор за обезцветяването на Rhodamine B.....	394
А.М. Аmani, Ю. Гасеми, А. Савардацаки, К. Зоморудиан, Е. Мирзаеи, Б. Заре, Х. Сеферман, Нов екологично съвместим метод за синтеза на 2,3-дихидрохиназолин-4(1h)-они във водна среда при ултразвуково въздействие, използвайки $\text{ZrOCl}_2$ -MCM-41 като високоефективен нанокатализатор/нанореактор .....	402
Н. Сингх, А. Ахмад, Спектроскопски изследвания на комплекси с пренос на заряда от 2,3-дихлоро-5,6-дициано-р-бензохинон с р-нитроанили.....	413
М. Шоахиб, С.У.А. Шах, Н. Али, И. Шах, М.Н. Умар, Шафиула, М.Н. Тахр, М. Гуас, Синтетични флавонови производни. антибактериални свойства и връзка между активност и структура .....	421
М. Бордбар, Ф. Ходайе, М. Табатабаеи, А. И. Фаал, З. Мехрилухан, С. Мохамед-Ганджи, Изследване на взаимодействието на ДНК с нов Cu(II) комплекс чрез спектроскопски, спектрофлуометрични, волтаперометрични методи и с кръгов дихроизъм .....	429
А. Голизаде, А. Малекзаде, М. Гуаси, Структурни, магнитни и каталитични свойства на кобалт-заместени мангантини перовскити .....	439
С.Р. Хасан, Н.К. Заман, И. Дахлан, Изследване на секционното поведение на модифициран анаеробен хибриден реактор с прегради (МАНВ).....	445
Д.А. Байсейтов, М.И. Тулепов, Л.Р. Сасикова, Ш.Е. Габдрашова, Г.А. Есен, К.К. Кудайбергенов, З.А. Мансуров, Сорбционен капацитет на сорбенти за отстраняване на тънки слоеве от нефт .....	450
И.К. Михайлова, С.В. Димитрова, Д. Д. Стоянова, Д. Р. Механджиев, Влияние на фазовия състав на носителя върху каталитичната активност на медно-кобалтови оксиди нанесени върху шлакоситаги.....	455
С. Иванова, Д. Цветкова, Валидиране на TLC-дензитометричен метод за контрол на качеството на estradiol valerate в лекарствени комбинации.....	460
П. А. Гатева, В. Т. Ангелова, Р. Т. Георгиева-Николова, Ц. Р. Веселинов, В. Х. Нанкова, М. М. Николова, Р. К. Хаджиолова, М. П. Славова, Синтетични канабимиметици, установявани в смески за пушене на територията на България– токсикологично значение .....	468
А. Ревеш, Ц. Силаги, Т. Спасов, Сорбция на водород в магнезиеви пластини деформирани чрез повърхностно механично изтриване .....	475
М. Лефахал, М. Бенахмед, Л. Джари, Н. Заабат, А.Е. Хай, М. Камел, М.-Г. Дижу Франка, Х. Лауе, С. Аккал, Химичен състав на <i>Limonium thouinii</i> (viv.) kuntze (Plumbaginaceae) и DPPH-активността за отстраняване на свободни радикали.....	479
О. Исмаил, Й.Г. Коджабай, Оценяване на методите и условията на сушене според кинетиката, качествата на цветовете и специфичната енергия на сушене на тънки слоеве от тиква .....	491
Ж.-Л. Яо, И.-П. Пей, Ж.-И. Луо, Р.-Х. Ху, И.-С. Яанг, Уен-Тонг Чен, Приготвяне, охарактеризиране и флуоресценция на две кадмиеви съединения с различни разгънати структури .....	496
У. Аббас, Х. Али Атия, М.А.М. Абдийн, Отклонения от закона на дарси при ненютонови бингамови флуиди с топлопренасяне между две успоредни плоскости .....	505
Т. Махмуд, Дж. Ахмед, А. Шахзад, Р. Али, З. Икбал, Конвективно топлопренасяне във вискозен флуид над разтегнат лист, поставен в термично еднородна среда.....	513
Е. А. Велчева, З. И. Главчева, Б. А. Стамболийска, ИЧ спектрални и структурни промени причинени от превръщането на ацетанилида в азанион .....	520
А.И. Гизбрехт, М.М. Асимов, Кинетика на лазерно-индуцираната фотодисоциация на оксигемоглобина в кръвта за биомедицински приложения .....	524

<i>А. Мираби, М.Р. Джамали, К. Каземи</i> , Определяне на следи от манган във водни проби чрез пламъкова атомно-абсорбционна спектрофотометрия след дисперсионна течно-течна микро-екстракция ....	531
<i>К.-У. Чанг, Дж. Ли, Ц.-С. Ян, Дж. Джуанг, Дж.-Л. Чен, К.-С. Йе, Дж. Ю, У.-П. Лю</i> , Нов метод за синтеза и фото-физични свойства на $\text{Ir}(\text{C}^{\wedge}\text{N})_3$ циклометалирани иридиеви фосфоресцентни комплекси.....	534
<i>З. Янг, И.Г. Уанг, И.Дж. Джинг, К.У. Уей, Ф.Ф. Ленг, Х. Ма, И.Л. Уанг, Дж. Кс. Чен</i> , Модифициране на шлюпки от фъстъци и тяхното приложение за адсорбция на тежки метали .....	542
<i>У. Гао, У.Ф. Уанг, М.К. Джамил, Р. Фарук, М.Р. Фарахани</i> , Обобщен анализ на свързаната атомна връзка с няколко молекулни графи .....	549
<i>У.Л. Ксу, И.Н. Янг, Дж. Уанг, М. Танг, И. Джуан, С.Дж. Пей</i> , Отстраняване на органична материя и механизъм на действие на системата за бърза инфилтрация.....	557
<i>И.В. Хуанг, К. Кю, К.И. Ню, Х.К. Гао, К. Хуанг, С.С. Ту</i> , Свойства, синтеза и отстраняване на ванадий от феро-манганови композитни материали .....	564
<i>М.У. Муцак, М. Имран, С. Башир, Ф. Канвал, Л. Миту</i> , Синтеза, структурни и биологични изследвания на наночастици от кобалтови ферити .....	570
<i>Б. Ерен, Й.Й. Гуркан</i> , Най-стабилните преходни състояния на молекулата на аминок-толуена .....	579
<b>ИНСТРУКЦИЯ ЗА АВТОРИТЕ</b> .....	580